Transient Free Radicals Studied by Laser Magnetic Resonance Spectroscopy

A thesis submitted for the degree of

Doctor of Philosophy

at the

University of Oxford

by

David Alan Gillett

Saint Edmund Hall

Michaelmas Term, 1994

Transient Free Radicals Studied by Laser Magnetic Resonance Spectroscopy

A thesis submitted for the degree of Doctor of Philosophy at the University of Oxford.

by

David Alan Gillett, Saint Edmund Hall

Michaelmas Term, 1994

Abstract

A liquid nitrogen cooled, carbon monoxide laser magnetic resonance spectrometer was used to study mid-infrared vibration-rotation transitions in the gaseous free radical NCO, in its $\tilde{X}^2\Pi$ state, at very high resolution. The use of an intracavity absorption cell made possible the observation of some transitions with sub-Doppler resolution. Developments to the spectrometer extended the range of operation of the CO laser. Most importantly, a CO laser operating on overtone transitions, $\Delta v = 2$, was operated in Oxford. The $\Delta v = 2$ CO laser operates over the range 2450–3800 cm^{-1} (4.08–2.63 μm), and the $\Delta v = 1$ CO laser over the range 1200–2100 cm^{-1} (8.33–4.76 μm).

NCO exhibits a Renner-Teller effect in its ground electronic state, an interaction between the motion of the electrons and the bending motion of the nuclei. Vibration-rotation transitions were observed in a sequence of bands involving the excitation of the out-of-phase stretching vibration, in the region of 1900 cm^{-1}. Some of the bands involved the excited bending vibration. The Zeeman effect behaviour of the molecular energy levels, particularly in the $^2\Sigma$ vibronic states, clearly showed the manifestation of the Renner-Teller effect. The Zeeman effect in the $^2\Sigma$ vibronic states was considered in detail. Many of the $^2\Sigma$ LMR spectra were recorded at sub-Doppler resolution. NCO is complicated to model, and unassigned LMR spectra remain.

A harmonic Renner-Teller model was developed for the analysis. It was implemented by constructing an explicit matrix representation of the single electronic state $\mathbf{N}^2$ effective Hamiltonian, which was diagonalised exactly. A new term in this Hamiltonian, describing centrifugal distortion corrections to the Renner-Teller coupling term, was developed for the $^2\Sigma$ vibronic states in order to account for anharmonic vibronic interactions.

Acknowledgements

First and foremost I thank my supervisor Dr. J.M. Brown, for his help and encouragement during my education as a spectroscopist. It has been my pleasure to have had the help and camaraderie of Dr. Jonathan Towle, and the part II students Meezanul Islam and Stephen Diggines. My colleagues Dr. Ger Van Den Hoek and Nicholas Lakin deserve a special mention, Ger for proof reading my thesis and Nick for his deft 'cut-and-paste' skills. Thanks to Dr. Kristine Hensel, who kindly transported my sleeping bag to Vancouver and taught it how to assign spectra, and to Dr. Rob 'Roy' Carter.

I am very grateful to Prof. Dr. W. Urban and his group at the Institut für Angewandte Physik der Universität Bonn, who supported my visit there in December, 1992. I thank Thomas Vogt, who worked with me during part of the study of NCO, and Dr. Claus Pfelzer, with whom I worked on the overtone CO laser. A special thanks to Dr. Eberhard Bachem and his wife Giesla, whose acquaintance it has been my great pleasure to have made. Thanks to Thomas, Claus and Ebus for introducing me to Kernbröt, Glühwein and Weihnachtsmarkt, but most of all the impressive (and alcoholic) Feuerzangenbowle.

Experimental spectroscopy is a highly technical subject and I am indebted to the staff of the electronics and mechanical workshops of the Physical Chemistry Laboratory, and to Steve Giles of the Clarendon Laboratory.

I thank British Gas plc. for a Graduate Research Scholarship, for funding to attend conferences, and for providing me with the opportunity to gain some experience of combustion modelling. Thanks to Mr. B. Cheyney, Dr. S. Hasko and Dr. C. Robinson of British Gas plc. I am very grateful to my College, Saint Edmund Hall, and to the Physical Chemistry Laboratory, for generous additional financial support. I specifically thank my undergraduate tutors, Prof. M.S. Child, FRS and Dr. F.J.C. Rossotti.

A personal thanks to my friends, "gloomy" Greg Mott, Julian Wooltorton, Christophe Watts, Ildikó Taksz, Juliet Davis (for having patience with a dancer with two left feet), Martin "The Doctor" Booth, Navaneethan Paramananthan, Shekhar Aiyar, Anjana Taggarse, Alexandra West, Georg Bruun, John and Helen Allison, and especially to Helen F., who also encouraged my interest in spectroscopy.

Finally, and most importantly, I am for ever indebted to my parents, Doris and the late James Alan Gillett. They have given me great financial support and encouragement during my education, without which my time at Oxford would not have been possible.

À l'avenir, et quoiqu'il y arrive.

Contents

I Introduction **1**

I.1 Subject Matter of this Thesis 1

I.2 The Importance of Free Radicals 1

I.2.1 Theoretical Studies 1

I.2.2 Astrophysical Chemistry 2

I.2.3 Combustion Studies 3

I.3 Biological Role of Free Radicals 6

I.4 Laser Magnetic Resonance 6

I.5 Mid-Infrared Laser Sources 8

I.5.1 The CO Laser 8

I.5.2 Diode Laser Spectrometers 9

I.5.3 Fourier Transform Spectrometers 9

I.6 Motivation for this Study 9

II Experimental Aspects of LMR Spectroscopy **14**

II.1 Introduction 14

II.2 Overview of the CO-LMR Spectrometer 15

II.3 The CO Laser System 15

II.3.1 General features 15

II.3.2 Laser Optics 23

II.3.3 The Laser Cavity 25

II.3.4 Gas Mixing System and Discharge 26

II.4 The Magnet System 29

II.4.1 Field Scanning and Measurement 29

II.4.2 Development of a New Magnet Power Supply 29
II.5 The Intracavity Absorption Cell 30
II.5.1 Arrangement of the Cell 30
II.5.2 The Generation of Gaseous Free Radicals 30
II.5.3 Sub-Doppler Spectroscopy 31
II.6 The Detection System 31
II.6.1 Phase-Sensitive Detection 31
II.6.2 The 2-f LMR Lineshape 32
II.6.3 The Modulation Coils 34
II.6.4 Detectors 34
II.7 LMR Measurements 34
II.7.1 Accuracy and Precision 34

III A Theoretical Model of a Linear Free Radical **40**
III.1 Introduction 40
III.2 The Renner-Teller Effect 41
III.2.1 Angular Momenta 41
III.2.2 Vibronic Coupling 42
III.2.3 The Molecular Orbital Basis of the Renner-Teller Effect 43
III.2.4 Spin-Orbit and Rotational Effects 48
III.2.5 The Classification of Vibronic Levels 49
III.3 The Nomenclature for Normal Vibrational Modes 50
III.3.1 Symmetrical Linear Triatomic Molecules 50
III.3.2 Unsymmetrical Linear Triatomic Molecules 50
III.3.3 A Note About the NCO Radical 51
III.4 The Calculation of Molecular Energy Levels 51
III.4.1 The Schrödinger Equation 51
III.4.2 The Born-Oppenheimer Separation 52
III.4.3 Representation of the Vibrational and Electronic Wave Functions 54
III.4.4 The Zero Order Hamiltonian 56
III.4.5 The Van Vleck Transformation 58
III.4.6 Basis Functions for a Renner-Teller Molecule 60

III.4.7 Types of Basis Function 61
III.5 The Renner-Teller Effective Hamiltonian 62
III.5.1 Matrix Elements 63
III.6 Vibrational Energy 65
III.6.1 The Vibrational Band Origin 67
III.7 The Spin-Orbit Hamiltonian 67
III.8 Molecular Rotation 69
III.8.1 General Features 69
III.8.2 The Rotational Hamiltonian 70
III.8.3 The $\mathbf{N}^2$ and $\mathbf{R}^2$ Hamiltonians 75
III.9 Rotational Matrix Elements 76
III.9.1 The Matrix Representation of $\mathbf{N^2}$ 76
III.9.2 The $\mathbf{N}^2$ Effective Rotational Hamiltonian 77
III.9.3 Centrifugal Distortion of the Spin-Orbit Coupling 77
III.9.4 The Spin-Rotation Interaction 78
III.9.5 The Complete Rotational Effective Hamiltonian 80
III.10 K-type Doubling 82
III.11 Nuclear Hyperfine Structure 83
III.12 The Zeeman Hamiltonian 83
III.12.1 Introduction 83
III.12.2 The Zeeman Effect 83
III.12.3 The Single State Effective Zeeman Hamiltonian 86
III.12.4 Parameters in the Effective Hamiltonian 88
III.12.5 Modelling the Zeeman Effect 91

IV Modelling the Renner-Teller States **98**
IV.1 Modelling the Unique States 98
IV.1.1 Spin-Orbit and Renner-Teller Effects 98
IV.1.2 Rotational Structure 99
IV.1.3 Zeeman Effect 103
IV.2 Modelling the $^2\Sigma$ Vibronic States 105
IV.2.1 Spin-Orbit and Renner-Teller Effects 105

IV.2.2 Rotational Structure 109
IV.2.3 Zeeman Effect 113
IV.3 Anharmonic Effects in the $^2\Sigma$ Vibronic States 123
IV.3.1 Introduction 123
IV.3.2 The Potential Function 124
IV.3.3 The $(010)^2\Sigma$ states 124
IV.3.4 The Fermi Resonance Hamiltonian 125
IV.3.5 Matrix Elements of $\mathcal{H}_{FR}^{\text{eff.}}$ 127
IV.3.6 The $(010) - (011), (031)$ Anharmonic Interactions 128
IV.3.7 Reduction to a Hamiltonian Spanning Only the v_2 Manifold . . . 129
IV.3.8 Generalisation to a New Effective Hamiltonian 131
IV.3.9 Contributions of the ν_1 and ν_3 Modes to Anharmonic Vibronic Interactions in the $(010)^2\Sigma$ States 133
IV.4 Intensities of LMR Transitions 135
IV.5 Computer Modelling 135
IV.5.1 Introduction 135
IV.5.2 The 'HANCO.FOR' Program 136
IV.5.3 The 'RENNER.FOR' Program 136
IV.5.4 Modelling of the Unique States 137
IV.5.5 Modelling of the $^2\Sigma$ States 137
IV.5.6 Tuning Rates and Intensities 140
IV.5.7 Data Analysis 140
IV.5.8 The 'LMRSIM.FOR' Program 141
IV.5.9 Computational Details 141

V The NCO Radical **146**
V.1 Introduction 146
V.2 Review of Previous Studies of NCO and CNO 147
V.2.1 Electronic Spectra 147
V.2.2 Ionisation and Thermodynamic Studies 149
V.2.3 Kinetic and Fluorescence Studies 150
V.2.4 Structural Studies 151

V.2.5 Infrared Studies 152
V.2.6 Microwave and EPR studies 154
V.2.7 Theoretical Studies 155
V.2.8 The CNO Radical 155
V.3 Production of the NCO Free Radical 156
V.3.1 Survey of Methods 156
V.3.2 Production of NCO for this Study 158
V.3.3 Comparison of the HNCO+F and HN_3+F Reactions 162
V.3.4 The Preparation of Isocyanic Acid 163
V.4 An LMR Study in the Region of the ν_1 Vibration 167
V.4.1 Background 167
V.4.2 The LMR Search 167

VI The $1_0^1 2_{v_2}^{v_2}$ Unique State Bands of NCO **178**
VI.1 The $1_0^1\,^2\Pi$ Band 178
VI.1.1 Observations 178
VI.1.2 Searches for Other 1_0^1 Transitions 182
VI.1.3 Final Analysis 184
VI.2 The $1_0^1 2_1^1\,^2\Delta$ Band 191
VI.2.1 Observations 191
VI.2.2 Searches for Other $1_0^1 2_1^1\,^2\Delta$ Band Resonances 194
VI.2.3 Final Analysis 197
VI.3 The $1_0^1 2_2^2\,^2\Phi$ Band 198
VI.3.1 Analysis 207
VI.4 Discussion of the Unique States 209
VI.4.1 Overview 209
VI.4.2 Band Origins 210
VI.4.3 Spin-Orbit Parameters 213
VI.4.4 Rotational and Spin-Rotational Parameters 214
VI.4.5 Hyperfine Parameters 216
VI.4.6 The Zeeman Parameter $\Delta g_L^{(1)}$ 216
VI.4.7 K-Type Doubling 217

VII The $1_0^1 2_1^1$ $\mu^2\Sigma$ and $1_0^1 2_1^1$ $\kappa^2\Sigma$ Bands **221**

VII.1 Introduction 221

VII.1.1 Structure of the $1_0^1 2_1^1\,{}^2\Sigma$ Bands 222

VII.1.2 Modelling the $1_0^1 2_1^1\,{}^2\Sigma$ bands 224

VII.1.3 Searching for Assignments 225

VII.1.4 Summary of Results 226

VII.2 Results and Analysis 226

VII.2.1 Assignments 226

VII.2.2 Final Analysis 244

VII.3 Discussion of the $1_0^1 2_1^1\,{}^2\Sigma$ Bands 253

VII.3.1 General 253

VII.3.2 Band Origin and Renner-Teller Parameters 253

VII.3.3 Rotational and Spin-Rotational Parameters 255

VII.3.4 Hyperfine Parameters 256

VII.3.5 Zeeman Parameters 257

VII.3.6 Unassigned Spectra 257

VIII Conclusions and Further Work **261**

VIII.1 The CO LMR Spectrometer 261

VIII.1.1 The CO Laser 261

VIII.1.2 Components of the Spectrometer 261

VIII.1.3 Recommendations for the Future 262

VIII.2 The Renner-Teller Effect 263

VIII.2.1 The Model Used in the Analysis 263

VIII.2.2 Future Recommendations 263

VIII.3 The NCO Radical 264

VIII.3.1 Observations 264

VIII.3.2 The Unique States 264

VIII.3.3 The $^2\Sigma$ Vibronic States 264

VIII.3.4 Future Studies, Including the N_3 Radical 265

VIII.3.5 A Postscript on the CCN Radical 266

A The Mechanism of CO Laser Action **267**

A.1 Introduction 267

A.2 The Gain Process 267

A.3 The Overtone CO Laser 270

A.4 The Vibrational Pumping Mechanism 272

A.5 Oxygen in the Plasma 274

B Further Experimental Details **277**

B.1 CO Laser Operating Conditions 277

B.1.1 Introduction 277

B.1.2 The Normal CO Laser 278

B.1.3 The Overtone CO Laser 280

B.2 Diffraction Gratings and Laser Alignment 283

B.2.1 The Diffraction Grating 283

B.2.2 Gratings in Oxford 285

B.3 Properties of the CO Laser Cavity 286

B.3.1 Resonator Structure 286

B.4 Detectors 290

B.4.1 The Normal CO Laser 290

B.4.2 The Overtone CO Laser 291

B.5 The Mean Free Path in the Absorption Cell 292

B.6 Modulation Effects Upon the 2-f Lineshape 293

B.6.1 Modulation Broadening 294

B.6.2 Modulation Induced Intensity Loss 294

B.7 The LMR Spectroscopic Lineshape 294

B.7.1 Doppler Limited Resonances 294

B.7.2 Sub-Doppler Resonances 298

B.7.3 Factors Limiting the Widths of Lamb-Dips 298

C Third Order Perturbation Estimates of the Renner-Teller Effect **303**

C.1 Quenching of the Orbital Angular Momentum 303

C.1.1 Derivation of the Third Order Correction 304

C.2 Application of the Correction Term 305

C.2.1 Unique States 305
C.2.2 $^2\Sigma$ Vibronic States 305
C.3 Third Order Contributions to the Renner Parameter 305

D The N^2 and R^2 Hamiltonians **308**

E *K*-Type Doubling **312**
E.1 Introduction 312
E.2 Λ-Type Doubling 313
E.2.1 Introduction 313
E.2.2 Matrix Elements 314
E.3 The *l*-Type Doubling Hamiltonian 314
E.3.1 Introduction 314
E.3.2 Matrix Elements 315
E.4 The *K*-Type Doubling Matrix 316
E.4.1 Matrix Representation 316
E.4.2 Λ-Type Doubling Contributions to the Zeeman Effect 316

F Nuclear Hyperfine Structure **320**
F.1 Introduction 320
F.2 Magnetic Hyperfine Structure 321
F.2.1 The Magnetic Hyperfine Effective Hamiltonian 321
F.2.2 Matrix Elements 321
F.2.3 Magnetic Hyperfine Parameters 323
F.3 Nuclear Quadrupolar Hyperfine Structure 324
F.3.1 Introduction 324
F.3.2 The Quadrupolar Effective Hamiltonian 324
F.3.3 Matrix Elements 325
F.3.4 Quadrupolar Hyperfine Parameters 326

G Other Data Included in the Analysis of NCO ($\tilde{X}^2\Pi$) **328**

Chapter I

Introduction

I.1 Subject Matter of this Thesis

This thesis is concerned with the study by infrared spectroscopy, and the theoretical modelling of, the transient free radical NCO in the gas phase. The extension of a mid-infrared CO laser source to operate in a region where there is a paucity of other radiation sources, is also reported.

I first want to set in context the importance of free radicals in nature, paying particular attention to NCO and also the similar species CCN [1]. It is important to understand how spectroscopic studies can be used to probe both the environment and structure of transient free radicals, leading to advances in the understanding of these matters. I then want to describe the spectroscopic technique of carbon monoxide laser magnetic resonance used for this study, and to compare this with other spectroscopic methods. The significance of this thesis is then discussed briefly.

The following chapters successively describe relevant experimental and theoretical details, followed by surveys of, and detailed experimental studies of, the NCO free radical.

I.2 The Importance of Free Radicals

I.2.1 Theoretical Studies

All molecular free radicals are chemically bound; some are highly labile, short-lived species whilst others, such as molecular oxygen, are relatively inert. All free radicals are

characterised by having open valence-shell electronic structures, with non-zero electron spin and/or orbital angular momentum. It is the interactions arising from this open-shell structure which make the study of free radicals of great theoretical importance. Spectroscopic observations provide a direct test, and prompt the development of, sophisticated theories of molecular structure.

A cornerstone of much molecular theory is the Born-Oppenheimer approximation [2, 3], which assumes that the light, fast moving electrons can adjust instantaneously to the motion of the slow, heavy nuclei. In a linear triatomic molecule with non-zero resultant electronic orbital angular momentum, there is a coupling between the electrons and the bending motion of the nuclei. This, the Renner-Teller effect [3], is a breakdown of the Born-Oppenheimer approximation. Spectroscopic observations of the molecular energy levels, and particularly those in an external magnetic field, provide information on the manifestation of the Renner-Teller interaction. A full understanding of such effects is required before larger molecules can be understood in depth; there is a very big jump in complexity on going simply from a diatomic molecule to a triatomic one.

I.2.2 Astrophysical Chemistry

Carbon, nitrogen and oxygen in the circumstellar environment

Of all the atoms in the universe, 98% are hydrogen and helium. Carbon, nitrogen and oxygen are the most abundant components of the remainder [4], estimated to be about 10^{-7} the abundance of hydrogen [4].

Carbon, nitrogen and oxygen are synthesised in late K-type stars via the so-called 'C-N-O' cycle and helium burning [4, 5]. These stars, typically 1–2 times the solar mass, are found mainly in the arms of galaxies [6]. Such stars are often called 'carbon stars' [7] because they have used up their hydrogen and helium and have begun to fuse carbon. The resulting partial gravitational collapse produces a contraction of the star's core, with the ejection of a shell of hot gas, forming a so-called 'red giant'. The ejected shell of gas, a so-called 'circumstellar envelope', initially has a typical density of $10^{10}\,\mathrm{atoms\,cm^{-3}}$ and a temperature of $2 \times 10^3\,\mathrm{K}$. As the gas expands and cools to below 100 K and the density drops below $10^5\,\mathrm{atoms\,cm^{-3}}$, stable polyatomic molecules can form. In this environment, ion and radical reactions involving hydrogen take place. Subsequent reactions with the

abundant C, N and O atoms lead to the formation of CN, HCN, H_2O and other such species [7]. The total abundance of C, N and O and their isotopes in the circumstellar environment, is of interest in the modelling of stellar structures [5]. Stellar models are likely to come under intense scrutiny given the recent observation [8, 9], which suggests the contradiction that the universe is younger than some of its oldest stars.

The HCCN species has been detected in the circumstellar envelope of the carbon star IRC + 10216 [10], and HNCO has also been detected in the astrophysical environment [7]. To date the radicals NCO and CCN have not been detected, a somewhat surprising fact since the strong ultraviolet radiation field would be expected to photolyse the above species. This possibly arises from a lack of accurate spectroscopic information and insufficient sensitivity of telescopes. Oliphant *et al.*[11] have started a search for the CCN radical in the envelope of IRC + 10216. This could be aided by the revised band origin determined recently, following a study of CCN by laser magnetic resonance [1].

Astrophysical uses of spectroscopic studies

Spectroscopy provides the only window for the observation of astrophysical molecules. The rotational temperatures and Doppler shifts deduced from spectroscopic observations, provide very important information on the astrophysical environment. High resolution studies provide accurate and precise frequencies for vibration-rotation transitions, which can then be detected in absorption against the bright stellar background. The required fractional accuracy for astrophysical searches is of the order of 3 parts per million (ppm) [12], corresponding to $6 \times 10^{-3}\,\mathrm{cm}^{-1}$ for a band origin of $1900\,\mathrm{cm}^{-1}$. Laser magnetic resonance studies can attain the required accuracy.

I.2.3 Combustion Studies

The environment of an atmospheric pressure flame is at the extreme opposite of temperature and pressure to the astrophysical environment; nevertheless there are remarkable similarities in the types of species present. The high temperature ($> 2 \times 10^3\,\mathrm{K}$) in the flame front (the region of greatest energy release) leads to the production of many hundreds of free radicals [13].

In burning a natural gas, it is desirable to covert the (mainly) methane to carbon

dioxide and water, with maximum thermal efficiency and whilst minimising pollution. Fuel bound nitrogen and sulphur, and nitrogen entrained from the air, lead to the formation of pollutants. The most important are NO, NO_2 and N_2O, so-called 'NO_x', which arises in two ways:

1. 'Thermal' (or 'Zeldovich') NO formation [13], in which nitrogen from the air is entrained and oxidised in the hot parts of the flame and on hot burner surfaces.

2. 'Prompt' NO formation [13], in which fuel bound nitrogen is oxidised via HCN and NCO. This occurs early on during the combustion cycle and is important in fuel-rich mixtures. A proposed 'prompt' NO formation scheme is shown in Fig.I.1, in which the importance of the NCO free radical can be seen.

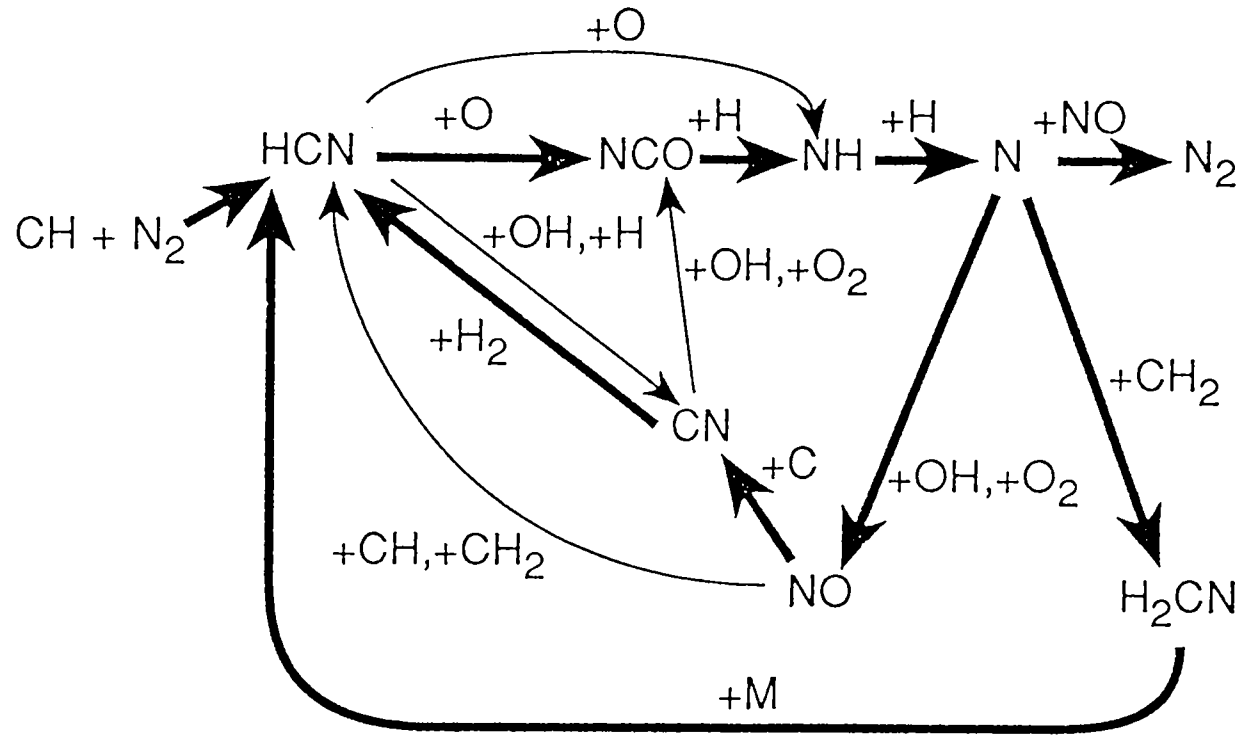

Figure I.1: The chemical scheme thought to produce 'prompt' NO in the combustion of a natural gas. The thickness of the arrows indicates the relative importance of the various reactions.

Attempts at NO_x reduction are based on modelling the flame and the burner design using two- and three- dimensional chemical fluid dynamics (CFD) computer models. The computer burden of the fluid dynamics and thermodynamics is very great, because the development of the flame has only very short term predictability, leading to "stiffness" in the model [14]. This means that the chemical scheme has to be simplified. The production of 'prompt' NO is very sensitive to the chemistry; therefore a careful choice

of steps is required for the simplified chemical scheme. This is further complicated by a lack of detailed knowledge of the kinetics of the key reactions taking place in the flame [13], so that many have to be estimated using thermodynamic relations. Attempts have been made to reduce NO_x emissions from industrial burners by injecting ammonia ("Thermal De-NO_x") or cyanuric acid, $(HNCO)_3$, ("RAPRENO$_x$") into the hot post-combustion gases [15]. Fig. I.2 shows the chemistry involved in the RAPRENO$_x$ scheme; again the NCO radical is a key intermediate in this process.

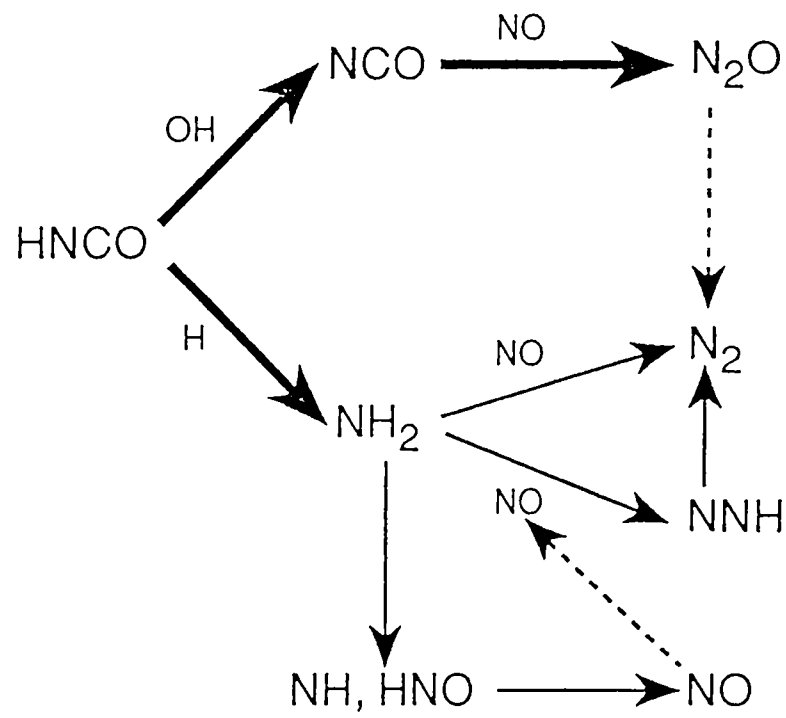

Figure I.2: The chemical scheme involved in the 'RAPRENO$_x$' NO_x reduction process. The thickness of the arrows indicates the relative importance of the reactions.

Spectroscopic observations are important in two ways

1. Tunable infrared diode lasers have been used to make quantitative concentration measurements of transient species (*e.g.* CH) in atmospheric pressure flames, *in situ* [16]. Similar studies have also been performed using optical laser induced fluorescence [17]. The quantitative results can be compared with the predictions of models. Laser magnetic resonance is unsuitable for such studies because it would not be very sensitive with the broad transition line profiles at atmospheric pressure.

2. High resolution studies at low pressures ($< 1.3\,\mathrm{kPa}\,(10\mathrm{Torr})$) can provide information on the vibrational energy levels of molecules. This can be used to estimate the activation energies and Arrhenius constants for reactions. A knowledge of the

bending vibrational frequency of polyatomic molecules is particularly useful in the QRRK [18, 19] and BAC-MP4 [20, 21] methods, for example.

I.3 Biological Role of Free Radicals

Free radicals also play a role in biological systems. Reactive species including free atomic oxygen and larger free radicals are often damaging to living tissues (*e.g.* in sunburn). The free radical nitric oxide, NO, has been found to be useful for the control of high blood pressure [22]. Compounds containing the NO group are introduced to the bloodstream where they generate free NO; this in turn stimulates the release of an enzyme inducing arterial muscle relaxation (vasodilation).

I.4 Laser Magnetic Resonance

Laser magnetic resonance (LMR) [23, 24] involves identifying a close coincidence (typically $\leq 0.7\,\mathrm{cm}^{-1}$, but dependent upon the range of the magnet) between a fixed frequency laser line and a transition in the molecule of interest. A magnetic field is then applied to the sample, employing the Zeeman effect to tune the transitions between the magnetic sub-levels into resonance with the laser line. A schematic diagram illustrating the principle of the technique is shown in Fig.I.3. The molecule must be paramagnetic in one or both of the energy levels, a requirement only satisfied by open-shell species. Therefore, LMR is exclusive to the study of free radicals.

The laser source is typically a molecular gas laser operating on pure rotational transitions (*e.g.* a CO_2 pumped methanol laser) or vibration-rotation transitions (*e.g.* CO_2 and CO lasers). The lines of such lasers are primary frequency standards for the infrared region, having been measured using heterodyne techniques, *e.g.* [25, 26]. This makes possible a highly accurate measurement of the absolute transition frequency. Furthermore, the excellent long term stability of molecular gas lasers enables measurements of very high precision and resolution to be made. The power of such lasers can be very high (several tens of Watts) [27], allowing saturation effects to be observed.

The use of an intracavity absorption cell brings further advantages,

- The sample is subjected to the full laser power.

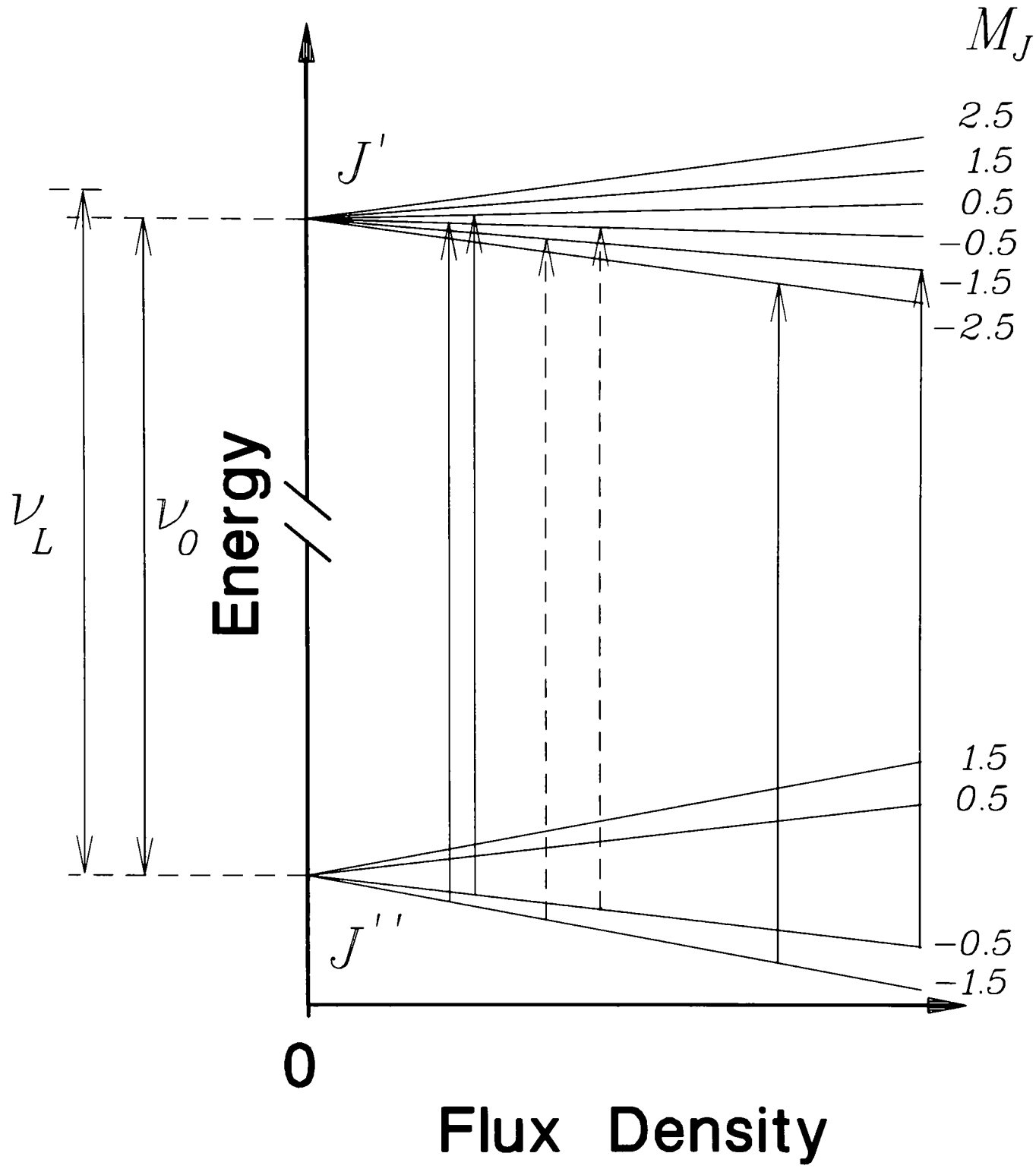

Figure I.3: The principle of laser magnetic resonance. ν_L is the laser frequency and ν_0 is the zero field transition frequency. Absorption occurs when the separation of two Zeeman components is equal to the laser frequency. For electric dipole transitions, there is a selection rule of $\Delta M_J = \pm 1$ (σ polarisation, solid arrows) and $\Delta M_J = 0$ (π polarisation, dashed arrows), when the electric vector of the laser radiation is perpendicular and parallel to the applied magnetic field, respectively.

- The laser radiation makes multiple passes through the absorption cell, amplifying the absorption.

- The counter-propagating, high power laser radiation makes it possible to saturate the transitions and resolve sub-Doppler features with very narrow linewidths.

The laser resonator is a nonlinear amplifier, and it must be remembered that it will also amplify any noise induced by the intracavity sample.

I.5 Mid-Infrared Laser Sources

I.5.1 The CO Laser

The CO laser operates between 1200 cm^{-1} and 2100 cm^{-1} on $\Delta v = 1$ transitions, and between 2450 cm^{-1} and 3800 cm^{-1} on $\Delta v = 2$ overtone transitions. The 'overtone' CO laser is a bright new source in the mid- to near- infrared [28] and it fills the gap in frequency coverage between the $\Delta v = 1$ CO laser and difference frequency, colour centre and HF lasers, which operate in the near-infrared [29].

The sensitivity of an intracavity CO-LMR spectrometer is typically about 1.5×10^9 molecules cm^{-3} for the NO radical [30]; using the intracavity system in Oxford, it has been possible to saturate weak magnetic dipole transitions in atoms [31]. The sensitivity is limited by the fact that the absorption is detected against the high power background of the laser. Extracavity CO-LMR spectrometers using 'zero-background' Faraday and Voigt detection [32] can improve the sensitivity to about 5×10^7 molecules cm^{-3}, but it is not possible to record sub-Doppler resonances with such an arrangement.

An advantage of CO-LMR is that it discriminates against absorption due to non-paramagnetic species. A disadvantage is that a diatomic molecular laser is being used, with laser lines every 2–3 cm^{-1}. Therefore, if a polyatomic molecule is being studied, several rotational transitions can fall between two CO laser lines and be too far away to tune into resonance. This can lead to problems in identifying the spectrum, since only fragments are observed. Therefore, it is useful to have information on the spectrum from a complementary technique to aid the LMR study.

I.5.2 Diode Laser Spectrometers

Diode lasers are excellent mid-infrared laser sources; they are tunable over specified ranges and the spectra are recorded at zero field, so that they are usually simpler to interpret than LMR spectra. Diode laser scans can be useful in providing band origins to guide LMR studies. The power of diode lasers is very low [29], typically a few μW, so that the sensitivity is several orders of magnitude lower than LMR. Temperature instabilities can cause the laser frequency to drift, leading to absolute frequency measurement errors. Recent developments [33] have produced diode laser systems with sub-MHz stability, a factor also aided by improved temperature control systems [34].

I.5.3 Fourier Transform Spectrometers

Fourier transform spectrometers can be used in the mid-infrared to record either absorption or fluorescence [29, 35]. The resolution is limited by the lengths of the arms of the interferometer; these are typically L = 0.5 m, giving a resolution ($\approx 1/2L$) of $10^{-3}\,\mathrm{cm}^{-1}$ [29]. Fourier transform methods also suffer from the possibility of absolute frequency errors, and the possibility of frequency dependent errors ($< 10^{-3}\,\mathrm{cm}^{-1}$), introduced by the use of cutoff filters [36]. The sensitivity is again much lower than that of LMR, though there is a $\sqrt{n}$ improvement in the signal-to-noise ratio when the scan is repeated n times.

I.6 Motivation for this Study

Pahnke [37] recorded the CO-LMR spectrum of the antisymmetric stretching vibration of the N_3 radical in its $\tilde{X}^2\Pi$ state. Many new spectra were observed, thought to originate from levels involving the excited bending vibration. Almost nothing is known about N_3 and it proved impossible to assign these spectra. The free radicals N_3 and NCO have very similar geometrical and electronic structures, and Renner-Teller effects. Therefore, it was hoped that a similar study of NCO, about which more is known, would lead to an understanding that could be applied to N_3. Furthermore, despite the fact that the positions of various vibrational levels of NCO were known to a few cm^{-1} from studies by ultraviolet spectroscopy, there was little knowledge on the vibration-rotation structure

and Zeeman effects in these levels.

This thesis reports the observation and analysis of several rotation-vibration bands of NCO. The most significant aspect is the observation and analysis for the first time, of Zeeman spectra of the $^2\Sigma$ vibronic bands. This has led to an understanding of these states and the nature of their magnetic moments.

Bibliography

[1] D.A. Gillett and J.M. Brown, *Can. J. Phys.* **72**, 1001–1006 (1994).

[2] M. Born and R. Oppenheimer, *Ann. Phys.* **84**, 457–484 (1927).

[3] G. Herzberg, "Molecular Spectra and Molecular Structure," Vol. III, "Electronic Spectra of Polyatomic Molecules," 2nd ed. (corrected), pp. 8ff, 26ff, Krieger Publishing, Malabar, Florida, 1991.

[4] N.N. Greenwood and A. Earnshaw, "Chemistry of the Elements," pp. 1–23, Pergamon Press, Oxford, 1984.

[5] M.F. El Eid, *Astron. Astrophys.* **285**, 915–928 (1994).

[6] T. Ponman, *Chemistry in Britain* **28**, 623–625 (1992).

[7] G. Winnewisser and E. Herbst, *Rep. Prog. Phys.* **56**, 1209–1273 (1993).

[8] W.L. Freedman, B.F. Madore, J.R. Mould, R. Hill, L. Ferrarese, R.C. Kennicutt, Jr., A. Saha, P.B. Stetson, J.A. Graham, H. Ford, J.G. Hoessel, J. Huchra, S.M. Hughes, G.D. Illingworth, *Nature* **371**, 757–762 (1994).

[9] G.H. Jacobs, *Nature* **371**, 741–742 (1994).

[10] M. Guélin and J. Cernicharo, *Astron. Astrophys.* **244**, L21–L24 (1991).

[11] N. Oliphant, A. Lee, P.F. Bernath and C.R. Brazier, *J. Chem. Phys.* **92**, 2244–2247 (1990).

[12] P. Thaddeus, Harvard–Smithsonian Institute for Astrophysics, Harvard University, Private Communication, 1994.

[13] J.A. Miller and C.T. Bowman, *Prog. Energy. Combust. Sci.* **15**, 287–338 (1989).

[14] W.H. Press, S.A. Teukolsky, W.T. Vetterling and B.P. Flannery, "Numerical Recipes in FORTRAN: The Art of Scientific Computing," 2nd ed., pp. 727ff, Cambridge University Press, Cambridge, 1992.

[15] J.A. Miller and C.T. Bowman, *Int. J. Chem. Kin.* **23**, 289–313 (1991).

[16] R.K. Hanson, P.L. Varghese, S.M. Schoenung and P.K. Falcone, "Absorption Spectroscopy of Combustion Gases Using a Tunable IR Diode Laser," *in* "Laser Probes for Combustion Chemistry," ACS Symposium Series, Vol. 134, (D. Crosley, Ed.), pp. 413–426, 1980.

[17] R.A. Copeland, D.R. Crosley and G.P. Smith, "Laser-Induced Fluorescence Spectroscopy of NCO and NH_2 in Atmospheric Pressure Flames," pp. 1195–1203, 20th Symposium (International) on Combustion/The Combustion Institute, 1984.

[18] A.M. Dean, *J. Phys. Chem.* **89**, 4600–4608 (1985).

[19] A.M. Dean and P.R. Westmoreland, *Int. J. Chem. Kin.* **19**, 207–228 (1987).

[20] C.F. Melius and J.S. Binkley, "Reactions of NH and NH_2 with O and O_2," *in* "The Chemistry of Combustion Processes," ACS Symposium Series, Vol. 249, (T.M. Sloane, Ed.), pp. 103–115, American Chemical Society, Washington D.C., 1984.

[21] J.A. Miller and C.F. Melius, *Int. J. Chem. Kin.* **24**, 421–432 (1992).

[22] A.R. Butler, *Chemistry in Britain* **26**, 419–421 (1990).

[23] P.B. Davies, *J. Phys. Chem.* **85**, 2599–2607 (1991).

[24] K.M. Evenson, R.J. Saykally, D.A. Jennings, R.F. Curl, Jr. and J.M. Brown, "Far Infrared Laser Magnetic Resonance," *in* "Chemical and Biochemical Applications of Lasers," Vol. V, (C.B. Moore, Ed.), pp. 95–138, Academic Press, New York, 1980.

[25] M. Schneider, J.S. Wells and A.G. Maki, *J. Mol. Spectrosc.* **141**, 351 (1990).

[26] M. Schneider, J.S. Wells and A.G. Maki, *J. Mol. Spectrosc.* **139**, 432–438 (1990).

[27] W. Urban, "Infrared Lasers for Spectroscopy," Institüt für Angewandte Physik der Universität Bonn, 1987.

[28] E. Bachem, A. Dax, T. Fink, A. Weidenfeller, M. Schneider and W. Urban, *Appl. Phys. B* **57**, 185–191 (1993).

[29] B.J. Howard and J.M. Brown, "High-Resolution Infrared Spectroscopy," *in* "Applied Laser Spectroscopy," (D.L. Andrews, Ed.), pp. 185–225, VCH Publishers, New York, 1992.

[30] D. Robinson, Ph.D. thesis, p. 55, University of Southampton, 1985.

[31] D.A. Gillett, S.J. Diggines and J.M. Brown, *J. Phys. B* **27**, 5175–5184 (1994).

[32] A. Hinz, J. Pfeiffer, W. Bohle and W. Urban, *Mol. Phys.* **45**, 1131–1139 (1982).

[33] M. Mürtz, M. Schaefer, M. Schneider, J.S. Wells, W. Urban, U. Schiessl and M. Tacke, *Opt. Comm.* **94**, 551–556 (1992).

[34] D. Li, N.J. Bowring and J.G. Baker, *Meas. Sci. Technol.* **4**, 1111–1116 (1993).

[35] E.H. Fink, K.D. Setzer, D.A. Ramsay, and M. Vervloet, *J. Mol. Spectrosc.* **80**, 19–28 (1989).

[36] M. Vervloet, Laboratoire de Photophysique Moléculaire, Université de Paris Sud, Orsay, Private Communication, 1993.

[37] R. Pahnke, D.Phil. thesis, University of Oxford, 1990.

Chapter II

Experimental Aspects of LMR Spectroscopy

II.1 Introduction

This chapter describes the Oxford intracavity carbon monoxide laser magnetic resonance (CO-LMR) spectrometer, the apparatus used to make all the mid-infrared LMR measurements reported in this thesis.

The first section gives an overview of the spectrometer; there follows a description of the CO laser system, including the first development in Oxford of a CO laser operating on $\Delta v = 2$ transitions. This is a powerful and promising new source in the 2500–3500 cm^{-1} region. Each major component of the spectrometer is then discussed, with the focus on aspects that are of importance in obtaining high quality LMR spectra. The final section discusses LMR signals and the accuracy and precision with which they can be measured.

Many improvements to the spectrometer have been made during the course of this study and they are described in this chapter. These have enabled the Oxford LMR spectrometer to operate well over a wide range in the mid-infrared. Furthermore, many important aspects of the spectrometer have not previously been considered fully. Therefore, two appendices accompany this chapter. The first, Appendix A, reviews the present model of CO laser action. An understanding of this model is essential in guiding the conditions required to operate the laser across a wide range of frequencies. The second, Appendix B, investigates important components of the spectrometer in detail.

II.2 Overview of the CO-LMR Spectrometer

The intracavity CO-LMR spectrometer was constructed by Robinson [1] in 1983; subsequent modifications to the grating and detector assembly were implemented by Towle [2]. A cross-section of the spectrometer is shown in Fig.II.1; it can be divided into four components, viz:

1. The CO laser system, shown in Fig.II.2.
2. The scanning d.c. magnet system, shown in Fig.II.3.
3. The intracavity absorption cell, shown in Fig.II.4.
4. The phase-sensitive detection system, shown in Fig.II.3.

II.3 The CO Laser System

II.3.1 General features

CO laser operation and coverage

The laser consists of a 2.4 m gain stabilised cavity in which the active medium is a 1.4 m long, liquid nitrogen cooled, flowing CO plasma contained within a triple-jacket, borosilicate glass tube. The gain tube has an i.d. of 16 mm; its ends are sealed by calcium fluoride windows at Brewster's angle[1]. The CO flow laser is a mid-infrared radiation source, and in this arrangement can produce radiation of great spectral purity. A schematic diagram of the CO laser system is shown in Fig.II.2

Laser action occurs on P-type vibration-rotation lines of CO in the $X^1\Sigma^+$ electronic state. The laser lines (denoted by the symbol $P(J'')_{v'-v''}$) are grouped in vibrational bands covering 1205–2116 cm^{-1} for $\Delta v = 1$ transitions [3, 4], see Fig.II.5, and 2459–3810 cm^{-1} for $\Delta v = 2$ transitions[2] [5], see Fig.II.6. The c.w., line-tunable overtone CO flow laser was first developed in Bonn. During the course of this work, an overtone laser

[1]The transmitted radiation is polarised when the angle between the incident beam and the normal to the window is Brewster's angle. This is 54° for CaF_2 in the mid-infrared [14].

[2]The CO laser operating on $\Delta v = 1$ and $\Delta v = 2$ transitions is referred to as the 'normal' and 'overtone' laser respectively.

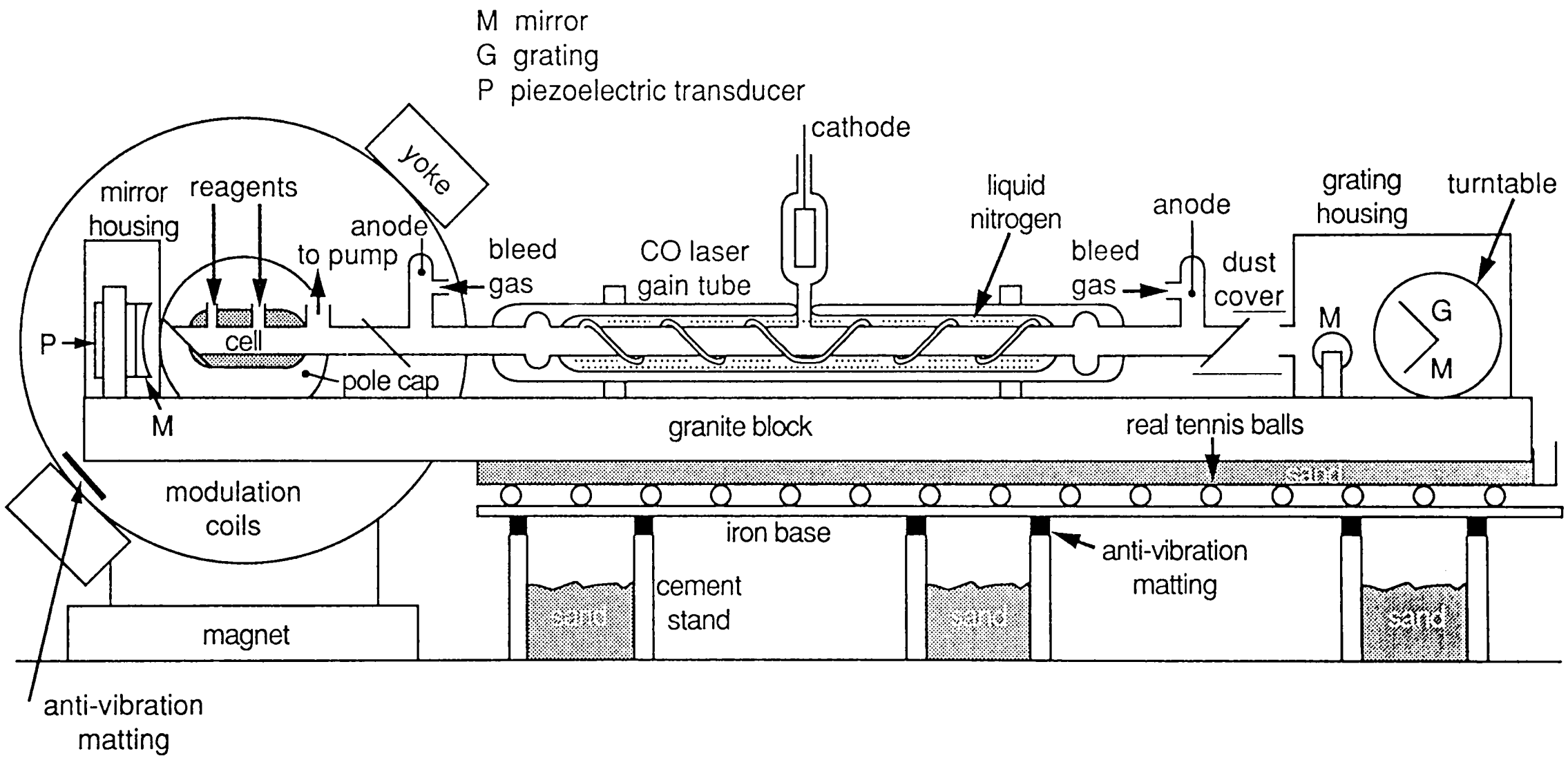

Figure II.1: A cross-section of the Oxford CO-LMR spectrometer.

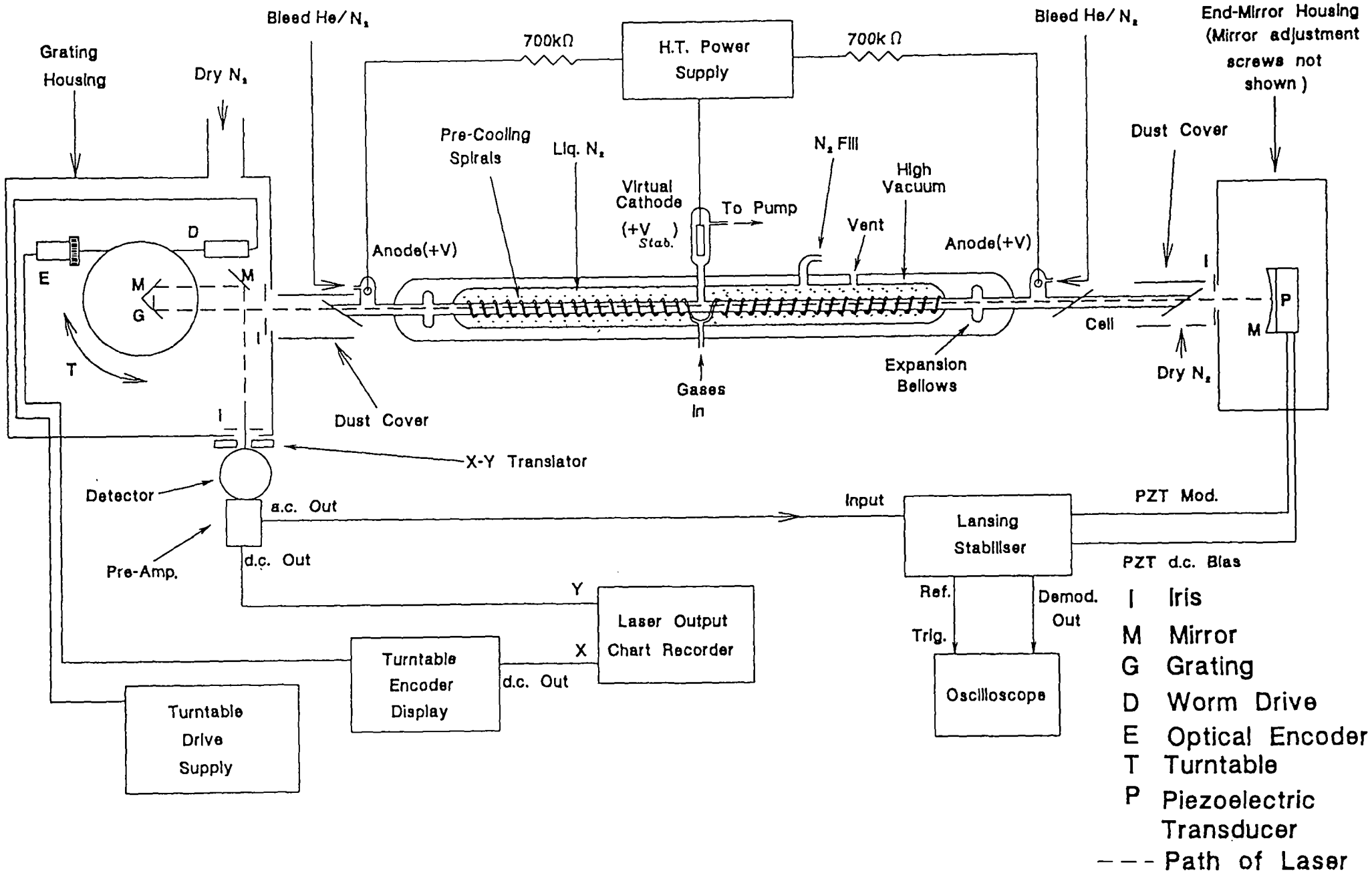

Figure II.2: A schematic diagram of the CO laser system.

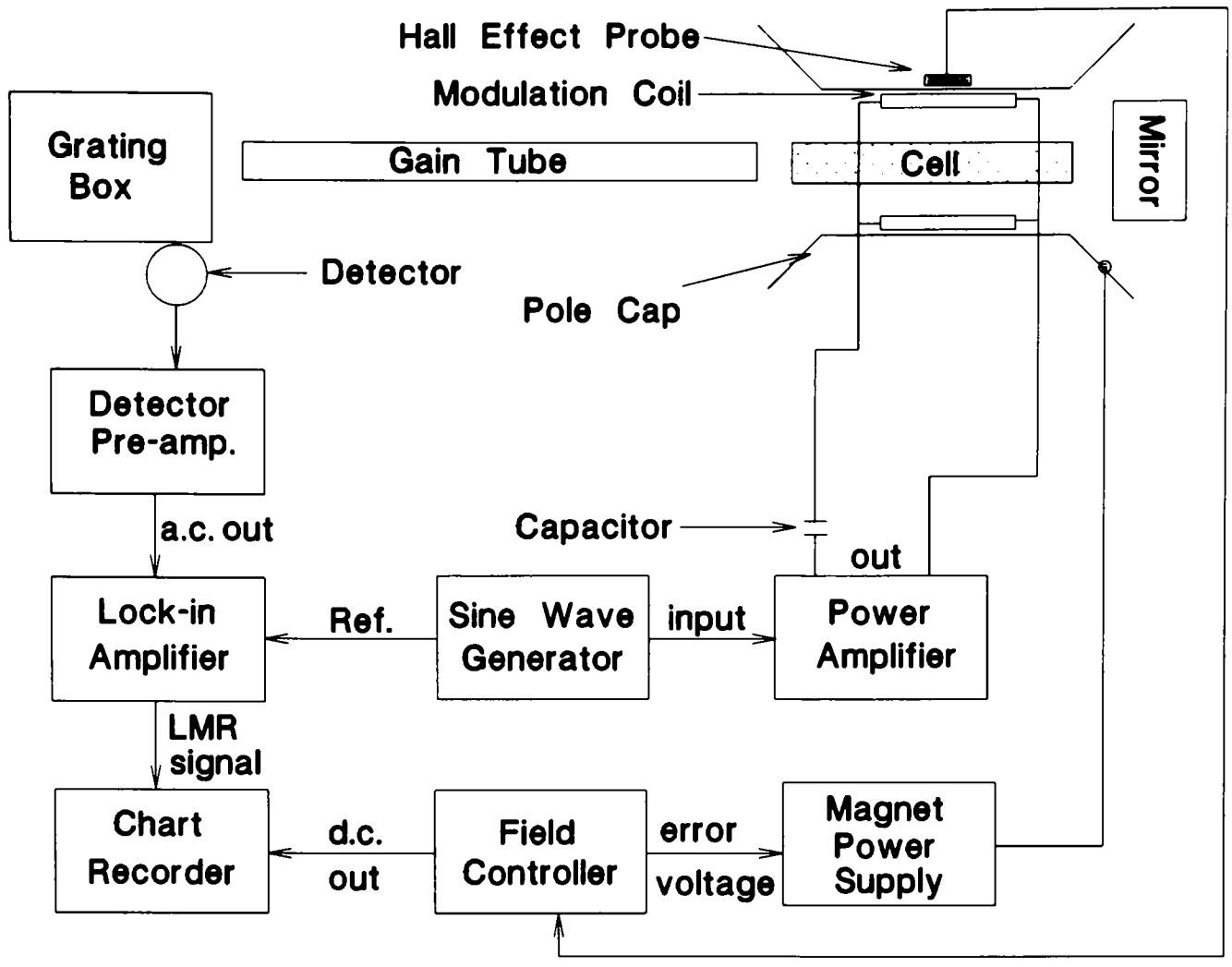

Figure II.3: A schematic diagram of the phase-sensitive detection system and the field control system.

was successfully started in the Oxford LMR spectrometer for the first time. The viability of the overtone laser was proved by its use to detect well known transitions due to CH [6, 7]. These were the $R_{1f}(7/2)$ transition on the $P(15)_{29-27}$ laser line, the $P_{2e}(7/2)$ transition on the $P(10)_{34-32}$ laser line, both in the fundamental band, and the $Q_1(3/2)$ hot-band transition on the $P(12)_{34-32}$ laser line. All these resonances were observed with Doppler limited resolution.

The normal CO laser has been operated on over 400 lines [8]; successive P lines are ca. 4 cm^{-1} apart ($B_e \approx 1.9$ cm^{-1}[9]) and the vibrational band spacing is about 26 cm^{-1} [9]. The vibrational bands overlap, resulting in a laser line every 2–3 cm^{-1} across most of the range. The spacing of successive P lines is similar for the overtone laser, but the vibrational band spacing is ca. 52 cm^{-1}. The conditions required to operate the overtone laser are critical; therefore only a narrow range of rotational lines show gain under a given set of conditions. As a result of this, lines in adjacent vibrational bands do not normally overlap. Overtone laser action has been observed on 330 lines in Bonn,

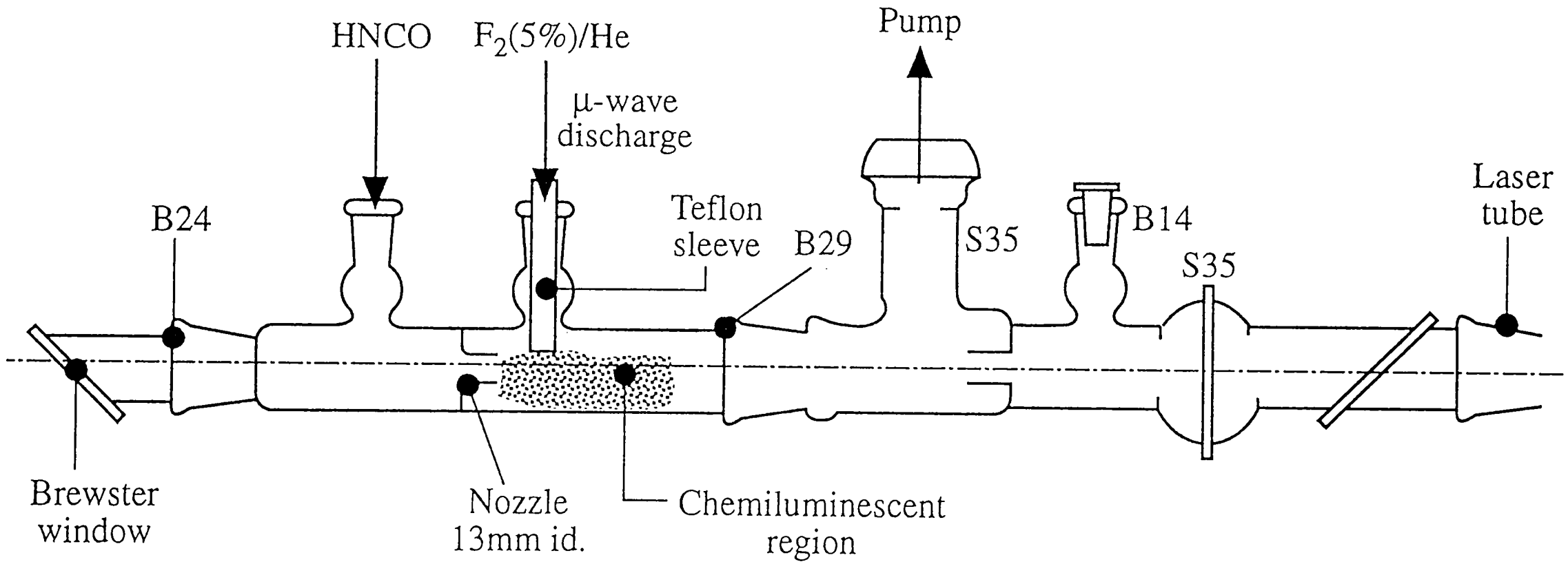

Figure II.4: A schematic diagram of the intracavity absorption cell, showing the arrangement for the production of the NCO free radical. The 'B' numbers refer to the cone joint sizes in millimeters. The centreline marks the optical axis of the laser.

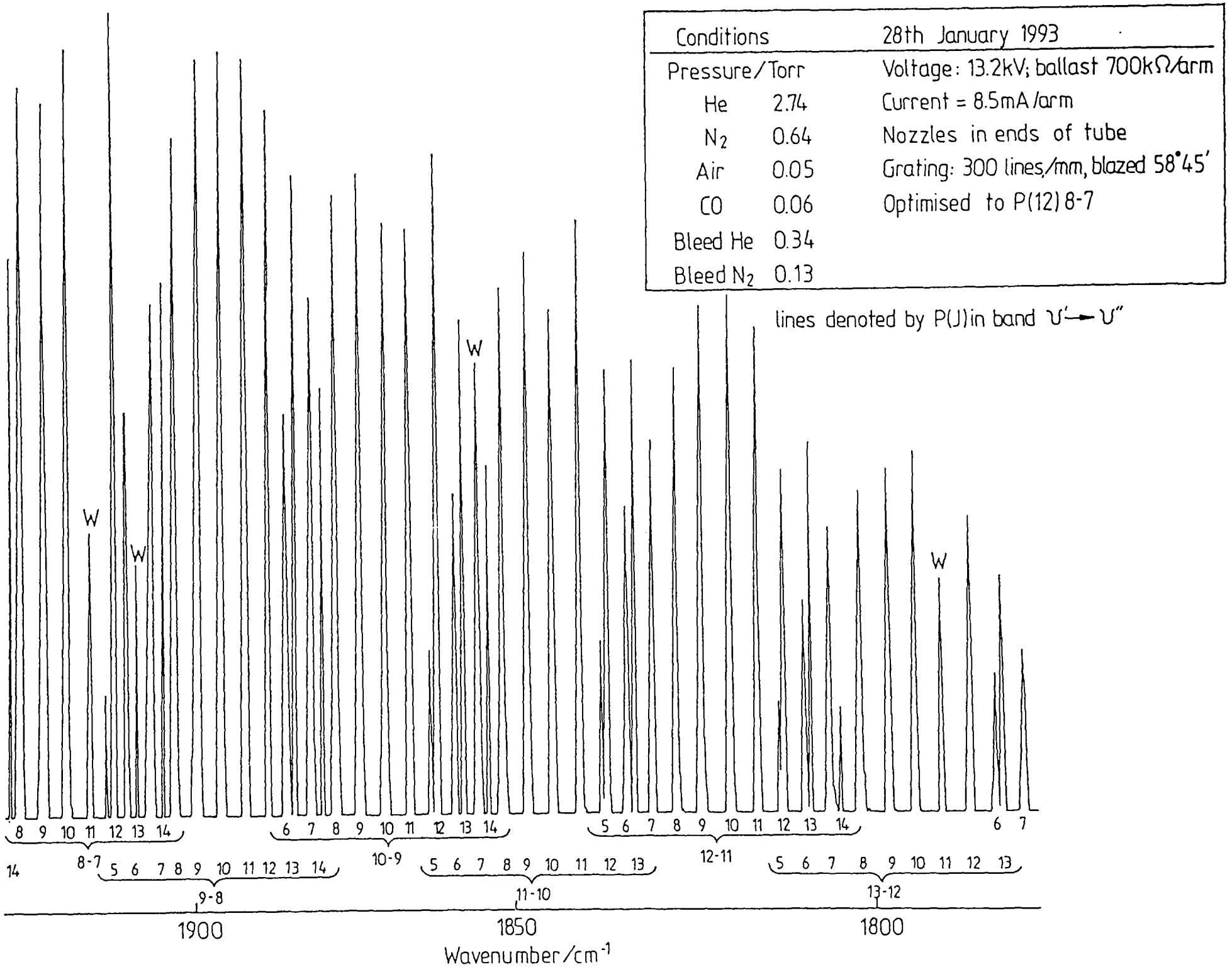

Figure II.5: A portion the $\Delta v = 1$ CO laser spectrum with conditions optimised to the $P(12)_{8-7}$ line. Fig.B.1 in Appendix B shows the same region optimised for higher J lines.

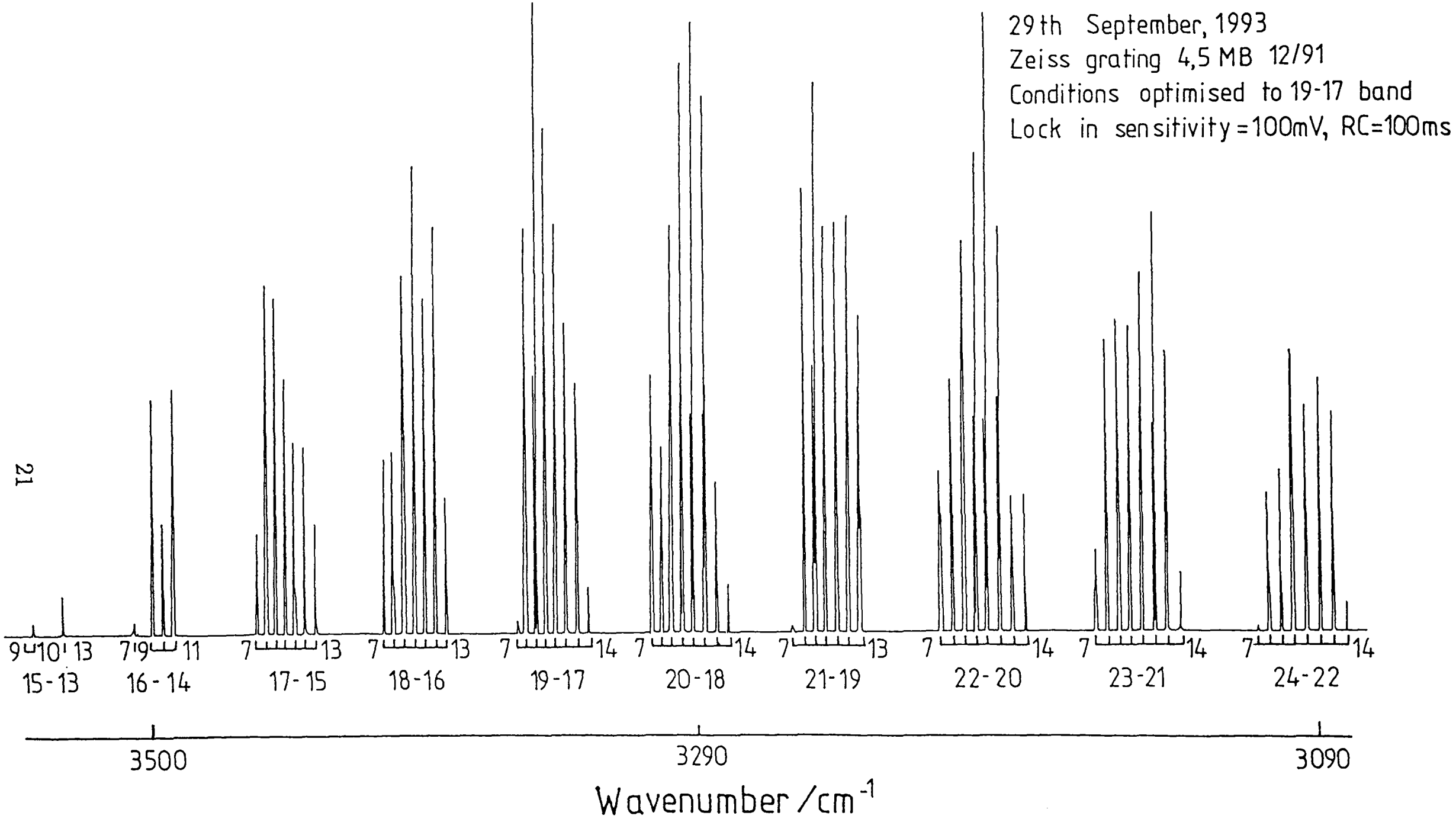

Figure II.6: A portion the $\Delta v = 2$ CO laser spectrum. The sharp appearance of the lines arises from the use of an intracavity chopped, lock-in amplifier method of monitoring the output of the laser. Fig.B.2 in Appendix B shows the longer wavelength region of the spectrum.

where it has been possible to extend the manifold of lines showing gain, so that some adjacent vibrational bands do now overlap [5].

CO laser power

The relation between out-coupled and intracavity laser powers requires a knowledge of the reflectivity characteristics of the diffraction grating; this was not pursued in the present study. Therefore, the intracavity laser power cannot easily be measured; for the normal laser it can be as high as 40 W on the strongest lines [8], down to a few hundred mW on the weakest lines. In Oxford, the power coupled out via the zeroth order of the grating has been measured as 120 mW for the normal laser on the $P(12)_{8-7}$ line, using an Ophir 30A-P-Cal power meter. If it is estimated that 1% of the laser power is coupled out, then this corresponds to an intracavity laser power of 12 W.

When a 2% out-coupling mirror replaced the end-mirror of the overtone laser in Bonn, a maximum output power of 550 mW was recorded [5]. No comparable measurement was made in Oxford, but monitoring the power coupled out by the zeroth order of the diffraction grating gave maximum output powers of 20 mW on both the $P(9)_{19-17}$ and $P(11)_{33-31}$ lines of the overtone laser. This gives an estimated intracavity power of 2 W. In a similar measurement in Bonn, Bachem [11] recorded an output power of 120 mW on the $P(11)_{33-31}$ line, suggesting an intracavity power of 12 W.

The beam waist of the laser [10], which is located at the diffraction grating, is in the range 2–3.5 mm, increasing with the wave number of the laser (see Appendix B).

The CO laser spectrum

As can be seen from Fig.II.5, the higher J laser lines are narrower than the lower J ones. This observation is explained by a reduction in the gain as J increases, a consequence of the population of higher J lines being divided up amongst more M_J components. This increased degeneracy provides more levels from which non-radiative relaxation can occur [12]. This observation is useful in assigning the CO laser spectrum.

Characteristic water absorptions, e.g. those in Fig.II.5, and readily produced LMR signals due to NO [1] and TeD [13], are also valuable fingerprints in the assignment of the normal laser spectrum. In the overtone laser region, water absorptions occur on the $P(10)_{25-23}$, $P(8)_{27-25}$ and $P(10)_{27-25}$ lines [5], see Fig.B.2 in Appendix B. The overtone

laser spectrum can be assigned by extrapolating a scale based upon these line positions, and by considering the observed J values of the manifold of lines showing gain, which tends to be the same in adjacent bands.

II.3.2 Laser Optics

CO laser line selection

The laser operates on a single rotation-vibration line, selected by rotating a blazed diffraction grating [14] in a Littrow autocollimation mount [15] on a motorised turntable. Laser reflection occurs on the first order of the grating. A small amount of radiation is coupled out via the zeroth order of the grating to a detector, using a pair of mirrors (see Fig.II.7). Appendix B gives further details of the Littrow mount and the gratings used in the spectrometer.

Laser optimisation

Fig.II.7 shows a drawing of the grating box assembly. The turntable can be mounted either on the side or the floor of the grating housing, so that the grating rulings are horizontal or vertical respectively. This results in laser radiation with its electric vector oscillating either parallel to (π-polarisation) or perpendicular to (σ-polarisation) the applied flux of the electromagnet, respectively. The Brewster's angle windows (Fig.II.2) are polarising elements and must be rotated to lie in the plane normal to the electric vector of the laser beam. The micrometer adjustable foot and the grating cam, see Fig.II.7, are used to align the grating correctly when it is first installed.

The open sections of the laser cavity and end-mirror/grating housings can be purged with dry nitrogen, allowing laser action to occur on CO lines coincident with water absorptions.

The end-mirror and grating can be optimised for the desired laser line. For the grating, this involves narrowing the iris at the end-mirror to about 4 mm diameter, slowly rotating the grating turntable to optimise the output power, and re-opening the iris. A similar procedure is then used to optimise the end-mirror, the grating box iris being narrowed before adjusting the end-mirror mounting screws; the iris is then reopened. Finally, the detector position is optimised by adjusting its X-Y micrometer mounting

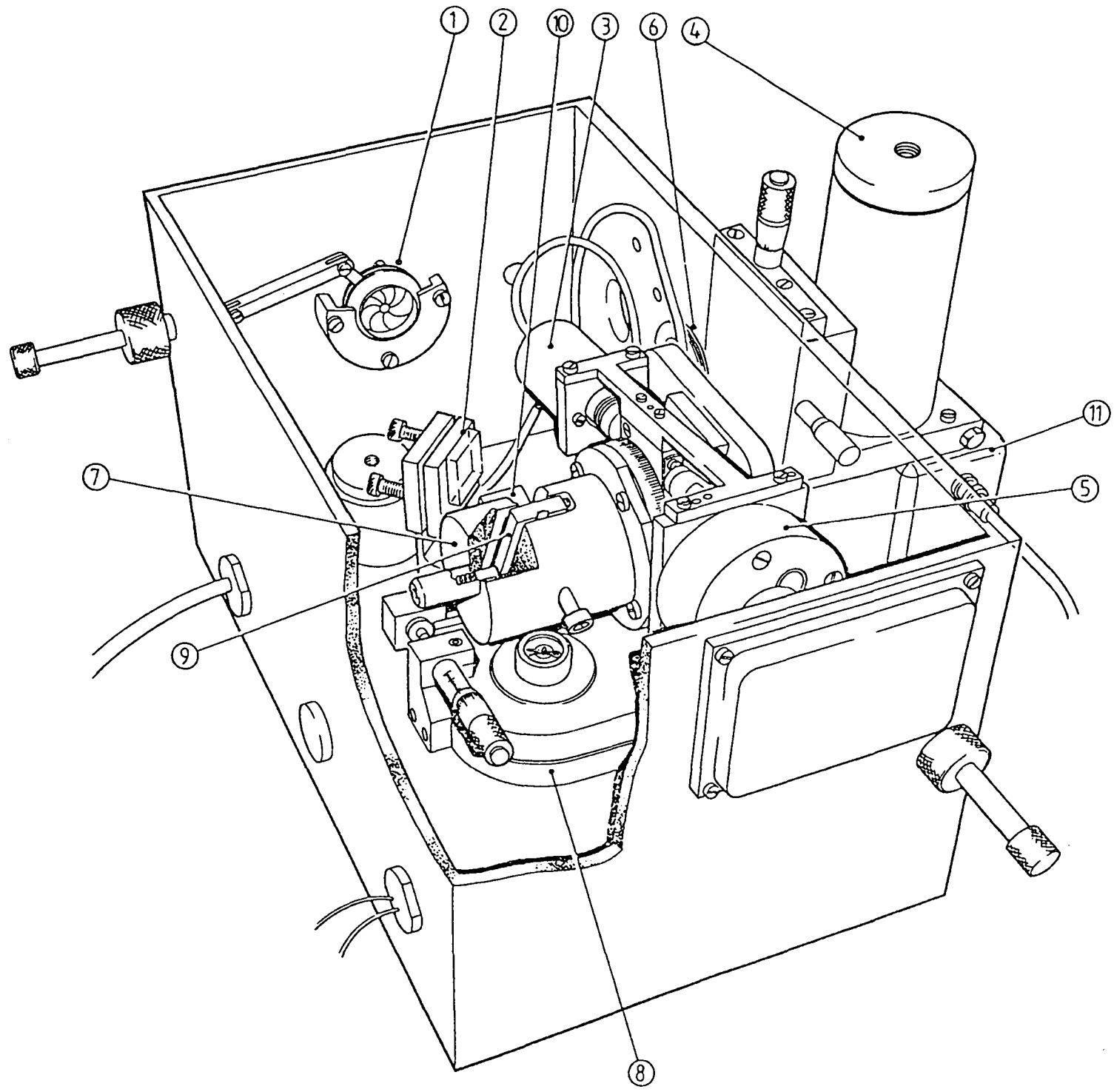

1	Inter Cavity Iris	7	Littrow Mount
2	Adjustable Mirror	8	Turntable with Micrometer Adjustment
3	Angle Encoder	9	Diffration Grating
4	Detector on X-Y Mount	10	90° Gold Mirror
5	Motor to Drive Littrow Mount	11	Detector Amplifier
6	Detector Iris		

Figure II.7: A drawing of the grating box assembly. The optics are shown in the arrangement for σ-polarisation (see text).

(see Fig.II.7).

The grating turntable drive is connected to an optical pulse encoder, producing 100 pulses for every 1° rotation of the turntable. A pulse counter allows the grating angle to be monitored. The counter also produces a d.c. output, which along with the pre-amplified d.c. output from the detector, allows the CO laser spectrum to be recorded. A slight backlash in the grating drive system (Fig.II.7) means that the angle encoder readout is not exactly reproducible.

II.3.3 The Laser Cavity

Single mode operation

The laser is operated in the fundamental axial mode (TEM_{00k}) [14, 15]; transverse modes are reduced below the gain threshold by narrowing intracavity irises at the end-mirror and grating housings. This is effective because the diffraction losses of transverse modes exceed those of axial modes.

The cavity mode is stabilised on the top of the gain curve of the CO laser transition by a Lansing 80.215 stabiliser. The Lansing modulates the piezo-ceramic transducer (PZT) upon which the cavity end-mirror[3] is mounted (Fig.II.1). Using a negative feedback loop, the Lansing monitors the effect of the PZT modulation on the a.c. output at the detector, and applies a d.c. bias voltage to move the PZT so as to gain-stabilise the cavity. The PZT can be biased between +0.5 and +1.5 kV. Outside of this range, the end-mirror must be adjusted manually using two fine adjustment screws in the end-mirror mount[4], or the adjacent $TEM_{00k\pm1}$ mode can be locked to the top of the gain curve.

Mode stability

An oscilloscope display of the de-modulated output of the Lansing stabiliser (see Fig.II.2) shows the region of the CO gain curve sampled by the PZT modulation. This trace appears flat when the mode is at the top of the profile of the gain curve. It is important

[3]The mirror is coated with Cu/Ni/Au (99% infrared reflectivity) and has a 10 m radius of curvature and a 25 mm diameter.

[4]The end-mirror screws have been re-designed and now include a universal joint mounting. This makes them much more stable. It is now possible to make the fine adjustments necessary when optimising the overtone laser.

that the laser remains gain-stabilised during an LMR scan; failure to do this can result in a frequency drift (mode-pulling [15]), and an almost invariable reduction in signal-to-noise ratio. It is often necessary to re-lock the stabiliser in the middle of an LMR scan, because both the cavity and the CO laser plasma are affected by the magnetic field.

The stability of the laser resonator is very sensitive to the effects of vibrations, since the mode spacing is of the order of a few microns and the free spectral range [14] of the cavity is 63 MHz. Therefore, the granite block upon which the laser components are mounted is supported by a tray filled with sand mounted upon real tennis balls[5] [16], an iron plate, rubber matting and sand-filled concrete tubes (see Fig.II.1).

The properties of the laser cavity and the stabilisation system are considered in greater detail in Appendix B.

II.3.4 Gas Mixing System and Discharge

Active medium of the CO laser

The laser plasma consists of helium, nitrogen, CO and a little oxygen (admitted as air) at a total pressure of 0.46–1.33 kPa (3.5–10 Torr). Typical gas compositions range from He 78.2%, N_2 19%, air 1.3%, CO 1.5% (total pressure 533 Pa (4 Torr)) in the 1900 cm^{-1} region, to He 89%, N_2 5.4%, air 0.8%, CO 4.8% (total pressure 1.133 kPa (8.5 Torr)) in the overtone laser region. The CO is held in an iron cylinder at high pressure; consequently iron pentacarbonyl is formed, an electron quencher and therefore a laser poison. Iron pentacarbonyl is removed by passing the CO through a heated alumina catalyst before entering the gas mixer.

Details of the gas mixtures required to access different regions of the laser spectrum are given in Appendix B.

Gas regulation

The gases are regulated by fine needle valves (Whitey B22-RS4) with ruby ball flow meter indicators. Before entering the gain tube, the gases pass through a baffled steel tank which damps any sudden pressure changes. The mixed gases are cooled and purified

[5] These hard balls are very effective at damping low frequency vibrations.

on entering the laser tube, passing through glass spirals immersed in the liquid nitrogen reservoir before entering the central gain tube.

A similar, smaller gas mixer allows helium and nitrogen to be bled in over the anodes at the sides of the tube. The bleed gases keep the electrodes clean and reduce self absorption of the low v laser bands, which occurs when CO diffuses out of the cooled excitation region. The bleed gas is essential when running the laser near to 2000 cm^{-1}, but is detrimental to the overtone laser[6].

A continual gas flow is maintained by an Edwards E2M28 two-stage vacuum pump ($28\,m^3hr^{-1}$ pump rate), which produces an ultimate vacuum of 0.1 Pa (1 mTorr). In order to obtain adequate pressures and a stable laser output, the gas flow rate is reduced by closing a choke flap after the tube outlet. The gas pressures are measured by an Edwards 10^{-3}–10 Torr barocel gauge between the tube outlet and the choke flap.

The normal CO laser operating above 2000 cm^{-1}

When running the normal laser below the 4–3 band, gain is improved by passing all the gases through electrically insulated, liquid nitrogen cooled copper coils, before entering the laser tube [3]. This is thought to purify and dry the gases. A glass insert is also placed in each end of the laser tube, see Fig.II.8, to discourage CO from diffusing out of the excitation region [3, 17]. With these modifications, lines in the 2–1 band became accessible.

Very recent developments in Bonn have greatly increased both the power and the number of laser lines accessible in the 2–1 and 1–0 bands [18]–[21], removing the need for the nozzle inserts. Briefly, a narrower gain tube (13 mmi.d.) is favoured, with a ribbed inner to increase viscous flow and aid cooling. Extra gas purging inlets are built into the sides of the tube, within the cooled region. The gas inlets to the tube are constricted in order to cause cooling of the gases by expansion as they enter the gain tube.

Electrical discharge

The plasma is maintained by a longitudinal, current stabilised d.c discharge (typically 14 – 20 kV). In order to avoid electrical ground loops [22], all three electrodes are main-

[6]It seems that the warm bleed gas is detrimental to the vibrational pumping which is critical for overtone laser action [5].

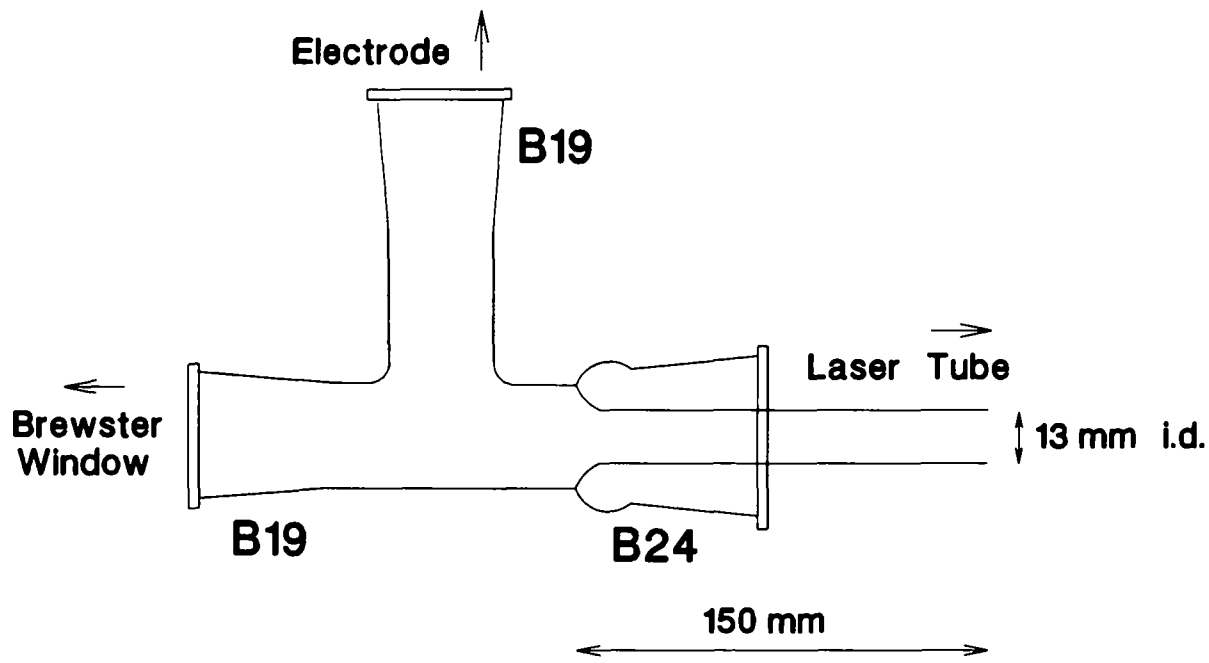

Figure II.8: The insert placed at each end of the laser tube when operating the $\Delta v = 1$ laser below the 4–3 band. The cone joint sizes are given in millimeters.

tained at positive potentials with respect to ground (Fig.II.2). The virtual cathode is at the voltage of the current stabilisation valves (1.5 – 3 kV). The total discharge current is typically in the range 8.5 – 25 mA. The current plays an important role in determining the translational temperature of the plasma and therefore the manifold of rotational lines on which laser action occurs in each vibrational band [12]. Lines in the range P(5) to P(17) have been observed in Oxford, dependent upon the current.

Each virtual anode arm of the discharge is loaded with a 700 kΩ ballast resistance in order to overcome the negative impedance characteristic of the plasma [3]. The ballast resistance plays two roles:

1. The resistor banks limit the current surges which may occur at the low voltages when the discharge is first struck.

2. At low currents (below 8.5 mA total, with the present resistors), the net impedance of the circuit becomes negative. The stabilisation valves in the power supply require a positive V/I characteristic and so runaway occurs and the discharge fails. Low currents are needed when running the normal laser below the 4–3 band, in order specifically to achieve a population inversion on these low vibrational levels.

A deficiency of oxygen in the plasma can cause the discharge to become unstable, observed as a pink coloration in the plasma. This can be avoided by starting with a slight excess of oxygen (3 Pa (0.02 Torr) excess), and by building up the CO pressure slowly

over a 20 minute period. For optimum, low-noise laser power, the oxygen level must be balanced so that it is just sufficient for the level of CO in the plasma. Appendix B discusses this in more detail.

II.4 The Magnet System

II.4.1 Field Scanning and Measurement

A schematic diagram of the magnet system is shown in Fig.II.3. The magnet is a Varian V3800 15″ diameter pole cap electromagnet with a 4″ pole gap. It produces a homogeneous (variation $< 0.1\,\mathrm{mT}$ over the region where free radicals are probed by the laser) magnetic flux density between 0 and 1.6 T. The magnet is operated by a Brüker B-H15 digital field controller, which scans the field in 4095 points over a specified range in a given time. The field controller monitors the field using a Hall effect probe [23] mounted on one of the pole caps of the magnet. The error between the actual and demanded field at a given point in the scan is used by the controller to regulate the current through the magnet.

Periodically, a calibration is carried out between the field measured by the controller and the field at the centre of the magnet gap, on the optical axis of the laser. A Brüker B-NM20 NMR oscillator is used for this purpose, its probe being held on the optical axis in a perspex mount. The calibration is used to correct the fields of LMR signals, using a cubic spline interpolation procedure [24].

II.4.2 Development of a New Magnet Power Supply

An important development during this study was the installation of a new magnet power supply, replacing the mechanically regulated Varian supply. The old supply had a long response time causing it to lag behind the field demanded by the controller. Occasional jumps in the mechanical system caused spikes on the LMR spectrum and non-linearities in the field scan. The new supply uses solid state, thyristor-controlled rectification [25] and transformation of the 3-phase input. This gives smooth, step-less current regulation with a very short response time.

II.5 The Intracavity Absorption Cell

II.5.1 Arrangement of the Cell

The absorption cell (Fig.II.1 and Fig.II.4) is mounted between the poles of the electromagnet, centered on the optical axis of the CO laser and co-symmetric with the gain tube, to which it is connected by a ball joint. Free radicals are sampled by the laser beam in the most homogeneous region of the magnetic field.

II.5.2 The Generation of Gaseous Free Radicals

The radicals studied in this thesis were formed by the reaction *in situ* between a precursor species in the cell, and labile atomic/molecular fragments formed by a microwave discharge through a flowing gas at the entrance to the cell, see Fig.II.4. The microwave discharge was a Microtron 200 (Electro-Medical Supplies) source delivering up to 75 W output at 2.45 GHz. A quarter-wave tunable, impedance matched cavity ("Evenson" cavity) was used to couple the microwave power into the flowing gas.

The species formed in these reactions have typical rotational temperatures no more then 100 K above room temperature. In the case of NCO production, 83 Pa (0.62) Torr of a 5% fluorine in helium mixture is passed through the microwave discharge, forming fluorine atoms which react with HNCO to form NCO. The mean free path for the fluorine atoms is about 60 μm; they travel at least 5 cm between the discharge and the reaction zone. Therefore, the atomic fluorine will be completely thermalised by the time it reacts with HNCO. This is considered in more detail in Appendix B.

Contamination of the Brewster windows can be greatly reduced by introducing an inert purging gas at the ends of the cell; as the purge gas passes through the constrictions, it maintains a pressure gradient away from the windows. The use of a nitrogen purge in the cell was found to reduce the intensity of NCO resonances and so was not used in this study.

A fresh flow of reagents is maintained in the cell by a Edwards E2M80 two-stage vacuum pump (80 m^3hr^{-1}). An in-line liquid nitrogen trap can be placed between the cell and the pump to reduce contamination and damage when using corrosive reagents. Pressures are measured at the outlet of the cell by an Edwards barocel gauge (10^{-3} –

10 Torr); the ultimate vacuum is typically 0.7 Pa (5 mTorr).

II.5.3 Sub-Doppler Spectroscopy

The intracavity arrangement means that the sample is subjected to counter-propagating beams of CO laser radiation along the optical axis of the laser cavity. This makes it possible to saturate strong transitions in molecules which have zero velocity component along this axis. These transitions can be observed as Lamb-dips burned into the Doppler absorption profile of the resonance [15]. The Lamb-dips are sensitive to collisional and modulation broadening, and to the frequency stability of the laser. These factors limit the saturation linewidth to ~ 10 MHz, as discussed in §II.7 and Appendix B.

II.6 The Detection System

II.6.1 Phase-Sensitive Detection

Construction

Fig.II.3 gives a schematic diagram of the detection system. A sine wave generator produces a 3.5 kHz waveform which is sent simultaneously to an EG & G model 5209 Lock-In Amplifier and an HH Electronics X800 MOS-FET power amplifier. When matched to a 4 Ω load, the MOS-FET amplifier can deliver an r.m.s. power of 780 W. The power amplifier drives a resonant LC circuit consisting of a capacitor (0.75 μF) and a pair of modulation coils (wired in parallel) mounted on the pole caps of the magnet. The parallel coils have an inductance of 2.1 mH at 1 kHz and a resistance of 1.54 Ω. At resonance, the capacitative and inductive impedances cancel; the modulation frequency is then [25]

$$f = \frac{1}{2\pi\sqrt{LC}}. \tag{II.1}$$

The maximum peak-to-peak modulation amplitude that can be obtained at present is 3 mT.

The CO laser and other components produce '$1/f$' noise which arises from resistances, semiconductor junctions and low frequency vibrations [27]. The $1/f$ noise peaks in the range 1–2 kHz, so it is desirable to make the modulation frequency as high as possible.

This can be achieved by reducing the size of the capacitance. The problem with this approach is that the peak-to-peak current and hence the modulation field, drop as the resonant frequency is increased [25]. As discussed below, this has serious consequences for the sensitivity of detection of slow tuning Doppler limited resonances.

Operation of phase-sensitive detection

The modulated field is superimposed upon the d.c. field of the scanning electromagnet, causing any LMR signals to show an intensity modulation, and so discriminating against other, non-paramagnetic absorptions. The applied modulation field has the time-dependent form $B_m \sin \omega t$, where $\omega = 2\pi f$ and B_m is half the peak-to-peak modulation amplitude. The effect upon the nonlinear transition profile, as observed at the detector, can be expressed as a Fourier series in the harmonics of ωt [23],

$$F(B) = \sum_{n=0}^{\infty} \{a_n(B) \cos n\omega_m t + b_n(B) \sin n\omega_m t\}, \qquad \text{(II.2)}$$

where B is the d.c. flux density. The n^{th} harmonic is proportional to the n^{th} derivative of the line profile. The pre-amplified a.c. output of the detector is sent to the lock-in amplifier which detects at twice the reference frequency, ($n = 2$). This, 2-f detection, occurs at $\approx 7\,\text{kHz}$, so the Fourier component of the $1/f$ noise at this frequency is lower than if 1-f detection at $\approx 3.5\,\text{kHz}$ were used.

II.6.2 The 2-f LMR Lineshape

Line profile

For a Doppler limited line profile in the frequency domain, with a Doppler width of $2\Delta\nu$, the *field-equivalent Doppler width* of a resonance in the magnetic field domain is $2\Delta B = 2\Delta\nu/(\partial\nu/\partial B)$, where $(\partial\nu/\partial B)$ is the Zeeman tuning rate (normally in MHzG^{-1}). The LMR spectrometer detects the second derivative of the Doppler profile, producing the 2-f lineshape shown in Fig.II.9. The spacing of the minima of the 2-f absorption signal observed in the LMR experiment is $2.94\Delta B$ for a Doppler limited resonance.

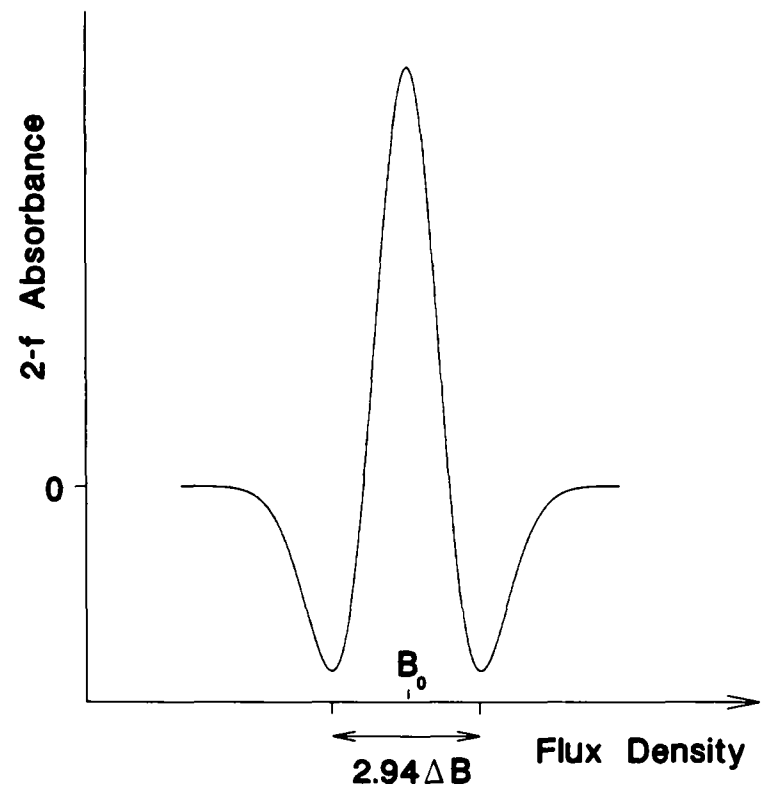

Figure II.9: A 2-f, Doppler limited LMR signal resonant at rest-frame field B_0. Modulation effects have been neglected.

Modulation effects

The 2-f signal amplitude is optimised when the peak-to-peak modulation field is about twice the field-equivalent Doppler width. Note that Lamb-dips appear as 2-f Lorentzian profiles burned into the Doppler limited 2-f profile. The field-equivalent Doppler width is typically between 8 mT and 20 mT, somewhat greater than the peak-to-peak modulation amplitude quoted in §II.6.1. Therefore, most Doppler limited resonances are under-modulated with the present experimental arrangement. This phenomenon leads to *modulation induced intensity loss* of signal [28], see Appendix B.

When the peak-to-peak modulation amplitude approaches the field-equivalent width of the signal, *modulation broadening* [29] becomes significant. This is of importance for sub-Doppler resonances (Lamb-dips), which are at least an order of magnitude narrower than Doppler limited resonances, and it explains the need to reduce the modulation amplitude in order to observe them. The observed widths of Lamb-dips are normally partly limited by modulation broadening, since the signal is lost at modulations low enough to avoid it. Modulation broadening is considered in detail in Appendix B.

II.6.3 The Modulation Coils

The modulation coils are wound on water cooled copper formers held in perspex mounts. Eddy currents in the copper lead to significant energy losses, reducing the modulation amplitude below the optimum value. This construction is necessary to cool the windings and prevent damage to them.

Lorentz forces arising from interactions between the a.c. and d.c. fields, cause the windings to oscillate at the modulation frequency. This oscillation produces acoustic noise, whose amplitude increases with the d.c. flux density. This causes vibrations which de-stabilise the laser cavity and become significant above 1 T.

II.6.4 Detectors

Three detectors are used to cover the complete wavelength range of the CO laser. For the normal laser, a liquid nitrogen cooled Hg:Cd:Te photoconductive detector is used to monitor the laser power and to record the LMR spectrum. A liquid nitrogen cooled In:Sb photovoltaic detector is used to record the overtone laser LMR spectrum. The power incident on the liquid nitrogen cooled detectors should be below 1 mW, or their a.c. responses will be reduced and the detector can be damaged. When starting the overtone laser and recording its output, the In:Sb detector is exchanged for a cheaper, pyroelectrical detector which is used with an intracavity chopper.

The detector mounting is skewed by placing some shim-metal plates between the X-Y translator and the grating box. This is necessary for the overtone laser, where a reflection from the detector window, back into the laser, can cause 'all-line' $\Delta v = 1$ laser action. The resulting high power would lead to serious damage to the detector and diffraction grating.

II.7 LMR Measurements

II.7.1 Accuracy and Precision

The accuracy and precision of a measurement determines the uncertainty assigned to an LMR datum in the analysis.

The accuracy of an LMR measurement is limited by four factors:

1. The frequency stability of the CO laser. The long term stability is typically 10 MHz when the gain stabilisation system is well adjusted[7] [30].

2. The field inhomogeneity in the region of the sample, typically ~ 0.1 mT as measured by an NMR probe.

3. There is a shift of ~ 3 mT in the field position of the resonance peak between up and down field scans. This arises because of magnet hysteresis and system response. The peak centre is taken to be the average from several pairs of up/down scans.

4. Collisional and other minor factors, which contribute ≤ 1 MHz error to a typical mid-infrared measurement at pressures below 133 Pa (1.0 Torr).

Measurement errors

The precision of the field measurement depends upon how accurately and precisely the centre of the resonance can be measured. A 2-f signal, as shown in Fig.II.9, has the advantage that the centre of the signal is marked by a peak rather than a baseline crossing which is the case with 1-f detection. The error in frequency measurement introduced by an error in field measurement is virtually constant for a range of Zeeman tuning rates, $\partial\nu/\partial B$. The field measurement error δB, of a broad, slow tuning resonance is greater than that for a narrow, fast tuning one; however the frequency error, $\delta B(\partial\nu/\partial B)$, is approximately constant. The limitations of this assumption are evident for certain transitions due to NCO, as discussed in §VII.2.1.

A Doppler limited resonance with a field-equivalent Doppler width of 10 mT, typically has a frequency-equivalent width of 100 MHz (assuming a tuning rate of 1 MHzG^{-1}). For a Lamb-dip with a modulation broadened/laser stability limited width of about 1 mT, the frequency equivalent width is about 10 MHz.

Pessimistically, a 2-f peak centre can be measured to a tenth of its width, giving measurement errors of about 10 MHz for a Doppler limited resonance and 1 MHz for a Lamb-dip resonance.

[7]Determined from studies of Lamb-dips resonances due to NO.

The field scan rate

When recording the LMR spectrum, it is important to use a magnet scan rate appropriate for the lock-in amplifier time constant, in order to avoid signal distortion. Poole [23] quotes a parameter

$$\alpha = \frac{\tau_0}{\tau_{1/2}}, \tag{II.3}$$

where τ_0 is the lock-in time constant and $\tau_{1/2}$ is half the time taken to scan between the half amplitude points of the signal. The distortion becomes significant for $\alpha \geq 0.05$. A slow scan rate also ensures that the response time of the magnet does not contribute significantly to field measurement errors.

Total uncertainties

When errors due to long term laser stability, field measurement errors and collisional broadening effects are taken together, the estimated total measurement uncertainties are 20 MHz for a Doppler limited resonance and 10 MHz for a Lamb-dip resonance. These are the uncertainties normally assigned to clearly resolved resonances. Exceptions are made when resonances are blended or when they are very fast tuning (and therefore very sensitive to systematic and random field measurement errors), or weak.

Bibliography

[1] D. Robinson, Ph.D thesis, University of Southampton, 1985.

[2] J.P. Towle, D.Phil thesis, pp. 4–18, 107–109, University of Oxford, 1992.

[3] B. Wu, T. George, M. Schneider, W. Urban and B. Nelles, *Appl. Phys. B* **52**, 163–167 (1991).

[4] T.X. Lin, W. Rohrbeck and W. Urban, *Appl. Phys. B* **26** 73–76 (1981).

[5] E. Bachem, A. Dax, T. Fink, A. Weidenfeller, M. Schneider and W. Urban, *Appl. Phys. B* **57**, 185–191 (1993).

[6] P.F. Bernath, *J. Chem. Phys.* **86**, 4838–4842 (1987).

[7] S.J. Diggines, Part II thesis, University of Oxford, Trinity 1994.

[8] W. Urban, *Laser und Optoelektron.* **23**, 56–61 (1991).

[9] K.P. Huber and G. Herzberg, "Molecular Spectra and Molecular Structure," Vol. IV, "Constants of Diatomic Molecules," p. 166, Van Nostrand-Reinhold, New York, 1979.

[10] A.E. Siegman, "Lasers," pp. 663–667, University Science Books, Mill Valley, CA, 1986.

[11] E. Bachem, Institut für Angewandte Physik der Universität Bonn, Private Communication, 1992.

[12] W. Urban, "Infrared Lasers for Spectroscopy," Institüt für Angewandte Physik der Universität Bonn, 1987.

[13] D.A. Gillett, J.P. Towle, M.N. Islam and J.M. Brown, *J. Mol. Spectrosc.* **163**, 459–482 (1994).

[14] E. Hecht, "Optics," 2nd ed., pp. 424–430, 581–585, Addison-Wesley, Reading, MA, 1989.

[15] W. Demtröder, "Laser Spectroscopy," Springer Series in Chemical Physics, Vol. 5, pp. 79–115, 132–139, 232–272, Springer-Verlag, Berlin, 1982.

[16] C. Ronaldson, "Tennis: A Cut Above the Rest," p. 24, Ronaldson Publications, Oxford, 1989.

[17] T. George, Diplomarbeit thesis, Institut für Angewandte Physik der Universität Bonn, 1990.

[18] S. Saupe, Diplomarbeit thesis, Institut für Angewandte Physik der Universität Bonn, 1991.

[19] T. George, B. Wu, A. Dax, M. Schneider and W. Urban, *Appl. Phys. B* **53**, 330–332 (1991).

[20] T. George, W. Urban and A. Le Floch, *J. Mol. Spectrosc.* **165**, 500–505 (1994).

[21] T. George, S. Saupe, M.H. Wappelhorst and W. Urban, *Appl. Phys. B* **59**, 159–166 (1994).

[22] J.H. Moore, C.C. Davis and M.A. Coplan, "Building Scientific Apparatus," pp. 443–445, Addison-Wesley, London, 1983.

[23] C.P. Poole, Jr., "Electron Spin Resonance," 2nd ed., pp. 220, 229–247, J. Wiley & Sons, New York, 1983.

[24] W.H. Press, B.P. Flannery, S.A. Teukolsky and W.T. Vetterling, "Numerical Recipes: The Art of Scientific Computing," pp. 31–38, 86–89, Cambridge University Press, Cambridge, 1986.

[25] J.M. Calvert and M.A.H. Mc Causland, "Electronics," pp. 69–70, 75–76, 127–129, J. Wiley & Sons, Chichester, 1982.

[26] P.W. Atkins, "Physical Chemistry," 3rd ed., pp. 647–653, Oxford University Press, Oxford, 1986.

[27] T. Coor, *J. Chem. Ed.* **45**, A533–A544, A583–A590 (1968).

[28] G.V.H. Wilson, *J. Appl. Phys.* **34**, 3276–3285 (1963).

[29] A.W. Johnson, *J. Magn. Reson.* **24**, 21–24 (1976).

[30] C. Pfelzer, Institut für Angewandte Physik der Universität Bonn, Private Communication, 1993.

Chapter III

A Theoretical Model of a Linear Free Radical

III.1 Introduction

This chapter describes how the energy levels and properties of linear triatomic free radicals in open shell states can be calculated. The expressions derived are applicable to $^2\Pi$ electronic states, *i.e.* those studied in this thesis. The parameters of the model relate to real physical features of the molecule.

The first section considers the nature of the Renner-Teller effect and its understanding in terms of molecular orbital theory. There follows a more formal treatment of the calculation of molecular energy levels, and its reduction to a tractable problem through the development of an effective Hamiltonian. The types of terms arising from this process are described; they will be of significance later in this chapter. The second section considers the effective Hamiltonian and a matrix representation for the harmonic Renner-Teller effect. The following sections deal with vibrational, spin-orbit and spin-rotational interactions, rotation, nuclear hyperfine structure, parity doubling and the Zeeman effect.

The energy level structures for the two types of Renner-Teller states studied in this thesis are then discussed in Chapter IV, including the evaluation of approximate expressions for the molecular parameters, energies and in particular the Zeeman interactions. The final sections discuss transition intensities, and the development of a sophisticated computer model of a Renner-Teller molecule.

III.2 The Renner-Teller Effect

III.2.1 Angular Momenta

In a non-rotating, linear triatomic molecule in an open shell state, there are three angular momenta of interest[1], **L**, **S** and **G**, [1], see Fig.III.1. The molecule-fixed z-axis is taken to be the axis along which the molecule lies in its equilibrium configuration [1].

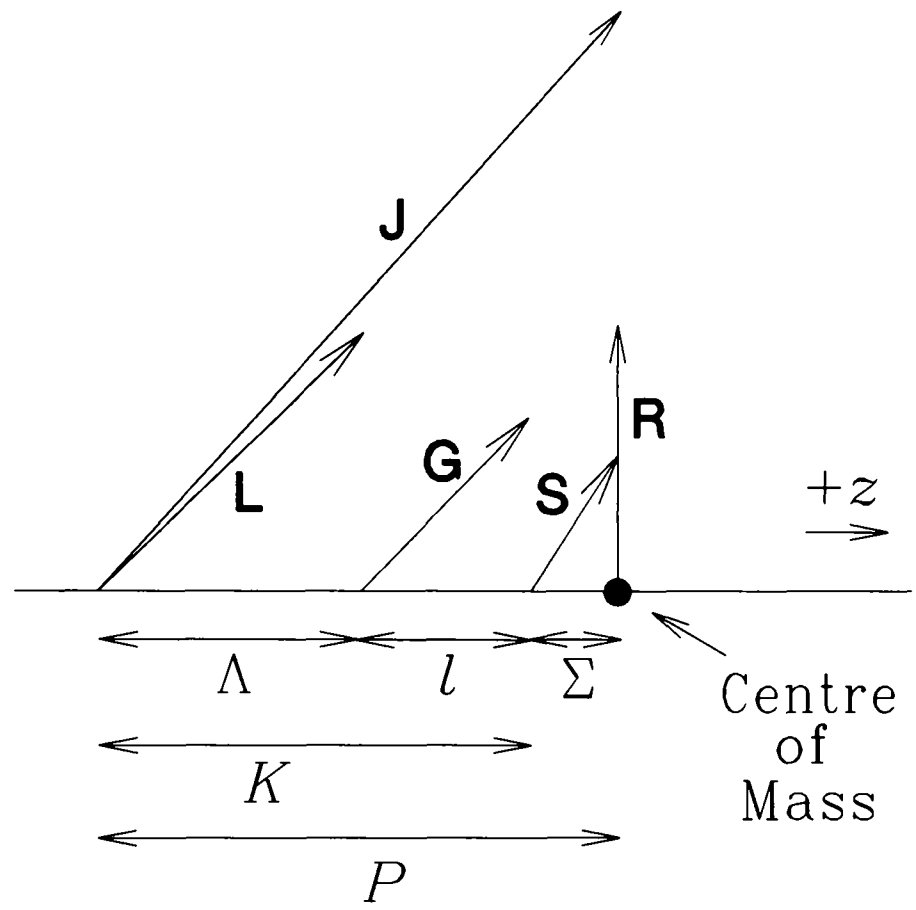

Figure III.1: A Hund's case (a) coupling scheme for a linear triatomic molecule in an orbitally degenerate electronic state. The rotational angular momentum **R** is discussed later.

There are electronic orbital and spin angular momenta, **L** and **S**. As in the case of a diatomic molecule, they precess about the z-axis, along which they have projections Λ and Σ, respectively [2]. In addition there is a vibrational angular momentum, **G**. This arises from the doubly degenerate bending mode of the nuclear framework, ν_2, which is coupled along the linear axis due to Coriolis interactions with the stretching modes [3, 4]. The degenerate bending normal co-ordinates [3, 5] can be labelled as Q_{2x} and Q_{2y}, corresponding to 'in-plane' and 'out-of-plane' bending [6, 7]. Q_{2x} and Q_{2y} are the components of a two-dimensional, isotropic harmonic oscillator [6, 7], as is shown in

[1]Rotation and nuclear spin are neglected at this point in the discussion.

Fig.III.2. **G** has a projection of l on the molecule-fixed z-axis, spanning

$$l = v_2, v_2 - 2, \cdots, -v_2. \tag{III.1}$$

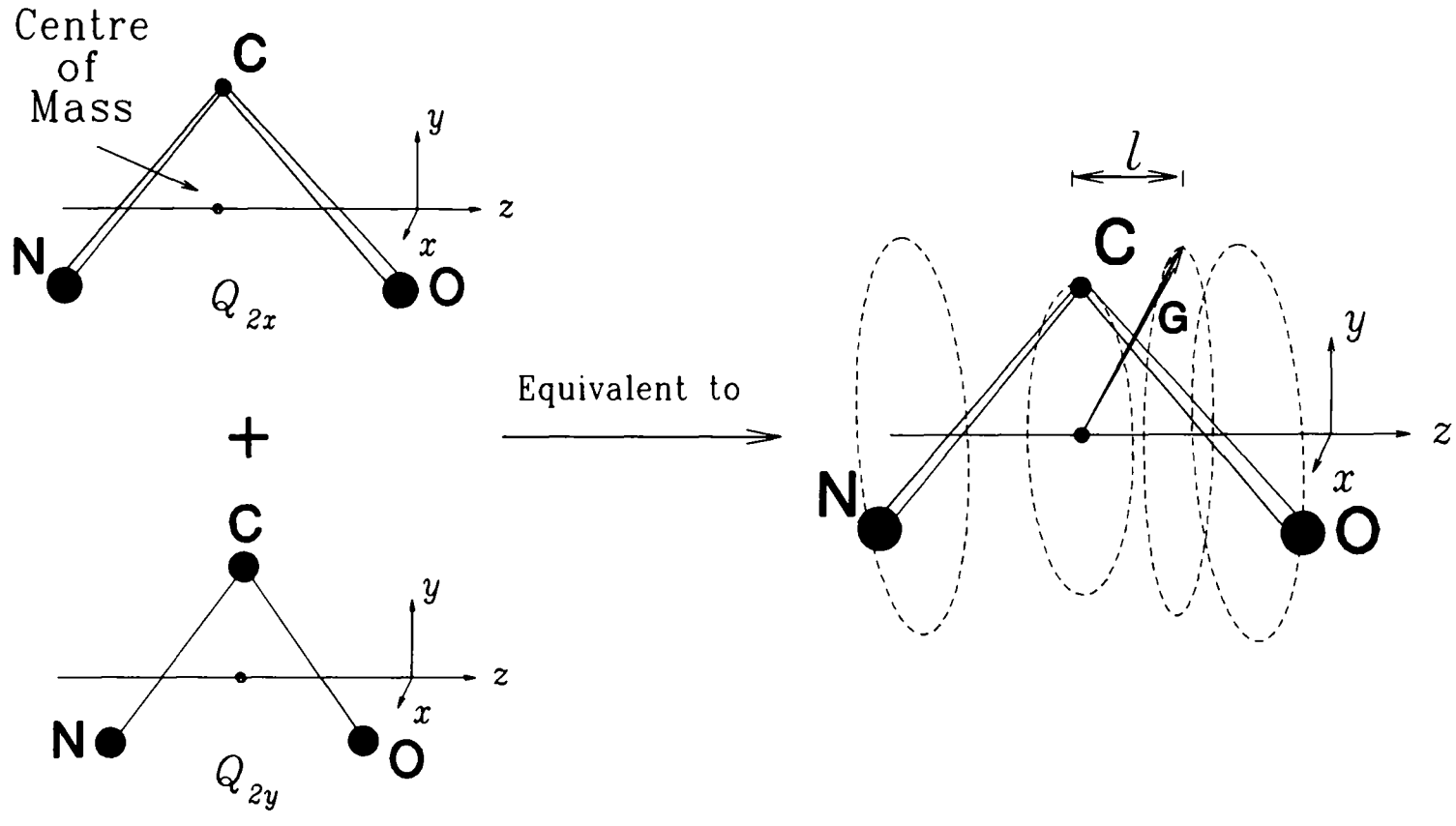

Figure III.2: A two-dimensional, isotropic harmonic oscillator. The two vibrational coordinates with a 90° phase difference can be expressed in terms of the vibrational angular momentum, **G**, and its projection on the z-axis, l. The bending amplitude is grossly exaggerated.

III.2.2 Vibronic Coupling

There is an electrostatic interaction between the electrons and nuclei which leads to a coupling between **G** and **L**; this a feature of the Renner-Teller effect [2]. This is an important interaction because it occurs between angular momenta of nuclear and electronic origin. Therefore, it causes a breakdown of the Born-Oppenheimer separation [8, 9], at least in those parts of the Hamiltonian concerned with the bending vibration. The interaction can be classified in terms of a vibronic quantum number K [2], where

$$K = \Lambda + l. \tag{III.2}$$

K is a rigorously good quantum number in the absence of rotation, which causes l-type interactions with other K states in the same and different v_2 manifolds [10].

The Renner-Teller effect lifts the degeneracy of the different K-components in a given v_2 manifold. In terms of the vector model, the different K values represent different relative orientations of **L** and **G**; each has a different interaction energy. Consider a $^2\Pi$ electronic state; for $v_2 = 0$, $l = 0$ and $\Lambda = \pm 1$, values of $K = \pm 1$ arise, giving a $^2\Pi$ vibronic state. For $v_2 = 2, l = \mp 2, 0, \Lambda = \pm 1$, the following states (denoted by $|\Lambda, l, K\rangle$ and grouped vertically in degenerate pairs) arise [10]:

$$\begin{array}{ccc} {}^2\Pi & {}^2\Pi & {}^2\Phi \\ |1,-2,-1\rangle & |1,0,1\rangle & |1,2,3\rangle \\ |-1,2,1\rangle & |-1,0,-1\rangle & |-1,-2,-3\rangle . \end{array}$$

The left-hand side of Fig.III.3 shows the scheme arising for $v_2 = 2$. The possible vibronic states arising in a given v_2 manifold can be predicted from group theory [11, 12]. The reducible representations of the vibronic state, Γ_{vibronic}, are given by the product of the electronic and bending vibrational symmetries[2], $\Gamma_{\text{elec.}} \otimes \Gamma_{\text{bend}}$. An 'ABC type' linear molecule belongs to the point group $C_{\infty v}$. The degenerate bending mode has Π symmetry; hence the vibrational species span the symmetric products of the reducible representation Π^x. The reason that only symmetric products are allowed is that the bending co-ordinate must be symmetric about the linear axis, *i.e.* it is an even function.

III.2.3 The Molecular Orbital Basis of the Renner-Teller Effect

Electronic configurations

Some insight into the nature of the Renner-Teller effect can be gained when the electronic wave function is described in terms of the electron occupancy of the molecular orbitals.

Consider the linear NCO molecule in its $\tilde{X}^2\Pi$ electronic state; its molecular orbitals can be modelled in terms of linear combinations of atomic orbitals. The dominant

[2]The stretching mode symmetries do not affect this result.

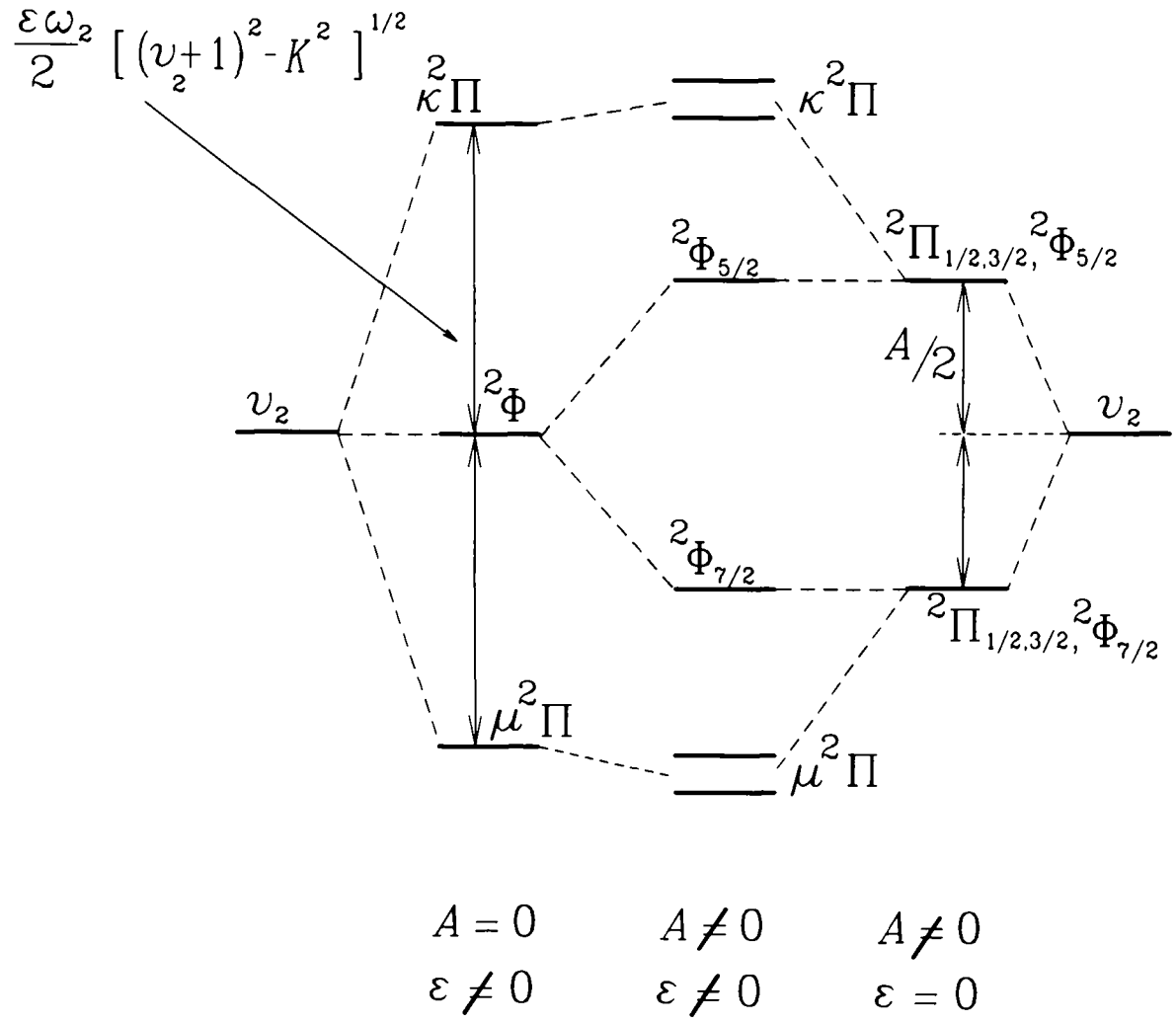

Figure III.3: The first order Renner-Teller and spin-orbit effects in the $v_2 = 2$ manifold. In this case both the Renner parameter ϵ, and the spin-orbit coupling constant A, are negative. The harmonic bending frequency is ω_2. See also [2].

electronic configuration of the ground state is then expected to be [13]–[15]

$$(1\sigma)^2\,(2\sigma)^2\,(3\sigma)^2\,(4\sigma)^2\,(5\sigma)^2\,(6\sigma)^2\,(1\pi)^4\,(7\sigma)^2\,(2\pi)^3\,.$$

The character of the $\tilde{X}^2\Pi$ electronic state arises from the unpaired electrons in the 2π orbital [11]. As is shown in Fig.III.4, this orbital is non-bonding and arises from an out-of-phase combination of N and O atom p_x and p_y orbitals. The molecular orbital has both an in-plane and out-of plane component; these are equivalent in the linear molecule.

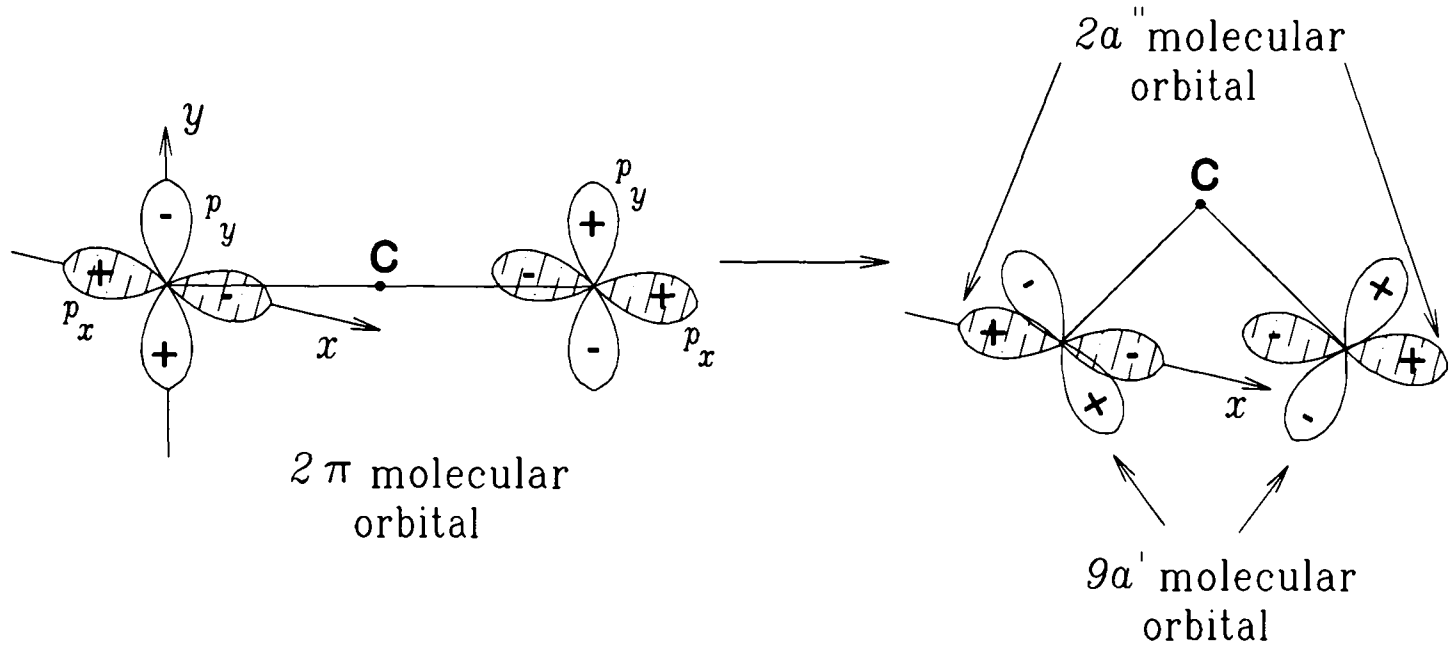

Figure III.4: The 2π molecular orbital in the linear molecule correlates with the out-of-plane $2a''$ and in-plane $9a'$ molecular orbitals in the bent molecule. The bending amplitude is grossly exaggerated.

Correlation of linear and bent electronic configurations

Consider bending the molecule in the yz-plane; the change in overlap of atomic orbitals will shift the energies of the molecular orbitals. This is shown by the Walsh diagram in Fig.III.5, which correlates the molecular orbitals of a bent (C_s) and a linear ($C_{\infty v}$) 'ABC' molecule, albeit somewhat schematically[3]. For small bending amplitudes, the molecular orbital energy orderings do not change. The important feature is the 2π orbital, whose in-plane (a') and out-of-plane (a'') components are not equivalent when the molecule is

[3]The Walsh diagram neglects spin-orbit coupling, electronic correlation, exchange interactions and also any steric factors.

bent, as shown in Fig.III.4. This means that the electronic wave function depends upon the bending angle. Two possible bent-molecule electronic configurations arise:

$$\cdots(2a'')^2(9a')^1$$

and

$$\cdots(2a'')^1(9a')^2.$$

The former is the lower in energy and places the unpaired electron in the plane of the bent molecule, giving a symmetric electronic wave function V'. The latter places the lone electron out of the plane of the molecule to give the unsymmetrical electronic wave function V''. The V potentials for the NCO radical are shown in Fig.III.6. They are degenerate in the linear configuration. This splitting into two electronic states is at the heart of the Renner-Teller effect. Vibronic and spin-orbit couplings mix together the eigenfunctions of the in-plane and out-of-plane potential curves [17].

Renner [16] first developed his theory using the V', V'' potentials and introduced the Renner parameter ϵ [16, 18] as a measure of the difference of the bending force constants λ_2 [18] for the two harmonic potential curves:

$$\epsilon = \frac{\lambda_2' - \lambda_2''}{\lambda_2' + \lambda_2''}, \tag{III.3}$$

where $\lambda_2 = 4\pi^2 c^2 \omega_2^2$. The magnitude of the force constant is a function of the curvature of the potential, therefore a negative value of ϵ is predicted for NCO, as has been determined, with V' being the lower potential curve when the molecule is bent. An interesting comparison can be made with the CCN free radical, a linear molecule with two electrons less than NCO. Its calculated ground state electronic configuration is

$$\cdots(1\pi)^4\,(7\sigma)^2\,(2\pi)^1\,.$$

In this case the lowest energy bent configuration is $\cdots(2a'')^1$, making V'' the lower energy curve and suggesting a positive value for ϵ, as has been determined.

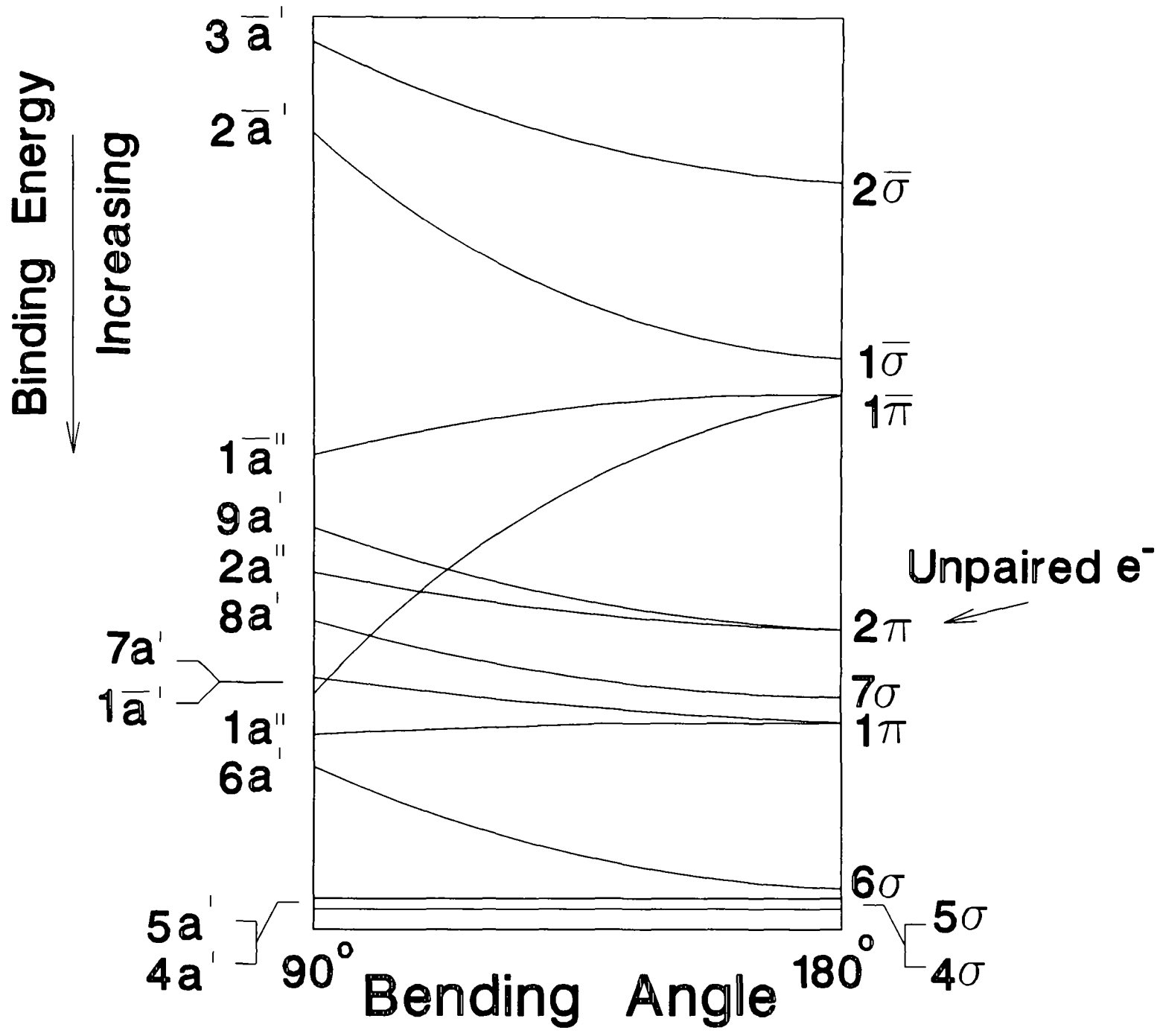

Figure III.5: A bent–linear Walsh correlation diagram for an 'ABC' molecule. The energy order of close-lying orbitals, *e.g.* 7σ and 1π, can change with the electronic configuration because spin-orbit coupling, electron correlations and steric factors are not considered.

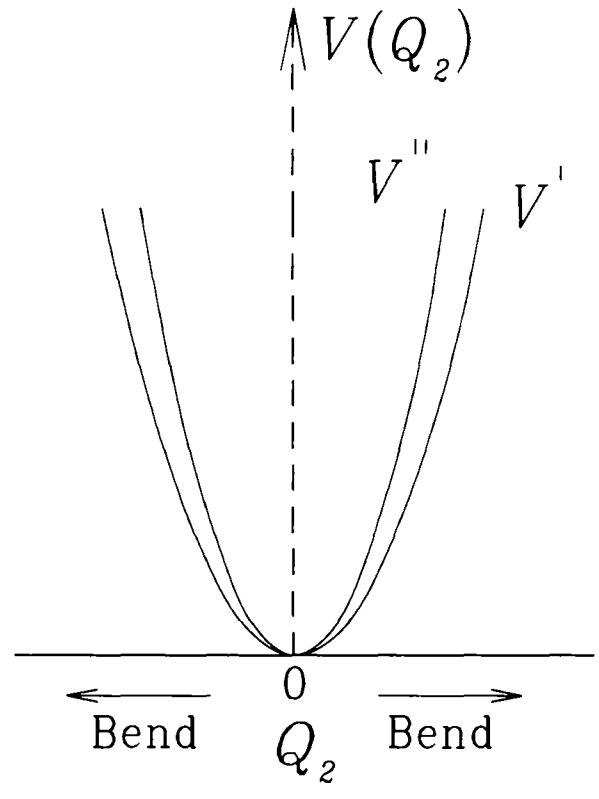

Figure III.6: For the NCO radical, the unpaired electron can lie in-plane or out-of plane as the molecule bends. This is the nature of the Renner-Teller effect, which gives rise to V'' and V' potential curves, respectively [16]. The order of the curves is correct for $\epsilon < 0$.

III.2.4 Spin-Orbit and Rotational Effects

Spin-Orbit coupling

When the magnetic spin-orbit coupling between **L** and **S** is considered, the quantum number [2, 10]

$$P = K + \Sigma \tag{III.4}$$

is defined, and the vibronic state is denoted by the term symbol

$$^{2S+1}|K|_P\,, \tag{III.5}$$

see Fig.III.3. This coupling scheme is called Hund's case (a), by analogy with the case of diatomic molecules [19], and is shown in Fig.III.1. The spin-orbit interaction is quenched by the Renner-Teller effect, and P can become ill-defined [10]. The states are then better described as mixtures of the spin-orbit components, denoted μ (lower energy) and κ (higher energy) after Hougen [10].

Rotation

When molecular rotation is considered, in the Hund's case (a) limit the good quantum number is J, where $\mathbf{J} = \mathbf{R}+\mathbf{L}+\mathbf{S}+\mathbf{G}$, with a z-axis projection P. When $\mathbf{S}$ is de-coupled from the molecule-fixed z-axis due to Renner-Teller and Zeeman interactions, the good rotational quantum number becomes the Hund's case (b) quantum number N rather than J, where $\mathbf{N} = \mathbf{L} + \mathbf{G} + \mathbf{R} = \mathbf{J} - \mathbf{S}$.

In the non-rotating molecule, there is a degeneracy of the states $|v_2, \Lambda, l, K; S\Sigma; JPM_J\rangle$ and $|v_2, -\Lambda, -l, -K; S, -\Sigma; J, -PM_J\rangle$; these pairs are known as Kramers doublets [2, 10]. Molecular rotation lifts this degeneracy to give K-type doubling [20], the analogue of Λ-type doubling [21] in diatomic molecules.

III.2.5 The Classification of Vibronic Levels

The K-states arising in a given v_2 manifold fall into three categories [10] when the Renner-Teller splitting is less than the spacing of adjacent v_2 manifolds. The categories are:

1. 'Unique' states with $K = v_2 + 1$. The unique state of a given K occurs in the lowest v_2 manifold for which this value of K arises. In these states there is no first order Renner-Teller effect; in the vector model it may be said that $\mathbf{L}$ and $\mathbf{G}$ do not oppose one another. The $^2\Phi$ vibronic states in Fig.III.3 provide an example.

2. $K = 0\,(^2\Sigma)$ vibronic states, which arise when v_2 is odd. In this case there is complete opposition between $\mathbf{L}$ and $\mathbf{G}$; the resulting states are often very close to Hund's case (b) in character. In general these states will show the largest Renner-Teller effect within the v_2 manifold.

3. 'Non-unique' states, which have $0 < K < v_2+1$. These states also show a first order Renner-Teller effect. The vibronic quenching of the orbital angular momentum again produces states close to Hund's case (b) in character. The $^2\Pi$ vibronic states in Fig.III.3 provide an example.

III.3 The Nomenclature for Normal Vibrational Modes

The references made to normal modes throughout this thesis are those for an unsymmetrical molecule. The convention of Herzberg [2, 22] is adopted as described below.

III.3.1 Symmetrical Linear Triatomic Molecules

The in-phase, symmetrical stretching normal mode is denoted ν_1, the bending normal mode is denoted ν_2 and the out-of-phase, antisymmetric stretching normal mode is denoted ν_3, see Fig.III.7 (note that for the in-phase stretching vibration there is no displacement of the central atom).

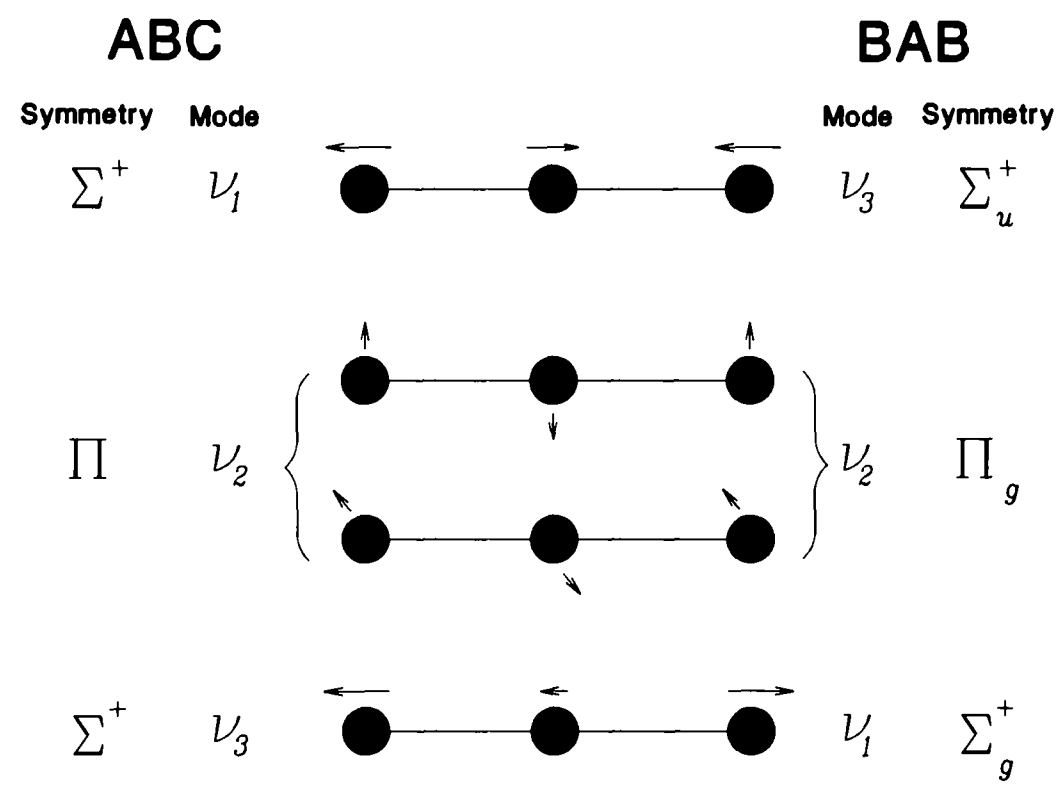

Figure III.7: Nomenclature for the normal modes of symmetrical and unsymmetrical linear triatomic molecules.

III.3.2 Unsymmetrical Linear Triatomic Molecules

The in-phase stretching normal mode is denoted ν_3, the bending normal mode is denoted ν_2 and the out-of-phase stretching normal mode is denoted ν_1, since this is generally the higher wave number stretching mode, see Fig.III.7. An unfortunate consequence of this convention is that the labelling of in-phase and out-of-phase stretching vibrations swaps over between linear BAB and ABC molecules.

III.3.3 A Note About the NCO Radical

It so happens that the stretching normal modes of NCO correspond very closely to the symmetric and antisymmetric stretching modes of a symmetrical linear triatomic molecule [23]. Therefore, it has been customary to name the normal modes as though they were those of a symmetrical molecule. This convention is not adopted here; instead the notation has reverted to the 'correct' form. This must be borne in mind when referring to previous studies of NCO.

III.4 The Calculation of Molecular Energy Levels

III.4.1 The Schrödinger Equation

In principle, the exact molecular energy levels, E_{exact}, can be found by solving the Schrödinger equation [24, 25] for the molecular system,

$$\mathcal{H}_{\text{exact}}\Psi = E_{\text{exact}}\Psi. \tag{III.6}$$

In Eq.(III.6), Ψ is the wave function containing all information about the system and $\mathcal{H}_{\text{exact}}$ is the exact Hamiltonian energy operator[4],

$$\mathcal{H}_{\text{exact}} = -\frac{\hbar^2}{2m}\nabla^2 + V, \tag{III.7}$$

where m is the mass, ∇^2 is the Laplacian kinetic energy operator[5] and V is the potential energy function.

The molecules of interest are many body molecular systems; it is not at present possible to solve Eq.(III.6) exactly for a greater than two-body system. Therefore, the *Born-Oppenheimer approximation* [8, 9] is invoked.

---

[4]Strictly Eq.(III.6) should be written in a Lorentz covariant gauge, with the Laplacian replaced by the D'Alembertian, $\Box^2 = \nabla^2 - \partial^2/\partial t^2$, and the Cartesian and temporal co-ordinates replaced by Minkowski four-vectors [25, 26]. Field quantisation effects should also be considered [26].

[5]In Cartesian co-ordinates, $\nabla = \partial/\partial x + \partial/\partial y + \partial/\partial z$.

III.4.2 The Born-Oppenheimer Separation

The Coulomb Hamiltonian

Fig.III.8 shows a triatomic molecule with a linear equilibrium configuration along the z-axis. The bond lengths of the molecule are frozen during its bending motion (stretching is neglected). The xz-plane is a reference plane; the plane containing the 'frozen' nuclei makes an angle φ with the reference plane. The plane containing the electronic coordinate and the z-axis, makes an angle ϑ with the reference plane [1].

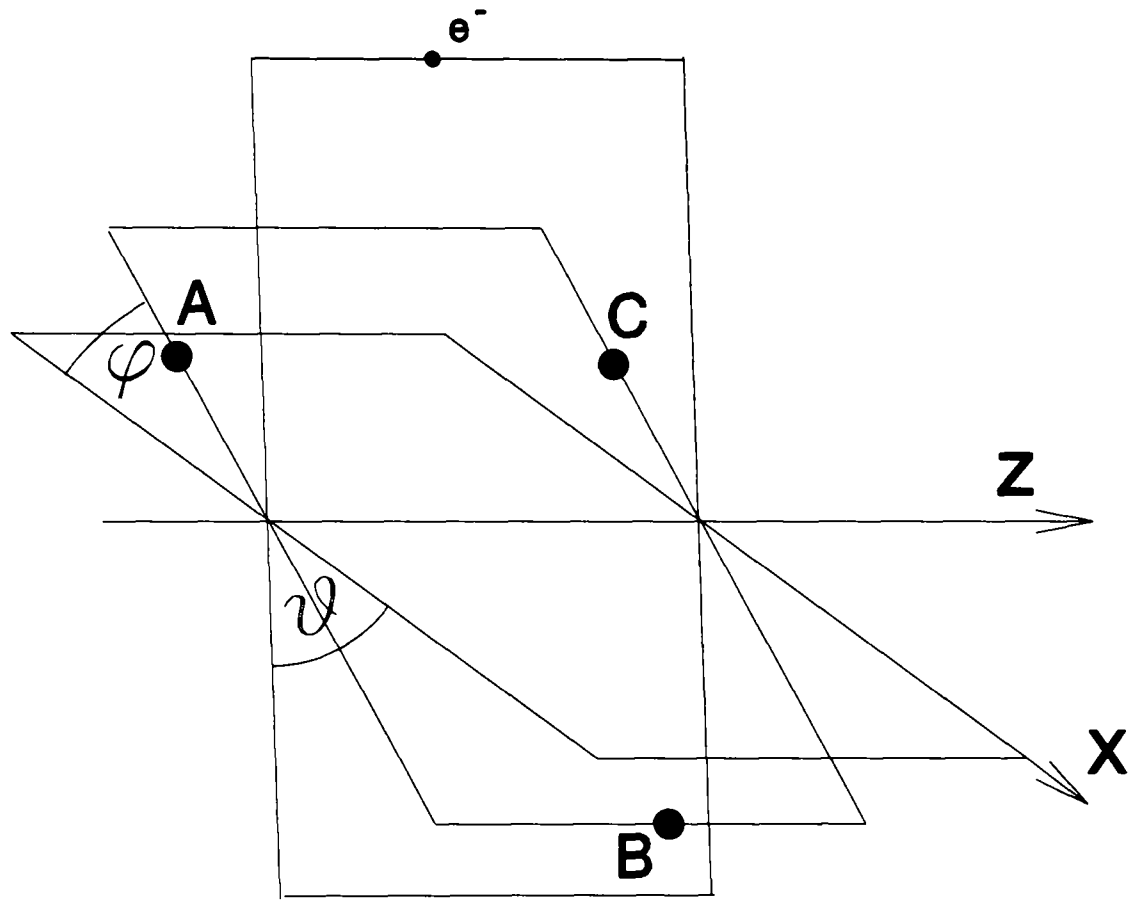

Figure III.8: An 'ABC' triatomic free radical, with a linear equilibrium configuration lying on the z-axis, frozen during its bending motion.

The major terms in the exact (but non-relativistic) molecular Hamiltonian arise from Coulombic interactions [1, 27]:

$$\mathcal{H} = \overbrace{-\frac{\hbar^2}{2m_e}\sum_{i=1}^{n}\nabla_i^2}^{T_e} \overbrace{-\frac{\hbar^2}{2}\sum_{\alpha=1}^{m}\frac{\nabla_\alpha^2}{M_\alpha}}^{T_n} \overbrace{+\sum_{\alpha,\beta(\alpha\neq\beta)}^{m}\frac{Z_\alpha Z_\beta e^2}{4\pi\epsilon_0 r_{\alpha\beta}}}^{V_{nn}(Q)} + \underbrace{\sum_{i,j(i\neq j)}\frac{e^2}{4\pi\epsilon_0 r_{ij}}}_{V_{ee}(r)} \underbrace{-\sum_{i=1}^{n}\sum_{\alpha=1}^{m}\frac{Z_\alpha e^2}{4\pi\epsilon_0 r_{i\alpha}}}_{V_{en}(r,Q)} . \tag{III.8}$$

Eq.(III.8) is written in Cartesian co-ordinates; the r_i are the inter-particle distances, Z_α refers to the atomic number of nucleus α, and m_e and M_α are the electronic and nuclear masses, respectively. The braces refer to the same terms expressed in internal electronic co-ordinates, r, and internal normal nuclear co-ordinates, Q [5]. T and V refer to kinetic and potential energies and e, n refer to electrons and nuclei, respectively.

Separation of nuclear and electronic terms

The solution of the Schrödinger equation using the Hamiltonian (III.8) is clearly a function of both the nuclear co-ordinates, Q, and the electronic co-ordinates, r:

$$\mathcal{H}(Q,r)\,\Psi = E\Psi. \tag{III.9}$$

An approximate solution can be found by neglecting the nuclear kinetic energy, T_n, which is a factor of m_e/M_α smaller than the electronic kinetic energy [1, 9, 27]. The wave function can then be factorised into two parts, one electronic and one nuclear:

$$\Psi_{\text{total}} = \psi_e \psi_n. \tag{III.10}$$

Furthermore, the assumption is made that the electronic energy only depends upon the equilibrium nuclear co-ordinates, and not the vibrational ones. This is the *crude adiabatic Born-Oppenheimer separation* [28]. The Schrödinger equation can then be solved for the electronic energy of the molecule in its linear equilibrium configuration (denoted by the superscript '0'):

$$\left[T_e + V_{ee}(r) + V_{en}\left(r, Q^0\right)\right] \psi_e^0(r) = E_e^0 \psi_e^0(r). \tag{III.11}$$

The resulting Born-Oppenheimer wave functions take the form [1]

$$\Psi^{BO} = \psi_e^0(r) \prod_i \chi_i(Q_i), \tag{III.12}$$

where the χ_i are the vibrational wave functions.

III.4.3 Representation of the Vibrational and Electronic Wave Functions

The degenerate bending vibration

The bending vibration is characterised by two degenerate normal co-ordinates, Q_{2x} and Q_{2y} (see Fig.III.2). The bending eigenvalues are solutions of the two-dimensional, isotropic harmonic oscillator equation [27, 29],

$$\left\{T_n + \frac{\lambda_2}{2}\left(Q_{2x}^2 + Q_{2y}^2\right)\right\}|v_2, l\rangle = (v_2 + 1)\, hc\omega_2\, |v_2, l\rangle\,, \tag{III.13}$$

where $\lambda_2 = 4\pi^2 c^2 \omega_2^2$ is the bending force constant and ω_2 is the harmonic bending wave number. It is convenient to transform the bending co-ordinates to polar form [29],

$$Q_2 = \left[Q_{2x}^2 + Q_{2y}^2\right]^{\frac{1}{2}} \text{ and } \varphi = \tan^{-1}\left(Q_{2y}/Q_{2x}\right). \tag{III.14}$$

The normalised form of the bending wave functions may then be written as [29]

$$|v_2, l\rangle = \chi_2\left(Q_2\right) = (-1)^{\frac{(v_2+|l|)}{2}}\, N_{v_2,|l|} e^{-\frac{\gamma_2 Q_2^2}{2}} Q_2^{|l|} L^{|l|}_{\left(\frac{v_2+|l|}{2}\right)}\left(\gamma_2 Q_2^2\right) e^{il\varphi}, \tag{III.15}$$

where N is a real, positive normalisation constant, and

$$G_z = Q_{2x}P_{2y} - Q_{2y}P_{2x} = -i\frac{h}{2\pi}\left(\frac{\partial}{\partial\varphi}\right), \tag{III.16}$$

with eigenvalue l. The P terms are the kinetic energy operators, which are the derivatives of the conjugate normal co-ordinate, for example

$$P_{2x} = -\frac{ih}{2\pi}\left(\frac{\partial}{\partial Q_{2x}}\right). \tag{III.17}$$

$L_s^r(x)$ is a Laguerre polynomial of degree $(s - r)$. The matrix elements of Q_2 [3, 5] have the dimensions of the quantity $\gamma_2^{-\frac{1}{2}}$, where

$$\gamma_i = \frac{2\pi\lambda_i^{\frac{1}{2}}}{h}. \tag{III.18}$$

Bending vibrational ladder operators

When evaluating matrix elements, it is useful to define the dimensionless normal coordinate operator [3]

$$q_i = \gamma_i^{\frac{1}{2}} Q_i, \tag{III.19}$$

whose matrix elements are dimensionless. The relevant constants can then be absorbed into those parameters of the Hamiltonian which are coefficients of the q_i. The matrix elements of q_2 are defined by the phase convention suggested by Di Lauro and Mills [29], to be real, positive quantities.

The ladder operators for the degenerate bending vibration are defined as

$$q_{2\pm} = \gamma_2^{\frac{1}{2}} Q_2 e^{\pm i\varphi} = q_{2x} \pm i q_{2y}, \tag{III.20}$$

and have the matrix elements given in Table III.1. The operator q_2^2 has matrix elements

Table III.1: The matrix elements[(a)] of the ladder operators $q_{2\pm}$ for a two-dimensional, isotropic harmonic oscillator.

$\Delta v_2 = +1$	$\Delta v_2 = -1$	Element
$\langle v_2+1, l+1 \vert q_{2+} \vert v_2, l\rangle$	$\langle v_2, l \vert q_{2-} \vert v_2+1, l+1\rangle$	$2^{-\frac{1}{2}}\left[v_2+l+2\right]^{\frac{1}{2}}$
$\langle v_2+1, l-1 \vert q_{2-} \vert v_2, l\rangle$	$\langle v_2, l \vert q_{2+} \vert v_2+1, l-1\rangle$	$2^{-\frac{1}{2}}\left[v_2-l+2\right]^{\frac{1}{2}}$

[(a)] The matrix elements are dimensionless.

diagonal in v_2 and l given by

$$\left\langle v_2, l \left| q_2^2 \right| v_2, l \right\rangle = \frac{1}{2} \left\langle v_2, l \left| [q_{2+}q_{2-} + q_{2-}q_{2+}] \right| v_2, l \right\rangle = (v_2+1), \tag{III.21}$$

there are also matrix elements of q_2 with $\Delta v_2 = \pm 2, \Delta l = 0, \pm 2$; they can be evaluated from Table III.1.

Representation of the electronic wave function

The electronic wave function can be expressed as a sum of the product of a radial function F and a spherical harmonic Y [30],

$$|\eta, \Lambda\rangle = \sum_L F_L(\iota_e) Y_{L,\Lambda}(\vartheta, \beta), \tag{III.22}$$

where η, L refers to the electronic state, and $\iota_e, \vartheta, \beta$ are the polar electronic co-ordinates in the molecule-fixed axis system. The projection along the molecule-fixed z-axis is defined by

$$L_z|\eta, \Lambda\rangle = -\frac{ih}{2\pi}\frac{\partial}{\partial\vartheta}|\eta, \Lambda\rangle = \Lambda|\eta, \Lambda\rangle \tag{III.23}$$

The ladder operators[6]

$$\Lambda_\pm^2 = e^{\pm 2i\vartheta} \tag{III.24}$$

can connect basis states with $\Delta\Lambda = \mp 2$ in the electronic manifold; for $\Lambda = \pm 1$ the matrix elements are [30]

$$\langle \eta\Lambda' = \pm 1|\, \Lambda_\pm^2\, |\eta\Lambda = \mp 1\rangle = -1. \tag{III.25}$$

The negative sign here produces a phase difference when compared with the conventions of Renner [16], Hougen [10], Pople and Longuet-Higgins [17] and Carrington *et al.*[1]. This is true for any matrix elements involving this operator.

III.4.4 The Zero Order Hamiltonian

The crude adiabatically Born-Oppenheimer separated wave functions [28] are the eigenfunctions of the zero order Hamiltonian [27]

$$\mathcal{H}^{(0)} = T_e + V_{ee}(r) + V_{en}\left(r, Q_2^0\right) + V_{nn}\left(Q_2^0\right) + T_n + \frac{1}{2}\lambda_2 Q_2^2, \tag{III.26}$$

where Q_2^0 refers to the linear equilibrium configuration of the molecule. Eq.(III.26) describes the energy of the molecule in its equilibrium configuration, but also includes a doubly degenerate harmonic bending potential which ideally is close to the average of V' and V'' shown in Fig.III.6. Note that in this approximation, the bending vibration

[6]The operators $\Lambda_\pm$ are not the same as $L_\pm$.

does not affect the electronic energy.

The effects of the interaction between nuclear and electronic motion, and the effects of the stretching vibrations, molecular rotation, spin-orbit coupling and the Zeeman effect can be introduced as a perturbation to the zero order eigensystem.

The Renner-Teller interaction

The interaction between the bending vibration and the electrons can be modelled by 'freezing' the molecule during its bending vibration. The relative displacement of the nuclei and electrons then leads to a non-uniform distribution of the nuclear and electronic charges. The electrostatic energy can then be expressed as a function of the angles between and separations of the nuclear and electronic charges [1, 31]. This expression can be resolved into to a product of spherical harmonics, using the spherical harmonic addition theorem [32]. The spherical harmonics can then be written as a series, a so-called *multipole expansion* [32]–[34]. Each term in the expansion has a radial Coulombic function and a Legendre function [34] which produces a polynomial expansion in $\cos(\vartheta - \varphi)$, see Fig.III.8. The form of the Renner-Teller Hamiltonian obtained up to the harmonic (quadrupolar) terms in the expansion is [1, 31]

$$\mathcal{H}_{RT}^{(1)} = \frac{V_{11}Q_2}{2}\left\{e^{i(\vartheta-\varphi)} + e^{-i(\vartheta-\varphi)}\right\} + V_{20}Q_2^2 + \frac{V_{22}Q_2^2}{2}\left\{e^{2i(\vartheta-\varphi)} + e^{-2i(\vartheta-\varphi)}\right\}. \quad \text{(III.27)}$$

The V terms are Coulombic terms and the angles are defined in Fig.III.8. Note that $Q_2 e^{\pm i(\vartheta-\varphi)} = Q_{2\mp}\Lambda_{\pm}$. The first term in Eq.(III.27) will only give a contribution to the Renner-Teller effect in second order; it is called the Herzberg-Teller term [27]. The second term is a correction to the bending energy, and the third term leads directly to a first order contribution to the Renner-Teller effect in the $\tilde{X}^2\Pi$ state. The Renner-Teller effective Hamiltonian for the $\tilde{X}^2\Pi$ state is produced by a Van Vleck or 'contact' transformation of a perturbation Hamiltonian including Eq.(III.27). Van Vleck's treatment is detailed in the original work [35]; more recent and extensive treatments are discussed in refs. [1, 27, 32, 36, 37].

The perturbation Hamiltonian

The rotational, single-electron spin-orbit and Zeeman interactions must also be considered as perturbations to the zero order system. The total perturbation Hamiltonian is then

$$\mathcal{H}^{(1)} = \mathcal{H}^{(1)}_{RT} + hcB\mathbf{R}^2 + hc\sum_i a_i \mathbf{l}_i.\mathbf{s}_i + \mathcal{H}^{(1)}_z, \tag{III.28}$$

where the explicit form of the Zeeman Hamiltonian, $\mathcal{H}_z$, is not given here but is described later in §III.12. The parameters B and a_i are the rotational constant and the microscopic spin-orbit coupling constant, respectively.

$\mathcal{H}^{(1)}$ generates matrix elements between the zero order eigenfunctions. The new eigenvalues and eigenfunctions can be obtained by diagonalising the matrix representation. A problem arises because there is an infinite number of configurations of the particles which constitute the molecule. Therefore, the zero order basis is infinite and an infinite matrix must be constructed and diagonalised. The problem is made tractable by performing a *Van Vleck* or *Contact* transformation as described below.

III.4.5 The Van Vleck Transformation

Restriction to a single electronic state

We focus on the ground $^2\Pi$ electronic state, ($\tilde{\mathrm{X}}^2\Pi$) and 'earmark' the block of the infinite matrix which spans all the spin, rotational and vibrational sub-states of $\tilde{\mathrm{X}}^2\Pi$. Degenerate perturbation theory is then applied to estimate the contribution of matrix elements between the $\tilde{\mathrm{X}}^2\Pi$ state and the infinite remainder. Pursuing this to the nth order of perturbation, reduces the significance of the remaining matrix elements between the $\tilde{\mathrm{X}}^2\Pi$ state and remote states to the order of $1/(\Delta E)^n$, where ΔE is the separation of these states. When additional terms become insignificant, the infinite remainder of states can be discarded.

Taken to third order, the Van Vleck transformation produces a *single state effective Hamiltonian* given by [36, 38]

$$\mathcal{H}^{\text{eff.}} = \mathcal{H}_0 + P_0\mathcal{H}'P_0 + P_0\mathcal{H}'a_0\mathcal{H}'P_0 + P_0\mathcal{H}'a_0\mathcal{H}'a_0\mathcal{H}'P_0 \tag{III.29}$$

$$- P_0\mathcal{H}'a_0^2\mathcal{H}'P_0\mathcal{H}'P_0 + \cdots. \tag{III.30}$$

where P_0 is the projection operator onto the zero order space of the $\tilde{X}^2\Pi$ state, $|0\rangle\langle 0|$,

$$a_0^k = \sum_{n\neq 0}^{\infty\,\dagger} \frac{|n\rangle\,\langle n|}{(E_0 - E_n)^k} \tag{III.31}$$

and $\mathcal{H}'$ is the perturbation Hamiltonian. The ket $|0\rangle$ refers to the $\tilde{X}^2\Pi$ state and the ket $|n\rangle$ refers to a remote state in the infinite remainder of states; the respective energies are E_0 and E_n. Each ket represents a block of states, within which all the sub-states are considered to be degenerate. The summation is restricted to all states outside the space of $|0\rangle$.

This procedure has isolated the $\tilde{X}^2\Pi$ state from all other electronic states. The matrix elements that used to connect the $\tilde{X}^2\Pi$ state with remote states have been replaced by effective operators. The effective operators act only within the $\tilde{X}^2\Pi$ state; the coefficients of these operators are parameters whose value represents the summation over remote states of the non-adiabatic matrix elements. Note that the effective operators have both diagonal and off-diagonal matrix elements within the space of the $\tilde{X}^2\Pi$ state. This is because the operators in Eq.(III.29) can project out from one place within the $\tilde{X}^2\Pi$ state to a remote state, and return to another place within the $\tilde{X}^2\Pi$ state.

Restriction to a single stretching vibrational level

A similar Van Vleck transformation can now be applied over the stretching vibrational sub-states of the $\tilde{X}^2\Pi$ state. This produces an effective Hamiltonian which operates in a single (v_1, v_3) level. The bending vibrational levels are not included in the vibrational transformation because the matrix representation will span these levels explicitly. This is necessary in order to model the harmonic Renner-Teller effect exactly.

Consequences of the Van Vleck transformation

The following sections are going to describe the terms in the effective Hamiltonian produced by the Van Vleck transformation. In each case, an indication will be given of the origin of the various terms.

In general, the terms involving the ladder operators $L_\pm$ are not written explicitly in the effective Hamiltonian; only terms involving L_z are retained. This is because the

matrix elements of $L_\pm$ cannot be evaluated easily. The operators $L_\pm$ project out to remote electronic states and their effects are absorbed into various terms in the effective Hamiltonian. These arise from operator products of second and higher order in the Van Vleck transformation, producing two types of term [39]:

1. Terms such as $a_i B l_{i,\mp} s_{i,\pm} N_\pm N_\mp$ and $a_i A l_{i,\pm} s_{i,\mp} L_\mp S_\pm$, where the l_i and s_i are the single electron (microscopic) spin and orbital angular momenta, and L and S are the macroscopic, adiabatic electron spin and orbital angular momenta. The parameters a_i and A are the microscopic and macroscopic spin-orbit coupling parameters, respectively. The terms shown contribute to the spin-rotation and spin-orbit parameters respectively. In both cases, the last two operators act within the $\tilde{X}^2\Pi$ electronic state and the matrix elements of $l_{i,\pm}$ and $s_{i,\pm}$, the non-adiabatic terms, are absorbed into the parameters.

   The important feature is that these operators return to basis states within the $\tilde{X}^2\Pi$ state which are characterised by the same value of Λ. The effects of these terms are congruent for basis functions with positive and negative space-fixed inversion parity.

2. Terms such as $a_i B l_{i,\pm} L_\pm s_{i,\mp} N_\mp$. These operators connect states within the $\tilde{X}^2\Pi$ block which differ in Λ by ± 2. The effect of such operator products is parity dependent; the example cited contributes to the term $p(N_+S_+ + N_-S_-)$ in the Λ-parity doubling effective Hamiltonian. Parity dependent effects will occur when ladder operators involving either **L** or **G** act twice in the same direction.

The operator products involving **G** are treated in a similar way in the vibrational Van Vleck transformation. The ladder operators $G_\pm$ project out to other (v_1, v_3) levels [3, 10] and give contributions in second and higher orders. The parity independent terms become absorbed into the vibrational dependences of the parameters, and the parity dependent terms give rise to l-parity doubling [20].

III.4.6 Basis Functions for a Renner-Teller Molecule

The representation of the Renner-Teller effective Hamiltonian, $\mathcal{H}^{\text{eff.}}_{RT}$ in §III.5, and the rotational, spin-rotational, spin-orbit and other terms in the effective Hamiltonian, is

constructed in parity conserving Hund's case (a) basis functions of the form

$$\frac{1}{\sqrt{2}}\left\{|\eta\Lambda; v_2 l; S\Sigma; JPM_J\rangle \pm (-1)^{(J-S-l)}\,|\eta, -\Lambda; v_2, -l; S, -\Sigma; J, -PM_J\rangle\right\}, \qquad \text{(III.32)}$$

where η refers to the electronic state, restricted to $\tilde{X}^2\Pi$ in this thesis. The upper and lower sign choice refers to positive and negative space-fixed inversion parity respectively, and $(-1)^{(J-S-l)}$ is a phase factor. The quantum number M_J is the projection of the total angular momentum J on a space-fixed Z-axis.

Phase convention

The phase factor is the eigenvalue of the space-fixed inversion operator, E^* [40, 41], which inverts the space-fixed co-ordinates of the basis wave function. The parity combinations are symmetric (positive parity) and antisymmetric (negative parity) under this operation. This phase convention differs from that of Hougen [10] and Pople [17] by producing a negative sign in all matrix elements in which $\Lambda_\pm^2$ acts.

III.4.7 Types of Basis Function

For a $^2\Pi$ electronic state, the basis functions characterising a vibronic state with a given (v_2, K), fall into two categories, each consisting of two spin functions. The two categories represent the only two ways in which a given value of K can arise for a particular value of v_2. The first category is denoted ψ_1 and is characterised by an l value of $l_1 = K - 1$,

$$\begin{aligned} |\psi_{1a}; v_2; \pm\rangle \quad = \quad & \frac{1}{\sqrt{2}}\left\{\left|1; v_2, l_1, K; S, \frac{1}{2}; J, K+\frac{1}{2}, M_J\right\rangle\right. \\ & \pm(-1)^p \left.\left|-1; v_2, -l_1, -K; S, -\frac{1}{2}; J, -\left(K+\frac{1}{2}\right), M_J\right\rangle\right\} \end{aligned} \qquad \text{(III.33)}$$

and

$$\begin{aligned} |\psi_{1b}; v_2; \pm\rangle \quad = \quad & \frac{1}{\sqrt{2}}\left\{\left|1; v_2, l_1, K; S, -\frac{1}{2}; J, K-\frac{1}{2}, M_J\right\rangle\right. \\ & \pm(-1)^p \left.\left|-1; v_2, -l_1, -K; S, \frac{1}{2}; J, -\left(K-\frac{1}{2}\right), M_J\right\rangle\right\} \end{aligned} \qquad \text{(III.34)}$$

The second type of function is denoted ψ_2 and is characterised by an l value of $l_2 = K+1 \equiv l_1+2$,

$$\begin{aligned} |\psi_{2a};v_2;\pm\rangle \quad &= \quad \frac{1}{\sqrt{2}}\left\{\left|-1;v_2,l_2,K;S,\frac{1}{2};J,K+\frac{1}{2},M_J\right\rangle\right. \\ &\pm(-1)^p \quad \left.\left|1;v_2,-l_2,-K;S,-\frac{1}{2};J,-\left(K+\frac{1}{2}\right),M_J\right\rangle\right\} \end{aligned} \tag{III.35}$$

and

$$\begin{aligned} |\psi_{2b};v_2;\pm\rangle \quad &= \quad \frac{1}{\sqrt{2}}\left\{\left|-1;v_2,l_2,K;S,-\frac{1}{2};J,K-\frac{1}{2},M_J\right\rangle\right. \\ &\pm(-1)^p \quad \left.\left|1;v_2,-l_2,-K;S,\frac{1}{2};J,-\left(K-\frac{1}{2}\right),M_J\right\rangle\right\} \end{aligned} \tag{III.36}$$

The basis set labels are given in Eq.(III.32). Note that in writing the basis functions K has been taken as an *unsigned* quantum number.

III.5 The Renner-Teller Effective Hamiltonian

Form of the Hamiltonian

Brown [27] has shown that the Van Vleck transformation leads to an effective Hamiltonian for the harmonic Renner-Teller effect of the form

$$\begin{aligned} \frac{\mathcal{H}_{RT}^{\text{eff.}}}{hc} \quad &= \quad \frac{T_n}{hc}+\frac{1}{2}\lambda_2^{\text{eff.}}Q_2^2+\frac{1}{2}\gamma_2\epsilon\omega_2Q_2^2\left\{e^{2i(\vartheta-\varphi)}+e^{-2i(\vartheta-\varphi)}\right\}+g_K\left(G_z+L_z\right)L_z \\ &+ \quad \Delta AL_zS_zQ_2^2+\Delta g_L^{(1)}L_ZQ_2^2\mu_BB_0, \end{aligned} \tag{III.37}$$

where $\lambda_2^{\text{eff.}} = 4\pi^2c^2[\omega_2^{(0)}+\Delta\omega_2^{(1)}-\Delta\omega_2^{(2)}]^2$ is the effective harmonic bending force constant. The last two terms in Eq.(III.37) are spin-orbit and Zeeman terms and will be defined and discussed later.

Bending vibrational terms

The contributions to the harmonic bending vibrational wave number, $\Delta\omega_2^{(1)}$ and $\Delta\omega_2^{(2)}$, arise in first and second order perturbation theory, respectively. The first term gives each electronic state a different bending wave number, the second is a contribution from

non-adiabatic vibronic interactions due to the Herzberg-Teller term in Eq.(III.27) [27].

The Renner parameter

The Renner parameter, ϵ, has both first and second order contributions [27]. The second order contribution arises from Herzberg-Teller interactions with Σ electronic states only. Theoretical calculations suggest that the first and second order contributions to ϵ are similar in magnitude but opposite in sign.

For example, ϵ for NCO has been determined in this study to be -0.1437. Chablo [42] has calculated *ab initio* values of the contributions to ϵ for NCO of $\epsilon^{(1)} = +0.714$ and $\epsilon^{(2)} = -0.748$, from the two terms in Eq.(III.27), predicting an effective value of $\epsilon = -0.0335$. The discrepancy between observation and prediction is thought to be indicative of the need to include higher order terms (in particular quartic ones) in the bending vibrational potential. Brown and Jørgensen [18, 43] have developed a detailed treatment of the Renner-Teller effect including these terms.

The g_K parameter

The g_K parameter is a K-dependent correction to the vibronic term values; it is given by [27]

$$g_K = \frac{\omega_2}{4\gamma_2} \sum_{\eta'=\Sigma,\Delta} \frac{(-1)^s \left|\langle \eta = \Pi | \, V_{11} \, | \eta' \rangle\right|^2}{(\Delta E)^2}. \tag{III.38}$$

The exponent s is even for Σ states and odd for Δ states; hence the observed value of g_K results from the difference of these contributions. The effect of g_K on the observed energy levels depends upon the balance of Renner-Teller and spin-orbit effects, as has been discussed by Brown [27].

III.5.1 Matrix Elements

The matrix elements of $\mathcal{H}^{\text{eff.}}_{RT}/hc$ can be evaluated using the results in Table III.2. The representation is diagonal in (v_1, v_3) and K but not in v_2.

The selection rules governing the matrix elements of $\mathcal{H}^{eff.}_{RT}$ are

$$\Delta v_2 = 0, \pm 2; \Delta v_1 = 0; \Delta v_3 = 0; \Delta K = 0; \Delta\Lambda = -\Delta l = \pm 2; \Delta\Sigma = 0; \Delta P = 0$$

Table III.2: The matrix elements[a] of the operators $q_{2\pm}^2\Lambda_{\mp}^2$.

$\langle\Lambda-2,v_2+2,l+2\vert\, q_{2+}^2\Lambda_-^2\,\vert\Lambda,v_2,l\rangle$	=	$-\frac{1}{2}\left[v_2+l+4\right]^{\frac{1}{2}}\left[v_2+l+2\right]^{\frac{1}{2}}$
$\langle\Lambda-2,v_2,l+2\vert\, q_{2+}^2\Lambda_-^2\,\vert\Lambda,v_2,l\rangle$	=	$-\left[v_2-l\right]^{\frac{1}{2}}\left[v_2+l+2\right]^{\frac{1}{2}}$
$\langle\Lambda-2,v_2-2,l+2\vert\, q_{2+}^2\Lambda_-^2\,\vert\Lambda,v_2,l\rangle$	=	$-\frac{1}{2}\left[v_2-l-2\right]^{\frac{1}{2}}\left[v_2-l\right]^{\frac{1}{2}}$
$\langle\Lambda,v_2+2,l\vert\, q_{2-}^2\Lambda_+^2\,\vert\Lambda-2,v_2,l+2\rangle$	=	$-\frac{1}{2}\left[v_2-l\right]^{\frac{1}{2}}\left[v_2-l+2\right]^{\frac{1}{2}}$
$\langle\Lambda,v_2,l\vert\, q_{2-}^2\Lambda_+^2\,\vert\Lambda-2,v_2,l+2\rangle$	=	$-\left[v_2-l\right]^{\frac{1}{2}}\left[v_2+l+2\right]^{\frac{1}{2}}$
$\langle\Lambda,v_2-2,l\vert\, q_{2-}^2\Lambda_+^2\,\vert\Lambda-2,v_2,l+2\rangle$	=	$-\frac{1}{2}\left[v_2+l\right]^{\frac{1}{2}}\left[v_2+l+2\right]^{\frac{1}{2}}$

[a] The matrix elements are dimensionless.

and it is diagonal in all other quantum numbers. The general form of the matrix elements, when expressed in the parity conserving basis functions ψ_1,ψ_2, and neglecting the terms in ΔA and $\Delta g_L^{(1)}$, which are discussed in §III.7 and §III.12, is

$$\langle\psi_1;v_2;\pm\vert\,\mathcal{H}_{RT}^{\text{eff.}}\,\vert\psi_1;v_2;\pm\rangle = n\omega_2+g_KK \tag{III.39}$$

$$\langle\psi_2;v_2;\pm\vert\,\mathcal{H}_{RT}^{\text{eff.}}\,\vert\psi_2;v_2;\pm\rangle = n\omega_2-g_KK \tag{III.40}$$

$$\langle\psi_2;v_2;\pm\vert\,\mathcal{H}_{RT}^{\text{eff.}}\,\vert\psi_1;v_2;\pm\rangle = -\frac{1}{2}\epsilon\omega_2\left[n^2-K^2\right]^{\frac{1}{2}} \tag{III.41}$$

$$\langle\psi_2;v_2\pm2;\pm\vert\,\mathcal{H}_{RT}^{\text{eff.}}\,\vert\psi_1;v_2;\pm\rangle = -\frac{1}{4}\epsilon\omega_2\left[n_m+\Lambda_mK\right]^{\frac{1}{2}}\left[n_m+\Lambda_mK+2\right]^{\frac{1}{2}} \tag{III.42}$$

where $n=(v_2+1)$ and the subscript m means that the quantum numbers are taken from the basis function with the smaller value of v_2. Note that there are no elements between *'a'* and *'b'* type spin functions, except when $K=0$. In the latter case there are no ψ_2 type basis functions, but $\mathcal{H}_{RT}^{\text{eff.}}$ connects the ψ_{1a} and ψ_{1b} basis functions to produce parity dependent Renner-Teller matrix elements. This is discussed in §IV.2.

The position occupied by the matrix elements for unique and non-unique states is shown in Fig.III.11. Explicit matrix representations are given in Chapter IV.

Higher order effects

Although $\mathcal{H}_{RT}$ only has matrix elements off-diagonal in v_2 by two, there will be higher order effects because these elements affect the zero order energies as demonstrated in Fig.III.10. The v_2+2 manifold is directly affected by the v_2+4 manifold; this affects the interaction between the v_2+2 and v_2 manifolds etc. Estimating these effects using

perturbation theory can be clumsy, and when the Renner-Teller splitting becomes comparable with the spacing of $\Delta v_2 = \pm 2$ levels, a second order perturbation treatment is not a good approximation to the exact result.

The work in this thesis adopts the more desirable method of setting up the matrix for the states of a given K in the manifold (v_1, v_2, v_3) and including explicitly the states of the same K in the manifolds (v_1, v_2', v_3), where $v_2' = v_2 \pm 2, v_2 \pm 4, v_2 \pm 6 \cdots$, truncated when including further members produces no significant change. The resulting matrix is then diagonalised to give the exact energies and eigenfunctions of $\mathcal{H}^0 + \mathcal{H}_{RT}^{\text{eff.}}$, plus other effective terms, such as spin-orbit, spin-rotation, rotational and Zeeman terms. An advantage of this approach is that the adiabatic Renner-Teller "quenching" effects on the spin-orbit and orbital Zeeman terms are modelled exactly and need not be estimated by perturbation theory (see Appendix C).

III.6 Vibrational Energy

The vibrational energy makes a direct contribution to the molecular energy levels. The harmonic contributions from vibrational mode i satisfy the harmonic oscillator equation [6]

$$\frac{\mathcal{H}_{\text{vib.}}^{\text{harm.}}}{hc} = \frac{1}{2}\left(P_i^2 + \omega_i q_i^2\right), \tag{III.43}$$

where $P_i = -(ih/2\pi)\partial/\partial Q_i$ is the kinetic energy operator conjugate to the normal co-ordinate Q_i, q_i is the corresponding dimensionless normal co-ordinate [3] and ω_i is the harmonic wave number. The total vibrational wave number can be expressed by the series expansion [2]

$$G(v_1 v_2 v_3) = \sum_{i=1}^{3} \omega_i \left(v_i + \frac{d_i}{2}\right) + \sum_{i=1}^{3}\sum_{j\geq i}^{3} x_{ij}\left(v_i + \frac{d_i}{2}\right)\left(v_j + \frac{d_j}{2}\right) + Bl^2 + g_{22}l^2 + \cdots, \tag{III.44}$$

where d_i is the degeneracy of vibrational mode i, and the x_{ij} are the first vibrational anharmonicities. Note that the harmonic contribution $\omega_2(v_2 + 1)$ has already been included in the Renner-Teller Hamiltonian and must only appear once in the actual matrix representation. Contributions to the x_{ij} parameters arise from anharmonic terms in the molecular potential energy function, and Coriolis terms. These contributions arise in

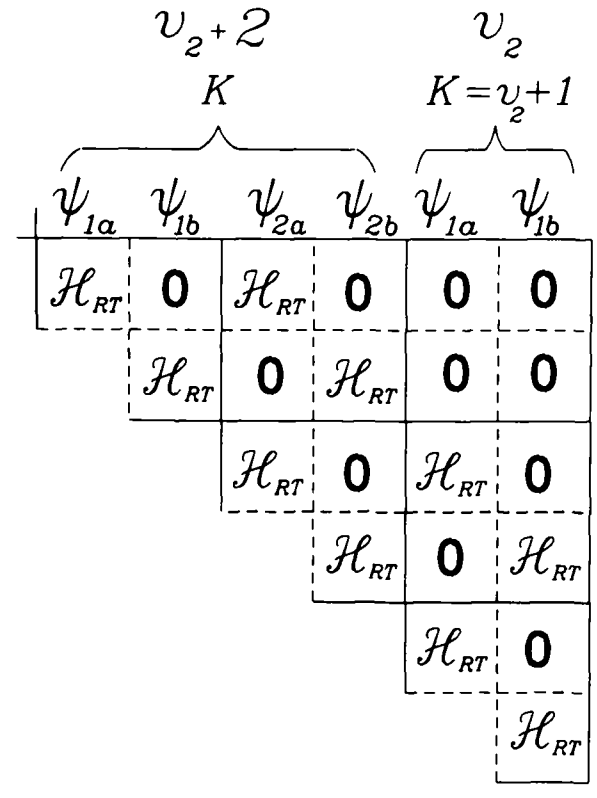

Figure III.9: A schematic representation of the position occupied by the Renner-Teller terms, collectively denoted $\mathcal{H}_{RT}$. A unique and a non-unique state are shown for comparison with Fig.III.11. The section shown is diagonal in J and (v_1, v_3).

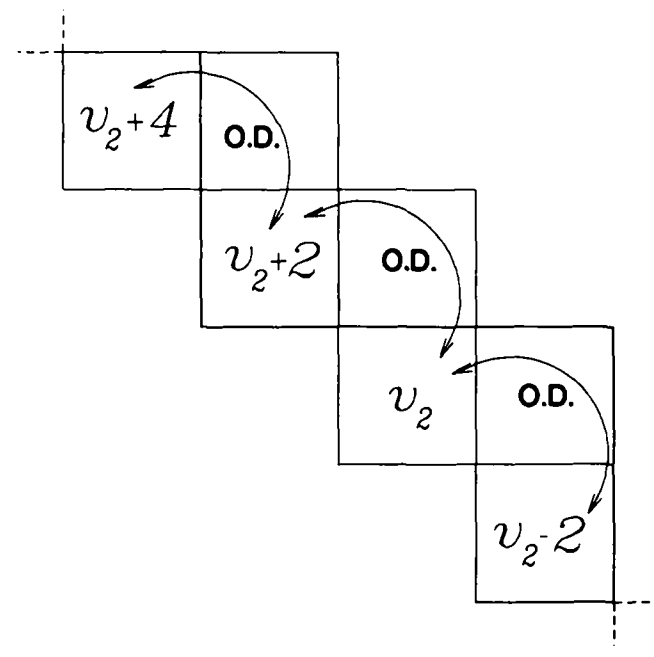

Figure III.10: The matrix elements of $\mathcal{H}_{RT}$ are only off-diagonal by $\Delta v_2 = \pm 2$, indicated by "O.D.". Higher order effects, indicated by the arrows, produce indirect effects from more remote v_2 levels with $\Delta v_2 = \pm 4, \Delta v_2 = \pm 6, \cdots$.

standard vibration-rotation theory, as discussed in [3].

The contribution Bl^2 arises from the Van Vleck transformation of the rotational Hamiltonian over the vibrational levels, as discussed in §III.8.2. This produces a contribution of order B; it has been neglected in the present study and so it is absorbed into the vibrational term values, producing a contribution of order α_B to the value of the vibrational band origin. Contributions of a similar magnitude arise from the neglect of terms involving $B\mathbf{L}^2$, as discussed in §III.8.2. The term $g_{22}l^2$ accounts for anharmonic vibrational angular momentum contributions [2]; it has been constrained to zero in this thesis since it is not determinable in the present study.

III.6.1 The Vibrational Band Origin

The vibrational transition $(v_1', v_2', v_3') \leftarrow (v_1'', v_2'', v_3'')$ is associated with a band origin,

$$\nu_0 = G(v_1', v_2', v_3') - G(v_1'', v_2'', v_3''). \tag{III.45}$$

Such a transition is denoted

$$1_{v_1''}^{v_1'} 2_{v_2''}^{v_2'} 3_{v_3''}^{v_3'}.$$

III.7 The Spin-Orbit Hamiltonian

The precession of the electrons about the linear z-axis (the "orbital motion") creates a magnetic field. The electron spin angular momentum has associated with it a magnetic moment which is aligned in this magnetic field, with a projection on the z-axis of $\Sigma = \pm 1/2$ for a single unpaired spin. This interaction is called spin-orbit coupling; it can be represented by the single electronic state, effective spin-orbit Hamiltonian [9]

$$\frac{\mathcal{H}_{SO}^{\text{eff.}}}{hc} = A_v L_z S_z = A_v \Lambda \Sigma, \tag{III.46}$$

where A is the macroscopic, adiabatic spin-orbit coupling parameter. The matrix elements of $\mathcal{H}_{SO}^{\text{eff.}}$ are completely diagonal in the $|\psi_1; v_1, v_2, v_3; \pm\rangle$ and $|\psi_2; v_1, v_2, v_3; \pm\rangle$ basis functions.

Off-diagonal spin-orbit interactions have been neglected in Eq.(III.46); they arise

through the operators

$$\sum_i a_i \left(l_{i,x}s_{i,x} + l_{i,y}s_{i,y}\right) = \sum_i a_i \frac{1}{2}\left[l_{i,+}s_{i,-} + l_{i,-}s_{i,+}\right], \tag{III.47}$$

where L_x, L_y and S_x, S_y have been expressed using the microscopic, single electron spin and orbital angular momentum operators for the ith electron [9], and a_i is the microscopic spin-orbit coupling parameter.

In a linear molecule there is no symmetric electrostatic field along the molecule-fixed x and y axes. As a consequence, $\mathbf{L}$ is not coupled along them and the operators L_x and L_y do not have well defined matrix elements[7] [44]. The effects of $L_\pm S_\mp$ are real nevertheless, and are absorbed into the spin-orbit coupling parameter A by the Van Vleck transformation used to decouple the single electronic state from all others. A similar transformation reduces $\mathcal{H}_{SO}^{\text{eff}}$ to operate in a single vibrational level; the elements off-diagonal in the vibrational quantum numbers are replaced by the vibrational dependence of A as discussed in §III.8.2.

Brown [27] has shown that an additional contribution to A arises from non-adiabatic Herzberg-Teller interactions projecting to remote Σ and Δ electronic states. This term was included in the Renner-Teller effective Hamiltonian, Eq.(III.37). The leading term arises in the third order of degenerate perturbation theory in the Van Vleck transformation used to form the Renner-Teller effective Hamiltonian:

$$\begin{aligned}
A^{(3)} \;=\; & \sum_{\eta''=\Sigma,\Delta} \left\{ \frac{1}{(\Delta E)^2} \langle \eta\Lambda; v_2 l; K | \mathcal{H}' | \eta''\Lambda''; v_2'' l''; K \rangle \right. \\
\times \; & \left. \langle \eta''\Lambda''; v_2'' l''; K | AL_zS_z | \eta''\Lambda''; v_2'' l''; K \rangle \langle \eta''\Lambda''; v_2'' l''; K | \mathcal{H}' | \eta\Lambda; v_2' l; K \rangle \right\} \\
- \; & \sum_{\eta''=\Sigma,\Delta} \left\{ \frac{1}{(\Delta E)^2} \langle \eta\Lambda; v_2 l; K | \mathcal{H}' | \eta''\Lambda''; v_2'' l''; K \rangle \right. \\
\times \; & \left. \langle \eta''\Lambda''; v_2'' l''; K | \mathcal{H}' | \eta\Lambda; v_2' l; K \rangle \langle \eta\Lambda; v_2' l; K | AL_zS_z | \eta\Lambda; v_2' l; K \rangle \right\},
\end{aligned} \tag{III.48}$$

where $\mathcal{H}'$ is the Herzberg-Teller term in Eq.(III.27). The resulting additional term in the

[7] In a spherically symmetric system, *i.e.* an atom, L_x, L_y and L_z are all well defined. In a cylindrically symmetric linear molecule, there is a symmetric electrostatic field only along the molecule-fixed z-axis. $\mathbf{L}$ is only coupled along this axis, and so only L_z is well defined. As a consequence, the matrix elements of L_x and L_y cannot be evaluated using standard angular momentum theory.

effective Hamiltonian is [27]

$$\Delta A Q_2^2 L_z S_z \rightarrow \Delta A \, (v_2 + 1) \, \Lambda\Sigma. \tag{III.49}$$

The parameter ΔA is a spin-orbit parameter with a coefficient of $(v_2 + 1)$, *i.e.* its dependence upon the quantum numbers in the basis set of the effective Hamiltonian is identical to that of α_{2_A} (see §III.8.2), into which it is absorbed[8]. Note that the connection to remote electronic states arises through the Herzberg-Teller term; the spin-orbit operator acts adiabatically and can be written in its macroscopic form in Eq.(III.48).

III.8 Molecular Rotation

III.8.1 General Features

The rotation of the molecular framework about its centre of mass produces a rotational angular momentum $\mathbf{R}$, as shown in Fig.III.1. Classically, $\mathbf{R}$ is given by a sum over the vector product of the distances of the particles in the system from the centre of mass, $\mathbf{r}_i$, and their linear momenta, $\mathbf{p}_i$, viz

$$\mathbf{R} = \sum_i \mathbf{r}_i \times \mathbf{p}_i, \tag{III.50}$$

where m_i is the mass of the ith particle. The dominant contribution to $\mathbf{R}$ is from the nuclei because the electrons are some 1.8×10^3 times lighter. Within the Born-Oppenheimer approximation, the electrons are dragged round with the nuclei and do not 'lag' behind, so they make a small adiabatic contribution to the rotational energy. Eq.(III.50) shows that $\mathbf{R}$ is perpendicular to the plane of rotation; in Fig.III.1, it points up or down in the plane of the paper (depending on the direction of rotation) when the molecule rotates into and out of the paper. The energy of such a rotor is given classically by the sum of the rotational energy about the three Cartesian inertial axes α,

$$E_{\text{rot.}} = \sum_{\alpha=1}^{3} \frac{\mathbf{R}_{(\alpha)}^2}{2I^{(\alpha)}}, \tag{III.51}$$

[8]Studies of isotopomers should allow ΔA to be separated, since it will have a different mass dependence to the Coriolis and anharmonic contributions to $\alpha_{2,A}$.

where $I^{(\alpha)} = \sum_i m_i \mathbf{r}_i^{(\alpha)2}$ is the moment of inertia about the axis α and the $\mathbf{r}_i^{(\alpha)}$ are measured along this axis. In a quantum mechanical system, the classical Hamilton function [24] for $\mathbf{R}$ is replaced by its Hamiltonian operator, $-\mathbf{R}h/2\pi$. The operator equivalent of Eq.(III.51) is the rotational Hamiltonian, in which the constants are absorbed into the rotational parameter for the equilibrium configuration of the molecule, $B_e^{(\alpha)}$ [3, 4]:

$$\frac{\mathcal{H}_{rot.}}{hc} = \sum_{\alpha=1}^{3} B_e^{(\alpha)} \mathbf{R}_{(\alpha)}^2, \tag{III.52}$$

with $B_e^{(\alpha)}$ in wave number units given by[9]

$$B_e^{(\alpha)} = \frac{h}{8\pi^2 I^{(\alpha)} c}. \tag{III.53}$$

Note from Fig.III.1 that for a linear molecule, the moment of inertia about the z-axis is extremely small[10] and that the moments of inertia about the x and y axes are equivalent. Therefore, the sum over α is dropped and a single rotational constant can be used. The B value is a characteristic of the spacing of rotational lines in the spectrum; its relation to the moment of inertia means that it contains information on the bond lengths in the molecule. Since $B_e \propto r^{-2}$, the rotational constant of a triatomic molecule is expected to be of the order of 25% of that of a diatomic molecule consisting of similar sized atoms. To quantify this, the rotational constant of CO is $\approx 1.9\,\mathrm{cm}^{-1}$ and that for NCO is $\approx 0.4\,\mathrm{cm}^{-1}$.

III.8.2 The Rotational Hamiltonian

Initial Hamiltonian

The rotational Hamiltonian operating over all states is

$$\frac{\mathcal{H}_{rot.}}{hc} = B\mathbf{R}^2 = B\left[\mathbf{J} - \mathbf{S} - \mathbf{L} - \mathbf{G}\right]^2 = B\left[\mathbf{N} - \mathbf{L} - \mathbf{G}\right]^2 \tag{III.54}$$

[9] As is discussed later, vibrational and Coriolis contributions [3] to B mean that Eq.(III.53) is not valid for the non-equilibrium configuration.

[10] In a linear molecule, a very small moment of inertia about the molecule-fixed z-axis arises mainly from the electrons. The rotational constant $B^{(z)}$ is so large that this can almost always be ignored. It is discussed in connection with microwave spectroscopy in [45].

In writing Eq.(III.54), Coriolis terms have been omitted; these are discussed below and are given explicitly in Watson's vibration-rotation Hamiltonian, described by Mills [3]. The operators in Eq.(III.54) can be expanded in terms of their orthonormal Cartesian components, also using the ladder operators

$$\hat{O}_{\pm} = \hat{O}_x \pm i\hat{O}_y.$$

It is also useful to define [44]

$$\left\langle \hat{O}_{\perp}^2 \right\rangle = \hat{\mathbf{O}}^2 - \hat{O}_z^2,$$

where $\hat{\mathbf{O}}$ represents a first rank (vector) operator. This enables Eq.(III.54) to be rewritten as

$$\begin{aligned} \frac{\mathcal{H}_{rot.}}{hc} &= B\mathbf{N}^2 + B\left[\left\langle L_{\perp}^2 \right\rangle + L_z^2\right] + B\left[\left\langle G_{\perp}^2 \right\rangle + G_z^2\right] - B\left[N_+L_- + N_-L_+\right] \\ &- B\left[N_+G_- + N_-G_+\right] + B\left[L_+G_- + L_-G_+\right]. \end{aligned} \tag{III.55}$$

Electronic Van Vleck transformation of $\mathcal{H}_{rot.}$

At this stage, the terms involving $L_{\pm}$ are absorbed into effective operators; they produce second order non-adiabatic electronic contributions to the rotational constant, the spin-rotation parameter and the Λ-type doubling parameters.

The term $B\langle L_{\perp}^2 \rangle$ cannot simply be evaluated in a cylindrically symmetric system, as was discussed in §III.7. This term is not J dependent and is a constant for a given state, so it can be absorbed into the term value. A choice is made not to include the term BL_z^2, which is also absorbed into the term value because it is J independent; this decision gives rise to the $\mathbf{N}^2$ effective Hamiltonian, rather than the $\mathbf{R}^2$ one. The subtle difference between these two formalisms is discussed below in §III.8.3 and in ref. [38].

A similar treatment of terms involving $L_{\pm}G_{\mp}$ gives second order electronic contributions to the vibronic term values and also to the vibrational dependences of the molecular parameters.

Vibrational Van Vleck transformation of $\mathcal{H}_{rot.}$

A Van Vleck transformation over the (v_1, v_2, v_3) levels of the $\tilde{X}^2\Pi$ state removes the terms in Eq.(III.55) involving the vibrational angular momentum $\mathbf{G}$. The ladder operators $G_\pm$ are [3, 4, 10] given by

$$G_\pm = \zeta^{(x)}_{2x,i}\left[q_{2\mp}p_i\left(\frac{\omega_i}{\omega_2}\right)^{\frac{1}{2}} + p_{2\pm}q_i\left(\frac{\omega_2}{\omega_i}\right)^{\frac{1}{2}}\right], \tag{III.56}$$

with $i = 1, 3$ and $\zeta^{(x)}_{2x,i}$ the Coriolis coupling constant between the bending mode and stretching mode i, about the molecule-fixed x-axis. The expression is obtained by noting that for a linear molecule, $\zeta^{(x)}_{2x,i} = -\zeta^{(x)}_{2y,i}$ [46]. $G_\pm$ projects out to other vibrational levels and produces a term proportional to $B(v_2 + 1)(v_i + 1/2)$, which is constant for a given vibrational level. This is a Coriolis contribution from the degenerate bending mode to the vibrational anharmonicity, $x_{2i}(v_2+1)(v_i+1/2)$. The term BG_z^2 also gives a contribution to the vibrational energy, as discussed in §III.6. In a similar manner, the operator $J_\pm G_\mp$ (contained within $N_\pm G_\mp$) gives rise to a second order, rotationally dependent term which is a Coriolis contribution to α_{i_B}. The operators $G_\pm S_\mp$ also produce a second order contribution to the spin-spin parameter[11] λ. In a doublet state there is only one unpaired electron spin and so λ is zero[12]. Parity dependent terms involving $G_\pm G_\pm$ give rise to second order contributions to the the l-type doubling parameter q^* [20].

Note that for the rotational Hamiltonian, the Van Vleck transformation also operates over the bending vibrational levels, so that the resulting effective rotational Hamiltonian operates in a single (v_1, v_2, v_3) level. The resulting $\mathbf{N}^2$ single-state effective rotational Hamiltonian is now

$$\mathcal{H}^{\text{eff.}}_{rot.} = B\mathbf{N}^2. \tag{III.57}$$

The effect of all other angular momenta has now been absorbed elsewhere, as described above.

In performing a Van Vleck transformation over the vibrational levels, the effect of the vibrational modes on the moment of inertia must be considered. This gives rise to centrifugal distortion effects as described next.

---

[11]The spin-spin effective Hamiltonian is $\mathcal{H}^{\text{eff.}}_{SS} = \frac{1}{3}\lambda_v(3S_z^2 - \mathbf{S}^2)$ [30].

[12]The approximation is made that there are no low-lying electronic states of higher spin multiplicity, so the adiabatic macroscopic spin operator can be used.

Centrifugal distortion

In a classical, rotating system there is a centripetal force $\mathbf{F} = -\sum_i m_i \mathbf{v}_i^2/\mathbf{r}_i$, which acts radially inwards. The equal and opposite reaction to this is the centrifugal force, which imparts a tendency for a rotating body to extend outwards, an effect known as centrifugal distortion. The important point is that the magnitude of this force increases non-linearly as the system rotates faster. In a quantum system, centrifugal distortion effects 'stretch' the molecule, so that its moment of inertia increases and its effective rotational constant decreases. The 'stretching' due to centrifugal distortion effectively samples other vibrational levels and mixes them into the vibrational level of interest.

The effect of the vibrational modes on the moment of inertia of the molecule can be modelled using the inverse inertial tensor, $\boldsymbol{\mu}$, developed by Watson and described by Mills [3]. The rotational constant can be written

$$B^{(\alpha)} = \frac{\mu_{\alpha\alpha}}{8\pi^2 c} = \frac{h}{8\pi^2 I^{(\alpha)} c}, \tag{III.58}$$

where the inverse inertial tensor is expressed as a Taylor series in the normal co-ordinates [3],

$$\mu_{\alpha,\beta} = \mu^{(e)}_{\alpha,\alpha}\delta_{\alpha,\beta} + \sum_r \frac{\partial \mu_{\alpha,\beta}}{\partial q_r} q_r + \sum_s \sum_r \frac{\partial^2 \mu_{\alpha,\beta}}{\partial q_r \partial q_s} q_r q_s + \cdots, \tag{III.59}$$

where the symbols α, β denote inertial axes. The derivatives of the $\boldsymbol{\mu}$ tensor are, for example, given by [3]

$$\frac{\partial \mu_{\alpha,\beta}}{\partial q_r} = -\frac{\left(\frac{\partial I^{(\alpha\beta)}}{\partial Q_r}\right)}{I^{(\alpha)} I^{(\beta)}} \gamma_r^{\frac{1}{2}}. \tag{III.60}$$

Terms such as Eq.(III.60) have $\Delta v_r = \pm 1$ and when included in the initial rotational Hamiltonian, they give rise to rotational terms when $B\mathbf{R}^2$ operates in second order in the vibrational Van Vleck transformation. These purely harmonic terms give rise to the first centrifugal distortion constant, D, with an effective Hamiltonian [30]

$$\frac{\mathcal{H}^{\text{eff.}}_{\text{CD}}}{hc} = -D\mathbf{N}^4. \tag{III.61}$$

In a linear 'ABC' type molecule, the in-phase stretching mode ν_3 produces the largest change in the size of the molecule (see §III.3). To a first approximation, only this mode

affects the moment of inertia. A perturbation theory estimate of D is given by [4]

$$D_e \approx \frac{4B_e^3}{\omega_3^2}, \tag{III.62}$$

where it is assumed that the ν_1 vibrational mode has negligible effect on the moment of inertia.

Higher terms in the expansion of $\boldsymbol{\mu}$ give rise to further centrifugal distortion parameters $H, L, \cdots$, which include anharmonic contributions. The magnitude of these terms is of order $(B_e/\omega_3)^{m-1}\omega_3$, where m is the power of $\mathbf{R}$. For example, assuming that the in-phase stretching mode gives the dominant contribution (since it has the greatest effect upon the inverse inertial tensor), with ω_3 typically $10^3\,\mathrm{cm}^{-1}$ and with $B_e \approx 0.5\,\mathrm{cm}^{-1}$, a value of $D_e \approx 5 \times 10^{-7}\,\mathrm{cm}^{-1}$ is estimated.

Vibrational dependence of the molecular parameters

The Van Vleck transformation over the vibrational levels of the single electronic state produces an effective Hamiltonian operating in a single vibrational level. This procedure introduces a vibrational dependence to the parameters, with contributions from harmonic and anharmonic potential energy terms as well as Coriolis terms [3].

The value of a parameter P in the vibrational level (v_1, v_2, v_3) is related to its equilibrium value P_e, by a series of vibrational dependence parameters such that

$$P_{(v_1,v_2,v_3)} = P_e + \sum_{i=1}^{3} \alpha_{i,P}\left(v_i + \frac{d_i}{2}\right) + \sum_{i=1}^{3}\sum_{j\geq i}^{3} \beta_{ij,P}\left(v_i + \frac{d_i}{2}\right)\left(v_j + \frac{d_j}{2}\right) + \cdots, \tag{III.63}$$

where d_i is the degeneracy of normal mode i. The sign of the alpha term is opposite to that adopted by Herzberg [2], but it is more logical since all the vibrational dependence terms now enter with a positive sign.

Summary of the single state effective rotational and centrifugal distortion Hamiltonians

In summary, an $\mathbf{N}^2$ single electronic and vibrational state effective rotational and centrifugal distortion Hamiltonian has been obtained, which can be written as

$$\frac{\mathcal{H}^{\text{eff.}}_{rot.} + \mathcal{H}^{\text{eff.}}_{CD}}{hc} = \left(B_v - D_v\mathbf{N}^2 + H_v\mathbf{N}^4 + L_v\mathbf{N}^6 + \cdots\right).\mathbf{N}^2. \tag{III.64}$$

The vibrational dependence of the molecular parameters is indicated here by the subscript v. The following subsection considers the alternative $\mathbf{R}^2$ formulation of the Hamiltonian, in which terms in the orbital angular momentum are retained during the Van Vleck transformation.

III.8.3 The $\mathbf{N}^2$ and $\mathbf{R}^2$ Hamiltonians

The rotational operator $\mathbf{R}$ can be expanded using simple vector addition (see Fig.III.1), to give

$$\mathbf{R} = \mathbf{J} - \mathbf{L} - \mathbf{S} - \mathbf{G}. \tag{III.65}$$

A problem arises in evaluating the matrix elements of $\mathbf{R}$ (and hence of $\mathbf{R}^2$) because this requires the evaluation of matrix elements involving $\mathbf{L}$. As discussed in §III.7, L_x and L_y do not have well defined matrix elements in a linear molecule.

One approach to this is to include $\mathbf{L}$ anyway, and to write $\mathcal{H}^{\text{eff.}}_{rot.}$ in terms of $\mathbf{R}^2$. The matrix elements involving $\mathbf{L}$ are carried throughout but only those involving L_z, *i.e.* Λ, are evaluated. This is called the $\mathbf{R}^2$ Hamiltonian formalism; it is described in [47].

A preferable approach is to use the $\mathbf{N}^2$ effective Hamiltonian [30, 38], first developed by Brown *et al.*[30], in which $\mathcal{H}^{\text{eff.}}_{rot.}$ is written in terms of $\mathbf{N}^2 = (\mathbf{R} - \mathbf{L} - \mathbf{G})^2$. Here it is explicit that $\mathbf{L}$ is not included. $\mathbf{N}$ is not the correct form of the rotational operator, but it differs from $\mathbf{R}$ only in terms involving $\mathbf{L}$ and $\mathbf{G}$. In the matrix representation of $\mathcal{H}^{\text{eff.}}_{rot.}$, the terms in $\mathbf{L}$ are not J-dependent, rather they are an additive constant for a given vibrational state[13]. The terms in $\mathbf{G}$ give contributions arising in standard vibration-rotation theory in both formulations of the Hamiltonian.

[13]In the centrifugal distortion terms, which involve $\mathbf{N}^4$ etc, this is not strictly true, but since the matrix elements of L_x, L_y are generally not known, they have to be neglected anyway.

The $\mathbf{N}^2$ Hamiltonian is used throughout in this thesis; everywhere that $\mathbf{R}$ would occur in an effective Hamiltonian, it is replaced by $\mathbf{N}$.

Both the $\mathbf{N}^2$ and the $\mathbf{R}^2$ formulations of the effective Hamiltonian will describe any data set equally well. The evaluation of L_z in the $\mathbf{R}^2$ Hamiltonian produces Λ dependent differences in the definitions of the parameters between the two formalisms. The parameters are simply inter-convertible using the formulae given in Appendix D. It is important to know which Hamiltonian is used in a particular analysis, and to correct the parameters accordingly before comparing them with others.

III.9 Rotational Matrix Elements

III.9.1 The Matrix Representation of $\mathbf{N}^2$

The rotational and centrifugal distortion terms require the matrix representation of

$$\mathbf{N}^2 = (\mathbf{J} - \mathbf{S})^2 . \tag{III.66}$$

which expands to give

$$\mathbf{N}^2 = \mathbf{J}^2 + \mathbf{S}^2 - 2J_z S_z - (J_+ S_- + J_- S_+) . \tag{III.67}$$

This allows $\mathbf{N}^2$ to be evaluated using operators with good Hund's case (a) eigenvalues, since N itself is not a good quantum number in the Hund's case (a) limit[14]. The matrix elements can be evaluated from the following standard results of angular momentum theory (in the molecule-fixed axis system) [32, 44]:

$$\mathbf{S}^2 |S\Sigma\rangle = S(S+1)|S\Sigma\rangle , \tag{III.68}$$

$$S_z |S\Sigma\rangle = \Sigma |S\Sigma\rangle , \tag{III.69}$$

$$S_\pm |S\Sigma\rangle = [(S \mp \Sigma)(S \pm \Sigma + 1)]^{\frac{1}{2}} |S\Sigma \pm 1\rangle , \tag{III.70}$$

$$\mathbf{J}^2 |JPM_J\rangle = J(J+1)|JPM_J\rangle , \tag{III.71}$$

$$J_z |JPM_J\rangle = P|JPM_J\rangle , \tag{III.72}$$

[14] $\mathbf{N}^2$ is diagonal in the Hund's case (b) limit.

$$J_{\pm}\,|JPM_J\rangle \;=\; [(J \pm P)\,(J \mp P + 1)]^{\frac{1}{2}}\,|JP \mp 1, M_J\rangle\,. \qquad \text{(III.73)}$$

The formulae given for S are perfectly general for angular momenta defined in the molecule-fixed axis system. The total angular momentum $\mathbf{J}$ is defined in the space-fixed system, giving rise to anomalous commutation relations [48] in the molecule-fixed Lie group [34] of $\mathbf{J}$, and hence an anomalous sign of its molecule-fixed ladder operators [48]–[50].

The representation of $\mathbf{N}^2$, evaluated in the parity conserving basis functions Eqs.(III.33)–(III.36) is

	$\lvert\psi_{xa}; v_1v_2v_3; \pm\rangle$	$\lvert\psi_{xb}; v_1v_2v_3; \pm\rangle$
$\lvert\psi_{xa}; v_1v_2v_3; \pm\rangle$	$\left(J+\frac{1}{2}\right)^2 - K$	$-z^{\frac{1}{2}}$
$\lvert\psi_{xb}; v_1v_2v_3; \pm\rangle$	Symmetric	$\left(J+\frac{1}{2}\right)^2 + K$

where $z = [(J + 1/2)^2 - K^2]$ and K is the vibronic quantum number (which is taken always to be positive for matrix elements in the ψ_1 and ψ_2 basis functions). The subscript 'x' in the kets is either 1 or 2.

III.9.2 The $\mathbf{N}^2$ Effective Rotational Hamiltonian

From the above representation, matrix elements of

$$\frac{\mathcal{H}^{\text{eff.}}_{rot.} + \mathcal{H}^{\text{eff.}}_{CD}}{hc} = \left[B - D\mathbf{N}^2 + H\mathbf{N}^4\right].\mathbf{N}^2 \qquad \text{(III.74)}$$

are readily evaluated.

III.9.3 Centrifugal Distortion of the Spin-Orbit Coupling

In the same way that rotation changes the size of the molecule and produces centrifugal distortion, it also produces a change in the electrostatic field along the linear axis of the molecule. This affects the spin-orbit interaction in a manner expressed by the centrifugal distortion of the spin-orbit coupling [30],

$$\frac{\mathcal{H}^{\text{eff.}}_{SOCD}}{hc} = \frac{A_{D_v}}{2}\left[\mathbf{N}^2 L_z S_z + L_z S_z \mathbf{N}^2\right] \qquad \text{(III.75)}$$

This effective Hamiltonian must be expressed as an hermitian average of the operators $\mathbf{N}^2$ and $L_z S_z$. This is because the matrix representation of an observable quantity must be hermitian (symmetric about the leading diagonal) [24]. Note that the matrix representation of this term differs between the ψ_1 and ψ_2 type basis functions.

III.9.4 The Spin-Rotation Interaction

First order interaction

The rotation of the molecule produces a small magnetic field to which the electron spin will couple weakly. This is the first order spin-rotation interaction [9], whose effective Hamiltonian is [30]

$$\frac{\mathcal{H}_{SR}^{\text{eff.}}}{hc} = \gamma_v^{(1)} \mathbf{N}.\mathbf{S}. \tag{III.76}$$

This expands to give

$$\frac{\mathcal{H}_{SR}^{\text{eff.}}}{hc} = \gamma_v^{(1)} \left[J_z S_z - \mathbf{S}^2 + \frac{1}{2} \left(J_+ S_- + J_- S_+ \right) \right]. \tag{III.77}$$

Second order interaction

The spin-rotation parameter γ, is observed to increase dramatically down a series of similar molecules consisting of progressively heavier atoms. The first order spin rotation interaction described above, is not expected to change significantly down such a series. The observed trend is explained by the non-adiabatic contribution to the effective spin-rotation Hamiltonian. This arises through a second order product of the rotational and spin orbit operators [9, 30, 51], in the Van Vleck transformation used to reduce the effective Hamiltonian to a single electronic state. It can be expressed by the degenerate perturbation theory projection operator

$$\frac{\mathcal{H}_{SR}^{\text{eff.}(2)}}{hc} = \sum_{n \neq 0} |0\rangle \frac{\langle 0| B N_{\pm} L_{\mp} |n\rangle \langle n| a_i l_{i,\pm} s_{i,\mp} |0\rangle}{E_0 - E_n} \langle 0|, \tag{III.78}$$

where $|0\rangle$ is the $\tilde{\mathrm{X}}^2\Pi$ state and $|n\rangle$ is one of the remote electronic states, denoted by primed quantum numbers. The spin-orbit coupling operator has been written in its microscopic form and there is an implicit summation over the i electrons.

The kets, *e.g.* $|0\rangle = |\eta\Lambda; v_2 l; S\Sigma; JPM_J\rangle$, can be factorised into products of orbital, vibrational and spin/rotational basis functions,

$$|0\rangle = |\eta\Lambda\rangle \sum_{v_2,l} |v_2, l\rangle \sum_{S,\Sigma,J,P,M_J} |S\Sigma; JPM_J\rangle \,. \tag{III.79}$$

The operators do not act upon $|v_2, l\rangle$ or $|J, M_J\rangle$, so the projection operator will be diagonal in these quantities and they are dropped in the following development. The operators $L_\mp$ and $l_{i,\pm}$ act only upon the orbital basis functions, and the $S_\pm$ and $s_{i,\mp}$ operators act only upon the spin functions, allowing Eq.(III.78) to be factorised to give

$$\begin{aligned} \frac{\mathcal{H}_{SR}^{\text{eff.}(2)}}{hc} &= \sum_{\eta',\Lambda'} |0\rangle \frac{a_i B \langle\eta\Lambda| L_\mp |\eta'\Lambda'\rangle \langle\eta'\Lambda'| l_{i,\pm} |\eta\Lambda\rangle}{E_0 - E_n} \\ &\times \sum_{S\Sigma'P'} \langle S\Sigma P| N_\pm |S\Sigma'P'\rangle \langle S\Sigma'P'| s_{i,\mp} |S\Sigma P\rangle \langle 0| \,. \end{aligned} \tag{III.80}$$

The inner summation runs over the complete set of spin and rotational functions in the electronic state η'. Assuming the spin wave functions to be normalised, the inner sum therefore exhibits closure over the ket and bra which form a representation of the spin group in η',

$$\sum_{S\Sigma'P'} |S\Sigma'P'\rangle \langle S\Sigma'P'| = 1. \tag{III.81}$$

Therefore, the projection operator reduces to a sum over the product of two matrix elements. The first is a non-adiabatic orbital matrix element, and the second is a spin-rotation matrix element operating only within the basis set of the effective Hamiltonian.

Assuming that there are no nearby electronic states of triplet or higher spin multiplicity, the microscopic operator $s_{i,\mp}$ can be replaced by the macroscopic operator $S_\mp$ to give

$$\frac{\mathcal{H}_{SR}^{\text{eff.}(2)}}{hc} = \sum_{\eta',\Lambda'} |0\rangle \underbrace{\frac{a_i B \langle\eta\Lambda| L_\pm |\eta'\Lambda'\rangle \langle\eta'\Lambda'| l_{i,\mp} |\eta\Lambda\rangle}{E_0 - E_n}}_{\gamma^{(2)}} \underbrace{\langle S\Sigma P| N_\pm S_\mp |S\Sigma P\rangle}_{\text{N.S}} \langle 0| \,. \tag{III.82}$$

This is a part of the spin-rotational effective Hamiltonian, with a second order contribution to the spin-rotation parameter, $\gamma^{(2)}$, as shown above. This contribution to the total γ is dominant even in Σ electronic states. The increase in magnitude of γ down a series

of progressively heavier atom molecules is explained by the increase in the spin-orbit coupling parameter, A (or $\sum_i a_i$). The complete effective spin-rotational Hamiltonian is a sum of the first and second (and higher) order contributions

$$\mathcal{H}_{SR}^{\text{eff.}} = \mathcal{H}_{SR}^{\text{eff.}(1)} + \mathcal{H}_{SR}^{\text{eff.}(2)} + \cdots, \tag{III.83}$$

where the observed value of γ is $\gamma^{(1)} + \gamma^{(2)} + \cdots$.

Kawaguchi *et al.*[52] have shown that there is also a fourth order contribution to γ. This contribution arises in a similar manner to the second order term above, but now the Herzberg-Teller vibronic term in Eq.(III.27) is included in the perturbation Hamiltonian and it acts twice.

The spin-rotation term has associated with it a centrifugal distortion given by

$$\frac{\mathcal{H}_{SRCD}^{\text{eff.}}}{hc} = \gamma_D \left[\mathbf{N}.\mathbf{S}\right].\mathbf{N}^2 \tag{III.84}$$

III.9.5 The Complete Rotational Effective Hamiltonian

Form of the matrix

The matrix representation of all the above terms plus the spin-orbit and Zeeman terms, is collectively denoted $\mathcal{H}'$. The representation of $\mathcal{H}'$ is diagonal in v_2 and also in the ψ_1, ψ_2 basis functions, *i.e.* $\langle \psi_{1a,1b} | \mathcal{H}' | \psi_{2a,2b} \rangle = 0$. The representation falls into 2×2 diagonal blocks as shown in Fig.III.11 and it exists for each basis state included in the matrix. For comparison, Fig.III.9 shows the position occupied by the Renner-Teller terms in the same matrix.

Tabulation of matrix elements

The explicit form of the rotational, spin-orbit, spin-rotation and centrifugal distortion matrix elements for the ψ_1 and ψ_2 basis functions (excluding the Renner-Teller and

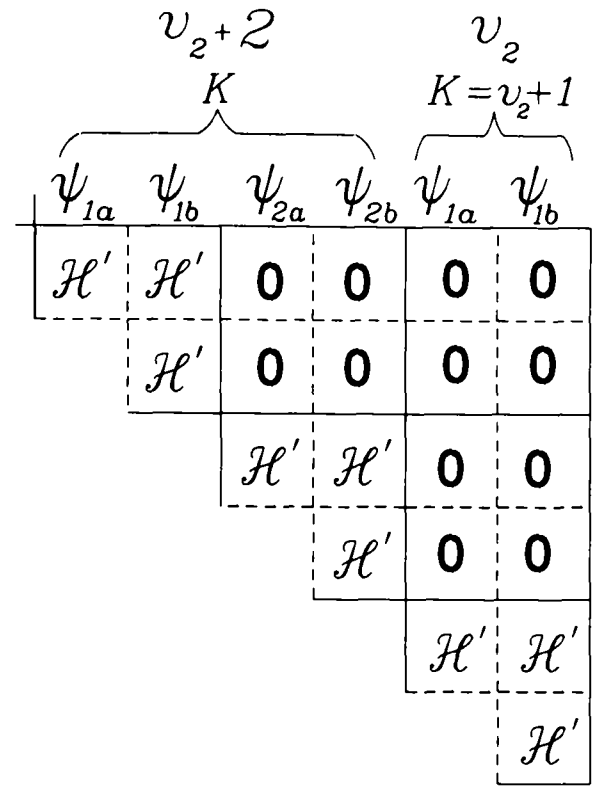

Figure III.11: A schematic representation of the position occupied by the rotational, spin-orbit, spin-rotation, centrifugal distortion and Zeeman terms, collectively denoted $\mathcal{H}'$. A unique and a non-unique state are shown. The representation of $\mathcal{H}'$ always falls into a 2×2 block-diagonal matrix form. The section shown is diagonal in J and (v_1, v_3); the matrix is symmetrical about the leading diagonal, so only one half is shown.

Zeeman terms) is given below:

$\lvert\psi_{1a}; v_1v_2v_3; \pm\rangle$	$\lvert\psi_{1b}; v_1v_2v_3; \pm\rangle$
$G(v_1, v_2, v_3)$ $+\frac{1}{2}\left[A_v + A_{D_v}\left\{\left(J+\frac{1}{2}\right)^2 - K\right\} + \gamma_v(K-1)\right.$ $\left.+\gamma_{D_v}\left\{\left(J+\frac{1}{2}\right)^2[K-2]+K\right\}\right]$ $+B_v\left\{\left(J+\frac{1}{2}\right)^2 - K\right\}$ $-\left(J+\frac{1}{2}\right)^2\left[D_v\left\{\left(J+\frac{1}{2}\right)^2 - 2K + 1\right\}\right.$ $\left.-H_v\left\{\left(J+\frac{1}{2}\right)^2\left[\left(J+\frac{1}{2}\right)+3(1-K)\right]-K\right\}\right]$	$-z^{\frac{1}{2}}\left[B_v - \frac{1}{2}\gamma_v - \frac{1}{2}\gamma_{D_v}\left\{\left(J+\frac{1}{2}\right)^2+1\right\}\right.$ $\left.-\left(J+\frac{1}{2}\right)^2\left\{2D_v - H_v\left[3\left(J+\frac{1}{2}\right)^2+1\right]\right\}\right]$
Symmetric	$G(v_1, v_2, v_3)$ $-\frac{1}{2}\left[A_v + A_{D_v}\left\{\left(J+\frac{1}{2}\right)^2 + K\right\} + \gamma_v(K+1)\right.$ $\left.-\gamma_{D_v}\left\{\left(J+\frac{1}{2}\right)^2[K+2]-K\right\}\right]$ $+B_v\left\{\left(J+\frac{1}{2}\right)^2 + K\right\}$ $-\left(J+\frac{1}{2}\right)^2\left[D_v\left\{\left(J+\frac{1}{2}\right)^2 + 2K + 1\right\}\right.$ $\left.-H_v\left\{\left(J+\frac{1}{2}\right)^2\left[\left(J+\frac{1}{2}\right)+3(1+K)\right]+K\right\}\right]$

and

$\lvert\psi_{2a}; v_1v_2v_3; \pm\rangle$	$\lvert\psi_{2b}; v_1v_2v_3; \pm\rangle$
$G(v_1, v_2, v_3)$ $-\frac{1}{2}\left[A_v + A_{D_v}\left\{\left(J+\frac{1}{2}\right)^2 - K\right\} - \gamma_v(K-1)\right.$ $\left.-\gamma_{D_v}\left\{\left(J+\frac{1}{2}\right)^2[K-2]+K\right\}\right]$ $+B_v\left\{\left(J+\frac{1}{2}\right)^2 - K\right\}$ $-\left(J+\frac{1}{2}\right)^2\left[D_v\left\{\left(J+\frac{1}{2}\right)^2 - 2K + 1\right\}\right.$ $\left.-H_v\left\{\left(J+\frac{1}{2}\right)^2\left[\left(J+\frac{1}{2}\right)+3(1-K)\right]-K\right\}\right]$	$-z^{\frac{1}{2}}\left[B_v - \frac{1}{2}\gamma_v - \frac{1}{2}\gamma_{D_v}\left\{\left(J+\frac{1}{2}\right)^2+1\right\}\right.$ $\left.-\left(J+\frac{1}{2}\right)^2\left\{2D_v - H_v\left[3\left(J+\frac{1}{2}\right)^2+1\right]\right\}\right]$
Symmetric	$G(v_1, v_2, v_3)$ $+\frac{1}{2}\left[A_v + A_{D_v}\left\{\left(J+\frac{1}{2}\right)^2 + K\right\} - \gamma_v(K+1)\right.$ $\left.+\gamma_{D_v}\left\{\left(J+\frac{1}{2}\right)^2[K+2]-K\right\}\right]$ $+B_v\left\{\left(J+\frac{1}{2}\right)^2 + K\right\}$ $-\left(J+\frac{1}{2}\right)^2\left[D_v\left\{\left(J+\frac{1}{2}\right)^2 + 2K + 1\right\}\right.$ $\left.-H_v\left\{\left(J+\frac{1}{2}\right)^2\left[\left(J+\frac{1}{2}\right)+3(1+K)\right]+K\right\}\right]$

where $z = [(J+1/2)^2 - K^2]$. The subscript v means the parameter value in the (v_1, v_2, v_3) manifold appropriate to the basis functions.

III.10 *K*-type Doubling

The Van Vleck transformation introduces both electronic and vibrational parity dependent terms in second and higher orders. The electronic terms give rise to Λ-type doubling through interactions with remote electronic states. The vibrational terms give rise to l-type doubling through Coriolis interactions with other vibrational levels. These rotationally induced effects split the degeneracy of states differing only in parity (Kramers' doublets [2]), to produce K-type doubling [20]. This has been included in the model presented here. The same terms also give rise to K-type resonance in which there is an interaction between states of different K within the same (v_1, v_2, v_3) manifold. Both effects are discussed briefly in Appendix E.

III.11 Nuclear Hyperfine Structure

The small effects of a nuclear spin **I**, give rise to hyperfine splittings in the LMR spectrum. These effects arise through coupling between the electrons and (principally) the nuclear magnetic dipole moment [53, 54] and electric quadrupole moment [53, 55]. Both interactions are discussed in Appendix F.

III.12 The Zeeman Hamiltonian

III.12.1 Introduction

The Zeeman effect is the change in energy of a system possessing a magnetic moment, due to the application of an external magnetic field. In an atomic or molecular system, the Zeeman effect removes the degeneracy of the M components of the total angular momentum.

In this section, B_r is used to denote the rotational parameter, so as to avoid confusion with other variables.

III.12.2 The Zeeman Effect

The Zeeman energy

A space-fixed magnetic field **B** of flux density B_0, defines the space-fixed Z-axis[15]. The energy of a magnetic dipole moment **m** in the field is the Zeeman energy [33]

$$E_z = -\mathbf{m}.\mathbf{B}. \tag{III.85}$$

The negative sign implies an energy minimum when the dipole and field vectors are parallel. The quantum analogue of Eq.(III.85) is the Zeeman Hamiltonian $\mathcal{H}_z$, which for a rotating molecule can be written [9, 39, 56]

$$\frac{\mathcal{H}_z}{hc} = B_0 \left\{ g_L^{(0)} \mu_B \mathbf{L}_Z + g_S \mu_B \mathbf{S}_Z - g_r^N \mu_B \mathbf{R}_Z - \mu_N \sum_\alpha g_{N_\alpha} \mathbf{I}_{\alpha,Z} \right\}. \tag{III.86}$$

[15] X, Y, Z and x, y, z denote space-fixed and molecule-fixed Cartesian axes, respectively.

This Hamiltonian operates over the infinite space of all basis states and must undergo a Van Vleck transformation.

The couple exerted on **J** by B_0 causes it to precess about the space-fixed Z-axis[16], with a projection of M_J on this axis. M_I is the projection of the nuclear spin angular momentum **I**, on the same axis; the summation over α covers all nuclei with non-zero spin. The nuclear spin is not included in the total angular momentum because the applied magnetic field easily decouples it from the molecular framework (see Appendix F). **I** is then quantized directly about the space-fixed Z-axis, independent of the orientation of the molecule in the magnetic field. This '**I**-decoupled' representation [54] is always appropriate for the LMR studies reported in this thesis.

Spherical tensor notation

The subscript 'Z' in Eq.(III.86) means projection of the angular momenta on the space-fixed Z-axis. Apart from the nuclear spin, the other angular momenta are coupled in the molecule-fixed frame. The space-fixed projections of these angular momenta are not simple, because the molecule-fixed frame is rotating with respect to the space-fixed one. This is dealt with by writing the angular momenta as spherical tensors [1, 32, 57]. For an angular momentum **A**, the entity $T^k_p(\mathbf{A})$ is a spherical tensor of rank k, with $2k+1$ spherical components spanning

$$p = k, k-1, \cdots, -k. \tag{III.87}$$

For a first rank tensor[17] (a vector), the spherical and Cartesian components are related by [39]

$$T^1_{p=0}(\mathbf{A}) = A_Z \tag{III.88}$$

$$T^1_{p=\pm 1}(\mathbf{A}) = \mp\frac{1}{\sqrt{2}}(A_X \pm iA_Y). \tag{III.89}$$

The indices p and q are used to denote the space-fixed and molecule-fixed spherical components[18], respectively. Eqs.(III.88) and (III.89) are valid in the molecule-fixed frame

[16] The couple is given by $\mathbf{J} \wedge \mathbf{B}$.

[17] All the angular momenta in $\mathcal{H}_z$ are first rank tensors.

[18] Brown and Howard [48] suggest the mnemonic 'space' and 'molequle'.

when p is replaced by q and (X, Y, Z) by (x, y, z). Note that it is possible to write B_0 for the magnetic flux density, since $T^1_{p=0}(\mathbf{B}) = B_0$ and $T^1_{p=\pm1}(\mathbf{B}) = 0$. The component of the vector $\mathbf{A}$ along the space-fixed Z-axis, $T^1_{p=0}(\mathbf{A})$, is required in $\mathcal{H}_z$, and can be expressed in terms of its molecule-fixed components by the rotational transformation [32, 40]

$$T^1_{p=0}(\mathbf{A}) = \sum_q \mathcal{D}^{(1)}_{p,q}(\omega)^* \, T^1_q(\mathbf{A}), \tag{III.90}$$

where $\mathcal{D}^{(1)}_{p,q}(\omega)^*$ is the complex conjugate of a first rank rotation matrix, ω representing the Euler rotation angles (α, β, γ). Rotation of the space-fixed axes about these angles maps them onto their molecule-fixed counterparts [32], as shown in Fig.III.12. The rotation matrix[19] is the tensor equivalent of a geometrical co-ordinate transformation using direction cosines. Details of the rotation matrices and spherical tensor reduction methods are given in [32, 57].

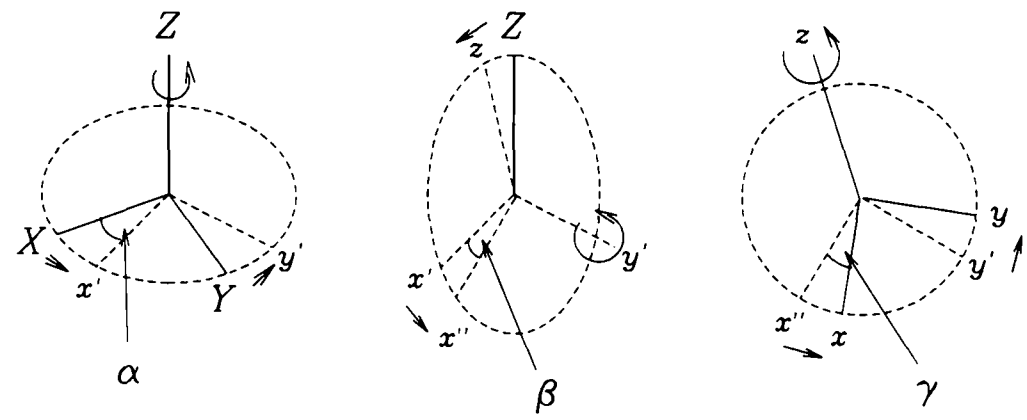

Figure III.12: A rotation about the Euler angles (α, β, γ) maps the space-fixed axes (X, Y, Z) onto the molecule-fixed axes (x, y, z). Note that the origin is common to both axis systems. Based on a diagram in ref. [32].

Terms in the Zeeman Hamiltonian

The Bohr magneton [58] $\mu_B = eh/4\pi m_e$, is the magnetic moment of a unit of orbital electronic angular momentum. The nuclear magneton [58] $\mu_N = \mu_B(m_e/m_p)$, is the analogous but much smaller quantity for the nucleus. The dimensionless Landé g-factors or gyromagnetic ratios, measure the size of the magnetic moments.

[19]The rotation matrices form an irreducible representation of the symmetric top rotational wave functions [32, 34, 57].

The g-factor for the orbital motion of the electrons is $g_L = 1.0$. This g-factor is modified by a relativistic correction [39, 59],

$$g_L^{(0)} = g_L \left(1 - \frac{m_e}{\sum_i M_i}\right)\left(1 - \frac{\langle T \rangle}{m_e c^2}\right), \tag{III.91}$$

where the M_i are the nuclear masses and $\langle T \rangle$ is the expectation value of the electron kinetic energy, which requires *ab initio* calculation. This relativistic correction is typically -1×10^{-4} for light atoms [59], but will become more important in heavy atoms with fast moving electrons. The spin g-factor for a free electron g_S, has a value of 2.00232 [58]; this includes relativistic and field quantisation corrections[20] [39, 59].

The rotational g-factor g_r^N, measures the magnetic moment arising from the rotation of the nuclei (excluding the electrons), and for a linear molecule is given by [9, 39, 59]

$$g_r^N = -m_e \frac{\sum_i Z_i \mathbf{r}_i^2}{I} \tag{III.92}$$

where Z_i is the atomic number of the ith nucleus, I is the moment of inertia and $\mathbf{r}_i$ is the displacement vector of the ith nucleus from the centre of mass, along the inertial (x or y) axis. The nuclear g-factor [9, 39, 59] is

$$g_N = \frac{\mu_I}{I}, \tag{III.93}$$

where the nuclear magnetic moment μ_I is a property of the nuclear structure.

III.12.3 The Single State Effective Zeeman Hamiltonian

Form of the Hamiltonian

When the Zeeman Hamiltonian is written in spherical tensor form and reduced to a single state $\mathbf{N}^2$ effective Hamiltonian, it takes the form[21] [41]

$$\frac{\mathcal{H}_z^{\text{eff.}}}{hc} = g_L \mu_B B_0 T^1_{p=0}(\mathbf{L}) + g_S \mu_B B_0 T^1_{p=0}(\mathbf{S}) - g_r \mu_B B_0 T^1_{p=0}(\mathbf{J} - \mathbf{S})$$

[20] To a first approximation, a spin 1/2 Fermion has a spin magnetic moment of $2\mu_B$. This is modified by relativistic and quantum electrodynamic effects [26].

[21] In [41], an $\mathbf{R}^2$ Hamiltonian is used. The $\mathbf{N}^2$ Hamiltonian here differs in the absence of a $g_r L_z$ term.

$$
\begin{aligned}
&+g_l\mu_B B_0 \sum_{q=\pm1} \mathcal{D}^{(1)}_{0,q}(\omega)^* T^1_q(\mathbf{S}) + g'_l\mu_B B_0 \sum_{q=\pm1} e^{-2iq\vartheta}\mathcal{D}^{(1)}_{0,-q}(\omega)^* T^1_q(\mathbf{S}) \\
&-g^{e'}_r \mu_B B_0 \sum_{q=\pm1}\sum_p e^{-2iq\vartheta}(-1)^p \mathcal{D}^{(1)}_{-p,-q}(\omega)^* T^1_p(\mathbf{J}-\mathbf{S})\mathcal{D}^{(1)}_{0,-q}(\omega)^* \\
&-g_N\mu_N B_0 T^1_{p=0}(\mathbf{I}) .
\end{aligned} \tag{III.94}
$$

The operator $e^{-2iq\vartheta}$ is the $\Lambda^2_{\mp}$ operator defined in Eq.(III.24), in which the angle ϑ is the electron azimuthal angle (see Fig.III.8).

Reduction of the spherical tensors produces a general form for the matrix elements in the **I**-decoupled scheme [41],

$$
\langle \eta\Lambda'; v_2 l; S\Sigma'; J'P'M_J; IM_I | \mathcal{H}^{\text{eff.}}_z | \eta\Lambda; v_2 l; S\Sigma; JPM_J; IM_I\rangle . \tag{III.95}
$$

They are given by [41]

$$
\begin{aligned}
&\mu_B B_0 \delta_{\Lambda',\Lambda} \textstyle\sum_q (-1)^{J'-M_J+J'-P'} \left[(2J'+1)(2J+1)\right]^{\frac{1}{2}} \\
\times\ &\begin{pmatrix} J' & 1 & J \\ -M_J & 0 & M_J \end{pmatrix}\begin{pmatrix} J' & 1 & J \\ -P' & q & P \end{pmatrix}\Big\{ g_L\Lambda\delta_{\Sigma',\Sigma} \\
+\ &(g_S+g_r+g_l)(-1)^{S-\Sigma'}\left[S(S+1)(2S+1)\right]^{\frac{1}{2}}\begin{pmatrix} S & 1 & S \\ -\Sigma' & q & \Sigma \end{pmatrix} - g_l\Sigma\delta_{\Sigma',\Sigma}\Big\} \\
-\ &(g_r\mu_B B_0 M_J + g_N\mu_N B_0 M_I)\,\delta_{J',J}\delta_{\Sigma',\Sigma}\delta_{\Lambda',\Lambda} \\
-\ &\mu_B B_0 \textstyle\sum_{q=\pm1}\delta_{\Lambda',\Lambda\mp2}(-1)^{J'-M_J}\left[(2J'+1)(2J+1)\right]^{\frac{1}{2}}\begin{pmatrix} J' & 1 & J \\ -M_J & 0 & M_J \end{pmatrix} \\
\times\ &\Big\{\left(g'_l - g^{e'}_r\right)(-1)^{S-\Sigma'}\begin{pmatrix} S & 1 & S \\ -\Sigma' & q & \Sigma \end{pmatrix}\left[S(S+1)(2S+1)\right]^{\frac{1}{2}}(-1)^{J'-P'} \\
\times\ &\begin{pmatrix} J' & 1 & J \\ -P' & -q & P \end{pmatrix} - g^{e'}_r\delta_{\Sigma',\Sigma}(-1)^{J'-P'}\textstyle\sum_{P''}\frac{1}{2}\Big[(-1)^{J'-P''} \\
\times\ &\begin{pmatrix} J' & 1 & J' \\ -P' & -q & P'' \end{pmatrix}\begin{pmatrix} J' & 1 & J \\ -P'' & -q & P \end{pmatrix}\left[J'(J'+1)(2J'+1)\right]^{\frac{1}{2}} \\
+\ &(-1)^{J-P''}\begin{pmatrix} J' & 1 & J \\ -P' & -q & P'' \end{pmatrix}\begin{pmatrix} J & 1 & J \\ -P'' & -q & P \end{pmatrix}\left[J(J+1)(2J+1)\right]^{\frac{1}{2}}\Big]\Big\} .
\end{aligned}
$$

The Wigner 3-j symbols

$$\begin{pmatrix} j_1 & k & j_2 \\ m_1 & q & m_2 \end{pmatrix}$$

are tabulated in [32, 57] and easily evaluated. The 3-j symbol has the properties [32, 40, 57]

$$|j_1 - j_2| < k < |j_1 + j_2| \text{ (the 'triangle' rule)} \tag{III.96}$$

$$m_1 + q + m_2 = 0, \tag{III.97}$$

implying the selection rule $\Delta J = 0, \pm 1$ for the matrix elements of the Zeeman Hamiltonian. The breakdown of J as a good quantum number is a consequence of **J** being defined as a space-fixed entity [48] with

$$J_Z \left| J, P, M_J \right\rangle = M_J \left| J, P, M_J \right\rangle, \tag{III.98}$$

and simultaneously being referred to the rotating molecule with

$$J_z \left| J, P, M_J \right\rangle = P \left| J, P, M_J \right\rangle. \tag{III.99}$$

In the absence of a magnetic field, this is possible since the orientation of the space-fixed axes is arbitrary. The imposition of a magnetic field defines uniquely the space-fixed Z-axis. Space is no longer spherically symmetric, so that the symmetry group of J [34] is reduced to one in which only M_J remains well-defined.

III.12.4 Parameters in the Effective Hamiltonian

Orbital and spin parameters

The effective Hamiltonian contains some modified parameters. The orbital g-factor contains non-adiabatic contributions, denoted Δg_L [27, 59, 60] so that

$$g'_L = g_L^{(0)} + (v_2 + 1)\, \Delta g_L^{(1)} + \text{other small terms.} \tag{III.100}$$

In a light atom Renner-Teller molecule, the dominant non-adiabatic contribution is $\Delta g_L^{(1)}$. It arises from Herzberg-Teller vibronic interactions combined with spin-orbit coupling in remote Σ and Δ electronic states, see Eqs.(III.27), (III.28) and (III.37). This non-adiabatic contribution first arises in the third order of perturbation theory in the Van Vleck transformation of the Renner-Teller Hamiltonian. Brown [27] has shown that it is related to the K-dependent vibronic parameter g_K by

$$\Delta g_L^{(1)} = -\frac{g_K}{\omega_2}. \tag{III.101}$$

Furthermore, $\Delta g_L^{(1)}$ is similar to the spin-orbit correction ΔA in Eq.(III.49). In the same manner, $\Delta g_L^{(1)}$ is an additional but inseparable contribution to the vibrational dependence of g_L, α_{2,g_L}. It is particularly important because α_{g_L} is otherwise expected to be negligible.

Other workers have included a parameter $\Delta g_L^{(2)}$, which arises from a perturbation approximation of Renner-Teller and Zeeman interactions from terms with $\Delta v_2 = \pm 2$ within the $^2\Pi$ electronic state [1]. This is not required in the model described here, because the matrix representation includes all of these terms explicitly. The matrix diagonalisation procedure then models this effect exactly, so that only the fundamental g-factors $g_L^{(0)}$ and $\Delta g_L^{(1)}$ need be known.

Rotational g-factor

As well as the nuclear contribution g_r^N, the total rotational g factor

$$g_r = g_r^N - g_r^e. \tag{III.102}$$

has an electronic contribution g_r^e [39, 59, 60]. This is a non-adiabatic term arising from the operators $L_\pm$ when the rotational operator $\mathbf{R}$ is expressed in terms of $\mathbf{J}$, $\mathbf{L}$, $\mathbf{S}$ and $\mathbf{G}$ during the Van Vleck transformation to isolate the single electronic state [1]. The effect of the vibrational angular momentum $\mathbf{G}$ has been neglected in $\mathcal{H}_z^{\text{eff.}}$; it would produce a small contribution to g_r. This is justified in the present case because g_r is very small ($< 10^{-3} g_L$), and therefore neglect of $\mathbf{G}$ will not introduce significant errors in mid-infrared studies.

Anistropic spin parameter

The anisotropic contribution to the spin magnetic moment, g_l, arises from non-adiabatic interactions with remote Σ and Δ electronic states [39, 41, 56, 60]. These arise in the Van Vleck transformation in third order, through products of the orbital Zeeman and spin-orbit operators. The origin of this term is similar to the second order spin-orbit contribution to the spin-rotation parameter, see §III.9.4, and the two are related by the well established Curl's relationship [56, 61]

$$g_l = -\frac{\gamma}{2B_r}, \tag{III.103}$$

which is moderately reliable in practice.

The Λ-type doubling g-factors, g_l' and $g_r^{e/}$ are discussed in Appendix E.4.2. Other very small, higher order perturbation contributions to $\mathcal{H}_z$ do arise; they are discussed in [9, 56] but have been neglected here.

Vibrational dependence of Zeeman parameters

The Zeeman parameters have a normal vibrational dependence; the subscript v has simply been omitted for clarity. Vibrational and centrifugal distortion effects on the Zeeman terms are expected to be small, because the parameters mostly originate from the electronic part of the Hamiltonian [56].

The matrix elements of $\mathcal{H}_z^{\text{eff}}$.

The matrix elements of $\mathcal{H}_z^{\text{eff}}$. diagonal in J are shown below, excluding the Λ-type doubling terms. The representation has been constructed in the parity conserving basis functions Eqs.(III.33)–(III.36), extended to included the **I**-decoupled quantum numbers I, M_I. Note that there are no matrix elements between ψ_1 and ψ_2 basis functions, and

the representation is diagonal in M_J and M_I.

$\lvert\psi_{1a}; v_1v_2v_3; \pm\rangle$	$\lvert\psi_{1b}; v_1v_2v_3; \pm\rangle$
$\frac{\mu_B B_0 M_J\left(K+\frac{1}{2}\right)}{J(J+1)}\left[g'_L + \frac{1}{2}(g_S + g_r)\right]$ $-g_r\mu_B B_0 M_J - g_I\mu_N B_0 M_I$	$\frac{\mu_B B_0 M_J z^{\frac{1}{2}}}{2J(J+1)}[g_S + g_r + g_l]$
Symmetric	$\frac{\mu_B B_0 M_J\left(K-\frac{1}{2}\right)}{J(J+1)}\left[g'_L - \frac{1}{2}(g_S + g_r)\right]$ $-g_r\mu_B B_0 M_J - g_I\mu_N B_0 M_I$

and

$\lvert\psi_{2a}; v_1v_2v_3; \pm\rangle$	$\lvert\psi_{2b}; v_1v_2v_3; \pm\rangle$
$-\frac{\mu_B B_0 M_J\left(K+\frac{1}{2}\right)}{J(J+1)}\left[g'_L - \frac{1}{2}(g_S + g_r)\right]$ $-g_r\mu_B B_0 M_J - g_I\mu_N B_0 M_I$	$\frac{\mu_B B_0 M_J z^{\frac{1}{2}}}{2J(J+1)}[g_S + g_r + g_l]$
Symmetric	$-\frac{\mu_B B_0 M_J\left(K-\frac{1}{2}\right)}{J(J+1)}\left[g'_L + \frac{1}{2}(g_S + g_r)\right]$ $-g_r\mu_B B_0 M_J - g_I\mu_N B_0 M_I$

III.12.5 Modelling the Zeeman Effect

The matrix representation of $\mathcal{H}_z$ has matrix elements with $\Delta J = 0, \pm 1$. This means that the matrix representation of a Renner-Teller state must span levels off-diagonal in J as well as v_2, as shown in Fig.III.13. When the rotational levels show Hund's case (a) behaviour, the Zeeman energy imparted to a rotational level can shift it by as much as $1\,\mathrm{cm}^{-1}$ at a flux density of $1.5\,\mathrm{T}$. With a typical rotational constant of $\approx 0.5\,\mathrm{cm}^{-1}$ for a light, linear triatomic molecule, Zeeman interactions between neighbouring rotational levels will become very important. Second and higher order interactions become significant, and accurate modelling of the Zeeman effect requires the matrix to span the levels $J, J \pm 1, J \pm 2, \cdots$. The size of the basis is determined from trial calculations; it is truncated when including further members produces no significant change in the calculated Zeeman effect. In the non-unique and $^2\Sigma$ vibronic states, the spin-orbit interaction is quenched by the Renner-Teller effect. This leads to behaviour close to Hund's case (b) and some dramatic consequences for the Zeeman effect, as discussed in §IV.2.3.

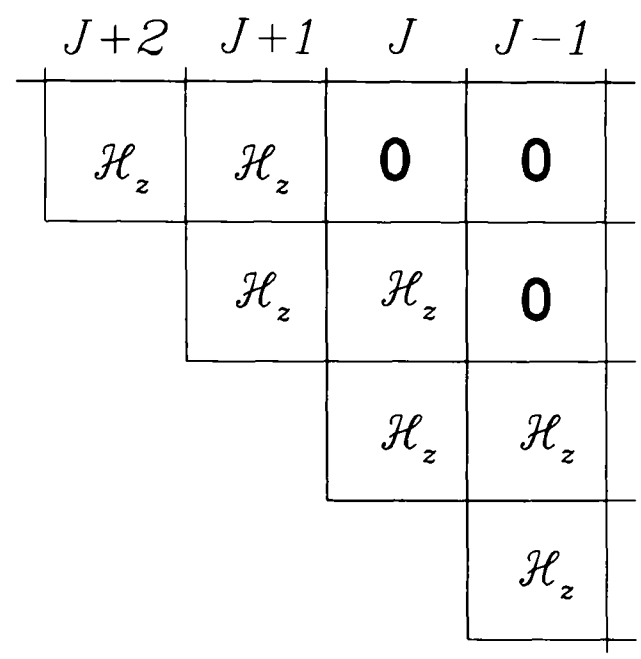

Figure III.13: A schematic representation of the J-space of the matrix representation, showing the position of the Zeeman terms, denoted $\mathcal{H}_z$. The matrix representation of the Zeeman Hamiltonian spans an arbitrary and potentially infinite number of rotational levels. The section shown is for a single vibrational level (v_1, v_2, v_3), for a single value of K.

Bibliography

[1] A. Carrington, A.R. Fabris, B.J. Howard and N.J.D. Lucas, *Mol. Phys.* **20**, 961–980 (1971).

[2] G. Herzberg, "Molecular Spectra and Molecular Structure," Vol. III, "Electronic Spectra of Polyatomic Molecules," 2nd ed. (corrected), Krieger Publishing, Malabar, Florida, 1991.

[3] I.M. Mills, "Vibration-Rotation Structure in Asymmetric- and Symmetric-Top Molecules," *in* "Molecular Spectroscopy: Modern Research." (K.N. Rao and C.W. Mathews, Eds.), pp. 115–140, Academic Press, New York, 1972.

[4] H.W. Kroto, "Molecular Rotation Spectra," Dover Publications, New York, 1992.

[5] E.B. Wilson, Jr., J.C. Decius and P.C. Cross, "Molecular Vibrations," pp. 289–291, Mc Graw-Hill, London, 1955.

[6] P.R. Bunker, "Molecular Symmetry and Spectroscopy," Academic Press, New York, 1979.

[7] W. Moffitt and A.D. Liehr, *Phys. Rev.* **106**, 1195–1200 (1957).

[8] M. Born and R. Oppenheimer, *Ann. Phys.* **84**, 457–484 (1927).

[9] A. Carrington, D.H. Levy and T.A. Miller, "Electron Resonance of Gaseous Diatomic Molecules," *in* "Advances in Chemical Physics," Vol. XVIII, (I. Prigogine and S.A. Rice, Eds.), pp. 149–248, J. Wiley and Sons, New York, 1970.

[10] J.T. Hougen, *J. Chem. Phys.* **36**, 519–534 (1962).

[11] S.F.A. Kettle, "Symmetry and Structure," J. Wiley & Sons, Chichester, 1985.

[12] P.W. Atkins, M.S. Child and C.S.G. Phillips, "Tables for Group Theory," Oxford University Press, Oxford, 1986.

[13] R.N. Dixon, *Phil. Trans. R. Soc. Lond. A* **252**, 165–192 (1960).

[14] D.A. Ramsay, "Electronic Spectra of Polyatomic Molecules and the Configurations of Molecules in Excited Electronic States," *in* "Determination of Organic Structures by Physical Methods," Vol. II, (F.C. Nachod and W.D. Phillips, Eds.), pp. 296ff., Academic Press, New York, 1962.

[15] A.D. Walsh, *J. Chem. Soc.*, 2260–2331 (1953).

[16] R. Renner, *Z. Phys.* **92**, 172–193 (1934).

[17] J.A. Pople and H.C. Longuet-Higgins, *Mol. Phys.* **1**, 372–383 (1958).

[18] J.M. Brown and F. Jørgensen, *Adv. Chem. Phys.* **52**, 117–180 (1983).

[19] G. Herzberg, "Molecular Spectra and Molecular Structure," Vol. I, "Spectra of Diatomic Molecules," 2nd ed. (corrected), pp. 221–224, 300–304, Krieger Publishing, Malabar, Florida, 1989.

[20] J.M. Brown, *J. Mol. Spectrosc.* **56**, 159–162 (1975).

[21] J.M. Brown and A.J. Merer, *J. Mol. Spectrosc.* **74**, 488–494 (1979).

[22] G. Herzberg, "Molecular Spectra and Molecular Structure," Vol. II, "Infrared and Raman Spectra of Polyatomic Molecules," Reprint (corrected), pp. 172–174, Krieger Publishing, Malabar, Florida, 1991.

[23] J. Werner, Ph.D. thesis, Institut für Angewandte Physik der Universität Bonn, 1987.

[24] P.W. Atkins, "Molecular Quantum Mechanics," 2nd ed., pp. 28ff., 88–99, 432, Oxford University Press, Oxford, 1983.

[25] L.L. Foldy, "Relativistic Wave Equations,"*in* "Pure and Applied Physics," Vol. 10 (part 3), (D.R. Bates, Ed.), pp. 1–46, Academic Press, New York, 1962.

[26] R.P. Feynman, "Quantum Electrodynamics," pp. 27ff, W.A. Benjamin, New York, 1962.

[27] J.M. Brown, *J. Mol. Spectrosc.* **68**, 412–422 (1977).

[28] H.C. Longuet-Higgins, *Advan. Spectrosc.* **2**, 429–472 (1961).

[29] C. Di Lauro and I.M. Mills, *J. Mol. Spectrosc.* **21**, 386–413 (1966).

[30] J.M. Brown, E.A. Colbourn, J.K.G. Watson and F.D. Wayne, *J. Mol. Spectrosc.* **74**, 294–318 (1979).

[31] B.J. Howard, Ph.D. thesis, University of Southampton, 1970.

[32] R.N. Zare, "Angular Momentum," J.Wiley & Sons, New York, 1988.

[33] B.I. Bleaney and B. Bleaney, "Electricity and Magnetism," 3rd ed., pp. 33–56, 98–129, 432–470, Oxford University Press, Oxford, 1987.

[34] G. Arfken, "Mathematical Methods for Physicists," 3rd ed., pp. 150–167, 251–252, 261–267, 637–676, Academic Press, San Diego, 1985.

[35] J.H. Van Vleck, *Phys. Rev.* **33**, 467–506 (1929).

[36] A. Messiah, "Quantum Mechanics," Vol. II, pp. 685–721, North-Holland, Amsterdam, 1966.

[37] L.D. Landau and E.M. Lifshitz, "Course of Theoretical Physics," Vol. 3, " Quantum Mechanics," 2nd ed. (revised), pp. 129–136, Pergamon Press, Oxford, 1965.

[38] J.M. Brown, A.S-C. Cheung and A.J. Merer, *J. Mol. Spectrosc.* **124**, 464–475 (1987).

[39] S. Davidson, Ph.D. thesis, University of Colorado, 1987.

[40] J.M. Brown, Physical Chemistry Laboratory, University of Oxford, unpublished notes on the space-fixed inversion operator, E^*.

[41] J.M. Brown, M. Kaise, C.M.L. Kerr and D.J. Milton, *Mol. Phys.* **36**, 553–582 (1978).

[42] A. Chablo, *J. Mol. Str. (Theochem)* **283**, 135–139 (1993).

[43] J.M. Brown and F. Jørgensen, *Mol. Phys.* **47**, 1065–1086 (1982).

[44] J.T. Hougen, "The Calculation of Rotational Energy Levels and Rotational Line Intensities in Diatomic Molecules," NBS Monograph 115, United States Department of Commerce, Washington D.C., 1970.

[45] W. Gordy and R.L. Cook, "Microwave Molecular Spectra," *in* "Chemical Applications of Spectroscopy," Vol. II, (W. West, Ed.), pp. 521–522, J. Wiley & Sons, New York, 1970.

[46] I.M. Mills, University of Reading, "Symmetry Relations between ζ's," Private Communication, 1994.

[47] R.N. Zare, A.L. Schmeltekopf, W.J. Harrop and D.L. Albritton, *J. Mol. Spectrosc.* **46**, 37–66 (1973).

[48] J.M. Brown and B.J. Howard, *Mol. Phys.* **31**, 1517–1525 (1976).

[49] J.H. Van Vleck, *Rev. Mod. Phys.* **23**, 213–227 (1951).

[50] O. Klein, *Z. Phys.* **58**, 730–734 (1929).

[51] H. Lefebvre-Brion and R.W. Field, "Perturbations in the Spectra of Diatomic Molecules," pp. 100, 229, Academic Press, Orlando, Florida, 1986.

[52] K. Kawaguchi, S. Saito and E. Hirota, *Mol. Phys.* **55**, 341–350 (1985).

[53] J.M. Brown, I.Kopp, C. Malmberg and B. Rydh, *Phys. Scr.* **17**, 55–67 (1978).

[54] R.A. Frosch and H.M. Foley, *Phys. Rev.* **88**, 1337–1349 (1952).

[55] R.L. Cook and F.C. Delucia, *Am. J. Phys.* **39**, 1433–1454 (1971).

[56] K.M. Evenson, R.J. Saykally, D.A. Jennings, R.F. Curl, Jr. and J.M. Brown, "Far Infrared Laser Magnetic Resonance," *in* "Chemical and Biochemical Applications of Lasers," Vol. V, (C.B. Moore, Ed.), pp. 95–138, Academic Press, New York, 1980.

[57] D.M. Brink and G.R. Satchler, "Angular Momentum," 3rd ed., Oxford University Press, Oxford, 1993.

[58] International Union of Pure and Applied Chemistry, Physical Chemistry Division, "Quantities, Units and Symbols in Physical Chemistry," 2nd ed., (I. Mills, T. Cvitaš, K. Homann, N. Kallay and K. Kucitsu, Eds.), Blackwell Scientific Publications, Oxford, 1993.

[59] L. Veseth, *J. Mol. Spectrosc.* **63**, 180–192 (1976).

[60] J.M. Brown and H. Uehara, *Mol. Phys.* **24**, 1169–1174 (1972).

[61] R.F. Curl, Jr., *Mol. Phys.* **9**, 585–597 (1965).

Chapter IV

Modelling the Renner-Teller States

IV.1 Modelling the Unique States

IV.1.1 Spin-Orbit and Renner-Teller Effects

Renner-Teller effect

The unique states have a vibronic quantum number of $K = v_2 + 1$, so they arise in the lowest v_2 level for which this vibronic species can occur. The restriction $|l| \leq v_2$ means that the unique states have no ψ_2 type basis functions; consequently there are no matrix elements of $\mathcal{H}_{RT}^{\text{eff.}}$ between the unique state basis functions in the (v_1, v_2, v_3) manifold of the unique states. States of the same vibronic symmetry arise in the $(v_1, v_2 + 2m, v_3)$ manifolds, where $m \geq 1$. These states are not unique and involve both ψ_1 and ψ_2 basis functions, and consequently show a large first order Renner-Teller effect. The unique states suffer a small Renner-Teller effect, because of the matrix elements that will mix their basis functions with the ψ_2 basis functions of the same K in the $(v_1, v_2 + 2, v_3)$ manifold:

$$\langle \psi_2; K = v_2 + 1; v_1, v_2 + 2, v_3 | \, \mathcal{H}_{RT}^{\text{eff.}} \, | \psi_1; K = v_2 + 1; v_1, v_2, v_3 \rangle \, .$$

The dominant contribution from these matrix elements to the unique state energy levels can be estimated by second order perturbation theory [1],

$$\frac{E^{(2)}}{hc} = -\frac{\epsilon^2 \omega_2}{8} n\,(n+1)\,, \tag{IV.1}$$

where $n = (v_2 + 1)$. The v_2 dependence of this contribution means that the unique states in higher vibrational manifolds will suffer significant quenching, *i.e.* when $E^{(2)} \sim 2hc\omega_2$. In this situation, the quantum number v_2 will not be a good label of the eigenfunctions. There are small additional harmonic Renner-Teller contributions to the unique states, arising in higher orders of perturbation theory. These can be modelled exactly by extending the matrix representation to include the $(v_1, v_2 + 4v_3), (v_1, v_2 + 6, v_3), \cdots$ levels of the same K.

Renner-Teller and spin-orbit matrix representation

The complete representation of all the matrix elements of $\mathcal{H}_{RT}^{\text{eff.}} + \mathcal{H}_{SO}^{\text{eff.}}$ for the unique states in the manifold (v_1, v_2, v_3), is shown in Fig.IV.1. The matrix can be extended beyond the $(v_1, v_2 + 2, v_3)$ manifold to include higher order effects.

Some workers, *e.g.* [2, 3], have analysed unique state spectra without including the Renner-Teller effect. As discussed in Appendix C, they determine an effective spin-orbit coupling parameter, related to the 'true' Renner-Teller free value[1] of the model determined in this study by [2]

$$A^{\text{eff.}} = A^{\text{true}} \left[1 - \frac{\epsilon^2}{8} n\,(n+1)\right]. \tag{IV.2}$$

IV.1.2 Rotational Structure

Hund's case (a) structure

When $|A| \gg BJ$ and $|A| \gg \epsilon^2\omega_2 n(n+1)/8$, the ψ_{1a} and ψ_{1b} basis functions are good descriptions of the eigenstates [1], since the off-diagonal matrix elements are small when compared with the separation between the diagonal ones. The quantum numbers v_2, K, J, P, M_J and M_I can then be used unambiguously to identify the eigenstates.

[1] In both cases A still contains non-adiabatic contributions, see §III.7.

	$\lvert\psi_{1a};v_2+2;\pm\rangle$	$\lvert\psi_{1b};v_2+2;\pm\rangle$	$\lvert\psi_{2a};v_2+2;\pm\rangle$	$\lvert\psi_{2b};v_2+2;\pm\rangle$	$\lvert\psi_{1a};v_2;\pm\rangle$	$\lvert\psi_{1b};v_2;\pm\rangle$
$\langle\psi_{1a};v_2+2;\pm\rvert$	$(n+2)\omega_2 + g_K K + {}^1\!/_2 A$	0	$-\frac{\varepsilon\omega_2}{2}[(n+2)^2 - K^2]^{\frac{1}{2}}$	0	0	0
$\langle\psi_{1b};v_2+2;\pm\rvert$	0	$(n+2)\omega_2 + g_K K - {}^1\!/_2 A$	0	$-\frac{\varepsilon\omega_2}{2}[(n+2)^2 - K^2]^{\frac{1}{2}}$	0	0
$\langle\psi_{2a};v_2+2;\pm\rvert$	$-\frac{\varepsilon\omega_2}{2}[(n+2)^2 - K^2]^{\frac{1}{2}}$	0	$(n+2)\omega_2 - g_K K - {}^1\!/_2 A$	0	$-\frac{\varepsilon\omega_2}{4}\{[n+K+2] \times [n+K]\}^{\frac{1}{2}}$	0
$\langle\psi_{2b};v_2+2;\pm\rvert$	0	$-\frac{\varepsilon\omega_2}{2}[(n+2)^2 - K^2]^{\frac{1}{2}}$	0	$(n+2)\omega_2 - g_K K + {}^1\!/_2 A$	0	$-\frac{\varepsilon\omega_2}{4}\{[n+K+2] \times [n+K]\}^{\frac{1}{2}}$
$\langle\psi_{1a};v_2;\pm\rvert$	0	0	$-\frac{\varepsilon\omega_2}{4}\{[n+K+2] \times [n+K]\}^{\frac{1}{2}}$	0	$n\omega_2 + g_K K + {}^1\!/_2 A$	0
$\langle\psi_{1b};v_2;\pm\rvert$	0	0	0	$-\frac{\varepsilon\omega_2}{4}\{[n+K+2] \times [n+K]\}^{\frac{1}{2}}$	0	$n\omega_2 + g_K K - {}^1\!/_2 A$

Figure IV.1: The complete matrix elements of the spin-orbit and Renner-Teller effective Hamiltonians for the unique state in the manifold (v_1, v_2, v_3). All the parameters have a vibrational dependence (not indicated for clarity). The quantum number $n = (v_2 + 1)$, and K is unsigned. The term ΔA is absorbed into $\alpha_{2,a}$ and so not shown separately. $\Delta g_L^{(1)}$ is not shown here because the Zeeman effect is considered later.

Approximate rotational term values

An approximate expression can be derived for the rotational term values of the unique states. Consider just the vibrational, Renner-Teller, spin-orbit, rotational and spin-rotational matrix elements (they are the most important) in §III.9.5, for the ψ_1 functions of a unique state:

$\lvert\psi_{1a}; K = v_2 + 1; v_1 v_2 v_3; \pm\rangle$	$\lvert\psi_{1b}; K = v_2 + 1; v_1 v_2 v_3; \pm\rangle$
$\frac{1}{2}\left[A + \gamma\left(K - 1\right)\right] + B\left[\left(J + \frac{1}{2}\right)^2 - K\right]$ $-\frac{\epsilon^2\omega_2}{8} n\left(n+1\right) + g_K K + G\left(v_1, v_2, v_3\right)$	$-z^{\frac{1}{2}}\left(B - \frac{1}{2}\gamma\right)$
$-z^{\frac{1}{2}}\left(B - \frac{1}{2}\gamma\right)$	$-\frac{1}{2}\left[A + \gamma\left(K + 1\right)\right] + B\left[\left(J + \frac{1}{2}\right)^2 + K\right]$ $-\frac{\epsilon^2\omega_2}{8} n\left(n+1\right) + g_K K + G\left(v_1, v_2, v_3\right)$

where $z = [(J + 1/2)^2 - K^2]$. The vibrational dependence of the parameters has been omitted for clarity. The effect of the $\Delta v_2 = 2$ Renner-Teller matrix elements has been estimated by second order perturbation theory.

Diagonalising the above matrix and expanding the square root up to the second binomial term gives expressions for the wave numbers of the rotational levels. For $A > 0$, the label $F_1(J)$ refers to levels with $P = K - 1/2$ and $F_2(J)$ to levels with $P = K + 1/2$:

$$F_1\left(J\right) = C' - \frac{1}{2}C'' + B^{\text{eff.}}_{P=K-1/2} J\left(J+1\right) \tag{IV.3}$$

$$F_2\left(J\right) = C' + \frac{1}{2}C'' + B^{\text{eff.}}_{P=K+1/2} J\left(J+1\right), \tag{IV.4}$$

where the effective rotational constant is

$$B^{\text{eff.}}_{P=K\pm1/2} = B\left[1 \pm \frac{\left(B - \frac{\gamma}{2}\right)^2}{B\left\{A + 2K\left(\frac{\gamma}{2} - B\right)\right\}}\right]. \tag{IV.5}$$

and

$$C' = G\left(v_1, v_2, v_3\right) - \frac{\epsilon^2\omega_2}{8} n\left(n+1\right) + g_K K + \frac{1}{2}\left(\frac{B}{2} - \gamma\right), \tag{IV.6}$$

$$C'' = \left[A + 2K\left(\frac{\gamma}{2} - B\right)\right]\left\{1 + \frac{2\left(B - \frac{1}{2}\gamma\right)^2\left(\frac{1}{4} - K^2\right)}{\left[A + 2K\left(\frac{\gamma}{2} - B\right)\right]^2}\right\}. \tag{IV.7}$$

The upper and lower sign choices refer to $P = K \pm 1/2$ respectively. When $A < 0$, the labels F_1 and F_2 swap over.

The expressions in Eq.(IV.3) and Eq.(IV.4) are characteristic of Hund's case (a) rotational structure, shown in Fig.IV.2. The vibration-rotation spectrum of such a system consists of a Q-branch close to but shaded to long wavelength, of the band origin, and P and R branches extending away from the band origin to lower and higher wave number, respectively.

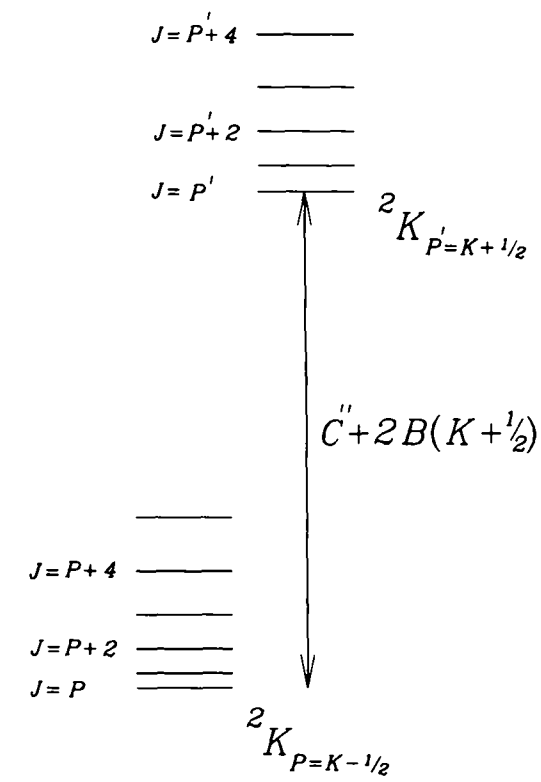

Figure IV.2: A schematic diagram of the Hund's case (a) rotational structure of the unique states in a $^2\Pi$ electronic state. The ground state is regular as shown ($A > 0$), making $P = K - 1/2$ the ground spin component. C'' is defined in Eq.(IV.7). The rotational spacings are grossly exaggerated and K-type doubling is not shown.

K-type doubling

The K-type doubling in the $(000)\,^2\Pi$ unique state has both Λ-type and l-type contributions. There are only Λ-type doubling matrix elements within the $(000)\,^2\Pi$ unique state block, but an equal or greater contribution to the K-type doubling in this state can come from l-type doubling in the $(020)\,^2\Pi$ states[2]. This arises in third order from products of

[2]This is because the l-type doubling parameter, q^*, is larger than the Λ-type doubling parameter, $q_{el.}$, by a factor of $\Delta E_i/\omega_2$, where ΔE_i represents the separation of remote Σ electronic states [4]. See Appendix E

the Renner-Teller and l-type doubling operators [4]. The K-type doubling parameter q is therefore a sum of the Λ-type doubling parameter $q_{el.}$ and the l-type doubling parameter q^*, even in the unique $(000)\,^2\Pi$ level. This has been discussed in detail by Brown [4].

IV.1.3 Zeeman Effect

Renner-Teller effect

In the model presented in this thesis, the orbital g factor in a given v_2 level is $g'_L = g_L^{(0)} + \Delta g_L^{(1)}(v_2+1)$. Workers who analyse unique state Zeeman spectra without including the Renner-Teller effect, determine an effective g_L value [5, 6] of $g_L^{\text{eff.}} = g'_L + \Delta g_L^{(2)}$. As discussed in Appendix C, $\Delta g_L^{(2)}$ is given by

$$\Delta g_L^{(2)} = -\frac{1}{8}\epsilon^2 n\,(n+1)\left[1+\frac{A}{\omega_2}\right]. \tag{IV.8}$$

Approximation of the Zeeman effect

In a Hund's case (a) system, the elements of the Zeeman Hamiltonian off-diagonal in P have a small effect, since the $P = K \pm 1/2$ components are well separated compared with the Zeeman energy. Consider the representation of $\mathcal{H}_z^{\text{eff.}}$ for the ψ_1 basis functions, given in §III.12.4. If the Zeeman matrix elements off-diagonal in J and P are neglected, an approximate expression can be derived for the magnetic moment of a Zeeman component of a rotational level [7]. This comes simply the diagonal matrix elements of the dominant Zeeman terms g_L and g_S, which can be expressed in terms of the parameter

$$g_J = \frac{P\left(g_L^{\text{eff.}}\Lambda + g_S\Sigma\right)}{J\,(J+1)}. \tag{IV.9}$$

The Zeeman energy of a component of a level is then approximately given by

$$E_z \approx g_J M_J \mu_B B_0. \tag{IV.10}$$

The Zeeman tuning rate of a transition $(v_1' v_2' v_3', J', M_J'' \pm 1) \leftarrow (v_1'' v_2'' v_3'', J'', M_J'')$ of frequency ν can then be approximated by

$$\frac{\partial \nu}{\partial B_0} = \Delta g_J M_J'' \pm g_J'. \tag{IV.11}$$

Zeeman effects in the $P = K \pm 1/2$ levels

The useful approximations in Eqs.(IV.9)–(IV.11) reveal two features about the Zeeman effect in unique state levels close to Hund's case (a):

1. In the $P = K - 1/2$ spin component, $g_J \approx 0$ since $g_L \approx 1, g_S \approx 2, \Lambda = +1, \Sigma = -1/2$. This accidental cancellation of the orbital and spin paramagnetism means that levels in this spin component have very low tunability. For the $J = 1/2$ level in the $(000)\,^2\Pi_{\frac{1}{2}}$ spin component, taking $g_L^{\text{eff.}} \approx 0.99$ gives $g_J \approx -7 \times 10^{-3}$. This means that a Q(1/2) transition can be tuned only by about $\pm 5 \times 10^{-3}\,\text{cm}^{-1}$ at a flux density of 1.5 T. Obviously, very close zero-field coincidences with CO laser lines would be required for resonance to be possible. Furthermore, the low tuning rate of any such resonances means that their field equivalent Doppler widths in an LMR spectrum would be several millitesla; hence they would be severely undermodulated and hard to detect.

2. Transitions in the $P = K + 1/2$ spin component are tunable. For a Q(3/2) transition in the $(000)\,^2\Pi_{\frac{3}{2}}$ spin component, $g_J \approx 0.8$. This means the transition can be tuned by up to $0.6\,\text{cm}^{-1}$ at 1.5 T and will have a field equivalent width of several tenths of a millitesla, making detection possible. The tuning rate of higher J lines drops off rapidly, since $g_J \propto 1/J(J+1)$. This factor normally dominates over line strength and population factors, to set an upper limit of $J'' \approx 11/2$ on observable transitions between Hund's case (a) states.

Q-branch LMR transitions

Eq.(IV.11) suggests that the tuning rate is independent of the magnetic field. For a Q-type vibration-rotation transition ($\Delta J = 0$), the tuning rate is also independent of M_J, so all the Zeeman components (for $\Delta M_J = \pm 1$) will be resonant at the same field. The matrix elements of $\mathcal{H}_z$ off-diagonal in J bring in a quadratic (and higher) dependence

upon M_J and B_0, so this is no longer exactly the case[3]. These effects are very significant in triatomic molecules, and produce a uniquely characteristic appearance for a given transition [8]. The ambiguity in the sign of the tuning rate in Eq.(IV.11) can often be resolved because the second order Zeeman effects produce a markedly different LMR spectrum in the two possible cases [8].

IV.2 Modelling the $^2\Sigma$ Vibronic States

IV.2.1 Spin-Orbit and Renner-Teller Effects

Basis functions

The $^2\Sigma$ vibronic states are characterised by a vibronic quantum number of $K = 0$. In a $^2\Pi$ electronic state of a Renner-Teller molecule, a pair of $^2\Sigma$ states arises in every vibrational manifold in which v_2 is odd. The $K = 0$ states only contain ψ_1 basis functions[4] because the l values are $l = -1$ and $l' = +1 = -l$. Explicitly, the parity conserving basis functions from Eqs.(III.33) and (III.34) are

$$\begin{aligned} |\psi_{1a};\pm\rangle \quad &= \quad \frac{1}{\sqrt{2}}\left\{\left|v_1 v_3;\Lambda=+1;v_2 l=-1;S\Sigma=+\frac{1}{2},JP=+\frac{1}{2},M_J\right\rangle\right. \\ &\left.\pm(-1)^{J+\frac{1}{2}}\left|v_1 v_3;\Lambda=-1;v_2 l=+1;S\Sigma=-\frac{1}{2},JP=-\frac{1}{2},M_J\right\rangle\right\} \quad \text{(IV.12)} \end{aligned}$$

and

$$\begin{aligned} |\psi_{1b};\pm\rangle \quad &= \quad \frac{1}{\sqrt{2}}\left\{\left|v_1 v_3;\Lambda=+1;v_2 l=-1;S\Sigma=-\frac{1}{2},JP=-\frac{1}{2},M_J\right\rangle\right. \\ &\left.\pm(-1)^{J+\frac{1}{2}}\left|v_1 v_3;\Lambda=-1;v_2 l=+1;S\Sigma=+\frac{1}{2},JP=+\frac{1}{2},M_J\right\rangle\right\} \quad \text{(IV.13)} \end{aligned}$$

Matrix representation

The Renner-Teller effect in the $K = 0$ states has matrix elements both diagonal and off-diagonal in v_2. The Renner-Teller effective Hamiltonian connects the parity inde-

[3]The Zeeman components of a Q-line are often still recognisably grouped close together, providing a characteristic signature.

[4]No basis function exists with $l = K + 1$ that cannot be expressed as a combination of the ψ_{1a} and ψ_{1b} basis functions.

pendent component of a $\psi_{1a}\,(\psi_{1b})$ basis function with the parity dependent component of a $\psi_{1b}\,(\psi_{1a})$ function. The complete matrix elements of $\mathcal{H}_{RT}^{\text{eff.}} + \mathcal{H}_{SO}^{\text{eff.}}$ for the $^2\Sigma$ states in the manifold (v_1, v_2, v_3), are given in in Fig.IV.3. The effect of the matrix elements off-diagonal in v_2 can be estimated using second order perturbation theory,

$$\frac{E^{(2)}}{hc} = -\frac{\epsilon^2 \omega_2 n}{8}, \tag{IV.14}$$

where $n = (v_2 + 1)$ as usual. The most important features are the large matrix elements of $\mathcal{H}_{RT}^{\text{eff.}}$ diagonal in v_2. Consider just the $K = 0$ matrix diagonal in v_2:

$\lvert\psi_{1a}; v_1 v_2 v_3; \pm\rangle$	$\lvert\psi_{1b}; v_1 v_2 v_3; \pm\rangle$
$+\frac{1}{2}A + n\omega_2$	$\mp\frac{1}{2}(-1)^{J+\frac{1}{2}}\,\epsilon\omega_2 n$
$\mp\frac{1}{2}(-1)^{J+\frac{1}{2}}\,\epsilon\omega_2 n$	$-\frac{1}{2}A + n\omega_2$

The substantial off-diagonal elements produce a very large mixing of the ψ_{1a} and ψ_{1b} basis functions. Therefore, the upper and lower eigenvalues cannot reliably be identified with eigenfunctions having a well defined value of the quantum number P. This is because the Renner-Teller effect has greatly quenched the spin-orbit interaction, so the electron spin is only weakly coupled to the linear axis of the molecule [1].

Transformation to the μ, κ basis set

The problem of eigenstate characterisation is resolved by applying a similarity transformation to the above representation [1], producing new basis functions. The transformation mixes just two basis functions, diagonal in all quantum numbers except P and Σ. The explicit form is

$$\left|\kappa^2\Sigma; v_1 v_2 v_3; J; \pm\right\rangle = \cos\beta\,|\psi_{1a}; v_1 v_2 v_3; J; \pm\rangle + \sin\beta\,|\psi_{1b}; v_1 v_2 v_3; J; \pm\rangle \tag{IV.15}$$

$$\left|\mu^2\Sigma; v_1 v_2 v_3; J; \pm\right\rangle = -\sin\beta\,|\psi_{1a}; v_1 v_2 v_3; J; \pm\rangle + \cos\beta\,|\psi_{1b}; v_1 v_2 v_3; J; \pm\rangle \tag{IV.16}$$

The labels κ and μ mean higher and lower $^2\Sigma$ energy levels, respectively, after Hougen [1]. Note that the κ and μ basis functions are orthonormal. The transformation variables

$\lvert\psi_{1a};v_2+2;\pm\rangle$	$\lvert\psi_{1b};v_2+2;\pm\rangle$	$\lvert\psi_{1a};v_2;\pm\rangle$	$\lvert\psi_{1b};v_2;\pm\rangle$	$\lvert\psi_{1a};v_2-2;\pm\rangle$	$\lvert\psi_{1b};v_2-2;\pm\rangle$
$(n+2)\omega_2 + \frac{1}{2}A$	$\mp(-1)^p\frac{\varepsilon\omega_2}{2}(n+2)$	0	$\mp(-1)^p\frac{\varepsilon\omega_2}{4}[n \times(n+2)]^{\frac{1}{2}}$	0	0
$\mp(-1)^p\frac{\varepsilon\omega_2}{2}(n+2)$	$(n+2)\omega_2 - \frac{1}{2}A$	$\mp(-1)^p\frac{\varepsilon\omega_2}{4}[n (n+2)]^{\frac{1}{2}}$	0	0	0
0	$\mp(-1)^p\frac{\varepsilon\omega_2}{4}[n (n+2)]^{\frac{1}{2}}$	$n\omega_2 + \frac{1}{2}A$	$\mp(-1)^p\frac{\varepsilon\omega_2}{2}n$	0	$\mp(-1)^p\frac{\varepsilon\omega_2}{4}[n \times(n-2)]^{\frac{1}{2}}$
$\mp(-1)^p\frac{\varepsilon\omega_2}{4}[n \times(n+2)]^{\frac{1}{2}}$	0	$\mp(-1)^p\frac{\varepsilon\omega_2}{2}n$	$n\omega_2 - \frac{1}{2}A$	$\mp(-1)^p\frac{\varepsilon\omega_2}{4}[n (n-2)]^{\frac{1}{2}}$	0
0	0	0	$\mp(-1)^p\frac{\varepsilon\omega_2}{4}[n (n-2)]^{\frac{1}{2}}$	$(n-2)\omega_2 + \frac{1}{2}A$	$\mp(-1)^p\frac{\varepsilon\omega_2}{2}(n-2)$
0	0	$\mp(-1)^p\frac{\varepsilon\omega_2}{4}[n \times(n-2)]^{\frac{1}{2}}$	0	$\mp(-1)^p\frac{\varepsilon\omega_2}{2}(n-2)$	$(n-2)\omega_2 - \frac{1}{2}A$

Figure IV.3: The complete matrix elements of the spin-orbit and Renner-Teller effective Hamiltonians for the $K = 0$ states in the manifold (v_1, v_2, v_3). All the parameters have a vibrational dependence (not indicated for clarity). The quantum number $n = (v_2 + 1)$, $p = (J - S - l) \equiv (J + 1/2)$ is a phase factor. The upper and lower sign choices are for positive and negative parities, respectively. The term ΔA is absorbed into $\alpha_{2,a}$ and so not shown separately. $\Delta g_L^{(1)}$ is not included because the Zeeman effect is discussed later.

are defined by

$$\cos 2\beta = \frac{A}{2r} \tag{IV.17}$$

$$\sin 2\beta = \frac{\mp(-1)^{J+\frac{1}{2}}\,\epsilon\omega_2 n}{2r} \tag{IV.18}$$

$$r = \frac{1}{2}\left[A^2 + \epsilon^2\omega_2^2 n^2\right]^{\frac{1}{2}}. \tag{IV.19}$$

The angular functions adjust the composition of the eigenfunctions so that the treatment is valid for any values of A and $\epsilon\omega_2$, as long as the vibrational manifolds remain well separated. This treatment is based on a similar, but not identical one developed by Hougen [1]. In particular, in the treatment here, the parity and phase factor have been taken inside the $\sin 2\beta$ term. The angle 2β covers the range $-\pi/2 \leq 2\beta \leq \pi/2$ for $A > 0$, and $\pi/2 \leq 2\beta \leq 3\pi/2$ for $A < 0$; consequently $-\pi/4 \leq \beta \leq \pi/4$ for $A > 0$ and $\pi/4 \leq \beta \leq 3\pi/4$ for $A < 0$.

The similarity transformation exactly diagonalises the Renner-Teller (diagonal in v_2) and spin-orbit matrix representation. The remaining Renner-Teller, rotational and Zeeman terms etc., are relatively minor perturbations to the new eigenfunctions and κ and μ remain good labels because they depend only upon the energy order. The transformed matrix is

$\lvert\kappa^2\Sigma; v_1v_2v_3; J; \pm\rangle$	$\lvert\mu^2\Sigma; v_1v_2v_3; J; \pm\rangle$
$+r + n\omega_2$	0
0	$-r + n\omega_2$

In the limit $A \to 0$ (*i.e.* $|\cos\beta| = |\sin\beta| = 1/\sqrt{2}$), the non-rotational κ and μ basis functions are orthonormal eigenfunctions of $\mathcal{H}_{RT}^{\text{eff.}}$. The states can then be described as $^2\Sigma^{(+)}$ and $^2\Sigma^{(-)}$ [1, 9, 10]; the former relates to the V' (in-plane) potential curve and the latter to the V'' (out-of-plane) one, see Fig.III.6. The superscript symmetry label describes the effect of the molecule-fixed σ_v symmetry operation on the vibronic wave function. When $\epsilon > 0$, the κ state is $^2\Sigma^{(+)}$ and the μ state is $^2\Sigma^{(-)}$; this is reversed for $\epsilon < 0$ [1]. The introduction of spin-orbit coupling generates matrix elements between the pure $^2\Sigma^{(\pm)}$ states, so the superscript $(+)$ and $(-)$ labels become imprecise [1].

IV.2.2 Rotational Structure

The μ, κ representation

The most important interactions in the $K = 0$ states in the absence of a magnetic field are the Renner-Teller, spin-orbit, rotational, and spin-rotational effects. The Hund's case (a) representation of these terms (see §III.9.5), can easily be transformed to the μ/κ representation. *Mutatis Mutandis*, the matrix representation is

$\lvert\kappa^2\Sigma; v_1v_2v_3; J; \pm\rangle$	$\lvert\mu^2\Sigma; v_1v_2v_3; J; \pm\rangle$
$r - \frac{1}{8}\epsilon^2\omega_2 n + G(v_1, v_2, v_3)$ $+B\left(J+\frac{1}{2}\right)\left[\left(J+\frac{1}{2}\right) - \sin 2\beta\right]$ $+\frac{1}{2}\gamma\left[\left(J+\frac{1}{2}\right)\sin 2\beta - 1\right]$ $+\frac{1}{2}A_D\left(J+\frac{1}{2}\right)^2 \sin 2\beta$	$-\left(J+\frac{1}{2}\right)\left[\left(B-\frac{1}{2}\gamma\right)\cos 2\beta$ $+\frac{1}{2}A_D \sin 2\beta\right]$
Symmetric	$-r - \frac{1}{8}\epsilon^2\omega_2 n + G(v_1, v_2, v_3)$ $B\left(J+\frac{1}{2}\right)\left[\left(J+\frac{1}{2}\right) + \sin 2\beta\right]$ $-\frac{1}{2}\gamma\left[\left(J+\frac{1}{2}\right)\sin 2\beta + 1\right]$ $-\frac{1}{2}A_D\left(J+\frac{1}{2}\right)^2 \cos 2\beta$

where the effect of the $\Delta v_2 = \pm 2$ matrix elements has been estimated by second order perturbation theory [1]. The $(\pm)$ parity choice is implicit in the $\sin 2\beta$ factors, see Eq.(IV.18).

Approximate rotational term values

The terms in A_D and γ can be neglected to a good approximation, since they are generally much smaller than those in B. In this case the approximate term values are given by

$$\begin{aligned} F(J,\pm) &= -\frac{\epsilon^2\omega_2 n}{8} + G(v_1, v_2, v_3) + B\left(J+\frac{1}{2}\right)^2 \\ &+ (-1)^s r\left[1 + \frac{B^2\left(J+\frac{1}{2}\right)^2}{r^2} - \frac{2B\left(J+\frac{1}{2}\right)\sin 2\beta}{r}\right]^{\frac{1}{2}}, \end{aligned} \qquad \text{(IV.20)}$$

where the exponent s is even or odd for the κ and μ states, respectively.

Hougen [1] showed that in the absence of an external field, the rotational levels can be described by both a Hund's case (a) expression, in which J and P are good quantum

numbers, and a Hund's case (b) expression in which N is good. In the limit $A \gg \epsilon\omega_2$, the former is most appropriate since the states approximate to Hund's case (a) or (c) ${}^2\Sigma_{\pm\frac{1}{2}}$ states. More typically, both spin-orbit and Renner-Teller effects are important and the states are closer to Hund's case (b), as is the case for NCO.

Hund's case (b) expression

A binomial expansion (to the third term) of the square root in Eq.(IV.20), retaining terms only up to B^2 [1], gives Hund's case (b) expressions [11] for the term values (in wave number) of

$$\kappa^2\Sigma \begin{cases} F_1(N) = -\frac{1}{8}\epsilon^2\omega_2 n + G(v_1,v_2,v_3) + \frac{1}{2}\gamma_\kappa^{\text{eff.}} + B_\kappa^{\text{eff.}} N(N+1) + \frac{1}{2}\gamma_\kappa^{\text{eff.}} N \\ F_2(N) = -\frac{1}{8}\epsilon^2\omega_2 n + G(v_1,v_2,v_3) + \frac{1}{2}\gamma_\kappa^{\text{eff.}} + B_\kappa^{\text{eff.}} N(N+1) - \frac{1}{2}\gamma_\kappa^{\text{eff.}}(N+1), \end{cases}$$

and

$$\mu^2\Sigma \begin{cases} F_1(N) = -\frac{1}{8}\epsilon^2\omega_2 n + G(v_1,v_2,v_3) + \frac{1}{2}\gamma_\mu^{\text{eff.}} + B_\mu^{\text{eff.}} N(N+1) + \frac{1}{2}\gamma_\mu^{\text{eff.}} N \\ F_2(N) = -\frac{1}{8}\epsilon^2\omega_2 n + G(v_1,v_2,v_3) + \frac{1}{2}\gamma_\mu^{\text{eff.}} + B_\mu^{\text{eff.}} N(N+1) - \frac{1}{2}\gamma_\mu^{\text{eff.}}(N+1), \end{cases}$$

where N is the Hund's case (b) quantum number. The parameters $\gamma_\kappa^{\text{eff.}}$ and $\gamma_\mu^{\text{eff.}}$ are effective ones and bear no relation to the true spin-rotation parameter, γ. The latter parameter was neglected in deriving these expressions. The effective parameters are defined by

$$B_\kappa^{\text{eff.}} = B\left[1 + \frac{B}{2r}\cos^2 2\beta\right], \tag{IV.21}$$

$$\gamma_\kappa^{\text{eff.}} = 2B\left[1 + \frac{B}{2r}\cos^2 2\beta - |\sin 2\beta|\right] \tag{IV.22}$$

and

$$B_\mu^{\text{eff.}} = B\left[1 - \frac{B}{2r}\cos^2 2\beta\right], \tag{IV.23}$$

$$\gamma_\mu^{\text{eff.}} = 2B\left[1 - \frac{B}{2r}\cos^2 2\beta - |\sin 2\beta|\right]. \tag{IV.24}$$

In both cases, $0 < \gamma^{\text{eff.}} < +2B$. The labels F_1, F_2 correlate[5] with J as follows:

$$F_1(N) \Longrightarrow J = N + \frac{1}{2} \tag{IV.25}$$

$$F_2(N) \Longrightarrow J = N - \frac{1}{2} \tag{IV.26}$$

A note on $\sin 2\beta$

In writing the term values and defining $\gamma^{\text{eff.}}$, $\sin 2\beta$ has been replaced by $|\sin 2\beta|$. This is a subtle point which can be appreciated by considering Eq.(IV.18) together with the parities of the $|F_1, N\rangle$ and $|F_2, N\rangle$ rotational levels and the sign of the Renner parameter.

Irrespective of the numerical sign of ϵ, the N dependent term involving $\sin 2\beta$ is *always* a negative quantity in the term value expressions for the F_1 levels of both the $\mu^2\Sigma$ and $\kappa^2\Sigma$ states. Similarly, the corresponding quantity for the F_2 levels is *always* a negative quantity.

Characteristics of the rotational levels

The above expressions give a spacing between adjacent N levels of $2B^{\text{eff.}}(N+1)$; this is the gross rotational structure. Each N level then has a much smaller (at least for low N) splitting of

$$F_1(N) - F_2(N) = \frac{1}{2}\gamma^{\text{eff.}}(2N+1), \tag{IV.27}$$

though this splitting is typically very much larger than the true spin-rotation splitting in a $^2\Sigma$ electronic state. The effective splitting parameter, $\gamma^{\text{eff.}}$, is always positive so that $|N, F_1\rangle$ always lies above $|N, F_2\rangle$. The rotational structure of the $K = 0$ states is shown in Fig.IV.4. Note that both the F_1 and F_2 levels belonging to the same N have the same parity. The parity alternates with N and can be deduced by noting that the $N = 0$ rotational level has the same parity as the nominal $^2\Sigma^{(\pm)}$ label of the vibronic state. In the absence of an external field, a rotational level can be identified uniquely by the quantum numbers v_1, v_2, v_3, N, parity and either of κ/μ or J.

The parameter $\gamma^{\text{eff.}}$ should not be confused with the true spin-rotation parameter γ, which has not been included in the term value expressions above[6]. The latter arises prin-

[5] These correlations are only exact in the absence of an external field.

[6] The true spin-rotation parameter γ is very much smaller than B, and has been neglected in these

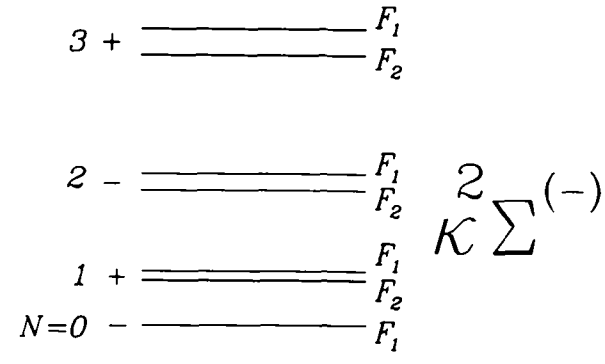

Figure IV.4: The Hund's case (b) rotational structure of the $K = 0$ states. The scheme shown is for $\epsilon < 0$; when $\epsilon > 0$ all the $+/-$ labels swap over. The rotational spacings are grossly exaggerated when compared with the κ/μ separation.

cipally from non-adiabatic spin-orbit interactions, whereas $\gamma^{\text{eff.}}$ arises from the residue of the Renner-Teller quenched spin-orbit interaction within the $^2\Pi$ electronic state.

Selection rules for vibration-rotation transitions in the $K = 0$ states

The selection rules for vibration-rotation transitions are

$$\Delta N = \pm 1; \Delta J = 0, \pm 1; F_1 \leftrightarrow F_1, F_2 \leftrightarrow F_2, F_1 \leftrightarrow F_2; \kappa \leftrightarrow \kappa, \mu \leftrightarrow \mu; \kappa \not\leftrightarrow \mu. \quad \text{(IV.28)}$$

The $\kappa \leftrightarrow \mu$ transitions are forbidden because they are analogous to $\Delta P = \pm 1$ transitions in a Hund's case (a) system. The vibration-rotation transition $(v_1' v_2' v_3', N', F_i') \leftarrow (v_1'' v_2'' v_3'', N'', F_i'')$ may be denoted by

$$1_{v_1''}^{v_1'} 2_{v_2''}^{v_2'} 3_{v_3''}^{v_3'} \; {}^{\Delta N}\Delta J_{F_i' F_i''}(N''), \quad \text{(IV.29)}$$

where P,Q and R are used for ΔJ (or ΔN) $= -1, 0, +1$, respectively, $i = 1, 2$ and the single and double primes denote the upper and lower levels. The possible transitions are therefore ${}^{\text{P}}\text{P}_{11}(N''), {}^{\text{P}}\text{P}_{22}(N''), {}^{\text{P}}\text{Q}_{12}(N''), {}^{\text{R}}\text{R}_{11}(N''), {}^{\text{R}}\text{R}_{22}(N'')$ and ${}^{\text{R}}\text{Q}_{21}(N'')$. It must be remembered that $N = 0$ has only an F_1 level, *i.e.* $J = 1/2$.

IV.2.3 Zeeman Effect

Matrix representation of the Zeeman effect

The Zeeman matrix diagonal in J and transformed to the μ/κ representation is

$\lvert\kappa^2\Sigma; v_1 v_2 v_3; J; \pm\rangle$	$\lvert\mu^2\Sigma; v_1 v_2 v_3; J; \pm\rangle$
$\frac{\mu_B B_0 M_J}{2J(J+1)} \left[g_L' \cos 2\beta + g_S \left\{ \frac{1}{2} + \left(J + \frac{1}{2}\right) \sin 2\beta \right\} \right]$	$-\frac{\mu_B B_0 M_J}{2J(J+1)} \left[g_L' \sin 2\beta - g_S \left(J + \frac{1}{2}\right) \cos 2\beta \right]$
Symmetric	$-\frac{\mu_B B_0 M_J}{2J(J+1)} \left[g_L' \cos 2\beta - g_S \left\{ \frac{1}{2} - \left(J + \frac{1}{2}\right) \sin 2\beta \right\} \right]$

Consider two adjacent levels, $J + 1$ and J, with the same parity, in the $\mu^2\Sigma$ state. These levels form the pair N, F_1 and N, F_2 (see Fig.IV.4). Neglecting the Zeeman matrix

approximate expressions. It is of course included in the computer model.

elements (§III.12.3) between the μ and κ states (which are well separated compared with the Zeeman energy), but including the matrix elements off-diagonal in J between N, F_1 and N, F_2 in the same state, the matrix representation for a given value of N is

$\lvert\mu^2\Sigma; v_1v_2v_3; N; F_1\rangle$	$\lvert\mu^2\Sigma; v_1v_2v_3; N; F_2\rangle$
$-\frac{\mu_B B_0 M_J}{2\left(N+\frac{1}{2}\right)\left(N+\frac{3}{2}\right)}\left[g'_L\cos 2\beta - g_S\left\{\frac{1}{2}+(N+1)\lvert\sin 2\beta\rvert\right\}\right]$	$-\mu_B B_0\left[\frac{\left(N+\frac{1}{2}\right)^2-M_J^2}{4\left(N+\frac{1}{2}\right)^2}\right]^{\frac{1}{2}} \times\left[g'_L\cos 2\beta-\frac{1}{2}g_S\left\{1+\lvert\sin 2\beta\rvert\right\}\right]$
Symmetric	$-\frac{\mu_B B_0 M_J}{2\left(N-\frac{1}{2}\right)\left(N+\frac{1}{2}\right)}\left[g'_L\cos 2\beta - g_S\left\{\frac{1}{2}-N\lvert\sin 2\beta\rvert\right\}\right]$

The corresponding matrix for the κ states is

$\lvert\kappa^2\Sigma; v_1v_2v_3; N; F_1\rangle$	$\lvert\kappa^2\Sigma; v_1v_2v_3; N; F_2\rangle$
$\frac{\mu_B B_0 M_J}{2\left(N+\frac{1}{2}\right)\left(N+\frac{3}{2}\right)}\left[g'_L\cos 2\beta + g_S\left\{\frac{1}{2}+(N+1)\lvert\sin 2\beta\rvert\right\}\right]$	$-\mu_B B_0\left[\frac{\left(N+\frac{1}{2}\right)^2-M_J^2}{4\left(N+\frac{1}{2}\right)^2}\right]^{\frac{1}{2}} \times\left[g'_L\cos 2\beta+\frac{1}{2}g_S\left\{1+\lvert\sin 2\beta\rvert\right\}\right]$
Symmetric	$\frac{\mu_B B_0 M_J}{2\left(N-\frac{1}{2}\right)\left(N+\frac{1}{2}\right)}\left[g'_L\cos 2\beta + g_S\left\{\frac{1}{2}-N\lvert\sin 2\beta\rvert\right\}\right]$

When the matrix elements of the Renner-Teller effect with $\Delta v_2 = \pm 2$ are ignored, their effect on g_L can be estimated using third order perturbation theory [12], see Eq.(C.4), Appendix C. The total effective g_L value for the $K = 0$ states is then approximately given by

$$g_L^{\text{eff.}} = g_L^{(0)}\left[1-\frac{\epsilon^2}{16}n^2\right] + \Delta g_L^{(1)} n, \tag{IV.30}$$

where $n = (v_2 + 1)$.

Comparison of the Zeeman effect in a $^2\Sigma$ vibronic state with that in a $^2\Sigma$ electronic state

It is instructive to compare the above Zeeman matrix with that for a $^2\Sigma$ electronic state [13]. In such a state, the case (b) eigenfunctions are given by the following combination

of Hund's case (a) basis functions:

$$|N,F_1\rangle = \frac{1}{\sqrt{2}}\left\{\left|\Lambda=0;S=+\frac{1}{2}\Sigma=+\frac{1}{2};J+1,\Omega=+\frac{1}{2}M_J\right\rangle + \left|\Lambda=0;S=+\frac{1}{2}\Sigma=-\frac{1}{2};J+1,\Omega=-\frac{1}{2}M_J\right\rangle\right\} \quad \text{(IV.31)}$$

$$|N,F_2\rangle = \frac{1}{\sqrt{2}}\left\{\left|\Lambda=0;S=+\frac{1}{2}\Sigma=+\frac{1}{2};J,\Omega=+\frac{1}{2}M_J\right\rangle - \left|\Lambda=0;S=+\frac{1}{2}\Sigma=-\frac{1}{2};J,\Omega=-\frac{1}{2}M_J\right\rangle\right\} \quad \text{(IV.32)}$$

and the matrix representation is

$\|^2\Sigma;N,F_1,M_J\rangle$	$\|^2\Sigma;N,F_2,M_J\rangle$
$BN(N+1)+\frac{1}{2}\gamma N$ $+g_S\mu_B B_0\frac{M_J}{2\left(N+\frac{1}{2}\right)}$	$g_S\mu_B B_0\left[\frac{\left(N+\frac{1}{2}\right)^2-M_J^2}{4\left(N+\frac{1}{2}\right)^2}\right]^{\frac{1}{2}}$
$g_S\mu_B B_0\left[\frac{\left(N+\frac{1}{2}\right)^2-M_J^2}{4\left(N+\frac{1}{2}\right)^2}\right]^{\frac{1}{2}}$	$BN(N+1)-\frac{1}{2}\gamma(N+1)$ $-g_S\mu_B B_0\frac{M_J}{2\left(N+\frac{1}{2}\right)}$

The obvious difference is the presence of orbital Zeeman terms in the $^2\Sigma$ vibronic states which are zero in a $^2\Sigma$ electronic state. In addition, the $^2\Sigma$ vibronic states are not generally 50:50 mixtures of the Hund's case (a) basis functions, unlike a pure $^2\Sigma$ electronic state.

A comparison of the Zeeman matrix elements in the electronic and vibronic $^2\Sigma$ states allows the coefficient equivalent to g_S in the $^2\Sigma$ electronic state to be defined for the $^2\Sigma$ vibronic states. As an example of this, the equivalent to g_S for the diagonal matrix element $\langle N,F_1|H_z|N,F_1\rangle$ in the $\mu^2\Sigma^{(+)}$ state is

$$g_{S\,\mu^2\Sigma,F_1}^{\text{equiv.}} = -\frac{1}{\left(N+\frac{3}{2}\right)}\left[g_L'\cos 2\beta - g_S\left\{\frac{1}{2}+(N+1)\left|\sin 2\beta\right|\right\}\right]. \quad \text{(IV.33)}$$

A similar term can be extracted for each position in the $\mu\,^2\Sigma$ and $\kappa\,^2\Sigma$ Zeeman matrices, and compared with g_S. These terms have been evaluated for several rotational levels

of NCO in the $(010)\,^2\Sigma$ states, and they are given in Tables IV.1 and IV.2. For the purpose of this comparison, g_L' was replaced by $g_L^{\text{eff.}}$, Eq.(IV.30), in order to account for the quenching effect of the Renner-Teller matrix elements off-diagonal by $\Delta v_2 = \pm 2$.

Table IV.1: Equivalents of g_S for the $(010)\,\mu^2\Sigma^{(+)}$ state of NCO.

$N =$	0	1	2	3	4	5	∞
$g_{F_1}^{\text{eff.}}{}^{(a,b)}$	2.146	1.968	1.892	1.849	1.822	1.803	1.700
$g_{F_2}^{\text{eff.}}$	–	0.363	1.255	1.433	1.509	1.552	1.700
$g_{F_1/F_2}^{\text{eff.}}{}^{(c)}$	–	2.369	2.369	2.369	2.369	2.369	2.369

(a) Evaluated using $A_{(010)} = -95.7246\,\text{cm}^{-1}$, $\epsilon\omega_2 = -76.7249\,\text{cm}^{-1}$, $\omega_2 = 534.063\,\text{cm}^{-1}$, $g_L^{\text{eff.}} = 0.98138$, $g_S = 2.002099$.

(b) For a $^2\Sigma$ electronic state, these values are all equal to g_S.

(c) Equivalent of g_S in the off-diagonal position, $\langle N, F_1 | H_z | N, F_2 \rangle$.

Table IV.2: Equivalents of g_S for the $(010)\,\kappa^2\Sigma^{(-)}$ state of NCO.

$N =$	0	1	2	3	4	5	∞
$g_{F_1}^{\text{eff.}}{}^{(a,b)}$	1.456	1.554	1.596	1.619	1.634	1.644	1.700
$g_{F_2}^{\text{eff.}}$	–	2.435	1.945	1.847	1.805	1.782	1.700
$g_{F_1/F_2}^{\text{eff.}}{}^{(c)}$	–	−1.333	−1.333	−1.333	−1.333	−1.333	−1.333

(a) Evaluated using the parameters given at the foot of Table IV.1.

(b) For a $^2\Sigma$ electronic state, these values are equal to g_S.

(c) Equivalent of g_S in the off-diagonal position, $\langle N, F_1 | H_z | N, F_2 \rangle$.

The complete expressions for the diagonal Zeeman matrix elements of the μ and $\kappa\,^2\Sigma$ states have been evaluated explicitly for the $N = 1$ levels and are given in Table IV.3. These expressions are the coefficients of $M_J \mu_B B_0$ and as such are effective g-factors for the $^2\Sigma$ vibronic states. For comparison, the effective g-factors for a $^2\Sigma$ electronic state are also given in Table IV.3. Note that the magnetic moment changes sign between the F_1 and F_2 components. As can be seen in Fig.IV.5, this reverses the energy ordering of the M_J components and the sign of the low field tuning rate for the M_J levels in the F_2 component. This phenomenon also occurs in a $^2\Sigma$ electronic state [13].

Table IV.3: Calculated diagonal Zeeman matrix elements for $N = 1$ levels of the $\mu^2\Sigma^{(+)}$ and $\kappa^2\Sigma^{(-)}$ states of NCO ($\tilde{X}^2\Pi$).

Zeeman Hamiltonian matrix element	Value $[cm^{-1}]^{(a,b)}$ $^2\Sigma$ Electronic state $[cm^{-1}]$	
$\langle \mu\,^2\Sigma, N, F_1 \vert H_z \vert \mu\,^2\Sigma, N, F_1 \rangle$	$+0.656 M_J \mu_B B_0$	$+0.667 M_J \mu_B B_0$
$\langle \mu\,^2\Sigma, N, F_2 \vert H_z \vert \mu\,^2\Sigma, N, F_2 \rangle$	$-0.121 M_J \mu_B B_0$	$-0.667 M_J \mu_B B_0$
$\langle \kappa\,^2\Sigma, N, F_1 \vert H_z \vert \kappa\,^2\Sigma, N, F_1 \rangle$	$+0.518 M_J \mu_B B_0$	$+0.667 M_J \mu_B B_0$
$\langle \kappa\,^2\Sigma, N, F_2 \vert H_z \vert \kappa\,^2\Sigma, N, F_2 \rangle$	$-0.812 M_J \mu_B B_0$	$-0.667 M_J \mu_B B_0$

$^{(a)}$Using $g_S = 2.002099$, $g_L^{\text{eff.}} = 0.98138$, $\cos 2\beta = -0.527828$, $|\sin 2\beta| = 0.849351$.

$^{(b)}\mu_B$ is the Bohr magneton, B_0 is the flux density.

Points to be noted from the comparison

The following points should be noted:

1. The equivalents of g_S, *e.g.* Eq.(IV.33), differ significantly from the value of g_S for a $^2\Sigma$ electronic state and can exceed g_S in magnitude. The $^2\Sigma$ vibronic states cannot be modelled as though they were $^2\Sigma$ electronic states because there are orbital Zeeman effects.

2. The equivalents of g_S in the diagonal positions are N dependent and tend to a finite, non-zero value as $N \rightarrow \infty$; the limiting values differ from g_S. The effective g-factors, *e.g.* Table IV.3, decrease as N increases, but more slowly than the g_J factor in the Hund's case (a) unique states, in which $g_J \rightarrow 0$ as $J \rightarrow \infty$. Therefore, the Hund's case (b) energy levels remain significantly tunable, even at high N. The tunability is also modified by off-diagonal Zeeman matrix elements not represented in the 2×2 matrices above. These become extremely significant as the flux density increases, as do higher order Zeeman effects which mediate interactions with the levels[7] $N \pm 2, N \pm 4, \cdots$, and also interactions between the μ and κ states. Therefore, the values quoted in Tables IV.1–IV.3 are only reliable in the low field limit, when the Zeeman energy is less than the separation of the levels $N \pm 2$.

3. The significance of the orbital Zeeman term decreases as N increases, so orbital Zeeman effects are most important for low N levels. This reflects the increasing

[7]The levels $N \pm 1, N \pm 3, \ldots$, have the opposite parity.

transition to pure Hund's case (b) behaviour as N increases.

Zeeman effect behaviour of the $\mu\,^2\Sigma$ and $\kappa\,^2\Sigma$ rotational levels

The behaviour of the $^2\Sigma$ vibronic levels in a magnetic field is shown in Figs. IV.5 and IV.6 for the $N = 1$ level in the $(010)\,^2\Sigma$ states of NCO. The modelling was performed using the 'RENNER.FOR' computer program (described in §IV.5), exactly diagonalising the complete effective Hamiltonian, which included basis members with $\Delta v_2 = \pm 4$ and $\Delta J = \pm 6$. The parameters were taken from the final analysis of the $1_0^1 2_1^1\,^2\Sigma$ bands of NCO, Table VII.4.

A similar calculation was performed for a molecule in a $^2\Sigma$ electronic state, using a diatomic molecule program constructed in a Hund's case (b) basis set, 'HUNDB.FOR' [14]. The rotational parameters used in this calculation were the effective ones for the $\mu^2\Sigma$ state of NCO, calculated from the formulae in §IV.2.2. The result of this calculation is shown in Fig.IV.7.

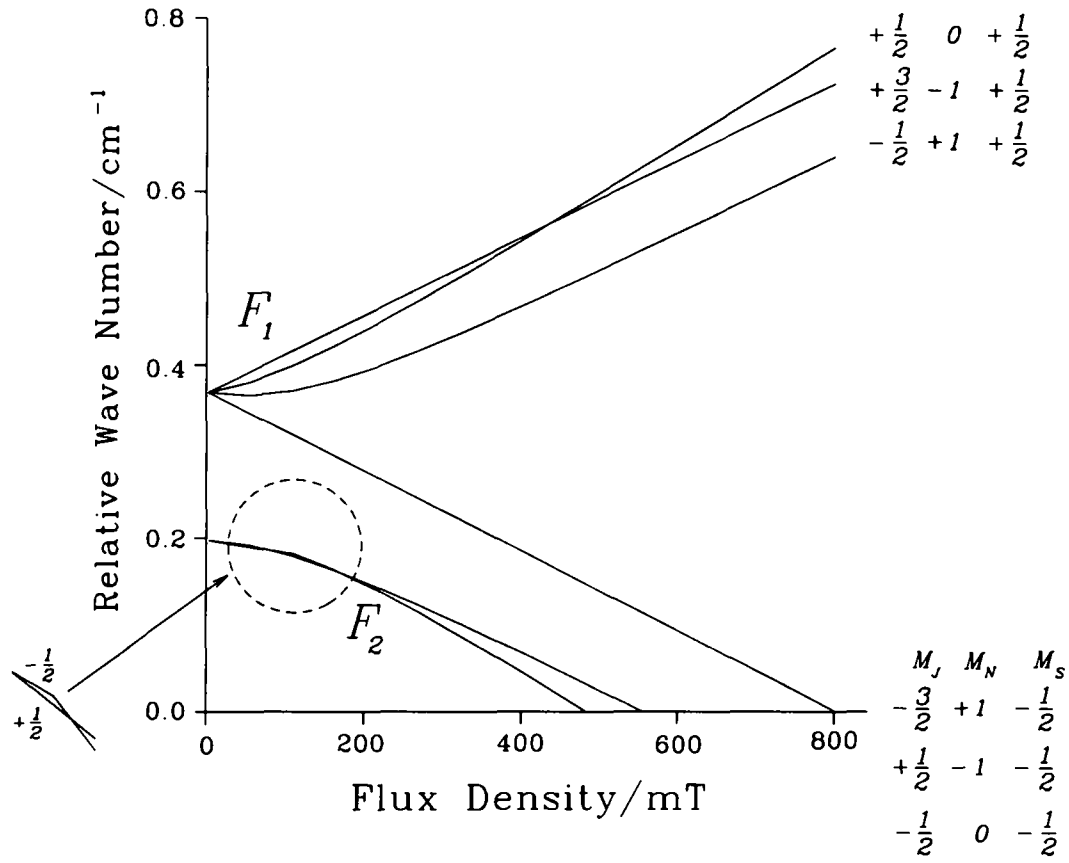

Figure IV.5: The Zeeman effect in the $N = 1$ level of the $(010)\,\mu^2\Sigma^{(+)}$ state of NCO. The major parameters used were $A_{(010)} = -95.7246\,\mathrm{cm}^{-1}$, $\epsilon\omega_2 = -76.7249\ \mathrm{cm}^{-1-1}$, $B = 0.39045284\ \mathrm{cm}^{-1-1}$, $g_S = 2.002099$, $g_L^{(0)} = 0.99989$, $\Delta g_L^{(1)} = -0.67765 \times 10^{-2}$, $g_l = 0.25 \times 10^{-2}$, and a basis set with $\Delta v_2 = \pm 4, \Delta J = \pm 6$ was used for the exact calculation.

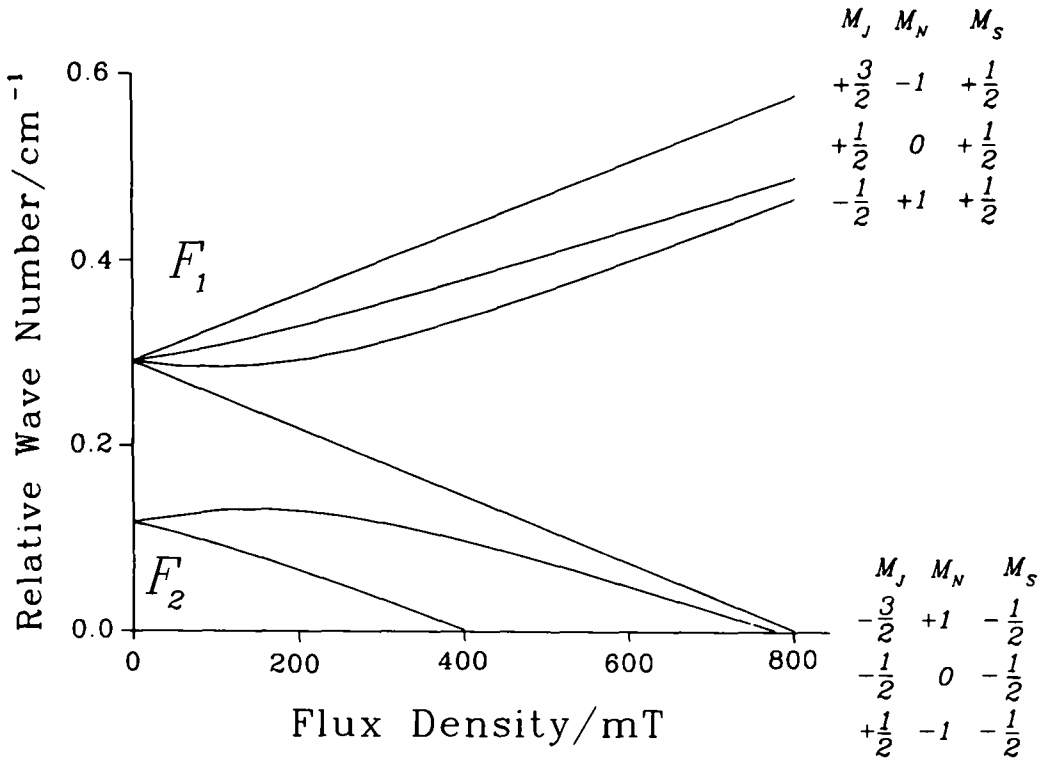

Figure IV.6: The Zeeman effect in the $N = 1$ level of the $(010)\,\kappa^2\Sigma^{(-)}$ state of NCO. The parameters used were the same as for Fig.IV.5. Both figures provide good examples of the molecular Paschen-Back effect (spin-decoupling).

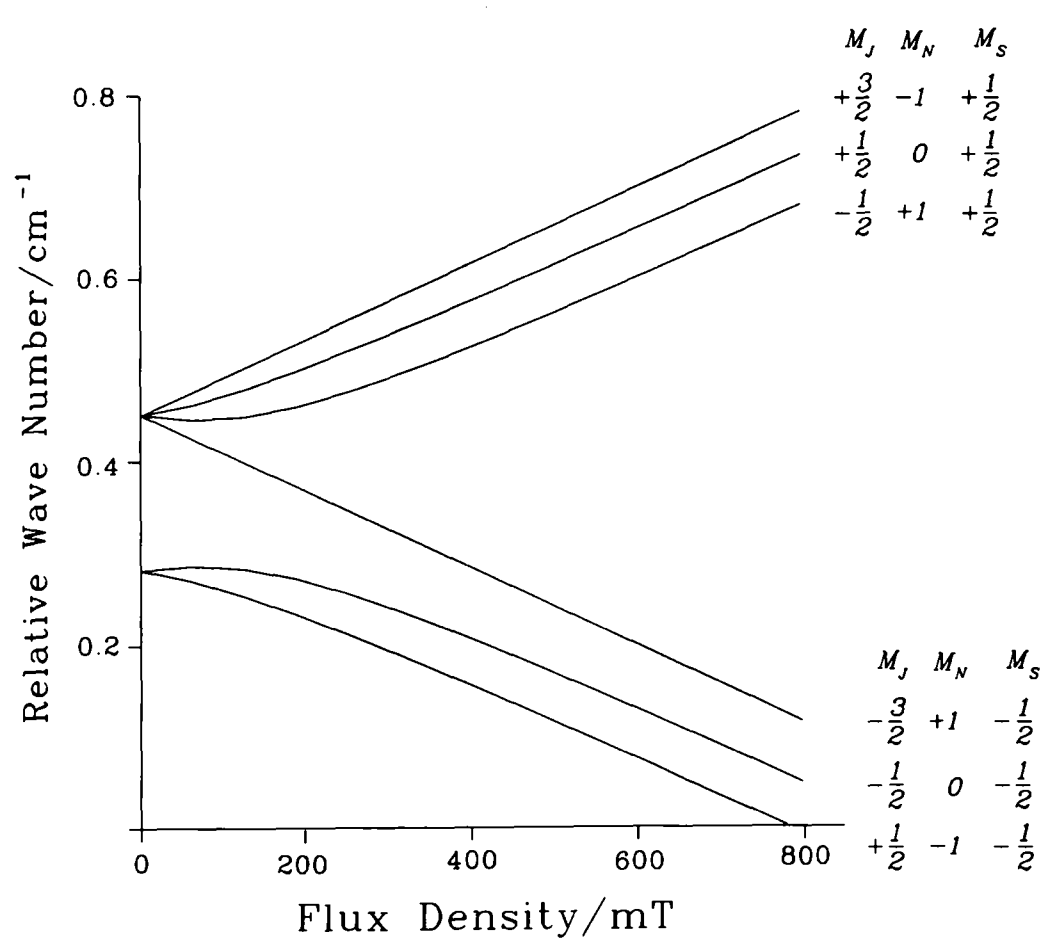

Figure IV.7: The Zeeman effect in the $N = 1$ level of a molecule in a $^2\Sigma$ electronic state. The parameters used were $B = 0.39021775\,\mathrm{cm}^{-1}, \gamma = \gamma_\mu^{\mathrm{eff.}} = 0.117172\,\mathrm{cm}^{-1}, g_S = 2.002099, g_l = 0.25 \times 10^{-2}$ and a basis set with $\Delta N = \pm 6$.

The levels of the $^2\Sigma$ electronic state show simpler Zeeman effect behaviour than those of NCO in the $K = 0$ states. The behaviour of the $\mu^2\Sigma$ states is the most complicated, since the M_J components cross over and do not tune parallel to one another at high fields. The $\kappa^2\Sigma$ levels are slightly simpler; this is in line with expectations for NCO that the $\mu\,^2\Sigma$ states can be considered as a relic of the "$^2\Pi_{\Omega=\frac{3}{2}}$" spin component and the $\kappa\,^2\Sigma$ states a relic of the "$^2\Pi_{\Omega=\frac{1}{2}}$" spin component, of a pure $^2\Pi$ electronic state. Therefore, the former are the most tunable.

Spin-Decoupling

As can be seen in Figs.IV.5 and IV.6, the Zeeman components split into two groups at high fields; this phenomenon is spin-decoupling, sometimes called the molecular Paschen-Back effect [7, 11, 15]. Consider the $N, F_1/N, F_2$ Zeeman matrices for the $^2\Sigma$ vibronic states. The element off-diagonal between F_1 and F_2 (*i.e.* $\Delta J = \pm 1$) becomes increasingly important as the flux density increases. The mixing of the F_1 and F_2 levels represents the decoupling of the electron spin along the molecule-fixed z-axis, to which it is only weakly coupled because the orbital angular momentum is quenched by the Renner-Teller effect. The torque exerted by an increasing external field couples the electron spin, $\mathbf{S}$, about the space-fixed Z-axis with a projection of M_S, in the same way that the nuclear spin is decoupled from the molecule-fixed z-axis and becomes space quantised.

The quantum number M_J remains good[8] and can be expressed in terms of the space-fixed projections of N and S [7],

$$M_J = M_N + M_S. \tag{IV.34}$$

Spin-decoupling occurs when the Zeeman energy is of the order of the $F_1 - F_2$ spacing ($\sim \frac{1}{2}\gamma^{\text{eff.}}\{2N + 1\}$), so the onset occurs at higher fields as N increases. The Zeeman components can be considered to be decoupled when they have passed the curved turning point in the Zeeman tuning diagram. This occurs at very low flux densities in Figs.IV.5 and IV.6, but can be seen in Fig.IV.8.

[8]Strictly it is $M_F = M_J + M_I$ that is always good, but nuclear spin is neglected here.

The breakdown of J

The levels N, F_1 and N, F_2 in the same state, which differ by 1 in J, are very close in energy, so the Zeeman effect destroys the goodness of J by mixing them together. F_1 and F_2 are no longer good labels for the identification of eigenstates, and an alternative means of identifying eigenstates has to be employed. Consider Fig.IV.8 which shows how the character of the eigenstates of a given N level varies with field[9]. At zero field, F_1 and F_2 are good labels; at a certain field B_0, the eigenstates are 50:50 mixtures of F_1 and F_2 and it is impossible to use these labels to distinguish them. Beyond this field the labels F_1 and F_2 have swapped levels non-adiabatically.

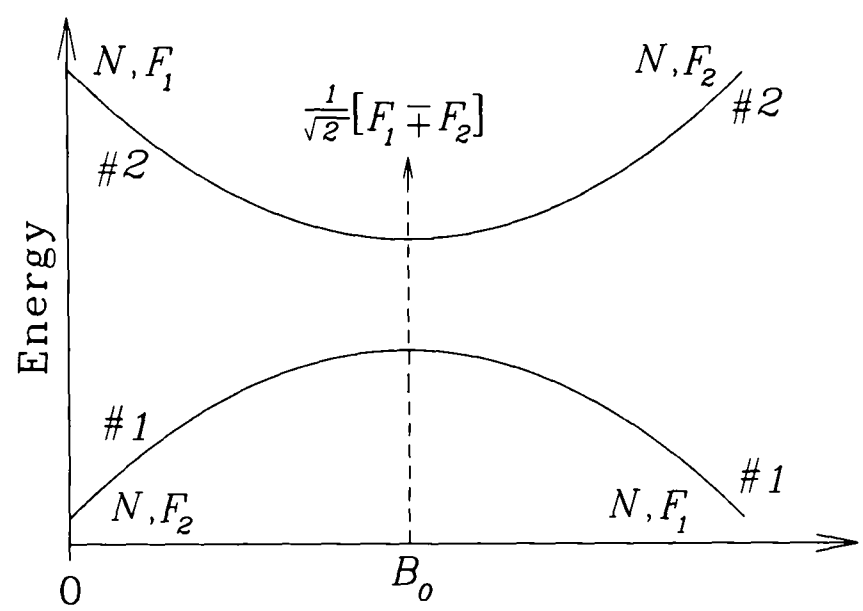

Figure IV.8: The heavy mixing of levels with $\Delta J = \pm 1$ due to the Zeeman effect in the $^2\Sigma$ vibronic states leads to a breakdown of the F_1/F_2 labels. The adiabatic energy level ordering labels $\#_1, \#_2$ remain good because of the non-crossing rule and are used to identify the energy levels. Note that both levels must have the same value of M_F (or M_J if nuclear spin is ignored).

$\#_i$ ordering

The alternative scheme is to identify the levels by '$\#_i$' ordering, where $\#_2$ correlates with N, F_1, M_J and $\#_1$ correlates with N, F_2, M_J *at zero field.* The label $\#_i$ adiabatically follows the energy level, not its character; since the levels never cross this is a foolproof scheme. When the character of the level is required (*e.g.* in intensity and Zeeman tuning

[9] Assuming that the only important off-diagonal Zeeman matrix element is the $N, F_1/N, F_2$ term.

rate calculations), this is of course still correctly given by the eigenvector coefficients of the basis functions for the level.

At high fields, the Zeeman components will tune into the region of the levels $N \pm 2$; N is then no longer a good quantum number. This can be overcome by an extension of the $\#_i$ ordering scheme to count the absolute ordering of several levels at zero field. In a similar manner, the $\#_i$ ordering scheme can be extended to count the ordering of nuclear hyperfine levels with the same values of $M_F = M_I + M_J$ within each $|N, F_i\rangle$ level.

Intensities of transitions in the $K = 0$ states

In a magnetic field, the $\mu, \kappa\,^2\Sigma$ levels are tunable over a much larger range of energies than the unique state levels. Unfortunately transitions between the $^2\Sigma$ levels tend to lose intensity with increasing flux density. This arises because of electron spin-decoupling effects. In the spin-decoupled (*i.e.* high field) limit, the selection rules on ΔM_J for electric dipole transitions become instead[10] [16]:

$$\sigma \text{ polarisation} : \quad \Delta M_N = \pm 1; \Delta M_S = 0 \tag{IV.35}$$

$$\pi \text{ polarisation} : \quad \Delta M_N = 0; \Delta M_S = 0 \tag{IV.36}$$

In the spin-decoupled limit, F_1 Zeeman components correlate with $M_S = +1/2$, with the exception of the component having $M_J = -(N + 1/2)$, which correlates with $M_S = -1/2$ [16]. All of the F_2 Zeeman components correlate with $M_S = -1/2$. Therefore, the following electric dipole induced LMR transitions arise:

1. Fast tuning $F_1 \leftrightarrow F_2$ transitions, whose Zeeman components almost all rapidly lose intensity due to spin-decoupling as the field increases. Nevertheless, such transitions may appear as very sharp resonances at low field.

   There are two types of these transitions; the first have $\Delta J = 0, \Delta N = \pm 1$, denoted $^{\mathrm{R}}Q_{21}$ and $^{\mathrm{P}}Q_{12}$. The components of these transitions involving $|F_1, M_J = -(N + 1/2)\rangle$ going to/from F_2 levels correlate with $\Delta M_S = 0$ and so retain intensity at higher fields, although they are slower tuning than the other $F_1 \leftrightarrow F_2$ transitions.

[10] Spin-orbit and spin-rotation interactions give a little intensity to transitions with $\Delta M_S \neq 0$.

The second type have $\Delta J = \pm 2, \Delta N = \pm 1$, denoted ${}^{P}O_{21}$ and ${}^{R}S_{12}$. These transitions are forbidden at zero field but gain intensity because of the field induced mixing of $|N, F_1, M_J\rangle$ and $|N, F_2, M_J\rangle$, which mixes the levels with $J = N \pm 1/2$. These transitions are very fast tuning but show rapid spin-decoupling, since they *always* correlate with $\Delta M_S = \pm 1$ in the high field limit.

2. Transitions of the type $F_1 \leftrightarrow F_1$ and $F_2 \leftrightarrow F_2$. These transitions correlate with $\Delta M_S = 0$ and so retain intensity at higher fields, although they are slow tuning. Such transitions would give broad Doppler limited resonances and are more likely to be detected in saturation as Lamb-dips, which would be better modulated in detection. Fast tuning $F_1 \leftrightarrow F_1$ transitions occur when one component involves the $M_J = -(N + 1/2)$ level; these are weak because they correlate with $\Delta M_S = \pm 1$.

IV.3 Anharmonic Effects in the $^2\Sigma$ Vibronic States

IV.3.1 Introduction

In order to aid the prediction of transitions in the $1_0^1 2_1^1$ $\mu^2\Sigma$ and $\kappa^2\Sigma$ vibronic bands of NCO, it was necessary to fit the microwave observations of the $(010)^2\Sigma$ levels. These observations were made by Kawaguchi *et al.*[17], who found it necessary to include anharmonic interactions in their model in order to describe the observations satisfactorily. These interactions impart slightly different rotational properties to the $\mu^2\Sigma$ and $\kappa^2\Sigma$ states.

This section develops a treatment of the anharmonic interactions between the $^2\Sigma$ vibronic states in the manifold (v_1, v_2, v_3) with those in the manifolds $(v_1 \pm 1, v_2', v_3)$ and $(v_1, v_2', v_3 \pm 1)$, where $v_2' = v_2, v_2 \pm 2$. The treatment is constructed in the Hund's case (a) parity conserving basis functions for the $K = 0$ states, ψ_{1a} and ψ_{1b} (see §IV.2.1). The problem is developed *ad hoc* for the $(010)\,^2\Sigma$ levels. A methodology similar to that introduced by Hougen [18] is used to develop the treatment.

When the anharmonic interactions are much smaller than both the Renner-Teller splitting and the vibrational energy level spacings, they can be expressed by a new effective Hamiltonian operating only within the v_2 manifolds. For the $^2\Sigma$ states in the manifold (v_1, v_2, v_3), the matrix elements span the representation (v_1, v_2', v_3), where $v_2' =$

$v_2, v_2 \pm 2$. The effective Hamiltonian takes the form of a centrifugal distortion of the Renner-Teller effect, characterised by a parameter $(\epsilon\omega_2)_D$, which bears no simple relation to $\epsilon\omega_2$.

A treatment of anharmonic interactions in the $(010)\,^2\Sigma$ vibronic levels was first developed by Kawaguchi *et al.*[19] for the analysis of BO_2. The effective Hamiltonian approach developed in this section is simpler to apply and relates much more clearly to the anharmonic interactions, than the previous formulation.

IV.3.2 The Potential Function

In the harmonic approximation, the vibrational wave functions $\chi(v_1, v_2, v_3)$ and $\chi(v_1', v_2, v_3')$ (where $v_i \neq v_i'$), are completely independent[11]. This is because the intra-molecular potential energy function contains no terms which are functions of more than one normal co-ordinate.

When cross terms between the normal co-ordinates ("anharmonic" terms) of power ≥ 3 are included in the potential function, this is no longer the case. In a Renner-Teller molecule, this gives rise to vibronic effects not included in standard vibration-rotation theory [20].

IV.3.3 The $(010)^2\Sigma$ states

Anharmonic interactions

The principal anharmonic interactions of interest in the $(010)\,^2\Sigma$ states have the selection rules $\Delta K = 0; \Delta v_1$ or $\Delta v_3 = \pm 1; \Delta v_2 = 0$. These interactions arise from the cubic anharmonic terms $Q_2^2 Q_1$ and $Q_2^2 Q_3$ in the potential energy expression [18, 20], where the Q_i are the mass-weighted normal co-ordinates [21] for normal mode i.

[11] The Renner-Teller effect leads to interactions between different v_2 levels within the harmonic approximation.

Fermi resonance

In many triatomic and polyatomic molecules, there are accidental near-degeneracies of vibrational energy levels, *e.g.* the dyad[12] $(v_1, 0, 1) - (v_1, 2, 0)$ of NCO [22]. The cubic anharmonic terms also give rise to interactions with the selection rules $\Delta K = 0; \Delta v_1$ or $\Delta v_3 = \pm 1; \Delta v_2 = \pm 2$, connecting vibronic levels of the same symmetry. Large perturbations can arise if the levels are near resonant. This particular type of anharmonic interaction is known as Fermi resonance [18, 23]; it also affects the $(010)\,^2\Sigma$ states but it is small since the (130) and (031) energy levels are far from resonance with (010).

IV.3.4 The Fermi Resonance Hamiltonian

Cubic anharmonic terms in the potential function

The in-plane and out-of-plane potential functions V' and V'' (see §III.2.3), of a triatomic Renner-Teller molecule in a $^2\Pi$ electronic state, can be expressed as a Taylor series in the normal co-ordinates; in Hougen's notation [18],

$$V' = \sum_i k'_i Q_i^2 + f'_{221} Q_2^2 Q_1 + f'_{223} Q_2^2 Q_3 + \cdots \tag{IV.37}$$

and

$$V'' = \sum_i k''_i Q_i^2 + f''_{221} Q_2^2 Q_1 + f''_{223} Q_2^2 Q_3 + \cdots. \tag{IV.38}$$

The k_i are the harmonic force constants and the f_{22i} are the cubic anharmonic force constants of interest for the problem to hand[13]. The anharmonic force constants are related by

$$f_{22i} \propto \left(\frac{\partial k_2}{\partial Q_i}\right)_{Q_i=0}. \tag{IV.39}$$

The magnitudes of the f_{22i} represent the strength of coupling between the bending mode ν_2 and the stretching mode ν_i [24]. In the same way that ϵ is the quotient of the difference and sum of the in-plane and out-of-plane harmonic bending force constants, Eq.(III.3),

[12] The term 'dyad' refers to the fact that two sets of (v_1, v_2, v_3) manifolds are involved in the Fermi resonance.

[13] The terms involving the bending co-ordinate are always even functions of Q_2, a consequence of the bending mode being symmetric about the linear axis.

anharmonic analogues of ϵ can be defined [18, 24],

$$\frac{\frac{1}{2}\left(f'_{22i} - f''_{22i}\right)}{\frac{1}{2}\left(f'_{22i} + f''_{22i}\right)} = \frac{\hat{\phi}_{22i}}{\phi_{22i}}. \tag{IV.40}$$

Dimensionless co-ordinates

The ϕ_{22i} are the reduced force constants introduced by Brown and Jørgensen [25, 26], and used by Sears *et al.*[24], for the average of the V' and V'' potential curves,

$$\phi_{22i} = \frac{1}{4\gamma_2\sqrt{2\gamma_i}}\left(f'_{22i} + f''_{22i}\right) \tag{IV.41}$$

$$\hat{\phi}_{22i} = \frac{1}{4\gamma_2\sqrt{2\gamma_i}}\left(f'_{22i} - f''_{22i}\right), \tag{IV.42}$$

where $\gamma_i = 4\pi^2 c\omega_i/h$. In working with the reduced force constants, the Q_i are replaced by the dimensionless normal co-ordinates [20],

$$q_i = \gamma_i^{\frac{1}{2}} Q_i. \tag{IV.43}$$

The Fermi resonance effective Hamiltonian

By direct analogy with the form of the Renner-Teller effective Hamiltonian, the Fermi resonance effective Hamiltonian can be written down [18]. In the dimensionless co-ordinate form adopted by Brown and Jørgensen [25, 26] and Sears *et al.*[24],

$$\frac{\mathcal{H}_{FR}^{\text{eff.}}}{hc} = \frac{1}{2}\left\{\phi_{221}q_1 + \phi_{223}q_3\right\} q_2^2 + \frac{1}{2}\left[\hat{\phi}_{221}q_1 + \hat{\phi}_{223}q_3\right] q_2^2 \left\{e^{2i(\vartheta-\varphi)} + e^{-2i(\vartheta-\varphi)}\right\} \tag{IV.44}$$

The first term has matrix elements diagonal in Λ, l and is a vibrational term; the second term is vibronic and has matrix elements with selection rules

$$\Delta K = 0; \Delta\Lambda = -\Delta l = \pm 2; \Delta v_2 = 0, \pm 2; \Delta v_i = \pm 1,$$

where $i = 1, 3$.

IV.3.5 Matrix Elements of $\mathcal{H}_{\mathbf{FR}}^{\mathbf{eff}}$

The matrix elements of Eq.(IV.44) can be evaluated using the matrix elements of $q_{2\pm}^2 \lambda_{\mp}^2$ given in Table III.2, and also [21]

$$\langle v_i + 1 | \, q_i \, | v_i \rangle = (v_i + 1)^{\frac{1}{2}} \, . \tag{IV.45}$$

Elements diagonal in Λ and l.

The matrix elements of $\mathcal{H}_{FR}$ diagonal in Λ and l are

$$\langle v_i + 1, v_j; \Lambda; v_2 l; S\Sigma; JPM_J | \, \mathcal{H}_{FR} \, | v_i, v_j; \Lambda; v_2 + 2, l; S\Sigma; JPM_J \rangle = W_{1,i} \left[(v_i + 1)(v_2 + l + 2)(v_2 - l + 2) \right]^{\frac{1}{2}} , \tag{IV.46}$$

$$\langle v_i + 1, v_j; \Lambda; v_2 l; S\Sigma; JPM_J | \, \mathcal{H}_{FR} \, | v_i, v_j; \Lambda; v_2 l; S\Sigma; JPM_J \rangle = 2W_{1,i} (v_i + 1)^{\frac{1}{2}} (v_2 + 1) , \tag{IV.47}$$

$$\langle v_i + 1, v_j; \Lambda; v_2 l; S\Sigma; JPM_J | \, \mathcal{H}_{FR} \, | v_i, v_j; \Lambda; v_2 - 2, l; S\Sigma; JPM_J \rangle = W_{1,i} \left[(v_i + 1)(v_2 + l)(v_2 - l) \right]^{\frac{1}{2}} . \tag{IV.48}$$

where $i, j = (1, 3)$ or $(3, 1)$. The vibrational Fermi resonance parameter in the dimensionless form[14] is $W_{1,i}$ [18], which is equivalent to ϕ_{22i}; the former symbol is more usual and will be adopted from now on.

Elements off-diagonal in Λ and l.

These matrix elements are

$$\langle v_i + 1, v_j; \Lambda; v_2 l; S\Sigma; JPM_J | \, \mathcal{H}_{FR} \, | v_i, v_j; \Lambda \mp 2, v_2 + 2, l \pm 2; S\Sigma; JPM_J \rangle = -W_{2,i} \left[(v_i + 1)(v_2 + 2 \pm l)(v_2 + 4 \pm l) \right]^{\frac{1}{2}} , \tag{IV.49}$$

$$\langle v_i + 1 v_j; \Lambda; v_2 l; S\Sigma; JPM_J | \, \mathcal{H}_{FR} \, | v_i, v_j; \Lambda \mp 2, v_2 l \pm 2; S\Sigma; JPM_J \rangle = -2W_{2,i} \left[(v_i + 1)(v_2 \mp l)(v_2 + 2 \pm l) \right]^{\frac{1}{2}} , \tag{IV.50}$$

$$\langle v_i + 1, v_j; \Lambda; v_2 l; S\Sigma; JPM_J | \, \mathcal{H}_{FR} \, | v_i, v_j; \Lambda \mp 2, v_2 - 2, l \pm 2; S\Sigma; JPM_J \rangle =$$

[14] If the Fermi resonance Hamiltonian is written in terms of Q_i rather than q_i, then $W_{1,i} = \phi_{22i}/(2\gamma_2\sqrt{2\gamma_i})$ and similarly for $W_{2,i}$.

$$-W_{2,i}\left[(v_i+1)\,(v_2 \mp l - 2)\,(v_2 \mp l)\right]^{\frac{1}{2}}. \quad \text{(IV.51)}$$

The vibronic Fermi resonance parameter in dimensionless form is $W_{2,i} = \hat{\phi}_{22i}$ [18]. The matrix elements involving $W_{2,i}$ take the opposite sign to those of Hougen [18]. This is a consequence of the representation of the electronic wave function used here, producing a negative sign in the eigenvalue of the ladder operator $\Lambda_{\pm}^2$ [27], see Eq.(III.25).

IV.3.6 The (010) – (011), (031) Anharmonic Interactions

Renner-Teller and spin-orbit matrix elements

The Renner-Teller and spin-orbit Hamiltonians can been reduced by a Van Vleck transformation to operate in a single stretching level (v_1, v_3) of the $\tilde{X}^2\Pi$ state. Their parameters then have the standard vibrational dependences $\alpha_{i,\epsilon\omega_2}$ and $\alpha_{i,A}$.

Rotational matrix elements

The rotational Hamiltonian must be considered at the stage before the Van Vleck transformation over the vibrational levels. The rotational constant can then be expressed as a Taylor series in the normal co-ordinates,

$$B(q) = B_e + \sum_i \left(\frac{\partial B_e}{\partial q_i}\right)_{q_i=0} q_i + \sum_i \sum_j \left(\frac{\partial^2 B_e}{\partial q_i \partial q_j}\right)_{q_i=0,q_j=0} q_i q_j + \cdots. \quad \text{(IV.52)}$$

The term linear in q_3 has the selection rule $\Delta v_3 = \pm 1$; it produces the standard rotational matrix elements (see §III.9), except that they are off-diagonal in v_3 and the coefficient B is replaced by $b_3(v_3+1)$, where $b_3 = \partial B_e/\partial q_3$. The parameter b_3 can be related to the derivative of the inverse inertial tensor, $\partial\mu/\partial q_3$ [20].

Matrix representation

The $(010)^2\,\Sigma$ states are connected by the $q_2^2 q_3$ anharmonic term to the $(011)\,^2\Sigma$ and $(030)\,^2\Sigma$ states.

Consider just the interactions diagonal in v_2. The matrix representation of the Renner-Teller, Fermi resonance, spin-orbit and rotational terms involved can be ex-

pressed in the parity conserving ψ_{1a} and ψ_{1b} basis functions for the $K = 0$ states,

$\lvert\psi_{1a};011;\pm\rangle$	$\lvert\psi_{1b};011;\pm\rangle$	$\lvert\psi_{1a};010;\pm\rangle$	$\lvert\psi_{1b};010;\pm\rangle$
$\frac{3}{2}\omega_1 + 2\omega_2 + \frac{1}{2}A$ $+B\left(J+\frac{1}{2}\right)^2$	$\mp(-1)^p\,\epsilon\omega_2$ $-B\left(J+\frac{1}{2}\right)$	$4W_{1,3}$ $+b_3\left(J+\frac{1}{2}\right)^2$	$\mp(-1)^p\,4W_{2,3}$ $-b_3\left(J+\frac{1}{2}\right)$
	$\frac{3}{2}\omega_1 + 2\omega_2 - \frac{1}{2}A$ $+B\left(J+\frac{1}{2}\right)^2$	$\mp(-1)^p\,4W_{2,3}$ $-b_3\left(J+\frac{1}{2}\right)$	$4W_{1,3}$ $+b_3\left(J+\frac{1}{2}\right)^2$
		$\frac{1}{2}\omega_1 + 2\omega_2 + \frac{1}{2}A$ $+B\left(J+\frac{1}{2}\right)^2$	$\mp(-1)^p\,\epsilon\omega_2$ $-B\left(J+\frac{1}{2}\right)$
			$\frac{1}{2}\omega_1 + 2\omega_2 - \frac{1}{2}A$ $+B\left(J+\frac{1}{2}\right)^2$

where $p = (J - S - l) \equiv J + 1/2$ is a phase factor.

IV.3.7 Reduction to a Hamiltonian Spanning Only the v_2 Manifold

Van Vleck transformation over the stretching levels

If the anharmonic interactions are small compared with both the Renner-Teller interaction and the spacing of the vibrational levels, a Van Vleck transformation can be applied over the (011) and (031) levels. This will reduce the matrix to one spanning only the (030) and (010) levels. The perturbation Hamiltonian for this purpose is

$$\mathcal{H}' = \mathcal{H}_{SO}^{\text{eff.}} + \mathcal{H}_{RT}^{\text{eff.}} + \mathcal{H}_{FR}^{\text{eff.}} + \mathcal{H}_{rot.}^{\text{eff.}}, \tag{IV.53}$$

where the rotational Hamiltonian is still off-diagonal in the vibrational space. The Van Vleck transformation is performed using the degenerate perturbation theory projection operator [28, 29] to third order, Eq.(III.29), which sums over all the possible perturbation pathways in the above matrix. For this purpose, the states within the (010) block are considered as a degenerate block, and the states within (011) are considered as another degenerate block. The following treatment operates on the matrix shown above.

Second order terms

The diagonal effective matrix elements introduced to the (010) block are

$$\begin{aligned}\tilde{H}^{(2)}_{aa} = \tilde{H}^{(2)}_{bb} &= -\frac{16}{\omega_3}\left[{W_{1,3}}^2 + {W_{2,3}}^2\right] - \frac{b_3^2\left(J+\frac{1}{2}\right)^2}{\omega_3}\left[1+\left(J+\frac{1}{2}\right)^2\right] \\ &\quad -\frac{8b_3W_{1,3}\left(J+\frac{1}{2}\right)^2}{\omega_3} \mp (-1)^p\,\frac{8b_3W_{2,3}\left(J+\frac{1}{2}\right)}{\omega_3},\end{aligned} \tag{IV.54}$$

where $\tilde{H}_{aa} = \langle\psi_{1a};010;\pm|\mathcal{H}'|\psi_{1a};010;\pm\rangle$ etc...

The first term in Eq.(IV.54) gives a contribution to the vibrational anharmonicities x_{22} and x_{23}. The second term is a contribution to the centrifugal distortion parameter D, and the third term is a contribution to the vibrational dependence of B, $\alpha_{2,B}$. These effects are already included in the standard vibration-rotation model [20], but the final term is a new one,

$$\pm\,(-1)^p\,(\epsilon\omega_2)_{D,3}\left(J+\frac{1}{2}\right), \tag{IV.55}$$

where the new parameter is

$$(\epsilon\omega_2)_{D,3} = -\frac{8b_3W_{2,3}}{\omega_3}, \tag{IV.56}$$

a centrifugal distortion of the Renner-Teller effect.

The off-diagonal terms in second order are (summing over the two possible pathways)

$$\begin{aligned}\tilde{H}^{(2)}_{ab} &= \pm\,(-1)^p\,\frac{32W_{1,3}W_{2,3}}{\omega_3} + \frac{8W_{1,3}b_3\left(J+\frac{1}{2}\right)}{\omega_3} + \frac{2b_3^2\left(J+\frac{1}{2}\right)^3}{\omega_3} \\ &\quad \pm\,(-1)^p\,\frac{8W_{2,3}b_3\left(J+\frac{1}{2}\right)^2}{\omega_3}.\end{aligned} \tag{IV.57}$$

The first term is a small, parity dependent anharmonic correction to the Renner-Teller effect; it is neglected here. The second term is a contribution to $\alpha_{2,B}$ and the third term contributes to D. The final term is again a centrifugal distortion of the Renner-Teller effect,

$$\mp\,(-1)^p\,(\epsilon\omega_2)_{D,3}\left(J+\frac{1}{2}\right)^2. \tag{IV.58}$$

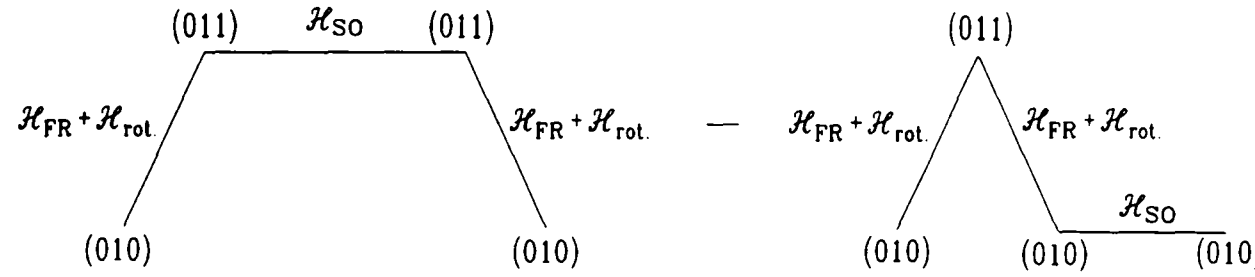

Figure IV.9: The origin of the principal third order perturbation contribution to anharmonic interactions between the $(010)\,^2\Sigma$ and $(011)\,^2\Sigma$ vibronic states.

Third order terms

There are many third order perturbation pathways to be considered. The only non-zero diagonal terms arise from the pathway shown in Fig.IV.9. This produces three terms,

$$\tilde{H}^{(3)}_{aa} = -\tilde{H}^{(3)}_{bb} = -\frac{A}{\omega_3^2}\left[16{W_{2,3}}^2 + b_3^2\left(J+\frac{1}{2}\right)^2 \pm (-1)^p\left(\epsilon\omega_2\right)_{D,3}\left(J+\frac{1}{2}\right)\right] \qquad \text{(IV.59)}$$

The first term is a small anharmonic vibronic contribution to the spin-orbit splitting and will be absorbed into the fitted value of $A^{\text{eff.}}$. The second term is a contribution to the centrifugal distortion of the spin-orbit interaction, A_D. The third term is an additional centrifugal distortion of the Renner-Teller effect,

$$\mp(-1)^p\,\frac{2\left(\epsilon\omega_2\right)_{D,3}AL_zS_z}{\omega_3}, \qquad \text{(IV.60)}$$

Third order off-diagonal terms have been neglected because they are both off-diagonal and of order ω_3^{-2}. Were such terms to be very significant, it would be an indication that the effective Hamiltonian was not a good approximation to the explicit treatment.

IV.3.8 Generalisation to a New Effective Hamiltonian

Interactions considered

The above treatment can be generalised to include the anharmonic interactions involving both the and ν_1 and ν_3 stretching modes. The effective matrix only spans the v_2 manifolds, the effects of levels off-diagonal in v_1, v_3 having been taken into account by a Van Vleck transformation.

The general treatment will model the anharmonic interactions between the $^2\Sigma$ vi-

bronic states in the level (v_1, v_2, v_3) and those in the levels $(v_1 \pm 1, v_2, v_3)$, $(v_1 \pm 1, v_2 \pm 2, v_3)$, $(v_1, v_2, v_3 \pm 1)$ and $(v_1, v_2 \pm 2, v_3 \pm 1)$.

The new effective Hamiltonian

The general form of the matrix elements of the centrifugal distortion of the Renner-Teller effect, whose matrix elements diagonal in v_2 were derived above, can be seen to arise from a new term in the effective Hamiltonian,

$$\frac{\mathcal{H}^{\text{eff.}}_{RTCD}}{hc} = \sum_i (\epsilon\omega_2)_{D,i} \left[1 + 2\frac{AL_zS_z}{\omega_i}\right] \frac{Q_2^2}{2} \left\{e^{2i(\vartheta-\varphi)} + e^{-2i(\vartheta-\varphi)}\right\} \mathbf{N}^2, \qquad \text{(IV.61)}$$

where the summation is over the stretching modes ν_1 and ν_3. In a study of this effect in a molecule, only one parameter $(\epsilon\omega_2)_D$ would be determined, where

$$(\epsilon\omega_2)_D = (\epsilon\omega_2)_{D,1} + (\epsilon\omega_2)_{D,3}. \qquad \text{(IV.62)}$$

In principle these two contributions are separable because the third order term,

$$+2(\epsilon\omega_2)_{D,i} AL_zS_z/\omega_i,$$

gives them a different dependence on the spin-orbit coupling parameter. This is only a minor contribution to the total parameter and so it would be difficult to separate the $i = 1$ and $i = 3$ contributions in this manner.

In writing the effective Hamiltonian, the vibrational co-ordinates have been converted back to the dimensioned form, Q_i. In doing so, the Fermi resonance parameters $W_{1,i}$ and $W_{2,i}$ (which are absorbed into $(\epsilon\omega_2)_D$) gain additional factors of $1/(2\gamma_2\sqrt{2\gamma_i})$, so that $(\epsilon\omega_2)_D$ is in units of wave number. The selection rules for the effective Hamiltonian are

$$\Delta K = 0; \Delta v_2 = 0, \pm 2; \Delta\Lambda = -\Delta l = \pm 2; \Delta\Sigma = \Delta P = 0, \pm 1, \qquad \text{(IV.63)}$$

so it operates only over the space of the bending vibrational levels. This is highly desirable because the matrix representation is compatible with that for the Renner-Teller effect (see Fig.IV.3), in that there is no need to extend the basis set to span levels off-diagonal in the stretching vibrational quantum numbers. Note that there is no

obvious relation between $\epsilon\omega_2$ and $(\epsilon\omega_2)_D$.

The complete matrix elements of the effective Hamiltonian are shown in Fig.IV.10. In the figure, the terms involving $+2(\epsilon\omega_2)_D A\Lambda\Sigma/\omega_i$ have been omitted for clarity. The elements off-diagonal in v_2 arise from the Van Vleck transformation of matrix elements with $\Delta v_2 = \pm 2, \Delta v_i = \pm 1$ $(i = 1, 3)$.

Matrix representation in the μ, $\kappa\,^2\Sigma$ basis

Taking just the terms diagonal in v_2, the matrix representation of $\mathcal{H}^{\text{eff.}}_{RTCD}$ for the $^2\Sigma$ states in the level (v_1, v_2, v_3) is

$\lvert\kappa^2\Sigma; v_1v_2v_3; J; \pm\rangle$	$\lvert\mu^2\Sigma; v_1v_2v_3; J; \pm\rangle$
$\pm(-1)^p \frac{1}{2}(\epsilon\omega_2)_D \left(J+\frac{1}{2}\right)$ $\times \left[n - \left(J+\frac{1}{2}\right)\sin 2\beta\right]$	$\mp(-1)^p \frac{1}{2}(\epsilon\omega_2)_D\, n \left(J+\frac{1}{2}\right)^2 \cos 2\beta$
Symmetric	$\pm(-1)^p \frac{1}{2}(\epsilon\omega_2)_D \left(J+\frac{1}{2}\right)$ $\times \left[n + \left(J+\frac{1}{2}\right)\sin 2\beta\right]$

where $n = (v_2+1)$ and again the small term involving $+2(\epsilon\omega_2)_D A\Lambda\Sigma/\omega_i$ has been omitted for clarity. As can be seen, the diagonal term in $(J+1/2)^2$ takes the opposite sign in the μ and $\kappa\,^2\Sigma$ states; this gives an equal but opposite contribution to the effective rotational constant in these states.

IV.3.9 Contributions of the ν_1 and ν_3 Modes to Anharmonic Vibronic Interactions in the $(010)^2\Sigma$ States

The size of the contribution to $(\epsilon\omega_2)_D$ from the in-phase and out-of-phase stretching modes depends upon $W_{2,i}$ and b_i. The latter parameter is related to the derivative of the inverse inertial tensor, $\partial\mu/\partial q_i$ [20]. As can be seen from Fig.III.7, for a molecule such as NCO, where the stretching vibrational modes are close to the antisymmetric and symmetric stretching modes of a 'BAB' molecule, b_3 is expected to be much larger than b_1, so that $(\epsilon\omega_2)_{D,3} \gg (\epsilon\omega_2)_{D,1}$. In a BAB molecule, the out-of-phase stretching mode will not contribute to $(\epsilon\omega_2)_D$.

	$\lvert\psi_{1a};v_2+2;\pm\rangle$	$\lvert\psi_{1b};v_2+2;\pm\rangle$	$\lvert\psi_{1a};v_2;\pm\rangle$	$\lvert\psi_{1b};v_2;\pm\rangle$	$\lvert\psi_{1a};v_2-2;\pm\rangle$	$\lvert\psi_{1b};v_2-2;\pm\rangle$
$\langle\psi_{1a};v_2+2;\pm\rvert$	$\pm(-1)^{p}\frac{(\varepsilon\omega_2)_D(n+2)}{2}\times(J+\frac{1}{2})$	$\mp(-1)^{p}\frac{(\varepsilon\omega_2)_D(n+2)}{2}\times(J+\frac{1}{2})^2$	$\pm(-1)^{p}\frac{(\varepsilon\omega_2)_D[n}{4}^{1/2}\times(n+2)]^{1/2}(J+\frac{1}{2})$	$\mp(-1)^{p}\frac{(\varepsilon\omega_2)_D[n}{4}^{1/2}\times(n+2)]^{1/2}(J+\frac{1}{2})^2$	0	0
$\langle\psi_{1b};v_2+2;\pm\rvert$	$\mp(-1)^{p}\frac{(\varepsilon\omega_2)_D(n+2)}{2}\times(J+\frac{1}{2})^2$	$\pm(-1)^{p}\frac{(\varepsilon\omega_2)_D(n+2)}{2}\times(J+\frac{1}{2})$	$\mp(-1)^{p}\frac{(\varepsilon\omega_2)_D[n}{4}^{1/2}\times(n+2)]^{1/2}(J+\frac{1}{2})^2$	$\pm(-1)^{p}\frac{(\varepsilon\omega_2)_D[n}{4}^{1/2}\times(n+2)]^{1/2}(J+\frac{1}{2})$	0	0
$\langle\psi_{1a};v_2;\pm\rvert$	$\pm(-1)^{p}\frac{(\varepsilon\omega_2)_D[n}{4}^{1/2}\times(n+2)]^{1/2}(J+\frac{1}{2})$	$\mp(-1)^{p}\frac{(\varepsilon\omega_2)_D[n}{4}^{1/2}\times(n+2)]^{1/2}(J+\frac{1}{2})^2$	$\pm(-1)^{p}\frac{(\varepsilon\omega_2)_D n}{2}\times(J+\frac{1}{2})$	$\mp(-1)^{p}\frac{(\varepsilon\omega_2)_D n}{2}\times(J+\frac{1}{2})^2$	$\pm(-1)^{p}\frac{(\varepsilon\omega_2)_D[n}{4}^{1/2}\times(n-2)]^{1/2}(J+\frac{1}{2})$	$\mp(-1)^{p}\frac{(\varepsilon\omega_2)_D[n}{4}^{1/2}\times(n-2)]^{1/2}(J+\frac{1}{2})^2$
$\langle\psi_{1b};v_2;\pm\rvert$	$\mp(-1)^{p}\frac{(\varepsilon\omega_2)_D[n}{4}^{1/2}\times(n+2)]^{1/2}(J+\frac{1}{2})^2$	$\pm(-1)^{p}\frac{(\varepsilon\omega_2)_D[n}{4}^{1/2}\times(n+2)]^{1/2}(J+\frac{1}{2})$	$\mp(-1)^{p}\frac{(\varepsilon\omega_2)_D n}{2}\times(J+\frac{1}{2})^2$	$\pm(-1)^{p}\frac{(\varepsilon\omega_2)_D n}{2}\times(J+\frac{1}{2})$	$\mp(-1)^{p}\frac{(\varepsilon\omega_2)_D[n}{4}^{1/2}\times(n-2)]^{1/2}(J+\frac{1}{2})^2$	$\pm(-1)^{p}\frac{(\varepsilon\omega_2)_D[n}{4}^{1/2}\times(n-2)]^{1/2}(J+\frac{1}{2})$
$\langle\psi_{1a};v_2-2;\pm\rvert$	0	0	$\pm(-1)^{p}\frac{(\varepsilon\omega_2)_D[n}{4}^{1/2}\times(n-2)]^{1/2}(J+\frac{1}{2})$	$\mp(-1)^{p}\frac{(\varepsilon\omega_2)_D[n}{4}^{1/2}\times(n-2)]^{1/2}(J+\frac{1}{2})^2$	$\pm(-1)^{p}\frac{(\varepsilon\omega_2)_D(n-2)}{2}\times(J+\frac{1}{2})$	$\mp(-1)^{p}\frac{(\varepsilon\omega_2)_D(n-2)}{2}\times(J+\frac{1}{2})^2$
$\langle\psi_{1b};v_2-2;\pm\rvert$	0	0	$\mp(-1)^{p}\frac{(\varepsilon\omega_2)_D[n}{4}^{1/2}\times(n-2)]^{1/2}(J+\frac{1}{2})^2$	$\pm(-1)^{p}\frac{(\varepsilon\omega_2)_D[n}{4}^{1/2}\times(n-2)]^{1/2}(J+\frac{1}{2})$	$\mp(-1)^{p}\frac{(\varepsilon\omega_2)_D(n-2)}{2}\times(J+\frac{1}{2})^3$	$\pm(-1)^{p}\frac{(\varepsilon\omega_2)_D(n-2)}{2}\times(J+\frac{1}{2})$

Figure IV.10: The complete matrix elements of the centrifugal distortion of the Renner-Teller effect, for the $^2\Sigma$ vibronic states in the level (v_1, v_2, v_3). The upper and lower sign choices are for positive and negative parities, respectively, $p = (J-S-l) \equiv J+1/2$ is a phase factor and $n = (v_2 + 1)$.

IV.4 Intensities of LMR Transitions

For a zero-field transition in a given vibration-rotation band, the relative intensity I is proportional to the rotational line-strength factor[15], S [30]. In an LMR spectrum, the line strength factor is divided up amongst the Zeeman components of the transition according to the M_J dependent factors from the square of a 3-j symbol [30, 31],

$$\begin{pmatrix} J' & 1 & J \\ -M'_J & p & M_J \end{pmatrix}^2,$$

which are given in Table IV.4. The space-fixed Z-axis ($p = 0$) is defined by the direction of the applied magnetic field, $\mathbf{B}$. When $T^1_{p=0}(\mathbf{E})$ of the laser radiation induces the transition, the selection rule can be seen to be $\Delta M_J = 0\,(\mathbf{E} \parallel \mathbf{B})$, and when it is induced by $T^1_{p=\pm1}(\mathbf{E})$ the selection rule is $\Delta M_J = \pm 1$ $(\mathbf{E} \perp \mathbf{B})$. These two extreme relative orientations are π and σ polarisation electric dipole LMR spectra, respectively.

Table IV.4: The M_J dependence of the intensity of the Zeeman components of an LMR transition.

ΔM_J	$R(J)$	$Q(J)$	$P(J)$
+1	$(J+M_J+1)(J+M_J+2)$	$(J+M_J)(J-M_J+1)$	$(J-M_J-1)(J-M_J)$
0	$(J+1)^2-M_J^2$	M_J^2	$J^2-M_J^2$
−1	$(J-M_J+1)(J-M_J)$	$(J-M_J)(J-M_J+1)$	$(J+M_J-1)(J-M_J)$

IV.5 Computer Modelling

IV.5.1 Introduction

Three programs were specially developed during this study; they are described below [14]. Various interpolation, extrapolation, polynomial root finding and matrix routines were used both in the programs and in the course of the analysis. These were double precision implementations of the routines given 'Numerical Recipes' [32, 33].

[15]There is also a population factor.

IV.5.2 The 'HANCO.FOR' Program

The initial predictions and assignments of the unique state LMR spectra were made using the program 'HANCO.FOR'. The Renner-Teller model was not implemented in this program, which was a modified form of the diatomic molecule program 'HUNDA.FOR' described in [34]. The following modifications were made *ad hoc*:

1. The quantum number Ω was replaced everywhere by P.

2. With the exception of the Zeeman terms, the quantum number Λ was replaced by K (which was always positive for this purpose).

The matrix elements were evaluated in a Hund's case (a) representation, using reduced spherical tensors, so the above changes produce the correct elements.

The unique state transitions in a Renner-Teller molecule can be modelled as the $v = 1 \leftarrow 0$ transition of a diatomic molecule. It is necessary to use effective spin-orbit and orbital Zeeman parameters for this purpose, approximately accounting for Renner-Teller mixing. These can be estimated to second order using Eqs.(IV.2) and (IV.8).

IV.5.3 The 'RENNER.FOR' Program

This program was used for all final analyses and for all work concerning the $K = 0$ states.

Format of the program

The program 'RENNER.FOR' used IMPLICIT REAL*8 , INTEGER*4 format throughout, with all FUNCTIONs declared in double precision. The only exception to this was for real arguments passed to the graphics package 'UNIRAS', which required a REAL*4 format. The program was run with self-contained matrix diagonalisation and inversion routines, which were double precision (REAL*8) implementations of those given in 'Numerical Recipes' [32, 33]. These routines were used for all calculations, however the facility easily to swap over to NAG version 15B routines was retained to allow checks to be made[16].

[16]The two sets of routines agreed to 1 part in 10^{13}.

Implementation of the theoretical model

The program implemented the Renner-Teller model developed in this and the previous chapter. The complete matrix representation was constructed in a parity conserving Hund's case (a) representation, *i.e.* the $\psi_{1a,b}$ and $\psi_{2a,b}$ basis functions, Eqs.(III.33)–(III.36). The Renner-Teller matrix elements were coded explicitly; all other matrix elements were coded using general, reduced spherical tensor expressions.

The complete matrix representation for a given state $|v_1, v_2, v_3,\ K,\ J,\ M_J,\ M_I, \pm\rangle$, at a given flux density, was constructed for a single vibronic species, *i.e.* diagonal in K, and then diagonalised. The basis set could be selected to span a number of vibrational levels $(v_1, v_2, v_3), (v_1, v_2 \pm 2, v_3), \cdots, (v_1, v_2 \pm \Delta v_2, v_3)$, Δv_2 even and ≥ 0; and rotational levels $J, J \pm 1, \cdots, J \pm \Delta J$, $\Delta J \geq 0$.

IV.5.4 Modelling of the Unique States

The unique state eigenvalues could be identified using the Hund's case (a) quantum numbers J, P, M_J, M_I and parity. These quantum numbers were found to remain good in a magnetic field.

IV.5.5 Modelling of the $^2\Sigma$ States

The unitary transformation

The quantum number P is not a good label for identifying the $^2\Sigma$ eigenstates. Therefore, the program transforms the basis into the μ and κ $^2\Sigma$ representation before diagonalisation.

The Hamiltonian is first constructed in the Hund's case (a) ψ_{a1}, ψ_{1b} basis functions and then a unitary transformation [35, 36] is applied to map the complete Hamiltonian matrix onto the μ, κ basis:

$$[\mathbf{H}'] = [\mathbf{U}]^T \,.\, [\mathbf{H}] \,.\, [\mathbf{U}] \,. \tag{IV.64}$$

$[\mathbf{H}]$ is the Hund's case (a) representation of the Hamiltonian and $[\mathbf{H}']$ is the μ, κ representation. The unitary transformation matrix[17], $[\mathbf{U}]$, takes each pair of basis functions

[17] For a unitary matrix, $[\mathbf{U}]^{-1} \equiv [\mathbf{U}]^T$.

$|\psi_{1a}; v_1, v_2, v_3; J; \pm\rangle$ and $|\psi_{1b}; v_1, v_2, v_3; J; \pm\rangle$ and applies the $\cos\beta$, $\sin\beta$ transformation detailed in Eqs.(IV.15) and (IV.16), to map them onto the μ, κ basis. The general form of the unitary matrix is shown in Fig.IV.11. The transformed Hamiltonian is then diagonalised; the resulting eigenvector coefficients refer to the μ, κ basis functions.

Evaluation of the quantum number N

For the $^2\Sigma$ states, J is not a good quantum number in a magnetic field, whereas the Hund's case (b) quantum number N remains good until the levels tune into the region of neighbouring levels with $N' = N \pm 2$.

At no point in the program is N used in the evaluation of matrix elements, however it is possible to evaluate N for a given eigenstate

$$|\Psi\rangle = \sum_n c_n |\phi_n\rangle ,$$

where the c_n are the eigenvector coefficients of the μ, κ basis functions. If the eigenstates are close to Hund's case (b) then the matrix representation of $\mathbf{N}^2$ can be used to evaluate the expectation value

$$[c_1\ c_2\ \cdots\ c_n].[\mathbf{U}]^T.[\mathbf{N}^2].[\mathbf{U}] \begin{bmatrix} c_1 \\ c_2 \\ \vdots \\ c_n \end{bmatrix} \approx N(N+1),$$

where $[\mathbf{N}^2]$ is in the ψ_{1a}, ψ_{1b} representation. This was used to identify the eigenstates with a given value of N; it proved reliable up to a flux density of about 1.4 T. Above this, the levels tune into the region of levels with $N \pm 2$ and N becomes ill-defined.

The F_1, F_2 states were identified using the '$\#_i$' ordering scheme described in §IV.2.3. The level correlating with F_1 at zero-field always lies above the F_2 level with the same values of N and M_J (assuming that $\Delta M_I = 0$ if nuclear hyperfine structure is considered).

$\cdots$	$\lvert\psi_{1a};v_1v_2{+}2v_3;JM_J;\pm\rangle$	$\lvert\psi_{1b};v_1v_2{+}2v_3;JM_J;\pm\rangle$	$\lvert\psi_{1a};v_1v_2v_3;J{+}1M_J;\pm\rangle$	$\lvert\psi_{1b};v_1v_2v_3;J{+}1M_J;\pm\rangle$	$\lvert\psi_{1a};v_1v_2v_3;JM_J;\pm\rangle$	$\lvert\psi_{1b};v_1v_2v_3;JM_J;\pm\rangle$	$\cdots$
$\cdots$	$\cos\beta$	$\sin\beta$	0	0	0	0	$\cdots$
$\cdots$	$-\sin\beta$	$\cos\beta$	0	0	0	0	$\cdots$
$\cdots$	0	0	$\cos\beta'$	$\sin\beta'$	0	0	$\cdots$
$\cdots$	0	0	$-\sin\beta'$	$\cos\beta'$	0	0	$\cdots$
$\cdots$	0	0	0	0	$\cos\beta''$	$\sin\beta''$	$\cdots$
$\cdots$	0	0	0	0	$-\sin\beta''$	$\cos\beta''$	$\cdots$

Figure IV.11: The form of the unitary transformation matrix [U], which maps the basis functions for the $K = 0$ states, $|\psi_{1a}\rangle$ and $|\psi_{1b}\rangle$, onto the $|\kappa\,^2\Sigma\rangle$ and $|\mu\,^2\Sigma\rangle$ basis functions. The dots indicate that the matrix extends over the whole basis set of the calculation.

IV.5.6 Tuning Rates and Intensities

The Zeeman tuning rates, $\partial E/\partial B_0$, of the eigenstate Ψ at a given flux density B_0 are evaluated using the Hellmann-Feynman theorem [35],

$$\frac{\partial E}{\partial B_0} = \left\langle \Psi \left| \frac{\partial \mathcal{H}_z}{\partial B_0} \right| \Psi \right\rangle, \tag{IV.65}$$

where $\mathcal{H}_z$ is the matrix representation of the Zeeman Hamiltonian. The expectation value is evaluated by pre- and post- multiplying the matrix representation of the derivative of the Zeeman Hamiltonian, $\partial \mathcal{H}_z/\partial B_0$, by the eigenvector coefficient column/row vector. For the $^2\Sigma$ vibronic states, the unitary transformation must also be applied to the ψ_{1a}, ψ_{1b} representation of $\partial \mathcal{H}_z/\partial B_0$ to map it onto the μ, κ basis.

The transition intensities are obtained in a similar manner; in this case the matrix representation of the rotation matrix [31] $\mathcal{D}_{pq}(\omega)^*$ is pre- and post- multiplied by the eigenvector coefficients for the initial and final states, respectively. The result is squared to give the rotational line strength factor [30, 31]

$$S = \left| \left\langle \sum_m c_m \psi'_m \left(J'_m, P'_m, M'_J\right) \right| \mathcal{D}^{(1)}_{0q}(\omega)^* \left| \sum_n c_n \psi_n \left(J''_n, P''_n, M''_J\right) \right\rangle \right|^2, \tag{IV.66}$$

where the ψ'_m and ψ''_n are the upper and lower basis functions of the eigenfunctions Ψ' and Ψ'', expressed here in terms of the Hund's case (a) basis functions. Eq(IV.66) is written for a single component of an LMR transition; for a zero-field transition the modulus is summed over M'_J and M''_J.

When dealing with the $^2\Sigma$ vibronic states, the unitary transformation was applied to $\mathcal{D}^{(1)}_{0q}(\omega)^*$; the basis functions in this case, ψ_n, refer to the μ, κ representation. In this case, the transformation matrix $[\mathbf{U}]^T$ refers to the final state and $[\mathbf{U}]$ refers to the initial state.

IV.5.7 Data Analysis

The assigned data were reduced to a set of parameters by a standard least-squares fitting procedure described in ref. [37]. A naturally weighted least-squares fit was used, the weight w_i being the inverse square of the estimated random experimental uncertainty,

$\tilde{\sigma}_i$, assigned to the ith datum.

The derivatives of the varied parameters were calculated for each transition in the same way as the Zeeman tuning rates, using the Hellmann-Feynman theorem. When dealing with the $^2\Sigma$ states, the derivative matrices were unitarily transformed to the μ, κ representation. The goodness of fit criterion was taken to be the measure [37]

$$\sigma_{\text{rel.}} = \sqrt{\frac{1}{(n-m)} \sum_{i=1}^{n} \frac{(y_i - \tilde{y}_i)^2}{\tilde{\sigma}_i^2}}. \tag{IV.67}$$

The number of degrees of freedom are $(n-m)$, where n is the number of data and m is the number of parameters being floated. The difference of the observed and calculated transition wave number (the "residual") of the ith datum is $(y_i - \tilde{y}_i)$. The measure $\sigma_{\text{rel.}}$ is unity when the quality of fit of the model is as good as can be expected given the estimated errors in the data. A value of $\sigma_{\text{rel.}}$ significantly less than unity indicates numerical over-fitting (too many parameters being floated), or a pessimistic estimate of the uncertainties. The residuals of the fit were recorded for each datum in the final output; the standard deviation of the residuals in each data class was also reported.

The parameters determined were output together with their unit standard deviations, given by the variance-covariance matrix, and their correlation coefficients, taken to be the diagonal elements of the inverse of this matrix [37].

IV.5.8 The 'LMRSIM.FOR' Program

This program used the intensity and tuning rate output of predictions made by the 'RENNER.FOR' or 'HANCO.FOR' programs, and produced graphical simulations of LMR spectra. 'LMRSIM.FOR' proved highly effective in guiding the assignment of several LMR spectra. The Doppler and Lamb-dip (Lorentzian) lineshapes were simulated as described in Appendix B.7, including the effects of detection system field modulation amplitude, sample mass and temperature.

IV.5.9 Computational Details

The programs used in this thesis were run on two machines. The smaller runs were performed on a DEC VAX 6000 Mainframe, running FORTRAN 6.2–108 under VMS

6.1. The program was compiled using the "/OPTIMIZE=(LEVEL=4)" option. The larger runs (and all final fits) were performed on a Convex C220, running the FORTRAN 77 vectorising compiler, fc version 8.0, under the Convex OS 8.0 system. The programs were compiled with the "-O2" option, leading to vectorisation where possible but not parallelisation. The outputs of the VAX and CONVEX runs were in agreement to better than 1 part in 10^{11}. The UNIRAS version 6.3b graphics library was used to produce the Zeeman tuning diagrams. Simulations of LMR spectra were performed on the VAX system, using the SIMPLEPLOT version 2-12 graphics library.

Bibliography

[1] J.T. Hougen, *J. Chem. Phys.* **36**, 519–534 (1962).

[2] P.S.H. Bolman, J.M. Brown, A. Carrington, I. Kopp and D.A. Ramsay, *Proc. R. Soc. Lond. A* **343**, 17–44 (1975).

[3] M. Fehér, C. Salud and J.P. Maier and A.J. Merer, *J. Mol. Spectrosc.* **150**, 280–281 (1991).

[4] J.M. Brown, *J. Mol. Spectrosc.* **56**, 159–162 (1975).

[5] A. Carrington, A.R. Fabris, B.J. Howard and N.J.D. Lucas, *Mol. Phys.* **20**, 961–980 (1971).

[6] P.B. Davies and I.H. Davies, *Mol. Phys.* **69**, 175–191 (1990).

[7] K.M. Evenson, R.J. Saykally, D.A. Jennings, R.F. Curl, Jr. and J.M. Brown, "Far Infrared Laser Magnetic Resonance," *in* "Chemical and Biochemical Applications of Lasers," Vol. V, (C.B. Moore, Ed.), pp. 95–138, Academic Press, New York, 1980.

[8] C.E. Barnes, J.M. Brown, A.D. Fackerell and T.J. Sears, *J. Mol. Spectrosc.* **92**, 485–496 (1982).

[9] J.A. Pople and H.C. Longuet-Higgins, *Mol. Phys.* **1**, 372–383 (1958).

[10] R. Renner, *Z. Phys.* **92**, 172–193 (1934).

[11] G. Herzberg, "Molecular Spectra and Molecular Structure," Vol. II, "Spectra of Diatomic Molecules," 2nd ed. (corrected), pp. 221–224, 300–304, Krieger Publishing, Malabar, Florida, 1989.5

[12] J.M. Brown, unpublished notes on the Renner-Teller effect, Physical Chemistry Laboratory, University of Oxford, 1994.

[13] N. Bazire, Part II thesis, University of Oxford, Trinity 1987.

[14] Copies of the computer programs are available from Dr. J.M. Brown, The Physical Chemistry Laboratory, University of Oxford, South Parks Road, Oxford OX1 3QZ, United Kingdom.

[15] E.U. Condon and G.H. Shortley, "The Theory of Atomic Spectra," pp. 378–396, Cambridge University Press, Cambridge, 1963.

[16] B.J. Boland, J.M. Brown, A. Carrington and A.C. Nelson, *Proc. R. Soc. Lond. A* **360**, 507–528 (1978).

[17] K. Kawaguchi, S. Saito and E. Hirota, *Mol. Phys.* **49**, 663–674 (1983).

[18] J.T. Hougen, *J. Chem. Phys.* **37**, 403–408 (1962).

[19] K. Kawaguchi, E. Hirota and C. Yamada, *Mol. Phys.* **44**, 509–528 (1981).

[20] I.M. Mills, "Vibration-Rotation Structure in Asymmetric- and Symmetric-Top Molecules," *in* "Molecular Spectroscopy: Modern Research." (K.N. Rao and C.W. Mathews, Eds.), pp. 115–140, Academic Press, New York, 1972.

[21] E.B. Wilson, Jr., J.C. Decius and P.C. Cross, "Molecular Vibrations," pp. 289–291, Mc Graw-Hill, London, 1955.

[22] D.R. Woodward, D.A. Fletcher and J.M. Brown, *Mol. Phys.* **68**, 261–262 (1989).

[23] E. Fermi, *Z. Phys.* **71**, 250–259 (1931).

[24] M. Wu, F.J. Northrup and T.J. Sears, *J. Chem. Phys.* **97**, 4583–4595 (1992).

[25] J.M. Brown and F. Jørgensen, *Adv. Chem. Phys.* **52**, 117–180 (1983).

[26] J.M. Brown and F. Jørgensen, *Mol. Phys.* **47**, 1065–1086 (1982).

[27] J.M. Brown, E.A. Colbourn, J.K.G. Watson and F.D. Wayne, *J. Mol. Spectrosc.* **74**, 294–318 (1979).

[28] A. Messiah, "Quantum Mechanics," Vol. II, pp. 685–721, North-Holland, Amsterdam, 1966.

[29] L.D. Landau and E.M. Lifshitz, "Course of Theoretical Physics," Vol. 3, " Quantum Mechanics," 2nd ed. (revised), pp. 129–136, Pergamon Press, Oxford, 1965.

[30] J.M. Brown, B.J. Howard and C.M.L. Kerr, *J. Mol. Spectrosc.* **60**, 433–436 (1976).

[31] R.N. Zare, "Angular Momentum," pp. 50–51, 62, 312–315, J. Wiley & Sons, New York, 1988.

[32] W.H. Press, B.P. Flannery, S.A. Teukolsky and W.T. Vetterling, "Numerical Recipes: The Art of Scientific Computing," 1st ed., pp.31–38, 86–89, 350–356, 360–363, Cambridge University Press, Cambridge, 1986.

[33] W.H. Press, S.A. Teukolsky, W.T. Vetterling and B.P. Flannery, "Numerical Recipes in FORTRAN: The Art of Scientific Computing," 2nd ed., pp.211–213, 365–368, 659–660, Cambridge University Press, Cambridge, 1992.

[34] J.P. Towle, D.Phil thesis, pp. 39–40, University of Oxford, 1992.

[35] P.W. Atkins, "Molecular Quantum Mechanics," 2nd ed., pp. 431, Oxford University Press, Oxford, 1983.

[36] G. Arfken, "Mathematical Methods for Physicists," 3rd ed., pp. 209–211, Academic Press, San Diego, 1985.

[37] D.L. Albritton, A.L. Schmeltekopf and R.N. Zare, "The Least-Squares Fitting of Spectroscopic Data," *in* "Molecular Spectroscopy: Modern Research," Vol. II, (K.N. Rao, Ed.), pp. 1–67, Academic Press, New York, 1976.

Chapter V

The NCO Radical

V.1 Introduction

NCO has been the subject of much study and might be called the 'prototype' 15 valence electron Renner-Teller molecule. Spectroscopic observations of NCO have prompted the development of increasingly sophisticated models of the Renner-Teller effect.

This chapter and Chapters VI and VII describe the observation and analysis of laser magnetic resonance (LMR) vibration-rotation spectra, involving the excitation of the out-of-phase stretching mode, ν_1, in the $\tilde{X}^2\Pi$ electronic state. The transitions observed take the form $(1, v_2, 0) \leftarrow (0, v_2, 0)$ with $\Delta K = 0$. Specifically, they involve the unique state vibronic bands $1_0^1\,{}^2\Pi$, $1_0^1 2_1^1\,{}^2\Delta$, $1_0^1 2_2^2\,{}^2\Phi$, and the $K = 0$ vibronic bands $1_0^1 2_1^1\,\mu^2\Sigma$ and $1_0^1 2_1^1\,\kappa^2\Sigma$. Fig.V.1 shows the levels observed, together with nearby levels which may lead to Fermi-resonances or avoided crossings. Note that there are other levels in this region but they have been omitted for clarity. The experimental observations are described and explained in terms of the Zeeman and Renner-Teller effects. Each band is analysed using the complete harmonic Renner-Teller model developed in Chapters III and IV, and the significance of the parameters determined is discussed.

This chapter reviews previous spectroscopic, kinetic/combustion and theoretical studies of NCO and the isomer CNO. Following this, the means of generating NCO are discussed, with attention focusing on the F + HNCO reaction used in this study. A survey is then given of the LMR study undertaken here, showing the region covered and the state of assignment of the many spectra recorded. Chapter VI concentrates on the LMR

study of the unique state bands, and Chapter VII describes the study of the much more complicated $K = 0$ state bands; the necessity of additions to the theory is discussed for the $K = 0$ states.

V.2 Review of Previous Studies of NCO and CNO

V.2.1 Electronic Spectra

NCO was first observed by Holland, Style and Ramsay in 1958 [11]. In a photolysis study at up to 9 eV, they observed the $\tilde{A}^2\Sigma^{(+)} - \tilde{X}^2\Pi$ and $\tilde{B}^2\Pi - \tilde{X}^2\Pi$ bands in absorption at 360–450 nm and 262–316 nm, respectively.

Dixon [12] thoroughly analysed the $\tilde{A}-\tilde{X}$ and $\tilde{B}-\tilde{X}$ transitions recorded in absorption, the former with good rotational resolution. The $\tilde{A} - \tilde{X}$ spectrum clearly showed an inverted $^2\Pi$ ground state with a Renner-Teller splitting of the (010) vibronic levels. No stretching vibrational levels were observed in the $\tilde{X}$ state, though the vibrations for the $\tilde{A}$ state were characterised fully. For the $\tilde{X}$ state, values of $\epsilon = -0.159(4)$ and $\omega_2 = 538.9(4)\,\mathrm{cm}^{-1}$, and rotational and spin-orbit parameters were determined. The electronic configuration of the X state is

$$(1\sigma)^2\,(2\sigma)^2\,(3\sigma)^2\,(4\sigma)^2\,(5\sigma)^2\,(6\sigma)^2\,(1\pi)^4\,(7\sigma)^2\,(2\pi)^3\,.$$

The $\tilde{A}^2\Sigma^{(+)}$ state arises from the transition $2\pi \leftarrow 7\sigma$, and the $\tilde{B}^2\Pi$ state from the $2\pi \leftarrow 1\pi$ transition.

An analysis of the electron paramagnetic resonance (EPR) spectrum of levels in the $\tilde{X}$ state by Carrington *et al.*[13] suggested a smaller value of ϵ than determined by Dixon. A reinvestigation of the $\tilde{A} - \tilde{X}$ absorption spectrum by Bolman *et al.*[14] at higher resolution ($3 \times 10^{-3}\,\mathrm{cm}^{-1}$ *cf.* Dixon's $0.03\,\mathrm{cm}^{-1}$), revealed a misassignment in the earlier work and duly obtained new parameters for the $\tilde{X}$ state of $\epsilon = -0.144(1)$, $\omega_2 = 535.4\,\mathrm{cm}^{-1}$, $g_K = 3.64\,\mathrm{cm}^{-1}$, and a term value $\nu(\tilde{A} - \tilde{X}) = 22754.06(5)\,\mathrm{cm}^{-1}$, amongst others. The new values were consistent with the EPR study. Bolman *et al.*[14] showed the need to include K-type resonance between $(010)\,^2\Delta$ and $(010)\,\mu, \kappa^2\Sigma$ vibronic states, revealed by deviations at high J (or N). In order to explain the observation of forbidden parallel transitions ($\Delta K = 0$) in the above study, Bolman and Brown [15]

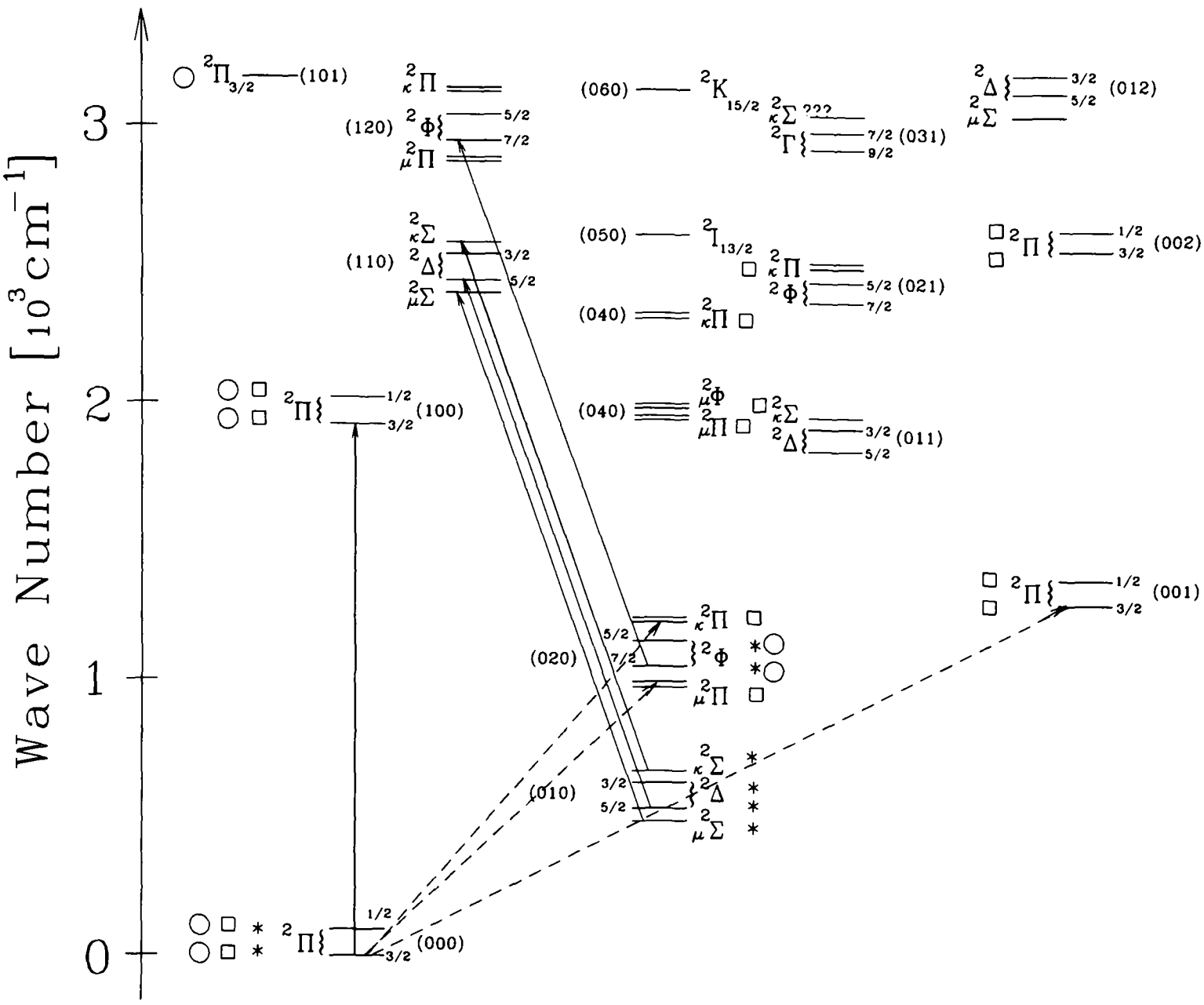

Figure V.1: Some low-lying levels of NCO ($\tilde{X}^2\Pi$). The transitions observed in this study are indicated by solid arrows. Levels possibly giving rise to Fermi-resonances, *e.g.* (020) – (001), or avoided crossings, are also shown. Dashed arrows indicate observations and assignments made by Werner *et al.*, [1]–[4], $*$ marks levels studied by microwave spectroscopy [5, 6], $\square$ indicates levels observed by SEP [7]–[9], and $\circ$ indicates levels observed in electronic fluorescence studies by FT-IR [10]. There are several other levels below $3,000\,\mathrm{cm}^{-1}$ *e.g.* the (030) manifold, which have been omitted for clarity.

proposed a vibronic coupling mechanism involving Herzberg-Teller mixing of remote Σ and Δ electronic states into the $\tilde{X}^2\Pi$ state.

Dixon *et al.*[16] determined the hyperfine splitting in the $\tilde{A}$ state; at low N this dominated the spin-rotation splitting, giving rise to observed transitions with $\Delta J = \pm 2$ in the $\tilde{A} - \tilde{X}$ spectrum. Charlton [17] performed an LIF study of the $\tilde{A} - \tilde{X}$ transition, determining an $\tilde{A}$ state lifetime of ~ 350 ns.

Dixon also recorded the $\tilde{B} - \tilde{X}$ absorption spectrum in a flash photolysis study [18]. The spectrum consisted of a progression of bands in the upper state in-phase stretching vibration, and showed predissociation; a band origin of $32781.1(3)\,\mathrm{cm}^{-1}$ was determined. The rotational analysis was achieved following an optical–optical double resonance study (OODR) [19]. The $Q_1 +^Q P_{21}$ head of the $\tilde{A} \leftarrow \tilde{X}$ transition was pumped and the $\tilde{B}(00^00) \leftarrow \tilde{A}(000)$ transition was probed. Levels in the $\tilde{B}$ state were perturbed by nearby levels of the $\tilde{A}$ state with $K \leq 2$. Parameters determined for the $\tilde{B}$ state include $A = -76.631(963)\,\mathrm{cm}^{-1}$. Sullivan *et al.*[20] determined lifetimes for NCO in the $\tilde{B}$ state levels (00^10) and (10^10) of 63 ns and ≤ 10 ns respectively, finding the $N(^2D) + CO$ dissociation limit to lie between these levels. An $\mathbf{R}^2$ Hamiltonian formulation was used for all the above studies.

V.2.2 Ionisation and Thermodynamic Studies

Dyke *et al.*[21] determined a value of $11.76(1)\,\mathrm{eV}$ for the first adiabatic ionisation energy of NCO, and observed states of NCO^+. They reported that *ab initio* calculations had difficulty modelling the geometries of the molecule, due to problems with treating multiple valence bonds by such methods. A time of flight photoelectron spectroscopy study of the anion NCO^- by Bradforth *et al.*[22] determined the electron affinity of NCO to be $3.609(5)\,\mathrm{eV}$; the changes in bond lengths from NCO^- to NCO were also determined. In a VUV photodissociation study of HNCO, Okabe *et al.*[23] found $NCO(\tilde{A})$ to be produced with a highly excited bending vibration. A bond dissociation energy of $D(N - CO) = 2.15(5)\,\mathrm{eV}$ was determined. Tokue and Ito [24] determined appearance onsets of $8.3(6)\,\mathrm{eV}$ and $9.2(6)\,\mathrm{eV}$ for NCO in the $\tilde{A}$ and $\tilde{B}$ states, in an electron impact dissociation study of HNCO. The states of the resulting NCO and NH fragments were correlated with HNCO. In a beam study of NCO photodissociation, Cyr *et al.*[25] determined $\Delta H_f(\mathrm{NCO}) = 128(4)\,\mathrm{kJmol}^{-1}$. The latest study by Ruscic and Berkowitz

[26] determined IP(NCO) = 11.759(6) eV and $119(2) \leq \Delta H_f(\mathrm{NCO}) \leq 137(3)\,\mathrm{KJmol}^{-1}$ in a photoelectron mass spectroscopy study of HNCO and NCO. They discuss in detail the significance of these results for the kinetics of NCO reactions and NO_x reduction strategies.

V.2.3 Kinetic and Fluorescence Studies

Of the numerous kinetic and combustion studies of NCO, Park and Hershberger [27] studied NCO/hydrocarbon reactions, Perry [28] studied NCO/ethene/oxygen reactions, and Louge and Hanson [29] discussed the high temperature kinetics of NCO. Louge *et al.*[30] discuss quantitative studies of NCO in the combustion environment, using LIF by pumping band heads in the $\tilde{\mathrm{A}} \leftarrow \tilde{\mathrm{X}}$ and $\tilde{\mathrm{B}} \leftarrow \tilde{\mathrm{X}}$ transitions, for which the oscillator strength was determined.

Argon laser LIF studies were performed by Anderson *et al.*[31] and Wong *et al.*[32], in atmospheric pressure CH_4/N_2O flames using a burner designed for combustion studies [33]. Recording fluorescence using a monochromator, they determined for the the first time gas phase stretching wave numbers of $\nu_1 = 1921.06(89)\,\mathrm{cm}^{-1}$ and $\nu_3 = 1270.3(27)\,\mathrm{cm}^{-1}$. A concentration profile of NCO through the flame was established. The studies inferred that in the flame environment, spin relaxation in the $\tilde{\mathrm{A}}$ state was much faster than electronic quenching. A similar study by Copeland and Crosley [34] provided a number of reliable term values for NCO in the $\tilde{\mathrm{X}}$ state (quoted to be accurate to $\pm 0.5\,\mathrm{cm}^{-1}$), for some of the vibronic states with $(v_1 \leq 1, v_2 \leq 2, v_3 \leq 1)$ and $K \leq 2$. Fermi resonances between the levels (001) – (020), (011) – (030), (101) – (120) and (111) – (130) were observed and modelled.

Woodward *et al.*[35]–[37] studied the $\tilde{\mathrm{A}} \leftarrow \tilde{\mathrm{X}}$ LIF spectrum and focused on the $(001)\,^2\Pi$–$(020)\,^2\Pi$ Fermi resonance. They determined parameters of $W_{1,3} = 22.72(91)\,\mathrm{cm}^{-1}$, $W_{2,3} = -0.32(32)\,\mathrm{cm}^{-1}$ and also parameters of $\epsilon\omega_{2,(020)} = -75.884(81)\,\mathrm{cm}^{-1}$, $G(001) = 1254.95(88)\,\mathrm{cm}^{-1}$ and $G(020) = 1069.70(44)\,\mathrm{cm}^{-1}$. An $\mathbf{N}^2$ Hamiltonian including the harmonic and anharmonic Renner-Teller effects and Fermi resonance interactions, was used.

Patel-Misra *et al.*[38]–[40] studied the reaction between cyanogen and oxygen atoms using LIF. They observed emission to many $\tilde{\mathrm{X}}$ vibronic states, with $(v_1 \leq 1, v_2 \leq 6, v_3 \leq 2)$ and $K \leq 5$. Term values were quoted relative to the lowest rotational levels in

these states; many were made from measurements of weak band heads and suffer from errors of several cm^{-1}. Using the same reaction, Wu, Northrup and Sears [7]–[9] performed both LIF and stimulated emission pumping (SEP) studies of NCO (ref. [41] explains the technique of SEP). Extensive term values were reported [7] for Π and Σ vibronic levels with $(v_1 \leq 3, v_2 \leq 6, v_3 \leq 3)$; the reported accuracy is $\pm 5\,cm^{-1}$ but when compared with known levels, these values are more accurate than those of Patel-Misra *et al.*[38, 39]. The levels $(v_1 00)$ with $v_1 \leq 3$ were studied with accuracy and precision by SEP, a perturbation being observed in the (300) level [7], probably due to $(240)\,\mu^2\Pi$. The remaining papers [8, 9] focus on the $(0v_2v_3)\,^2\Pi$ and $^2\Sigma$ vibronic levels with $v_1 = 0, v_2 \leq 4, v_3 \leq 2$, and the Fermi resonances involved. A very sophisticated $\mathbf{N}^2$ effective Hamiltonian model was used for the final analysis [9], including the harmonic and anharmonic Renner-Teller effects and K-type resonance/doubling. The parameters determined include $\omega_2 = 534.063(31)\,cm^{-1}$, $\omega_3 = 1260.22(13)\,cm^{-1}$, $A_e = -96.660\,cm^{-1}$ and $\epsilon\omega_2 = -78.370(29)\,cm^{-1}$, $g_K = 3.7672\,cm^{-1}$, $W_{1,3} = 27.230\,cm^{-1}$ and $W_{2,3} = 2.995(32)\,cm^{-1}$. A calculation of the in-plane and out-of-plane harmonic bending potential curves V' and V'' (see Fig.III.6), was also performed.

Using a radiofrequency discharge, or LIF, to produce NCO($\tilde{A}$), Hemmerling and Vervloet [10] performed a similar study to that of Bolman *et al.*[14], except recorded in emission using FT-IR. This had the advantage of being able to access levels in the $\tilde{X}$ state whose population would be too small for them to be observed in absorption. Accurate term values ($\pm 10^{-2}\,cm^{-1}$), spin-orbit and rotational parameters were determined for the unique vibronic states in $(0v_20)$, with $v_2 \leq 2$, the $^2\Pi$ vibronic states (101), (100), (100), and also $(011)\mu^2\Sigma^{(+)}$. A Fermi resonance was observed between the states $(011)\,\mu^2\Sigma^{(+)}$ and $(030)\,\kappa^2\Sigma^{(-)}$. An analysis was performed for the Fermi-resonant levels $(020)\,\mu, \kappa^2\Pi$ and $(001)\,^2\Pi$; the results were in good agreement with those of Woodward *et al.*[35]. Band heads involving $\tilde{X}$ state vibronic levels with $(v_1 \leq 1, v_2 \leq 4, v_3 \leq 1)$ were measured, and $\nu(\tilde{A} - \tilde{X}) = 22754.020(1)\,cm^{-1}$ was determined. The authors do not make clear whether they used an $\mathbf{N}^2$ or an $\mathbf{R}^2$ effective Hamiltonian.

V.2.4 Structural Studies

Misra *et al.*[42] studied the $(^0100)\tilde{A} \leftarrow (^1000)\tilde{X}$ transition of ^{14}NCO and ^{15}NCO in absorption. They determined bond lengths for NCO in the $\tilde{X}$ state of $r_{NC} = 0.1200(\pm 8)\,nm$

and $r_{NC} = 0.1206(\mp 8)\,\mathrm{nm}$. Werner [1] details force field calculations by Milligan and Jacox [43] and Dyke *et al.*[21], quoting bond force constants of $F_{CO} = 1.293\,\mathrm{mdyn\,nm^{-1}}$, $F_{CN} = 1.082\,\mathrm{mdyn\,nm^{-1}}$, $F_{CN-CO} = 0.256\,\mathrm{mdyn\,nm^{-1}}$ and $F_{NCO} = 0.0434\,\mathrm{mdyn\,nm^{-1}}$ (expressed in the symmetry co-ordinates of NCO). The force field calculations showed that the in-phase and out-of-phase stretching vibrations of NCO correspond closely to the symmetric and antisymmetric vibrations of a symmetric linear triatomic molecule. The dimensionless normal, internal stretching co-ordinates quoted by Werner [1] are

$$q_1 = -(1.24\Delta r_{CN} - 1.68\Delta r_{CO})$$

$$q_3 = -(2.79\Delta r_{CN} + 2.66\Delta r_{CO}),$$

where Δr is the bond displacement from equilibrium, with Coriolis coupling parameters determined to be $\zeta_{2,1} = 0.99816$ and $\zeta_{2,3} = 0.06068$.

V.2.5 Infrared Studies

Matrix isolation studies

The first such study was by Milligan and Jacox [43], who performed experiments in which HNCO was photolysed in neon, argon, nitrogen and CO matrices. The UV absorption spectrum was recorded and many bands were assigned to the $\tilde{A}-\tilde{X}$ and $\tilde{B}-\tilde{X}$ transitions of NCO. The studies in an argon matrix gave the first vibrational wave numbers for the $\tilde{X}$ state of $\nu_1 = 1922\,\mathrm{cm^{-1}}$, $\nu_2 = 487\,\mathrm{cm^{-1}}$ and $\nu_3 = 1265\,\mathrm{cm^{-1}}$. Isotopic studies allowed a force field calculation to be performed. Isotopic shifts in the vibrational wave numbers were determined to be $\Delta\nu_1 = -52\,\mathrm{cm^{-1}}, \Delta\nu_2 = -13\,\mathrm{cm^{-1}}$ for $^{14}N^{13}C^{16}O$; $^{15}N^{12}C^{16}O$ was also studied. The major photolysis product of NCO (at 253.7 nm) was found to be N + CO.

A study of the $\tilde{A} - \tilde{X}$ emission spectrum of NCO in an argon matrix by Bondybey and English [44], determined reliable term values for a number of vibronic levels with $(v_1 \leq 2, v_2 \leq 4, v_3 \leq 2)$ and $K \leq 2$, in the $\tilde{X}$ state, indicating very small matrix site shifts. They also observed the radiative lifetime of the $\tilde{A}^2\Sigma^{(+)}$ state to be 170 ns, $\tilde{A} \rightarrow \tilde{X}$ vibronic relaxation being slow. Rapid relaxation was observed between Fermi resonant levels in the $\tilde{A}$ state, with fluorescence originating only from the lowest level of each

Fermi polyad.

Studies in the 1900 cm^{-1} region

Barnes *et al.*[45] recorded CO-LMR spectra in the 1900 cm^{-1} region. The resonances observed were assigned to the $1_0^1\,^2\Pi_{\frac{3}{2}}$ and $1_0^1 2_1^1\,^2\Delta_{\frac{5}{2}}$ sub-bands. A diode laser study by Brüggemann [47, 48] extended Barnes' work by observing transitions in both the $1_0^1\,^2\Pi_{\frac{3}{2}}$ and $1_0^1\,^2\Pi_{\frac{1}{2}}$ sub-bands. An $\mathbf{N}^2$ effective Hamiltonian was used in both analyses, but the Renner-Teller effect was not accounted for, so effective parameters were determined. A few weak, unassigned transitions remained from these studies [49].

Studies in the 950–1300 cm^{-1} and 1650–1850 cm^{-1} regions

Seebass [2], Werner [1] and Müschenborn [3] thoroughly searched the 980 cm^{-1} region using CO_2 LMR, and the 1200–1300 cm^{-1} region using CO-LMR, in Bonn. Many complicated LMR spectra were observed, some of them qualitatively similar to the observations reported in this thesis.

The spectra were all recorded with Doppler limited resolution, using a variety of detection methods [50]. Transitions were assigned to the sub-bands $3_0^1\,^2\Pi_{\frac{3}{2}}$, $2_0^2\,(\mu^2\Pi \leftarrow^2 \Pi_{\frac{3}{2}})$, $2_0^2\,(\kappa^2\Pi \leftarrow^2 \Pi_{\frac{3}{2}})$ and possibly $2_1^1 3_0^1\,^2\Delta_{\frac{5}{2}}$. The only analysis to be published in the open literature was of the $3_0^1\,^2\Pi$ band [4], for which a band origin of 1272.9707 cm^{-1} was determined. The theses of Seebass [2] and Werner [1] report many more complete assignments and 'partial' assignments, in which a Fortrat diagram [2] was used to show that a series of spectra observed on different laser lines belonged to a common system. The analyses were performed using an $\mathbf{N}^2$ effective Hamiltonian, and Werner [1] included where necessary the Fermi resonances between the dyads (001) – (020), (011) – (030), (101) – (120) and (111) – (031). The Fermi resonances give rise to large changes in the g_L value, for example $g_{L,(000)} = 0.988773$ and $g_{L,(001)} = 0.779773$. Werner [1] used a matrix representation of the Renner-Teller effect (elements diagonal in v_2 only), including K-type doubling and anharmonic effects, and explicitly spanning the Fermi-resonant stretching levels.

Many unassigned spectra still remain; a large number of these are displayed in the thesis of Müschenborn [3], but it appears that the original spectra may no longer be held in Bonn [49]. Copies of a few of the spectra are held in Oxford [51], including some in

the $1650 - 1850\,\mathrm{cm}^{-1}$ and $1900\,\mathrm{cm}^{-1}$ regions. Werner [1] identified some likely bands for the unassigned spectra, viz: $2_1^3\,{}^2\Delta$, $2_1^3\,{}^2\Sigma$, $2_1^1 3_0^1\,{}^2\Delta$ and $2_1^1 3_0^1\,{}^2\Sigma$. One must also consider transitions from the level $(000)\,{}^2\Pi_{\frac{1}{2}}$ to tunable upper state levels, as well as the sub-band $2_2^2 3_0^1\,{}^2\Phi_{\frac{7}{2}}$. Transitions in CF fall in the $1200\,\mathrm{cm}^{-1}$ region [52] and must be borne in mind since Werner and Seebass sometimes used CF_4 as a source of fluorine atoms for the HNCO + F reaction.

V.2.6 Microwave and EPR studies

Carrington *et al.*[13, 53, 54] recorded the gas phase EPR spectrum for the three unique $(K = v_2 + 1)$ states in $(0, v_2, 0)$, $v_2 \leq 2$, of NCO in the $\tilde{\mathrm{X}}$ state. Second and third order perturbation terms were used to interpret the effective g factors using an $\mathbf{R}^2$ effective Hamiltonian [13]. The ^{14}N hyperfine splitting ($\sim 20\,\mathrm{MHz}$) was resolved in their study, but not the K-type doubling.

Saito and Amano [55], Amano and Hirota [56] and Saito [57] observed pure rotational transitions in the $(000)\,{}^2\Pi$ and $(010)^2\Delta$ vibronic states. Kawaguchi *et al.*[5, 6] extended these observations and also observed the $(020)\,{}^2\Phi$ and $(010)\,{}^2\Sigma$ vibronic states. The K-type doubling was resolved for transitions in the $(000)\,{}^2\Pi$ level, and nuclear hyperfine structure was resolved in all the states. An $\mathbf{R}^2$ effective Hamiltonian was used for the analysis, including perturbation terms required to account for anharmonic interactions between the $^2\Sigma$ vibronic states in the manifolds (010), (011) and (110).

Davies and Davis [58] recorded the far-infrared LMR spectrum of the $\tilde{\mathrm{X}}\,{}^2\Pi_{\frac{3}{2}}$ spin-component in the (000) vibrational level. The pure rotational transitions $J = 29/2 \leftarrow 27/2$ and $J = 43/2 \leftarrow 41/2$ were observed, with resolved K-type doubling and in some cases hyperfine structure. Their analysis was performed using an $\mathbf{R}^2$ effective Hamiltonian.

A microwave-optical double resonance (MODR)/inter-modulated fluorescence (IMF) study by Suzuki *et al.*[59] characterised the rotational properties of the (000) level of the $\tilde{\mathrm{A}}\,{}^2\Sigma^{(+)}$ electronic state at sub-Doppler resolution. The data were analysed using an $\mathbf{R}^2$ effective Hamiltonian, yielding precise $\tilde{\mathrm{A}}$ state parameters, including ^{14}N hyperfine parameters. The interpretation of the hyperfine parameters was that the unpaired electron occupied the 7σ molecular orbital, which was a $2s/2p$ hybrid, with the electron spin (Pauli) density localised on the nitrogen atom.

V.2.7 Theoretical Studies

A good summary of theoretical studies of NCO is given in [60], which investigates properties of the electronic spectrum of NCO and suggests that there should be high lying $^2\Pi$, $^4\Sigma^-$ and $^4\Pi$ electronic states. An *ab initio* study of NCO^+ by Cai *et al.*[61] explained the UV photoelectron spectrum of NCO [21]. Perić *et al.*[62] performed an *ab initio* study of NCO in its $\tilde{X}$ state, including configuration interaction. They modelled the vibronic levels and spin-orbit splittings of levels up to $\sim 10^4\,cm^{-1}$, and showed that they could be associated with the in-plane and out of plane potential curves V' and V'' (see Fig.III.6). The dipole moment of NCO in the $\tilde{X}$ state was calculated to be 0.650 D, compared with a value of 0.742(5) D determined by Carrington *et al.*[13]. The most recent and sophisticated *ab initio* calculation was by Li *et al.*[63], who determined potential curves and vibronic levels for the $\tilde{A}$ and $\tilde{X}$ states. The bond lengths and their vibrational dependences were well modelled, whereas the vibrational wave numbers were $60 - 140\,cm^{-1}$ higher than observed. The $\tilde{A} - \tilde{X}$ origin was predicted to within 1% of the observed value, and an off-diagonal orbital matrix element of $\langle L_x \rangle = \langle L_y \rangle 0.626\hbar$ was calculated.

A study by Koch and Frenking [64] calculated adiabatic and vertical electron affinities of 3.71 eV and 4.01 eV for NCO, in excellent agreement with experiment. A state-of-the-art *ab initio* calculation by East and Allen [65] gave a heat of formation for NCO of $\Delta H_f = 131(2)\,KJmol^{-1}$; the paper discusses the detailed kinetics of many reactions involving NCO in the combustion of fuels. There have also been studies of the dynamic Renner-Teller effect involving the inelastic scattering of NCO by helium [66, 67].

V.2.8 The CNO Radical

Very little is known about the unstable fulminate radical, a structural isomer of NCO. The $\tilde{A}^2\Pi - \tilde{X}^2\Pi$ transition of CNO has been observed in matrix [68] and gas phase [69] studies, with $\nu(\tilde{A} - \tilde{X}) = 12611.8\,cm^{-1}$. These studies gave no information about the vibrational intervals in the $\tilde{X}$ state. CNO is linear in the ground state, in which it has an as yet unquantified Renner-Teller effect.

Marian *et al.*[70] calculated the $\tilde{B}^2\Pi$ state to be bound, but to suffer an avoided crossing near to the equilibrium position of the $\tilde{X}$ state. This will make its observation by

absorption spectroscopy very difficult, due to predissociation. Maclagan [78] calculated harmonic vibrational wave numbers for CNO of $\omega_1 = 2245\,\mathrm{cm}^{-1}$, $\omega_2 = 389\,\mathrm{cm}^{-1}$ and $\omega_3 = 1179\,\mathrm{cm}^{-1}$ in a study of the proton affinities of NCO and CNO. The accuracy of these values may be gauged by noting that the values calculated for NCO are $\omega_1 = 1958\,\mathrm{cm}^{-1}$, $\omega_2 = 555\,\mathrm{cm}^{-1}$ and $\omega_3 = 1406\,\mathrm{cm}^{-1}$.

CNO is normally generated from highly explosive fulminates. The most elegant preparations of fulminic acid, HCNO, are given in refs. [72, 73], with other details in ref. [74]. Winnewisser [75] has supplied vapour pressure data on HCNO and recommends condensing it on the inside of the absorption cell and reacting it with fluorine atoms to generate CNO. The LMR spectrum should be interesting.

V.3 Production of the NCO Free Radical

V.3.1 Survey of Methods

In the earliest gas phase spectroscopic studies, NCO was produced by the flash photolysis of ethyl isocyanate C_2H_5NCO [11], or isocyanic acid HNCO [12], at pressures of $\sim 2.6\,\mathrm{kPa}(20\,\mathrm{Torr})$. Misra *et al.*[42] generated NCO in a flash photolysis experiment using $400\,\mathrm{Pa}\,(3\,\mathrm{Torr})$ HCN and $130\,\mathrm{Pa}\,(1\,\mathrm{Torr})$ ozonised oxygen ($3\%O_3$), buffered with $6.7\,\mathrm{kPa}\,(50\,\mathrm{Torr})$ Ar. This reaction probably generates NCO in a similar way to the cyanogen/oxygen reaction described below.

Many optical, infrared, microwave, EPR and LMR studies have used the reaction between gaseous HNCO and fluorine atoms [76]. The atomic fluorine is normally generated by passing a microwave discharge through a flowing mixture either of fluorine in helium or CF_4. The reaction can also be effected by passing an electrical discharge through a mixture of HNCO in fluorine buffered with helium. Typical pressures in such reactions are $\sim 150\,\mathrm{Pa}\,(1.1\,\mathrm{Torr})$, of which 5% is fluorine and 3% HNCO.

Three other preparative methods are of interest, because unlike the above techniques they can produce large concentrations of NCO in highly vibrationally excited levels. Copeland and Crosley [34] used an atmospheric pressure CH_4/N_2O flame to generate NCO. The flame was maintained on a slot burner specially designed for spectroscopic studies of the combustion process [33]. The relative intensities of their LIF spectra of

the $\tilde{A}$–$\tilde{X}$ transition, suggested the NCO was formed in a variety of vibrational levels in the $\tilde{X}$ state. This is to be expected from the estimated flame temperature of 2400 K. This method is not well suited to mid-infrared LMR. At atmospheric pressures, the line broadening would lead to the severely under-modulated detection of the resonances.

Hemmerling and Vervloet [10] produced NCO from a radiofrequency (r.f.) discharge at 30 MHz through 90 Pa (0.7 Torr) of ethyl isocyanate. The $\tilde{A}$–$\tilde{X}$ emission spectrum was observed directly from the discharge, and it was found that levels up to (040) in the $\tilde{X}$ state were populated by emission from the $\tilde{A}$ state. Experience with r.f. discharges in the intracavity LMR spectrometer has shown that there is a strong interaction between the discharge and the field modulation coils mounted on the pole caps. This causes a very high noise level, rendering the method of no use with the present experimental arrangement.

Patel-Misra *et al.*[39], and subsequently Sears *et al.*[7], produced NCO by the reaction

$$CN^{\bullet}_{(g)} + O^{\bullet}_{2(g)} \longrightarrow NCO^{\bullet}_{(g)} + O^{\bullet}_{(g)}. \qquad (V.1)$$

The CN radicals were generated by the 193 nm (ArF excimer) photolysis of cyanogen, C_2N_2. The optimum total pressure was 19 Pa (0.1 Torr). A thorough analysis of the relative intensities of the LIF spectra of the $\tilde{A}$–$\tilde{X}$ transition was undertaken by Sauder *et al.*[40]. The results implied that the above reaction formed NCO in the highly excited vibrational levels ($v_1 \leq 2, v_2 \leq 6, v_3 \leq 1$) in the $\tilde{X}$ state. Detailed studies of the thermodynamics and energy partitioning in this reaction have been undertaken by Phillips *et al.*[77] and Macdonald *et al.*[78]. This reaction is very promising for future studies of NCO by LMR, in which it might be desirable to access the higher vibrational levels. Recent restrictions have banned cyanogen from being marketed commercially, though it could still be prepared with the requisite skills and safety procedures [79].

In matrix isolation studies, NCO has been prepared in several ways [44]. The thermal decomposition of cyanuric acid, the cyclic trimer of HNCO, deposited at 1 part in 5000 in an argon matrix, produces NCO when photolysed. A similar method in which NH_3 and CO are condensed in Ar at ratios of 1:5:1000, has also been used. The condensation of the microwave discharge products of N_2 + Ar (1:500–2000) with CO/Ar is also successful.

V.3.2 Production of NCO for this Study

The HNCO+F reaction

The NCO($\tilde{X}$) produced for the LMR study reported here was generated in the intracavity absorption cell of the LMR spectrometer (see Fig.II.4) by the reaction

$$F^{\bullet}_{(g)} + HNCO_{(g)} \longrightarrow HF_{(g)}\,(v \leq 2) + NCO^{\bullet}_{(g)}. \qquad (V.2)$$

A detailed study of this reaction has been undertaken by Wategaonkar and Setser [76]. A rate constant of $3.4 \times 10^{-11}\,\mathrm{mol^{-1}cm^3s^{-1}}$ (at 300 K) and an enthalpy of $\Delta H^0_0 = -102.9\,\mathrm{kJmol^{-1}}$, were determined. They found that the nascent NCO was not highly vibrationally excited and the HF was produced with $v \leq 2$. The reaction is thought to be dominated by direct abstraction rather than addition-elimination via the $[FHNCO]^{\ddagger}$ complex. The authors of the study suggest that NCO concentrations of $3\text{–}5\times10^{12}$ molecules $\mathrm{cm^{-3}}$ can be generated, a factor of about 10^3 above the threshold for detection by intracavity CO-LMR [80].

NCO is the major reaction product, but with excess fluorine the reaction

$$F^{\bullet}_{(g)} + NCO^{\bullet}_{(g)}\left(\tilde{X}\right) \longrightarrow NF^{\bullet}_{(g)}\left(X^3\Sigma^-\right) + CO_{(g)} \qquad (V.3)$$

leads to the build up of the NF radical via the FNCO intermediate. Bimolecular self reactions of NCO produce small amounts of N_2 and CO. Other reaction channels producing HNF, NH_2, NH, CF and CN appear to be very small.

When [F]≤[HNCO], NCO is by far the major product. The 'cleanliness' of the reaction means that there is little chance of LMR spectra being due to species other than NCO. Nevertheless, it is useful to consider the vibrational wave numbers in the ground electronic state of a few of these species and they are given in Table V.1. As can be seen, such species pose a greater problem for studies involving the ν_3 vibration in the region of $1200\,\mathrm{cm^{-1}}$ [1, 2, 4].

An interesting observation of the kinetic study [76] was the report that the addition of a small amount of nitrogen to the reaction mixture may aid the excitation of NCO. This is thought to operate via a scheme involving nitrogen atoms and exchange energy transfer from $N_2(A^3\Sigma^+_u)$ to NCO. This has not been tried in the present study since

Table V.1: Approximate wave numbers[a] of the fundamental vibration-rotation bands in the $\tilde{X}$ states of paramagnetic species, other than NCO, possibly formed from the F+HNCO reaction.

Species	$\nu_1\,[cm^{-1}]$	$\nu_2\,[cm^{-1}]$	$\nu_3\,[cm^{-1}]$
CF	1285.9	—	—
CN	2042.4	—	—
NH	3125.6	—	—
NF	1123.4	—	—
NH_2	3219.4	1497.2	3301.1
NF_2	1074.3	573.4	930.7

[a] References [81] and [82].

article [76] was published some time after the LMR study reported here.

Experimental details

The experimental arrangement of the absorption cell is shown in Fig.II.4. Atomic fluorine was generated by passing a microwave discharge ('Evenson' cavity, 50 W, 2450 MHz,) through a flowing mixture of fluorine and helium (BOC Special Gases, research grade):

$$F_{2(g)}\,(5\%)\,/He_{(g)} \overset{\text{microwave}}{\longrightarrow} 2F^{\bullet}_{(g)}. \qquad (V.4)$$

The pressure of the fluorine/helium mixture was regulated by a stainless steel micrometer needle valve (Whitey SS-22RS4).

The fluorine mixture entered the cell through a borosilicate glass tube, lined with a thin walled Teflon tube from ~1 cm below the microwave discharge cavity. The discharge products were delivered ~2–3 mm above the path of the laser beam. The Teflon tube was intended to minimise the wall removal of fluorine atoms. Fluorine readily reacts with SiO_2 in the glass; a quartz inlet tube was found to be particularly unsuitable for this reason.

The preparation of HNCO is described in §V.3.4. The HNCO sample was held as a liquid in a 50:50 (by volume) ethylene glycol ($(CH_2OH)_2$)/water slush trap at −36.5 °C to −48 °C. The HNCO vapour was drawn directly off the sample through a fully open

Young Teflon tap (*i.e.* no regulation), and entered the cell near the Brewster's angle window at the mirror-box end of the laser cavity. The reaction took place downstream of the constriction in the cell (see Fig.II.4). A constant flow of reagents was maintained by an $80\,m^3hr^{-1}$ two-stage rotary vacuum pump, protected from corrosive products by a liquid nitrogen cooled trap placed before the inlet. The trap was removed to a fume cupboard at the end of each experiment, and allowed to warm up.

Reaction conditions

The reaction produced an intense violet-blue chemiluminescence, due to the $\tilde{A}$–$\tilde{X}$ emission of NCO [76]; this extended some 2–3 cm downstream of the point at which the reagents first mixed. It proved important to centre the chemiluminescence on the optical axis of the laser. This was achieved by careful positioning of the Teflon tube delivering the microwave discharge products. The tube was held in place by a wrapping of Teflon tape jammed between it and the interior of the base of the glass inlet tube.

The optimal total pressure in the absorption cell for all the signals recorded was 86 Pa (0.645 Torr). The ultimate vacuum pressure was $\sim$ 2 Pa (15 mTorr); fluorine/helium mixture was admitted to a pressure of 83 Pa (0.623 Torr) and the addition of HNCO raised the pressure by $\sim$ 3 Pa (23 mTorr) to 86 Pa (0.645 Torr). Pressures were measured at the cell outlet using an Edwards 0–10 Torr barocel capacitance manometer. The same pressure conditions proved optimal for the recording of both Lamb-dip and Doppler limited resonances. There was no evidence of significant pressure broadening of Lamb-dips.

The most important feature when recording Lamb-dips, sometimes resolving the ^{14}N hyperfine splitting, was a low detection system modulation amplitude. For Doppler limited resonances the peak-to-peak modulation amplitude gave the largest signals at about 3 mT (the maximum), whereas for Lamb-dips the optimum was typically below 0.5 mT. In the latter case, the lower modulation amplitude limit was set by a trade-off between improved resolution and loss of signal intensity. On some of the most intense signals, a peak-to-peak modulation amplitude as low as 0.13 mT was attained.

The HNCO sample typically lasted 2–4 hours, depending upon the yield in the preparation. The NCO generation took some minutes to build up at the start of each experiment. This was due to the slow warming of the sample (which had been held in a liquid nitrogen trap) and the boiling off of various contaminants. The deposition of cyanuric

acid polymer and dirt on the cell and windows meant that they had to be thoroughly cleaned after 2–3 experiments.

NO contamination

When running the experiment in π-polarisation, weak resonances due to low concentrations of the NO molecule were observed. These arose from very small traces of air present in the commercial fluorine/helium cylinder (the signal was present when the HNCO sample was turned off). The LMR experiment is most sensitive in π-polarisation and since NO is a very strong absorber, this observation is not surprising. Confusion between NO and NCO-LMR spectra was avoided by recording the scans with and without HNCO, and by noting the well characterised positions of NO resonances in the region of interest [80].

Corrosion of the glass inlet tube by fluorine eventually led to the entrainment of air into the cell from the region of the microwave discharge cavity. This could be detected by checking periodically during the experiment for the presence of NO (*e.g.* the low field NO σ-polarisation resonances on the $P(13)_{9-8}$ CO laser line), and by monitoring the pressure in the cell. Furthermore, most laser lines were studied on several different occasions.

Variations of the method of NCO generation

In early experiments, the F_2/He mixture was replaced by CF_4 (BOC research grade). The signal-to-noise of the NCO signals was at least a factor of five poorer than when F_2/He was used. Experiments were also performed in which the microwave discharge was replaced by an intracavity d.c. discharge [83]. A larger reaction cell was used for this experiment, containing a pair of parallel plate brass electrodes (24 mm long×16 mm high, 20 mm spacing). The plates were centered on the optical axis of the laser and parallel to the pole faces of the magnet, to minimise the effects of Lorentz forces. The F_2/He and HNCO were admitted to the cell (total pressure 80–110 Pa (0.6–0.83 Torr)) and discharged at a current of 5–25 mA. The NCO signal intensity increased with current; the upper limit was 25 mA, set by the fact that the silver solder on the electrodes started to melt. The total pressure could not be reduced below 25 Pa (0.19 Torr) for the same reason. Vibration of the electrodes de-stabilised the CO laser, and interactions between the d.c. discharge and the a.c. modulation coils caused noise which increased with flux

density. The best signal-to-noise ratio of the $3_0^1\,^2\Pi\,P(5/2)$ transition of NCO at 742 mT (σ-polarisation) on the $P(17)_{7-6}$ laser line, was at least two orders of magnitude below that obtained with the microwave discharge method.

Vogt [84] produced NCO by passing a d.c. discharge through ethyl isocyanate/helium in the absorbtion cell of an extracavity, Faraday detection LMR spectrometer in Bonn [50]. The signal-to-noise ratios of the observed resonances were several orders of magnitude poorer than when the F_2/HNCO/microwave method was used with the intracavity LMR spectrometer in Oxford.

V.3.3 Comparison of the HNCO+F and HN_3+F Reactions

In an analogous LMR study, Pahnke [87] prepared N_3 by the reaction

$$HN_{3(g)} + F^{\bullet}_{(g)} \longrightarrow N_{3(g)}^{\bullet} + HF_{(g)}\,(v \leq 4)\,, \tag{V.5}$$

but observed more hot-band spectra than in the present study. This reaction has been studied in detail by Habdas *et al.*[88]. From their study, an approximate rate constant of $1.1 \times 10^{-10}\,\mathrm{mol^{-1}cm^3s^{-1}}$ and an enthalpy of $\Delta H_0^0 \approx -183\,\mathrm{kJmol^{-1}}$ can be calculated. The reaction has only a very low (or zero) activation energy. In the same manner as the NCO reaction, N_3 formation is thought to proceed mainly via direct abstraction. The main difference between the NCO and N_3 reactions is that the latter proceeds faster and is more exothermic, the N–H bond energy being less in HN_3 than in HNCO.

Habdas *et al.*[88] found no evidence of highly vibrationally excited N_3 being formed, but in his LMR study, Pahnke [87] observed absorption from N_3 levels with $(0, 0, v_3 \leq 3)$ and (010). The intensity of the antisymmetric stretching mode hot-bands indicated a non-equilibrium nascent vibrational population of N_3. Consider Fig.V.2, which shows the geometric structures of HN_3, N_3, HNCO and NCO. Given the remarkable similarity between the azide and isocyanate radicals and their precursors, one would expect to observe hot-bands of the antisymmetric stretching mode in the LMR spectrum of NCO. This has not been the case, absorption being observed from levels with $(0, v_2 \leq 2, 0)$; this is also borne out by EPR [13] and microwave [6] studies in which the F+HNCO reaction was used to generate NCO. Parameters determined from observations of the $(v_1, 0, 0)$; $v_1 \leq 3$ levels of NCO($\tilde{\mathrm{X}}$) by Sears *et al.*[7] enabled highly reliable predictions

of detectable resonances in the 1_1^2 and 1_2^3 hot-bands to be made. Despite a thorough search, no spectra were observed which could be assigned to these bands. Possible reasons for this difference between N_3 and NCO are:

1. As can be seen, the change in bond length from HN–X to N–X (X=NN, CO) is greater for the azide species. This will certainly give a greater 'kick' to the anti-symmetric stretching mode of the azide species than to the out-of-phase stretching mode of the isocyanate species. Nevertheless, it is surprising that the difference is so pronounced.

2. The reaction dynamics (approach angle of the F atom) are different for the two reactions and favour the excitation of the ν_3 mode of N_3 more than the ν_1 mode of NCO.

3. The higher lying vibrational levels of N_3 are populated by the reaction channel in which the addition-elimination complex $[HFNX]^{\ddagger}$ is formed, allowing energy to flow into the ν_3 mode.

4. There could be another species present in the discharge which resonantly transfers energy to the ν_3 mode of the N_3 radical ($\sim 1645\,cm^{-1}$), but not to the ν_1 mode of NCO ($\sim 1923\,cm^{-1}$).

5. The ν_3 hot-bands of NCO are effectively quenched.

V.3.4 The Preparation of Isocyanic Acid

Reaction

Isocyanic acid was prepared by the reaction between orthophosphoric acid (H_3PO_4) and saturated potassium cyanate solution (KNCO), in a vacuum system:

$$H_3O^+_{(aq)} + NCO^-_{(aq)} \longrightarrow HNCO_{(g)} + H_2O_{(aq)}. \qquad \text{(V.6)}$$

Side reactions including hydrolysis, lead to the production of carbon dioxide, ammonia, hydrogen cyanide and cyanuric acid, the cyclic trimer of HNCO. The polymerisation of

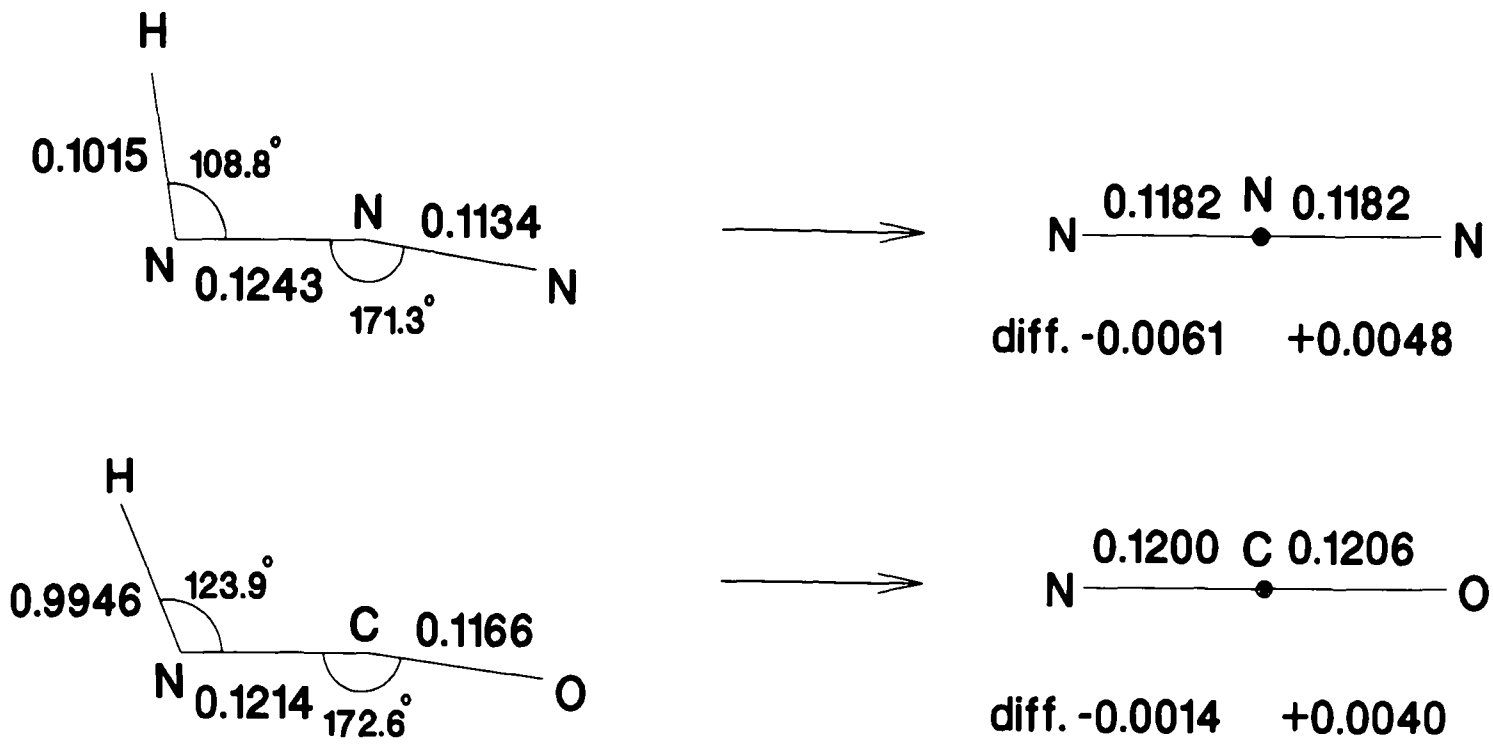

Figure V.2: The structures of HN_3, N_3, HNCO and NCO. The bond lengths and their changes upon formation of the free radicals are given in nanometers. Structures were taken from refs. [42], [85] and [86].

HNCO to cyanuric acid, a white granular material, is catalysed by the presence of water and the polymer itself [89].

Sullivan *et al.*[20] and Davies and Davis [58] produced HNCO by heating together potassium cyanate and stearic acid to 80°C in a flask and freezing out the products. This method tends to generate large amounts of carbon dioxide [76] and was not used in the present study.

Apparatus

The preparation line is shown in Fig.V.3. Manometers M_1 and M_2 were used to monitor the pressures in the reaction flask and manifolds, respectively. A 3 litre reaction flask and a splash trap were used to prevent the vigorously splashing reaction mixture from spilling over into the collection traps. Traps A and B were cooled to between $-36.5\,°C$ and $-48\,°C$ by ethylene glycol/water (50:50 by volume) slush traps in Dewars. These traps froze out the water and hydrogen cyanide, and condensed out most of the ammonia. It was important that they remained cold during the reaction, preventing water from being carried over into the collection trap and leading to polymerisation of the HNCO. The large amount of material deposited necessitated the use of 255 mm long B40 boiling tubes for the traps, with a 175 mm long inner delivery arm of 9 mm i.d. This minimised

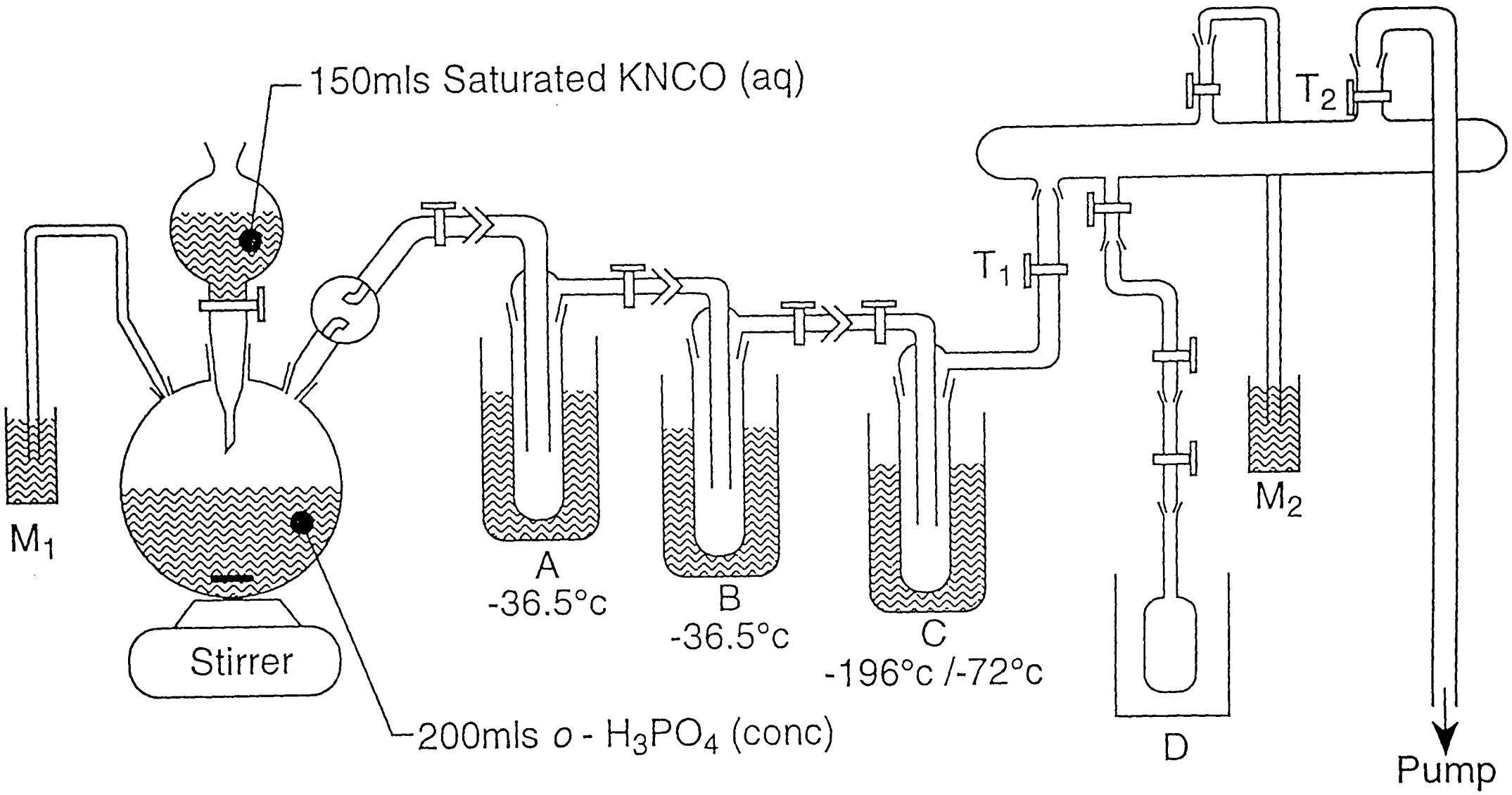

Figure V.3: The isocyanic acid preparation line.

the risk of an ice plug blocking the delivery tube and halting the preparation. Trap C was used to collect and purify the product, whence it was finally distilled over into trap D. Trap D had a long, thin 'neck' allowing it to be lowered into a large Dewar of liquid nitrogen for overnight storage of the HNCO. The components of the preparation line were connected by Quickfit-to-plastic tubing fittings (not shown), and all components could be isolated by Young type Teflon taps. This enabled a blocked trap or dropping funnel to be isolated, cleared, re-evacuated and returned to the line without spoiling the preparation.

Procedure

It proved important to ensure the line was free of cyanuric acid polymer and dry, with an ultimate vacuum pressure $< 13\,\mathrm{Pa}\,(100\,\mathrm{mTorr})$. 200 ml of orthophosphoric acid (Merck 'AnalaR', 80%) were placed in the flask with a Teflon stirrer flea and allowed to degas for at least 3 hours. A saturated solution of potassium cyanate (Aldrich, > 98%) was prepared by adding about 97 g to 130 ml demineralised water and stirring vigorously. It proved best to add a slight excess and to filter the solution. The filtrate ($\sim$ 150 ml) was poured into the dropping funnel.

With traps A and B in place and trap C cooled by liquid nitrogen, the KNCO solution was dropped in at the rate of 1 drop per second. The pressure at M_1 was maintained below 665 Pa (5 Torr) during the reaction and monitored in case a trap should become blocked. When the addition was complete, tap T_1 was closed and the left hand side of the system vented to the fume cupboard. The product was then purified, first to remove components more volatile than HNCO and then to remove any traces of water or HCN (see Table.V.2). Tap T_2 was closed and trap C replaced by an ethanol/CO_2 bath at $-72\,^{\circ}\mathrm{C}$. The sample was warmed in this bath for 15 minutes. Tap T_2 was then opened, the sample pumped on for 15 minutes and then the tap was closed again. Trap D was immersed in liquid nitrogen and the product was allowed to distill over from trap C. During this process, the ethanol/CO_2 bath was lowered to a few millimeters below trap C. The cooling provided by the bath avoided the sudden bumping of the liquid HNCO, which would otherwise spread throughout the line and polymerise in an exothermic reaction. The cooling also retained any residual water and the last 1–2 ml of residue were discarded. It proved advantageous to store the product overnight in

a large Dewar of liquid nitrogen, pumping on it with the reaction cell vacuum pump. Presumably this aided the degassing of highly volatile contaminants.

Table V.2: Melting and boiling points of species formed in the preparation of HNCO [90, 91].

Species	T_m [°C]	T_b [°C]
CO_2	–	−78.2
HNCO	−81.0	+23.5
NH_3	−78.2	−33.2
HCN	−14.2	+25.9

V.4 An LMR Study in the Region of the ν_1 Vibration

V.4.1 Background

The LMR spectrum of the 1_0^1 band of NCO was first recorded by Barnes *et al.*[45, 46], using an extracavity spectrometer. Brüggemman [47, 48] later recorded the band using a diode laser spectrometer. In both of these studies weak, unassigned lines were observed [45, 49]. Advances in CO laser technology, and the many developments made to the Oxford spectrometer, have considerably increased the laser power, sensitivity and mode stability compared to the device used by Barnes. Therefore, it was hoped that the weak, unassigned signals noted in the previous studies would be greatly enhanced in the present work, as has been the case. The unassigned signals were expected to originate from bands of the form $1_0^1 2_{v_2}^{v_2} 3_{v_3}^{v_3}$, which should be shifted to lower wave number than the 1_0^1 fundamental band ($\sim 1923\,\mathrm{cm}^{-1}$), because of anharmonic vibrational effects.

V.4.2 The LMR Search

The search commenced by re-recording the 1_0^1 band resonances observed by Barnes on $^{12}C^{16}O$ laser lines. This provided a good means of optimising the production chemistry. The search covered as many lines as possible in the 1930–1835 cm^{-1} region. Table V.3

gives full details, including on which CO laser lines resonances were observed, and the status of assignment. As the complexity of the assignment procedure became evident, the most intense work focused on the 1900–1923 cm^{-1} region, where the $1_0^1 2_1^1$ bands were expected to lie.

The spectra for most laser lines were recorded on several occasions; a few lines have been missed out and remain to be covered. Some laser lines had an intrinsically high noise baseline, usually the P(5), P(16) and P(17) laser lines, which require extreme gas and current conditions in the CO plasma, in order for gain to be achieved. An indication of noisy laser conditions is the observation of a 'flickering' of the blue corona at the cathode. Furthermore, the P(16) and P(17) laser lines often required the intracavity iris to be fully open in order to give adequate laser power for spectroscopy. This reduced the mode purity of the laser and was therefore a source of noise. Gain was achieved on water absorbed laser lines by purging the sections of the laser cavity open to the atmosphere with nitrogen from a cylinder.

As will be seen in the following chapters, many of the spectra are extremely complicated. Therefore, most laser lines were studied in both σ and π polarisation. The two polarisations provide complementary information, which can be useful when many resonances are convoluted due to two or more transitions being resonant on the same laser line. Furthermore, π polarisation spectra are often simpler since there are fewer Zeeman components than in the corresponding σ spectrum.

Survey LMR scans typically covered 0–1.6 T in 10 minutes, with a lock-in amplifier time constant of 300 ms. An up and a down scan were performed each time. The noise baseline increased logarithmically with field; typical lock-in sensitivities were 100 μV for $B < 0.6$ T, 300 μV for 0.6 T $< B <$ 1.2 T and 1 mV or 3 mV above 1.2 T. Above $\sim$ 1.3 T the noise level was sufficient to obscure all but the strongest signals.

Accurate measurements were performed with a scan rate of $\sim$ 20 mTmin^{-1} with a time constant of 300 ms. Measurements were taken to be the average of several upward and downward scans, since there was a shift of $\sim$ 3 mT between peak positions in the upward and downward scans. The resonant fields were corrected to give the fields at the center of the cavity, since the field controller used a Hall probe mounted on a pole cap of the magnet.

Assignments have so far been made to the unique states and to the $K = 0$ $^2\Sigma$ states of

Table V.3: Details of the $^{12}C^{16}O$ LMR search in the region of the ν_1 fundamental of $NCO(\tilde{X}^2\Pi)$.

Laser Line	$\tilde{\nu}_L$ [cm^{-1}]	Searched		Resonances		Assigned		Unassigned	
		σ^a	π^a	σ	π	σ	π	σ	π
$P(14)_{7-6}$	1931.4052	•	•						
$P(8)_{8-7}$	1929.5857	•	•						
$P(15)_{7-6}$	1927.2958	•	•						
$P(9)_{8-7}$	1925.7111	•	•						
$P(16)^{(w)}_{7-6}$	1923.1535	•	•	•	•	•	•		
$P(10)_{8-7}$	1921.8028	•	•		•				•
$P(17)_{7-6}$	1918.9787	•	•	•	•	•	•		
$P(11)^{(w)}_{8-7}$	1917.8610	•	•	•	•	•	•		
$P(5)_{9-8}$	1915.1976	•	•	•	•			•	•
$P(12)_{8-7}$	1913.8859	•	•	•	•	•	•		
$P(6)_{9-8}$	1911.4599	•	•	•	•			•	•
$P(13)^{(w)}_{8-7}$	1909.8775	•	•	•	•	•	•	•	•
$P(7)_{9-8}$	1907.6880	•	•	•	•	•	•	•	
$P(14)_{8-7}$	1905.8360	•	•	•	•	•	•	•	•
$P(8)_{9-8}$	1903.8822	•	•	•	•	•	•		
$P(15)_{8-7}$	1901.7616	•	•	•	•			•	•
$P(9)_{9-8}$	1900.0426	•	•		•				•
$P(16)_{8-7}$	1897.6545	•	•		•				•
$P(10)_{9-8}$	1896.1694	•	•	•	•			•	•
$P(17)^{(w)}_{8-7}$	1893.5147	•	•	•	•	•		•	•
$P(11)_{9-8}$	1892.2626	•	•	•	•			•	•
$P(5)_{10-9}$	1889.4666	•	•	•	•			•	•
$P(12)_{9-8}$	1888.3225	•	•	•	•			•	•
$P(6)_{10-9}$	1885.7638	•	•	•	•			•	•
$P(13)^{*}_{9-8}$	1884.3492	•	•	•	•			•	•
$P(7)_{10-9}$	1882.0270	•	•	•	•			•	•
$P(14)_{9-8}$	1880.3428	•	•	•	•			•	•
$P(8)_{10-9}$	1878.2562	•	•	•				•	

Table V.3 Continued...

CO Laser Line	$\tilde{\nu}$ [cm^{-1}]	Searched		Resonances		Assigned		Unassigned	
		$\sigma^{(a)}$	$\pi^{(b)}$	σ	π	σ	π	σ	π
$P(15)^{*}_{9-8}$	1876.3034	•	•	•	•			•	•
$P(9)_{10-9}$	1874.4516	•	•	•	•			•	•
$P(16)_{9-8}$	1872.2313		•						
$P(10)_{10-9}$	1870.6134	•	•	•	•			•	•
$P(17)^{(w)}_{9-8}$	1868.1266		•		•				•
$P(11)_{10-9}$	1866.7417	•	•	•	•			•	•
$P(5)^{*}_{11-10}$	1863.8144		•		•				•
$P(12)_{10-9}$	1862.8366	•	•	•				•	
$P(6)^{*}_{11-10}$	1860.1467	•	•	•				•	
$P(13)_{10-9}$	1858.8983		•		•				•
$P(7)^{*}_{11-10}$	1856.4449		•						
$P(14)_{10-9}$	1854.9270		•		•				•
$P(8)_{11-10}$	1852.7091		•		•				•
$P(15)_{10-9}$	1850.9227		•		•				•
$P(9)_{11-10}$	1848.9396		•						
$P(16)_{10-9}$	1846.8857		•		•				•
$P(10)^{(w)}_{11-10}$	1845.1364		•		•				•
$P(17)_{10-9}$	1842.8160		•						
$P(11)_{11-10}$	1841.2997		•		•				•
$P(5)_{12-11}$	1838.2426		•						
$P(12)_{11-10}$	1837.4297								
$P(6)_{12-11}$	1834.6099	•							

$^{(a)}\sigma$ and π polarisation have the selection rules $\Delta M_J = \pm 1$ and $\Delta M_J = 0$, respectively.

$^{(w)}$Laser lines attenuated by atmospheric water vapour.

*Resonances due to NO were sometimes observed.

NCO. The assignments to the $K = 0$ states were made as a result of a very complicated modelling procedure. Chapters VI and VII describe the assignment procedure, analysis and discussion of the various bands to which resonances have been assigned. Chapter VII also discusses some of the unassigned spectra [92], and possible assignments to be investigated as a continuation of this work.

Bibliography

[1] J. Werner, Ph.D. thesis, Institut für Angewandte Physik der Universität Bonn, 1987.

[2] W. Seebass, Ph.D. thesis, Institut für Angewandte Physik der Universität Bonn, October 1986.

[3] H.J. Müschenborn, Diplomarbeit thesis, Institut für Angewandte Physik der Universität Bonn, 1986.

[4] J. Werner, W. Seebass, M. Koch, R.F. Curl, W. Urban and J.M. Brown, *Mol. Phys.* **56**, 453–461 (1985).

[5] K. Kawaguchi, S. Saito and E. Hirota, *Mol. Phys.* **49**, 663–674 (1983).

[6] K. Kawaguchi, S. Saito and E. Hirota, *Mol. Phys.* **55**, 341–350 (1985).

[7] F.J. Northrup, M. Wu and T.J. Sears, *J. Chem. Phys.* **96**, 7218–7228 (1992).

[8] M. Wu, F.J. Northrup and T.J. Sears, *J. Chem. Phys.* **97**, 4583–4595 (1992).

[9] M. Wu and T.J. Sears, *Mol. Phys.* **82**, 503–521 (1994).

[10] B. Hemmerling and M. Vervloet, *Mol. Phys.* **78**, 1423–1447 (1993).

[11] R. Holland, D.W.G. Style, R.N. Dixon and D.A. Ramsay, *Nature*, **182**, 336–337 (1958).

[12] R.N. Dixon, *Phil. Trans. R. Soc. Lond. A* **252**, 165–192 (1960).

[13] A. Carrington, A.R. Fabris, B.J. Howard and N.J.D. Lucas, *Mol. Phys.* **20**, 961–980 (1971).

[14] P.S.H. Bolman, J.M. Brown and A. Carrington, *Proc. R. Soc. London A* **343**, 17–44 (1975).

[15] P.S.H. Bolman and J.M. Brown, *Chem. Phys. Lett.* **21**, 213–216 (1973).

[16] R.N. Dixon, N. Little, M.J. Trenouth and C.M. Western, *Chem. Phys. Lett.* **121**, 41–44 (1985).

[17] T.R. Charlton, T. Okamura and B.A. Thrush, *Chem. Phys. Lett.* **89**, 98–100 (1982).

[18] R.N. Dixon, *Can. J. Phys.* **38**, 10–17 (1960).

[19] R.N. Dixon, M.J. Trenouth and C.M. Western, *Mol. Phys.* **60**, 779–792 (1987).

[20] B.J. Sullivan, G.P. Smith and D.R. Crosley, *Chem. Phys. Lett.* **96**, 307–310 (1983).

[21] J.M. Dyke, N. Jonathan, A.E. Lewis, J.D. Mills and A. Morris, *Mol. Phys.* **50**, 77–89 (1983).

[22] S.E. Bradforth, E.H. Kim, D.W. Arnold and D.M. Neumark, *J. Chem. Phys.* **98**, 800–810 (1993).

[23] H. Okabe, *J. Chem. Phys.* **53**, 3507–3515 (1970).

[24] I. Tokue and Y. Ito, *Chem. Phys.* **89**, 51–57 (1984).

[25] D.R. Cyr, R.E. Continetti, R.B. Metz, D.L. Osborn and D.M. Neumark, *J. Chem. Phys.* **97**, 4937–4947 (1992).

[26] B. Ruscic and J. Berkowitz, *J. Chem. Phys.* **100**, 4498–4508 (1994).

[27] J. Park and J.F. Hershberger, *Chem. Phys. Lett.* **218**, 537–543 (1994).

[28] R.A. Perry, 25th Symposium (International) on Combustion/The Combustion Institute, pp. 913–918 (1993).

[29] M.Y. Louge and R.K. Hanson, *Combustion and Flame* **58**, 291–300 (1984).

[30] M.Y. Louge, R.K. Hanson, E.C. Rea and R.A. Booman, *J. Quant. Spectrosc. Radiat. Transfer* **32**, 353–362 (1984).

[31] W.R. Anderson, J.A. Vanderhoff, A.J. Kotlar, M.A. Dewilde and R.A. Beyer, *J. Chem. Phys.* **77**, 1677–1685 (1982).

[32] K.N. Wong, W.R. Anderson, A.J. Kotlar and J.A. Vanderhoff, *J. Chem. Phys.* **81**, 2970–2974 (1984).

[33] R.A. Beyer and M.A. DeWilde, *Rev. Sci. Instrum.* **53**, 103–104 (1982).

[34] R.A. Copeland and D.R. Crosley, *Can. J. Phys.* **62**, 1488–1501 (1985).

[35] D.R. Woodward, D.A. Fletcher and J.M. Brown, *Mol. Phys.* **68**, 261–262 (1989).

[36] D.R. Woodward, D.A. Fletcher and J.M. Brown, *Mol. Phys.* **62**, 517–536 (1987).

[37] D.R. Woodward, D.Phil thesis, University of Oxford, 1986.

[38] D. Patel-Misra, D.G. Sauder, P.J. Dagdigian and D.R. Crosley, *J. Chem. Phys.* **95**, 2222 (1991).

[39] D. Patel-Misra, D.G. Sauder and P.J. Dagdigian, *J. Chem. Phys.* **93**, 5448–5456 (1990).

[40] D.G. Sauder, D. Patel-Misra and P.J. Dagdigian, *J. Chem. Phys.* **95**, 1696–1707 (1991).

[41] F.J. Northrup and T.J. Sears, *Ann. Rev. Phys. Chem.* **43**, 127–152 (1992).

[42] P. Misra, C.W. Mathews and D.A. Ramsay, *J. Mol. Spectrosc.* **130**, 419–423 (1988).

[43] D.E. Milligan and M.E. Jacox, *J. Chem. Phys.* **47**, 5157–5169 (1967).

[44] V.E. Bondybey and J.H. English, *J. Chem. Phys.* **67**, 2868–2873 (1977).

[45] C.E. Barnes, J.M. Brown, A.D. Fackerell and T.J. Sears, *J. Mol. Spectrosc.* **92**, 485–496 (1982).

[46] C.E. Barnes, Ph.D. thesis, University of Southampton, 1981.

[47] R. Brüggemann, Diplomarbeit thesis, Institut für Angewandte Physik der Universität Bonn, 1988.

[48] R. Brüggemann, M. Petri, H. Fischer, D. Mauer, D. Reinert and W. Urban, *Appl. Phys. B* **48**, 105–110 (1989).

[49] T. Vogt, Institut für Angewandte Physik der Universität Bonn, Private Communications, 1991 and 1992.

[50] A. Hinz, J. Pfeiffer, W. Bohle and W. Urban, *Mol. Phys.* **45**, 1131–1139 (1982).

[51] Some programs and LMR spectra from Bonn are held by Dr. J.M. Brown, the Physical Chemistry Laboratory, University of Oxford, South Parks Road, Oxford OX1 3QZ, United Kingdom

[52] M.A. Gondal, W. Rohrbeck and W. Urban, *J. Mol. Spectrosc.* **100**, 290–302 (1983).

[53] A. Carrington, A.R. Fabris and N.J.D. Lucas, *J. Chem. Phys.* **49**, 5545–5547 (1968).

[54] A. Carrington, A.R. Fabris and N.J.D. Lucas, *Mol. Phys.* **16**, 195–197 (1969).

[55] S. Saito and T. Amano, *J. Mol. Spectrosc.* **34**, 383–389 (1970).

[56] T. Amano and E. Hirota, *J. Chem. Phys.* **57**, 5608–5610 (1972).

[57] S. Saito, Symposium on Structural Chemistry, Paper 19C10, Tokyo, 1974.

[58] P.B. Davies and I.H. Davis, *Mol. Phys.* **69**, 175–191 (1990).

[59] T. Suzuki, *J. Mol. Spectrosc.* **120**, 414–419 (1986).

[60] B.F. Minaev, N.M. Ivanova and Z.M. Muldahmetov, *Spectroscopy Lett.* **22**, 901–923 (1989).

[61] Z.-L. Cai, Y.-F. Wang and H.-M. Xiao, *Chem. Phys. Lett.* **190**, 381–385 (1992).

[62] M. Péric, B.A. Hess and R.J. Buenker *Mol. Phys.* **58**, 1001–1011 (1986).

[63] Y. Li, S. Carter, G. Hirsch and R.J. Buenker, *Mol. Phys.* **80**, 145–152 (1993).

[64] W. Koch and G. Frenking, *J. Phys. Chem.* **91**, 49–53 (1987).

[65] A.L.L. East and W.D. Allen, *J. Chem. Phys.* **99**, 4638–4650 (1993).

[66] R.G. Macdonald and K. Liu, *J. Chem. Phys.* **97**, 978–990 (1992).

[67] R.G. Macdonald and K. Liu, *J. Chem. Phys.* **98**, 3716–3725 (1993).

[68] V.E. Bondybey, J.H. English, C.W. Mathews and R.J. Contolini, *Chem. Phys. Lett.* **82**, 208–211 (1981).

[69] D.A. Ramsay and M. Winnewisser, *Chem. Phys. Lett.* **96**, 502–504 (1983).

[70] C. Marian, B.A. Hess, S. Schöttke and R.J. Buenker, *J. Mol. Spectrosc.* **124**, 190–198 (1987).

[71] R.G.A.R. Maclagan, *J. Phys. Chem.* **97**, 4614–4615 (1993).

[72] C. Wentrup, B. Gerecht and H. Riehl, *Angew. Chem. Int. Ed. Engl.* **18**, 467–468 (1979).

[73] F. De Sarlo, A. Brandi, A. Guarna, A. Goti and S. Corezzi, *Tetrahedron Lett. Engl.* **24**, 1815–1816 (1989).

[74] H. Wieland and H. Heß, *Chem. Ber.* **42**, 1346–1363 (1909).

[75] B.P. Winnewisser, Physikalisch-Chemisches Institut, Justus-Liebig-Universität, Gießen, Private Communications, 1981 and 1992.

[76] S. Wategaonkar and D.W. Setser, *J. Phys. Chem.* **97**, 10028–10034 (1993).

[77] L.F. Phillips, I.W.M. Smith, R.P. Tuckett and C.J. Whitham, *Chem. Phys. Lett* **183** 254–263 (1991).

[78] R.G. Macdonald, K. Liu, D.M. Sonnenfroh and Di-Jai Liu, *Can. J. Chem.* **72**, 660–672 (1994).

[79] N.N. Greenwood and A. Earnshaw, "Chemistry of the Elements," pp. 336–338, Pergamon Press, Oxford, 1984.

[80] D. Robinson, Ph.D. thesis, University of Southampton, 1983.

[81] K.P. Huber and G. Herzberg, "Molecular Spectra and Molecular Structure," Vol. IV, "Constants of Diatomic Molecules,", Van Nostrand-Reinhold, New York, 1979.

[82] G. Herzberg, "Molecular Spectra and Molecular Structure," Vol. III, "Electronic Spectra and Electronic Structure of Polyatomic Molecules," 2nd ed. (corrected), Krieger Publishing, Malabar, Florida, 1991.

[83] D.A. Gillett, Part II thesis, University of Oxford, Trinity 1990.

[84] Thomas Vogt, Diplomarbeit thesis, Institut für Angewandte Physik der Universität Bonn, 1993.

[85] B.P. Winnewisser, *J. Mol. Spectrosc.* **82**, 220–223 (1980).

[86] C.R. Brazier, P.F. Bernath, J.B. Burkholder and C.J. Howard, *J. Chem. Phys.* **89**, 1762–1767 (1988).

[87] R. Pahnke, D. Phil thesis, University of Oxford, 1990.

[88] J. Habdas, S. Wategaonkar and D.W. Setser, *J. Phys. Chem.* **91**, 451–458 (1987).

[89] J.Y.P. Mui and R.A. Back, *Can. J. Phys.* **41**, 826–830 (1963).

[90] "CRC Handbook of Chemistry and Physics," 75th ed., (D.R. Lide and H.P.R. Frederikser, Eds.), CRC Press inc., Baca Raton, 1993.

[91] "Revised Nuffield Advanced Science Book of Data," (H. Ellis, Ed.), Longman, Harlow, 1984.

[92] All the LMR spectra recorded in this study are held by Dr. J.M. Brown, The Physical Chemistry Laboratory, University of Oxford, Oxford OX1 3QZ, United Kingdom.

Chapter VI

The $1_0^1 2_{v_2}^{v_2}$ Unique State Bands of NCO

VI.1 The $1_0^1\,{}^2\Pi$ Band

VI.1.1 Observations

The first infrared study of this band was the LMR study by Barnes *et al.*[1]. A $^{12}C^{16}O$ laser was used in an extracavity LMR spectrometer in Southampton, and a $^{12}C^{18}O$ laser in an intracavity LMR spectrometer in Ottawa. The $^{12}C^{16}O$ LMR spectra were re-recorded at the start of the present study and where improved measurements could be made (*e.g.* by saturation), the old ones were replaced.

Improvements in the Dunham coefficients for CO since the study of Barnes *et al.* have led to revisions in some of the CO laser wave numbers [2]–[5]. These changes, typically $\pm 10^{-4}\,\mathrm{cm}^{-1}$, are most significant for the $^{12}C^{18}O$ laser lines.

Table VI.1 summarises the LMR observations of the $1_0^1\,{}^2\Pi$ band made in this study. As in previous Zeeman studies, all the observations were restricted to the $^2\Pi_{\frac{3}{2}}$ sub-band. One new transition has been detected, the P(7/2) on the $P(11)_{8-7}$ laser line. In addition, the transitions on the $P(16)_{7-6}$ and $P(17)_{7-6}$ laser lines have been studied in π polarisation for the first time. Many of the resonances were saturated, and at low modulation amplitudes the ^{14}N nuclear hyperfine structure was resolved as a triplet splitting. As in previous mid-infrared studies, the K-type doubling was not resolved.

The best signal-to-noise ratio was at least 500:1, achieved for the P(5/2) resonance

Table VI.1: Summary of LMR observations of the $1_0^1\,^2\Pi_{\frac{3}{2}}$ sub-band

Transition	Laser Line	$\tilde{\nu}_L\,[\mathrm{cm}^{-1}]$
R(3/2)	$P(16)_{7-6}$*	1923.1535
R(5/2)	$P(16)_{7-6}$*	1923.1535
P(5/2)	$P(17)_{7-6}$	1918.9787
P(7/2)	$P(11)_{8-7}$*	1917.8610

*Water absorbed laser line.

at 742 mT on the $P(17)_{7-6}$ laser line in σ polarisation, with a time constant of 300 ms. Fig.VI.1 shows the LMR spectrum of the P(7/2) transition recorded in π polarisation. This transition was predicted by Barnes [6], who failed to observe it because of limitations in the spectrometer and/or the NCO production. In Fig.VI.1, all the resonances appear as Lamb-dips, giving an indication of the improvements made since the original study, and in particular the advantages of an intracavity spectrometer.

A Zeeman tuning diagram for the P(7/2) transition is shown in Fig.VI.2. As can be seen, the components of the transition tune linearly with field, exactly what one expects for a Hund's case (a) coupling scheme. The flux density range of the diagram is low enough for second-order Zeeman effects to be unimportant. An approximate formula for the tuning rate (gradient) of the transitions in π polarisation is

$$\left(\frac{\partial\nu}{\partial B}\right)_{\pi} = (g'_J - g''_J)\, M_J \mu_B. \tag{VI.1}$$

An effective g_L value of 0.988892 can be estimated using the parameters from Table VI.4 with Eq.(IV.8). Using Eq.(IV.9), values of $g_{J=5/2} = 0.34113$ and $g_{J=7/2} = 0.18952$ can be calculated. The approximate tuning rates calculated from Eq.(VI.1) are compared in Table VI.2 with the exact tuning rates calculated using the Hellmann-Feynman theorem in the final analysis; the agreement is very good at low flux densities.

The lower the tuning rate, the more the transition line profile is spread out in the magnetic field domain and the broader the resonance. The field-width of a Lamb-dip can be measured to give an indication of the experimentally limited linewidth. The separation of the extrema of the dip at 842 mT is 12.1 mT. This dip consists of three hyperfine

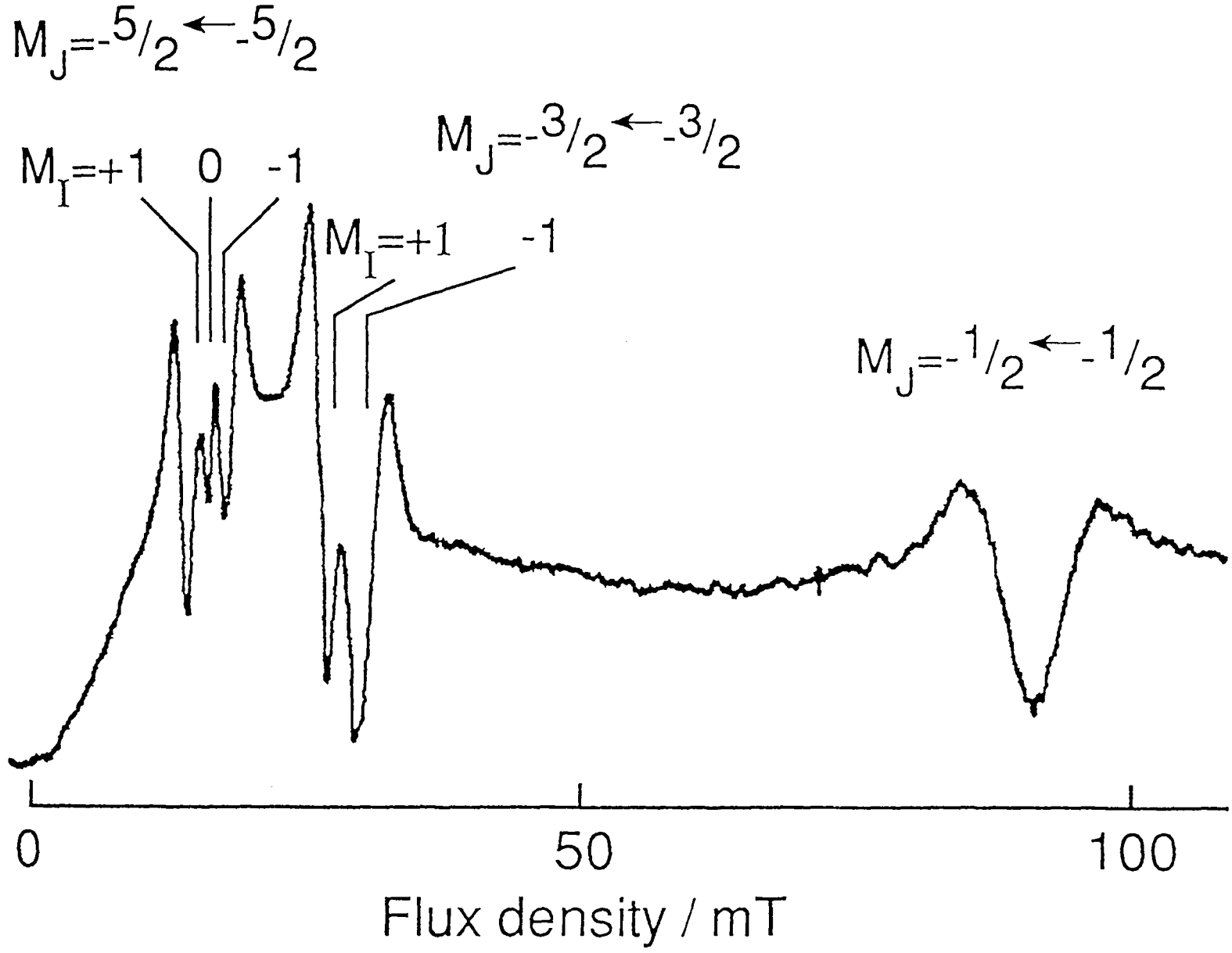

Figure VI.1: Resonances due to the P(7/2) line of the $1^1_0\,^2\Pi_{\frac{3}{2}}$ sub-band of NCO($\tilde{\mathrm{X}}$). The resonances appear in saturation as Lamb-dips burned into the Doppler profile. The ^{14}N hyperfine structure is partly resolved for the two lower field resonances. The spectrum was recorded on the $P(11)_{8-7}$ laser line in π polarisation at a scan rate of 17 mTmin^{-1} with a time constant of 1 s and a peak-to-peak modulation amplitude of 2 mT. The ordinate is the 2-f absorption signal.

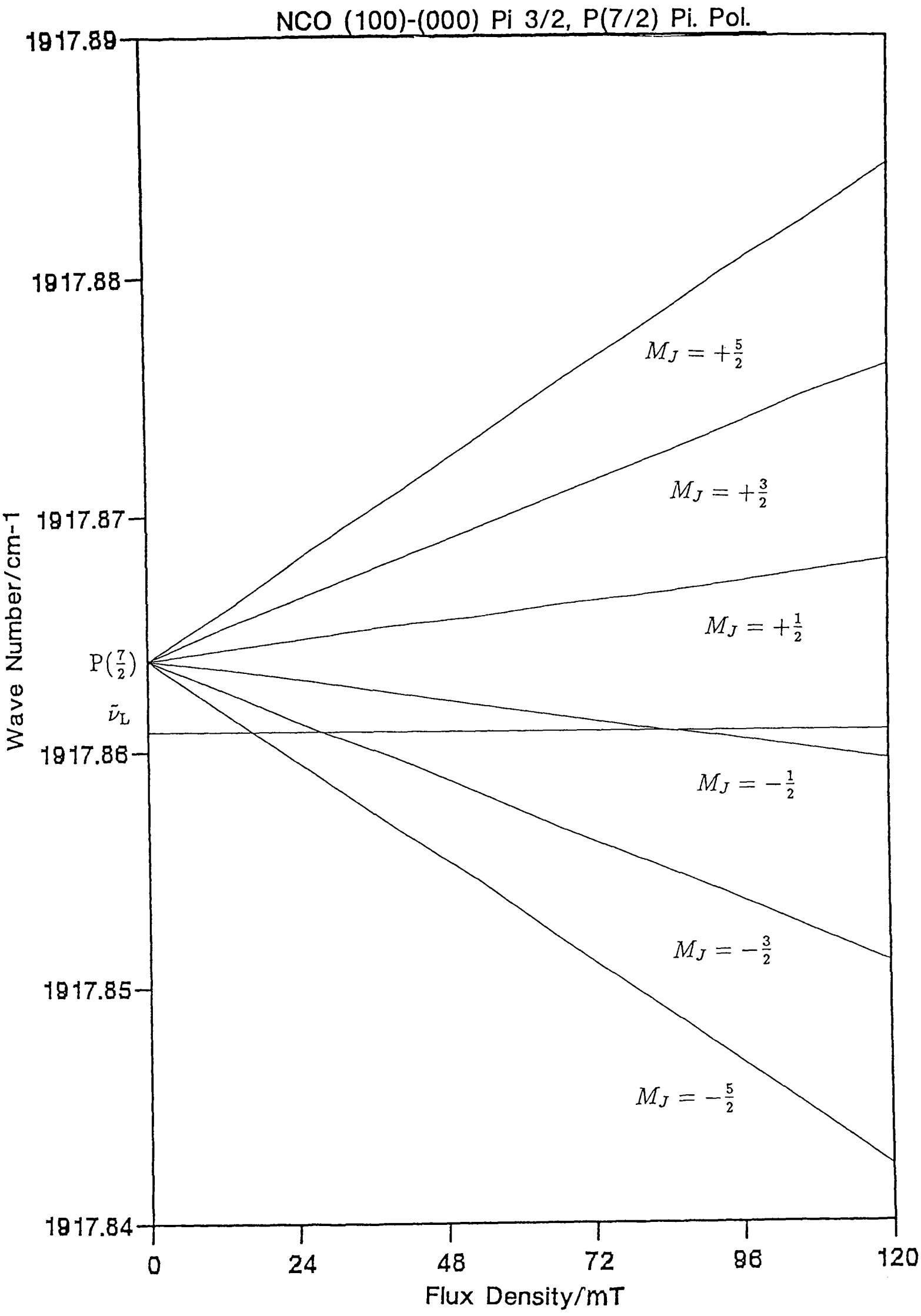

Figure VI.2: A Zeeman tuning diagram of the $1_0^1\,{}^2\Pi_{\frac{3}{2}}$ P(7/2) transition in π polarisation.

Table VI.2: First-order and exact tuning rates of the observed π polarisation resonances of the $1_0^1\,^2\Pi_{\frac{3}{2}}$ P(7/2) transition.

M_J	First Order[a]	Exact[a]
−2.5	−0.531	−0.526
−1.5	−0.318	−0.319
−0.5	−0.106	−0.108

[a] $\partial\nu/\partial B$ in MHz G^{-1}.

components; neglecting the broadening due to their overlap, the frequency equivalent separation of the extrema of the dip is 13 MHz. This corresponds to the FWHM of a Lorentzian profile and it is in good agreement with the estimated experimentally limited uncertainty of 10 MHz discussed in §II.7.

Only the two lower field transitions in Fig.VI.1 show resolved nuclear hyperfine structure. The small spacing of the hyperfine components ($\sim$ 2 mT) causes a small second derivative in the region of the central component, which is sometimes obscured in 2-f detection, as exemplified by the resonances for $M_J = -3/2$. In the dip at 842 mT, the hyperfine structure is lost completely due to the much lower tuning rate of this transition. The assignment of the hyperfine structure components was achieved in the first instance by making predictions using the diatomic program described in §IV.5.2, with hyperfine parameters taken from the EPR [7] and microwave studies [8].

VI.1.2 Searches for Other 1_0^1 Transitions

In the study of Pahnke [9], a P(25/2) transition was observed in the $3_0^1\,^2\Pi_{\frac{3}{2}}$ sub-band of N_3. The spectrum was observed as a progression of Lamb-dips showing K-type doubling. This is somewhat unexpected for transitions between Hund's case (a) energy levels and may be peculiar to Renner-Teller molecules. Interest was focused on assigning any such transitions to the 1_0^1 band of NCO. There were several candidate spectra and it was very important to exclude this possibility before attempting to assign them to more complicated bands.

An example is the spectrum recorded on the $P(12)_{8-7}$ laser line, shown in Fig.VII.10. The P(17/2) line of the $1_0^1\,^2\Pi_{\frac{3}{2}}$ sub-band lies close to this laser line, its + and −

parity components having predicted zero field wave numbers of 1913.8036 cm^{-1} and 1913.8035 cm^{-1}, respectively. Predictions suggested that this transition was not sufficiently near to the $P(12)_{8-7}$ laser line at 1913.8859 cm^{-1} to be tuned into resonance, but any small perturbation could easily change this. Therefore, a spectrum was modelled by moving a 'false' frequency line until it was crossed by the transition. The characteristics of the transition, including the width of the Lamb-dips and the obvious 'doubling' of the real spectrum, were not well modelled by the simulation. In particular, the predicted K-type doubling was far smaller than the observed 'doubling'. This spectrum was later assigned to the $1_0^1 2_1^1\,^2\Sigma$ band, as discussed in Chapter VII.

Consideration was also given to the $1_0^1\,^2\Pi_{\frac{1}{2}}$ sub-band. Although unlikely to be observed due to low tunability and extremely under-modulated linewidths, resonances are possible [10]. A very close ($\sim 10^{-3}$ cm^{-1}) coincidence with a CO laser line could possibly give rise to a spectrum consisting of Lamb-dips, which are much narrower than Doppler profiles, and therefore more likely to be detected. In addition, the K-type doubling is larger in the $P = 1/2$ spin component than in the $P = 3/2$ spin component. Careful predictions suggested that no such resonances occurred; the nearest coincidences were with CO laser lines on which no candidate spectra had been observed. As a guide, the P(17/2) transition referred to above but now for the $P = 1/2$ sub-band, was simulated. The zero field K-type splitting was 2.5×10^{-3} cm^{-1}, and typical tuning rates were of the order of 10^{-2} $MHzG^{-1}$. For Lamb-dips with a width of $\sim$ 10 MHz, the field-equivalent width would be around 100 mT.

The predictions discussed above were performed using the parameters obtained from a fit including FIR LMR data [11] of the $J = 29/2 \leftarrow 27/2$ and $J = 43/2 \leftarrow 41/2$ $(000)\,^2\Pi_{\frac{3}{2}}$ transitions, and diode laser observations of both the $1_0^1\,^2\Pi_{\frac{3}{2}}$ and $1_0^1\,^2\Pi_{\frac{1}{2}}$ sub-bands. The former data provide a very accurate measurement of the K-type doubling, and the latter fix the position of the $P = 1/2$ levels, which are absent in the LMR studies.

Sears *et al.*[12] observed the $(v_1, 0, 0)$ levels with $v_1 \leq 3$, in an SEP experiment. The vibrational, spin-orbit and rotational parameters quoted in this reference enabled predictions of the $1_1^2\,^2\Pi$ and $1_2^3\,^2\Pi$ bands to be made, with an estimated accuracy of $\pm 5 \times 10^{-3}$ cm^{-1}. Searches for these transitions on the $P(17)_{8-7}$, $P(11)_{9-8}$ and $P(12)_{9-8}$ CO laser lines, were unsuccessful despite intensive efforts. This indicates very low populations in the $v_1 = 1$ and $v_1 = 2$ levels of NCO. Transitions have been detected on these laser

lines, but none are consistent with resonances from the ν_1 hot-bands. Table VI.3 gives the calculated zero field wave numbers of these transitions, since their detection by LMR would be important.

Table VI.3: Predicted zero field wave numbers of transitions in the $1_1^2\,^2\Pi_{\frac{3}{2}}$ and $1_2^3\,^2\Pi_{\frac{3}{2}}$ "hot" sub-bands. The estimated accuracy is $\pm 5 \times 10^{-3}\,\mathrm{cm}^{-1}$.

Transition	$1_1^2\,\tilde{\nu}\,[\mathrm{cm}^{-1}]$	$1_2^3\,\tilde{\nu}\,[\mathrm{cm}^{-1}]$
$\mathrm{R}(\frac{5}{2})$	1893.511	1861.978
$\mathrm{R}(\frac{3}{2})$	1892.764	1861.234
$\mathrm{Q}(\frac{3}{2})$	1890.857	1859.341
$\mathrm{Q}(\frac{5}{2})$	1890.841	1859.327
$\mathrm{P}(\frac{5}{2})$	1888.934	1857.434
$\mathrm{P}(\frac{7}{2})$	1888.149	1856.658

VI.1.3 Final Analysis

Data set

The data set for the final analysis comprised:

1. The LMR data recorded in this study and the study of Barnes *et al.*[1]. Lamb-dips were assigned an uncertainty of $2 \times 10^{-4}\,\mathrm{cm}^{-1}$ and Doppler limited resonances were assigned an uncertainty of $6.7 \times 10^{-4}\,\mathrm{cm}^{-1}$.

2. The diode laser data of Brüggemmann *et al.*[13]. These observations cover both the $1_0^1\,^2\Pi_{\frac{3}{2}}$ and $1_0^1\,^2\Pi_{\frac{1}{2}}$ sub-bands. These observations allow the determination of the spin-orbit splitting in the $(100)\,^2\Pi$ level. Each datum was assigned an uncertainty of $2 \times 10^{-3}\,\mathrm{cm}^{-1}$. Diode laser observations can sometimes suffer from an absolute wave number offset which arises in the calibration procedure. No such effect was found here, after comparing the observed wave numbers with those calculated from parameters determined from an analysis of the LMR, EPR and microwave data.

3. Optical combination differences taken from Bolman *et al.*[14] were included to define the spin-orbit splitting in the $(000)\,\tilde{\mathrm{X}}^2\Pi$ level. A representative series was

chosen from the $00^00 \leftarrow 00^10$ band of the $\tilde{A} \leftarrow \tilde{X}$ transition. The combination differences were calculated from

$$^{R}R_{11}(J) - {}^{Q}R_{12}(J)$$

and

$$^{R}Q_{21}(J) - {}^{Q}Q_{22}(J)$$

and they correspond to $(000)\,^2\Pi_{\frac{1}{2}}(J) - (000)\,^2\Pi_{\frac{3}{2}}(J)$ in the $\tilde{X}$ state. Each datum was assigned an uncertainty of $10^{-2}\,\mathrm{cm}^{-1}$.

4. The FIR-LMR observations of Davies and Davis [11]. These were observed in the $(000)\,^2\Pi_{\frac{3}{2}}$ level and serve to fix the K-type doubling at intermediate J values. Resonances below 800 mT were assigned an uncertainty of 200 kHz, and those above 800 mT were assigned an uncertainty of 600 kHz as in [11].

5. The microwave observations of Kawaguchi *et al.*[8], Amano and Hirota [15] and Saito [16]. The observations cover both the $(000)\,^2\Pi_{\frac{3}{2}}$ and $(000)\,^2\Pi_{\frac{1}{2}}$ levels. All of these observations are detailed in ref. [8], which also gives the experimental uncertainty assigned to each datum.

6. The EPR observations of Carrington *et al.*[7]. These observations cover the $J = 3/2$ level of $(000)\,^2\Pi_{\frac{3}{2}}$. Each datum was assigned an uncertainty of 300 kHz.

Details of the fit and the parameters

The final analysis used the harmonic Renner-Teller model developed in Chapters III and IV. A least-squares multivariate fit was performed to the above data to determine a number of parameters. A basis set with $\Delta J = \pm 4$ and $\Delta v_2 = \pm 4$ was used fully to take into account the Zeeman and Renner-Teller effects in the $\tilde{X}$ state.

In the fit, 18 parameters were determined and 15 were constrained; they are detailed in Table VI.4. The LMR data section of the fit is given in Table VI.5; the remaining data are detailed in Appendix G.

The quality of fit relative to the estimated experimental uncertainties was $\sigma_{\mathrm{rel.}} = 1.59$, see Eq.(IV.67). This is quite close to unity but it indicates that some data do not fit

quite so well as expected. This predominantly occurs in the microwave data set, Table G.3, though these transitions fit at least as well as in the original analysis [8], implying that the authors of [8] were optimistic in their assessment of measurement errors. The standard deviation of the new LMR data was 7 MHz and that of Barnes' LMR data was 20 MHz, indicating that all the LMR data were well described by the model.

The vibrational wave numbers ω_2 and ω_3 were taken from the Renner-Teller analysis of Wu and Sears [17], as was the vibronic parameter g_K. Values of $\epsilon\omega_2$ and $\alpha_{1,\epsilon\omega_2}$ were taken from the fit of the $1_0^1 2_1^1\,{}^2\Sigma$ bands described in Chapter VII. The parameters α_{1,g_K} and $\alpha_{2,A}$ were determined from the fit of the $1_0^1 2_1^1\,{}^2\Delta$ band, described in §VI.2. The values of $A_{(000)}, \alpha_{1,A}, \alpha_{2,A}, \alpha_{1,g_K}, \epsilon\omega_2$ and $\alpha_{1,\epsilon\omega_2}$ were iterated between these three fits until consistent values were obtained.

The centrifugal distortion K-type doubling parameters, p_D and q_D, were constrained to perturbation theory estimates given by

$$p_D = -\frac{pD}{B} \tag{VI.2}$$

$$q_D = -4\frac{qD}{B} \tag{VI.3}$$

and were included to avoid distortion of the FIR-LMR data. The electron spin and orbital g-factors, g_S and $g_L^{(0)}$, were constrained to the values calculated for NCO in [7]. The anisotropic spin g-factor, g_l, was constrained to the estimate given by Curl's relationship, Eq.(III.103). The Λ-type doubling g factor g_l', was calculated using Eq.(E.9), but for $g_r^{e\prime}$ the relation

$$g_r^{e\prime} = -\frac{q_{\text{el.}}}{B} \tag{VI.4}$$

was used. The K-type doubling parameter q contains both Λ-type and l-type contributions, whereas the Zeeman effect of concern is electronic in origin (Λ-type). $q_{\text{el.}}$ was estimated by the perturbation theory relation

$$q_{\text{el.}} = -\frac{pB}{A}, \tag{VI.5}$$

and it is an order of magnitude smaller than q. The nuclear g-factor for ^{14}N was taken from ref. [18].

Table VI.4: Parameters from the analysis of the $1_0^1\,^2\Pi$ band of NCO ($\tilde{X}^2\Pi$). The units are cm^{-1} where appropriate.

Parameter	Value	Correlation[a]	Kawaguchi *et al.*[8]
ν_0	1921.36457(43)[b]	31.064	
$\omega_2^{(c)}$	534.063		
$\omega_3^{(c)}$	1260.22		
$\epsilon\omega_{2(000)}^{(c)}$	−76.7249		
$\alpha_{1,\epsilon\omega_2}^{(c)}$	1.29142		
$g_{K(000)}^{(c)}$	3.7672		
$\alpha_{1,g_K}^{(c)}$	−0.15525		
$A_{(000)}$	−96.0881(23)	50.250	−96.080[c,d]
$\alpha_{1,A}$	−1.38713(82)	28.750	
$\alpha_{2,A}^{(c)}$	0.3635		
$B_{(000)}$	0.389514206(12)	4.632	0.389514242(47)
$\alpha_{1,B}$	$-0.33457(28) \times 10^{-2}$	1.573	
$D_{(000)}$	$0.15140(19) \times 10^{-6}$	20.567	$0.15251(73) \times 10^{-6}$
$H_{(000)}$	$0.101(29) \times 10^{-11}$	15.290	
$\gamma_{(000)}$	$-0.10711(94) \times 10^{-2}$	50.804	$-0.10724(52) \times 10^{-2}$
$(p+2q)_{(000)}$	$0.253612(21) \times 10^{-2}$	1.447	$0.25357(29) \times 10^{-2}$
$q_{(000)}$	$-0.4938(18) \times 10^{-4}$	1.320	$-0.4940(61) \times 10^{-4}$
$(p_D+2q_D)_{(000)}^{(c)}$	-0.18948×10^{-8}		
$q_{D(000)}^{(c)}$	0.7677×10^{-10}		
$a_{(000)}$	$0.208019(69) \times 10^{-2}$	3.406	$0.20781(11) \times 10^{-2}$ [d]
$b_{(000)}$	$0.10206(75) \times 10^{-2}$	1.560	$0.10407(18) \times 10^{-2}$
$(b+c)_{(000)}$	$-0.5661(14) \times 10^{-3}$	3.645	$-0.5671(36) \times 10^{-3}$
$d_{(000)}$	$0.295154(42) \times 10^{-2}$	1.180	$0.295184(83) \times 10^{-2}$
$eQq_{0(000)}$	$-0.7374(41) \times 10^{-4}$	1.070	$-0.7288(76) \times 10^{-4}$
$eQq_{2(000)}$	$-0.539(17) \times 10^{-3}$	1.025	$0.5404(32) \times 10^{-3}$

Table VI.4 continued...

Parameter	Value	Correlation[a]
$g_{S_{(000)}}^{(c)}$	2.002099	
$g_{L_{(000)}}^{(0)\,(c)}$	0.999890	
$\Delta g_{L_{(000)}}^{(1)}$	$-0.6767(36) \times 10^{-2}$	1.048
$g_{r\,(000)}$	$-0.531(76) \times 10^{-4}$	1.278
$g_{l\,(000)}^{(c)}$	0.1375×10^{-2}	
$g_{r\ (000)}^{e\prime\,(c)}$	0.1371075×10^{-4}	
$(g_l' - g_r^{e\prime})_{(000)}^{(c)}$	0.380893×10^{-2}	
$g_{N_{(000)}}^{(c)}$	0.4037607	

[a] The correlation parameter $\kappa_i = (\chi^{-1})_{ii}$, where χ is the matrix of correlation coefficients.

[b] The numbers in parentheses are one standard deviation of the parameter in units of the least significant decimal place.

[c] Parameter constrained to this value (see text).

[d] Converted to 'true' value using Eq.(IV.2).

Table VI.5: Mid-infrared LMR observations of the $1_0^1\,^2\Pi_{\frac{3}{2}}$ sub-band of NCO $(\tilde{X})^2\Pi$ included in the fit of the $1_0^1\,^2\Pi$ band. Data from this study and ref. [1].

Transition	$M'_J \leftarrow M''_J$	M_I[a]	$\tilde{\nu}_L$[b] [cm^{-1}]	$B_{obs.}$ [T]	$\frac{\partial\nu}{\partial B}$[c] [MHzG^{-1}]	$(o-c)$[d,e] [10^{-5}cm^{-1}]
R($\frac{5}{2}$)	$\frac{5}{2} \leftarrow \frac{5}{2}$	1	1923.1535	0.7621[g]	−0.391	− 26
R($\frac{5}{2}$)	$\frac{5}{2} \leftarrow \frac{5}{2}$	0	1923.1535	0.7639[g]	−0.391	− 28
R($\frac{5}{2}$)	$\frac{5}{2} \leftarrow \frac{5}{2}$	−1	1923.1535	0.7660[g]	−0.391	− 26
R($\frac{5}{2}$)	$\frac{3}{2} \leftarrow \frac{3}{2}$	1	1923.1535	1.1807[g]	−0.306	− 14
R($\frac{5}{2}$)	$\frac{3}{2} \leftarrow \frac{3}{2}$	−1	1923.1535	1.1844[g]	−0.306	− 16
R($\frac{5}{2}$)	$\frac{3}{2} \leftarrow \frac{5}{2}$		1923.1535	0.47537	−0.692	57
R($\frac{5}{2}$)	$\frac{1}{2} \leftarrow \frac{3}{2}$		1923.1535	0.62539	−0.552	32
R($\frac{5}{2}$)	$-\frac{1}{2} \leftarrow \frac{1}{2}$		1923.1535	0.94241	−0.379	52
R($\frac{3}{2}$)	$-\frac{1}{2} \leftarrow -\frac{3}{2}$		1923.1535	1.19700	1.687	115
R($\frac{5}{2}$)	$\frac{3}{2} \leftarrow \frac{5}{2}$		1922.9829	1.36822	−0.440	− 11
R($\frac{5}{2}$)	$\frac{1}{2} \leftarrow \frac{3}{2}$		1922.9829	1.54517	−0.579	50
R($\frac{3}{2}$)	$-\frac{1}{2} \leftarrow -\frac{3}{2}$		1922.9829	0.89083	1.649	103
R($\frac{3}{2}$)	$\frac{1}{2} \leftarrow -\frac{1}{2}$		1922.9829	1.27942	1.342	− 13
R($\frac{3}{2}$)	$-\frac{1}{2} \leftarrow -\frac{3}{2}$		1922.5565	0.07500	1.464	104
R($\frac{3}{2}$)	$\frac{1}{2} \leftarrow -\frac{1}{2}$		1922.5565	0.13300	0.867	28
R($\frac{3}{2}$)	$-\frac{5}{2} \leftarrow -\frac{3}{2}$		1922.5565	0.23430	0.483	27
R($\frac{3}{2}$)	$\frac{3}{2} \leftarrow \frac{1}{2}$		1922.5565	0.43040	0.353	24
P($\frac{5}{2}$)	$\frac{3}{2} \leftarrow \frac{3}{2}$	1	1918.9787	1.4115[g]	0.315	− 31
P($\frac{5}{2}$)	$\frac{3}{2} \leftarrow \frac{3}{2}$	−1	1918.9787	1.4144[g]	0.316	− 21
P($\frac{5}{2}$)	$\frac{3}{2} \leftarrow \frac{1}{2}$	1	1918.9787	0.7407[g]	1.147	− 26
P($\frac{5}{2}$)	$\frac{3}{2} \leftarrow \frac{1}{2}$	0	1918.9787	0.7426[g]	1.147	− 26
P($\frac{5}{2}$)	$\frac{3}{2} \leftarrow \frac{1}{2}$	−1	1918.9787	0.7444[g]	1.147	− 21
P($\frac{5}{2}$)	$\frac{3}{2} \leftarrow \frac{1}{2}$		1918.6774	0.04110	1.427	147
P($\frac{5}{2}$)	$\frac{1}{2} \leftarrow -\frac{1}{2}$		1918.6774	0.07810	0.769	63
P($\frac{5}{2}$)	$\frac{3}{2} \leftarrow \frac{5}{2}$		1918.6774	0.13390	0.452	65
P($\frac{5}{2}$)	$-\frac{3}{2} \leftarrow -\frac{1}{2}$		1918.5802	0.15586	−1.488	8
P($\frac{5}{2}$)	$-\frac{1}{2} \leftarrow \frac{1}{2}$		1918.5802	0.26457	−0.928	45

Table VI.5 continued:

Transition	$M'_J \leftarrow M''_J$	M_I[a]	$\tilde{\nu}_{\mathrm{L}}$[b] $[\mathrm{cm}^{-1}]$	$B_{\mathrm{obs.}}$ [T]	$\frac{\partial\nu}{\partial B}$[c] $[\mathrm{MHzG}^{-1}]$	$(o-c)$[d,e] $[10^{-5}\mathrm{cm}^{-1}]$
$\mathrm{P}(\frac{5}{2})$	$-\frac{3}{2} \leftarrow -\frac{5}{2}$		1918.5802	0.47659	−0.497	65
$\mathrm{P}(\frac{5}{2})$	$\frac{1}{2} \leftarrow \frac{3}{2}$		1918.5802	0.70980	−0.491	53
$\mathrm{P}(\frac{7}{2})$	$-\frac{5}{2} \leftarrow -\frac{5}{2}$	1	1917.8610	0.0163[g]	−0.534	27
$\mathrm{P}(\frac{7}{2})$	$-\frac{5}{2} \leftarrow -\frac{5}{2}$	0	1917.8610	0.0180[g]	−0.529	28
$\mathrm{P}(\frac{7}{2})$	$-\frac{5}{2} \leftarrow -\frac{5}{2}$	−1	1917.8610	0.0198[g]	−0.526	28
$\mathrm{P}(\frac{7}{2})$	$-\frac{3}{2} \leftarrow -\frac{3}{2}$	1	1917.8610	0.0294[g]	−0.320	40
$\mathrm{P}(\frac{7}{2})$	$-\frac{3}{2} \leftarrow -\frac{3}{2}$	−1	1917.8610	0.0326[g]	−0.318	34
$\mathrm{P}(\frac{7}{2})$	$-\frac{1}{2} \leftarrow -\frac{1}{2}$		1917.8610	0.0842[g]	−0.108	7
$\mathrm{P}(\frac{7}{2})$	$-\frac{5}{2} \leftarrow -\frac{7}{2}$		1917.8610	0.0347[g]	−0.255	1
$\mathrm{P}(\frac{7}{2})$	$\frac{1}{2} \leftarrow \frac{3}{2}$		1917.8610	0.0536[g]	−0.170	11

[a] $\Delta M_I = 0$.

[b] $^{12}\mathrm{C}^{16}\mathrm{O}$ or $^{12}\mathrm{C}^{18}\mathrm{O}$ laser wave number.

[c] Tuning rate at resonance.

[d] Residuals of the fit.

[e] Uncertainties: Lamb-dips $2 \times 10^{-4}\,\mathrm{cm}^{-1}$, Doppler limited resonances $6.7 \times 10^{-4}\,\mathrm{cm}^{-1}$.

[g] Measurement made on a Lamb (sub-Doppler saturation) dip.

VI.2 The $1_0^1 2_1^1\,{}^2\Delta$ Band

VI.2.1 Observations

A previous LMR study by Barnes *et al.*[1] observed the Q(5/2) line in the $P = 5/2$ sub-band, using a $^{12}C^{18}O$ intracavity LMR system in Ottawa.

In the present study a significant number of new vibration-rotation observations have been made in this band; they are summarised in Table VI.6. As expected the observations are restricted to the $P = 5/2$ sub-band. Some of the resonances recorded in π polarisation were saturated, resolving the ^{14}N hyperfine structure. The best signal-to-noise ratio was for the R(5/2) line in π polarisation; about 45:1 with a 300 ms time constant.

Table VI.6: Summary of LMR observations of the $1_0^1 2_1^1\,{}^2\Delta_{\frac{5}{2}}$ sub-band

Transition	Laser Line	$\tilde{\nu}_L$ [cm^{-1}]
R(5/2)	$P(13)_{8-7}$	1909.8775
P(7/2)	$P(8)_{9-8}$	1903.8822

Initial predictions and assignments were made using the program described in §IV.5.2. The approximate parameters for these calculations were constrained to the values for the $1_0^1\,{}^2\Pi$ band, except for the rotational, spin-orbit and Zeeman parameters, which were constrained to the values determined in ref. [1].

The first assignment was made on the $P(13)_{8-7}$ laser line, to the σ polarisation spectrum shown in Fig.VI.3. At least two transitions in other bands overlap the R(5/2) spectrum, leading to a complicated pattern in which the simple structure of the R(5/2) line is not easily recognised. The assignment was made with the aid of the simulation shown in Fig.VI.4. As can be seen in Figs.VI.3 and VI.4, the two lower field resonances are heavily convoluted and their measurements were not included in the fit. The same laser line was also studied in π polarisation; the spectrum is shown in Fig.VI.5, where the three components of the R(5/2) transition stand out clearly. In the limit of Hund's case (a) behaviour, the intensity of the π polarisation components is expected to be proportional to $[(J+1)^2 - M_J^2]$, *i.e.* a ratio of 3:5:6 for $M_J = -2.5, -1.5$ and -0.5, respectively. In fact when the area under the peaks is considered, the $M_J = -2.5$ and

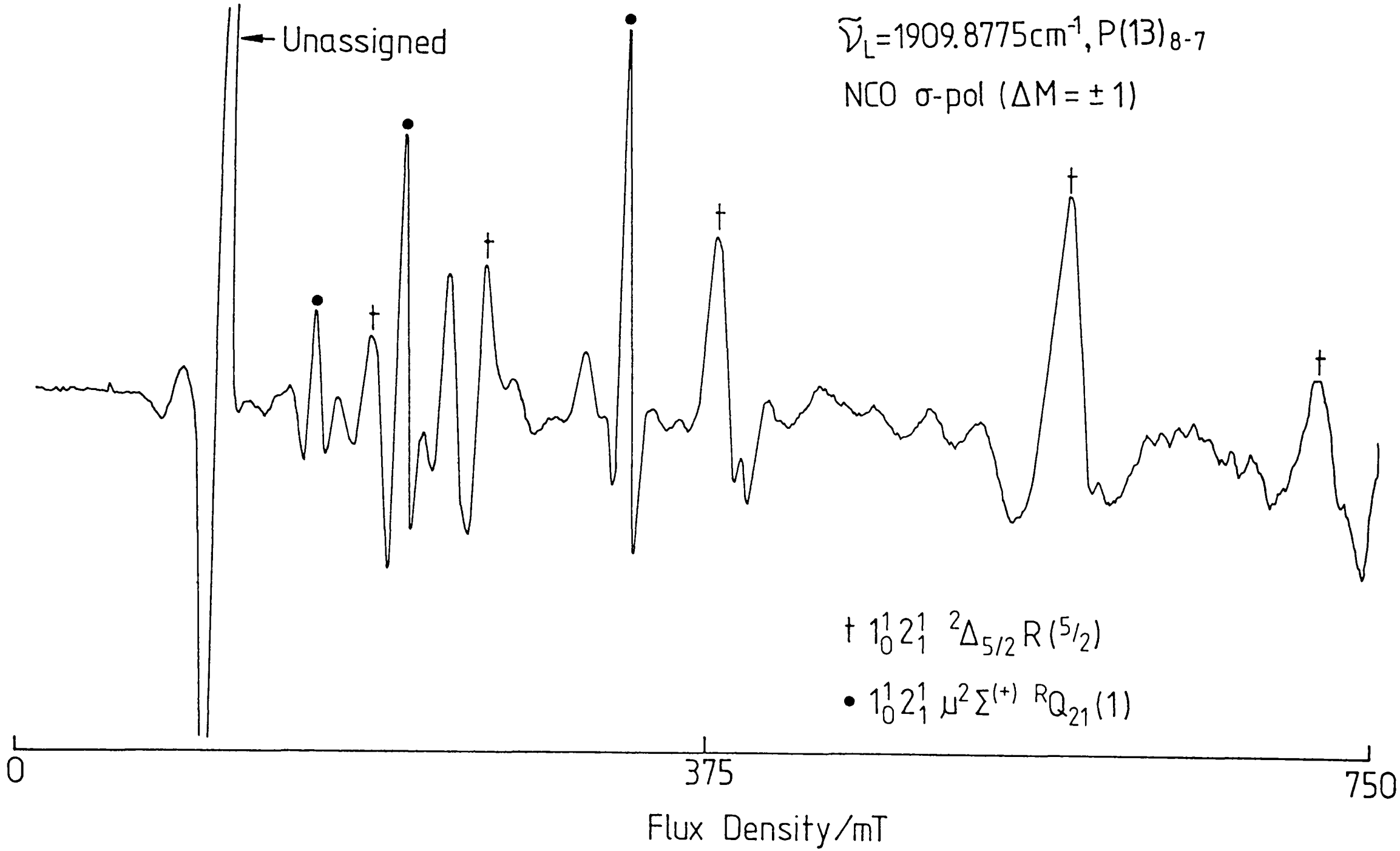

Figure VI.3: The spectrum recorded on the $P(13)_{8-7}$ laser line in σ polarisation. A survey scan is shown, recorded with a time constant of 300 ms at a scan rate of 100 mTmin^{-1}. The assignments are indicated; note the curious line-shape of the unassigned feature at low field.

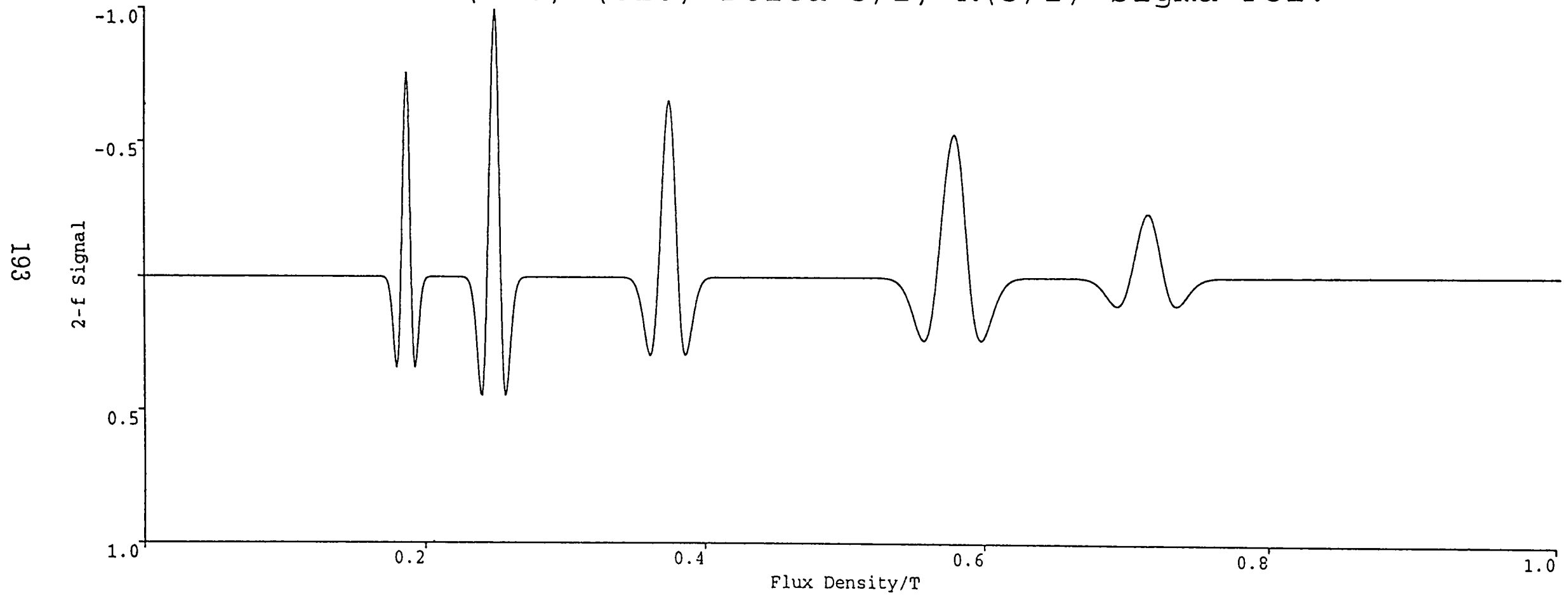

Figure VI.4: A simulation of the $1_0^1 2_1^1 {}^2\Delta_{\frac{5}{2}}$ R(5/2) spectrum recorded on the $P(13)_{8-7}$ laser line in σ polarisation.

$M_J = -1.5$ resonances are similar in intensity and the $M_J = -0.5$ resonance is weaker by a factor of about 2. This is explained by saturation effects, which become increasingly important as the transitions become slower tuning; the highest field component has a Lamb-dip on the top. The relative intensities also depend upon the detection system, which has a poorer response to broader resonances, and also upon non-linear Zeeman effects, which mix in the characteristics of other rotational levels as the flux density increases.

A Zeeman tuning diagram for the R(5/2) transition in σ polarisation is shown in Fig.VI.6. This tuning diagram extends to a higher flux density than the one in Fig.VI.2 and the higher order (*i.e.* non-linear) Zeeman effects are clearly evident. The Zeeman terms off-diagonal in J impart a quadratic dependence of the tuning rate upon the flux density and M_J values of the transition. In NCO, the rotational levels are separated by $\sim 0.8\,\mathrm{cm}^{-1}$; this is comparable to the Zeeman energy, so these interactions are quite significant. The first-order estimates of the tuning rates are no longer accurate in such cases. This effect has some useful consequences; in the limit of a linear tuning rate, the laser line could lie above or below the zero field transition frequency by an equal amount. Both situations would give the same LMR spectrum, and without being able to determine the sign of the tuning rate it would be impossible to resolve this ambiguity. The effect of the higher order Zeeman terms is to make these two situations distinct, so that only one position of the laser line is consistent with the observed spectrum.

Resonances due to the P(7/2) and P(9/2) transitions were detected on the $P(8)_{9-8}$ laser line. The signal-to-noise ratio of these resonances was much lower than for the R(5/2) line, due to the logarithmic increase in baseline noise above 1 T. In the first-order tuning rate approximation, the g_J factor exhibits a $1/J(J+1)$ dependence. Therefore, the P(7/2) $M_J = -5/2 \leftarrow -3/2$ and P(9/2) $M_J = 5/2 \leftarrow 3/2$ resonances are expected to have a field-equivalent Doppler width ratio of 0.64:1. The measured ratio is 0.60:1, in quite good agreement.

VI.2.2 Searches for Other $1_0^1 2_1^1\,{}^2\Delta$ Band Resonances

Predictions of other resonances in both the $P = 5/2$ and $P = 3/2$ sub-bands, were made. One close coincidence was a possible candidate for an unassigned transition on the $P(17)_{7-6}$ laser line. The R(31/2) transition of the $P = 5/2$ sub-band was predicted

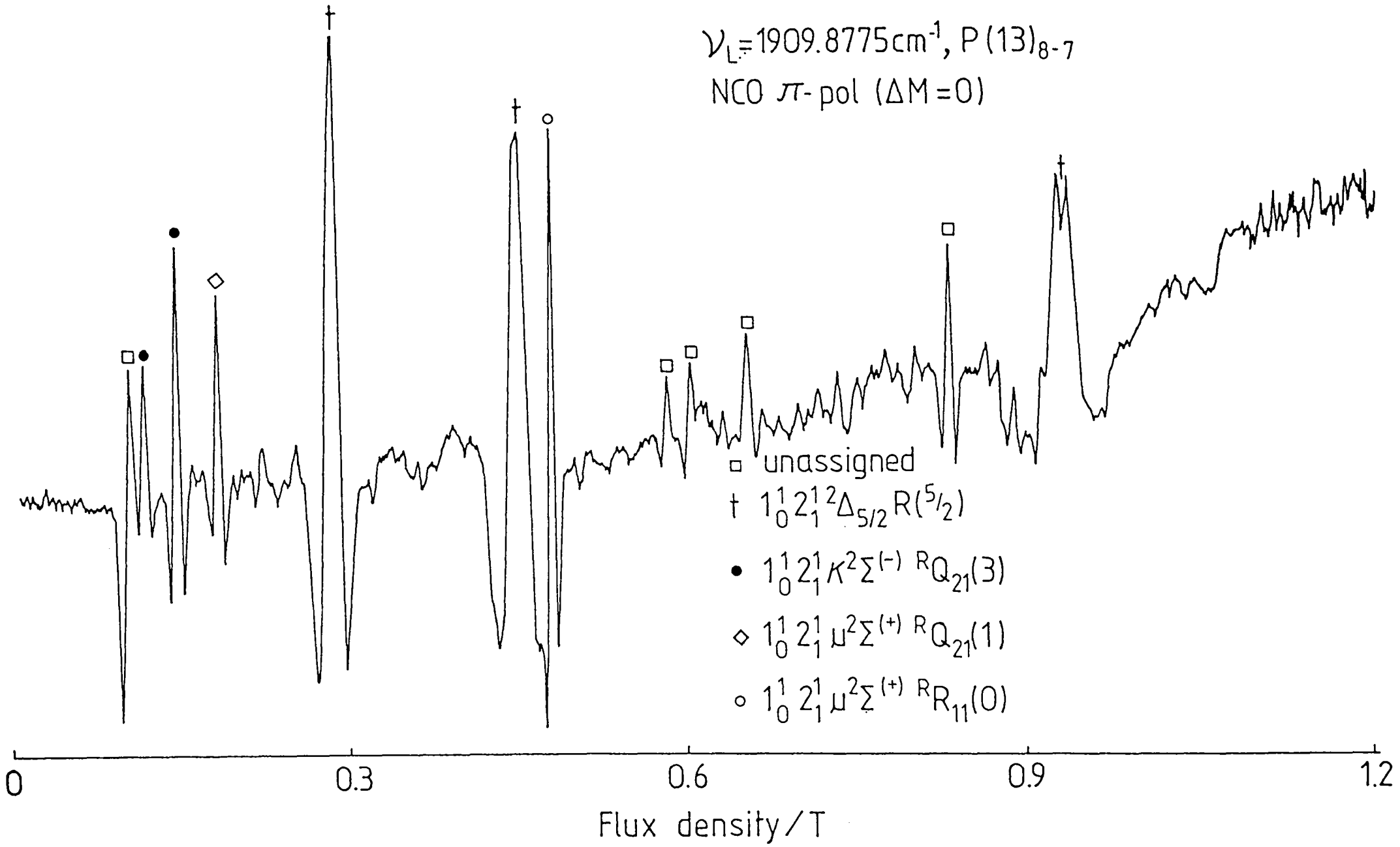

Figure VI.5: The spectrum recorded on the $P(13)_{8-7}$ laser line in π polarisation.

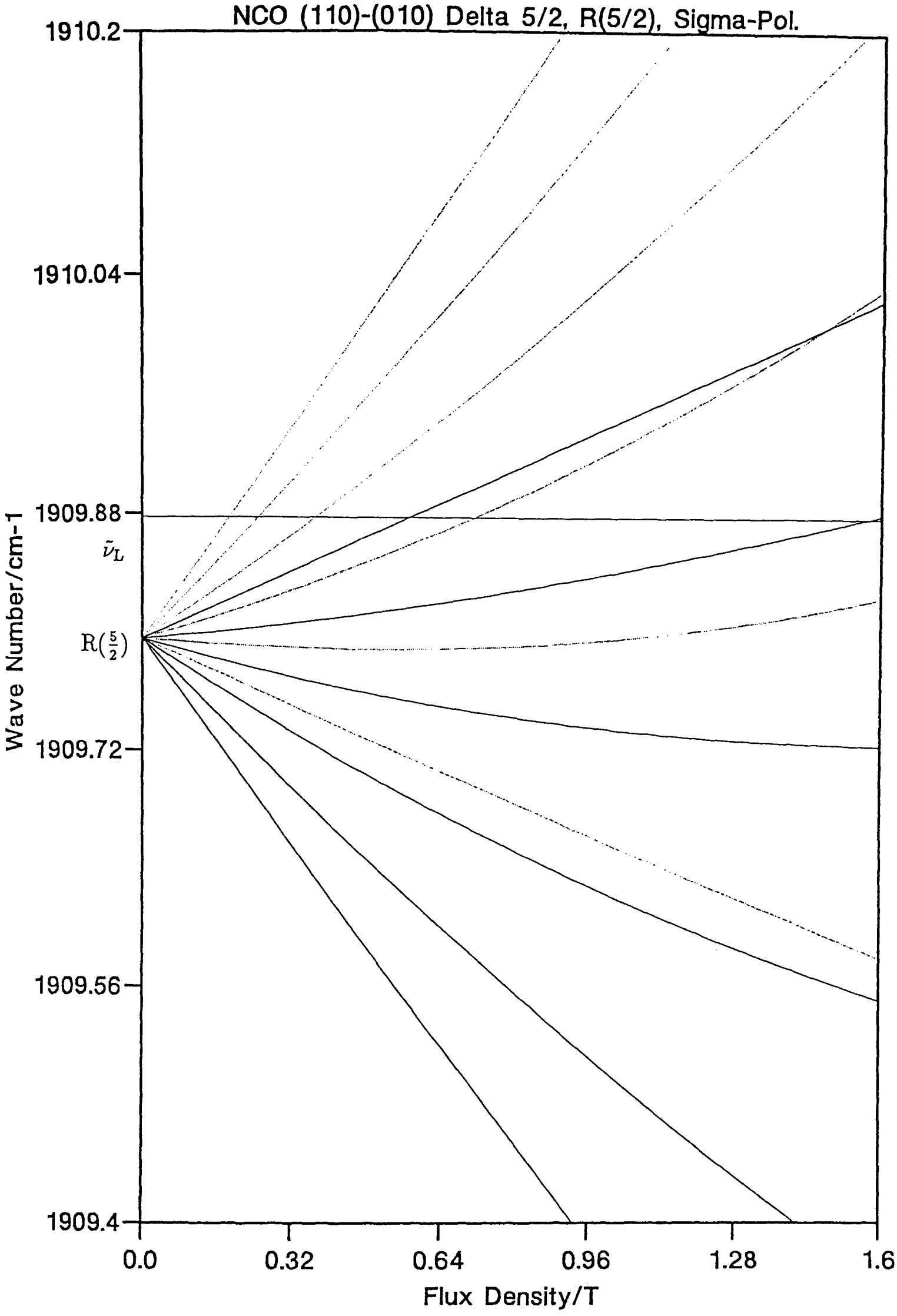

Figure VI.6: A Zeeman tuning diagram of the $1_0^1 2_1^1\,{}^2\Delta_{\frac{5}{2}}$ R(5/2) transition in σ polarisation. The solid and dotted lines indicate transitions for which $\Delta M_J = +1$ and $\Delta M_J = -1$, respectively.

to be resonant on this line, starting at about 1.25 T; the observed spectrum commences at about 700 mT. Extensive simulations in which a 'false' laser line was moved to bring the transition into resonance at different fields, showed the R(31/2) transition to be inconsistent with the observed spectrum. This spectrum was later assigned to the $1_0^1 2_1^1\,{}^2\Sigma$ band, as described in Chapter VII.

VI.2.3 Final Analysis

Data set

The data set for the final analysis consisted of the following:

1. The LMR observations from this study and from the study of Barnes *et al.*[1]. Doppler limited resonances were assigned an uncertainty of $6.67 \times 10^{-4}\,\mathrm{cm}^{-1}$ and Lamb-dips were assigned an uncertainty of $2 \times 10^{-4}\,\mathrm{cm}^{-1}$.

2. Optical combination differences taken from Bolman *et al.*[14], to define the spin-orbit splitting in the $(010)\,{}^2\Delta$ level. A representative series was chosen from the $01^10\,{}^2\Pi \leftarrow 01^20^2\,{}^2\Delta$ band of the $\tilde{\mathrm{A}} \leftarrow \tilde{\mathrm{X}}$ transition. The differences were calculated from

$$ {}^{\mathrm{R}}\mathrm{R}_{11}(J,\pm) - {}^{\mathrm{Q}}\mathrm{R}_{12}(J,\pm) $$

and

$$ {}^{\mathrm{R}}\mathrm{Q}_{21}(J,\pm) - {}^{\mathrm{Q}}\mathrm{Q}_{22}(J,\pm)\,. $$

The parity labels refer to the l-type doubling in the $\tilde{\mathrm{A}}$ state. Each datum was assigned an uncertainty of $10^{-2}\,\mathrm{cm}^{-1}$.

3. The microwave observations of Kawaguchi *et al.*[8], giving information about $(010)\,{}^2\Delta_{\frac{5}{2}}$ and $(010)\,{}^2\Delta_{\frac{3}{2}}$. The uncertainties are detailed in ref. [8].

4. The EPR observations of Carrington *et al.*, covering the $J = 5/2\,(010)\,{}^2\Delta_{\frac{5}{2}}$ level. Each datum was assigned an uncertainty of 300 kHz.

No K-type doubling was observed in any of these studies and so all such parameters were constrained to zero.

Details of the fit and the parameters

A basis set truncated at $\Delta J = \pm 4$ and $\Delta v_2 = \pm 4$ was used for the final fit. 11 parameters were determined and 14 were constrained; they are detailed in Table VI.7. The LMR data section of the fit is given in Table VI.8; the remaining data sets are given in Appendix G.

The fit contained 115 weighted data points and 21 zero-weighted ones. The standard deviation relative to the experimental uncertainties was $\sigma_{\text{rel.}} = 1.10$, see Eq.(IV.67), very close to the optimum value of 1.0. This suggests the uncertainties have been assessed well and the model describes the data very well. The standard deviation of the LMR data section was 9 MHz.

The band origin

A choice was made to constrain the band origin ν_0 to the value determined from the analysis of the $1_0^1 2_1^1\,{}^2\Sigma$ bands described in Chapter VII. Both bands involve the same vibrational levels; in the complete harmonic Renner-Teller model developed in Chapters III and IV, they have the same vibrational band origin. Furthermore, there is no contribution from the g_K term to the term values of the $^2\Sigma$ vibronic states (consider the matrices tabulated in §III.9.5). The value of α_{1,g_K} was not known *a priori*, therefore the band origin determined for the $1_0^1 2_1^1\,{}^2\Delta$ band should differ from that for the $1_0^1 2_1^1\,{}^2\Sigma$ bands by $2\alpha_{1,g_K}$. Therefore, the $1_0^1 2_1^1\,{}^2\Delta$ band origin was constrained to the value determined for the $1_0^1 2_1^1\,{}^2\Sigma$ bands and α_{1,g_K} was determined instead.

$A_{(000)}$ was constrained to the value for the $1_0^1\,{}^2\Pi$ band and $\alpha_{2,A}$ was determined. The Zeeman parameter g_l was calculated from Curl's relationship, Eq.(III.103). All other constrained parameters were held at the values used in the analysis of the $1_0^1\,{}^2\Pi$ band.

VI.3 The $1_0^1 2_2^2\,{}^2\Phi$ Band

The first observation of vibration-rotation transitions in this band is reported here. Following the success with the $K = 1$ and $K = 2$ unique states, predictions were made to see if any other spectra had been observed in the $1_0^1 2_{v_2}^{v_2}$ sequence of unique state bands. These bands are recognisable by virtue of their Hund's case (a) Zeeman effect behaviour,

Table VI.7: Parameters from the analysis of the $1_0^1 2_1^1\ ^2\Delta$ band of NCO ($\tilde{X}^2\Pi$). Parameters are quoted in cm^{-1} where applicable.

Parameter	Value	Correlation[a]	Kawaguci*et al.* [8]
$\nu_0^{(b)}$	1907.84852		
$\omega_{2(b)}$	534.063		
$\omega_3^{(b)}$	1260.22		
$\epsilon\omega_{2(010)}^{(b)}$	-76.7249		
$\alpha_{1,\epsilon\omega_2}^{(b)}$	1.29142		
$g_{K(010)}^{(b)}$	3.7672		
α_{1,g_K}	$-0.15525(29)$[c]	59.475	
$A_{(000)}$	-96.0881[c]		-96.080[b,d]
$\alpha_{1,A}^{(b)}$	-1.38713		
$\alpha_{2,A}^{(b)}$	0.3635(21)	16.420	
$B_{(010)}$	0.390547110(34)	15.429	0.390546224(74)
$\alpha_{1,B}$	$-0.3318(42) \times 10^{-2}$	59.473	
$D_{(010)}$	$0.15757(56) \times 10^{-6}$	13.505	$0.1588(12) \times 10^{-6}$
$H_{(010)}^{(b)}$	0.101×10^{-11}		
$\gamma_{(010)}$	$-0.26415(88) \times 10^{-2}$	17.213 $-0.25634(62) \times 10^{-2}$	
$a_{(010)}$	$0.205392(67) \times 10^{-2}$	1.665	$0.20522(14) \times 10^{-2}$ [d]
$b_{(010)}$	$0.1020(17) \times 10^{-2}$	1.185	$0.10441(42) \times 10^{-2}$
$(b+c)_{(010)}$	$-0.5296(14) \times 10^{-3}$	1.908	$-0.5170(85) \times 10^{-3}$
$eQq_{0(010)}$	$-0.750(11) \times 10^{-4}$	1.388	$-0.744(26) \times 10^{-4}$
$g_{S(010)}^{(b)}$	2.002099		
$g_{L,(010)}^{(0)\ (b)}$	0.999890		
$\Delta g_{L(010)}^{(1)}$	$-0.67765(94) \times 10^{-2}$	1.000	
$g_{r(010)}^{(b)}$	-0.531×10^{-4}		
$g_{l(010)}^{(b)}$	0.338180×10^{-2}		
$g_{N(010)}^{(b)}$	0.4037607		

[a] The correlation parameter $\kappa_i = (\chi^{-1})_{ii}$, where χ is the matrix of correlation coefficients.

[b] Parameter constrained to this value (see text).

[c] The numbers in parentheses give one standard deviation of the parameter in units of the least significant decimal place.

[d] Converted to the 'true' value using Eq.(IV.2).

Table VI.8: Mid-infrared LMR observations of the $1_0^1 2_1^1\,{}^2\Delta_{\frac{5}{2}}$ sub-band of NCO $(\tilde{X})^2\Pi$ included in the fit of the $1_0^1 2_1^1\,{}^2\Delta$ band. Data from this study and ref. [1].

Transition	$M'_J \leftarrow M''_J$	$M_I{}^{(a)}$	$\tilde{\nu}_L{}^{(b)}$ [cm^{-1}]	$B_{obs.}$ [T]	$\frac{\partial\nu}{\partial B}{}^{(c)}$ [MHzG^{-1}]	$(o-c)^{(d,e)}$ [10^{-5}cm^{-1}]
R($\frac{5}{2}$)	$-\frac{5}{2} \leftarrow -\frac{5}{2}$	1	1909.8775	0.2774$^{(g)}$	0.884	18
R($\frac{5}{2}$)	$-\frac{5}{2} \leftarrow -\frac{5}{2}$	0	1909.8775	0.2797$^{(g)}$	0.883	8
R($\frac{5}{2}$)	$-\frac{5}{2} \leftarrow -\frac{5}{2}$	−1	1909.8775	0.2814$^{(g)}$	0.883	12
R($\frac{5}{2}$)	$-\frac{3}{2} \leftarrow -\frac{3}{2}$	1	1909.8775	0.4410$^{(g)}$	0.585	− 4
R($\frac{5}{2}$)	$-\frac{3}{2} \leftarrow -\frac{3}{2}$	0	1909.8775	0.4430$^{(g)}$	0.585	− 6
R($\frac{5}{2}$)	$-\frac{3}{2} \leftarrow -\frac{3}{2}$	−1	1909.8775	0.4450$^{(g)}$	0.585	− 8
R($\frac{5}{2}$)	$-\frac{7}{2} \leftarrow -\frac{5}{2}$		1909.8775	0.5727	0.428	49
R($\frac{5}{2}$)	$\frac{3}{2} \leftarrow \frac{1}{2}$		1909.8775	0.7133	0.419	− 5
R($\frac{5}{2}$)	$-\frac{1}{2} \leftarrow -\frac{1}{2}$	1	1909.8775	0.9250$^{(g)}$	0.352	−14
R($\frac{5}{2}$)	$-\frac{1}{2} \leftarrow -\frac{1}{2}$	−1	1909.8775	0.9285$^{(g)}$	0.352	−10
Q($\frac{5}{2}$)	$\frac{3}{2} \leftarrow \frac{5}{2}$		1906.8558	0.8636	−0.864	−73
Q($\frac{5}{2}$)	$\frac{1}{2} \leftarrow \frac{3}{2}$		1906.8558	0.8851	−0.822	−55
Q($\frac{5}{2}$)	$-\frac{1}{2} \leftarrow \frac{1}{2}$		1906.8558	0.9079	−0.785	5
Q($\frac{5}{2}$)	$-\frac{3}{2} \leftarrow -\frac{1}{2}$		1906.8558	0.9287	−0.752	20
Q($\frac{5}{2}$)	$-\frac{5}{2} \leftarrow -\frac{3}{2}$		1906.8558	0.9499	−0.723	51
P($\frac{7}{2}$)	$-\frac{5}{2} \leftarrow -\frac{3}{2}$		1903.8822	1.0912	−1.369	3
P($\frac{7}{2}$)	$-\frac{3}{2} \leftarrow -\frac{1}{2}$		1903.8822	1.3769	−1.154	49
P($\frac{9}{2}$)	$\frac{7}{2} \leftarrow \frac{5}{2}$		1903.8822	1.1823	0.720	5
P($\frac{9}{2}$)	$\frac{5}{2} \leftarrow \frac{3}{2}$		1903.8822	1.4489	0.605	−12

(a) $\Delta M_I = 0$.

(b) $^{12}C^{16}O$ or $^{12}C^{18}O$ laser wave number.

(c) Tuning rate at resonance.

(d) Residuals of the fit.

(e) Uncertainties: Lamb-dips 2×10^{-4} cm^{-1}, Doppler limited resonances 6.67×10^{-4} cm^{-1}.

(g) Measurement made on a Lamb (sub-Doppler saturation) dip.

and the Q(7/2) and Q(9/2) lines of the $1_0^1 2_2^2\,{}^2\Phi_{\frac{7}{2}}$ sub-band were identified.

The difference in the vibrational band origin of two successive members of the unique state sequence $1_0^1 2_{v_2}^{v_2}$ can be expressed by the equation

$$x_{12} = [G(1, v_2 + 1, 0) - G(0, v_2 + 1, 0)] - [G(1, v_2 + 1, 0) - G(0, v_2, 0)], \qquad \text{(VI.6)}$$

where x_{12} is the component of the vibrational anharmonicity tensor involving the ν_1 and ν_2 vibrations. Taking the difference of the $1_0^1\,{}^2\Pi$ and $1_0^1 2_1^1\,{}^2\Delta$ band origins gives $x_{12} = 13.516\,\mathrm{cm}^{-1}$. Therefore, the origin of the $1_0^1 2_2^2\,{}^2\Phi$ band is expected to lie this amount below the origin of the Δ band, at $1894.33\,\mathrm{cm}^{-1}$.

Based on this estimate, predictions were made using the program described in §IV.5.2, with effective Zeeman [7] and spin-orbit parameters [8]. The rotational parameters were taken from [8] and converted to the values for an $\mathbf{N}^2$ Hamiltonian. Other parameters were constrained to the values determined for the $1_0^1\,{}^2\Pi$ band.

The Q(7/2) transition was predicted to be resonant at about 300 mT on the $P(17)_{8-7}$ laser line. A simulation suggested that the M_J structure would not be resolved and so a single peak with a width of $10 - 15\,\mathrm{mT}$ should be observed. No features were observed which fitted this description. Simulations were then performed in which a 'false' laser line was moved in increments of $\sim 0.1\,\mathrm{cm}^{-1}$, shifting the resonant field of the transition. This produced a simulation corresponding to the feature observed from 1.0–1.2 T in the spectrum shown in Fig.VI.7; a simulation is shown in Fig.VI.8 for comparison. The pattern somewhat resembles a 'damped oscillation', the Zeeman components of the Q(7/2) line becoming weaker and more overlapped as the flux density increases. This appearance is a result of second-order Zeeman effects, which produce an unmistakable pattern. The agreement between the simulation and the observed spectrum is excellent. All the resonances were observed with Doppler-limited resolution.

Consider the Zeeman tuning diagram shown in Fig.VI.9. The ambiguity in the sign of the tuning rate of the Q(7/2) transition was resolved by noting that the Q(9/2) line is expected to be resonant at about 1.5 T if the resonances are negatively tuning. This was indeed observed, as can be seen in Figs.VI.7 and VI.8. The Q(9/2) line is distinctive because the second-order Zeeman effects produce a much smaller splitting of the M_J structure than for the Q(7/2) line; in the former the M_J structure is not resolved with

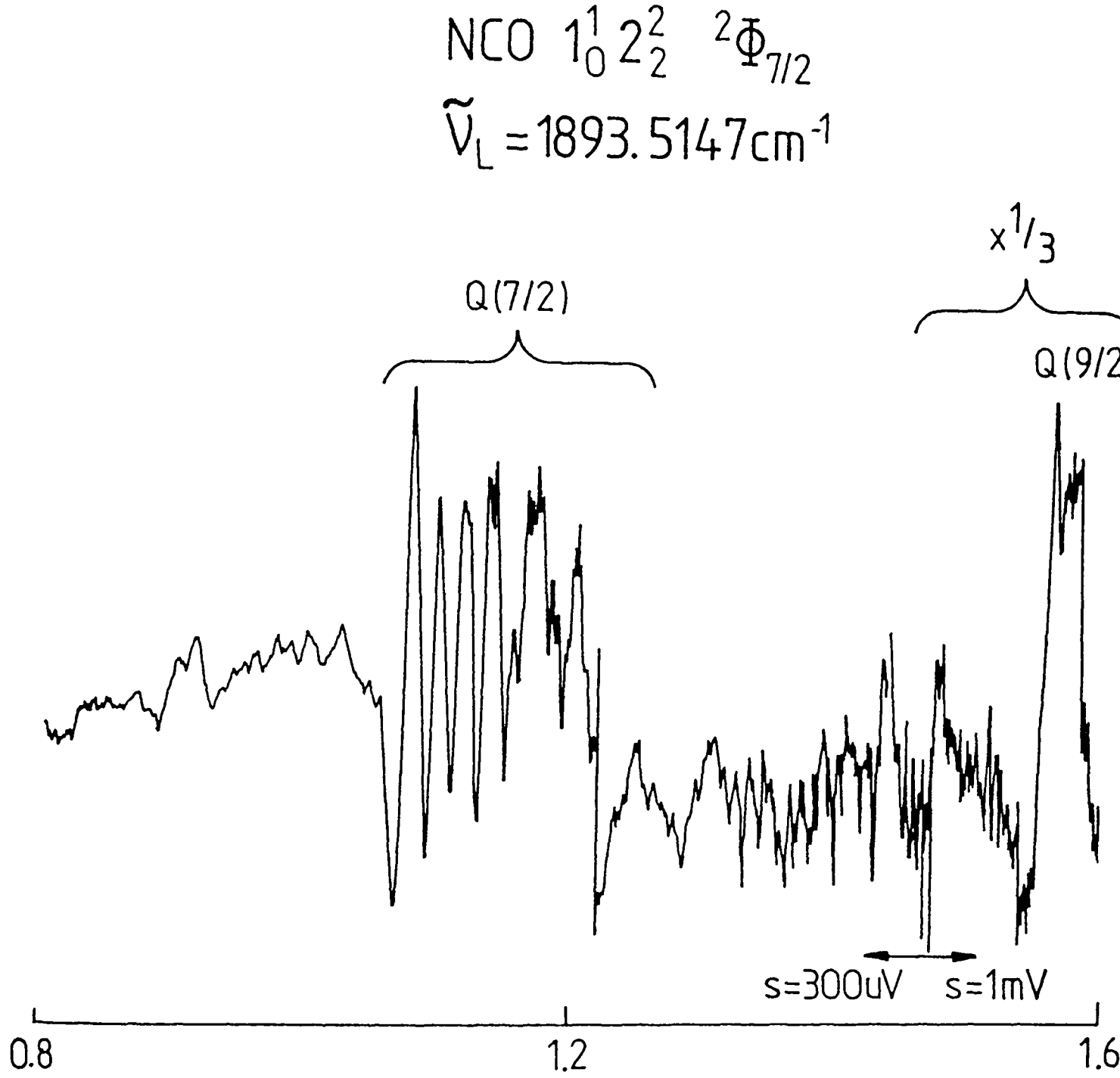

Figure VI.7: The $1_0^1 2_2^2\,^2\Phi_{\frac{7}{2}}$ Q(7/2) and Q(9/2) lines recorded on the $P(17)_{8-7}$ laser line in σ polarisation. Note the poor signal-to-noise ratio, a feature of the high flux densities, laser plasma conditions and the population of the (020) levels. A change of lock-in output sensitivity occurs at about 1.5 T.

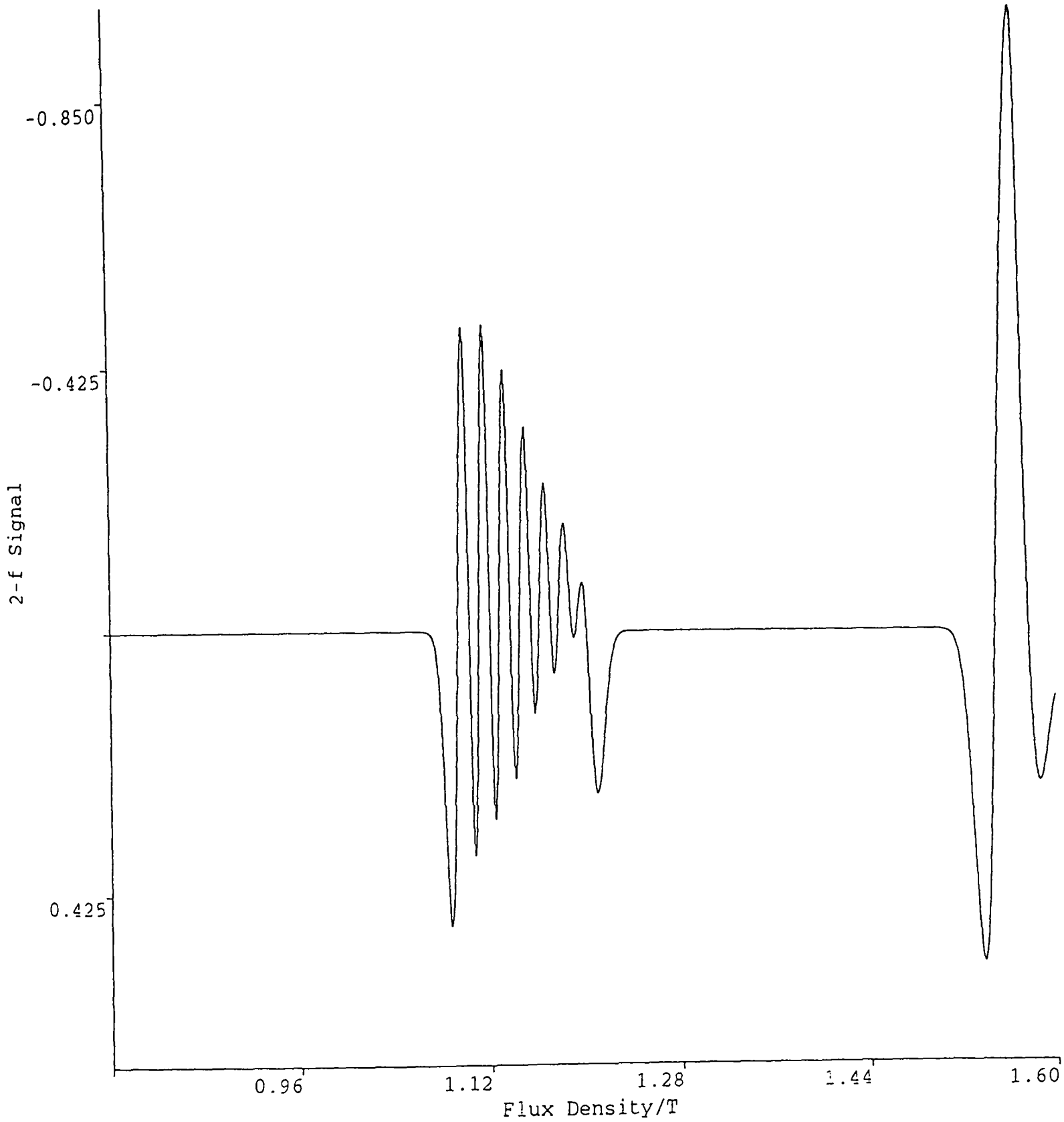

Figure VI.8: A simulation of the spectrum recorded on the $P(17)_{8-7}$ laser line in σ polarisation.

Doppler limited resolution. The Q(11/2) line should be resonant above 1.6 T, just beyond the range of the electromagnet. A π polarisation LMR spectrum is not expected for Q lines; Eq.(VI.1) shows that the first order tuning rate for such transitions is zero.

The best signal-to-noise ratio was 8:1, observed for the Q(9/2) line with a 300 ms time constant. The $P(17)_{7-6}$ laser line only shows gain under conditions which generate quite a high noise baseline. Therefore, measurements of the Q(7/2) line could only be made on the five lowest field Zeeman components, the remainder being lost in the noise.

Searches were made for predicted resonances due to the R(7/2), R(9/2) and P(11/2) transitions. None were detected due to the poor signal-to-noise ratio for this band, a symptom of the decrease in lower state population from (000) to (020). The Q lines show up clearly because they are fast tuning and their Zeeman components tend to be superimposed, giving a large signal in the LMR experiment. The components of the R and P lines are split well apart and are mostly slower tuning than the Q lines, hence the greater signal-to-noise ratio required to detect them. I have detailed the expected coincidences in Table VI.9; it would be useful to detect them in future studies in order to improve the determination of the rotational constant B_{120}.

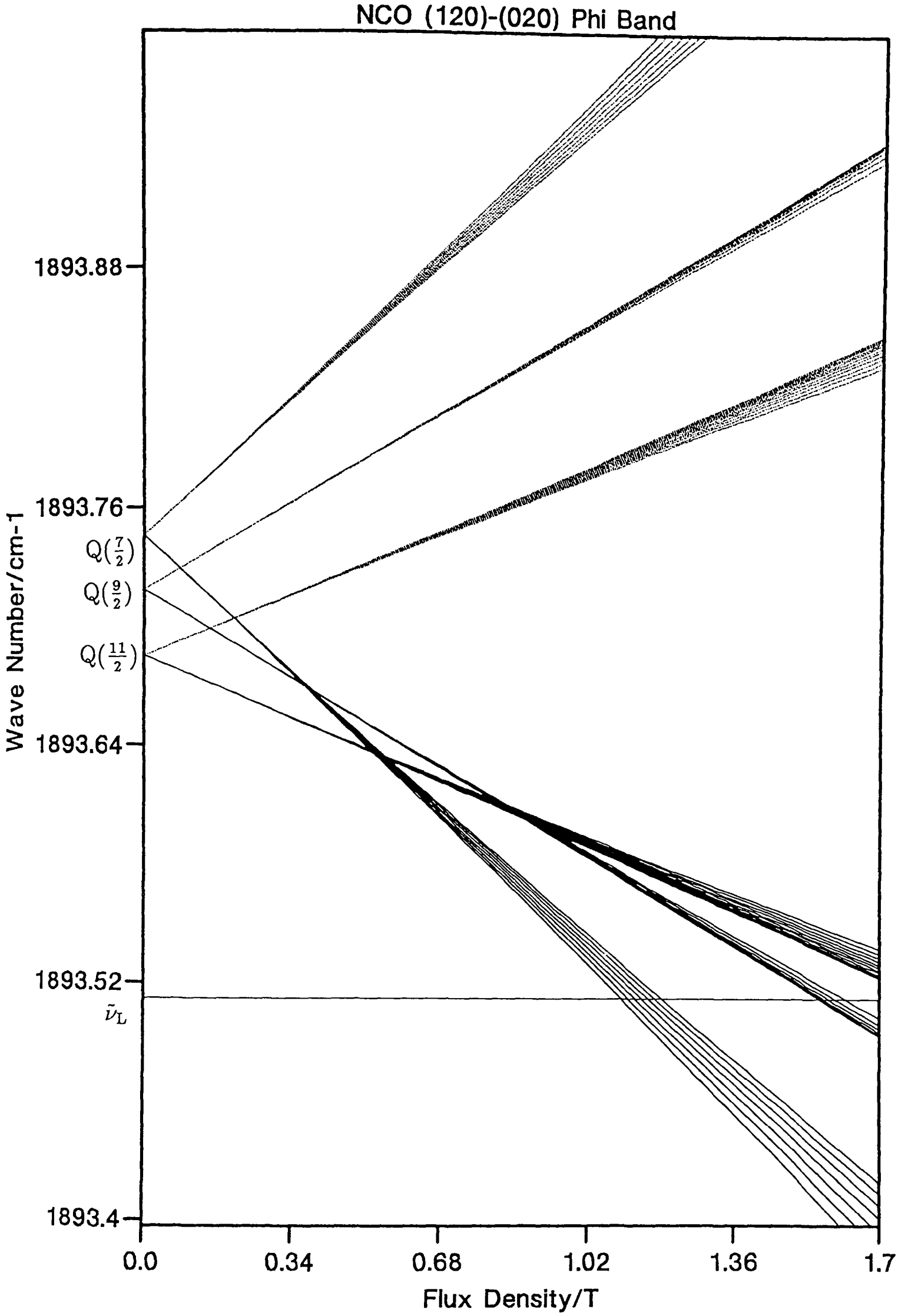

Figure VI.9: A Zeeman tuning diagram showing the first three Q lines in the $1_0^1 2_2^2\,{}^2\Phi_{\frac{7}{2}}$ sub-band, in σ polarisation.

Table VI.9: Predicted P and R line resonances in the $1_0^1 2_2^2\,{}^2\Phi_{\frac{7}{2}}$ sub-band of NCO ($\tilde{\mathrm{X}}$). Only the σ polarisation predictions are tabulated.

Transition	$M'_J \leftarrow M''_J$	$B_{\mathrm{pred.}}$ [T]	$(\frac{\partial\nu}{\partial B})^a$ [MHzG^{-1}]	Intensity^b
	$\mathrm{P}(16)_{8-7},\ \tilde{\nu}_{\mathrm{L}} = 1897.6545\,\mathrm{cm}^{-1}$			
$\mathrm{R}(\frac{9}{2})$	$\frac{7}{2} \leftarrow \frac{9}{2}$	1.2380	−0.755	0.58×10^{-2}
$\mathrm{R}(\frac{9}{2})$	$\frac{5}{2} \leftarrow \frac{7}{2}$	1.4612	−0.637	0.17×10^{-1}
$\mathrm{R}(\frac{7}{2})$	$-\frac{5}{2} \leftarrow -\frac{7}{2}$	1.0915	1.161	0.39×10^{-2}
$\mathrm{R}(\frac{7}{2})$	$-\frac{3}{2} \leftarrow -\frac{5}{2}$	1.3021	1.002	0.12×10^{-1}
	$\mathrm{P}(5)_{10-9},\ \tilde{\nu}_{\mathrm{L}} = 1889.4666\,\mathrm{cm}^{-1}$			
$\mathrm{P}(\frac{11}{2})$	$\frac{9}{2} \leftarrow \frac{7}{2}$	0.1284	0.802	0.50×10^{-2}
$\mathrm{P}(\frac{11}{2})$	$\frac{7}{2} \leftarrow \frac{5}{2}$	0.1505	0.684	0.15×10^{-1}
$\mathrm{P}(\frac{11}{2})$	$\frac{5}{2} \leftarrow \frac{3}{2}$	0.1819	0.565	0.30×10^{-1}
$\mathrm{P}(\frac{11}{2})$	$\frac{3}{2} \leftarrow \frac{1}{2}$	0.2299	0.446	0.50×10^{-1}
$\mathrm{P}(\frac{11}{2})$	$\frac{1}{2} \leftarrow -\frac{3}{2}$	0.3124	0.326	0.75×10^{-1}
$\mathrm{P}(\frac{11}{2})$	$\frac{9}{2} \leftarrow \frac{11}{2}$	0.4097	−0.251	0.28
$\mathrm{P}(\frac{11}{2})$	$-\frac{1}{2} \leftarrow -\frac{3}{2}$	0.4900	0.204	0.11
$\mathrm{P}(\frac{11}{2})$	$\frac{7}{2} \leftarrow \frac{9}{2}$	0.7911	−0.126	0.23
$\mathrm{P}(\frac{11}{2})$	$-\frac{3}{2} \leftarrow -\frac{5}{2}$	1.2177	0.070	0.14

[a] Predicted tuning rate at resonance.

[b] Predicted line strength factor.

VI.3.1 Analysis

Data set

The data set for the final analysis of the $1_0^1 2_2^2\,{}^2\Phi$ band comprised:

1. The LMR observations from this study, each assigned an uncertainty of $6.67 \times 10^{-4}\,\mathrm{cm}^{-1}$. For the Q(9/2) line, the Zeeman structure was not resolved. Therefore, the center of the line profile was assigned to the $M_J = -1/2 \leftarrow M_J = 1/2$ transition, since the resonances are negatively tuning.

2. The microwave observations of Kawaguchi *et al.*[8], who observed rotational transitions in both the $(020)\,{}^2\Phi_{\frac{7}{2}}$ and $(020)\,{}^2\Phi_{\frac{5}{2}}$ spin components. The experimental uncertainties are reported in their study.

3. The EPR observations of Carrington *et al.*[7], for the level $(020)\,{}^2\Phi_{\frac{7}{2}}$ $J = 7/2$. Each datum was assigned an uncertainty of 300 kHz.

Details of the fit and the parameters

In the final fit, a basis set with $\Delta J = \pm 4$ and $\Delta v_2 = \pm 4$ was used; 9 parameters were determined and 16 were constrained. The constrained parameters were taken from the $1_0^1\,{}^2\Pi$ band, except for g_l, which was again estimated using Curl's relationship, Eq.(III.103). The parameters determined are detailed in Table VI.10 and the LMR data section of the fit is given in Table VI.11. The remaining date sets are given in Appendix G.

As can be seen, the agreement between the estimated and calculated band origins is excellent, within $0.06\,\mathrm{cm}^{-1}$, see Eq.(VI.6). The spin-orbit coupling parameter was estimated by using the values of $A_{(000)}$ and $\alpha_{2,A}$ determined from the $1_0^1\,{}^2\Pi$ and $1_0^1 2_0^1\,{}^2\Delta$ fits. This yields a value of $\mathrm{A}_{020} = -96.0881\,\mathrm{cm}^{-1}$ as the 'true' (Renner-Teller free) spin-orbit coupling parameter.

Several possible parameter determinations were considered. The second order Zeeman splitting, and to some extent the separation of the Q(7/2) and Q(9/2) lines, depends upon $\Delta g_L^{(1)}$. The variation of $\alpha_{1,\Delta g_L^{(1)}}$ was tried to see if it improved the modelling of the Q(7/2) line in particular. This parameter did not have a significant effect; since it is an electronic parameter it is not expected to be significant if the upper and lower levels

Table VI.10: Parameters from the analysis of the $1_0^1 2_2^2\,{}^2\Phi$ band of NCO ($\tilde{X}^2\Pi$).

Parameter	Value [cm^{-1}]	Correlation[a]	Kawaguchi *et al.*[8]
ν_0	1894.3938(32)[b]	20.159	
$\omega_2^{(c)}$	534.063		
$\omega_3^{(c)}$	1260.22		
$\epsilon\omega_{2(020)}^{(c)}$	-76.7249		
$\alpha_{1,\epsilon\omega_2}^{(c)}$	1.29142		
$g_K^{(c)}$	3.7672		
$\alpha_{1,g_K}^{(c)}$	-0.15525		
$A_{(000)}^{(c)}$	-96.0881		$-96.080^{(c,d)}$
$\alpha_{1,A}^{(c)}$	-1.38713		
$\alpha_{2,A}^{(c)}$	0.3635		
$B_{(020)}$	0.39160400(17)	25.854	0.39160132(11)
$\alpha_{1,B}$	$-0.309(22) \times 10^{-2}$	20.158	
$D_{(020)}$	$0.1613(20) \times 10^{-6}$	25.173	$0.1604(14) \times 10^{-6}$
$H_{(020)}^{(c)}$	0.101×10^{-11}		
$\gamma_{(020)}$	$-0.47424(92) \times 10^{-2}$	1.331	$-0.44485(75) \times 10^{-2}$
$a_{(020)}$	$0.20266(68) \times 10^{-2}$	1.342	$0.20262(53) \times 10^{-2}$ [d]
$b_{(020)}^{(c)}$	0.10206×10^{-2}		$0.10407(18) \times 10^{-2}$
$(b+c)_{(020)}$	$-0.480(13) \times 10^{-3}$	1.314	$-0.4336(18) \times 10^{-3}$[c]
$eQq_{0(020)}$	$-0.761(79) \times 10^{-4}$	1.089	$-0.724(81) \times 10^{-4}$
$g_{S(020)}^{(c)}$	2.002099		
$g_{L(020)}^{(0)\,(c)}$	0.999890		
$\Delta g_{L(020)}^{(1)}$	$-0.6552(13) \times 10^{-2}$	1.000	
$g_{r(020)}^{(c)}$	-0.531×10^{-4}		
$g_{l(020)}^{(c)}$	0.60551×10^{-2}		
$g_{N(020)}^{(c)}$	0.4037607		

[a] The correlation parameter $\kappa_i = (\chi^{-1})_{ii}$, where χ is the matrix of correlation coefficients.

[b] The numbers in parentheses give one standard deviation of the parameter in units of the least significant figure.

[c] Parameter constrained to this value (see text).

[d] Converted to the 'true' value using Eq.(IV.2).

Table VI.11: LMR observations[a] of the $1_0^1 2_1^1\,{}^2\Phi_{\frac{7}{2}}$ sub-band of NCO $(\tilde{X})^2\Pi$ included in the least-squares fit of the $1_0^1 2_2^2\,{}^2\Phi$ band.

Transition	$M'_J \leftarrow M''_J$	$B_{\text{obs.}}$ [T]	$\frac{\partial\nu}{\partial B}$[b] [MHzG^{-1}]	$(o-c)^{(c,d)}$ [10^{-4}cm^{-1}]
$Q(\frac{7}{2})$	$\frac{5}{2} \leftarrow \frac{7}{2}$	1.0890	−0.664	−24
$Q(\frac{7}{2})$	$\frac{3}{2} \leftarrow \frac{5}{2}$	1.1106	−0.644	−12
$Q(\frac{7}{2})$	$\frac{1}{2} \leftarrow \frac{3}{2}$	1.1304	−0.626	− 4
$Q(\frac{7}{2})$	$-\frac{1}{2} \leftarrow \frac{1}{2}$	1.1509	−0.608	6
$Q(\frac{7}{2})$	$-\frac{3}{2} \leftarrow -\frac{1}{2}$	1.1812	−0.592	34
$Q(\frac{9}{2})$	$-\frac{1}{2} \leftarrow \frac{1}{2}$	1.5660	−0.399	0

[a] Observed on the $P(17)_{8-7}$ $^{12}C^{16}O$ laser line at 1893.5147 cm^{-1}.

[b] Tuning rate at resonance.

[c] Residuals of the fit.

[d] Each datum assigned an uncertainty of 0.667×10^{-3} cm^{-1}.

are unperturbed. The separation of the two Q lines depends mainly upon $\alpha_{1,B}$ and this parameter was finally chosen as the one to be varied instead.

The fit contained 45 weighted data points and the standard deviation relative to the estimated experimental uncertainties was $\sigma_{rel.} = 2.65$, see Eq.(IV.67). The standard deviation of the LMR data set was 54 MHz, almost three times the estimated uncertainty for Doppler limited resonances. In addition, the residuals of the LMR data show a small, M_J-dependent bias. This is understandable given the poor signal-to-noise ratio of the LMR spectrum. It could be argued that the uncertainty of the LMR data should be revised in this case, but an increase due to poor signal-to-noise is not easy to quantify *a priori*.

VI.4 Discussion of the Unique States

VI.4.1 Overview

The parameters determined from the analyses of the $1_0^1\,{}^2\Pi$, $1_0^1 2_1^1\,{}^2\Delta$ and $1_0^1 2_2^2\,{}^2\Phi$ bands are compared in Table VI.12. Each band has been analysed separately, using the $\mathbf{N}^2$ single electronic state effective Hamiltonian described in Chapters III and IV. The Renner-

Teller effect and the vibrational energy were treated within the harmonic approximation, whereas anharmonic contributions to the other interactions were included using standard rotation-vibration theory [19]. It is hoped that a global fit of all data will be possible at a later stage, by extending the model to include anharmonic Renner-Teller effects, Fermi and K-type resonances.

The vibrational dependence of g_K and the origin of the $1_0^1 2_2^2\,^2\Phi$ band have been determined for the first time. Included with the LMR data were extensive sets of microwave, EPR and FIR-LMR data together with optical combination differences. Such a data set minimises the need to constrain parameters, allowing the minimum of the parameter surface to be found in the least-squares fits. There was no indication of instability in the fits, nor of convergence on false parameter minima. The use of a basis set with $\Delta v_2 = \pm 4$ and an exact matrix diagonalisation procedure, has taken into account the Renner-Teller effect. This has allowed the determination of fundamental parameters more accurately than when they are deduced from the effective parameters determined in an analysis neglecting the Renner-Teller effect.

The parameters in Table VI.12 are compared below with those of other workers. The Renner-Teller effect has been neglected in most of these analyses, and so their effective A and g_L values have been converted to the 'true' values using Eqns.(IV.2) and (IV.8). Bolman *et al.*[14] and Kawaguchi *et al.*[8] used an $\mathbf{R}^2$ Hamiltonian in their analysis, so for the purposes of comparison their parameters have been converted to those for an $\mathbf{N}^2$ Hamiltonian, using the formulae in Appendix D. Copeland and Crosley [20], Patel-Misra *et al.*[21] and Hemmerling and Vervloet [22] do not state explicitly which Hamiltonian was used for their analyses; their parameters have been treated as though they were for an $\mathbf{N}^2$ Hamiltonian.

VI.4.2 Band Origins

The $1_0^1\,^2\Pi$ band origin of $1921.36457(43)\,\mathrm{cm}^{-1}$ determined here compares with values of $1920.60645(19)\,\mathrm{cm}^{-1}$ determined by Barnes *et al.*[1], $1921.8(5)\,\mathrm{cm}^{-1}$ determined by Copeland and Crosley [20], $1921.30323(59)\,\mathrm{cm}^{-1}$ by Bruggemann [13], $1921.350(10)\,\mathrm{cm}^{-1}$ by Sears *et al.*[12] and $1921.282(3)\,\mathrm{cm}^{-1}$ by Hemmerling and Vervloet [22]. With the exception of Barnes *et al.*[1], all the other band origins are in good agreement; the discrepancy in the former study arises because the band origin is an effective one with $\alpha_{1,A}$

Table VI.12: A comparison of parameters from the analyses of the $1_0^1\,^2\Pi$, $1_0^1 2_1^1\,^2\Delta$ and $1_0^1 2_2^2\,^2\Phi$ bands of NCO ($\tilde{X}$).

Parameter[a]	$1_0^1\,^2\Pi$	$1_0^1 2_1^1\,^2\Delta$	$1_0^1 2_2^2\,^2\Phi$
ν_0	1921.36457(43)	1907.84852	1894.3938(32)
$A_{(0,v_2,0)}$	−96.0881(23)	−95.7246(29)[b]	−95.3611(58)[b]
$\alpha_{1,A}$	−1.38713(82)	−1.38713[c]	−1.38713[c]
$B_{(0,v_2,0)}$	0.389514206(12)	0.390547110(34)	0.39160400(17)
$10^2\alpha_{1,B}$	−0.33457(28)	−0.3318(42)	−0.309(22)
$10^6 D_{(0,v_2,0)}$	0.15140(19)	0.15757(56)	0.1613(20)
$10^2\gamma_{(0,v_2,0)}$	−0.10711(94)	−0.26415(88)	−0.47424(92)
$10^2 a_{(0,v_2,0)}$	0.208019(69)	0.205392(67)	0.20266(68)
$10^3 b_{F,(0,v_2,0)}$	0.492(10)[d]	0.503(18)[d]	0.5203(4)[d,e]
$10^2 c_{(0,v_2,0)}$	−0.15867(89)[d]	−0.15496(18)[d]	−0.1501(13)[d]
$10^4 eQq_{0,(0,v_2,0)}$	−0.7374(11)	−0.750(11)	−0.761(79)
$10^2\Delta g_{L,(0,v_2,0)}^{(1)}$	−0.6767(36)	−0.67765(94)	−0.6552(13)
$10^2 g_{l,(0,v_2,0)}$	0.137500[g]	0.338180[g]	0.60551[g]

[a] Parameter values in cm^{-1} where appropriate.

[b] Calculated from $A_{(000)}$ and $\alpha_{2,A}$.

[c] Constrained to the value determined for the $1_0^1\,^2\Pi$ band.

[d] Calculated from b and $b+c$, where $b_F = b + c/3$.

[e] In the $1_0^1 2_2^2\,^2\Phi$ band, b was constrained to $b_{(000)}$.

[g] Estimated from Curl's relationship and used in the final fit.

constrained to zero. The value determined in this thesis must be regarded as the most reliable, because α_{1,g_K} has been determined for the first time, separating this vibronic contribution from the band origin.

Similar comparisons for the $1_0^1 2_1^1\,^2\Delta$ band origin (determined here to be $1907.84852\,\mathrm{cm}^{-1}$) are $1907.8(10)\,\mathrm{cm}^{-1}$ from Copeland and Crosley [20] and a value of $1905.5(10)\,\mathrm{cm}^{-1}$ for the $J = 5/2 - J = 5/2$ interval in the $P = 5/2$ sub-band, determined by Patel-Misra *et al.*[21]. The latter is $1.6\,\mathrm{cm}^{-1}$ lower than the value calculated here, indicating errors in the band head measurements used by Patel-Misra *et al.*[21] to determine their term values.

The $1_0^1 2_2^2\,^2\Phi$ band origin of $1894.3938(32)\,\mathrm{cm}^{-1}$ compares with $1888.8(10)\,\mathrm{cm}^{-1}$ estimated from Patel-Misra *et al.*[21], again indicating errors in their study. This is supported by the vibrational term value of $1065.5\,\mathrm{cm}^{-1}$ determined for $(020)\,^2\Phi$ by Hemmerling and Vervloet [22], which compares with term values of $1051\,\mathrm{cm}^{-1}$ and $1444\,\mathrm{cm}^{-1}$ determined for the spin components $(020)\,^2\Phi_{\frac{7}{2}}$ and $(020)\,^2\Phi_{\frac{5}{2}}$ by Patel-Misra *et al.*[21].

The physical interpretation of the trend in band origins is that as the bending amplitude increases, anharmonic effects reduce the frequency of the out-of-phase stretching mode. A χ^2 linear regression fit of the three band origins in Table VI.12 yields a vibrational anharmonicity of $x_{12} = -13.51\,\mathrm{cm}^{-1}$ and a residue of $(\omega_1 + 2x_{11} + x_{13}/2) = 1934.88\,\mathrm{cm}^{-1}$. These values compare well with $-14.6\,\mathrm{cm}^{-1}$ and $1936.7\,\mathrm{cm}^{-1}$ from Copeland and Crosley [20], and with $x_{12} = -13.48\,\mathrm{cm}^{-1}$ from Barnes *et al.*[1]. Taking $x_{11} = -14.78\,\mathrm{cm}^{-1}$ from Sears *et al.*[12] and $x_{13} = -24.8\,\mathrm{cm}^{-1}$ from Copeland and Crosley [17] gives a revised estimate of $\omega_1 = 1976.8\,\mathrm{cm}^{-1}$.

The calculation above allows a prediction to be made of the zero field wave number of the Q(9/2) line of the $1_0^1 2_3^3\,^2\Gamma_{\frac{9}{2}}$ band. This is calculated to be at $1880.43\,\mathrm{cm}^{-1}$, close to the $\mathrm{P}(14)_{9-8}$ laser line at $1880.3428\,\mathrm{cm}^{-1}$. No observed resonance could be assigned to this transition.

The vibrational anharmonicity x_{12} arises from anharmonic terms in the molecular potential energy, and from Coriolis terms. Mills [19] has shown that the contributions arise from cubic anharmonic terms in second order, and quartic terms in first order, plus Coriolis terms [19]:

$$x_{12} = \frac{1}{4}\left[\phi_{1122} + \frac{\phi_{111}\phi_{122}}{\omega_1} - \frac{\phi_{113}\phi_{322}}{\omega_3}\right] + \frac{\phi_{122}}{2\left(\omega_1^2 - 4\omega_2^2\right)} + B\left(\zeta_{1,2}\right)^2\left[\frac{\omega_1}{\omega_2} + \frac{\omega_2}{\omega_1}\right]. \quad \text{(VI.7)}$$

The ϕ_{ijk} are the reduced force constants for the normal co-ordinate term $q_i q_j q_k$ in the molecular potential energy expression [19]. Werner [23] has calculated a value of $\zeta_{1,2} = 0.99816$ for NCO, and taking $\omega_3 = 1260.22\,\mathrm{cm}^{-1}$ [17], the last term in Eq.(VI.7), the Coriolis contribution, is calculated to be $1.541\,\mathrm{cm}^{-1}$. An accurate knowledge of the various harmonic and anharmonic vibrational and vibration-rotation parameters would allow an inversion of the vibration-rotation parameters to obtain the form of potential function for NCO.

The parameters $\nu_0(1_0^1\,^2\Pi)$ and x_{12} are not sufficient to reproduce the unique state band origins in Table VI.12 to within their error limits. This is in part due to the need to consider the higher vibrational anharmonicities y_{ijk}, however contributions of a similar magnitude are expected arise from anharmonic Renner-Teller effects [24, 25], K-type [26] and Fermi resonances [27]. There are also K dependent terms, such as Bl^2, absorbed into the vibrational term values; these will give contributions of order $\alpha_{1,B} l^2$ to the band origins.

VI.4.3 Spin-Orbit Parameters

The value of $A_{(000)} = -96.0881(23)\,\mathrm{cm}^{-1}$ determined here is a 'Renner free' value for the $\tilde{\mathrm{X}}$ state. It still contains non-adiabatic vibronic and spin-other-orbit contributions which are absorbed into it by the Van Vleck transformation. The effective values obtained by other workers can be converted to the 'true' values using Eq.(IV.2). The value determined by Bolman *et al.*[14] is then $-96.079(1)\,\mathrm{cm}^{-1}$, Sears *et al.*[12] determined $-96.0770(6)\,\mathrm{cm}^{-1}$ and Hemmerling and Vervloet [22] $-96.084(1)\,\mathrm{cm}^{-1}$. The value of $\alpha_{1,A} = -1.38713(82)\,\mathrm{cm}^{-1}$ determined here is in good agreement with Bruggemann [13], $-1.39833(73)\,\mathrm{cm}^{-1}$, but the value calculated from Sears *et al.*[12] is $-1.510(11)\,\mathrm{cm}^{-1}$.

For the $1_0^1 2_1^1\,^2\Delta$ and $1_0^1 2_2^2\,^2\Phi$ bands, no accurate information was available on the spin-orbit splitting in the upper state; for these fits $\alpha_{1,A}$ was constrained to the value for the $1_0^1\,^2\Pi$ band. This is expected to be reliable since, as can be seen from Table VI.12, $\alpha_{1,B}$ is almost independent of v_2. Bolman *et al.*[14] determined a value of $A_{(010)} = -95.668(2)\,\mathrm{cm}^{-1}$, and Copeland and Crosley a value of $-95.50(40)\,\mathrm{cm}^{-1}$. The value of $A_{(010)}$ determined here is slightly larger, $-95.7246\,\mathrm{cm}^{-1}$, and indicates the effect of higher order Renner-Teller effects in the $\Delta v_2 = \pm 4$ basis set. Kawaguchi *et al.*[8] estimated $A_{(020)} = -95.240\,\mathrm{cm}^{-1}$ by extrapolating the results of Bolman *et al.*[14]. Hemmerling

and Vervloet [22] recently determined $A_{(020)}$ to be $-95.299\,\mathrm{cm}^{-1}$, in excellent agreement with the value of $-95.3611\,\mathrm{cm}^{-1}$ estimated in this thesis.

The increase in A upon excitation of the out-of-phase stretching mode implies a small change in the electronic wave function, with an increase in unpaired electron density on the more electronegative O and N atoms. A simple molecular orbital picture places the unpaired electron in a non-bonding π orbital consisting of atomic $2p$ orbitals, with a node near to the carbon atom. If excitation of the out-of-phase stretching mode made the molecule more nearly symmetrical, then the carbon atom contribution to the spin-orbit coupling would be reduced. The unpaired electron would implicitly localise more on the terminal atoms. The arguments used here are quite simplistic and an *ab initio* calculation is required fully to understand this observation.

In contrast, A decreases upon v_2 excitation. This is expected to be due to the effect of the non-adiabatic Renner-Teller term $(v_2+1)\Delta A$, Eq.(III.37), which represents vibronic (Herzberg-Teller) mixing with excited electronic states, mainly the $\tilde{\mathrm{A}}\,^2\Sigma^+$ state.

VI.4.4 Rotational and Spin-Rotational Parameters

The rotational constant

The rotational parameters are predominantly determined by the microwave data included in the fits. The values determined here are in excellent agreement with the original work [8], in which the significance of the parameters is discussed at length. For example, Kawaguchi *et al.*[8] determined a value of $B_{(020)} = 0.391601319\,\mathrm{cm}^{-1}$, very close to the value in Table VI.12. The v_2 dependence of B has both the normal anharmonic and Coriolis contributions [19], and contributions from the expectation value $\langle G_\perp^2 \rangle$, which will be K-dependent.

From a consideration of the molecular geometry, B is expected to increase with v_2 excitation. As the bending amplitude increases, the average values of the I_{xx} and I_{yy} components of the inertial tensor will decrease and hence increase B. The centrifugal distortion parameter D measures the derivative of the inverse inertial tensor w.r.t. the normal co-ordinates, $D \propto (\sum_i \partial I_{ii}/\partial Q_k)$, indicating that the derivatives w.r.t. Q_2 are increasing with v_2. The estimate $D \approx 4B^3/\omega_3^2 = 0.148 \times 10^{-6}\,\mathrm{cm}^{-1}$ is in this case a very good approximation to the values in Table VI.12. Exciting the out-of-phase stretching

mode increases the length of the molecule, and thus decreases B.

The spin-rotation parameter

The spin-rotation parameter shows a strong v_2 dependence. Kawaguchi *et al.*[8] have explained this in terms of a fourth order vibronic contribution arising in the Van Vleck transformation. Using a slightly different notation to Kawaguchi *et al.*[8], in the spirit of the ΔA correction developed by Brown [28], the fourth order term in the effective Hamiltonian may be written $\Delta\gamma Q_2^2$. The origin of the term is similar to the second order spin-orbit contribution to γ (§III.9.4), but the perturbation Hamiltonian is now

$$\mathcal{H}^{(4)} = a_i l_{i,\pm} s_{i,\mp} + B N_\mp N_\pm + \frac{V_{11}}{2}\left\{e^{i(\vartheta-\varphi)} + e^{-i(\theta-\phi)}\right\}. \qquad \text{(VI.8)}$$

The fourth-order term operates over a multiplicity of pathways and is therefore complicated to evaluate. The observed value of γ is a sum of the first, second and fourth order contributions:

$$\gamma^{\text{obs.}} = \gamma^{(1+2)} + \Delta\gamma\,(v_2 + 1)\,. \qquad \text{(VI.9)}$$

A χ^2 linear regression fit of the γ values in Table VI.12 yielded $\Delta\gamma = -0.184 \times 10^{-2}\,\text{cm}^{-1}$ and a value of $0.864 \times 10^{-3}\,\text{cm}^{-1}$ for $\gamma^{(1+2)}$. This treatment models the trend in γ tolerably well, but two points must be borne in mind. Firstly, A and γ are highly correlated. Secondly, A_D has been constrained to zero in this and previous analyses of the unique states. Therefore, γ is an effective parameter [29], which may be denoted $\tilde{\gamma}$ where

$$\tilde{\gamma} = \gamma^{\text{true}} - \frac{A_D\,[A\Lambda^2 - 2B\Lambda K]}{2B}. \qquad \text{(VI.10)}$$

There is a weak K dependence of $\tilde{\gamma}$ in Eq.(VI.10), from the term $A_D\Lambda K$. The value of $A_D = -0.1121 \times 10^{-3}\,\text{cm}^{-1}$ determined for the $1_0^1 2_1^1\,{}^2\Sigma$ bands described later, suggests that this contribution is smaller than the fourth order term. With this value for A_D, and taking the value for $\gamma^{(1+2)}$ estimated above, a value for γ^{true} of $-0.0131\,\text{cm}^{-1}$ can be estimated.

The effect on the energy levels of terms involving A_D and γ, has the same J dependence. Therefore, the two parameters are only weakly separable due to higher order

effects involving the Renner-Teller interaction in the $\tilde{X}$ state[1]. These effects were not sufficiently pronounced to achieve a meaningful separation in the present study.

VI.4.5 Hyperfine Parameters

A thorough discussion of the hyperfine parameters has been given by Kawaguchi *et al.*[8] and their conclusions are essentially unchanged in the present study. There are however a few new points to be raised here.

The hyperfine parameters are essentially electronic in origin and so their vibrational dependences are expected to be small. Any v_1 dependence was too small to be significant in the CO-LMR study, where the hyperfine splittings are comparable to the resolution of the spectrometer. The hyperfine parameters in Table VI.12 were essentially determined by the EPR, microwave and FIR LMR data.

A small increase in the Fermi contact parameter with v_2 can be seen in Table VI.12. This indicates an increase of nitrogen atomic s orbital character in the molecular orbital occupied by the unpaired electron. The trend in the quadrupolar coupling parameter eQq_0 also indicates an change in the total electron density in the region of the nitrogen nucleus. The v_2 dependence of the hyperfine parameters may be a result of non-adiabatic effects involving vibronic coupling. For example, Kawaguchi *et al.*[8] have shown that the nuclear spin-electron orbital coupling parameter, a (see Appendix F), has a correction Δa analogous to ΔA in §III.37.

VI.4.6 The Zeeman Parameter $\Delta g_L^{(1)}$

The values of $\Delta g_L^{(1)}$ reported here are the first to be determined in a least-squares fit. The best previous estimates were by Bolman *et al.*[14], who calculated $\Delta g_L^{(1)} = -0.66 \times 10^{-2}$, -0.67×10^{-2} and -0.68×10^{-2} for the (000) $K = 1$, (010) $K = 2$ and (020) $K = 3$ unique state levels. The $g_L^{\text{eff.}}$ values determined by Barnes *et al.*[1], 0.988773 and 0.973200 for the bands $1_0^1\,{}^2\Pi$ and $1_0^1 2_1^1\,{}^2\Delta$ respectively, are in excellent agreement with the values determined here, though the estimate of $\Delta g_L^{(1)} = -0.689 \times 10^{-2}$ deduced from their values is slightly higher than the average value in Table VI.12.

[1]Studies of isotopomers make the separation possible and this has been effected for some diatomic molecules, *e.g.* [30].

$\Delta g_L^{(1)}$ is a vibronic contribution to $\alpha_{2,A}$ and should be independent of K. The values determined for the $1_0^1\,{}^2\Pi$ and $1_0^1 2_1^1\,{}^2\Delta$ bands are indeed in good agreement, but the value for the $1_0^1 2_2^2\,{}^2\Phi$ band is slightly lower than expected. This might arise from a perturbation to $(020)\,{}^2\Phi$ from the $(100)\,{}^2\Pi - (020)\,{}^2\Pi$ Fermi resonance, or it might be caused by K-type resonance effects. It must also be remembered that $\Delta g_L^{(1)}(v_2+1)$ is only the leading third order correction to $g_L^{(0)}$. It arises from the neglect of ω_2 in the binomial expansion of the denominators $(-\Delta E \pm hc\omega_2)^{-2}$ in the third order perturbation expression [28]. Higher terms in the binomial expansion will be K and Λ dependent, similar in form to the g_K term. The first such term is expected to be $\sim \Delta g_L^{(1)}/40$ in magnitude.

The relation between g_K and $\Delta g_L^{(1)}$, given by Eq.(III.38), gives an estimate of $\Delta g_L^{(1)} = -0.705 \times 10^{-2}$, within 5% of the average value in Table VI.12. This equation also proved reliable in estimating $\Delta g_L^{(1)}$ for the CCN radical, enabling its Zeeman spectrum to be modelled [31].

VI.4.7 *K*-Type Doubling

The values of $(p+2q)_{(000)}$ and $q_{(000)}$ in Table VI.12 are in excellent agreement with those of Kawaguchi *et al.*[8], who determined $(p+2q)_{(000)} = 0.253688 \times 10^{-2}\,\mathrm{cm}^{-1}$ and $q_{(000)} = -0.4940\,\mathrm{cm}^{-1}$, and with Davies and Davis who determined $q_{(000)} = -0.5017\,\mathrm{cm}^{-1}$.

The value of $q_{(000)} = -0.4938 \times 10^{-4}\,\mathrm{cm}^{-1}$ determined here for $(000)\,{}^2\Pi$ contains an electronic contribution $q_{\mathrm{el.}} \approx pB/A = -0.1068 \times 10^{-4}\,\mathrm{cm}^{-1}$. This implies a value for the effective l-type doubling parameter of $q^*_{(000)} = -0.3870 \times 10^{-4}\,\mathrm{cm}^{-1}$. Brown [26] gives the formula

$$q^*_{(000)} = \frac{B^2\epsilon}{\omega_2} \sum_{n=1,3} (\zeta_{n,2})^2 \left\{ 1 - \frac{4\omega_2^2}{(\omega_n + \omega_2)^2} \right\}. \qquad \text{(VI.11)}$$

Taking $\zeta_{1,2} = 0.99816$ and $\zeta_{2,3} = 0.06068$ from the force field calculations quoted by Werner [23], a value of $q^* = -0.3340 \times 10^{-4}\,\mathrm{cm}^{-1}$ is calculated, in good agreement with the value deduced here.

Bibliography

[1] C.E. Barnes, J.M. Brown, A.D. Fackerell and T.J. Sears, *J. Mol. Spectrosc.* **92**, 485–496 (1982).

[2] M. Schneider, J.S. Wells and A.G. Maki, *J. Mol. Spectrosc.* **141**, 351 (1990).

[3] M. Schneider, J.S. Wells and A.G. Maki, *J. Mol. Spectrosc.* **139**, 432–438 (1990).

[4] M. Schneider, K.M. Evenson, M.D. Vanek, D.A. Jennings, J.S. Wells, A. Stahn and W. Urban, "$^{12}C^{16}O$ Laser Frequency Tables for the 34.2 to 62.3 THz (1139 to 2079 cm^{-1}) Region," NBS Technical Note 1321, National Bureau of Standards, U.S. Department of Commerce, Washington D.C., 1988.

[5] Computer list of CO laser lines for $^{12}C^{16}O$, $^{12}C^{18}O$, $^{13}C^{16}O$ and $^{13}C^{18}O$, calculated from Dunham Coefficients. Institut für Angewandte Physik der Universität Bonn, Private communication 1992/1993.

[6] C.E. Barnes, Ph.D. thesis, University of Southampton, 1981.

[7] A. Carrington, A.R. Fabris, B.J. Howard and N.J.D. Lucas, *Mol. Phys.* **20**, 961–980 (1971).

[8] K. Kawaguchi, S. Saito and E. Hirota, *Mol. Phys.* **55**, 341–350 (1985).

[9] R. Pahnke, D. Phil thesis, University of Oxford, 1990.

[10] J.P. Towle, D.Phil thesis, University of Oxford, 1992.

[11] P.B. Davies and I.H. Davis, *Mol. Phys.* **69**, 175–191 (1990).

[12] F.J. Northrup, M. Wu and T.J. Sears, *J. Chem. Phys.* **96**, 7218–7228 (1992).

[13] R. Brüggemann, Diplomarbeit thesis, Institut für Angewandte Physik der Universität Bonn, 1988.

[14] P.S.H. Bolman, J.M. Brown and A. Carrington, *Proc. R. Soc. Lond. A* **343**, 17–44 (1975).

[15] T. Amano and E. Hirota, *Mol. Phys.* **57**, 5608– (1972).

[16] S. Saito, Symposium on Structural Chemistry, Paper 19C10, Tokyo, 1974.

[17] M. Wu and T.J. Sears, *Mol. Phys.* **82**, 503–521 (1994).

[18] International Union of Pure and Applied Chemistry, Physical Chemistry Division, "Quantities, Units and Symbols in Physical Chemistry," 2nd ed., (I. Mills, T. Cvitaš, K. Homann, N. Kallay and K. Kucitsu, Eds.), Blackwell Scientific Publications, Oxford, 1993.

[19] I.M. Mills, "Vibration-Rotation Structure in Asymmetric- and Symmetric-Top Molecules," *in* "Molecular Spectroscopy: Modern Research." (K.N. Rao and C.W. Mathews, Eds.), pp. 115–140, Academic Press, New York, 1972.

[20] R.A. Copeland and D.R. Crosley, *Can. J. Phys.* **62**, 1488–1501 (1985).

[21] D. Patel-Misra, D.G. Sauder and P.J. Dagdigian, *J. Chem. Phys.* **93**, 5448–5456 (1990).

[22] B. Hemmerling and M. Vervloet, *Mol. Phys.* **78**, 1423–1447 (1993).

[23] J. Werner, Ph.D. thesis, Institut für Angewandte Physik der Universität Bonn, 1987.

[24] J.M. Brown and F. Jørgensen, *Adv. Chem. Phys.* **52**, 117–180 (1983).

[25] J.M. Brown and F. Jørgensen, *Mol. Phys.* **47**, 1065–1086 (1982).

[26] J.M. Brown *J. Mol. Spectrosc.* **56**, 159–162 (1975).

[27] J.T. Hougen, *J. Chem. Phys.* **37**, 403–408 (1962).

[28] J.M. Brown, *J.Mol. Spectrosc.* **68**, 412–422 (1977).

[29] J.M. Brown and J.K.G. Watson, *J. Mol. Spectrosc.* **65**, 65–74 (1977).

[30] D.A. Gillett, J.P. Towle, M.N. Islam and J.M. Brown, *J. Mol. Spectrosc.* **163**, 459–482 (1994).

[31] D.A. Gillett and J.M. Brown, *Can. J. Phys.* **72**, 1004–1006 (1994).

Chapter VII

The $1_0^1 2_1^1\,\mu^2\Sigma$ and $1_0^1 2_1^1\,\kappa^2\Sigma$ Bands

VII.1 Introduction

The following sections describe the search for, the assignment of and the analysis of transitions in the $1_0^1 2_1^1\,\mu^2\Sigma$ and $1_0^1 2_1^1\,\kappa^2\Sigma$ bands of NCO, recorded using CO laser magnetic resonance.

The $1_0^1 2_1^1\,{}^2\Sigma$ bands are the most complex systems studied in this thesis. The first rigorous understanding of LMR spectra due to such transitions in a Renner-Teller molecule, is presented here. The levels involved show complicated Zeeman effect behaviour, with the result that many of the LMR spectra have a spectacular appearance. These observations are of special interest because the observation of Zeeman spectra of Hund's case (b) systems is somewhat rare [1, 2].

The unique state LMR spectra of NCO could have been analysed by a diatomic molecule program constructed in a Hund's case (a) basis set, but then only effective parameters would have been determined. This cannot be done for the $^2\Sigma$ bands, even if a Hund's case (b) basis set is used. This is because there is a large, first order Renner-Teller effect and an orbital contribution to the Zeeman effect in the $^2\Sigma$ vibronic levels. The latter two effects have no analogue in a $^2\Sigma$ electronic state. The success of the explicit Renner-Teller modelling approach to enable the analysis of the $1_0^1 2_1^1\,{}^2\Sigma$ bands of NCO provides powerful justification for the model developed in Chapters III and IV. The implementation of this model in the computer program 'RENNER.FOR', (§IV.5), was used for all the work described below.

VII.1.1 Structure of the $1_0^1 2_1^1\,{}^2\Sigma$ Bands

The $K = 0$ states show Hund's case (b) rotational structure and Zeeman effects, described in §IV.2. The splitting into μ (lower) and κ (upper) components of each $K = 0$ level means there are two vibronic bands, $1_0^1 2_1^1\,\mu^2\Sigma^{(+)}$ and $1_0^1 2_1^1\,\kappa^2\Sigma^{(-)}$. The association of the (+) and (−) labels with the μ and κ states in NCO arises because the Renner-Teller parameter is negative.

Each band consists of transitions for which $\Delta N = \pm 1$, where N is the Hund's case (b) quantum number. For $N > 0$ each level has two spin components, F_1 correlating with $J = N + 1/2$ and F_2 correlating with $J = N - 1/2$ at zero field; for N=0 only F_1 arises. At zero field, for $\Delta N = +1$ there are R and Q type ΔJ transitions, *i.e.* $F_1 \leftrightarrow F_1$, $F_1 \leftrightarrow F_2$ and $F_2 \leftrightarrow F_2$. Similarly, for $\Delta N = -1$ there are Q and P type ΔJ transitions. In a magnetic field, the quantum number J breaks down and O and S type transitions become weakly allowed due to mixing of the F_1, F_2 spin-components of the same N. These correlate at zero field with forbidden transitions for which $\Delta J = \pm 2$.

Fig.VII.1 shows a zero field simulation of the first few lines in the $1_0^1 2_1^1\,\mu^2\Sigma^{(+)}$ and $1_0^1 2_1^1\,\kappa^2\Sigma^{(-)}$ vibration-rotation bands. This is an accurate diagram calculated from the parameters obtained in the final analysis described later. This should set in context the nature of the bands and the transitions that occur. The structure is very different to that of the Hund's case (a) unique state vibration-rotation bands. Firstly, there is no $P = K \pm 1/2$ sub-band structure or K-type doubling. Secondly, the Q lines do not fall close together, shaded slightly to long wavelength of the band origin, as they would in a band arising from transitions between Hund's case (a) energy levels.

Note that the effective origins of the μ and κ bands are displaced from the band origin, ν_0. If the effect of the Renner-Teller matrix elements with $\Delta v_2 = \pm 2$ is estimated using second order perturbation theory, then an approximate expression can be derived for the effective band origins,

$$\begin{aligned}\nu_{\text{eff.}}\left(1_0^1 2_1^1\,{}^2\Sigma\right) &= \nu_0^{\text{true}} - \frac{\omega_2}{4}\left[\epsilon_{110}^2 - \epsilon_{010}^2\right] \\ &\pm \frac{1}{2}\left[\left\{A_{(110)}^2 + 4\left(\epsilon\omega_{2(110)}\right)^2\right\}^{\frac{1}{2}} - \left\{A_{(010)}^2 + 4\left(\epsilon\omega_{2(010)}\right)^2\right\}^{\frac{1}{2}}\right] \quad \text{(VII.1)}\end{aligned}$$

where the upper and lower sign choice is for κ and μ, respectively. As can be seen from

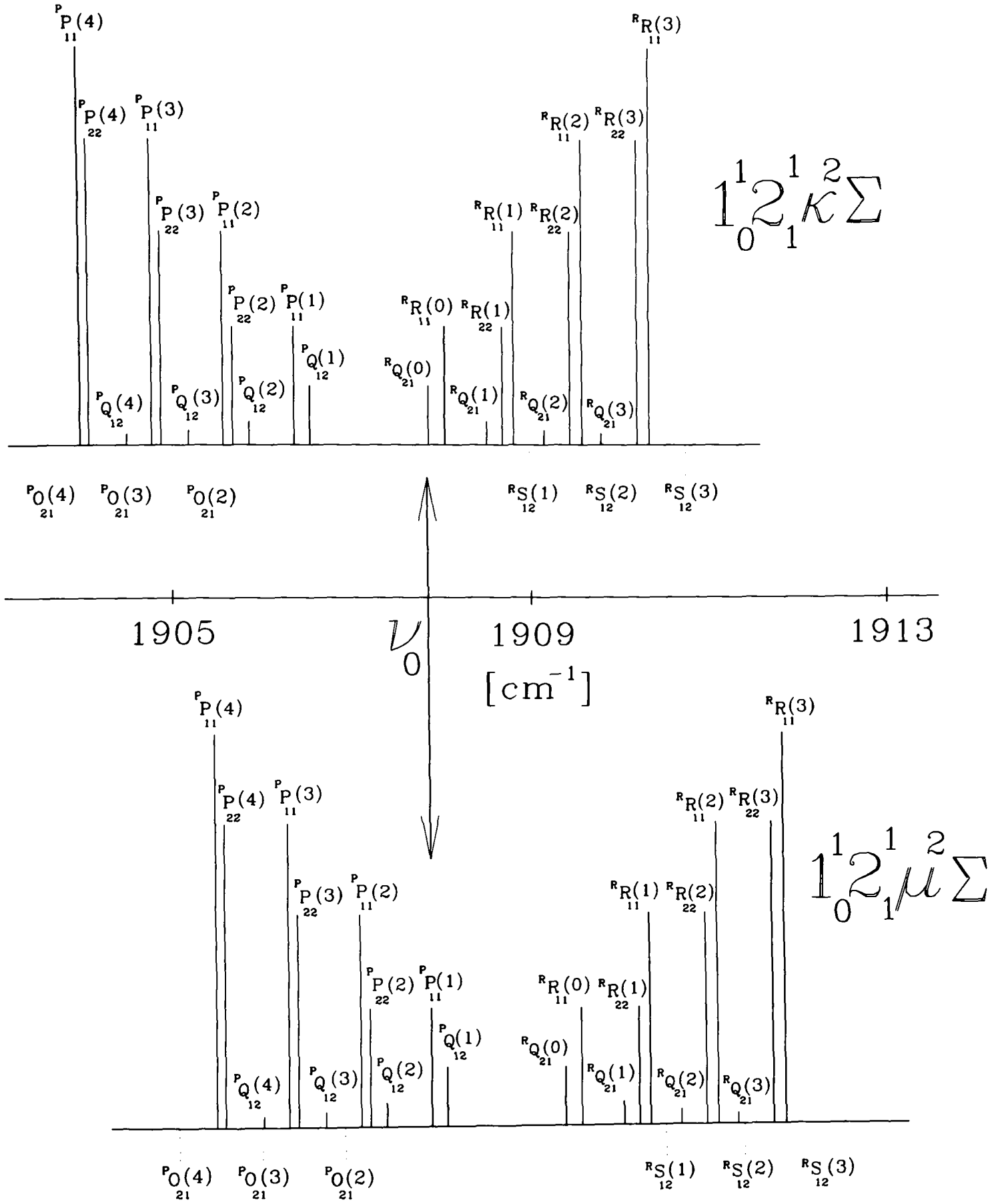

Figure VII.1: An accurate zero field stick diagram of the first few lines in the $1^1_0 2^1_1\,{}^2\Sigma$ vibration-rotation bands of NCO. The two bands show classic Hund's case (b) structure. The heights of the solid lines are proportional to the line strength factors $S_{J',J''}$. The transitions indicated by dotted lines are forbidden at zero field but become weakly allowed in a magnetic field; their intensities are not indicated. ν_0 indicates the band origin (see text). The transitions are denoted ${}^{\Delta N}\Delta J_{F_i',F_i''}(N'')$.

Fig.VII.1, in NCO these effects result in $\mu^{\rm P}{\rm P}(N)$ being near to $\kappa^{\rm P}{\rm P}(N-2)$ and $\mu^{\rm R}{\rm R}(N)$ being near to $\kappa^{\rm R}{\rm R}(N+2)$. The effective band origin for the $1_0^1 2_1^1\,{}^2\Delta$ band is similarly given by

$$\nu^{\rm eff.}\left(1_0^1 2_1^1\,{}^2\Delta\right) \;=\; \nu_0^{\rm true} - \frac{3\omega_2}{4}\left[\epsilon_{110}^2 - \epsilon_{010}^2\right] + 2\alpha_{1,g_K}. \qquad \text{(VII.2)}$$

VII.1.2 Modelling the $1_0^1 2_1^1\,{}^2\Sigma$ bands

The 'RENNER.FOR' program was used in the mode in which $N, \mu/\kappa, F_1/F_2$ and parity were read in, with the eigenstates being identified by N and energy ordering, $\#_i$, as described in §IV.2.3. A basis set with $\Delta J = \pm 6, \Delta v_2 = \pm 2$ was used for initial predictions. The large ΔJ basis was used because levels undergoing spin-decoupling can tune several $\rm cm^{-1}$ in a magnetic field, so it is necessary to consider a wide manifold of neighbouring rotational levels of the same parity.

A refit was performed of the rotational transitions observed in the levels (010) $\mu, \kappa\ {}^2\Sigma$, by Kawaguchi *et al.*[3]. This provided very accurate lower state rotational and spin-rotational parameters. The vibrational dependences $\alpha_{1,B}$ and $\alpha_{1,A}$, and the Zeeman parameter $\Delta g_L^{(1)}$, were taken to be the values determined from preliminary fits of the $1_0^1 2_1^1\,{}^2\Delta$ band, as was the spin-orbit splitting $A_{(010)}$.

At the outset, there was no high resolution information on the $1_0^1 2_1^1\,{}^2\Sigma$ band origin ν_0, nor on α_{1,g_K} or $\alpha_{1,\epsilon\omega_2}$. Therefore, the absolute band origins and the effective μ, κ origins were uncertain. The effective band origins were expected to be similar to the origin of the $1_0^1 2_1^1\,{}^2\Delta$ band, but could differ by several $\rm cm^{-1}$. Estimates of ν_0 for the ${}^2\Sigma$ bands were made by considering the term values available from LIF studies [4]–[6]. The term values reported by Copeland and Crosley proved the most accurate for predicting the band origins of the unique states, so their term values were used, giving a band origin of $1908.5(16)\,\rm cm^{-1}$. Bearing in mind the effects of the value of $\alpha_{1,A}$ determined for the $1_0^1 2_1^1\,{}^2\Delta$ band, the estimate of the $1_0^1 2_1^1\,{}^2\Sigma$ band origin was revised to $1908.83\,\rm cm^{-1}$.

The predictions based on the above estimated parameters were expected to give reliable relative spacings of lines within each band, but the uncertainties in the band origin and the relative positions of the μ and κ bands could still have introduced several $\rm cm^{-1}$ of systematic error. A decision was made to model only the μ state; being the lower ${}^2\Sigma$ state it should be the more populated.

VII.1.3 Searching for Assignments

Candidate $1^1_0 2^1_1\,{}^2\Sigma$ band spectra were observed on many laser lines, but the most probable were those on the $P(12)_{8-7}$, $P(6)_{9-8}$, $P(13)_{8-7}$, $P(7)_{9-8}$ and $P(8)_{9-8}$ laser lines. Resonances on some of these lines had already been assigned to the $1^1_0 2^1_1\,{}^2\Delta$ band, implying the $^2\Sigma$ band transitions should be nearby. The unassigned resonances consisted either of very sharp, fast tuning lines often in no regular pattern, or regular progressions of Lamb-dips with apparent doublings. These were thought to arise from Hund's case (b) behaviour, and could possibly also have arisen from the $1^1_0 2^2_2\,\mu, \kappa^2\Pi$ bands. A stick diagram of the predicted zero field $1^1_0 2^1_1\,{}^2\Sigma$ spectrum could be moved over a 'map' of the CO laser lines by $\pm 2\,\mathrm{cm}^{-1}$ and still give several positions with close zero field coincidences to the above laser lines.

Many Zeeman tuning diagrams (similar to Fig.VII.4) were produced, each covering a $1\,\mathrm{cm}^{-1}$ interval moving outwards from the band origin. The predictions covered the 0–1 T range, since there were few candidate transitions above 1 T. Many 'false' laser lines were then drawn across these diagrams, covering many possible intersections between the laser line and the transitions. A field prediction was then performed for each 'false' laser line, and the intensity and tuning rate output was used to perform a simulation of the Doppler limited LMR spectrum in both π and σ polarisations.

About 300 'false' lines were modelled in the range $1900 - 1912\,\mathrm{cm}^{-1}$. The calculations were performed on a CONVEX vectorising mainframe, but nevertheless became extremely time consuming as the N values involved increased (and so the number of Zeeman components), since in each $1\,\mathrm{cm}^{-1}$ interval up to 10 different transitions had to be considered. Moving the 'false' laser line by as little as $0.01\,\mathrm{cm}^{-1}$ could completely change the appearance of the simulations. This was because the tuning rates and intensities of resonances changed rapidly with field due to spin-decoupling effects.

A comparison of the simulations and observations produced no direct assignment. The problem with the simulations was the wide range of tuning rates of the predicted resonances. The $F_1 - F_1$ and $F_2 - F_2$ transitions are very slow tuning ($\sim 0.1\,\mathrm{MHzG}^{-1}$), and though strong they produce very broad LMR spectra. In contrast, the $F_1 - F_2$ transitions, though weak, typically have very large tuning rates, in excess of $2\,\mathrm{MHzG}^{-1}$. In simulations, their LMR spectra appeared as very sharp lines whose height suppressed the appearance of the $F_1 - F_1$ and $F_2 - F_2$ resonances into the baseline of the simulations.

In the light of this, further predictions were made in which only the $F_1 - F_1$ and $F_2 - F_2$ transitions were included. Considering the low tuning rates and the strength of these transitions, it was considered that they might appear as Lamb-dips since the Doppler profile would be severely under-modulated. Indeed, some of the candidate spectra matched this description. Therefore, simulations were performed in which the resonances appeared as Lamb-dips. This approach was successful after about 80 different simulations, as is described below. The sensitivity of the simulation to incremental changes in laser wave number was again noted; this feature made the initial assignments unambiguous, as will be seen from the complex Zeeman tuning diagrams shown below.

VII.1.4 Summary of Results

Following the initial assignment, several LMR spectra were assigned to the $1_0^1 2_1^1\,{}^2\Sigma$ bands. These are summarised in Table VII.1. The following results section discusses the assignments made, the first one being the $1_0^1 2_1^1\,\mu^2\Sigma\,{}^{\mathrm{P}}\mathrm{P}_{11}(6)$ transition on the $\mathrm{P}(8)_{9-8}$ laser line.

VII.2 Results and Analysis

VII.2.1 Assignments

Spectrum on the $\mathrm{P}(8)_{9-8}$ laser line

The predictions of Lamb-dip spectra eventually produced a simulation looking like the part of Fig.VII.2 below 650 mT, arising from the $\mu^{\mathrm{P}}\mathrm{P}_{11}(6)$ transition. The spectrum shows the second derivative signal as a function of the applied flux density. The dips at about 565 mT and 613 mT stood out unambiguously in both the simulation and the observed spectrum. Therefore, these two measurements were used in a fit to determine ν_0 and either of $\alpha_{1,A}$ or $\alpha_{1,\epsilon\omega_2}$ (they fitted to the data equally well). A re-prediction of the spectrum was then made, which showed that the features at higher fields, due to the $\mu^{\mathrm{P}}\mathrm{P}_{22}(6)$ transition, were brought exactly into their observed positions, see Fig.VII.3. Note that this was achieved with no $F_2 - F_2$ transitions in the fit, giving great confidence in the assignment. The preliminary parameters determined at this stage were close to the final ones given in Table VII.4. Furthermore, a weak Doppler limited resonance due

Table VII.1: Summary of LMR observations of the $1_0^1 2_1^1\,\mu^2\Sigma$ and $1_0^1 2_1^1\,\kappa^2\Sigma$ bands.

Transition[(a)]	Laser Line	$\tilde{\nu}_{\rm L}$ [cm^{-1}]
$\mu^{\rm R}R_{11}(13)$	$P(17)_{7-6}$	1918.9787
$\kappa^{\rm R}R_{22}(8)$	$P(12)_{8-7}$	1913.8859
$\mu^{\rm R}R_{22}(6)$	$P(12)_{8-7}$	1913.8859
$\kappa^{\rm R}Q_{21}(3)$	$P(13)_{8-7}$	1909.8775
$\mu^{\rm R}Q_{21}(1)$	$P(13)_{8-7}$	1909.8775
$\mu^{\rm R}R_{11}(0)$	$P(13)_{8-7}$	1909.8775
$\kappa^{\rm R}Q_{21}(0)$	$P(7)_{9-8}$	1907.6880
$\mu^{\rm P}P_{11}(1)$	$P(7)_{9-8}$	1907.6880
$\mu^{\rm P}Q_{12}(2)$	$P(7)_{9-8}$	1907.6880
$\kappa^{\rm P}P_{11}(1)$	$P(14)_{8-7}$	1905.8360
$\kappa^{\rm P}Q_{12}(2)$	$P(14)_{8-7}$	1905.8360
$\kappa^{\rm P}Q_{12}(3)$	$P(14)_{8-7}$	1905.8360
$\mu^{\rm P}P_{11}(3)$	$P(14)_{8-7}$	1905.8360
$\mu^{\rm P}O_{21}(3)$	$P(14)_{8-7}$	1905.8360
$\mu^{\rm P}Q_{12}(4)$	$P(14)_{8-7}$	1905.8360
$\kappa^{\rm P}P_{11}(4)$	$P(8)_{9-8}$	1903.8822
$\mu^{\rm P}P_{11}(6)$	$P(8)_{9-8}$	1903.8822
$\mu^{\rm P}P_{22}(6)$	$P(8)_{9-8}$	1903.8822

[(a)]Denoted ${}^{\Delta N}\Delta J_{F_i' F_i''}(N'')$.

to the $\kappa^{\mathrm{P}}\mathrm{P}_{11}(4)$ transition was observed at about 490 mT, as predicted. This fast tuning, Doppler-limited resonance involves the $M_J = -7/2$ component of $N = 3, F_1$ in the upper state. In the high field limit, this correlates with the $N = 3, F_2$ components, for which $M_S = -1/2$. Since the lower state M_J component correlates with $M_S = +1/2$ in the decoupled limit, the transition loses intensity as the field increases because the $\Delta M_S = 0$ selection rule becomes important. This transition can be clearly seen in Fig.VII.4. The final support for the assignment comes from the prediction and observation of just one resonance in π polarisation, the $M_J = -7/2$ component of $\kappa^{\mathrm{P}}\mathrm{P}_{11}(4)$. A simulation of the observed σ polarisation spectrum is shown in Fig.VII.3; it matches the observed spectrum very well, though the convolution of the Lamb-dips at around 700 mT is not exactly reproduced. The two lowest field Lamb-dips in the simulation are blended in the observed spectrum, presumably a result of modulation and other experimental contributions to the width of the Lamb-dips.

A tuning diagram for the observed spectrum is shown in Fig.VII.4 and Fig.VII.5. In many ways the properties of the levels speak for themselves– the non-linear Zeeman effects and relative disposition of zero field transitions together produce an unambiguous pattern. Attempts at switching the assignments between μ and κ, and F_1 and F_2 etc., and trials of the same type of transition but with different N values, showed other possibilities to be inconsistent.

A choice was made to determine $\alpha_{1,\epsilon\omega_2}$ rather than $\alpha_{1,A}$. There are two reasons for this, firstly $\alpha_{1,A}$ should be the same as for the $1_0^1 2_1^1\,{}^2\Delta$ band, and secondly varying $\alpha_{1,\epsilon\omega_2}$ brought ν_0 very close to the value for the ${}^2\Delta$ band, whereas varying $\alpha_{1,A}$ increased the difference between the two band origins.

It is interesting to consider Fig.VII.2 and to ask why the transitions should appear as such very strong Lamb-dips. In spite of their low tunability, the transitions are very strong (in the spin-decoupled limit they correlate with $\Delta M_S = 0$ and so retain intensity), and with the high intra-cavity power of the CO laser, the upper state and lower state populations must become very nearly equal. The residues of the Doppler profiles (Field-equivalent Doppler widths ~ 40 mT) can just be seen; such wide profiles were severely under-modulated under the recording conditions. The Lamb-dips have widths of ~ 7.5 mT, giving experimentally limited 'natural' line widths of ~ 19 MHz. This is slightly larger than a similar estimate of 13 MHz made for a transition in the

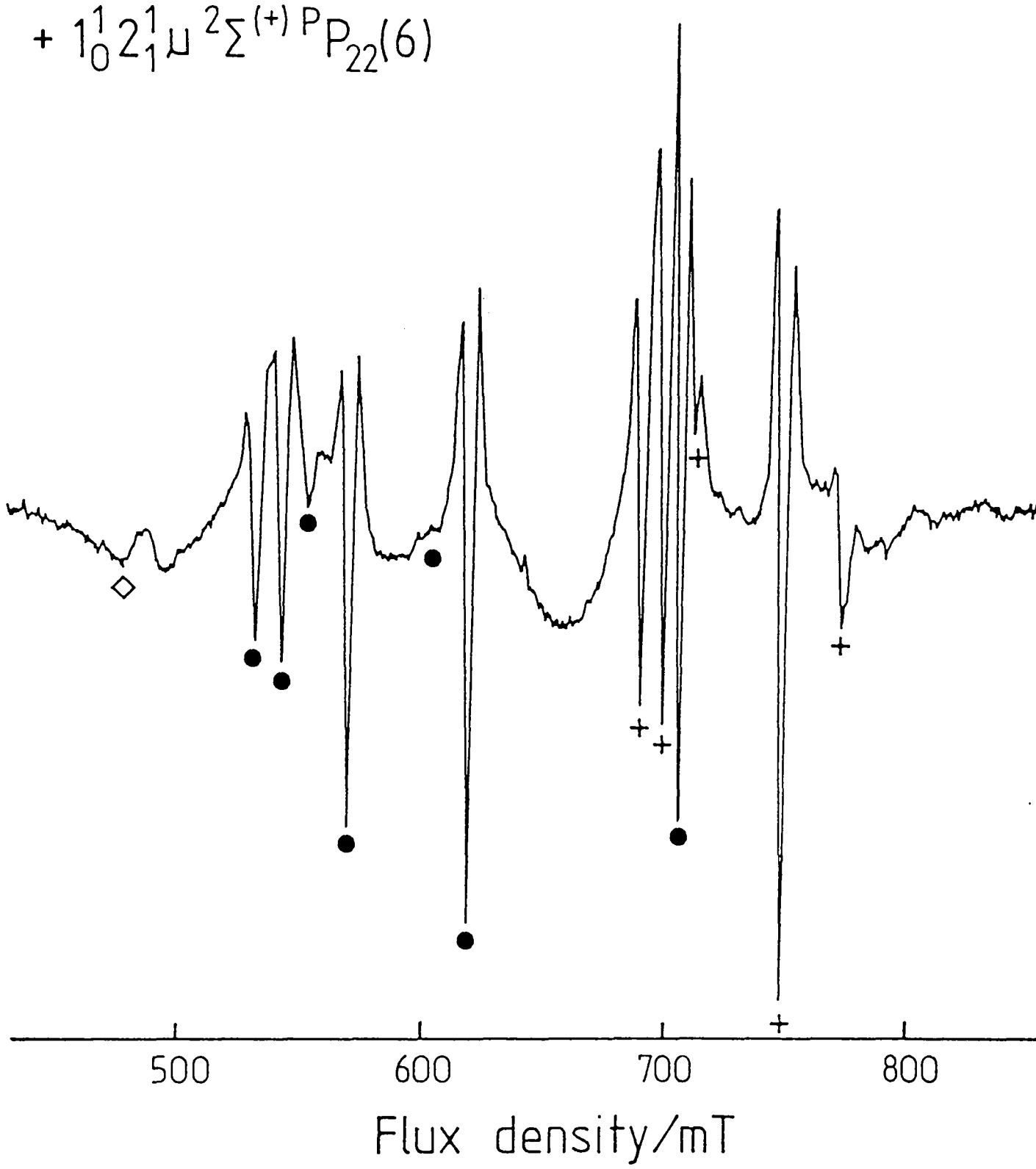

Figure VII.2: The spectrum recorded on the $P(8)_{9-8}$ laser line in σ polarisation. All resonances except the two very weak ones, appear as strong Lamb-dips. The spectrum was recorded with a 300 ms time constant, a peak-to-peak modulation of 1.1 mT and a scan rate of 53 mTmin^{-1}. The ordinate is the 2-f LMR signal.

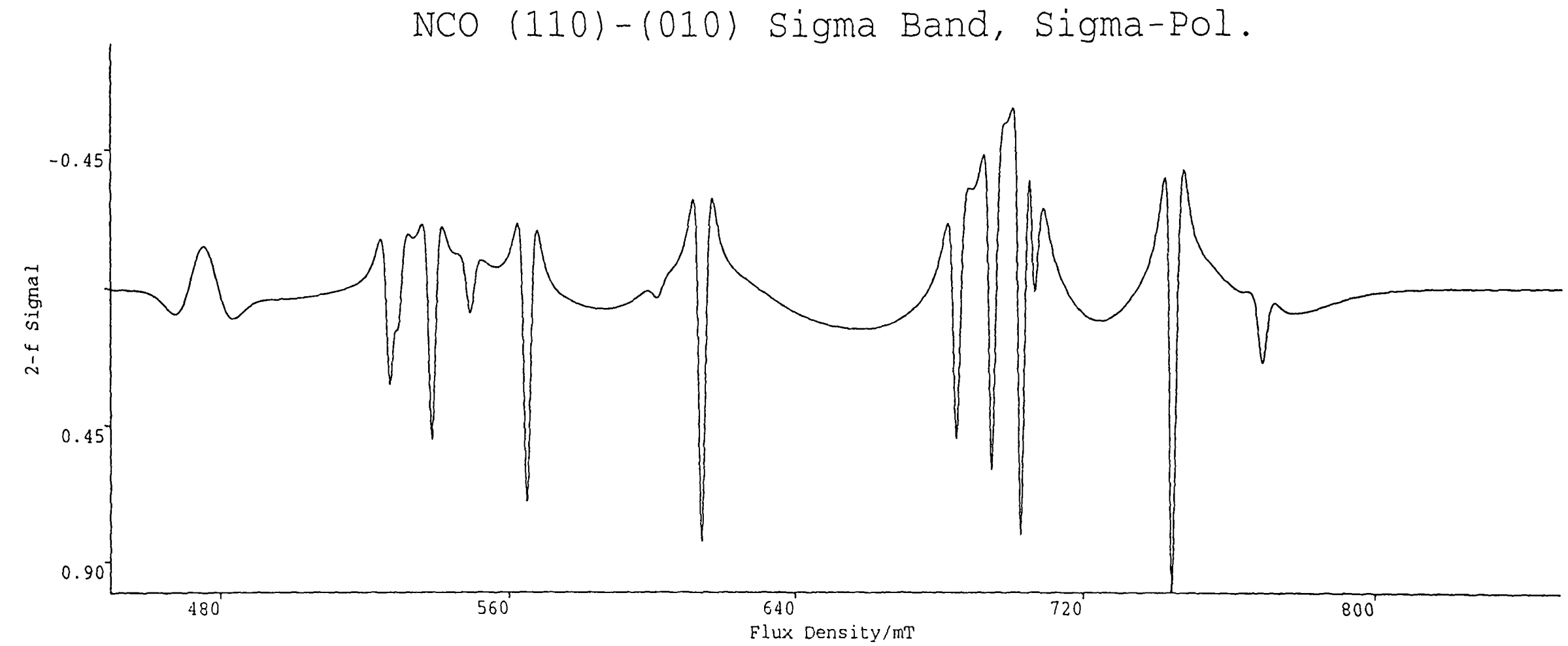

Figure VII.3: A simulation the spectrum observed on the $P(8)_{9-8}$ laser line in σ polarisation. The residual Doppler profiles appear weaker in the observed spectrum because the modulation effects are not perfectly modelled. The first two dip are blended and partially resolved here, but not resolved in the observed spectrum.

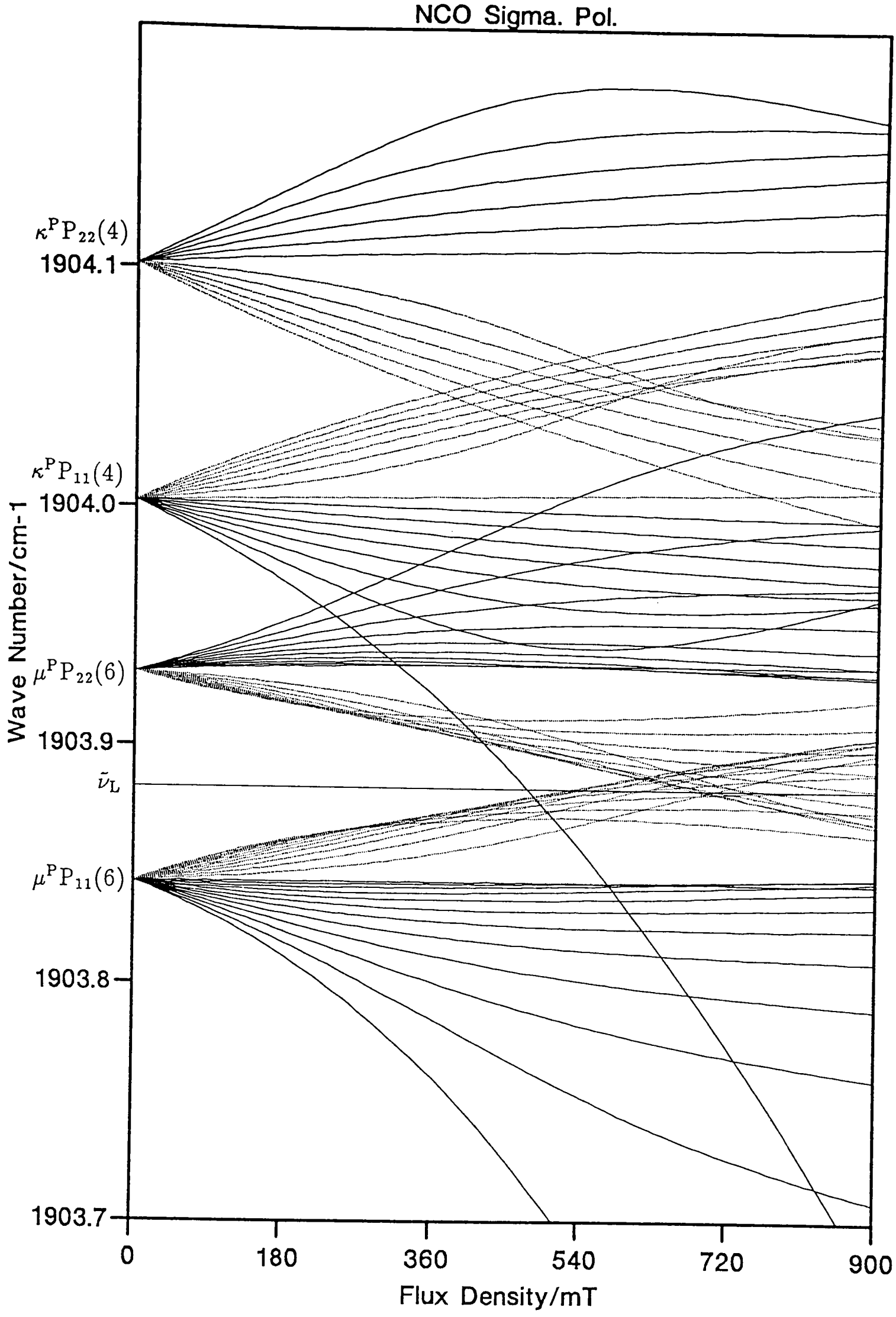

Figure VII.4: A Zeeman tuning diagram for the spectrum observed on the $P(8)_{9-8}$ laser line in σ polarisation. Solid and dotted lines indicate $\Delta M_J = +1$ and -1, respectively.

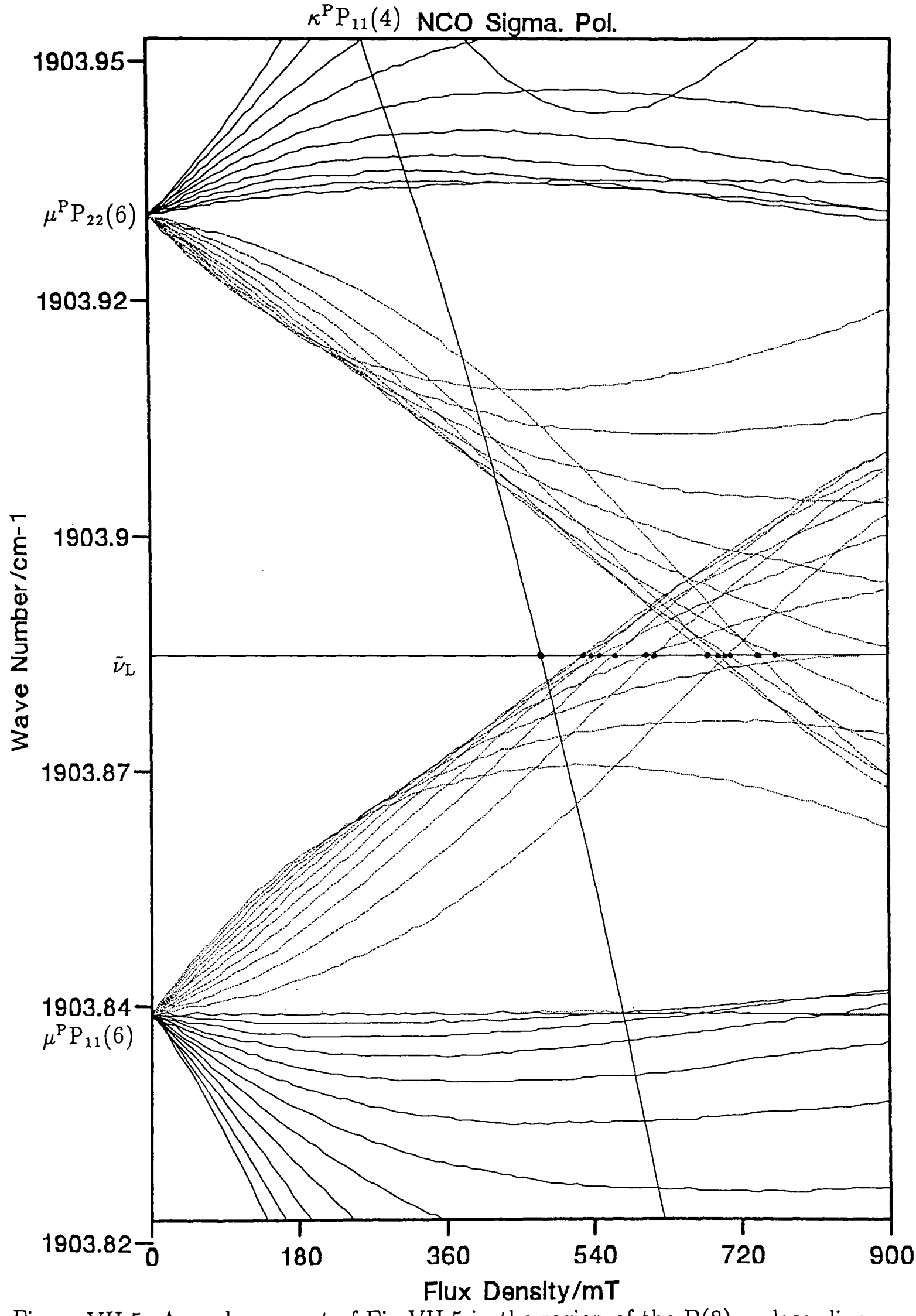

Figure VII.5: An enlargement of Fig.VII.5 in the region of the $P(8)_{9-8}$ laser line.

$1_0^1\,^2\Pi_{\frac{3}{2}}$ sub-band. There are two possible explanations for this. Firstly, modulation broadening effects and secondly the overlap of the three ^{14}N hyperfine components. The hyperfine structure was not resolved on any of the dips in this band, presumably because the dips are so broad that the turning points in the 2-f lineshape, which mark the three hyperfine components, are lost. Instead, the convolution of the three components produces a slight broadening compared with the dip for a single hyperfine component.

Spectrum on the $P(7)_{9-8}$ laser line

The assignments made above allowed a preliminary determination of the band origin and also $\alpha_{1,\epsilon\omega_2}$ and $\alpha_{1,B}$. Predictions made from the revised parameters immediately suggested a very important assignment for the spectrum shown in Fig.VII.6, recorded in π polarisation.

This spectrum was previously very misleading, since the intensities and positions of the three resonances approximately fit to the first three lines of a Q(7/2) transition in π polarisation. Such a transition can be observed if there is a large α_{1,g_L} due to a perturbation[1]. This explanation proved to be incorrect; there are three different transitions involved, as is shown by the Zeeman tuning diagram in Fig.VII.7. The fourth resonance, crossing the laser line at about 600 mT, was too weak to be seen.

The resonance at 445 mT is a blend of the $M_J = +3/2$ and $M_J = +1/2$ components of $\mu^{\rm P}Q_{12}(2)$. In order to reduce the measurement error for these fast tuning transitions, a simulation of the resonance was performed and the relative position of the two components was calculated as a function of the observed maximum and width of the lineshape.

Fig.VII.6 is a very important spectrum because it contains clear resonances from lines in both the $1_0^1 2_1^1\,\mu^2\Sigma$ and $1_0^1 2_1^1\,\kappa^2\Sigma$ bands. This enables the relative position of the two bands to be fixed accurately. The resonances are much faster tuning than any transitions in the $P = K + 1/2$ sub-bands of the unique states, which exhibit Hund's case (a) behaviour. The transitions in Fig.VII.6 are tuning at up to 3.1 MHzG^{-1}; the tuning rate of a free electron is $\pm 2\mu_B$, equivalent to ± 2.8 MHzG^{-1}. This gives a clear indication of orbital contributions to the Zeeman effect, though 'repulsion' between levels with the

[1]In the absence of a perturbation, the tuning rate for such a transition $\propto (g' - g'') \approx 0$.

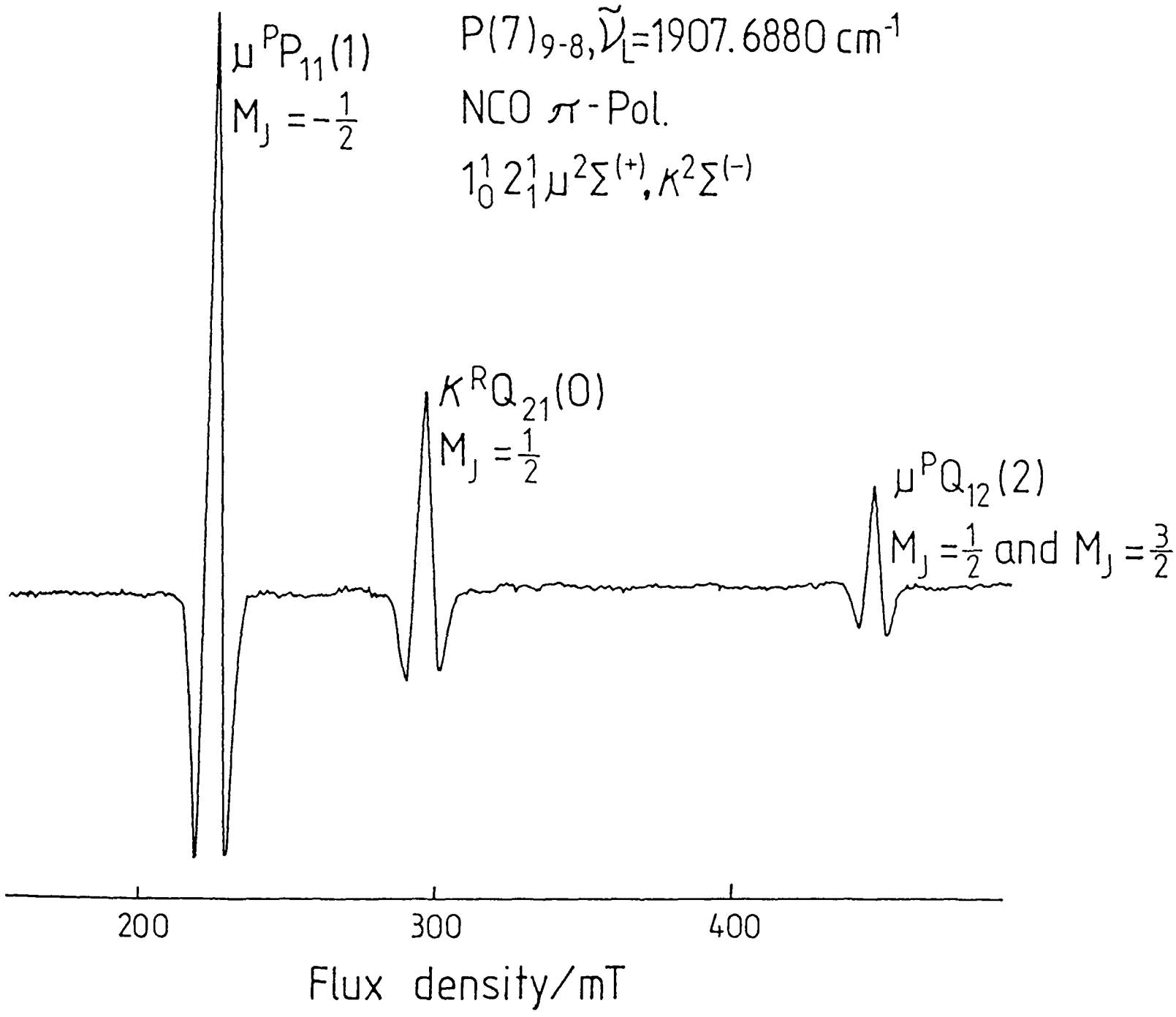

Figure VII.6: The spectrum observed on the $P(7)_{9-8}$ laser line in π polarisation. The resonances are all Doppler limited and very fast tuning. The spectrum was recorded with a 300 ms time constant, a peak-to-peak modulation of 1.5 mT and a scan rate of $60\,\mathrm{mT\,min^{-1}}$.

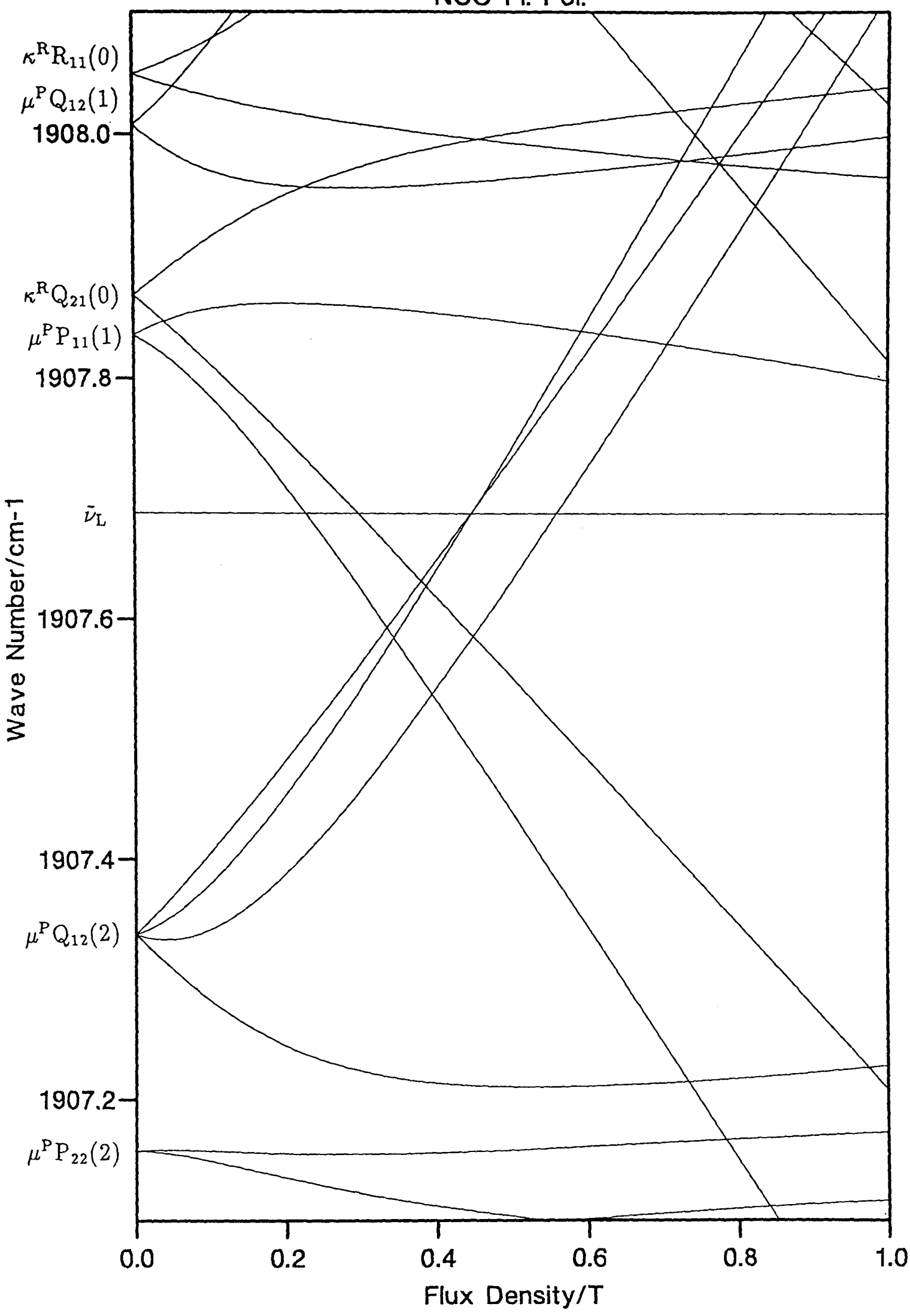

Figure VII.7: A Zeeman tuning diagram explaining the spectrum observed on the $P(7)_{9-8}$ laser line in π polarisation.

same M_J (or M_N, M_S) will also make a contribution.

Based on a revised, preliminary fit including these observations, the σ polarisation spectrum shown in Fig.VII.8 was also assigned. The features of this spectrum are very well modelled by the simulation shown in Fig.VII.9. In the simulation, there is a 'triplet' of transitions at about 460 mT; in the observed spectrum, the first and weakest component is lost in the baseline noise.

Whilst the visual agreement between the observed and simulated spectrum is excellent, the observed resonances in Fig.VII.8 occur at systematically lower fields than predicted. The π polarisation spectrum is quite well modelled, the systematic errors showing up mostly in the σ polarisation spectrum. This is an indication that the Zeeman effect is not being modelled quite correctly.

The data residuals in the analysis of the σ polarisation spectrum (see Table VII.3) suggested that the zero field frequency of $\mu^{\mathrm{P}}\mathrm{Q}_{12}(2)$ was about 116 MHz higher than calculated (when an average of the residuals of the components of this transition was taken), so its resonances should be about 4 mT higher than observed. In addition, the zero field frequency of $\mu^{\mathrm{P}}\mathrm{P}_{11}(1)$ appears to be 221 MHz lower than predicted (see Table VII.3), so its resonance should be 7.6 mT higher, and $\kappa^{\mathrm{R}}\mathrm{Q}_{21}(0)$ is predicted to be 71 MHz lower than observed, so its resonance should be 4 mT higher. These discrepancies are too small to question the assignments (other assignments were tried, by swapping $\kappa^{\mathrm{R}}\mathrm{Q}_{21}(0)$ and $\mu^{\mathrm{P}}\mathrm{P}_{11}(1)$, for example, and fitting resonances from these two transitions alone). Removing the $\mathrm{P}(8)_{9-8}$ spectrum from the fit did not aid this problem, nor did just fitting the μ or κ data separately. The problem appears to arise because the $F_1 - F_2$ interval is being measured by these transitions, *i.e.* the interval approximated by Hougen's $\gamma_{\mathrm{eff.}}$ in §IV.2.2, is not sufficient to describe the $F_1 - F_2$ interval. Varying Zeeman and spin-rotation parameters did not resolve the problem. Therefore, it appears that the problem might be due to some specific perturbation in one of the levels involved, or due to K-type resonance contributions to the Zeeman effect and zero field frequencies of the levels. Anharmonic contributions to the Renner-Teller effect might also be important. These possibilities are discussed later; the following paragraph considers the problem of field measurement errors with fast tuning resonances.

The very wide range of tuning rates in the $1^1_0 2^1_1\,\Sigma$ band contributed to problems in fitting the very fast tuning resonances. The Lamb-dip transitions are very slow tuning

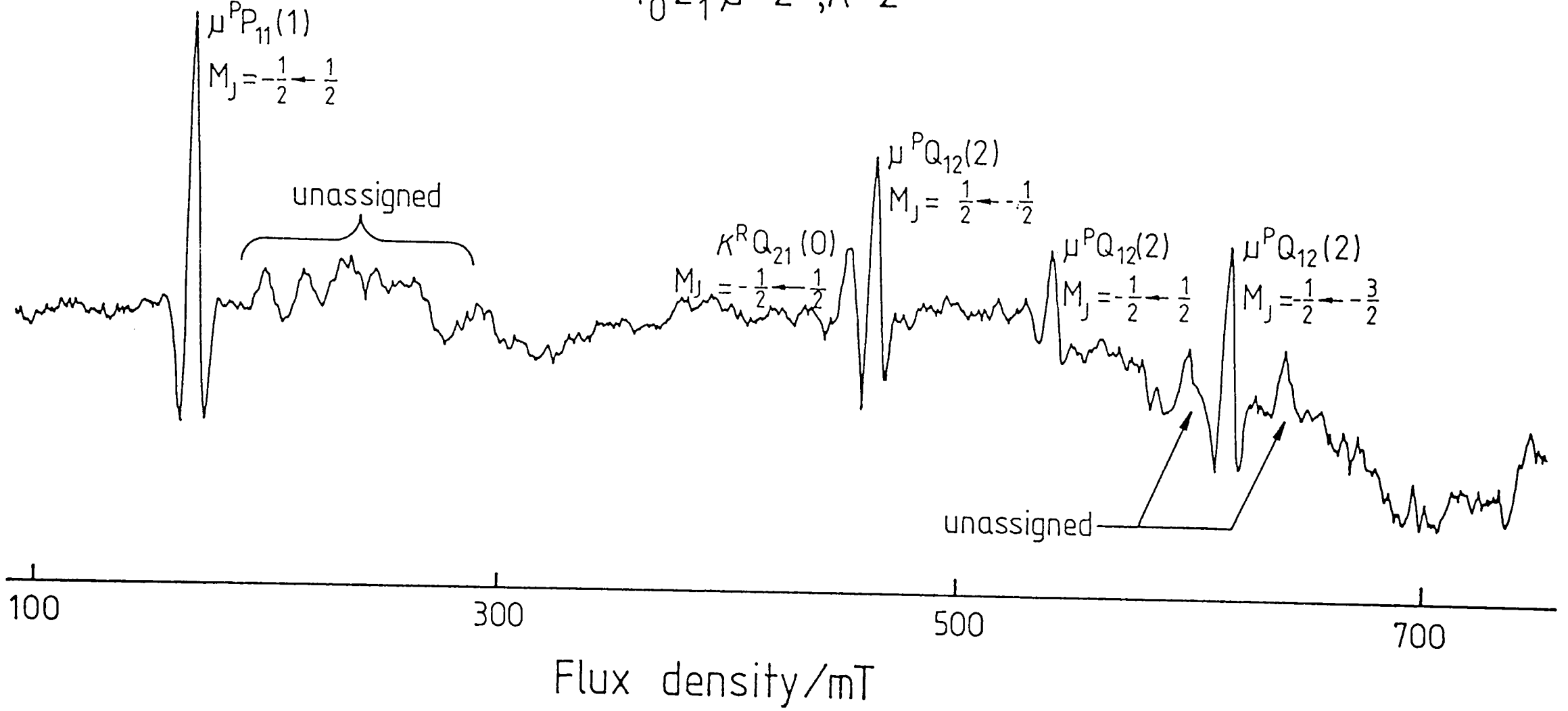

Figure VII.8: The spectrum observed on the $P(7)_{9-8}$ laser line in σ polarisation. The resonances are all Doppler limited. The spectrum was recorded with a 300 ms time constant, a peak-to-peak modulation of 3 mT and a scan rate of 75 mTmin^{-1}.

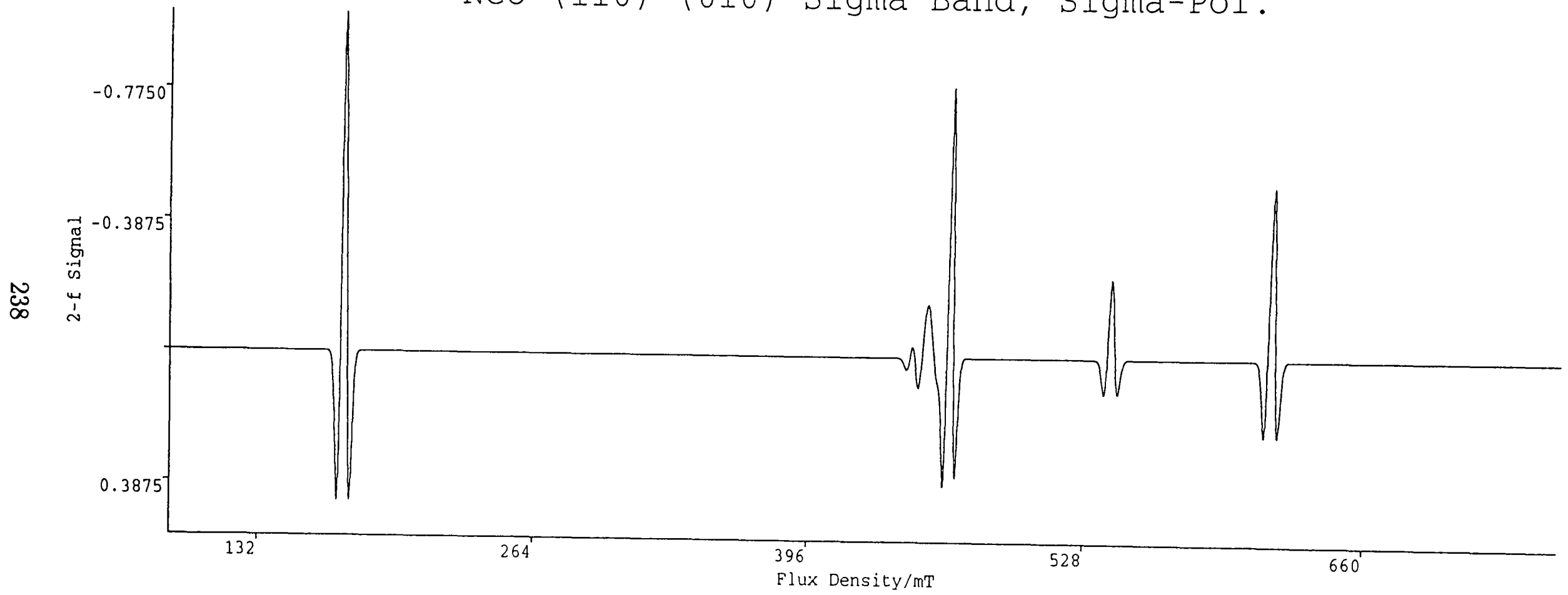

Figure VII.9: A simulation of the spectrum observed on the $P(7)_{9-8}$ laser line in σ polarisation. The weakest component of the three resonances at about 470 mT, is not observed in the spectrum (Fig.VII.8) because of the limited signal-to-noise.

and therefore, their measurement uncertainties are limited by long term laser stability and line broadening, rather than field measurement errors. The fast tuning resonances, however, are extremely sensitive to field measurement errors and this had to be borne in mind when assessing their uncertainties in the analysis. The appropriate uncertainties are discussed later.

Spectrum on the $P(12)_{8-7}$ laser line

Further predictions were made using the parameters obtained from fits of the assignments discussed above. In view of the large residuals in the analysis of some of the resonances on the $P(7)_{9-8}$ laser line, the fits were performed using the data on the $P(8)_{9-8}$ laser line only, or the $P(7)_{9-8}$ laser line only, or both. The predictions made from the parameters obtained in all three cases, were concurrent. They suggested that the $\mu^{R}R_{22}(6)$ transition produced the lower field progression in Fig.VII.10, followed by a similar progression from the $\kappa^{R}R_{22}(8)$ transition. A similar spectrum was predicted in both σ and π polarisations, in excellent agreement with observation. Before this assignment was made, another possibility was considered for this and other similar spectra. The obvious doublings in such spectra could also have been a K-type doubling rather than a spin-rotation splitting, from a band involving non-unique $^2\Pi$ vibronic states, particularly $1_0^1 2_2^2\,\mu, \kappa\,^2\Pi$.

Fig.VII.10 shows the σ polarisation spectrum. All the resonances appear as Lamb-dips, with almost no residual Doppler profile being visible. As can be seen, the point at which the progressions begin is somewhat uncertain, since the first few weak dips are probably lost in the baseline noise. For the μ transition, the primary progression comes to a definite end at about 290 mT, as predicted. The Zeeman components are then simply assigned by working backwards to lower field and comparing with the predictions. For the κ progression, the large noise above 1 T means that the identification of the end of the progression is less certain, though the last observed line was at 880 mT, within 10 mT of the prediction (which was sufficiently good to be unambiguous, given the spacing of lines).

It is necessary to be careful when making assignments to such progressions of slow tuning ($\sim 0.1\,\mathrm{MHzG^{-1}}$) transitions , because a small uncertainty in zero field frequency

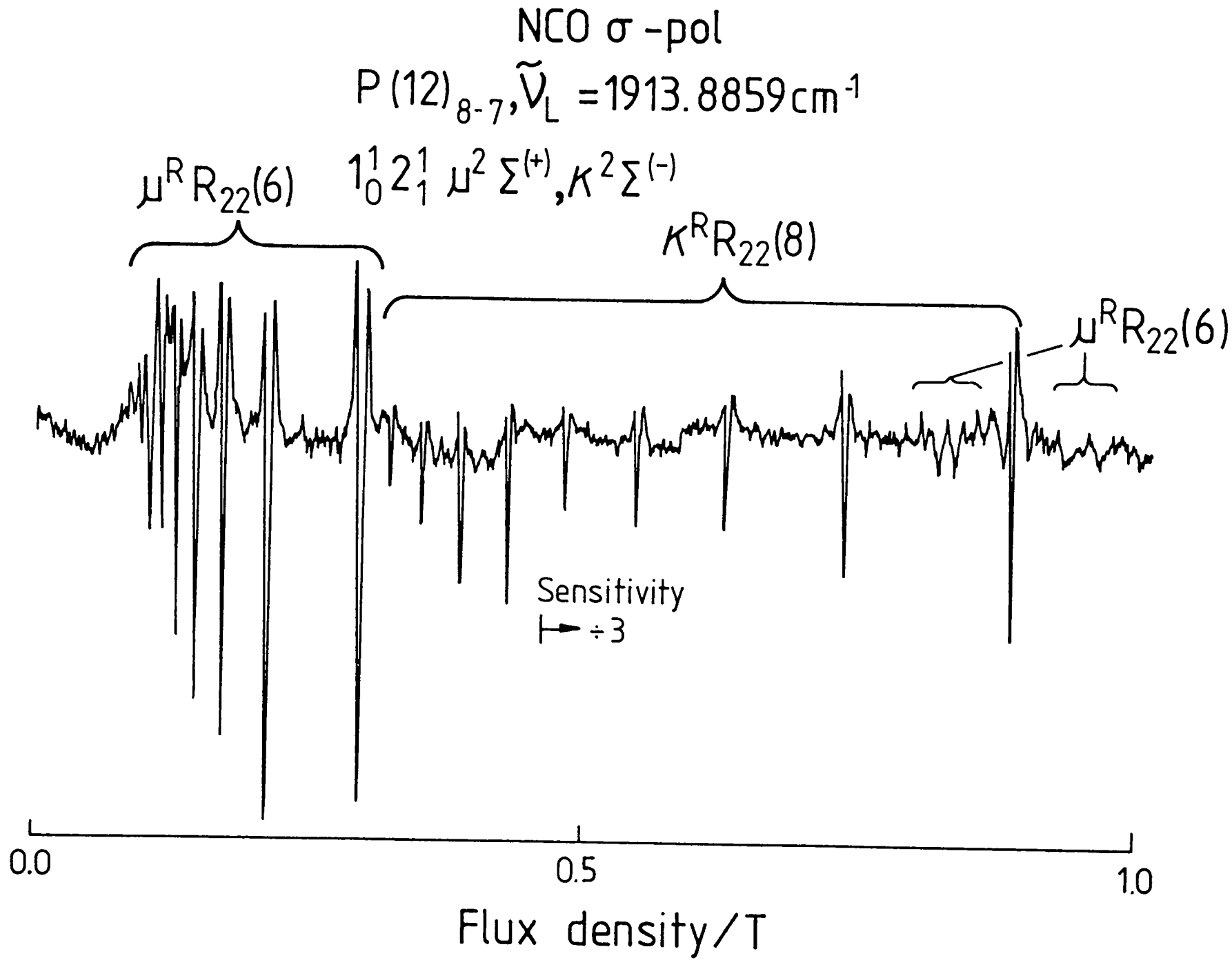

Figure VII.10: The spectrum observed on the $P(12)_{8-7}$ laser line in σ polarisation. The resonances are all Lamb-dips. The spectrum was recorded with a 300 ms time constant, a peak-to-peak modulation of 1.1 mT and a scan rate of 10 mTmin^{-1}.

($\Delta\nu$) can translate into a large uncertainty in flux density (ΔB), since

$$\Delta B = \frac{\Delta\nu}{\left(\frac{\partial\nu}{\partial B}\right)}. \tag{VII.3}$$

Above 1 T, the disagreement between predicted and calculated fields can be over 10 mT, but this is typically less than 1/3 of the spacing between adjacent resonances. At lower fields, the uncertainties and spacings of resonances can be comparable, so it is better to start the assignment with the high field resonances.

A procedure was established which helped to confirm whether the members of the progressions were assigned correctly. A plot was made of the spacing between adjacent members in the progression as a function of their resonant fields, using the empirical relation

$$B_n = m\,(B_n - B_{n-1}) + B_{n=1}. \tag{VII.4}$$

Here, $B_n > B_{n-1}$, $B_{n=1}$ is the resonant field of the lowest field member of the progression and m is the gradient. The assumptions are that at the beginning of the progression, the first term in Eq.(VII.4) becomes very small (<1 mT), as is the case in these progressions, and that the function is linear. The plots were in fact slightly but smoothly curved, easily allowing an extrapolation to give the resonant field for the first member of the progression. For the κ series the result of such a plot was in agreement with the predictions, *i.e.* that the 880 mT resonance is the end of the progression, and that the first few resonances (between the last two peaks of the primary μ progression) are lost in the baseline noise. This strategy was also used to aid the assignment of the π polarisation spectrum.

A Zeeman tuning diagram which explains the σ polarisation spectrum is shown in Fig.VII.11. The major progression for the μ transition involves Zeeman transitions with $\Delta M_J = -1$. Note however, that some transitions with $\Delta M_J = +1$ bend round to be resonant in the range 800–900 mT. These were indeed observed, as indicated in Fig.VII.10. It is the agreement of these subtle features with observation, which gives great confidence in the assignments made to the $1^1_0 2^1_1\,{}^2\Sigma$ band.

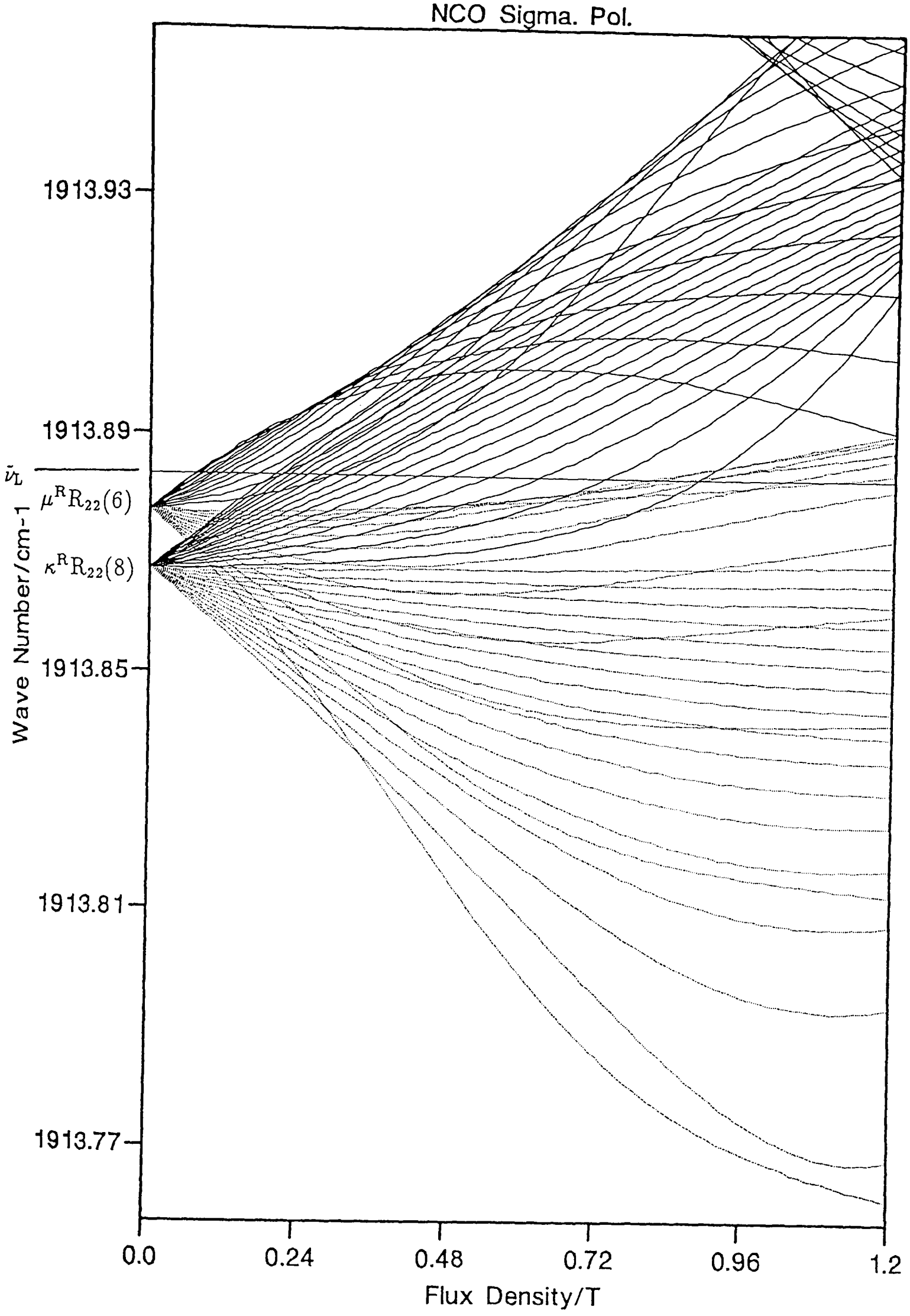

Figure VII.11: A Zeeman tuning diagram explaining the spectrum observed on the $P(12)_{8-7}$ laser line in σ polarisation. Solid and dashed lines indicate $\Delta M_J = +1$ and $\Delta M_J = -1$, respectively.

Spectrum on the $P(17)_{8-7}$ laser line

A single progression of Lamb-dips was observed on this laser line (not shown), extending from 0.76 T to 1.4 T. Again the progression was assigned with the aid of field predictions based on the preliminary analysis of the above data. Eq.(VII.4) was used to confirm the assignment of the Zeeman components. The spectrum is due to the $\mu^{R}R_{11}(13)$ transition; as predicted, resonances were only observed in σ polarisation. The first few resonances were obscured by the extremely strong resonance due to a component of the $1_0^1\,^2\Pi_{\frac{3}{2}}$ P(5/2) line at 742 mT.

A measurement of the width of one of these slow tuning ($\sim 0.16\,\mathrm{MHzG^{-1}}$) dips gave an experimentally limited linewidth of 17 MHz. This is a reliable estimate since the dip was 10 mT wide and unlikely to suffer from modulation broadening (peak-to-peak modulation $\sim$ 3mT). The tuning rates of these resonances are very similar to those for the $\mu^{R}R_{22}(6)$ resonances. Unlike a Hund's case (a) system, there is no strong dependence of the tuning rate on $1/J(J+1)$ (or $1/N(N+1)$ here). Given a close zero field coincidence with a CO laser line ($\sim 0.02\,\mathrm{cm^{-1}}$), high N transitions can be tuned into resonance more easily than low N ones. This is because the $F_1 - F_2$ splitting is larger ($\propto N+1$), and as discussed in §IV.2.3, this means that the transitions retain intensity up to higher fields.

Other assignments

The spectra recorded on the $P(13)_{8-7}$ laser line, see Figs.VI.3 and VI.5, show some very sharp, Doppler limited resonances. These were assigned, with the aid of field predictions and spectrum simulations, to components of the $\kappa^{R}Q_{21}(3)$, $\mu^{R}Q_{21}(1)$ and $\mu^{R}R_{11}(0)$ transitions. In Fig.VI.5, there are two resonances near to 450 mT; the broader one is the $M_J = -3/2$ component of $1_0^1 2_1^1\,^2\Delta_{\frac{5}{2}}$ R(5/2), and the much sharper one is the $M_J = -1/2$ component of $1_0^1 2_1^1\,\mu^2\Sigma\,^{R}R_{11}(0)$. The ratio of the widths of these two peaks is 3.3:1, compared with a ratio of 4.8:1 for the inverse of the resonant tuning rates. This indicates significant modulation broadening of the μ resonance for the conditions under which Fig.VI.5 was recorded. Other components were also predicted to be resonant with the laser line, but predictions suggested they would be much weaker (due to spin-decoupling), and indeed they were not observed.

Some of the resonances on the $P(14)_{8-7}$ laser line at $1905.8360\,\mathrm{cm^{-1}}$ were also as-

signed to the $1_0^1 2_1^1\,{}^2\Sigma$ bands. The π polarisation spectrum is shown on Fig.VII.12, and a Zeeman tuning diagram in Fig.VII.13. This diagram illustrates the complexity of performing LMR spectroscopy on the $^2\Sigma$ bands; at certain points there can be a very high density of Zeeman components from different transitions. This is why it was so difficult initially to make assignments to this band. The relative position of μ and κ transitions was somewhat uncertain, and obviously the appearance of the tuning diagram is very sensitive to this. The resonances observed on the $P(14)_{8-7}$ laser line are fast tuning and were not measured with sufficient precision to include in the fit. Table VII.2 details the approximate resonant flux densities of the transitions. Not every resonance in the tuning diagram was observed, due to the fact that some had become almost totally spin-decoupled and so lost intensity. The σ polarisation spectrum (not shown) is less 'clean' and has many unassigned resonances which appear as very broad, strong lines.

Table VII.2: Approximate flux densities ($\pm 3\,\mathrm{mT}$) of resonances assigned to the $1_0^1 2_2^1\,{}^2\Sigma$ bands. Observed on the $P(14)_{8-7}$ laser line at $1905.8360\,\mathrm{cm}^{-1}$.

Transition	$M_J'' \leftarrow M_J'$	$B_{\mathrm{obs.}}$ [T]	$(\frac{\partial\nu}{\partial B})$ [MHzG^{-1}]
$\kappa^{\mathrm{P}}Q_{12}(3)$	$\frac{5}{2} \leftarrow \frac{5}{2}$	0.8736	2.212
$\kappa^{\mathrm{P}}Q_{12}(2)$	$-\frac{3}{2} \leftarrow -\frac{3}{2}$	0.0749	−1.781
$\kappa^{\mathrm{P}}Q_{12}(2)$	$-\frac{3}{2} \leftarrow -\frac{1}{2}$	0.1101	−1.130
$\kappa^{\mathrm{P}}P_{11}(1)$	$-\frac{1}{2} \leftarrow -\frac{1}{2}$	0.9325	−2.079
$\kappa^{\mathrm{P}}P_{11}(1)$	$-\frac{1}{2} \leftarrow \frac{1}{2}$	0.9087	−1.881
$\mu^{\mathrm{P}}Q_{12}(4)$	$-\frac{7}{2} \leftarrow -\frac{7}{2}$	0.2190	−1.662
$\mu^{\mathrm{P}}O_{21}(3)$	$\frac{1}{2} \leftarrow \frac{1}{2}$	0.2568	−2.206
$\mu^{\mathrm{P}}O_{21}(3)$	$-\frac{1}{2} \leftarrow -\frac{1}{2}$	0.3233	−2.233
$\mu^{\mathrm{P}}P_{11}(3)$	$-\frac{5}{2} \leftarrow -\frac{5}{2}$	0.7851	−2.419

VII.2.2 Final Analysis

The data set for the final analysis comprised

1. The LMR observations reported here, except those on the $P(14)_{8-7}$ laser line. Lamb-dips were assigned an uncertainty of $2 \times 10^{-4}\,\mathrm{cm}^{-1}$, and Doppler limited

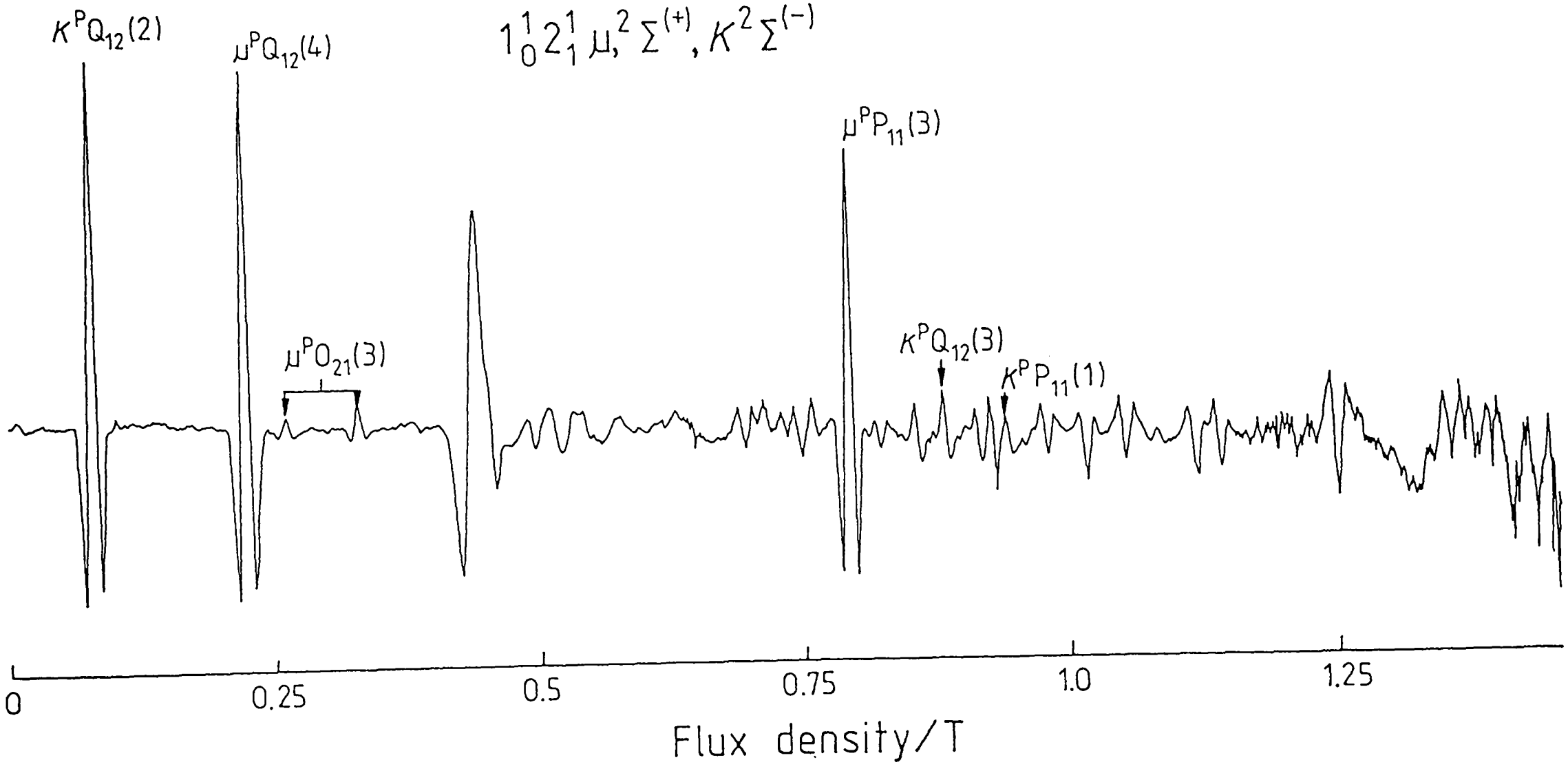

Figure VII.12: The spectrum recorded on the $P(14)_{8-7}$ laser line in π polarisation.

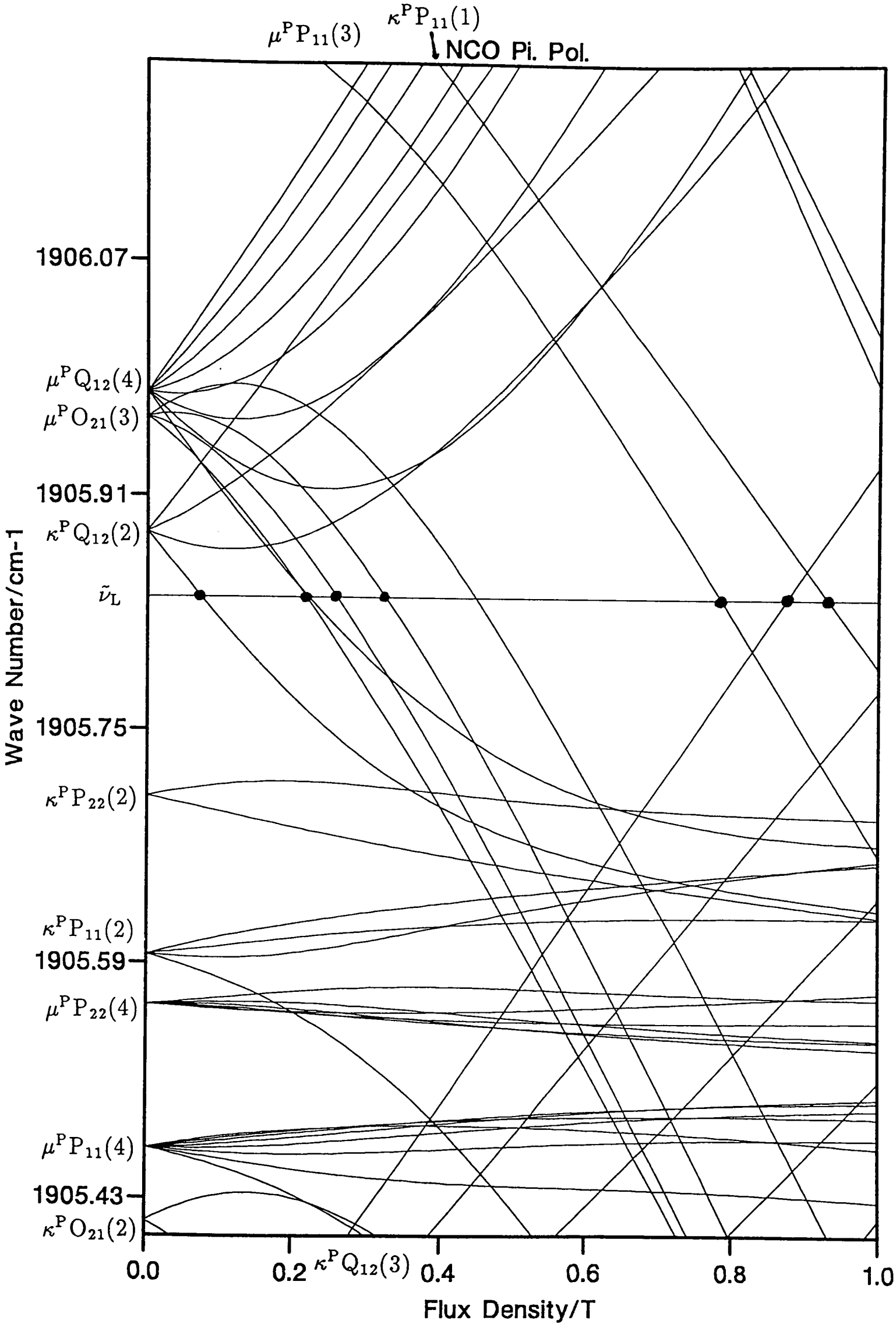

Figure VII.13: A Zeeman tuning diagram explaining some of the resonances observed on the $P(14)_{8-7}$ laser line in π polarisation. The observed resonances are marked with a •.

resonances an uncertainty of $6.67 \times 10^{-4}\,\mathrm{cm}^{-1}$, with the following exceptions. The two blended Lamb-dips on the $P(8)_{9-8}$ laser line were assigned an uncertainty of $3 \times 10^{-4}\,\mathrm{cm}^{-1}$ and assigned to the same resonant field. Some of the fast tuning $F_1 - F_2$ Doppler limited resonances were assigned a larger uncertainty of $1 \times 10^{-3}\,\mathrm{cm}^{-1}$, in order to account for the increased measurement errors of very fast tuning resonances.

2. Optical combination differences giving the $(010)\,\kappa^2\Sigma - (010)\,\mu^2\Sigma$ interval. These were calculated from the $(01^10)\,^2\Pi - (01^00)\,\mu^2\Sigma^{(+)}$ and $(01^10)\,^2\Pi - (01^00)\,\kappa^2\Sigma^{(-)}$ bands of the $\tilde{\mathrm{A}} \leftarrow \tilde{\mathrm{X}}$ transition observed by Bolman *et al.*[7]. These data allow a determination of $\epsilon\omega_2$ in the (010) level. Several series were used to form the combination differences, since many of the lines are blended. Each combination difference calculated from un-blended data was assigned an uncertainty of $10^{-2}\,\mathrm{cm}^{-1}$.

3. Microwave observations of the $(010)\,\mu^2\Sigma$ and $(010)\,\kappa^2\Sigma$ states, made by Kawaguchi *et al.*[3]. These fixed the lower state rotational and spin-rotational parameters. Each datum was assigned an uncertainty of 40 kHz.

The data were included in a multivariate fit to a set of parameters. A basis set with $\Delta v_2 = \pm 4$ and $\Delta J = \pm 6$ was found to be sufficient to model the Renner-Teller and Zeeman effects (using a larger basis had no significant effect). The overall standard deviation of the fit relative to the estimated experimental uncertainties was $\sigma_{\mathrm{rel.}} = 2.35$, Eq.(IV.67). The LMR data are given in Table VII.3, and the optical combination differences and microwave data in Appendix G. The standard deviations were 44 MHz for the LMR data, $0.026\,\mathrm{cm}^{-1}$ for the optical combination differences and 119 kHz for the microwave data. The value for the LMR data reflects the large residuals of the $F_1 - F_2$ transitions discussed earlier. An inspection of the residuals for the $F_1 - F_1$ and $F_2 - F_2$ transitions shows that they are typically 1–5 MHz, indicating an excellent fit. There is some systematic biasing of the residuals for the $F_1 - F_1, F_2 - F_2$ transitions, indicating that the Zeeman effect is well modelled but there is a slight failure to model the zero field wave number of the transition ($\sim$ 10 MHz error). The microwave data are modelled to well within the precision required for the LMR study, but the residuals are slightly larger than in the original study [3]. This is because Kawaguchi *et al.*[3] allowed the determination of separate centrifugal distortion constants for the μ and κ states; this

was not done here.

A total of 15 parameters were determined, with 14 constrained parameters; they are detailed in Table VII.4.

The constrained parameters were taken from the analysis of the $1_0^1 2_1^1\,{}^2\Delta$ band, except for g_l, which was estimated using Curl's relationship, Eq.(III.103). The parameters $A_{(000)}, \alpha_{2,A}, \epsilon\omega_2, \alpha_{1,\epsilon\omega_2}$ and α_{1,g_K} were obtained by iteration between the fits of the $1_0^1\,{}^2\Pi$, $1_0^1 2_1^1\,{}^2\Delta$ and $1_0^1 2_1^1\,{}^2\Sigma$ bands. The band origin determined here is the 'true' value for $1_0^1 2_1^1$, since the vibronic contribution involving g_K vanishes for $K = 0$. Therefore, this value was used in the fit of the $1_0^1 2_1^1\,{}^2\Delta$ band.

An attempt was made simultaneously to determine the values both of $A_{(010)}$ and $\epsilon\omega_{2,(010)}$. The value of A determined did not differ significantly from the value for the ${}^2\Delta$ band, was poorly determined and very highly correlated with several parameters, and did not improve the fit. Therefore, this parameter was constrained to the value determined for $1_0^1 2_1^1\,{}^2\Delta$.

The microwave data required the determination of $(\epsilon\omega_2)_D$, which accounts for anharmonic interactions between the (010), (110) and (011) ${}^2\Sigma$ states, §IV.3. The v_1 dependence of this parameter made a significant improvement to the fit of the LMR data at high N, indicating a 13% decrease in the anharmonic interactions upon excitation of the out-of-phase stretching mode. The parameter γ_D was also determined in the analysis, primarily from the microwave data. Kawaguchi *et al.*[3] did not determine this parameter.

The Zeeman parameters were not varied in the fit, $\Delta g_L^{(1)}$ being constrained to the value for the ${}^2\Delta$ band; this parameter is expected to be K independent. Attempts at improving the fit of the $F_1 - F_2$ data by varying $g_L^{(0)}, g_S, \Delta g_L^{(1)}, g_r$ and g_l and their v_1 dependences, were not successful. In particular, the fit was not very sensitive to variation of $\Delta g_L^{(1)}$, giving justification for its being constrained.

Table VII.3: Mid-infrared LMR observations of the $1_0^1 2_1^1\,\mu, \kappa^2\Sigma$ bands of NCO $(\tilde{X})^2\Pi$ included in the fit of the $^2\Sigma$ bands.

Transition[a]	$M'_J \leftarrow M''_J$	$\tilde{\nu}_L$[b] [cm^{-1}]	$B_{obs.}$ [T]	$\frac{\partial\nu}{\partial B}$[c] [MHzG^{-1}]	$(o-c)$[d,e] [10^{-5}cm^{-1}]
$\mu^R R_{11}(13)$	$-\frac{7}{2} \leftarrow -\frac{5}{2}$	1918.9787	0.7659	−0.141	− 5
$\mu^R R_{11}(13)$	$-\frac{9}{2} \leftarrow -\frac{7}{2}$	1918.9787	0.7830	−0.145	− 3
$\mu^R R_{11}(13)$	$-\frac{11}{2} \leftarrow -\frac{9}{2}$	1918.9787	0.8031	−0.148	− 3
$\mu^R R_{11}(13)$	$-\frac{13}{2} \leftarrow -\frac{11}{2}$	1918.9787	0.8273	−0.151	− 4
$\mu^R R_{11}(13)$	$-\frac{15}{2} \leftarrow -\frac{13}{2}$	1918.9787	0.8580	−0.154	0
$\mu^R R_{11}(13)$	$-\frac{17}{2} \leftarrow -\frac{15}{2}$	1918.9787	0.8942	−0.157	− 1
$\mu^R R_{11}(13)$	$-\frac{19}{2} \leftarrow -\frac{17}{2}$	1918.9787	0.9400	−0.160	0
$\mu^R R_{11}(13)$	$-\frac{21}{2} \leftarrow -\frac{19}{2}$	1918.9787	0.9967	−0.164	− 9
$\mu^R R_{11}(13)$	$-\frac{23}{2} \leftarrow -\frac{21}{2}$	1918.9787	1.0754	−0.170	− 6
$\mu^R R_{11}(13)$	$-\frac{25}{2} \leftarrow -\frac{23}{2}$	1918.9787	1.1877	−0.180	− 3
$\mu^R R_{11}(13)$	$-\frac{27}{2} \leftarrow -\frac{25}{2}$	1918.9787	1.3746	−0.207	11
$\kappa^R R_{22}(8)$	$\frac{13}{2} \leftarrow \frac{13}{2}$	1913.8859	0.4731	0.096	− 23
$\kappa^R R_{22}(8)$	$\frac{11}{2} \leftarrow \frac{11}{2}$	1913.8859	0.5293	0.088	− 15
$\kappa^R R_{22}(8)$	$\frac{9}{2} \leftarrow \frac{9}{2}$	1913.8859	0.6033	0.080	− 21
$\kappa^R R_{22}(8)$	$\frac{7}{2} \leftarrow \frac{7}{2}$	1913.8859	0.6903	0.074	− 19
$\kappa^R R_{22}(8)$	$\frac{5}{2} \leftarrow \frac{5}{2}$	1913.8859	0.7951	0.069	− 18
$\kappa^R R_{22}(8)$	$\frac{3}{2} \leftarrow \frac{3}{2}$	1913.8859	0.9157	0.066	− 12
$\kappa^R R_{22}(8)$	$\frac{1}{2} \leftarrow \frac{1}{2}$	1913.8859	1.0501	0.066	− 7
$\kappa^R R_{22}(8)$	$-\frac{1}{2} \leftarrow -\frac{1}{2}$	1913.8859	1.1864	0.069	1
$\kappa^R R_{22}(8)$	$-\frac{3}{2} \leftarrow -\frac{3}{2}$	1913.8859	1.3099	0.077	15
$\kappa^R R_{22}(8)$	$-\frac{5}{2} \leftarrow -\frac{5}{2}$	1913.8859	1.4136	0.090	25
$\kappa^R R_{22}(8)$	$-\frac{7}{2} \leftarrow -\frac{7}{2}$	1913.8859	1.4882	0.110	44
$\kappa^R R_{22}(8)$	$-\frac{1}{2} \leftarrow \frac{1}{2}$	1913.8859	0.3167	0.160	7
$\kappa^R R_{22}(8)$	$-\frac{3}{2} \leftarrow -\frac{1}{2}$	1913.8859	0.3475	0.152	− 1
$\kappa^R R_{22}(8)$	$-\frac{5}{2} \leftarrow -\frac{3}{2}$	1913.8859	0.3834	0.144	− 5
$\kappa^R R_{22}(8)$	$-\frac{7}{2} \leftarrow -\frac{5}{2}$	1913.8859	0.4257	0.138	− 5
$\kappa^R R_{22}(8)$	$-\frac{9}{2} \leftarrow -\frac{7}{2}$	1913.8859	0.4780	0.133	− 9
$\kappa^R R_{22}(8)$	$-\frac{11}{2} \leftarrow -\frac{9}{2}$	1913.8859	0.5371	0.129	13
$\kappa^R R_{22}(8)$	$-\frac{13}{2} \leftarrow -\frac{11}{2}$	1913.8859	0.6192	0.132	10
$\kappa^R R_{22}(8)$	$-\frac{15}{2} \leftarrow -\frac{13}{2}$	1913.8859	0.7270	0.143	7

Table VII.3 continued:

Transition[(a)]	$M'_J \leftarrow M''_J$	$\tilde{\nu}_{\mathrm{L}}$[(b)] [cm^{-1}]	$B_{\mathrm{obs.}}$ [T]	$\frac{\partial\nu}{\partial B}$[(c)] [$\mathrm{MHzG}^{-1}$]	$(o-c)$[(d,e)] [$10^{-5}\mathrm{cm}^{-1}$]
$\kappa^{\mathrm{R}}\mathrm{R}_{22}(8)$	$-\frac{17}{2} \leftarrow -\frac{15}{2}$	1913.8859	0.8797	0.182	11
$\mu^{\mathrm{R}}\mathrm{R}_{22}(6)$	$\frac{11}{2} \leftarrow \frac{11}{2}$	1913.8859	0.1744	0.083	− 12
$\mu^{\mathrm{R}}\mathrm{R}_{22}(6)$	$\frac{9}{2} \leftarrow \frac{9}{2}$	1913.8859	0.1874	0.087	− 8
$\mu^{\mathrm{R}}\mathrm{R}_{22}(6)$	$\frac{7}{2} \leftarrow \frac{7}{2}$	1913.8859	0.2062	0.090	− 11
$\mu^{\mathrm{R}}\mathrm{R}_{22}(6)$	$\frac{5}{2} \leftarrow \frac{5}{2}$	1913.8859	0.2283	0.093	− 11
$\mu^{\mathrm{R}}\mathrm{R}_{22}(6)$	$\frac{3}{2} \leftarrow \frac{3}{2}$	1913.8859	0.2572	0.096	− 12
$\mu^{\mathrm{R}}\mathrm{R}_{22}(6)$	$\frac{1}{2} \leftarrow \frac{1}{2}$	1913.8859	0.2941	0.099	− 9
$\mu^{\mathrm{R}}\mathrm{R}_{22}(6)$	$-\frac{1}{2} \leftarrow -\frac{1}{2}$	1913.8859	0.3457	0.101	− 8
$\mu^{\mathrm{R}}\mathrm{R}_{22}(6)$	$-\frac{3}{2} \leftarrow -\frac{3}{2}$	1913.8859	0.4226	0.105	− 13
$\mu^{\mathrm{R}}\mathrm{R}_{22}(6)$	$-\frac{5}{2} \leftarrow -\frac{5}{2}$	1913.8859	0.5411	0.107	− 13
$\mu^{\mathrm{R}}\mathrm{R}_{22}(6)$	$-\frac{7}{2} \leftarrow -\frac{7}{2}$	1913.8859	0.7528	0.105	− 17
$\mu^{\mathrm{R}}\mathrm{R}_{22}(6)$	$\frac{3}{2} \leftarrow \frac{5}{2}$	1913.8859	0.0794	0.208	47
$\mu^{\mathrm{R}}\mathrm{R}_{22}(6)$	$\frac{1}{2} \leftarrow \frac{3}{2}$	1913.8859	0.0874	0.199	37
$\mu^{\mathrm{R}}\mathrm{R}_{22}(6)$	$-\frac{1}{2} \leftarrow \frac{1}{2}$	1913.8859	0.0962	0.190	32
$\mu^{\mathrm{R}}\mathrm{R}_{22}(6)$	$-\frac{3}{2} \leftarrow -\frac{1}{2}$	1913.8859	0.1067	0.181	29
$\mu^{\mathrm{R}}\mathrm{R}_{22}(6)$	$-\frac{5}{2} \leftarrow -\frac{3}{2}$	1913.8859	0.1203	0.171	25
$\mu^{\mathrm{R}}\mathrm{R}_{22}(6)$	$-\frac{7}{2} \leftarrow -\frac{5}{2}$	1913.8859	0.1383	0.159	21
$\mu^{\mathrm{R}}\mathrm{R}_{22}(6)$	$-\frac{9}{2} \leftarrow -\frac{7}{2}$	1913.8859	0.1637	0.147	20
$\mu^{\mathrm{R}}\mathrm{R}_{22}(6)$	$-\frac{11}{2} \leftarrow -\frac{9}{2}$	1913.8859	0.2055	0.132	14
$\mu^{\mathrm{R}}\mathrm{R}_{22}(6)$	$-\frac{13}{2} \leftarrow -\frac{11}{2}$	1913.8859	0.2902	0.116	6
$\mu^{\mathrm{R}}\mathrm{R}_{22}(6)$	$\frac{9}{2} \leftarrow \frac{7}{2}$	1913.8859	0.8084	0.055	− 7
$\mu^{\mathrm{R}}\mathrm{R}_{22}(6)$	$\frac{7}{2} \leftarrow \frac{5}{2}$	1913.8859	0.8238	0.063	− 8
$\mu^{\mathrm{R}}\mathrm{R}_{22}(6)$	$\frac{5}{2} \leftarrow \frac{3}{2}$	1913.8859	0.8894	0.068	− 4
$\kappa^{\mathrm{R}}\mathrm{Q}_{21}(3)$	$-\frac{7}{2} \leftarrow -\frac{7}{2}$	1909.8775	0.1132[(f)]	2.053	111
$\kappa^{\mathrm{R}}\mathrm{Q}_{21}(3)$	$\frac{3}{2} \leftarrow \frac{3}{2}$	1909.8775	0.1416[(f)]	−2.291	−225
$\mu^{\mathrm{R}}\mathrm{Q}_{21}(1)$	$\frac{1}{2} \leftarrow \frac{1}{2}$	1909.8775	0.1786[(f)]	−2.400	−234
$\mu^{\mathrm{R}}\mathrm{Q}_{21}(1)$	$\frac{1}{2} \leftarrow \frac{3}{2}$	1909.8775	0.1505[(g)]	−2.254	−505
$\mu^{\mathrm{R}}\mathrm{Q}_{21}(1)$	$-\frac{1}{2} \leftarrow \frac{1}{2}$	1909.8775	0.1972[(f)]	−2.353	−424
$\mu^{\mathrm{R}}\mathrm{Q}_{21}(1)$	$-\frac{3}{2} \leftarrow -\frac{1}{2}$	1909.8775	0.3208[(f)]	−2.182	−355
$\mu^{\mathrm{R}}\mathrm{R}_{11}(0)$	$-\frac{1}{2} \leftarrow -\frac{1}{2}$	1909.8775	0.4726[(f)]	2.812	− 43

Table VII.3 continued:

Transition[a]	$M'_J \leftarrow M''_J$	$\tilde{\nu}_L$[b] [cm^{-1}]	$B_{obs.}$ [T]	$\frac{\partial\nu}{\partial B}$[c] [$MHzG^{-1}$]	$(o-c)$[d,e] [$10^{-5}cm^{-1}$]
$\kappa^R Q_{21}(0)$	$\frac{1}{2} \leftarrow \frac{1}{2}$	1907.6880	0.2941[g]	−1.973	− 21
$\kappa^R Q_{21}(0)$	$-\frac{1}{2} \leftarrow \frac{1}{2}$	1907.6880	0.4489[g]	−1.691	−236
$\mu^P P_{11}(1)$	$-\frac{1}{2} \leftarrow -\frac{1}{2}$	1907.6880	0.2235[g]	−2.551	−144
$\mu^P Q_{12}(2)$	$\frac{3}{2} \leftarrow \frac{3}{2}$	1907.6880	0.4447[f]	2.578	− 15
$\mu^P Q_{12}(2)$	$\frac{1}{2} \leftarrow \frac{1}{2}$	1907.6880	0.4456[f]	3.052	− 27
$\mu^P P_{11}(1)$	$-\frac{1}{2} \leftarrow \frac{1}{2}$	1907.6880	0.1653[g]	−2.917	−738
$\mu^P Q_{12}(2)$	$\frac{1}{2} \leftarrow -\frac{1}{2}$	1907.6880	0.4597[g]	3.115	430
$\mu^P Q_{12}(2)$	$-\frac{1}{2} \leftarrow \frac{1}{2}$	1907.6880	0.5359[g]	2.723	400
$\mu^P Q_{12}(2)$	$-\frac{1}{2} \leftarrow -\frac{3}{2}$	1907.6880	0.6127[g]	2.771	326
$\kappa^P P_{11}(4)$	$-\frac{7}{2} \leftarrow -\frac{7}{2}$	1903.8822	0.6233[g]	−1.242	78
$\kappa^P P_{11}(4)$	$-\frac{7}{2} \leftarrow -\frac{5}{2}$	1903.8822	0.4803[g]	−1.125	142
$\mu^P P_{11}(6)$	$-\frac{1}{2} \leftarrow -\frac{3}{2}$	1903.8822	0.5268[h]	0.208	− 7
$\mu^P P_{11}(6)$	$\frac{1}{2} \leftarrow -\frac{1}{2}$	1903.8822	0.5268[h]	0.184	6
$\mu^P P_{11}(6)$	$-\frac{3}{2} \leftarrow -\frac{5}{2}$	1903.8822	0.5381	0.227	− 4
$\mu^P P_{11}(6)$	$\frac{3}{2} \leftarrow \frac{1}{2}$	1903.8822	0.5489	0.151	− 8
$\mu^P P_{11}(6)$	$-\frac{5}{2} \leftarrow -\frac{7}{2}$	1903.8822	0.5650	0.240	− 4
$\mu^P P_{11}(6)$	$\frac{5}{2} \leftarrow \frac{3}{2}$	1903.8822	0.6053[g]	0.104	− 18
$\mu^P P_{11}(6)$	$-\frac{7}{2} \leftarrow -\frac{9}{2}$	1903.8822	0.6133	0.251	− 1
$\mu^P P_{11}(6)$	$-\frac{9}{2} \leftarrow -\frac{11}{2}$	1903.8822	0.7023	0.269	− 2
$\mu^P P_{22}(6)$	$-\frac{5}{2} \leftarrow -\frac{7}{2}$	1903.8822	0.6855	−0.213	8
$\mu^P P_{22}(6)$	$-\frac{7}{2} \leftarrow -\frac{9}{2}$	1903.8822	0.6947	−0.245	4
$\mu^P P_{22}(6)$	$-\frac{9}{2} \leftarrow -\frac{11}{2}$	1903.8822	0.7437	−0.282	6
$\mu^P P_{22}(6)$	$-\frac{1}{2} \leftarrow -\frac{3}{2}$	1903.8822	0.7687	−0.132	7

[a] Transitions are denoted $^{\Delta N}\Delta J_{F'_i F''_i}(N'')$.

[b] $^{12}C^{16}O$ laser wave number.

[c] Tuning rate at resonance.

[d] Residuals of the fit.

[e] Unless indicated otherwise, measurement made on a Lamb-dip and assigned an uncertainty of $2 \times 10^{-4}\,cm^{-1}$.

[f] Doppler limited measurement assigned an uncertainty of $1 \times 10^{-3}\,cm^{-1}$.

[g] Doppler limited measurement assigned an uncertainty of $6.67 \times 10^{-4}\,cm^{-1}$.

[h] Blended Lamb-dip measurement assigned an uncertainty of $3 \times 10^{-4}\,cm^{-1}$.

Table VII.4: Parameters from the analysis of the $1_0^1 2_1^1\,\mu,\kappa\,^2\Sigma$ bands of NCO ($\tilde{X}^2\Pi$).

Parameter	Value [cm^{-1}]	Correlation[a]	Kawaguchi *et al.*[3]
ν_0	1907.84852(44)[b]	56.087	
ω_2	534.063[c]		
ω_3	1260.22[c]		
$\epsilon\omega_{2,(010)}$	−76.7249(23)	59.253	
$\alpha_{1,\epsilon\omega_2}$	1.29141(49)	54.068	
$(\epsilon\omega_2)_{D,(010)}$	$0.37524(37) \times 10^{-3}$	72.408	
$\alpha_{1,(\epsilon\omega_2)_{D,(010)}}$	$-0.487(54) \times 10^{-4}$	78.913	
g_K	3.7672[c]		
α_{1,g_K}	−0.15525[c]		
$A_{(000)}$	−96.0881[c]		
$\alpha_{1,A}$	−1.38713[c]		
$\alpha_{2,A}$	0.3635[c]		
$A_{D,(010)}$	$0.1121(12) \times 10^{-3}$	70.967	
$B_{(010)}$	0.39045284(11)	8.234	0.390480482(76)
$\alpha_{1,B}$	$-0.32478(49) \times 10^{-2}$	79.831	
D_{010}	$0.1538(14) \times 10^{-6}$	7.200	$0.1544(16) \times 10^{-6}$
H_{010}	0.101×10^{-11}[c]		
$\gamma_{(010)}$	$-0.19668(67) \times 10^{-2}$	60.695	$-0.18259(11) \times 10^{-2}$
$\gamma_{D,(010)}$	$0.318(19) \times 10^{-6}$	3.605	
$a_{(010)}$	$0.21342(70) \times 10^{-2}$	1.168	$0.21168(46) \times 10^{-2}$
$b_{(010)}$	$0.9846(50) \times 10^{-3}$	2.386	$0.9827(63) \times 10^{-3}$
$(b+c)_{(010)}$	$-0.565(10) \times 10^{-3}$	2.217	$-0.5604(80) \times 10^{-3}$
$eQq_{0,(010)}$	$-0.665(43) \times 10^{-4}$	1.122	$-0.677(37) \times 10^{-3}$
$g_{S,(010)}$	2.002099[c]		
$g_{L,(010)}^{(0)}$	0.999890[c]		
$\Delta g_{L,(010)}^{(1)}$	-0.67765×10^{-2}[c]		
$g_{r,(010)}$	-0.532×10^{-4}[c]		
$g_{l,(010)}$	0.2518637×10^{-2}[c]		
$g_{N,(010)}$	0.4037607[c]		

[a] The correlation parameter $\kappa_i = (\chi^{-1})_{ii}$, where χ is the matrix of correlation coefficients.

[b] The numbers in parentheses are one standard deviation of the parameter in units of the least significant decimal place.

[c] Parameter constrained to this value (see text).

VII.3 Discussion of the $1_0^1 2_1^1\,{}^2\Sigma$ Bands

VII.3.1 General

The first observation and analysis of vibration-rotation transitions in the $1_0^1 2_1^1\,\mu^2\Sigma^{(+)}$ and $1_0^1 2_1^1\,\kappa^2\Sigma^{(-)}$ bands has been accomplished successfully. The analysis of this system required several factors fully to be taken into account, viz

- Modelling of the energy level structure and Zeeman effect behaviour of the $^2\Sigma$ bands required an explicit model of the Renner-Teller effect to be constructed. The energy levels exhibit the complications of orbital contributions to the magnetic moment and spin-decoupling effects.

- The Zeeman effects in the $^2\Sigma$ levels are highly non-linear, because the separation of adjacent rotational levels is comparable with the Zeeman energy.

- The $F_1 - F_1$ and $F_2 - F_2$ resonances appear as strongly saturated Lamb-dips, since they are slow tuning and have large line strength factors. The $F_1 - F_2$ transitions lose intensity with field due to spin-decoupling; they are predominantly observed at low fields as sharp, Doppler limited resonances.

- The $1_0^1 2_1^1\,{}^2\Sigma$ transitions fall in a region overlapped by several hot-bands of NCO, for example $1_0^1 2_1^1\,{}^2\Delta$. Therefore, many of the LMR spectra result from a superposition of resonances from transitions in different bands, some of whose character is still unknown.

- Adjacent rotational transitions in both the μ and κ $1_0^1 2_1^1\,{}^2\Sigma$ bands can be resonant on the same laser line. Taken together with the above point, this makes the recognition of any predicted patterns very difficult.

VII.3.2 Band Origin and Renner-Teller Parameters

The band origin obtained, $1907.84852(44)\,\mathrm{cm}^{-1}$ is about $1\,\mathrm{cm}^{-1}$ lower than the estimated value used initially to search for assignments to this band. Recalling Eq.(VII.1), the effective band origins are $1908.6579\,\mathrm{cm}^{-1}$ for $1_0^1 2_1^1\,\mu^2\Sigma^{(+)}$ and $1907.2231\,\mathrm{cm}^{-1}$ for $1_0^1 2_1^1\,\kappa^2\Sigma^{(-)}$. These values compare with an effective band origin of $1907.8140\,\mathrm{cm}^{-1}$ for

$1_0^1 2_1^1\,{}^2\Delta$. The effective band origins for the $1_0^1\,{}^2\Pi$ and $1_0^1 2_2^2\,{}^2\Phi$ bands are $1921.2553\,\mathrm{cm}^{-1}$ and $1894.0660\,cm^{-1}$, respectively.

Considering the parameters in Table VII.4, the Renner-Teller parameter $\epsilon\omega_2$ decreases upon excitation of the out-of-phase stretching mode, from $-76.7249(23)\,\mathrm{cm}^{-1}$ to $-75.4335(28)\,\mathrm{cm}^{-1}$, a decreases of 1.7%. From these, values of $\epsilon_{(010)} - 0.143662(13)$ and $\epsilon_{(110)} = -0.141245(13)$ are calculated. The vibronic parameter g_K also decreases, from $3.7672\,\mathrm{cm}^{-1}$ to $3.6120\,\mathrm{cm}^{-1}$ (determined for $1_0^1 2_1^1\,{}^2\Delta$), a change of 4.1%, but note that only the change in g_K is really determined here, since the lower state value was constrained in the fit. The changes in $\epsilon\omega_2$ and g_K are in the same sense, in that both indicate a smaller net vibronic interaction in the (110) vibrational level than in the (010) level. The g_K parameter is purely non-adiabatic and α_{1,g_K} indicates a decrease in Herzberg-Teller coupling to remote electronic states upon excitation of the ν_1 vibrational mode. The parameter $\epsilon\omega_2$ has both adiabatic and non-adiabatic contributions; it shows a smaller relative change than g_K, indicating that the adiabatic contribution is affected less than the non-adiabatic one by excitation of the ν_1 vibrational mode. These trends are in line with an increased localisation of the unpaired electron on the terminal atoms as the ν_1 vibrational mode is excited. This is because if the unpaired electron is localised on the terminal atoms, it will be less affected by the the bending mode, which has greatest amplitude at the centre of mass of the molecule.

A comparable diode laser study of $BO_2(\tilde{X}^2\Pi_g)$ was made by Kawaguchi *et al.*[8]. Using constrained values of $\epsilon\omega_2 = -86.4\,\mathrm{cm}^{-1}$ and $\epsilon = -0.19$, they determined $\alpha_{3,\epsilon\omega_2} = 7.8218(6)\,\mathrm{cm}^{-1}$ and $\alpha_{3,g_K} = -0.1825\,\mathrm{cm}^{-1}$. The change in $\epsilon\omega_2$ is in the same sense as that determined for NCO.

In other studies of NCO, Bolman *et al.*[7] determined $\epsilon\omega_2 = -76.91(2)\,\mathrm{cm}^{-1}$, $\epsilon = -0.144(1)$ and $g_K = 3.64\,\mathrm{cm}^{-1}$. The values determined by Hemmerling and Vervloet [9] were $\epsilon\omega_2 = -76.062(24)\,\mathrm{cm}^{-1}$. Sears *et al.*[10] determined $\epsilon\omega_2 = -78.370(29)\,\mathrm{cm}^{-1}$, $g_K = 3.7672(87)\,\mathrm{cm}^{-1}$ and $\epsilon = -0.146743(63)$. The latter values were determined using a model including anharmonic effects, explaining the larger value of $\epsilon\omega_2$.

VII.3.3 Rotational and Spin-Rotational Parameters

Rotational parameters

The rotational parameters determined here are in quite good agreement with the work of Kawaguchi *et al.*[3]. For example, they determined $B_{(010)} = 0.39047986(7)\,\mathrm{cm}^{-1}$ (corrected for an $\mathbf{N}^2$ Hamiltonian), compared with a value of $0.39045284(11)\,\mathrm{cm}^{-1}$ determined here. The differences arise for two reasons. Firstly, Kawaguchi *et al.*[3] attempted to account for K-type resonance between $(110)\,^2\Delta$ and $(110)\,^2\Sigma$ by determining separate centrifugal distortion parameters for the μ and κ states. Secondly, in their treatment of the Renner-Teller effect and anharmonic interactions, only the leading terms of these effects up to the fourth order in perturbation theory were taken into account, whereas the treatment used here is exact for the harmonic part of the Renner-Teller effect. In the present study, a very accurate upper state rotational constant of $B_{(110)}(^2\Sigma) = 0.3872050(50)\,\mathrm{cm}^{-1}$ has been determined, see Table VII.4.

The spin-rotation parameter

The value of $\gamma = -0.19668(67)\,\mathrm{cm}^{-1}$ determined in the fit presented here compares with a value of $-0.1825930(11)\,\mathrm{cm}^{-1}$ determined by Kawaguchi *et al.*[3]. The difference partly arises from Kawaguchi's use of perturbation approximations, but also from the separation of A_D and γ in the present study. This is made possible by terms involving the centrifugal distortion of the spin-orbit coupling Hamiltonian, $\mathcal{H}_{\mathrm{socd}}$, and the spin-rotation Hamiltonian, $\mathcal{H}_{\mathrm{sr}}$, in combination with the Renner-Teller Hamiltonian.

In the study by Kawaguchi *et al.*[3], three perturbation parameters were defined, $\gamma_{\mathrm{vib.}}$, s and t, to account for anharmonic interactions between the (010), (011) and (110) $^2\Sigma$ vibronic states. A value of A_D can be estimated from their study using their definitions of

$$s = Z \sin 2\beta + \frac{A_D}{2} \cos 2\beta + \text{Coriolis terms} \qquad \text{(VII.5)}$$

$$\gamma_{\mathrm{vib.}} = Z + \frac{A_D}{2} \sin 2\beta \cos 2\beta. \qquad \text{(VII.6)}$$

The parameter Z is a Fermi resonance parameter [3]. The angular functions are defined in §IV.2.1 of this thesis; taking $\sin 2\beta = -0.8484$ and $\cos 2\beta = -0.5293$, and neglecting

the Coriolis terms, an estimate of $A_D = 0.291 \times 10^{-3}\,\mathrm{cm}^{-1}$ can be calculated from their values of $s = -10.4831\,\mathrm{MHz}$ and $\gamma_{\mathrm{vib.}} = 11.593\,\mathrm{MHz}$. The value determined in the present study is $A_D = 0.1121(12) \times 10^{-3}\,\mathrm{cm}^{-1}$. The difference between the two values arises not only because of the exact model used here, see §IV.3, but also for two other reasons. Firstly because γ_D was also determined here, and secondly because the three parameters $s, \gamma_{\mathrm{vib.}}$ and t used by Kawaguchi *et al.*[3] are to a good approximation combinations of just two more fundamental parameters. In the model presented in this thesis, the two fundamental parameters are represented by A_D and $(\epsilon\omega_2)_D$. If NCO is approximated to a 'BAB' molecule, neglecting the terms involving $+2AL_zS_z/\omega_i$ given in Eq.(IV.60), and using $W_{2,3} = 2.995\,\mathrm{cm}^{-1}$ given by Sears [10], the value determined for $(\epsilon\omega_2)_D$ gives an estimate of $b_3 = -0.9868 \times 10^{-2}\,\mathrm{cm}^{-1}$. This parameter is a measure of $(\partial B/\partial Q_3)$, the change in the rotational constant for a unit change in the mass weighted in-phase stretching co-ordinate.

The rotational parameters determined for the $1_0^1 2_1^1\,{}^2\Sigma$ bands are smaller than those for the $1_0^1 2_1^1\,{}^2\Delta$ bands. This is in part due to different Coriolis contributions arising from terms absorbed into the parameters, such as $B\langle G_\perp^2\rangle$ (see §III.8.2). Kawaguchi *et al.*[3] have attempted to explain the remaining part of this difference in terms of third and fourth order contributions in the Van Vleck transformation over the vibrational levels. The Hamiltonian for this is $\mathcal{H}_{\mathrm{RT}} + \mathcal{H}_{\mathrm{rot.}} + \mathcal{H}_{\mathrm{FR}}$, where $\mathcal{H}_{\mathrm{FR}}$ is the Fermi Resonance Hamiltonian (see §IV.3).

VII.3.4 Hyperfine Parameters

A Fermi contact parameter of $b_F = 0.468(55) \times 10^{-3}\,\mathrm{cm}^{-1}$ can be calculated from Table VII.4, with $c = -0.155(15) \times 10^{-2}\,\mathrm{cm}^{-1}$. The value of b_F is significantly smaller than the corresponding value for $1_0^1 2_1^1\,{}^2\Delta$, implying less s orbital character in the π orbital occupied by the unpaired electron in the $^2\Sigma$ vibronic states. Quite surprisingly, the a parameter is slightly larger than in the $^2\Delta$ state, indicating a greater nuclear spin-electron orbital coupling in the $^2\Sigma$ states. The axial component of the nuclear quadrupolar coupling tensor eQq_0, is slightly smaller for the $^2\Sigma$ levels than for the $^2\Delta$ state, indicating a smaller field gradient due to all the electrons in the region of the nitrogen nucleus, in the $^2\Sigma$ vibronic states.

VII.3.5 Zeeman Parameters

The fit was not very sensitive to the variation of $\Delta g_L^{(1)}$, which was therefore constrained to the value determined for the $1_0^1 2_2^1\, ^2\Delta$ band. Given the large spin-decoupling effects, one would expect sensitivity to g_S or $\alpha_{1,gS}$, but attempts to determine these parameters did not improve the fit significantly and they were not well determined.

The fit of the $F_1 - F_2$ transitions might be improved by including K-type resonance contributions to the zero field frequencies (involving p and q, see Appendix E), and similar contributions to the Zeeman effect (involving g_l' and $g_r^{e\prime}$, see Appendix E). Such contributions might give the necessary shifts of up to 220 MHz required to bring the $F_1 - F_2$ transitions into line. In order to gauge the size of such effects, the predicted K-type doubling in the $1_0^1\, ^2\Pi_{\frac{3}{2}}$ sub-band was about 75 MHz at low J. The parameter $q_{\text{vib.}}$ will be larger for $v_2 = 1$ than for $v_2 = 0$, so this explanation is quite plausible and will be the next stage in the analysis. If this fails to resolve the problem, then further investigations of harmonic and anharmonic contributions to the vibronic, rotational and Zeeman energies will be required. This will be accomplished by considering terms arising in the electronic and vibrational stages of the Van Vleck transformation to produce an effective Hamiltonian.

VII.3.6 Unassigned Spectra

There are too many unassigned spectra to describe here. The following paragraphs précis the general types of features observed and possible assignments.

The spectra recorded on the $P(13)_{8-7}$ laser line show some unassigned resonances, see Figs.VI.3 and VI.5. At low field there is a resonance looking like an inverted first derivative line-shape. Such a resonance can only arise from the overlap of several fast tuning Zeeman components. On the neighbouring $P(6)_{9-8}$ laser line, a similar resonance was observed at low field, followed by many (> 100) fast tuning lines. Such patterns can arise from 'anticrossing transitions', in which the Zeeman components from the rotational levels in two different vibronic levels are accidentally near-resonant. Components with the same value of M_J interact and avoid each other by bending away sharply, and many vibration-rotation transitions tend to 'pile up' in a narrow field range of the LMR spectrum. An example of such effects in the far-infrared LMR spectrum of HCO is

given in ref. [11]. The analysis such spectra will require the identification of which levels are likely to be near-resonant; the well known Fermi resonance (001) – (020) and also the (101) – (120) resonance, are good candidates. Note also from Fig.V.1 that the levels $(001)\,^2\Pi_{\frac{3}{2}}$ and $(011)\,^2\Delta_{\frac{3}{2}}$ are within $12\,\mathrm{cm}^{-1}$ of each other, and that there are various levels at similar energies to those of (110). It is possible that the band $2_0^1 3_0^1 (^2\Delta_{\frac{3}{2}} \leftarrow ^2 \Pi_{\frac{3}{2}})$ could be observed, though it would only be vibronically allowed, gaining intensity through an anharmonic terms of the form $Q_2^2 Q_3$, where the Q_i are the normal co-ordinates.

The spectrum on the $P(14)_{8-7}$ laser line shown in Fig.VII.12, and the corresponding σ polarisation spectrum, also show several unassigned features. The broad feature at about 400 mT resolves at low modulation into a series of Lamb-dips progressing to higher fields (some can be seen). At higher fields, there is another progression of Lamb-dips. Qualitatively, such progressions of Lamb-dips are indicative of $F_1 - F_1$ and $F_2 - F_2$ type transitions, but they do not arise from the $1_0^1 2_1^1\,^2\Sigma$ bands. The next most likely candidates are the transitions $1_0^1 2_2^2\,\mu, \kappa^2\Pi$; certainly this is the region in which they would be expected, near to $1_0^1 2_2^2\,^2\Phi$. The $P(15)_{8-7}$ laser line (not displayed) shows a progression of Doppler limited resonances with an apparent doubling. This might be a K-type doubling, which is expected to be large for $^2\Pi$ vibronic states; these bands would exhibit Hund's case (b) Zeeman effects, which have been shown here to give rise to such features. The levels (011) and (020) have been well characterised by Werner [12], so reliable LMR predictions can be made. This will require the inclusion of K-type doubling and resonance, and the expansion of the matrix explicitly to include the necessary Fermi resonances. This is going to be done as a continuation of this work. Other possibilities are the bands $1_0^1 3_1^1\,^2\Pi$ (see Fig.V.1), and $1_0^1 2_3^3\,^2\Sigma$, but the population of the lower levels is expected to be small given that $1_1^2\,^2\Pi$ was not detected at all in this study.

Proceeding to lower wave number in the LMR search, there are progressions of Lamb-dips and occasional strong signals. These might arise from very high N/J transitions in the bands already discussed, or from transitions in other weakly populated hot-bands, or from some other molecule. Thorough predictions should 'weed-out' any $1_0^1 2_1^1\,^2\Sigma$ transitions at high $N(> 40)$. In some cases it may be impossible to make assignments, since the spectra are so weak that the start and end of the progressions cannot be seen clearly.

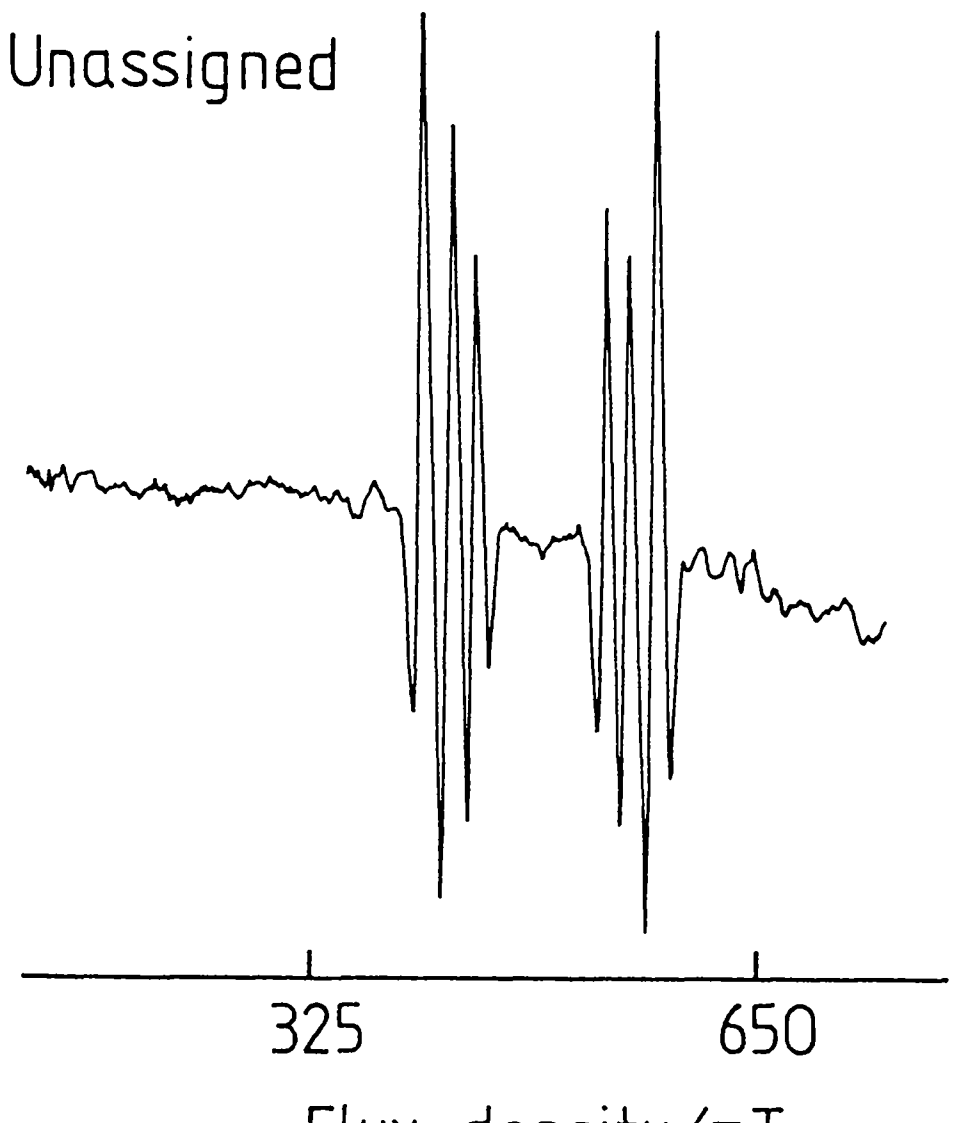

Figure VII.14: The unassigned spectrum observed on the $P(10)_{11-10}$ laser line in π polarisation. This laser line is partly water absorbed and the laser cavity was purged with dry nitrogen when recording this spectrum.

In the region of 1870 cm^{-1}, some sharp transitions consisting of pairs of Doppler limited doublets/triplets were observed. The laser lines concerned were $P(17)_{9-8}$, $P(16)_{10-9}$ and $P(10)_{11-10}$ at 1868.1266 cm^{-1}, 1846.8857 cm^{-1} and 1845.1364 cm^{-1} respectively, in π polarisation. An example is shown in Fig.VII.14. A matrix isolation study [13] suggested that the $1_0^1\,^2\Pi$ band of $N^{13}CO$ should be in this region ($\sim$ 52 cm^{-1} below $N^{12}CO$). The splitting might be the ^{13}C hyperfine splitting, but no convincing assignments could be made to these spectra. In addition, the π orbital occupied by the unpaired electron has a node near to the carbon nucleus, so the ^{13}C hyperfine splitting is expected to be small (*i.e.* < 10 mT).

Bibliography

[1] N. Bazire, Part II thesis, University of Oxford, Trinity 1987.

[2] B.J. Boland, J.M. Brown, A. Carrington and A.C. Nelson, *Proc. R. Soc. Lond. A* **360**, 507–528 (1978).

[3] K. Kawaguchi, S. Saito and E. Hirota, *Mol. Phys.* **49**, 663–674 (1983).

[4] R.A. Copeland and D.R. Crosley, *Can. J. Phys.* **62**, 1488–1501 (1985).

[5] D. Patel-Misra, D.G. Sauder and P.J. Dagdigian, *J. Chem. Phys.* **93**, 5448–5456 (1990).

[6] F.J. Northrup, M. Wu and T.J. Sears, *J. Chem. Phys.* **96**, 7218–7228 (1992).

[7] P.S.H. Bolman, J.M. Brown and A. Carrington, *Proc. R. Soc. Lond. A* **343**, 17–44 (1975).

[8] K. Kawaguchi, E. Hirota and C. Yamada, *Mol. Phys.* **44**, 509–528 (1981).

[9] B. Hemmerling and M. Vervloet, *Mol. Phys.* **78**, 1423–1447 (1993).

[10] M. Wu and T.J. Sears, *Mol. Phys.* **82**, 503–521 (1994).

[11] J.M. Brown and H.E. Radford, *J. Mol. Spectrosc.* **148**, 20–37 (1991).

[12] J. Werner, Ph.D. thesis, Institut für Angewandte Physik der Universität Bonn, 1987.

[13] D.E. Milligan and M.E. Jacox, *J. Chem. Phys.* **47**, 5157–5169 (1967).

Chapter VIII

Conclusions and Further Work

VIII.1 The CO LMR Spectrometer

VIII.1.1 The CO Laser

An overtone ($\Delta v = 2$) CO laser has been started in Oxford for the first time. This has been used successfully to detect well known vibration-rotation transitions in the fundamental and hot bands of CH. These observations, made with Doppler limited resolution, proved the viability of the overtone CO-LMR spectrometer. The maximum output power of the overtone laser was measured to be 120 mW, giving an estimated intracavity power of 6 W, based on 2 % out-coupling into the zeroth order of the diffraction grating.

The $\Delta v = 1$ CO laser is now operable over almost its entire range. The only exceptions to this are the 1–0 band (around 2100 cm^{-1}) and the 1200–1300 cm^{-1} region. In Appendix B, I have given a detailed description of the physical parameters and *ad hoc* modifications required to operate the laser across its various regions. I hope this permanent record will be of use to my successors.

VIII.1.2 Components of the Spectrometer

The vacuum and gas mixing systems have been completely rebuilt, leading to an order of magnitude improvement in the ultimate vacuum in the laser gain tube, and greater control and day-to-day reproducibility of the gas mixture. The end-mirror adjustment screws of the laser resonator were re-designed with universal joints, giving improved

stability of the laser resonator. A new magnet power supply has been installed; this thyristor-controlled device is much smoother running and has a very much faster response than the previous, mechanically regulated device. The latter modification has reduced distortion and non-linearities in the LMR scan, which produced field measurement errors.

The development of the CO laser described above is a result both of these improvements and those made by previous workers.

VIII.1.3 Recommendations for the Future

- Replace the present gain tube (16 mm i.d.) by one with an i.d. of 13 mm; the reason for this is shown in Fig.B.5. The narrower gain tube will give a lower plasma temperature, increasing the gain. This should be particularly effective for the overtone laser. The new tube should also have extra bleed gas inlets to aid running the $\Delta v = 1$ laser above 2000 cm^{-1}. A ribbed gain tube interior is also desirable, since this generates viscous flow in the plasma, aiding cooling.

- A wider choice of diffraction gratings, each optimised for a particular region. This would be particularly useful for the 1–0 band of the CO laser, where the first order reflectivity of the grating is critical in achieving gain.

- To rebuild the end-mirror mount, if possible giving sub-micron sensitivity to the adjustment screws.

- To rebuild the modulation coils, in an effort to increase the peak-to-peak modulation amplitude to about 13 mT. This should enable the optimum detection of Doppler profiles over a wide range of tuning rates. This is already in progress; the Oxford Magnet Group of Mr. H. Jones, The Clarendon Laboratory, University of Oxford, is designing new coils for the system. They are using computer aided design to optimise the modulation amplitude in the region of the sample cell. Improved fabrication procedures for the windings should eliminate the need for water cooled copper formers, which obviously lead to large losses via eddy currents.

VIII.2 The Renner-Teller Effect

VIII.2.1 The Model Used in the Analysis

An implementation of a model of the harmonic Renner-Teller effect for a linear triatomic molecule in a $^2\Pi$ electronic state, has been presented. This model is based on the $\mathbf{N}^2$ effective Hamiltonian developed by J.M. Brown. The inclusion of spin-orbit coupling, rotation, spin-rotation, centrifugal distortion, K-type doubling, nuclear hyperfine and Zeeman effects has been described. A new term in the effective Hamiltonian has been developed to treat anharmonic interactions in the $^2\Sigma$ vibronic states.

The application of this model to the unique ($K = v_2 + 1$) and $^2\Sigma$ ($K = 0$) vibronic states has been considered in detail. The Zeeman effect in the $^2\Sigma$ vibronic states has been investigated for the first time. The behaviour of the $^2\Sigma$ vibronic states is characteristic of a system approximating to Hund's (b) coupling, but distinct from and more complicated than the Zeeman effect in a $^2\Sigma$ electronic state.

VIII.2.2 Future Recommendations

A computer program 'RENNER.FOR' was developed to implement the model. The program proved extremely successful in modelling the Zeeman and zero field observations of NCO in its $\tilde{X}^2\Pi$ state. In order to be able to model higher lying vibronic levels, and to include other effects, the following modifications to 'RENNER.FOR' are proposed:

- The expansion of the matrix representation to span all the vibronic K-states within each (v_1, v_2, v_3) manifold in the basis set. This will allow the inclusion of K-type resonance matrix elements, including K-type resonance Zeeman terms.

- Fermi resonances where required, for example the dyad $(020)\,^2\Pi$–$(021)\,^2\Pi$. The matrix representation should span the complete manifold of each Fermi polyad.

- The inclusion, where required, of quartic anharmonic Renner-Teller terms, based on the model developed by J.M. Brown and F. Jørgensen.

VIII.3 The NCO Radical

VIII.3.1 Observations

A large number of laser magnetic resonance spectra were recorded in a search of the $1830\,\mathrm{cm}^{-1}$–$1930\,\mathrm{cm}^{-1}$ region. Some of these have been assigned to transitions in the $\tilde{X}^2\Pi$ state of NCO, as summarised below.

VIII.3.2 The Unique States

The LMR spectra in the unique states were assigned with the aid of predictions based on existing observations of the $1_0^1\,^2\Pi$ and $1_0^1 2_1^1\,^2\Delta$ bands. The previous observations have been significantly extended and improved, for example by the observation of Lamb-dips, resolving the ^{14}N nuclear hyperfine structure. Observations of the $1_0^1 2_2^2\,^2\Phi$ band have been made for the first time. All of the unique state LMR spectra show classic Hund's case (a) Zeeman effect behaviour, but with significant nonlinear Zeeman effects due to the spacing of adjacent rotational levels being comparable with the Zeeman energy. This gave many of the spectra characteristic appearances. All the LMR observations were restricted to the $P = K + 1/2$ spin component, because the $P = K - 1/2$ spin component is non-tunable.

The observations have been analysed together with existing mid- and far- infrared LMR data, mid-infrared diode laser data, microwave data and EPR data. The matrix representation for this purpose spanned a basis set with $\Delta v_2 = \pm 4$ and $\Delta J = \pm 4$. Truncation at this point was found not to introduce significant error.

VIII.3.3 The $^2\Sigma$ Vibronic States

Transitions in the $^2\Sigma$ vibronic bands $1_0^1 2_1^1\,\mu^2\Sigma^{(+)}$ and $1_0^1 2_1^1\,\kappa^2\Sigma^{(-)}$ were very complicated to assign. It was only possible to model these systems once the complete Renner-Teller model had been implemented in 'RENNER.FOR'. Even then, it took a long time to make the first assignment. There are four reasons for this:

1. There are two $^2\Sigma$ bands, μ and κ. There was no sufficiently accurate knowledge *a priori* of either the absolute band origin or of the relative origin of the μ and

κ bands. Therefore, it was not known what pattern of rotational lines would be produced from the superposition of the two systems.

2. There are transitions from other bands in the region of the $^2\Sigma$ bands; these are not always easy to differentiate.

3. The Zeeman effect in the $^2\Sigma$ states is very complicated, showing spin-decoupling behaviour. It was not obvious at first that the $F_1 - F_1$ and $F_2 - F_2$ transitions would appear as Lamb-dips, whereas the $F_1 \leftrightarrow F_2$ transitions would appear as very sharp lines. It was initially thought that only the latter would be observed, the Doppler profiles of the other transitions being too broad to detect.

4. Several hundred 'blind' field predictions and spectrum simulations had to be performed before a possible assignment came to light. Many of these runs were extremely computer intensive, especially those involving several higher N levels with many Zeeman components.

The analysis proved very satisfying, reproducing the most subtle features of the observations. Small but significant (in LMR terms) residuals remain for the $F_1 - F_2$ transitions. Two possibilities might be considered to explain this:

- The effects of K-type resonance. The ability to model this will be included in the 'RENNER.FOR' program shortly.

- Anharmonic terms or other terms not projected onto the space of the effective Hamiltonian. This study provides an example of experimental results revealing potential inadequacies in the present theoretical understanding.

VIII.3.4 Future Studies, Including the N_3 Radical

Efforts will continue to analyse the unassigned spectra of NCO. The $1_0^1 2_2^2\,^2\Pi$ bands will be considered next; the upper and lower states are involved in Fermi resonances, which must be modelled. Given that no resonances due to the 1_1^2 hot bands were observed, it is unlikely that the observed spectra will originate from levels of NCO more than 1900 cm^{-1} above the ground state. Some of the spectra are so weak or noisy that they might never be assignable.

At the outset, it was hoped that understanding NCO would aid in the assignment of the similar LMR spectrum of the azide radical N_3, which is a Renner-Teller molecule isoelectronic with NCO. As it has turned out, NCO itself has been something of a Pandora's box. Nevertheless, the understanding of the $^2\Sigma$ vibronic states gained here, and the computer model developed, should allow progress to be made on explaining the LMR data of N_3 reported in the thesis of Ralph Pahnke (Oxford, 1990).

VIII.3.5 A Postscript on the CCN Radical

A similar LMR study of CCN led to the observation of the Q(3/2) and Q(5/2) lines in the $1_0^1\,^2\Pi_{\frac{3}{2}}$ sub-band of CCN ($\tilde{X}^2\Pi$). This Renner-Teller molecule is similar to NCO but has 13 valence electrons instead of 15, and consequently positive Renner-Teller and spin-orbit coupling parameters.

As a postscript to this thesis, the 'RENNER.FOR' program has been used to predict transitions in the $1_0^1 2_1^1\,^2\Delta$ band of CCN. These successfully guided Dr. M. Fehér (group of Prof. J.P. Maier, Basel) to record the band with a mid-infrared diode laser. Further predictions with the program have led to the observation and assignment of the $1_0^1\,^2\Sigma$ bands, whose detailed analysis is still in progress. An increase in the residuals at high J indicates the need to include K-type resonance in the model.

Appendix A

The Mechanism of CO Laser Action

A.1 Introduction

Patel was the first to observe pulsed [1] and later continuous wave [2, 3] CO laser action in the mid-infrared. The laser action was assigned to vibration-rotation transitions within the very deep potential well of the $X^1\Sigma^+$ electronic state[1]. Since then, many workers, most notably the group of Urban in Bonn, have developed the CO laser. It has become a powerful mid-infrared spectroscopic source of unrivalled power, range and quality.

A.2 The Gain Process

In the liquid nitrogen cooled plasma gain tube, cooling of CO occurs by convection. Helium, the major constituent of the plasma, is particularly efficient in this respect because of its high thermal conductivity. Rapid translational-rotational relaxation occurs[2], resulting in a translational/rotational temperature of ca. 120 K [5]. If it is assumed that there are only small rovibrational interactions in the X state, then a very similar rotational population distribution will be found in each vibrational level.

For gain on a vibration-rotation transition, an inversion of population, N, is required

[1]The $X^1\Sigma^+$ electronic state has $D_0 = 89.4 \times 10^3$ cm^{-1}, $\omega_e = 2170$ cm^{-1} and $\omega_e x_e = 13$ cm^{-1} [4].

[2]Since the rotational and thermal quanta are of similar magnitudes, rapid collisional energy transfer occurs between these degrees of freedom.

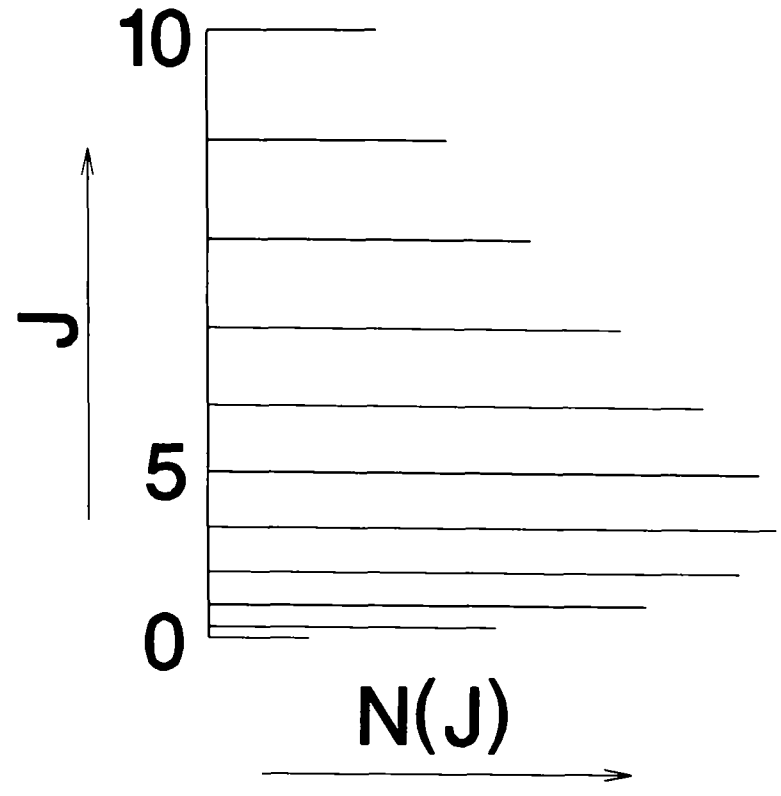

Figure A.1: The relative rotational population distribution in a vibrational level of CO, at a rotational temperature of 120 K [4].

between two rotation-vibration levels:

$$N(v', J') > N(v'', J'') . \tag{A.1}$$

If the total population in level v is $N_v = \sum_J N(v, J)$, the degeneracy-weighted population distribution amongst the rotational levels is given by[3],

$$N(v, J) = \frac{N_v (2J+1)}{q^r (B, T)} e^{-\frac{hcBJ(J+1)}{kT}} . \tag{A.2}$$

Where k is Boltzmann's constant (in JK^{-1}), B is the rotational constant in wave numbers and

$$q^r (B, T) = \sum_J (2J+1) e^{-\frac{hcBJ(J+1)}{kT}} , \tag{A.3}$$

is the rotational partition function for CO [6]. A typical rotational population distribution is shown in Fig.A.1.

The field stimulating the emission of radiation quantises the M_J components of the rotational levels involved, so emission occurs from a single M_J state. For this reason, the $(2J+1)$ weighting factor is dropped when considering the population inversion required

[3]Centrifugal distortion terms are neglected in these expressions.

for laser action[4]. Hence Eq.(A.1) becomes

$$\frac{N_{v'}}{q^r\left(B_{v'},T\right)}e^{-\frac{hcB_{v'}J'(J'+1)}{kT}} > \frac{N_{v''}}{q^r\left(B_{v''},T\right)}e^{-\frac{hcB_{v''}J''(J''+1)}{kT}}. \tag{A.4}$$

Fluorescence emission studies of a CO plasma [7] have shown that there is no inversion of the vibrational population. A plateau of vibrational levels is found, for which $N_{v+1}/N_v \approx 0.9$. For positive rotational temperatures (negative temperatures do not occur here), Eq.(A.4) can only be satisfied for $J' < J''$. This is why laser action only occurs on P-type lines; as is shown in Fig.A.2, gain is made possible by a *partial inversion of population.* Patel [3] derived a formula for the small signal gain of the CO laser; a simplified form for R and P lines is

$$\begin{aligned}\alpha^{v',J'}_{v'',J'\pm1} &= \frac{8\pi^3c^3}{3h\left(2\pi kT/m\right)^{1/2}}K_{v'v''}S_{J'J'\pm1}\times \\ &\left[\frac{N_{v'}}{q^r\left(B_{v'},T\right)}e^{-\frac{hcB_{v'}J'(J'+1)}{kT}} - \frac{N_{v''}}{q^r\left(B_{v''},T\right)}e^{-\frac{hcB_{v''}J'(J'+1\pm1)}{kT}}\right].\end{aligned} \tag{A.5}$$

Here, $S_{J'J'\pm1} = J'$ or $J'+1$ for R and P lines respectively, m is the molecular mass (in a.u.) and $K_{v'v''}$ is the vibrational transition moment $< v'|\boldsymbol{\mu}|v'' >$, where $\boldsymbol{\mu}$ is the electric dipole moment operator. Fig.A.3 shows an example of the gain distribution calculated from Eq.(A.5); in reality, the maximum gain occurs at a higher J value than predicted by Eq.(A.5). This is due to saturation effects, which are more significant for lower J values since they have a lower degeneracy. The manifold of lines showing gain is determined by the temperature of the plasma. In a liquid nitrogen cooled laser, the observed range of rotational lines in the band v'–v'' is P(5) to P(17)[5]. CO lasers using a pentane coolant [8], or a liquid nitrogen cooled sand diffusion system [9], can access higher rotational lines, though the gain is generally lower at the higher temperature.

---

[4]The degeneracy contributes to the total intensity of the stimulated emission.

[5]The J manifold is principally determined by the discharge current, and also the helium and CO pressures for P(16) and P(17) lines.

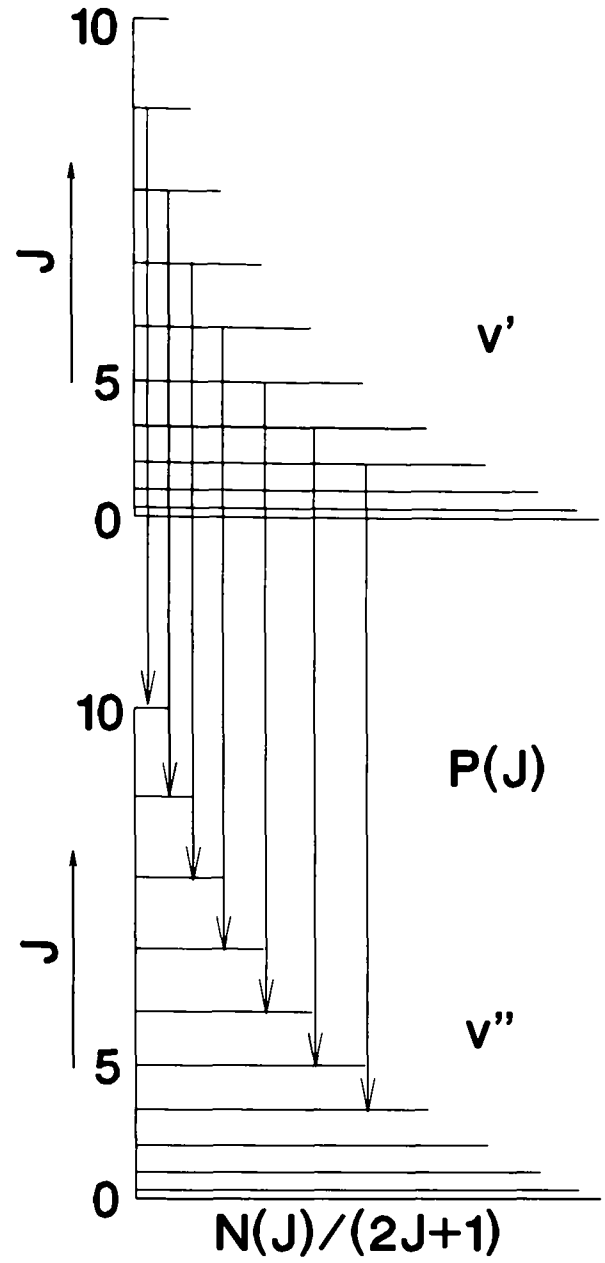

Figure A.2: A partial inversion of the Boltzmann population can give rise to gain on P-type rotation-vibration transitions.

A.3 The Overtone CO Laser

C.W. laser action has been obtained on both $\Delta v = 1$ and $\Delta v = 2$ transitions [5], for which the maximum intracavity powers are 30–40 W and 15 W, respectively[6] [5]. There are two reasons why the gain of the overtone laser is less than that of the normal laser.

The first is a population factor; for $N_{v+1}/N_v \approx 0.9$, then $N_{v+2}/N_v \approx 0.8$. This makes the partial inversion harder to achieve.

The second factor is the reduced vibrational transition moment, $K_{v'v''}$ in Eq.(A.5), when compared to that for the $\Delta v = 1$ transition. The $X^1\Sigma^+$ potential can be expressed

[6]The intracavity power can be measured by monitoring the reflection from one of the Brewster's angle windows in the cavity, or the zeroth order of a grating with known reflectivity. The power is quoted for a 1 m gain medium.

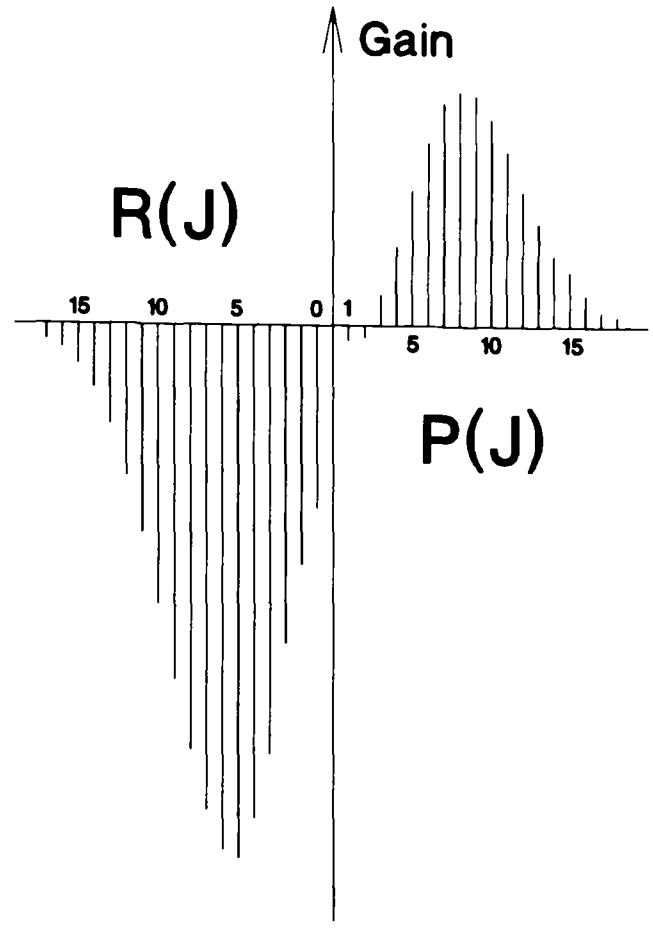

Figure A.3: The gain distribution for a CO plasma at 120 K, calculated from Patel's formula.

as a Taylor series in the vibrational co-ordinate Q,

$$V = \frac{1}{2}\lambda Q^2 + aQ^3 + bQ^4 + \cdots, \tag{A.6}$$

where λ, a and b are force constants, *e.g.* $a = \partial^3 V/\partial Q^3$. The first term in Eq.(A.6) is the harmonic term. The term in Q^3 has matrix elements with $\Delta v = \pm 1$ and is the major contributor to the mechanical anharmonicity, $\omega_e x_e$ [10]. This term gives some harmonic character to $\Delta v = 2$ transitions. The relative size of the harmonic and anharmonic terms for CO can be gauged by comparing ω_e and $\omega_e x_e$, 2170 cm^{-1} and 13 cm^{-1} respectively. A similar anharmonic contribution arises in the electric dipole moment operator $\boldsymbol{\mu}$,

$$\boldsymbol{\mu} = \boldsymbol{\mu}_e + \left(\frac{\partial \boldsymbol{\mu}}{\partial Q}\right) Q + \frac{1}{2}\left(\frac{\partial^2 \boldsymbol{\mu}}{\partial Q^2}\right) Q^2 + \cdots. \tag{A.7}$$

The third term in Eq.(A.7) contributes to the electrical anharmonicity [10], and gives intensity to $\Delta v = 2$ transitions. The matrix element $< v+1|\boldsymbol{\mu}|v' >$ is proportional to $v'^{1/2}$ [11]. Hence the vibrational transition moment $K_{v+2,v} =< v+2|\boldsymbol{\mu}|v >$ has a v' dependence. For this reason, the overtone laser favours higher vibrational bands; it has

been operated on bands with $v' = 10$ to 37.

A.4 The Vibrational Pumping Mechanism

CO laser action has been observed on a large number of vibrational bands from $v' = 1$–37. This is possible because the population ratio $N_{v'}/N_{v''}$ is close to unity over a large number of vibrational levels, corresponding to a vibrational temperature of $T_{\text{vib}} \approx 4 \times 10^4$ K [5]. The present understanding is that vibrational pumping occurs by two mechanisms.

The first involves slow electrons in the plasma (1–2 eV), which are captured by CO. The unstable CO^- ion autoionises to form $CO(X^1\Sigma^+)$ with $v = 0 - 8$. The addition of small amounts of oxygen is very important in this respect [12]. The O_2^+ ion becomes dominant in the plasma, because O_2 has a low ionisation potential. The ion undergoes recombination/ionisation reactions which thermalise the electrons in the plasma, favouring vibrational rather than electronic excitation of CO.

The second mechanism is an anharmonic vibrational-vibrational pumping mechanism which populates many vibrational levels, which are metastable[7]. The mechanism is known as Treanor pumping [13, 14]. Consider a collision between two CO molecules in vibrational states v_1 and v_2 ($v_1 > v_2$). Collisionally induced vibrational energy transfer occurs after every 50–100 such collisions [5]; there are two possible outcomes:

$$\text{CO}(v_1) + \text{CO}(v_2) \longrightarrow \begin{cases} \text{CO}(v_1 + 1) + \text{CO}(v_2 - 1) + \Delta E \ (a) \\ \text{CO}(v_1 - 1) + \text{CO}(v_2 + 1) - \Delta E \ (b) \end{cases} \tag{A.8}$$

In an anharmonic system, as shown in Fig.A.4, $E(v+1) - E(v)$ decreases with increasing v. Hence in Eq.(A.8), path (a) is exothermic whilst path (b) is endothermic and requires an activation energy. If the plasma is cooled so that $kT < \Delta E$, path (a) dominates and vibrational pumping occurs. The smaller the values of (v_1, v_2), the smaller ΔE and hence the colder the plasma must be to initiate pumping. As (v_1, v_2) increase, the process becomes ever nearer resonance and the rate of pumping increases. The result of many such collisions is to produce a wide 'Treanor plateau' of vibrational levels with very similar populations, typically from $v = 8$ to $v = 35$. An example of such a Treanor

[7]The large size of the vibrational quanta *cf.* the rotational and translational quanta means that it takes ca. 10^5 collisions to equilibrate the vibrational and translational energies [5].

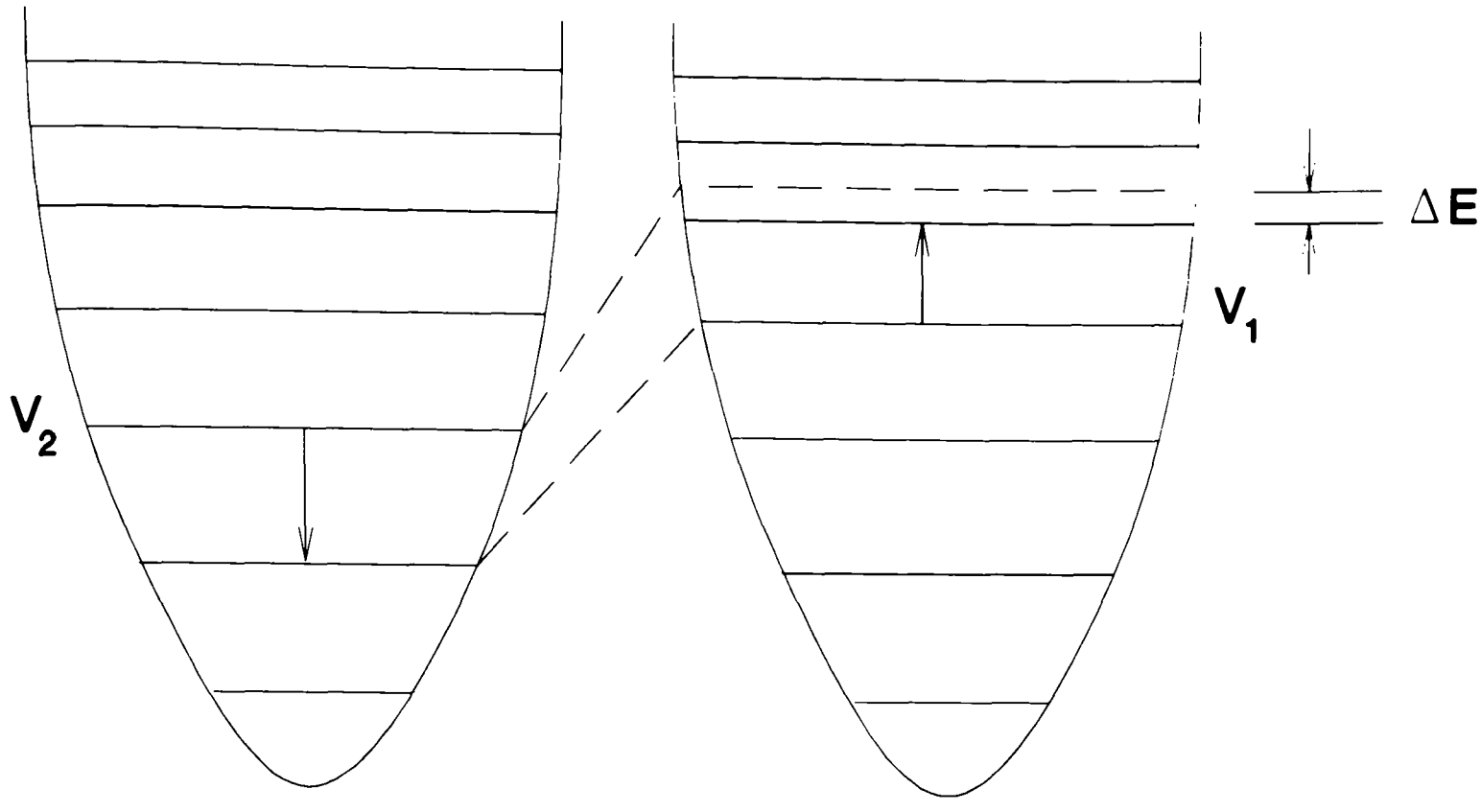

Figure A.4: The collisionally induced anharmonic vibrational pumping process known as 'Treanor pumping'.

plateau is shown in Fig.A.5; this is the region where laser action can occur. The limit of the plateau is near to $v' = 37$, where the $A^1\Pi$ state crosses the X state [5], leading to increased vibrational relaxation rates above this level. Treanor pumping also occurs between N_2 and CO. The larger vibrational spacing in N_2 means that the pumping is near-resonant with low v levels of CO. A simplified model of the vibrational processes in the active medium of a CO laser was provided by Berdyshev *et al.*[15].

A high partial pressure of CO ($\approx 67\,\mathrm{Pa}\,(0.5\,\mathrm{Torr})$) is required to operate the normal laser on the higher vibrational bands (long wavelengths), and it is essential for the operation of the overtone laser (as can be seen, the rate of Treanor pumping is second order in [CO]). Conversely, a very low CO partial pressure ($< 4\,\mathrm{Pa}\,(0.03\,\mathrm{Torr})$), a high nitrogen content and a very efficiently cooled plasma (hence a low discharge current and high helium partial pressure) are critical when operating the laser below the $5-4$ vibrational band. The purity of the gases is important; it can be improved by freezing out laser poisons using liquid nitrogen traps before the inlet to the tube.

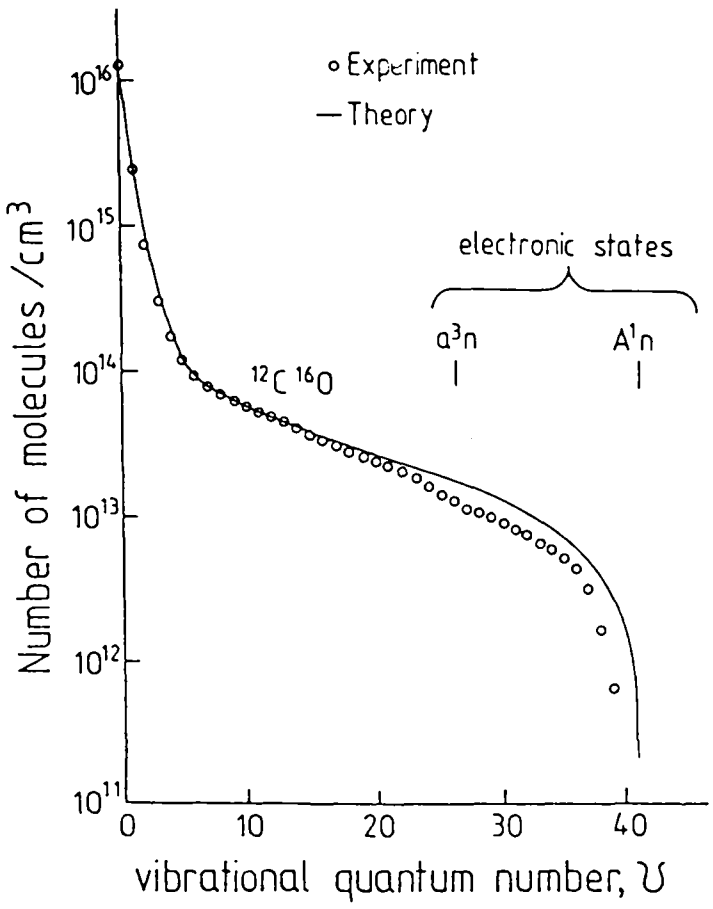

Figure A.5: The experimental and calculated vibrational population distribution of a liquid nitrogen cooled CO plasma, showing the "Treanor plateau".

A.5 Oxygen in the Plasma.

Apart from its role as an electron thermaliser, oxygen removes the carbon formed from dissociated CO,

$$CO \rightleftharpoons C + O. \tag{A.9}$$

This accounts for most of the oxygen requirement of the laser. The balance of oxygen is very important. If too much is admitted, it acts as a vibrational quencher of CO [12]. The correct balance must be found, normally by starting the laser with a slight excess of oxygen and then reducing it gradually. For the overtone laser, a change of 2.7 Pa (0.02 Torr) in the partial pressure of air can make the difference between an air excess/shortage and the optimum for stable laser output. A shortage of air is observed as a pink coloration which grows outwards from the centre of the gain tube; the discharge becomes very unstable and laser action ceases. When this occurs, the tube must be pumped out whilst maintaining a helium discharge, before re-starting the laser. The addition of too much oxygen can lead to the formation of explosive, ultramarine blue ozone downstream of the gas inlets to the gain tube.

Bibliography

[1] C.K.N. Patel and J.R. Kerl, *Appl. Phys. Lett.* **5**, 81–83 (1964).

[2] C.K.N. Patel, *Appl. Phys. Lett.* **7**, 246–247 (1964).

[3] C.K.N. Patel, *Phys. Rev.* **141**, 71–83 (1966).

[4] K.P. Huber and G. Herzberg, "Molecular Spectra and Molecular Structure," Vol. IV, "Constants of Diatomic Molecules," pp. 158–169, Van Nostrand-Reinhold, New York, 1979.

[5] W. Urban, *Laser und Optoelektron.* **23**, 56–61 (1991).

[6] P.W. Atkins, "Physical Chemistry," 3rd ed., pp. 528–532, Oxford University Press, Oxford, 1986.

[7] R. Farrenq and C. Rossetti, *Chem. Phys.* **92**, 401–416 (1985).

[8] A.Hinz, D. Zeitz, W. Bohle and W. Urban, *Appl. Phys. B* **36**, 1–4 (1985).

[9] G. Nelke, Diplomarbeit thesis, Institut für Angewandte Physik der Universität Bonn, 1992.

[10] G. Herzberg, "Molecular Spectra and Molecular Structure," Vol. I, "Spectra of Diatomic Molecules," 2nd ed. (corrected), pp. 92–97, Krieger, Malabar, FL, 1989.

[11] P.R. Bunker, "Molecular Symmetry and Spectroscopy," p. 200, Academic Press, New York, 1979.

[12] W.L. Morgan and E.R. Fisher, *Phys. Rev. A* **16**, 1186–1198 (1977).

[13] C.E. Treanor, J.W. Rich and R.G. Rehm, *J. Chem. Phys.* **48**, 1798–1807 (1968).

[14] J.W. Rich, *J. App. Phys.* **42**, 2719–2730 (1971).

[15] A.V. Berdyshev, I.V. Kochetov and A.P. Napartovich, *Sov. J. Chem. Phys. Engl. (Khimicheskaya Fizika)* **7**, 751–764 (1990).

Appendix B

Further Experimental Details

B.1 CO Laser Operating Conditions

B.1.1 Introduction

This section discusses the conditions required to operate the CO laser in its various wave number regions. The appropriate diffraction grating was selected for the region of interest. The gain tube had a 16 mm i.d.; gas pressures were measured between the tube outlet and the choke-flap, using a 10^{-3}–10 Torr barocel gauge. The ultimate vacuum was better than 0.8 Pa (6 mTorr) with the flap closed, and when 533 Pa (4 Torr) of helium were admitted to the tube under these conditions[1], the measured exhaust rate to atmosphere of the pump was $16.25(\pm 0.35)\,\mathrm{l hr^{-1}}$.

The pressures for laser operation were recorded when the laser tube was cooled by liquid nitrogen, with the choke-flap after the tube outlet closed. The gas inlet pressures were 1.5 bar for He and N_2, atmospheric pressure for air and 1.1 bar for CO. The gases were admitted in the order He, N_2, air, CO and the cumulative pressures were recorded.

The laser power supply had ballast resistors of 700 kΩ in each of its two anode arms (see Fig.II.2). The footnotes in the following tables give the stabilisation voltage, total voltage and total current of the CO laser power supply. These parameters are quite sensitive to the composition of the plasma.

[1] With the flap open, the ultimate vacuum was < 1 mTorr.

Table B.1: Optimal gas pressures for the Oxford $\Delta v = 1$ CO laser in the 1900 cm^{-1} region.

Gas	Cumulative Pressure [Torr]	
	Low $J^{(a)}$	High $J^{(b)}$
Bleed helium	0.34	0.28
Bleed nitrogen	0.47	0.36
Helium	3.21	2.97
Nitrogen	3.85	4.65
Air	3.90	4.89
Carbon Monoxide	3.96	5.11

$^{(a)}V_{\text{stab.}} = 2.0\,\text{kV}$, $V_{\text{tot.}} = 13.2\,\text{kV}$, $I_{\text{tot.}} = 17\,\text{mA}$.

$^{(b)}V_{\text{stab.}} = 2.0\,\text{kV}$, $V_{\text{tot.}} = 16.5\,\text{kV}$, $I_{\text{tot.}} = 23\,\text{mA}$.

B.1.2 The Normal CO Laser

1900 cm^{-1} region

Table B.1 gives the optimum gas conditions for the CO laser in the 1900 cm^{-1} region. Two sets of conditions are given; the low J set produced the spectrum shown in Fig.II.5, and the high J set produced the spectrum shown in Fig.B.1. Both spectra were recorded with 'nozzle' inserts (Fig.II.8) in the sides of the tube, designed to prevent diffusion of CO out of the cooled part of the gain tube [1].

The higher J spectrum is less clean than the low J one. This is because the intracavity irises must be opened wider for the high J lines, on which gain is more critical. This can lead to transverse mode oscillation on the stronger lines. Urban [2] has speculated that some of the spikes in the high J spectrum arise from laser action in naturally abundant ^{13}CO.

2000 cm^{-1} region

Table B.2 gives the optimum gas conditions required for this region. Both the 'nozzle' inserts and electrically insulated, liquid nitrogen cooled copper coils at the gas inlets, were used to run the laser in this region [1]. Precise optical alignment and the cleanliness of the intracavity components were essential factors in achieving laser action in the 2–1

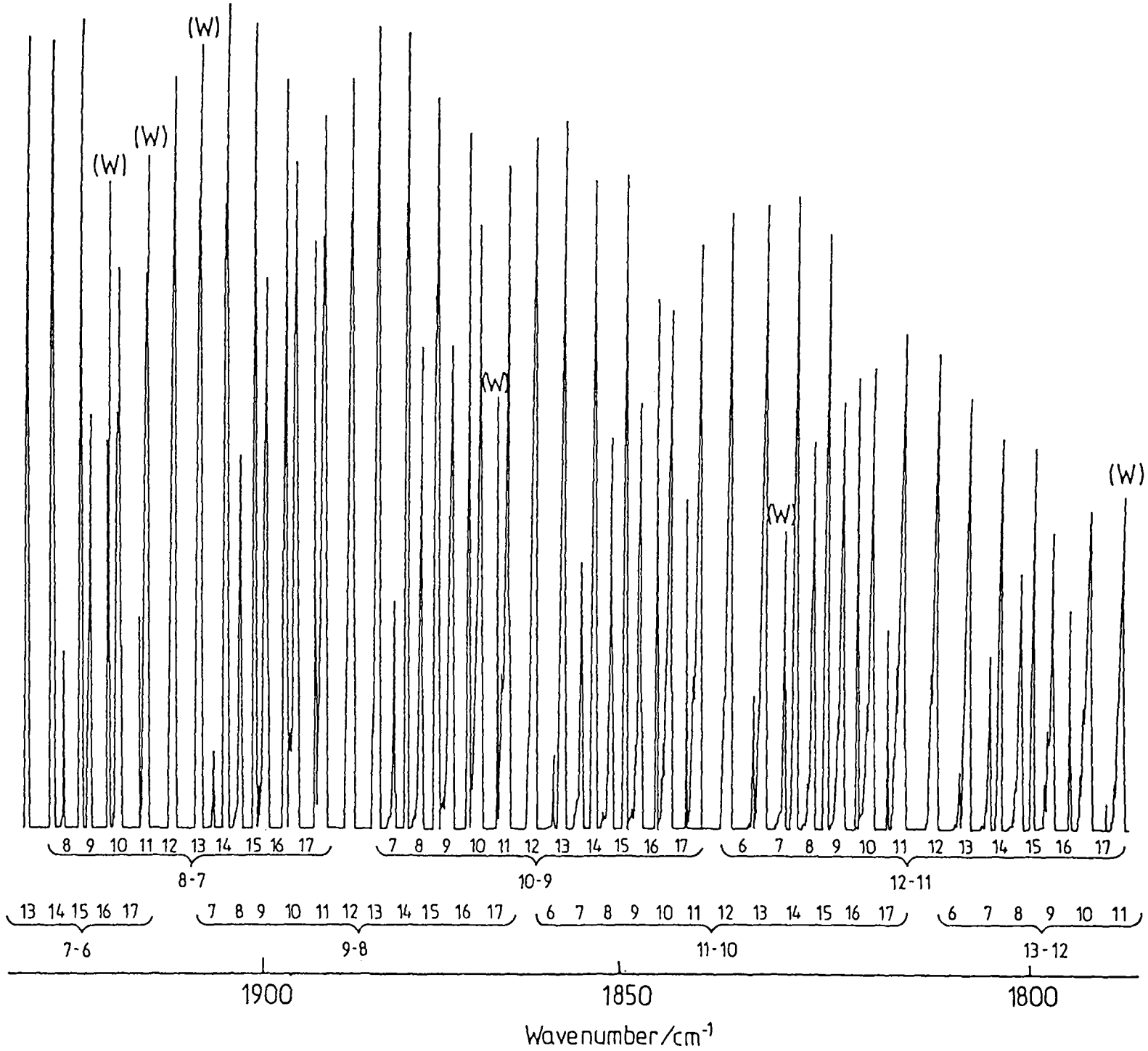

Figure B.1: The CO laser spectrum in the 1900 cm^{-1} region, with conditions optimised for high J lines. Contrast this with Fig.II.5 in Chapter II, which shows the same region optimised for lower J lines.

band. In this region, when the Littrow wavelength of the grating coincides with a CO laser line, an increase is observed in the fluorescence from the plasma at right angles to the optical axis. Laser action has been attained on the P(9) to P(11) lines of the (2,1) band, the P(11) being observed by Hensel and Hughes [3] when the laser cavity was purged with dry nitrogen.

Table B.2: Optimal gas pressures for the Oxford $\Delta v = 1$ CO laser below the 4–3 band[a].

Gas	Cumulative Pressure [Torr]
Helium	3.21
Nitrogen	4.23
Air	4.25[b]
Carbon Monoxide	4.29
Bleed Helium	4.47
Bleed Nitrogen	4.53

[a] $V_{\text{stab.}} = 2.0\,\text{kV}$, $V_{\text{tot.}} = 11.7\,\text{kV}$, $I_{\text{tot.}} = 9.0\,\text{mA}$.

[b] Approximate value.

Other regions

Laser action in the 1800–1200 cm^{-1} region requires pressures which vary progressively between those given for the 1900 cm^{-1} region and those required for the overtone laser, as the wave number decreases.

B.1.3 The Overtone CO Laser

Conditions

The gas pressures and discharge currents for operating the overtone laser in various regions are given in Table B.3. The air pressures may require minor adjustments, since they are very critical. No gases were bled in over the electrodes, since this was detrimental to laser action. The total current could not be reduced below 8.5 mA since the discharge became unstable, a manifestation of its negative impedance characteristic.

Table B.3: Optimal gas pressures for the Oxford overtone CO laser.

Gas	Cumulative Pressure [Torr]		
	19–17 Band[a]	33–31 Band[b]	
		Low J	High J[c]
Helium	7.51	6.96	7.08
Nitrogen	7.96	8.46	7.89
Air	8.04	8.52	7.95
Carbon Monoxide	8.50	9.06	8.53

[a] $V_{\text{stab.}} = 1.91\,\text{kV}$, $V_{\text{tot.}} = 12.8\,\text{kV}$, $I_{\text{tot.}} = 10.5\,\text{mA}$.

[b] $V_{\text{stab.}} = 2.45\,\text{kV}$, $V_{\text{tot.}} = 13.4\,\text{kV}$, $I_{\text{tot.}} = 8.8\,\text{mA}$.

[c] Current increased to 15 mA, giving gain on the $P(15)_{29-27}$ line.

Range of overtone laser action

With conditions optimised for the 19–17 band, laser action was observed from the 15–13 to 27–25 bands, the output power falling off above the 24–22 band. Fig.II.6 shows the overtone laser spectrum under these conditions. With conditions optimised for the 33–31 band, coverage extended from the 34–32 to the 16–14 bands, though the power dropped on the lower bands. A wide survey overtone laser spectrum is shown in Fig.B.2; it was recorded with conditions optimised for the 33–31 band and should be compared with Fig.II.6.

Output power

The maximum power coupled out via the zeroth grating order on the $P(11)_{33-31}$ line was measured to be 20 mW. This compares with a power of 140 mW measured by Bachem in Bonn [4], using the same grating but a 13 mm i.d. gain tube. The $P(11)_{33-31}$ line gave the greatest output power in both studies. The lowest output power was on the $P(15)_{29-27}$ line, $\approx 1\,\text{mW}$; this line was used to detect transitions in CH, indicating that the intracavity power is reasonable. This can occurs when the diffraction grating has a high first order reflectivity and a low zeroth order reflectivity at a given frequency, see §B.2.1.

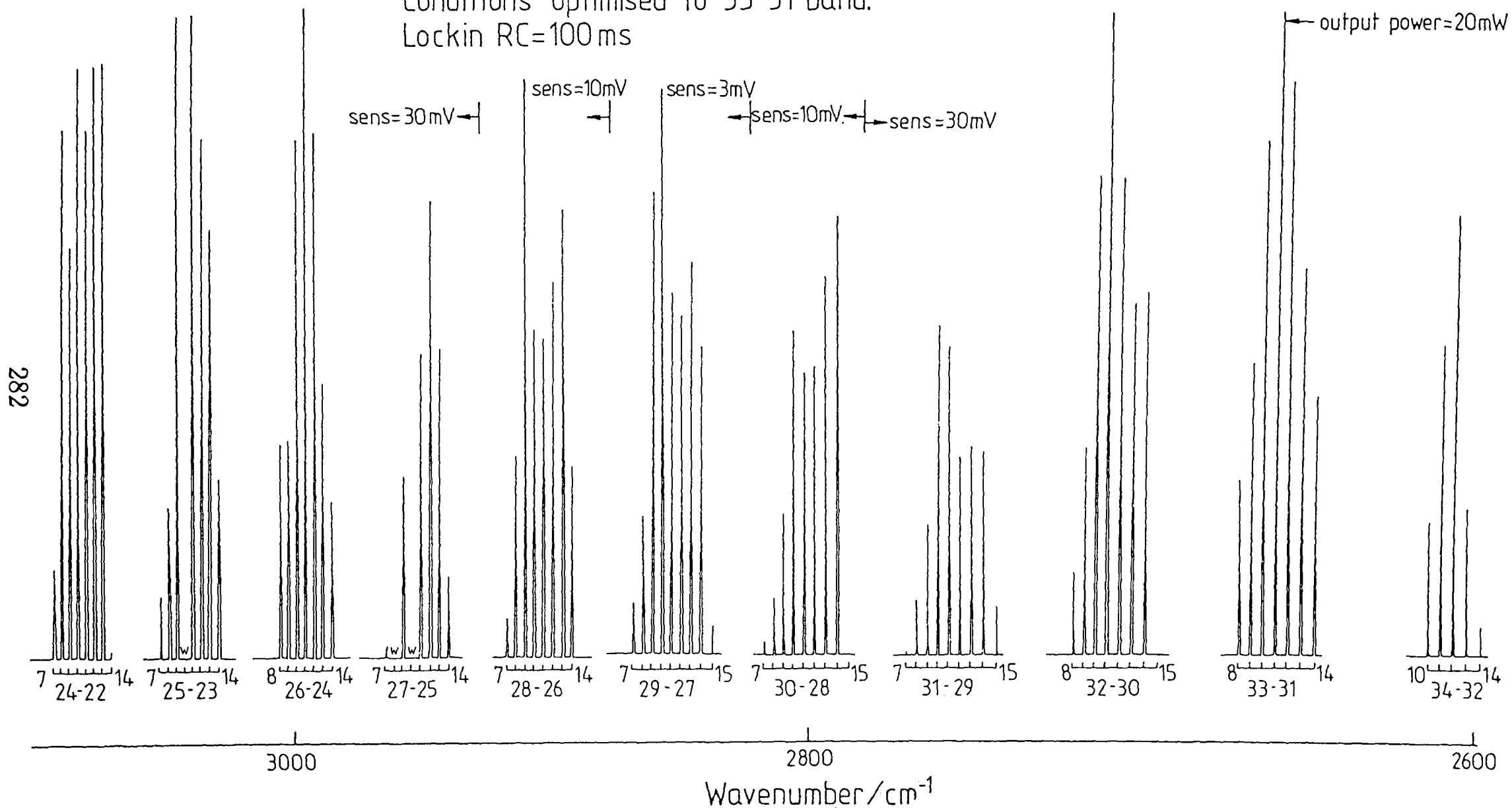

Figure B.2: Part of the CO overtone laser spectrum, with conditions optimised to the 33–31 band. The characteristic water absorption lines (marked W) are used to assign the spectrum.

B.2 Diffraction Gratings and Laser Alignment

B.2.1 The Diffraction Grating

The grating equation

The general equation for a ray of wavelength λ incident at an angle α to the normal of a diffraction grating, and refracted in the n^{th} order, at an angle β to the normal is [5]

$$d\,(\sin\alpha \pm \sin\beta) = n\lambda, \tag{B.1}$$

where the positive sign is taken when α and β are on the same side of the normal; d is the groove spacing.

The Littrow condition

If the grating is aligned such that the first order reflection on the same side of the normal as the incident beam, passes back along the incident path, then $\alpha = \beta$, the *Littrow condition* [6],

$$2d\sin\alpha = \lambda. \tag{B.2}$$

This is shown in Fig.B.3; in this arrangement the grating acts as a wavelength selective mirror, selection is performed by rotating the grating.

Blazing

The ruled surface of the grating is *blazed* at an angle γ (Fig.B.3). The blaze angle is chosen such that in the Littrow arrangement, the incident and first order radiation is at near normal incidence to the blazed surface. The specular reflection from this surface then coincides with the first order of the grating, channeling most of the refracted intensity into this order. This makes the grating highly reflective in the first order. Obviously this only occurs for near-normal incidence to the blazed surface, i.e. when the angle of incidence to the grating, α (also the angle of inclination of the grating from the vertical), is approximately the blaze angle.

The reflectivity of the grating in its first order falls off away from the blaze angle,

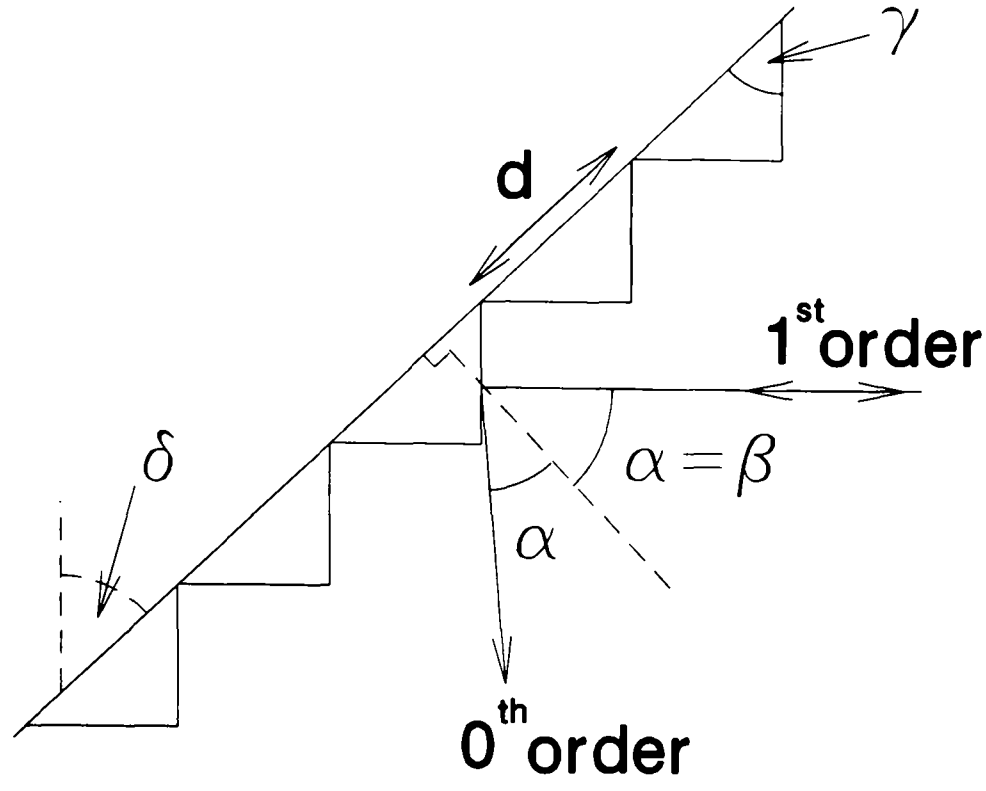

Figure B.3: A blazed diffraction grating optimised for the first order and shown in a Littrow autocollimation arrangement with an angle of incidence close to the blaze angle. There is another (weak, non-Littrow) first order ray on the opposite side of the grating normal and not shown.

which must be chosen for the region of interest[2] [4]. The groove spacing, d, is chosen so that $d \sim 0.7\lambda$, in order to ensure efficient refraction and to give high resolution[3].

Autocollimation

In the zeroth order, the grating acts as a plane mirror, *i.e.* $\alpha = -\beta$ (see Fig.B.3). A mirror at 90° to the grating can pick up the zeroth order beam, returning it parallel to the incoming first order beam but displaced in space. This is a so-called *autocollimation* arrangement [5]; it is used to couple the zeroth order radiation out to a detector. In this context, it should be noted that a high first order reflectivity of the grating will give a low zeroth order output power [8, 9]. This means that when the CO laser spectrum appears to be weak, the intracavity power can still be high.

[2]In practice, the optimum blaze angle depends upon the quality of the ruling engine used to produce the grating, and the ruling density. This makes grating production somewhat 'trial and error'.

[3]This is found to be optimal in the 10 μm region [7].

B.2.2 Gratings in Oxford

Specification

Four gratings are used for the CO LMR spectrometer:

1. 450 lines mm^{-1}, blazed for 4.5 μm, covering the 2500 – 3500 cm^{-1} region. This is the overtone laser grating; its properties have been characterised in Bonn, where it is referred to in literature as Zeiss grating #12 (4,5 MB) [4, 10]. The overtone laser grating has a special coating which is not reflective in the region of the normal CO laser, only allowing the lower gain overtone laser to operate[4].

2. 300 lines mm^{-1}, with $\gamma = 58°45'$, covering the 1500 – 2100 cm^{-1} region.

3. 150 lines mm^{-1}, with $\gamma = 23°45'$, covering the 1300 – 1500 cm^{-1} region.

4. 200 lines mm^{-1}, blazed for 9.3 μm, covering the 1200 – 1400 cm^{-1} region.

Alignment

There are two diffracted beams in each order of the grating, one of which is made more intense by the blazed surface. It is therefore important to mount the grating so that the intense reflections of an alignment He:Ne laser will be sent down the laser cavity.

Figs.II.1 and II.7 should be consulted in relation to the following text. With the tube and cell evacuated, an alignment He:Ne laser is mounted in place of the PZT mounted end-mirror, the iris at the mirror box is narrowed, and a center-hole plate is mounted at the grating box iris. With the He:Ne spot aligned on the optical axis, the grating is brought to normal incidence. The micrometer at the foot of the grating turntable is then adjusted so that the spot reflected back from the grating tracks exactly through the centre of the mirror box iris. The grating is then scanned forwards to the highest visible order that gives a clear spot. A cam screw in the grating holder itself is then adjusted so that this spot tracks exactly through the centre of the mirror box iris. This procedure must often be iterated several times to get a perfect grating alignment. The grating should then be set to its blaze angle and the autocollimation spot should then

[4]This is important because if $\Delta v = 2$ shows gain, then $\Delta v = 1$ will have a very much higher gain.

be aligned on the detector element, by adjusting the 45° out-coupling mirror and the detector's X-Y translator.

Overtone laser

For the overtone laser, it is also necessary to align the end-mirror before starting the laser. An intracavity beam-splitter is placed in the grating box so that it pivots on the optical axis. The beam-splitter is a microscope cover slip loosely mounted in an aluminium mount which sits on a pressurised 'O'-ring. The end-mirror is now replaced and the He:Ne laser sent into the grating box from a hole adjacent to the detector. The He:Ne spot must strike the beam-splitter on its pivot axis; an intermediate external mirror aids this. The He:Ne laser spot must now be aligned to pass unhindered through the cell and tube, and through the narrowed intracavity irises, by adjusting the beam-splitter and the external mirror. There are generally two spots seen on the mirror box, arising from reflections at each face of the beam splitter. One of them is chosen arbitrarily and aligned. The end-mirror screws are then adjusted so that the mirror's diffracted reflection is centered upon the entrance to the grating box.

With this accomplished and the irises opened and centre plate removed, it should be possible to start the overtone laser by scanning the grating with the Lansing stabiliser on 'slow' PZT modulation; the mirror adjustment screws should not be touched since this alignment is very critical. A special pyroelectrical detector and intracavity chopper are used when starting the laser; they are described in §B.4.2.

B.3 Properties of the CO Laser Cavity

B.3.1 Resonator Structure

The half symmetric resonator

The laser cavity forms a stable half-symmetric resonator [11], as is shown in Fig.B.4. The grating is the plane mirror M_1 with radius of curvature $R_1 = \infty$, M_2 is the end-mirror with radius of curvature R_2, and L is the length of the cavity. The criterion for laser oscillation is that an integral number of half wavelengths must fit into the cavity, and that the superposition of wavefronts must be coherent at the mirror surfaces (i.e. it must

obey Huygens' principle [5]).

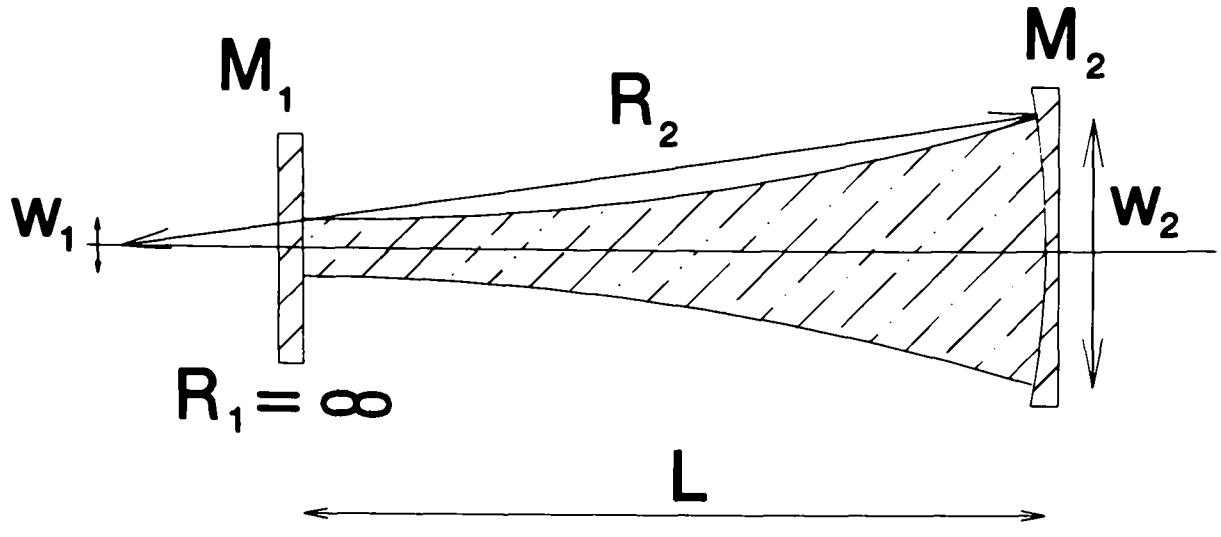

Figure B.4: The CO laser cavity as a half symmetric resonator.

Mode structure

The cavity can sustain a number of modes, which can be divided into two groups [5, 6, 11]:

1. Longitudinal modes TEM_{00k}, with a mode spacing of $c/2L$ Hz between TEM_{00k} and $\mathrm{TEM}_{00k\pm1}$. These modes have a spatially coherent, Gaussian intensity profile and have the smallest angular divergence of any modes. The Oxford CO laser cavity is 2.4 m long and so has a free spectral range of 62.5 MHz. Table B.3.1 gives the Doppler width of CO at $T_{\mathrm{trans}} = 120\,\mathrm{K}$ for a range of wave numbers. Hence under the gain curve of a CO transition there will typically be 1–3 longitudinal modes, but only the central one will have a gain above the lasing threshold.

2. Transverse modes TEM_{ijk} will also occur. These modes have (i, j) nodes in the planes orthogonal to the optical axis of the laser. They have an incoherent intensity distribution, the peak intensity lying away from the optical axis of the laser. The modes are shifted but close to, the TEM_{00k} modes. The spacing TEM_{ijk}–$\mathrm{TEM}_{ijk\pm1}$ is again $c/2L$ Hz.

Single axial mode operation

In order to record accurate, high-quality LMR spectra (particularly Lamb-dips), it is essential that the laser runs only in the TEM_{00k} mode. Furthermore, during an LMR

Table B.4: Doppler widths of CO gain profiles at $T_{\text{trans}} = 120\,\text{K}$.

Laser Wave Number $[\text{cm}^{-1}]$	Doppler Width [MHz]
1200	53
1600	71
2000	89
2500	111
3000	133
3500	156

scan, one mode must remain locked to the center of the CO gain curve, using the Lansing stabilisation system. The PZT modulation amplitude must be correctly adjusted on the Lansing stabiliser; if it is too large, it can cause excessive broadening of Lamb-dips, since it modulates the resonant frequency of the cavity.

When both longitudinal and transverse modes oscillate, gain stabilisation becomes unreliable. There is consequently an increase in laser noise (and a possible shift in laser frequency), as seen by a degradation in the signal-to-noise ratio of the LMR spectrum. Furthermore, the off-axis intensity distribution of the axial modes means that they do not probe the free radicals in the most homogeneous region of the magnetic field.

Intracavity irises enable the laser to be run only in the axial mode (TEM_{00k}), since narrowing the irises increases diffraction losses on other TEM_{ijk} modes more than on the TEM_{00k} modes, so that the former are suppressed are below the gain threshold for laser action [6].

Laser beam spot sizes

For a Gaussian beam in the TEM_{00k} mode, the spot sizes at the mirrors M_1 and M_2 are given by w_1 and w_2 respectively (see Fig.B.4), where

$$w_1^2 = \frac{L\lambda}{\pi}\sqrt{\frac{g}{1-g}} \tag{B.3}$$

and

$$w_2^2 = \frac{L\lambda}{\pi}\sqrt{\frac{1}{g\,(1-g)}}, \tag{B.4}$$

with $g = 1 - L/R_2$ [11]. The smallest spot size is w_1, the *beam waist*[5] of the laser. The variation of beam spot size with wave number and radius of curvature of M_2 has been evaluated in Table B.3.1. A mirror with $R_2 = 10\,\mathrm{m}$ was used for all the measurements made during this study.

Table B.5: Beam spot sizes for the Oxford CO-LMR spectrometer.

Laser Wave Number	$R_2 = 10\,\mathrm{m}$		$R_2 = 5\,\mathrm{m}$	
$\tilde{\nu}\,[\mathrm{cm}^{-1}]$	$w_1\,[\mathrm{mm}]$	$w_2\,[\mathrm{mm}]$	$w_1\,[\mathrm{mm}]$	$w_2\,[\mathrm{mm}]$
1200	3.4	3.9	2.6	3.6
1500	3.0	3.5	2.3	3.2
1800	2.7	3.2	2.1	2.9
2100	2.5	2.9	1.9	2.7
2500	2.3	2.7	1.8	2.5
3000	2.1	2.4	1.6	2.3
3500	2.0	2.3	1.5	2.1

Effect of gain tube diameter

Bachem [12] has shown that the power of the overtone laser can be improved dramatically by using a gain tube with a 13 mm i.d. instead of one with an i.d. of 16 mm. Fig.B.5 explains this; for a narrower gain tube, the translational temperature in the region of the laser mode will be lower than in a wider gain tube. This gives more efficient Treanor pumping and hence improved gain. There is a limit on how narrow the gain tube can be; if the i.d. approaches the diameter of the laser mode, then diffraction losses become significant. A mirror with a smaller radius of curvature can aid this, but then the volume of gain medium used by the narrower laser beam, and hence the power, is reduced. A glass tube cannot be made perfectly straight, and it seems that the optimum is a 13 mm i.d. tube and an end-mirror with a 10 m radius of curvature [12]. It would be desirable to install such a tube in Oxford.

[5]The beam waist is defined at the narrowest point of the TEM_{00k} laser beam. The beam waist defines the diameter of a circle within which $1 - 1/e$ of the normalised power of the beam is contained [11].

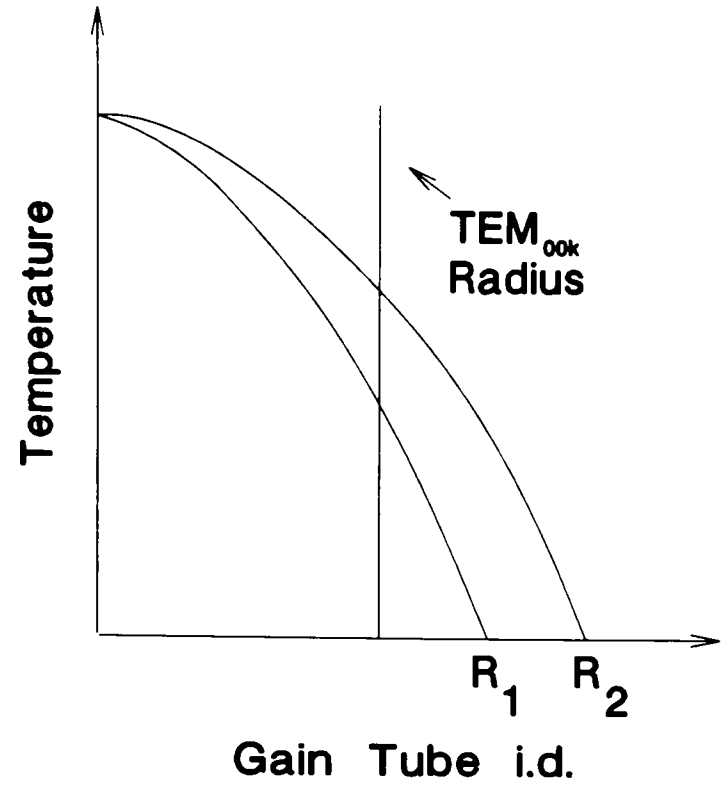

Figure B.5: Schematic diagram of the effect of the gain tube diameter on the temperature of the active medium in the region of the TEM_{00k} laser beam. Reproduced from [12] with the permission of E. Bachem.

B.4 Detectors

B.4.1 The Normal CO Laser

An Infrared Associates Hg:Cd:Te photo-conductive, liquid nitrogen cooled detector (model HCT 6-8, serial # H-2527) with a 1 mm^2 element and a 10° field-of-view, is used for the normal CO laser. This detector is suitable for monitoring both the d.c. and a.c. outputs of the spectrometer. The detector saturates when the incident power approaches 1 mW, therefore it is important to collimate the incident power, since the a.c. LMR signal is small and superimposed upon the d.c. background of the laser power. For this purpose, there is an iris at the entrance to the detector mounting (see Fig.II.7). The detector is held in a grounded copper housing which acts as a Faraday cage.

A standard pre-amplifier with a ±10 V, stabilised and filtered external power supply, provides a d.c. output for the chart recorder (for recording the CO laser spectrum) and two a.c. outputs, one for the Lansing stabiliser and one for the lock-in amplifier used to detect the LMR signal.

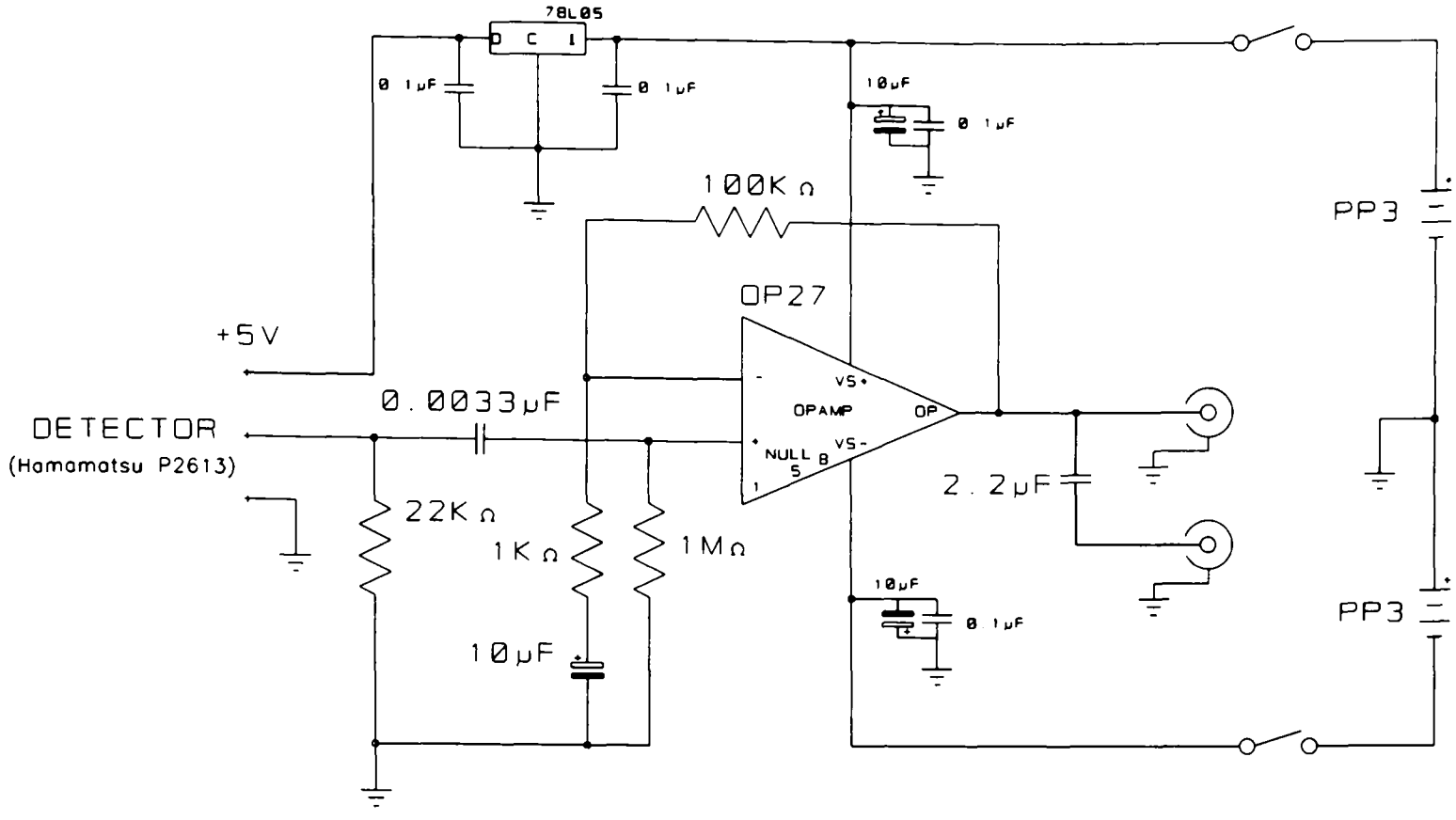

Figure B.6: The Pyroelectrical detector and pre-amplifier. The device is powered by a 9 V battery. Drawing courtesy of [13].

B.4.2 The Overtone CO Laser

Starting the overtone laser and recording its spectrum

When starting the overtone laser, there is a danger that a reflection from the window of the detector will cause all-line $\Delta v = 1$ laser action; the resulting high power would damage the In:Sb detector described below. For this reason, the detector described below is used to start the overtone laser and record its spectrum.

The CO overtone laser spectrum is recorded with a pyroelectrical detector based on a Hamamatsu photonics infrared sensitive diode (P2613), which operates at room temperature. A diagram of the detector and amplifier is shown in Fig.B.6. An intracavity chopper is used to provide a reference signal at 70 Hz, which is sent to a lock-in amplifier together with the pre-amplified detector output. The lock-in amplifier produces a 1-f signal corresponding to the CO laser output; its response is nonlinear in incident power. The pyroelectrical detector has a slow, small a.c. response and is not sufficiently sensitive for recording the LMR spectrum.

Recording the overtone laser LMR spectrum

With the overtone laser running on the desired line, the pyroelectrical detector is swapped over for the recording of the LMR spectrum.

An Infrared Associates In:Sb, liquid nitrogen cooled photo-voltaic detector (model IS-1.0, serial # GIL-598-S-IS) gives optimal sensitivity in the range of the overtone laser. The detector has a $1\,\mathrm{mm}^2$ element area and 10° field-of-view. The In:Sb detector can be damaged by an incident power on its element in excess of 1 mW; it must always be mounted skewed, so that a reflection off its window will not go back into the gain tube and give rise to al-line $\Delta v = 1$ laser action, whose power would destroy the detector. The detector is held in a copper housing which acts as a Faraday cage.

The In:Sb detector element is very sensitive and no current must flow through it; for this reason it requires the special pre-amplifier shown in Fig.B.7. The main component is a pair of Siliconix DPAD1 low-leakage, low reverse current diodes, mounted on a Teflon disk to minimise earth leakage. The gain of this pre-amplifier is very high and must be adjusted so that the laser power does not saturate it; this occurs when the pre-amplifier's d.c. output nears 14 V. A pre-amplifier gain of 10^3 or at the most 10^4 proves adequate; the output saturates at a gain of 10^5. The pre-amplifier provides the same outputs as the one for the Hg:Cd:Te detector.

B.5 The Mean Free Path in the Absorption Cell

The mean free path in a gas is given by [14]

$$\lambda = \frac{\bar{c}}{Z} = \frac{kT}{\sigma p \sqrt{2}}, \tag{B.5}$$

where Z is the collision frequency, p the pressure and $\bar{c} = (8kT/\pi\mu)^{1/2}$ is the mean speed of a Maxwell molecular velocity distribution for a gas of molecules with a reduced mass μ. The collision cross-section is $\sigma = \pi d^2$, where d is the 'hard sphere' molecular diameter.

In a typical experiment to produce NCO, a mixture of 5% fluorine in helium at a pressure of 83 Pa (0.62 Torr) was flowed through the microwave discharge. If it is assumed that collisions between helium and fluorine atoms are dominant, the mean free path of atomic fluorine, the species of interest, can be calculated. Atkins [14] gives collision

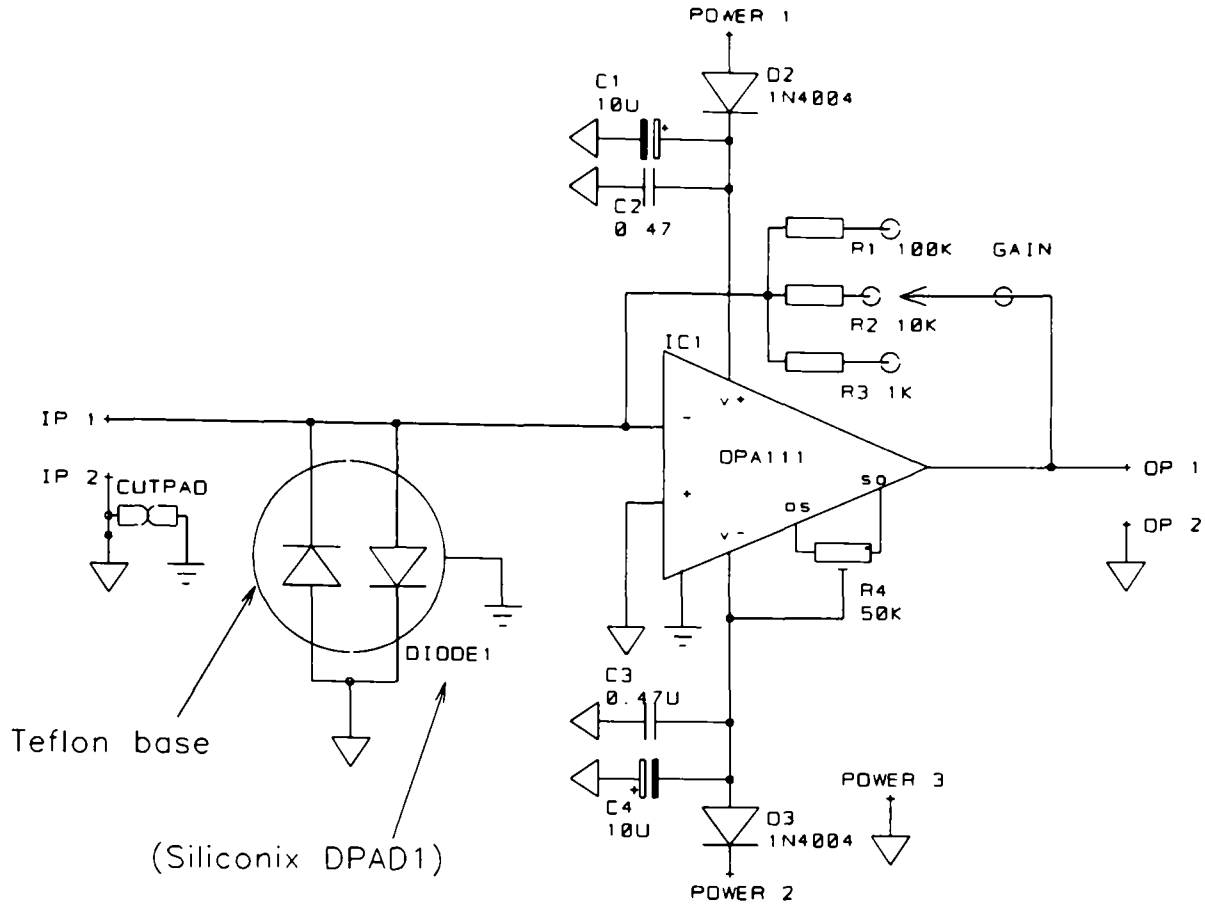

Figure B.7: The special low-noise, ultra-low leakage current pre-amplifier for the In:Sb detector. Power is supplied via a $\pm 15\,\mathrm{V}$ d.c. output from the EG+G model 5209 lock-in amplifier. Ferrite cores can be placed around the power inputs further to filter out noise. Drawing courtesy of [13].

cross-sections for helium and neon of $0.21\,\mathrm{nm}^2$ and $0.24\,\mathrm{nm}^2$, respectively. Assuming that fluorine and neon atoms are of similar size, the helium-fluorine collision cross-section is then $\sigma_{\mathrm{F/He}} = \pi(d_{\mathrm{F}} + d_{\mathrm{He}})^2/4 = 0.22\,\mathrm{nm}^2$; hence the mean-free path at $300\,\mathrm{K}$ is $161\,\mu\mathrm{m}$. This is much shorter than the several cm which the fluorine atoms must travel before reacting with HNCO; in addition, wall collisions will occur. Therefore, the fluorine atoms will be thermalised on entering the region probed by the laser beam.

B.6 Modulation Effects Upon the 2-f Lineshape

As discussed in §II.6, in the LMR experiment, resonances are detected at twice the modulation frequency (2-f detection). A problem with the use of higher harmonics in a phase-sensitive detection system is that the coefficients of the contribution of the n^{th} harmonic to the LMR signal, a_n and b_n in Eq.(II.2), generally decrease with n so that the absolute signal is less.

Two effects must be considered, both of which are functions of the normalised modulation amplitude,

$$\text{Normalised M.A.} = \frac{B_m}{\Delta B}, \tag{B.6}$$

where ΔB is the field-equivalent Half-Width-Half-Maximum (HWHM) of the resonance and B_m is half the peak-to-peak modulation amplitude (see §B.7).

B.6.1 Modulation Broadening

Modulation broadening becomes significant when the normalised M.A. exceeds unity. With the present modulation coils, it is normally only significant for Lamb-dip signals. Johnson [15] has investigated this effect for 2-f signals and the results are shown in Fig.B.8. Modulation broadening is homogeneous and modifies ΔB by a factor σ_m.

B.6.2 Modulation Induced Intensity Loss

The optimal signal pick-up for 2-f detection occurs at a normalised M.A. of ≈ 2 [16]. For a typical Doppler limited LMR signal with an FWHM of 10 mT, this requires a peak-to-peak M.A. of ≈ 20 mT. The present modulation coils produce a maximum peak-to-peak M.A.[6] of 3 mT, and so most resonances are severely under-modulated. Fig.B.9 shows how the signal amplitude depends upon the normalised M.A.; the effect can be modelled by an intensity factor I_m.

B.7 The LMR Spectroscopic Lineshape

B.7.1 Doppler Limited Resonances

Frequency domain

The motion of the absorbing molecules with respect to the stationary laboratory frame gives rise to a Doppler shift of the transition frequency. Molecules with a velocity component away from the radiation source experience a 'red' shift and those moving towards it experience a 'blue' shift [6]. At translational equilibrium, the velocity distribution of the

[6] A search coil is used to calibrate the peak-to-peak modulation field as a function of the current delivered to the resonant circuit. This is described in Ref. [17].

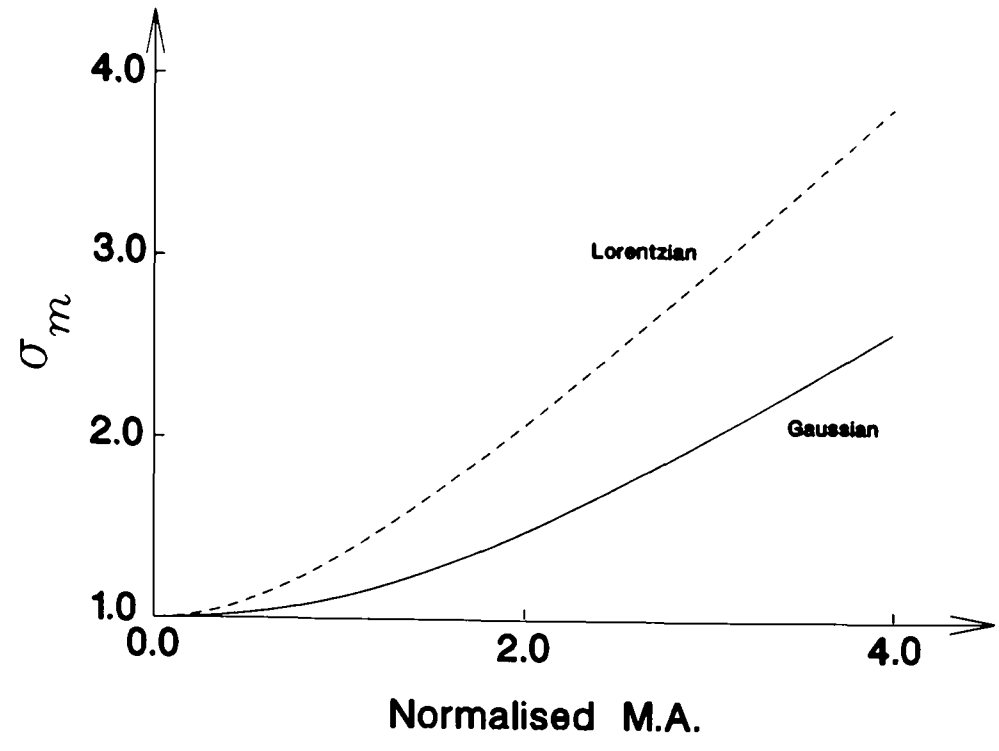

Figure B.8: The modulation broadening factor σ_m,for a 2-f lineshape as a function of the normalised modulation amplitude.

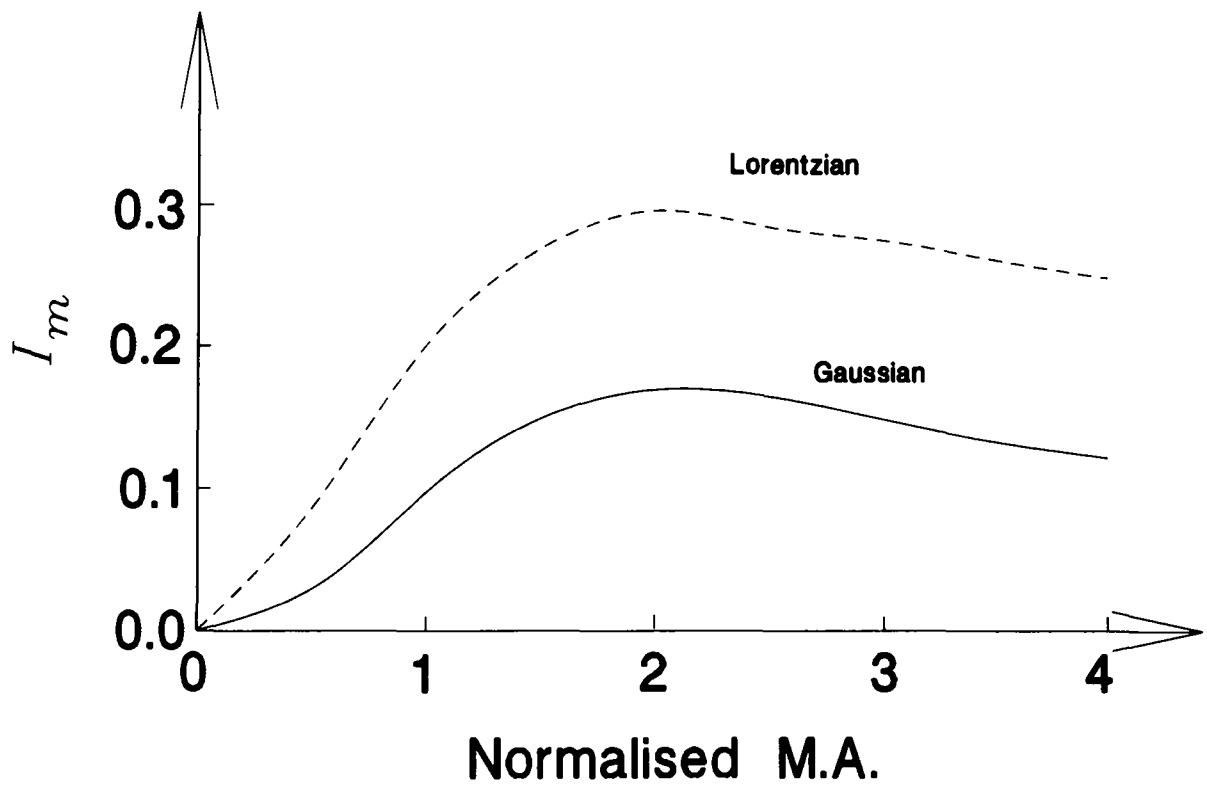

Figure B.9: The modulation induced intensity factor I_m, for a 2-f lineshape as a function of the normalised modulation amplitude. The peak of a "0-f" profile has an intensity factor of 1.0.

molecules is given by a Maxwell distribution [14]. The resulting spectroscopic lineshape is a 'Doppler profile' centered about the rest-frame transition frequency, ν_0, as shown in Fig.B.10. The analytical form of the absorbance profile, in which the area is proportional to the transition intensity, is given by [6, 15]

$$I(\nu) = \frac{I_0}{\Delta\nu}\left(\frac{\ln 2}{\pi}\right)^{\frac{1}{2}} e^{-\ln 2\left(\frac{\nu-\nu_0}{\Delta\nu}\right)^2}. \tag{B.7}$$

In Eq.(B.7), ν and ν_0 are the Doppler shifted and inertial rest-frame transition frequencies respectively, and $\Delta\nu$ is the HWHM in the frequency domain. The profile is characterised by a *Doppler width* of $2\Delta\nu$ [6], given by

$$\text{Doppler Width} = 2\Delta\nu = \frac{\nu_0}{c}\left(\frac{8N_A kT\ln 2}{M}\right)^{\frac{1}{2}} \text{ Hz}, \tag{B.8}$$

where N_A is Avogadro's number and M is the molecular mass in Kg. For NCO at 300 K and 1900 cm^{-1}, the Doppler width is 109 MHz. For comparison, ^{130}TeH under the same conditions has a Doppler width of 62 MHz.

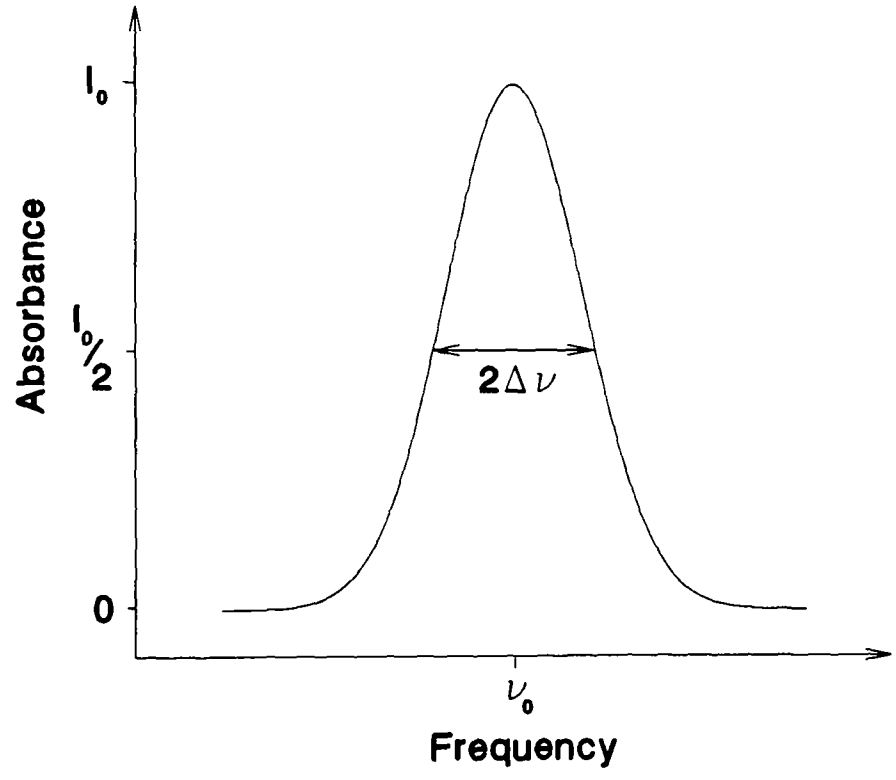

Figure B.10: The intensity normalised Doppler profile of a transition with an inertial rest-frame frequency of ν_0.

Magnetic field domain

The Doppler profile easily can be transformed into the magnetic field domain. It is then characterised by a field-equivalent HWHM, ΔB, and an intensity I_0 for a Zeeman component of the transition. The analytical form of the profile is

$$I(B) = \frac{I_m I_0}{\sigma_m \Delta B} \left(\frac{\ln 2}{\pi}\right)^{\frac{1}{2}} e^{-\ln 2\left(\frac{B-B_0}{\sigma_m \Delta B}\right)^2}, \tag{B.9}$$

where the field-equivalent HWHM (half the field-equivalent Doppler width) is

$$\Delta B = \Delta\nu/(\partial\nu/\partial B), \tag{B.10}$$

and B and B_0 are the Doppler shifted and rest-frame resonant fields, respectively. The factors σ_m and I_m account for modulation broadening and modulation-induced intensity loss respectively, as was discussed in §B.6.

The Oxford LMR spectrometer uses 2-f detection, generating a signal proportional to the second derivative of Eq.(B.9). This takes the form

$$I''(B) = -2\ln 2\left\{I(B) + \left(\frac{B-B_0}{\sigma_m \Delta B}\right) I'(B)\right\}. \tag{B.11}$$

An example of such a profile (neglecting modulation effects) is shown in Fig.II.9.

Widths of LMR signals

Zeeman components of the same zero-field transition will have different tuning rates at resonance and hence different field-equivalent HWHM's. For example, with a Doppler width of 100 MHz, tuning rates of 1.8 $\mathrm{MHzG^{-1}}$, 0.5 $\mathrm{MHzG^{-1}}$ and 0.1 $\mathrm{MHzG^{-1}}$, give respective field widths of $\Delta B = 56$ G, $\Delta B = 200$ G and $\Delta B = 1000$ G.

Transitions which are several hundreds of Gauss wide are difficult to detect; they are both under-modulated in the Oxford LMR spectrometer and the peak amplitude of the signal, $I(B_0)$, as given by Eq.(B.11), is reduced as ΔB increases.

Simulating LMR spectra

The line profile given by Eq.(B.11), proved adequate for the simulation of Doppler limited LMR spectra. Simulations aided the assignment of NCO spectra (and others), and were used to refine the field measurements of the convoluted LMR spectrum of CCN [18].

B.7.2 Sub-Doppler Resonances

Saturation

Molecules moving with zero velocity component along the optical (z) axis of the laser do not experience a Doppler shift in the transition frequency. In the intracavity configuration, such molecules are subjected to counter-propagating beams of laser radiation, both of which pump an absorption resonance at the same field B_0. If the transition is strong and the single mode laser power is high, it is possible to equalise the upper and lower state populations.

When $B \neq B_0$, two different velocity groups absorb laser radiation, whilst at B_0, only one velocity group with $v_z = 0$ absorbs radiation. The saturation effect is nonlinear, so the laser intensity absorbed at B_0 does not lead to twice the absorption. This gives rise to an inhomogeneous drop in the absorption at B_0, which appears as a Lamb-dip [6] 'burned' into the Doppler profile (apparently, but not really, in emission relative to the Doppler absorption profile).

B.7.3 Factors Limiting the Widths of Lamb-Dips

Lifetime broadening

The natural lifetime broadening of mid-infrared transitions is very small [19], of the order of

$$\delta\nu_{\text{natural}} \approx A/4\pi. \tag{B.12}$$

Here, A is the Einstein spontaneous emission rate constant[7][19] for the upper state,

$$A = \frac{64\pi^4\nu^3 \times 10^{-7}}{3hc} |\boldsymbol{\mu}|^2 \text{ s}^{-1}, \tag{B.13}$$

where ν is in Hertz and $\boldsymbol{\mu}$ is the electric transition dipole moment in Cm. A typical vibration-rotation transition at 1900 cm^{-1}, with a dipole moment of 0.1 D (3.3×10^{-5} Cm), has $\Delta\nu \approx 1.71$ Hz.

Collisional broadening

In the production of NCO, 2.7 Pa (0.02 Torr) of HNCO was added to the 83 Pa (0.62 Torr) of 5% fluorine in helium. Assuming that 2.7 Pa(0.02 Torr) of NCO was formed, and that collisions of NCO with He were dominant, the collision frequency of one NCO molecule with all He atoms is given by [14]

$$Z_{\text{NCO/He}} = \sigma_{\text{NCO/He}}\bar{c}\left(\frac{p_{He}}{kT}\right) \text{ s.}^{-1} \tag{B.14}$$

Atkins [14] gives a value of $\sigma = 0.52\,\text{nm}^2$ for CO_2; assuming the same value for NCO gives $\sigma_{\text{NCO/He}} = 0.35\text{nm}^2$. This yields $Z_{\text{NCO/He}} = 9.2 \times 10^6\text{s}^{-1}$. Replacing A with Z in Eq.(B.12) gives a collision broadening of $\Delta\nu \approx 0.75$ MHz at a total pressure of 86 Pa (0.64 Torr).

Observing and modelling Lamb-dips

In this work, saturation was only observed at pressures below 133 Pa (1 Torr). Studies of Lamb-dips of NO by LMR in Bonn [20] have shown the minimum HWHM of the dips to be $\sim$ 5 MHz. The largest contributions to this value arise from the long term stability of the laser cavity, the modulation of the PZT mounted cavity end-mirror used by the Lansing stabiliser, and the broadening due to the phase-sensitive detection field modulation. The latter can be reduced, but at the expense of losing signal intensity.

A value of 5 MHz can be assigned to ΔB_s, the effective saturation HWHM. The

[7]Spontaneous emission is induced by the component of the zero-point background field at the transition frequency. Lifetime broadening is a consequence of Heisenberg's uncertainty principle.

Lamb-dip signal can be approximated to a Lorentzian emission curve of the form

$$I(B) = \left(\frac{I_m I_0}{\pi}\right) \frac{\sigma_m \Delta B_s}{(\sigma_m \Delta B_s)^2 + (B - B_0)^2} \tag{B.15}$$

so that the form of the 2-f lineshape is

$$\begin{aligned} I''(B) &= \frac{2}{(\sigma_m \Delta B_s)^2 + (B - B_0)^2} \times \\ &\left\{ I(B) \frac{\left[(B - B_0)^2 - (\sigma_m \Delta B_s)^2\right]}{(\sigma_m \Delta B_s)^2 + (B - B_0)^2} - (B - B_0) I'(B) \right\}. \end{aligned} \tag{B.16}$$

Other line profile effects

It should be noted that at longer wavelengths, for example in the far-infrared and at longer wavelengths, it is important to consider pressure induced shifts in the rest frame transition frequency. These can require the numerical evaluation of more complicated Voigt etc... lineshapes [6, 21]. These effects are only just detectable at low pressures in the far-infrared, and are probably too small to be significant in low pressure ($<$ 660 Pa (5 Torr)) mid-infrared studies.

High laser powers can also produce small Stark shifts and broadenings (induced by the **E** field of the radiation) in the transition [6]. Again such effects are only just detectable in the far-infrared and they have been neglected here.

Bibliography

[1] B. Wu, T. George, M. Schneider, W. Urban and B. Nelles, *Appl. Phys. B* **52**, 163–167 (1991).

[2] W. Urban, Institut für Angewandte Physik der Universität Bonn, Private Communication, 1992.

[3] K.D. Hensel and R.A. Hughes, Physical Chemistry Laboratory, University of Oxford, Private Communication, 1994.

[4] E. Bachem, Institut für Angewandte Physik der Universität Bonn, Private Communication, 1992.

[5] E. Hecht, "Optics," 2nd ed., pp. 79–87, 393–394, 424–430, 581–585, Addison-Wesley, Reading, MA, 1989.

[6] W. Demtröder, "Laser Spectroscopy," pp. 79–115, 132–139, 232–272, "Springer Series in Chemical Physics," Vol. 5, Springer-Verlag, Berlin, 1982.

[7] K.M. Evenson, National Institute of Standards Technology, Boulder, Colorado, Private Communication, 1994.

[8] W. Urban, "The CO-Overtone Laser A Spectroscopic Source in a Most Interesting Wavelength Region," *in* "Applied Laser Spectroscopy," (W. Demtröder and M. Inguscio, Eds.), pp. 127–135, Plenum Press, New York, 1990.

[9] E. Bachem, A. Dax, T. Fink, A. Weidenfeller, M. Schneider and W. Urban, *Appl. Phys. B* **57**, 185–191 (1993).

[10] A. Weidenfeller, Diplomarbeit thesis, Institut für Angewandte Physik der Universität Bonn, 1990.

[11] A.E. Siegman, "Lasers," pp. 462–273, 663–675, 744–752, 758–775, University Science Books, Mill Valley, CA, 1986.

[12] E. Bachem, Ph.D thesis, Institut für Angewandte Physik der Universität Bonn, 1992.

[13] Electronics workshop (J. Jessup *et al.*), Physical Chemistry Laboratory, University of Oxford, 1994.

[14] P.W. Atkins, "Physical Chemistry", 3rd ed., pp. 647–653, 831 Oxford University Press, Oxford, 1986.

[15] A.W. Johnson, *J. Magn. Reson.* **24**, 21–24 (1976).

[16] G.V.H. Wilson, *J. Appl. Phys.* **34**, 3276–3285 (1963).

[17] J.P. Towle, D.Phil thesis, p. 9, University of Oxford, 1992.

[18] D.A. Gillett and J.M. Brown, *Can. J. Phys.* **72**, 1004–1006 (1994).

[19] P.W. Atkins, "Molecular Quantum Mechanics," 2nd ed., pp. 196–202, 442–443, Oxford University Press, Oxford, 1983.

[20] M. Havenith-Neven, Institut für Angewandte Physik der Universität Bonn, Private Communication, 1992.

[21] C.H. Townes and A.L. Schawlow, "Microwave Spectroscopy," pp. 336–375, Dover Publications, New York, 1975.

Appendix C

Third Order Perturbation Estimates of the Renner-Teller Effect

C.1 Quenching of the Orbital Angular Momentum

Renner-Teller interactions within the $^2\Pi$ electronic manifold result in a quenching of the orbital angular momentum vector, **L**. Physically this can be attributed to coupling between **L** and the vibrational angular momentum vector, **G**.

If the state of interest is a non-unique state ($K < v_2 + 1$), the matrix elements of the Renner-Teller effective Hamiltonian diagonal in v_2 must be considered explicitly. The effect of the matrix elements of the Renner-Teller effective Hamiltonian off-diagonal in v_2 is smaller and can be estimated by perturbation theory. This has not been done in this thesis; rather the complete matrix was constructed and diagonalised exactly. Many other workers however, particularly in the study of the unique states, have chosen not to include the matrix elements of $\mathcal{H}_{RT}^{\text{eff.}}$ off-diagonal by $\Delta v_2 = \pm 2$. They have instead approximated their contribution using an estimate derived from third order perturbation theory [1]. The spin-orbit coupling parameter A, the nuclear spin-electronic orbital magnetic hyperfine coupling parameter a, and the orbital g-factor, g_L are affected by this interaction.

C.1.1 Derivation of the Third Order Correction

The leading contribution to the Renner-Teller quenching due to the matrix elements with $\Delta v_2 = \pm 2$ arises in the third order of perturbation theory. The perturbation Hamiltonian operating in the single $^2\Pi$ electronic state is

$$\mathcal{H}' = \mathcal{H}_{RT}^{\text{eff.}} + L_z, \tag{C.1}$$

The effect of the Renner-Teller matrix elements with $\Delta v_2 = \pm 2$ is to reduce the expectation value of the projection orbital angular momentum along the molecule-fixed z-axis, Λ.

Consider a basis state $|\eta\Lambda; v_2 l K\rangle$; the interaction with states $|\eta\Lambda; v_2 \pm 2; l' K\rangle$ are of concern. This is given to third order by

$$\begin{aligned}
\left\langle L_z^{(3)} \right\rangle \;=\; & \sum_{v_2'=v_2\pm 2} \Bigg\{ \frac{1}{4\omega_2^2} \langle \eta\Lambda; v_2 l; K | \, \mathcal{H}_{RT}^{\text{eff.}} \, | \eta, -\Lambda; v_2' l'; K \rangle \\
& \times \; \langle \eta, -\Lambda; v_2' l'; K | \, L_z \, | \eta, -\Lambda; v_2' l'; K \rangle \, \langle \eta, -\Lambda; v_2' l'; K | \, \mathcal{H}_{RT}^{\text{eff.}} \, | \eta, \Lambda; v_2 l; K \rangle \\
& - \; \frac{1}{4\omega_2^2} \langle \eta\Lambda; v_2 l; K | \, \mathcal{H}_{RT}^{\text{eff.}} \, | \eta, -\Lambda; v_2' l'; K \rangle \\
& \times \; \langle \eta, -\Lambda; v_2' l'; K | \, \mathcal{H}_{RT}^{\text{eff.}} \, | \eta, \Lambda; v_2 l; K \rangle \, \langle \eta, \Lambda; v_2 l; K | \, L_z \, | \eta, \Lambda; v_2 l; K \rangle \Bigg\}
\end{aligned} \tag{C.2}$$

The result is

$$\left\langle L_z^{(3)} \right\rangle = -\frac{\epsilon^2 \Lambda}{16} \left(n^2 + 2\Lambda K + \Lambda^2 K^2 \right), \tag{C.3}$$

so that the orbital quenching reduces Λ to an effective value of

$$\Lambda^{\text{eff.}} = \Lambda \left[1 - \frac{\epsilon^2 \Lambda}{16} \left(n^2 + 2\Lambda K + \Lambda^2 K^2 \right) \right]. \tag{C.4}$$

C.2 Application of the Correction Term

C.2.1 Unique States

For a unique state, the third order correction is the first and most significant; since $\Lambda = 1$ and $K = v_2 + 1$,

$$\Lambda^{\text{eff.}} = 1 - \frac{\epsilon^2}{8} n\,(n+1)\,. \tag{C.5}$$

In an analysis of the unique states neglecting the Renner-Teller effect, a value of $\Lambda^{\text{eff.}} = 1$ is used so that the above correction affects the parameter instead. For example, the effective spin-orbit coupling parameter determined in such analysis, $A^{\text{eff.}}$, is related to the 'true' un-quenched value by

$$A^{\text{eff.}} = A^{\text{true}} \left[1 - \frac{\epsilon^2}{8} n\,(n+1)\right], \tag{C.6}$$

and similarly for the magnetic hyperfine parameter a. Bolman *et al.*[2] derived a similar correction for the orbital g-factor in the unique states, Eq.(IV.8). In their expression they also included the spin-orbit coupling parameter in the denominator of the perturbation expression, giving a slightly modified form for $\Lambda^{\text{eff.}}$.

C.2.2 $^2\Sigma$ Vibronic States

In the $K = 0$ states, the effective value of Λ is

$$\Lambda^{\text{eff.}} = \Lambda \left[1 - \frac{\epsilon^2}{16} n^2\right]. \tag{C.7}$$

It must be remembered that there is a much larger first order Renner-Teller effect in these states.

C.3 Third Order Contributions to the Renner Parameter

Brown [1] has shown that if the $\Delta v_2 = \pm 2$ matrix elements are omitted from a study in which $\epsilon\omega_2$ is determined, then there is a third order Renner-Teller contribution to the

value of $\epsilon\omega_2$. The effective value determined is given to third order by

$$\epsilon^{\text{eff.}}\omega_2 = \epsilon^{\text{true}}\omega_2 \left[1 + \frac{\epsilon^2_{\text{true}}}{16}\left(2 - K^2\right)\right]. \tag{C.8}$$

Therefore, if $\epsilon\omega_2$ is obtained from the analysis of $K = 0$ states, an effective value of

$$\epsilon^{\text{eff.}} = \epsilon_{\text{true}}\left(1 + \frac{\epsilon^2_{\text{true}}}{8}\right) \tag{C.9}$$

is obtained.

Bibliography

[1] J.M. Brown, Physical Chemistry Laboratory, University of Oxford, unpublished notes on the Renner-Teller effect, 1993.

[2] P.S.H. Bolman, J.M. Brown, A. Carrington, I. Kopp and D.A. Ramsay, *Proc. R. Soc. Lond. A* **343**, 17–44 (1975).

Appendix D

The $\mathbf{N^2}$ and $\mathbf{R^2}$ Hamiltonians

Tables D.1 and D.2 on the following pages give the interconversion formulae for parameters determined in the $\mathbf{N^2}$ and $\mathbf{R^2}$ Hamiltonian formalisms. The parameter T (or T^*) is the vibrational or electronic term value; in both formalisms it includes the contribution

$$\left\langle v' \left| B\left(r\right) \left\{ L_x^2 + L_y^2 \right\} \right| v \right\rangle ,$$

where the v are the vibrational levels. This arises from the inability to evaluate the off-diagonal matrix elements of the orbital angular momentum operator, $\mathbf{L}$. The size of this contribution is of the order of the rotational constant, B. Therefore band origins, which are differences of term values, contain an uncertainty of the order of α_B. This contribution will have a different mass dependence to the pure term value, so in principle it can be separated by comparing the band origins of isotopomeric molecules. There is a similar contribution to the band origin, of order $\alpha_B l^2$, arising from second order terms similar to those for $\mathbf{L}$ above, but involving the components of the vibrational angular momentum, G_x, G_y and G_z. References [1] and [2] describe the simple inter-relation between the $\mathbf{N^2}$ and $\mathbf{R^2}$ formalisms.

Table D.1: Interconversion of parameters from the $\mathbf{R}^2$ to the $\mathbf{N}^2$ Hamiltonians.

$\mathbf{N}^2$		$\mathbf{R}^2$
$T^{(a)}$	=	$T^* - B^*\Lambda^2 - D^*\Lambda^4 - H^*\Lambda^6$
B	=	$B^* + 2D^*\Lambda^2 + 3H^*\Lambda^4$
D	=	$D^* + 3H^*\Lambda^2$
H	=	H^*
$A^{(b)}$	=	$A^* - \gamma^* - A_D^*\Lambda^2 + \gamma_D^*\Lambda^2$
γ	=	$\gamma^* - \gamma_D^*\Lambda^2$
γ_D	=	γ_D^*
A_D	=	$A_D^* - \gamma_D^*$
λ	=	$\lambda^* - \lambda_D^*\Lambda^2$
λ_D	=	λ_D^*
β	=	$\beta^* - \beta_D^*\Lambda^2$
β_D	=	β_D^*

[a] The parameters without asterisks are $\mathbf{N}^2$ values; those with asterisks are $\mathbf{R}^2$ values.

[b] In some $\mathbf{R}^2$ Hamiltonians, the spin-rotation Hamiltonian is written $\gamma\mathbf{N}.\mathbf{S}$. In this case $A = A^*$.

[c] β is a hyperfine or Λ-type doubling parameter.

Table D.2: Interconversion of parameters from the $\mathbf{N}^2$ to the $\mathbf{R}^2$ Hamiltonians.

$\mathbf{R}^2$		$\mathbf{N}^2$
$T^{*(a)}$	=	$T + B\Lambda^2 - D\Lambda^4 + H\Lambda^6$
B^*	=	$B - 2D\Lambda^2 + 3H\Lambda^4$
D^*	=	$D - 3H\Lambda^2$
H^*	=	H
$A^{*(b)}$	=	$A + \gamma + A_D\Lambda^2 + \gamma_D\Lambda^2$
γ^*	=	$\gamma + \gamma_D\Lambda^2$
γ_D^*	=	γ_D
A_D^*	=	$A_D + \gamma_D$
λ^*	=	$\lambda + \lambda_D\Lambda^2$
λ_D^*	=	λ_D
β^*	=	$\beta + \beta_D\Lambda^2$
β_D^*	=	β_D

[a] The parameters without asterisks are $\mathbf{N}^2$ values; those with asterisks are $\mathbf{R}^2$ values.

[b] In some $\mathbf{R}^2$ Hamiltonians, the spin-rotation Hamiltonian is written $\gamma\mathbf{N}.\mathbf{S}$. In this case $A^* = A$.

[c] β is a hyperfine or Λ-type doubling parameter.

Bibliography

[1] J.M. Brown, A.S-C. Cheung and A.J. Merer, *J. Mol. Spectrosc.* **124**, 464–475 (1987).

[2] T.D. Varberg and K.M. Evenson, *J. Mol. Spectrosc.* **157**, 55–67 (1993).

Appendix E

K-Type Doubling

E.1 Introduction

K-type doubling [1] is a rotationally induced splitting of states which are degenerate in the non-rotating molecule. These states are characterised by the same value of K but have opposite space-fixed inversion parity, for example the Kramers doublets $|\psi_{1a}; J; +\rangle$ and $|\psi_{1a}; J; -\rangle$. The physical origin of K-type doubling can be attributed to the electromagnetic field created by rotation of the molecule. This additional field along the direction of the rotational angular momentum $\mathbf{R}$, starts to decouple the angular momenta from the molecule-fixed z-axis. This destroys Λ, Σ, l and K as good quantum numbers. There are two consequences for a Π electronic state:

1. A parity dependent interaction with remote $^2\Sigma$ electronic states. The interacting levels in the $^2\Pi$ and $^2\Sigma$ electronic states must have the same parity. The rotational levels of a $^2\Pi$ state occur in $\pm$ parity pairs and so only the level with the same parity as the remote $^2\Sigma$ state level with which it interacts, is affected. This interaction causes a splitting of basis states with the same value of $|\Lambda|$ but with opposite space-fixed inversion parities; it is known as Λ-type doubling.

2. Parity dependent Coriolis and vibrational interactions within the $^2\Pi$ electronic state cause a splitting of basis states characterised by the same value of $|l|$ but with opposite space-fixed inversion parities. This interaction is known as l-type doubling.

Together these effects are known as K-type parity doubling. The observed K-type doubling is a combination of both effects and the two contributions cannot be separated easily [1].

In addition, a mixing occurs between states of different K in a given vibrational manifold (v_1, v_2, v_3); this is known as K-type resonance [2, 3]. Adam *et al.*[5] have observed K-type resonance effects in the Renner-Teller molecule BO_2; it appears that these effects can become large when $A \gg \epsilon\omega_2$.

The effective Hamiltonians for the two contributions to K-type doubling in $^2\Pi$ electronic states are now considered.

E.2 Λ-Type Doubling

E.2.1 Introduction

Λ-type doubling arises in the electronic Van Vleck transformation through the operators $a_i l_{i,\pm} s_{i,\mp} a_j l_{j,\pm} s_{j,\mp}$, $BN_\pm N_\mp a_i l_{i,\pm} s_{i,\mp}$ and $BN_\pm, N_\mp BN_\pm N_\mp$ [4], which give rise to second-order, parity dependent terms [6]–[11].

The single state, Λ-type doubling effective Hamiltonian for a Π electronic state can be written as [10]

$$\frac{\mathcal{H}_{LD}^{\text{eff.}}}{hc} = \frac{o}{2}\left[S_+^2 + S_-^2\right] - \frac{p}{2}\left[N_+ S_+ + N_- S_-\right] + \frac{q_{\text{el.}}}{2}\left[N_+^2 + N_-^2\right]. \tag{E.1}$$

where the parameters are those of Mulliken and Christy [8] and Brown and Merer [10]. The Hamiltonian can be expanded in terms of operators with good Hund's case (a) eigenvalues to give

$$\frac{\mathcal{H}_{LD}^{\text{eff.}}}{hc} = \frac{1}{2}\left(o + p + q_{\text{el.}}\right)\left[S_+^2 + S_-^2\right] - \frac{1}{2}\left(p + 2q_{\text{el.}}\right)2\left[J_+ S_+ + J_- S_-\right] + \frac{1}{2}q_{\text{el.}}\left[J_+^2 + J_-^2\right]. \tag{E.2}$$

The selection rules of the effective Hamiltonian are

$$\Delta\Lambda = \pm 2; \Delta K = 0, \pm 2; \Delta l = 0; \begin{cases} \Delta\Sigma = \pm 1 \text{ and } \Delta P = \mp 1 \\ \Delta\Sigma = 0 \text{ and } \Delta P = \pm 2. \end{cases}$$

The Hamiltonian is diagonal in all other quantum numbers. For a $^2\Pi$ electronic state remote from states of higher spin multiplicity, the eigenvalues of $S_{\pm}^2$ are zero and the first term in Eq.(E.2) need not be considered further.

E.2.2 Matrix Elements

The matrix elements of the Hamiltonian (E.2) are

$$\begin{aligned}&\langle \eta\Lambda'; v_2 l; S\Sigma \pm 1; JP \mp 1, M_J | \, \mathcal{H}_{ld}^{\text{eff.}} \, | \eta\Lambda; v_2 l; S\Sigma; JP, M_J \rangle \\ &= -\frac{1}{2}\left(p + 2q_{\text{el.}}\right)\left[J\left(J+1\right) - P\left(P \mp 1\right)\right]^{\frac{1}{2}}\left[S\left(S+1\right) - \Sigma\left(\Sigma \pm 1\right)\right]^{\frac{1}{2}} \qquad \text{(E.3)}\end{aligned}$$

and

$$\begin{aligned}&\langle \eta\Lambda'; v_2 l; S\Sigma; JP \mp 2, M_J | \, \mathcal{H}_{ld}^{\text{eff.}} \, | \eta\Lambda; v_2 l; S\Sigma; JP, M_J \rangle \\ &= \frac{q_{\text{el.}}}{2}\left[J\left(J+1\right) - \left(P \mp 1\right)\left(P \mp 2\right)\right]^{\frac{1}{2}}\left[J\left(J+1\right) - P\left(P \mp 1\right)\right]^{\frac{1}{2}}. \qquad \text{(E.4)}\end{aligned}$$

The quantum number $\Lambda' = \Lambda \pm 2$; this sign choice is independent of those in the brackets above.

Consideration of the selection rules shows that, for $\Delta K = 0$, the operators in Eq.(E.2) can only connect states characterised by $\pm|\Lambda|$ when $|K| = 1$, *i.e.* only for $^2\Pi$ vibronic states within the $^2\Pi$ electronic state.

E.3 The *l*-Type Doubling Hamiltonian

E.3.1 Introduction

In the vibrational Van Vleck transformation of the total Hamiltonian to reduce it to operate in a single vibrational manifold (v_1, v_2, v_3), l-type doubling is introduced. This arises through operators of the form $-2BG_{\pm}N_{\mp}$, which project to states off-diagonal in v_2 and v_i $(i = 1, 3)$. These operators give a parity dependent contribution to the basis of the effective Hamiltonian, in second order [2].

The effective Hamiltonian for l-type doubling, operating in a single vibrational level

of a Π electronic state, can be written [1, 2]

$$\frac{\mathcal{H}_{ld}^{\text{eff.}}}{hc} = \frac{q^*}{2}\left[N_+^2 + N_-^2\right]. \tag{E.5}$$

where the l-type doubling parameter is q^*. Eq.(E.5) expands to give

$$\frac{\mathcal{H}_{ld}^{\text{eff.}}}{hc} = \frac{q^*}{2}\left[\left(J_+^2 + J_-^2\right) + \left(S_+^2 - S_-^2\right) - 2\left(J_+S_+ + J_-S_-\right)\right]. \tag{E.6}$$

In a $^2\Pi$ state, the eigenvalues of $S_\pm^2$ are zero since $S_+|S, \Sigma_{\text{max.}}\rangle = 0$ and $S_+|S, \Sigma_{\text{min.}}\rangle = 0$, assuming that there are no nearby electronic states of different spin multiplicity, so that the macroscopic operator $\mathbf{S}$ can be used.

E.3.2 Matrix Elements

The operators $J_\pm S_\pm$ and $J_\pm^2$ give rise to matrix elements with the selection rules

$$\Delta\Lambda = 0; \Delta K = 0, \pm 2; \Delta l = \pm 2; \begin{cases} \Delta\Sigma = \pm 1 \text{ and } \Delta P = \mp 1 \\ \Delta\Sigma = 0 \text{ and } \Delta P = \pm 2. \end{cases}$$

The matrix elements are

$$\begin{aligned} &\langle \eta\Lambda; v_2 l'; S\Sigma \pm 1; JP \mp 1, M_J | \, \mathcal{H}_{ld}^{\text{eff.}} \, | \eta\Lambda; v_2 l; S\Sigma; JP, M_J \rangle \\ &= -q^* \left[J\left(J+1\right) - P\left(P \mp 1\right)\right]^{\frac{1}{2}} \left[S\left(S+1\right) - \Sigma\left(\Sigma \pm 1\right)\right]^{\frac{1}{2}} \end{aligned} \tag{E.7}$$

and

$$\begin{aligned} &\langle \eta\Lambda; v_2 l'; S\Sigma; JP \mp 2, M_J | \, \mathcal{H}_{ld}^{\text{eff.}} \, | \eta\Lambda; v_2 l; S\Sigma; JP, M_J \rangle \\ &= \frac{q^*}{2} \left[J\left(J+1\right) - \left(P \mp 1\right)\left(P \mp 2\right)\right]^{\frac{1}{2}} \left[J\left(J+1\right) - P\left(P \mp 1\right)\right]^{\frac{1}{2}}, \end{aligned} \tag{E.8}$$

where $l' = l \pm 2$; this sign choice is independent of that for Σ and P in the brackets above.

For $\Delta K = 0$, the selection rule for K-type doubling, states states characterised by $\pm|l|$ can only be connected by the l-type doubling Hamiltonian when $K = \pm 1$, *i.e.* $^2\Pi$ vibronic states. To connect states characterised $\pm|l|$ in states of higher K requires the

Van Vleck transformation producing $\mathcal{H}_{ld}$ to operate in the $2K^{\text{th}}$ order, so the l-type doubling is much smaller in for example, $^2\Delta$ vibronic states, than it is in $^2\Pi$ vibronic states.

E.4 The K-Type Doubling Matrix

E.4.1 Matrix Representation

As discussed above, K-type (Λ-type + l-type) doubling can only arise from the above effective Hamiltonian for a $^2\Pi$ vibronic state within the $^2\Pi$ electronic manifold [1]. Tabulated here is the complete matrix representation of $\mathcal{H}_{ld}^{\text{eff.}} + \mathcal{H}_{LD}^{\text{eff.}}$ for such a state. The matrix elements have been evaluated in the parity conserving Hund's case (a) basis functions for a Renner-Teller molecule, Eqs.(III.33)–(III.36):

$K=\pm 1$

$\lvert\psi_{1a};v_1v_2v_3;\pm\rangle$	$\lvert\psi_{1b};v_1v_2v_3;\pm\rangle$	$\lvert\psi_{2a};v_1v_2v_3;\pm\rangle$	$\lvert\psi_{2b};v_1v_2v_3;\pm\rangle$
0	$\pm\frac{1}{2}(-1)^p q z^{\frac{1}{2}}\left(J+\frac{1}{2}\right)$	0	$\pm\frac{1}{2}(-1)^p q^* z^{\frac{1}{2}}\left(J+\frac{1}{2}\right)$
	$\mp\frac{1}{2}(-1)^p (p+2q)\left(J+\frac{1}{2}\right)$	$\pm\frac{1}{2}(-1)^p q^* z^{\frac{1}{2}}\left(J+\frac{1}{2}\right)$	$\mp(-1)^p q^*\left(J+\frac{1}{2}\right)$
		0	0
			0

Note how, in the unique $^2\Pi$ state ($v_2 = 0$), there are no ψ_2 type basis functions. The above matrix collapses to a 2×2 matrix which has only Λ-type doubling matrix elements. In fact, there is still an l-type contribution to the K-type doubling in the unique $^2\Pi$ vibronic state. This arises in third order due to Renner-Teller interactions between the unique $^2\Pi$ state and the non-unique $^2\Pi$ states with $v_2 = 2$; this has been discussed by Brown [1].

E.4.2 Λ-Type Doubling Contributions to the Zeeman Effect

For $v_2 = 0, K = 1$, there is a significant K-type doubling. An additional, parity dependent Zeeman contribution arises from the operators responsible for Λ-type doubling in combination with the orbital Zeeman term [4], [12]–[15]. When reduced to an effective Hamiltonian, this effect is characterised by two g-factors, g_l' and $g_r^{e'}$, the Zeeman

analogues of the Λ-type doubling parameters, p and $q_{\mathrm{el.}}$.

The general expression for the matrix elements of these terms is given in Eq.(III.94) and subsequent equations. For the unique $^2\Pi$ vibronic state ($v_2 = 0$), there are only ψ_1 type basis functions and the Λ-type doubling Zeeman matrix representation is

	$\|\psi_{1a}; K=1; v_1v_2=0; v_3; \pm\rangle$	$\|\psi_{1b}; K=1; v_1v_2=0; v_3; \pm\rangle$
	0	$\mp(-1)^x \frac{\mu_B B_0 M_J g_r^{e'}\left(J+\frac{1}{2}\right)z^{\frac{1}{2}}}{2J(J+1)}$
	Symmetric	$\pm(-1)^x \frac{\mu_B B_0 M_J \left(g_l'-g_r^{e'}\right)\left(J+\frac{1}{2}\right)}{2J(J+1)}$

where $x = (J - S - l)$ is a phase factor. Brown [12] has derived approximate relations for these g-factors,

$$g_l' = \frac{p_r}{2B_r} \tag{E.9}$$

$$g_r^{e'} = -\frac{q_r}{B_r}. \tag{E.10}$$

There are also K-type resonance contributions to the Zeeman effect, again involving the above g-factors. These interactions will be off-diagonal in K within a given (v_1, v_2, v_3) manifold. Such effects are expected to be very small at low J, and have been ignored in this work.

Bibliography

[1] J.M. Brown, *J. Mol. Spectrosc.* **56**, 159–162 (1975).

[2] I.M. Mills, "Vibration-Rotation Structure in Asymmetric- and Symmetric-Top Molecules," *in* "Molecular Spectroscopy: Modern Research." (K.N. Rao and C.W. Mathews, Eds.), pp. 115–140, Academic Press, New York, 1972.

[3] P.S.H. Bolman, J.M. Brown, A. Carrington, I. Kopp and D.A. Ramsay, *Proc. R. Soc. Lond. A* **343**, 17–44 (1975).

[4] S. Davidson, Ph.D. thesis, University of Colorado, 1987.

[5] A.G. Adam, A.J. Merer and D.M. Steunenberg, *J. Chem. Phys.* **92**, 2848–2861 (1990).

[6] R. de L. Kronig, *Z. Phys.* **50**, 347–362 (1928).

[7] J.H. Van Vleck, *Phys. Rev.* **33**, 467–506 (1929).

[8] R.S. Mulliken and A. Christy, *Phys. Rev.* **38**, 87–119 (1931).

[9] J.M. Brown and D.J. Milton, *Mol. Phys.* **31**, 409–422 (1976).

[10] J.M. Brown and A.J. Merer, *J. Mol. Spectrosc.* **74**, 488–494 (1979).

[11] J.M. Brown, A.S-C. Cheung and A.J. Merer, *J. Mol. Spectrosc.* **124**, 464–475 (1987).

[12] K.M. Evenson, R.J. Saykally, D.A. Jennings, R.F. Curl, Jr. and J.M. Brown, "Far Infrared Laser Magnetic Resonance," *in* "Chemical and Biochemical Applications of Lasers," Volume V, (C.B. Moore, Ed.), Vol. V, pp. 95–138, Academic Press, New York, 1980.

[13] A. Carrington, A.R. Fabris, B.J. Howard and N.J.D. Lucas, *Mol. Phys.* **20**, 961–980 (1971).

[14] A. Carrington, D.H. Levy and T.A. Miller, "Electron Resonance of Gaseous Diatomic Molecules," *in* "Advances in Chemical Physics," Vol. XVIII, pp. 149–248 (I. Prigogine and S.A. Rice, Eds.), J. Wiley & Sons, New York, 1970.

[15] J.M. Brown and H. Uehara, *Mol. Phys.* **24**, 1169–1174 (1972).

Appendix F

Nuclear Hyperfine Structure

F.1 Introduction

The presence of nuclei with non-zero spin gives rise to additional angular momenta in the molecule. Considering just one nuclear spin in the molecule, **I**, there are two possible angular momentum coupling schemes:

1. The **I**-coupled scheme, appropriate in the absence of applied electric or magnetic fields. In this case the total angular momentum is

$$\mathbf{F} = \mathbf{J} + \mathbf{I}, \tag{F.1}$$

and the basis functions are modified to include nuclear spin, giving the Hund's case $(a)_\alpha$ [1] basis functions

$$|\eta\Lambda; v_2 l; S\Sigma; JP; IFM_F\rangle\,, \tag{F.2}$$

where the quantum number M_F is the projection of **F** on the space-fixed Z-axis.

2. The **I**-decoupled scheme, appropriate in an applied magnetic or electric field. The molecule-fixed total angular momentum is now **J**, because **I** is not coupled to the molecular framework and is considered separately. The Hund's case $(a)_\beta$ [1] basis functions take the form

$$|\eta\Lambda; v_2 l; S\Sigma; JPM_J; IM_I\rangle\,. \tag{F.3}$$

The nuclear magneton [2] is $\mu_N \approx 1.8 \times 10^{-3}\mu_B$; because the electron density in the region of the nucleus is small, the interaction between the nuclear spin and the electrons is generally very small. This interaction is rapidly overwhelmed by an external field, which exerts a torque to couple the nuclear spin about the space-fixed Z-axis. This is why an **I**-decoupled basis set is used when describing LMR/EPR and Stark effect spectra[1].

F.2 Magnetic Hyperfine Structure

F.2.1 The Magnetic Hyperfine Effective Hamiltonian

The interaction between the nuclear spin magnetic moment and the electron orbital and spin magnetic moments gives rise to a splitting of the rotational levels, typically of 10–100 MHz in magnitude.

The nuclear magnetic moment is a polar tensor [3] and has even parity under space-fixed inversion. The requirement that the operator be symmetric under space fixed inversion means that only odd ranked terms arise in the multipolar expansion [3, 5] of the magnetic hyperfine interaction. The first term in the expansion is the magnetic dipolar term. An effective Hamiltonian for this interaction has been developed by Brown *et al.*[4], based on the model first developed by Frosch and Foley [1]; it is

$$\frac{\mathcal{H}_{hfs}^{\text{eff.}}}{hc} = aI_zL_z + b_F\mathbf{I}.\mathbf{S} + \frac{1}{3}c\,(I_zS_z - \mathbf{I}.\mathbf{S}) - \frac{1}{2}d\,(S_+I_+ + S_-I_-)\,. \tag{F.4}$$

F.2.2 Matrix Elements

When expressed in reduced spherical tensors, the matrix elements in the **I**-coupled scheme,

$$\langle \eta\Lambda'; v_2 l; S\Sigma'; J'P'; IFM_F|\,\mathcal{H}_{hfs}^{\text{eff.}}\,|\eta\Lambda; v_2 l; S\Sigma; JP; IFM_F\rangle \tag{F.5}$$

[1] At low fields the nuclear spin may still be partly coupled. This can lead to problems in identifying the eigenstates using decoupled basis set quantum numbers. Care must be exercised in such calculations.

are given by

$$
\begin{aligned}
& \delta_{\Lambda',\Lambda}\left\{(-1)^{J+I+F}\left[I\left(I+1\right)\left(2I+1\right)\left(2J'+1\right)\left(2J+1\right)\right]^{\frac{1}{2}}\right. \\
\times\ & \left\{\begin{array}{ccc} F & J & I \\ 1 & I & J' \end{array}\right\} \sum_q (-1)^{J'-P'} \left(\begin{array}{ccc} J' & 1 & J \\ -P' & q & P \end{array}\right) \left[a\Lambda\delta_{\Sigma',\Sigma}+\delta_{P',P}\right. \\
+\ & b_F\,(-1)^{S-\Sigma'} \times \left(\begin{array}{ccc} S & 1 & S \\ -\Sigma' & q & \Sigma \end{array}\right) \left[S\left(S+1\right)\left(2S+1\right)\right]^{\frac{1}{2}} + \tfrac{(30)^{\frac{1}{2}}}{3} c \\
\times\ & (-1)^q\,(-1)^{S-\Sigma'} \left(\begin{array}{ccc} S & 1 & S \\ -\Sigma' & q & \Sigma \end{array}\right) \left(\begin{array}{ccc} 1 & 2 & 1 \\ -q & 0 & q \end{array}\right) \\
\times\ & \left.\left[S\left(S+1\right)\left(2S+1\right)\right]^{\frac{1}{2}}\right]\Big\} - d\sum_{q=\pm 1} \delta_{\Lambda',\Lambda\mp 2}\,(-1)^{J+I+F} \\
\times\ & \left[I\left(I+1\right)\left(2I+1\right)\left(2J+1\right)\left(2J'+1\right)\right]^{\frac{1}{2}} \left\{\begin{array}{ccc} F & J & I \\ 1 & I & J' \end{array}\right\} \\
\times\ & (-1)^{J'-P'} \left(\begin{array}{ccc} J' & 1 & J \\ -P' & -q & P \end{array}\right) (-1)^{q+S-\Sigma'} \left(\begin{array}{ccc} S & 1 & S \\ -\Sigma' & q & \Sigma \end{array}\right) \\
\times\ & \left[S\left(S+1\right)\left(2S+1\right)\right]^{\frac{1}{2}}.
\end{aligned}
$$

The matrix elements are diagonal in F, M_F but off-diagonal by $\Delta J = 0, \pm 1$. The matrix elements in the **I**-decoupled scheme are obtained when the phase factor and Wigner 6-j symbol

$$(-1)^{J+I+F} \left\{\begin{array}{ccc} F & J & I \\ 1 & I & J' \end{array}\right\}$$

are replaced by [6]

$$\sum_q (-1)^p\,(-1)^{J'-M'_J}\,(-1)^{I-M'_I} \left(\begin{array}{ccc} J' & 1 & J \\ -M'_J & p & M_J \end{array}\right) \left(\begin{array}{ccc} I & 1 & I \\ -M'_I & -p & M_I \end{array}\right).$$

In the decoupled scheme the selection rule on J is unchanged. The matrix elements are off-diagonal in M_J and M_I, but the states constituting the basis set are all characterised by the same value of the projection of the total angular momentum, $M_F = M_I + M_J$.

F.2.3 Magnetic Hyperfine Parameters

The Frosch and Foley parameters [1, 4], involve the spherical polar co-ordinates of the electrons, (r_i, Θ_i), which are the azimuthal angle and position vector of the ith electron from the *centre of mass of the nucleus in question.* The parameter a is the nuclear spin–electronic orbital coupling parameter,

$$a\left[\mathrm{cm}^{-1}\right] = 10^{-2}\frac{\mu_0}{2\pi hc}\sum_i \mu_B g_N \mu_N \left\langle \frac{1}{r_i^3} \right\rangle . \tag{F.6}$$

The summation extends over all the unpaired electrons, and μ_0 is the permeability of free space. $\langle 1/r^3 \rangle$ is the expectation value of the radial operator function in m^{-3}, which can be calculated by *ab initio* methods [7].

The Fermi contact parameter b_F, is a direct measure of the unpaired electron density in the region of the nucleus. It is only non-zero when the molecular orbital(s) occupied by the unpaired electron(s) contain some character of spherically symmetric s atomic orbitals. The parameter

$$b_F\left[\mathrm{cm}^{-1}\right] = 10^{-2}\frac{2\mu_0}{3hc}\sum_i g_{s_i}\mu_B g_N \mu_N \left\langle \delta\left(\mathbf{r}_i\right)\right\rangle , \tag{F.7}$$

where g_{s_i} is the microscopic spin g-factor for the ith electron and $\delta(\mathbf{r}_i)$ is the Dirac delta function [3], which is 1 in the nucleus and 0 outside it.

There are two additional parameters, c and d, the latter having parity dependent matrix elements. These parameters represent the through space dipole–dipole interaction of the nuclear and electronic spins, where

$$c\left[\mathrm{cm}^{-1}\right] = 10^{-2}\frac{3\mu_0}{8\pi hc}\sum_i g_{S_i}\mu_B g_N \mu_N \left\langle \frac{3\cos^2\Theta_i - 1}{r_i^3} \right\rangle , \tag{F.8}$$

and

$$d\left[\mathrm{cm}^{-1}\right] = 10^{-2}\frac{3\mu_0}{8\pi hc}\sum_i g_{S_i}\mu_B g_N \mu_N \left\langle \frac{\sin^2\Theta_i}{r_i^3} \right\rangle . \tag{F.9}$$

The magnetic hyperfine parameters are specific and sensitive probes of the unpaired electron density in the region of the nucleus[2]. Very often the magnitude of these pa-

[2]There is no net magnetic dipolar coupling if there are no unpaired electrons.

rameters in the molecule can be related to the hyperfine parameters of the free atoms, shedding light on the atomic parentage of the molecular orbitals.

F.3 Nuclear Quadrupolar Hyperfine Structure

F.3.1 Introduction

The nuclear quadrupole moment arises from a non-spherical nuclear charge distribution, which can only occur for $I \geq 1$. The nuclear electrostatic field is a polar tensor [3], with odd space-fixed inversion parity; the requirement that it must be symmetric under space-fixed inversion, means that only even-ranked tensors arise in the multipolar expansion of the nuclear-electronic electrostatic interaction [5].

The first term is the zeroth rank (monopolar) Coulombic interaction, which forms the zero-order Hamiltonian, Eq.(III.26), in which all the basis functions are diagonal. The second rank term is the interaction of the nuclear quadrupole moment with the electric field gradient due to the electrons.

F.3.2 The Quadrupolar Effective Hamiltonian

The quadrupolar effective Hamiltonian is[3] [4, 8]

$$\frac{\mathcal{H}_Q}{hc} = T^2\left(\operatorname{grad}\mathbf{E}\right).T^2\left(\mathbf{Q}\right), \tag{F.10}$$

where $\mathbf{E} = -\operatorname{grad} V$ is the electric field associated with the electrostatic potential V. The single state effective quadrupolar Hamiltonian is

$$\frac{\mathcal{H}_Q^{\text{eff.}}}{hc} = \frac{eq_0Q}{4I\left(2I-1\right)}\left(3I_z^2 - \mathbf{I}^2\right) + \frac{eq_2Q}{8I\left(2I-1\right)}\left(I_+^2 + I_-^2\right). \tag{F.11}$$

The axial and off-axial field gradient coupling constants are defined in the molecule-fixed reference frame by [8, 9]

$$q_0 = -2\left\langle \eta\Lambda = 1\right| T^2_{q=0}\left(\operatorname{grad}\mathbf{E}\right)\left|\eta\Lambda = 1\right\rangle, \tag{F.12}$$

[3]The gradient of a vector quantity $\mathbf{E}$ is $\operatorname{grad}\mathbf{E} = \nabla\mathbf{E}$, where ∇ is the Laplacian vector operator [5].

and

$$q_2 = 2\sqrt{6}\,\langle \eta\Lambda = \mp 1|\, T^2_{q=\pm 2}\,(\mathrm{grad}\,\mathbf{E})\,|\eta\Lambda = \pm 1\rangle\,, \tag{F.13}$$

where Hund's case (a) basis functions are used in the brackets. The cylindrical symmetry about the molecule-fixed z-axis of a linear molecule means that $T^2_{q=\pm 1}(\mathrm{grad}\,\mathbf{E})$ does not generate a first order contribution to the effective quadrupolar Hamiltonian, though it will produce non-adiabatic corrections in second order.

The nuclear quadrupole moment Q is defined in the space-fixed reference frame for $M_I = I$,

$$Q = \frac{2}{e}\,\langle \cdots, I, M_I = I|\, T^2_{p=0}\,(\mathbf{Q})\,|\cdots, I, M_I = I\rangle\,. \tag{F.14}$$

Q is positive for an oblate nucleus and negative for a prolate one.

F.3.3 Matrix Elements

The matrix elements of $\mathcal{H}^{\mathrm{eff.}}_Q$,

$$\langle \eta\Lambda'; v_2 l; S\Sigma; J'P'; IFM_F|\, \mathcal{H}^{\mathrm{eff.}}_Q\,|\eta\Lambda; v_2 l; S\Sigma; JP; IFM_F\rangle \tag{F.15}$$

are given by the spherical tensor expression [4]

$$\begin{aligned}
& \tfrac{1}{2}eQ \begin{pmatrix} I & 2 & I \\ -I & 0 & I \end{pmatrix}^{-1} \times (-1)^{J+I+F} \begin{Bmatrix} F & J & I \\ 2 & I & J' \end{Bmatrix} [(2J'+1)(2J+1)]^{\frac{1}{2}} \\
\times \quad & \Bigg[\delta_{\Lambda',\Lambda}\delta_{P',P}\tfrac{1}{2}q_0\,(-1)^{J'-P} \begin{pmatrix} J' & 2 & J \\ -P & 0 & P \end{pmatrix} \\
+ \textstyle\sum_{q=\pm 2} \times \quad & \delta_{\Lambda',\Lambda\mp 2}\tfrac{1}{2(6)^{\frac{1}{2}}}q_2\,(-1)^{J'-P'} \begin{pmatrix} J' & 2 & J \\ -P' & -q & P \end{pmatrix} \Bigg]\,.
\end{aligned}$$

The selection rules are $\Delta J = 0, \pm 1, \pm 2$, $\Delta F = 0, \Delta M_F = 0$. The matrix elements in the decoupled scheme are obtained by replacing the 6-j symbol and its preceding phase factor by [6]

$$\sum_q (-1)^p\,(-1)^{J'-M'_J}\,(-1)^{I-M'_I} \begin{pmatrix} J' & 2 & J \\ -M'_J & p & M_J \end{pmatrix} \begin{pmatrix} I & 2 & I \\ -M'_I & -p & M_I \end{pmatrix}$$

The selection rule on J is unchanged in the decoupled scheme. The matrix elements are off-diagonal in M_J and M_I, but all the states constituting the basis set are characterised by the same value of the projection of the total angular momentum, $M_F = M_I + M_J$.

F.3.4 Quadrupolar Hyperfine Parameters

The quadrupole parameters provide a sensitive probe of the environment of the total electron density in the region of the nucleus, since

$$q \propto -\frac{\partial^2 V}{\partial \mathbf{r}^2}, \tag{F.16}$$

where V is the electrostatic field due to the electrons.

Bibliography

[1] R.A. Frosch and H.M. Foley, *Phys. Rev.* **88**, 1337–1349 (1952).

[2] International Union of Pure and Applied Chemistry, Physical Chemistry Division, "Quantities, Units and Symbols in Physical Chemistry," 2nd ed., (I. Mills, T. Cvitaš, K. Homann, N. Kallay and K. Kucitsu, Eds.), Blackwell Scientific Publications, Oxford, 1993.

[3] G. Arfken, "Mathematical Methods for Physicists," 3rd ed., pp. 81, 128–135, 481–484, 637–676, Academic Press, San Diego, 1985.

[4] J.M. Brown, I. Kopp, C. Malmberg and B. Rydh, *Phys. Scr.* **17**, 55–67 (1978).

[5] B.I. Bleaney and B. Bleaney, "Electricity and Magnetism," 3rd ed., pp. 33–56, 98–129, 432–470, Oxford University Press, Oxford, 1987.

[6] J.M. Brown and J.E. Schubert, *J. Mol. Spectrosc.* **95**, 194–212 (1982).

[7] W. Weltner, Jr., "Magnetic Atoms and Molecules," Van Nostrand-Reinhold, New York, 1983.

[8] R.N. Zare, "Angular Momentum," J. Wiley & Sons, New York, 1988.

[9] J.M. Brown, Physical Chemistry Laboratory, University of Oxford, unpublished notes on quadrupolar hyperfine structure.

Appendix G

Other Data Included in the Analysis of NCO ($\tilde{X}^2\Pi$)

This appendix details the large body of other data not recorded in this study, but included in the final fits of the $1_0^1\,^2\Pi$, $1_0^1 2_1^1\,^2\Delta$, $1_0^1 2_2^2\,^2\Phi$ $1_0^1 2_1^1\,^2\Sigma$ bands. The data sets comprise virtually all existing high resolution data on NCO in its $\tilde{X}\,^2\Pi$ state. Source references are given in Chapters VI and VII.

Table G.1: EPR observations[a] of $(000)\,^2\Pi_{\frac{3}{2}}$, $J = 3/2$ NCO ($\tilde{X}^2\Pi$), included in the fit of the $1_0^1\,^2\Pi$ band.

$M'_J \leftarrow M''_J$	M_I[b]	$B_{\text{obs.}}$ [T]	$\frac{\partial\nu}{\partial B}$[c] [MHzG^{-1}]	$(o-c)$[d,e] [kHz]
$\frac{3}{2} \leftarrow \frac{1}{2}$	1	0.790286	1.204	134
$\frac{3}{2} \leftarrow \frac{1}{2}$	0	0.792161	1.204	117
$\frac{3}{2} \leftarrow \frac{1}{2}$	−1	0.794129	1.204	108
$\frac{1}{2} \leftarrow -\frac{1}{2}$	1	0.835507	1.076	60
$\frac{1}{2} \leftarrow -\frac{1}{2}$	0	0.837435	1.076	101
$\frac{1}{2} \leftarrow -\frac{1}{2}$	−1	0.839352	1.076	− 47
$-\frac{1}{2} \leftarrow -\frac{3}{2}$	1	0.878159	0.981	−116
$-\frac{1}{2} \leftarrow -\frac{3}{2}$	0	0.880145	0.981	−116
$-\frac{1}{2} \leftarrow -\frac{3}{2}$	−1	0.881993	0.981	−155

[a] Observed at a frequency of 9270.00 MHz.

[b] $\Delta M_I = 0$.

[c] Tuning rate at resonance.

[d] Residuals of the fit.

[e] 300 kHz uncertainty assigned to each datum.

Table G.2: Far-infrared LMR observations of $(000)\,^2\Pi_{\frac{3}{2}}$ NCO ($\tilde{X}^2\Pi$), included in the fit of the $1_0^1\,^2\Pi$ band.

$M'_J \leftarrow M''_J$	$M_I{}^{(a)}$ Parity	$B_{\text{obs.}}$ [T]	$\frac{\partial\nu}{\partial B}{}^{(b)}$ [MHzG^{-1}]	$(o-c)^{(c,d)}$ [kHz]
	$\nu_L = 337192.1\,\text{MHz}$			
	$J = \frac{29}{2} \leftarrow \frac{27}{2}$			
$-\frac{27}{2} \leftarrow -\frac{27}{2}$	$- \leftarrow +$	0.12618	0.038	119
$-\frac{25}{2} \leftarrow -\frac{25}{2}$	$- \leftarrow +$	0.13654	0.035	40
$-\frac{21}{2} \leftarrow -\frac{21}{2}$	$- \leftarrow +$	0.16240	0.029	125
$-\frac{23}{2} \leftarrow -\frac{23}{2}$	$+ \leftarrow -$	0.17529	0.032	− 357
$-\frac{19}{2} \leftarrow -\frac{19}{2}$	$- \leftarrow +$	0.17992	0.027	44
$-\frac{21}{2} \leftarrow -\frac{21}{2}$	$+ \leftarrow -$	0.19135	0.029	− 138
$-\frac{17}{2} \leftarrow -\frac{17}{2}$	$- \leftarrow +$	0.20184	0.024	− 92
$-\frac{19}{2} \leftarrow -\frac{19}{2}$	$+ \leftarrow -$	0.21215	0.027	− 270
$-\frac{15}{2} \leftarrow -\frac{15}{2}$	$- \leftarrow +$	0.22931	0.021	− 147
$-\frac{17}{2} \leftarrow -\frac{17}{2}$	$+ \leftarrow -$	0.23662	0.024	− 94
$-\frac{11}{2} \leftarrow -\frac{11}{2}$	$+ \leftarrow -$	0.36943	0.015	− 251
$-\frac{9}{2} \leftarrow -\frac{9}{2}$	$- \leftarrow +$	0.38596	0.012	− 111
$-\frac{9}{2} \leftarrow -\frac{9}{2}$	$+ \leftarrow -$	0.45418	0.012	− 219
$-\frac{7}{2} \leftarrow -\frac{7}{2}$	$- \leftarrow +$	0.50187	0.009	− 118
$-\frac{7}{2} \leftarrow -\frac{7}{2}$	$+ \leftarrow -$	0.59176	0.009	− 231
$-\frac{5}{2} \leftarrow -\frac{5}{2}$	$- \leftarrow +$	0.72230	0.006	− 65
$-\frac{5}{2} \leftarrow -\frac{5}{2}$	$+ \leftarrow -$	0.85560	0.006	− 131
$-\frac{25}{2} \leftarrow -\frac{27}{2}$	$- \leftarrow +$	0.06956	0.068	692
$-\frac{23}{2} \leftarrow -\frac{25}{2}$	$- \leftarrow +$	0.07325	0.065	247
$-\frac{21}{2} \leftarrow -\frac{23}{2}$	$- \leftarrow +$	0.07679	0.062	102
$-\frac{5}{2} \leftarrow -\frac{7}{2}$	$- \leftarrow +$	0.11994	0.039	201
$-\frac{9}{2} \leftarrow -\frac{11}{2}$	$+ \leftarrow -$	0.12236	0.045	617
$\frac{1}{2} \leftarrow -\frac{1}{2}$	$+ \leftarrow -$	0.18034	0.031	− 348
$\frac{5}{2} \leftarrow \frac{3}{2}$	$- \leftarrow +$	0.18653	0.025	− 79
$\frac{3}{2} \leftarrow \frac{1}{2}$	$+ \leftarrow -$	0.19760	0.028	− 205
$\frac{7}{2} \leftarrow \frac{5}{2}$	$- \leftarrow +$	0.20964	0.023	− 135

Table G.2 continued:

$M'_J \leftarrow M''_J$	M_I[a]	Parity	$B_{\text{obs.}}$ [T]	$\frac{\partial\nu}{\partial B}$[b] [MHzG^{-1}]	$(o-c)$[c,d] [kHz]
$\frac{5}{2} \leftarrow \frac{3}{2}$		$+ \leftarrow -$	0.21904	0.025	− 166
$\frac{9}{2} \leftarrow \frac{7}{2}$		$- \leftarrow +$	0.23912	0.020	− 175
$\frac{7}{2} \leftarrow \frac{5}{2}$		$+ \leftarrow -$	0.24560	0.023	− 96
$\frac{13}{2} \leftarrow \frac{11}{2}$		$+ \leftarrow -$	0.38935	0.014	− 217
$\frac{15}{2} \leftarrow \frac{13}{2}$		$- \leftarrow +$	0.41066	0.011	− 98
$\frac{15}{2} \leftarrow \frac{13}{2}$		$+ \leftarrow -$	0.48239	0.011	− 160
$\frac{17}{2} \leftarrow \frac{15}{2}$		$- \leftarrow +$	0.54000	0.009	− 93
$-\frac{29}{2} \leftarrow -\frac{27}{2}$		$- \leftarrow +$	0.59668	0.009	− 148
$\frac{17}{2} \leftarrow \frac{15}{2}$		$+ \leftarrow -$	0.63520	0.008	− 208
$-\frac{29}{2} \leftarrow -\frac{27}{2}$		$+ \leftarrow -$	0.69804	0.009	− 285
$\frac{19}{2} \leftarrow \frac{17}{2}$	−1	$- \leftarrow +$	0.78730	0.006	− 68
$-\frac{27}{2} \leftarrow -\frac{25}{2}$		$- \leftarrow +$	0.91950	0.006	− 528
$\frac{15}{2} \leftarrow \frac{15}{2}$		$- \leftarrow +$	0.18349	−0.021	471
$\frac{11}{2} \leftarrow \frac{11}{2}$		$+ \leftarrow -$	0.19306	−0.015	157
$\frac{13}{2} \leftarrow \frac{13}{2}$		$- \leftarrow +$	0.21047	−0.018	308
$\frac{9}{2} \leftarrow \frac{9}{2}$		$+ \leftarrow -$	0.23508	−0.012	145
$\frac{11}{2} \leftarrow \frac{11}{2}$		$- \leftarrow +$	0.24650	−0.015	63
$\frac{7}{2} \leftarrow \frac{7}{2}$		$- \leftarrow +$	0.38394	−0.010	204
$\frac{5}{2} \leftarrow \frac{5}{2}$		$+ \leftarrow -$	0.41327	−0.007	88
$\frac{5}{2} \leftarrow \frac{5}{2}$		$- \leftarrow +$	0.52691	−0.007	184
$\frac{3}{2} \leftarrow \frac{3}{2}$		$+ \leftarrow -$	0.65584	−0.005	123
$\frac{3}{2} \leftarrow \frac{3}{2}$		$- \leftarrow +$	0.82582	−0.005	222
$\frac{1}{2} \leftarrow \frac{1}{2}$		$+ \leftarrow -$	1.3800	−0.003	− 52
$\frac{1}{2} \leftarrow \frac{1}{2}$		$- \leftarrow +$	1.6634	−0.003	320
$-\frac{1}{2} \leftarrow \frac{1}{2}$		$- \leftarrow +$	0.12009	−0.031	169
$-\frac{7}{2} \leftarrow -\frac{5}{2}$		$+ \leftarrow -$	0.12738	−0.023	222
$-\frac{9}{2} \leftarrow -\frac{7}{2}$		$- \leftarrow +$	0.18510	−0.020	212
$-\frac{13}{2} \leftarrow -\frac{11}{2}$		$+ \leftarrow -$	0.19741	−0.015	115
$-\frac{11}{2} \leftarrow -\frac{9}{2}$		$- \leftarrow +$	0.21399	−0.018	212

Table G.2 continued:

$M'_J \leftarrow M''_J$	$M_I{}^{(a)}$	Parity	$B_{\text{obs.}}$ [T]	$\frac{\partial\nu}{\partial B}{}^{(b)}$ [MHzG^{-1}]	$(o-c)^{(c,d)}$ [kHz]
$-\frac{15}{2} \leftarrow -\frac{13}{2}$		$+ \leftarrow -$	0.24254	−0.012	141
$-\frac{13}{2} \leftarrow -\frac{11}{2}$		$- \leftarrow +$	0.25337	−0.015	180
$-\frac{17}{2} \leftarrow -\frac{15}{2}$		$- \leftarrow +$	0.40596	−0.010	498
$\frac{29}{2} \leftarrow \frac{27}{2}$		$+ \leftarrow -$	0.41722	−0.007	124
$-\frac{19}{2} \leftarrow -\frac{17}{2}$	−1	$+ \leftarrow -$	0.44446	−0.007	1
$\frac{29}{2} \leftarrow \frac{27}{2}$		$- \leftarrow +$	0.54242	−0.006	338
$-\frac{19}{2} \leftarrow -\frac{17}{2}$	1	$- \leftarrow +$	0.57282	−0.007	290
$\frac{27}{2} \leftarrow \frac{25}{2}$		$+ \leftarrow -$	0.69521	−0.004	258
$-\frac{21}{2} \leftarrow -\frac{19}{2}$		$+ \leftarrow -$	0.77047	−0.004	− 11
$\frac{27}{2} \leftarrow \frac{25}{2}$		$- \leftarrow +$	0.90737	−0.004	329

$$\nu_L = 500029.2\,\text{MHz}$$
$$J = \tfrac{43}{2} \leftarrow \tfrac{41}{2}$$

$-\frac{41}{2} \leftarrow -\frac{41}{2}$		$+ \leftarrow -$	0.42523	0.018	− 31
$-\frac{39}{2} \leftarrow -\frac{39}{2}$		$+ \leftarrow -$	0.44690	0.017	30
$-\frac{37}{2} \leftarrow -\frac{37}{2}$		$+ \leftarrow -$	0.47143	0.017	11
$-\frac{35}{2} \leftarrow -\frac{35}{2}$		$+ \leftarrow -$	0.49862	0.016	23
$-\frac{33}{2} \leftarrow -\frac{33}{2}$		$+ \leftarrow -$	0.52882	0.015	86
$-\frac{39}{2} \leftarrow -\frac{39}{2}$		$- \leftarrow +$	0.55128	0.018	− 301
$-\frac{31}{2} \leftarrow -\frac{31}{2}$		$+ \leftarrow -$	0.56384	0.014	35
$-\frac{37}{2} \leftarrow -\frac{37}{2}$		$- \leftarrow +$	0.58072	0.017	− 176
$-\frac{29}{2} \leftarrow -\frac{29}{2}$		$+ \leftarrow -$	0.60379	0.013	− 14
$-\frac{35}{2} \leftarrow -\frac{35}{2}$		$- \leftarrow +$	0.61430	0.016	− 163
$-\frac{29}{2} \leftarrow -\frac{29}{2}$		$- \leftarrow +$	0.74399	0.013	− 171
$-\frac{23}{2} \leftarrow -\frac{23}{2}$		$+ \leftarrow -$	0.76447	0.010	86
$-\frac{27}{2} \leftarrow -\frac{27}{2}$		$- \leftarrow +$	0.80040	0.012	− 165
$-\frac{21}{2} \leftarrow -\frac{21}{2}$		$+ \leftarrow -$	0.83840	0.009	210
$-\frac{25}{2} \leftarrow -\frac{25}{2}$		$- \leftarrow +$	0.86290	0.011	208
$-\frac{19}{2} \leftarrow -\frac{19}{2}$		$- \leftarrow +$	1.1531	0.008	− 215

Table G.2 continued:

$M'_J \leftarrow M''_J$	$M_I{}^{(a)}$ Parity	$B_{\text{obs.}}$ [T]	$\frac{\partial\nu}{\partial B}{}^{(b)}$ [MHzG^{-1}]	$(o-c)^{(c,d)}$ [kHz]
$-\frac{15}{2} \leftarrow -\frac{15}{2}$	$+ \leftarrow -$	1.1988	0.006	− 57
$-\frac{17}{2} \leftarrow -\frac{17}{2}$	$- \leftarrow +$	1.3014	0.007	− 504
$-\frac{13}{2} \leftarrow -\frac{13}{2}$	$+ \leftarrow -$	1.4191	0.005	−1046
$-\frac{15}{2} \leftarrow -\frac{15}{2}$	$- \leftarrow +$	1.4789	0.006	164
$-\frac{11}{2} \leftarrow -\frac{11}{2}$	$+ \leftarrow -$	1.6850	0.004	173
$-\frac{13}{2} \leftarrow -\frac{13}{2}$	$- \leftarrow +$	1.7355	0.005	4
$-\frac{29}{2} \leftarrow -\frac{31}{2}$	$+ \leftarrow -$	0.22895	0.033	240
$-\frac{27}{2} \leftarrow -\frac{29}{2}$	$+ \leftarrow -$	0.23544	0.033	147
$-\frac{25}{2} \leftarrow -\frac{27}{2}$	$+ \leftarrow -$	0.24039	0.032	656
$\frac{5}{2} \leftarrow \frac{3}{2}$	$+ \leftarrow -$	0.41515	0.018	90
$-\frac{1}{2} \leftarrow -\frac{3}{2}$	$- \leftarrow +$	0.44893	0.021	− 157
$\frac{9}{2} \leftarrow \frac{7}{2}$	$+ \leftarrow -$	0.45929	0.017	− 29
$\frac{1}{2} \leftarrow -\frac{1}{2}$	$- \leftarrow +$	0.46800	0.020	− 70
$\frac{9}{2} \leftarrow \frac{7}{2}$	$- \leftarrow +$	0.56655	0.017	− 147
$\frac{17}{2} \leftarrow \frac{15}{2}$	$+ \leftarrow -$	0.57966	0.013	15
$\frac{11}{2} \leftarrow \frac{9}{2}$	$- \leftarrow +$	0.59761	0.016	− 125
$\frac{19}{2} \leftarrow \frac{17}{2}$	$+ \leftarrow -$	0.62046	0.012	− 22
$\frac{13}{2} \leftarrow \frac{11}{2}$	$- \leftarrow +$	0.63116	0.015	52
$\frac{19}{2} \leftarrow \frac{17}{2}$	$- \leftarrow +$	0.76530	0.012	− 157
$\frac{25}{2} \leftarrow \frac{23}{2}$	$+ \leftarrow -$	0.78280	0.010	10
$\frac{21}{2} \leftarrow \frac{19}{2}$	$- \leftarrow +$	0.82040	0.011	62
$\frac{27}{2} \leftarrow \frac{25}{2}$	$+ \leftarrow -$	0.85460	0.009	194
$\frac{23}{2} \leftarrow \frac{21}{2}$	$- \leftarrow +$	0.89440	0.010	− 806
$\frac{29}{2} \leftarrow \frac{27}{2}$	$+ \leftarrow -$	0.94440	0.008	57
$\frac{25}{2} \leftarrow \frac{23}{2}$	$- \leftarrow +$	0.96220	0.010	96

(a) $\Delta M_I = 0$.

(b) Tuning rate at resonance.

(c) Residuals of the fit.

(d) Uncertainties: 200 kHz for $B_{\text{obs.}} < 800$ mT, otherwise 600 kHz.

Table G.3: Microwave observations of $(000)\,^2\Pi$ NCO ($\tilde{X}^2\Pi$), included in the fit of the $1_0^1\,^2\Pi$ band.

$J' \leftarrow J''$	$F' \leftarrow F''$	Parity	$\nu_{\text{obs.}}$ [MHz]	$(o-c)^{(a)}$ [kHz]
		$^2\Pi_{\frac{1}{2}}$		
$\frac{3}{2} \leftarrow \frac{1}{2}$	$\frac{5}{2} \leftarrow \frac{3}{2}$	$- \leftarrow +$	35120.68(2)$^{(b)}$	− 7
$\frac{3}{2} \leftarrow \frac{1}{2}$	$\frac{3}{2} \leftarrow \frac{1}{2}$	$- \leftarrow +$	35137.76(5)	12
$\frac{3}{2} \leftarrow \frac{1}{2}$	$\frac{3}{2} \leftarrow \frac{3}{2}$	$- \leftarrow +$	35155.98(8)	73
$\frac{3}{2} \leftarrow \frac{1}{2}$	$\frac{1}{2} \leftarrow \frac{1}{2}$	$- \leftarrow +$	35160.32(4)	− 8
$\frac{3}{2} \leftarrow \frac{1}{2}$	$\frac{5}{2} \leftarrow \frac{3}{2}$	$+ \leftarrow -$	35208.33(5)	− 12
$\frac{3}{2} \leftarrow \frac{1}{2}$	$\frac{3}{2} \leftarrow \frac{1}{2}$	$+ \leftarrow -$	35284.76(6)	26
$\frac{3}{2} \leftarrow \frac{1}{2}$	$\frac{3}{2} \leftarrow \frac{3}{2}$	$+ \leftarrow -$	35125.76(3)	− 48
$\frac{3}{2} \leftarrow \frac{1}{2}$	$\frac{1}{2} \leftarrow \frac{1}{2}$	$+ \leftarrow -$	35236.20(4)	− 19
$\frac{5}{2} \leftarrow \frac{3}{2}$	$\frac{7}{2} \leftarrow \frac{5}{2}$	$+ \leftarrow -$	58578.53(8)	64
$\frac{5}{2} \leftarrow \frac{3}{2}$	$\frac{5}{2} \leftarrow \frac{3}{2}$	$+ \leftarrow -$	58581.98(2)	38
$\frac{5}{2} \leftarrow \frac{3}{2}$	$\frac{3}{2} \leftarrow \frac{1}{2}$	$+ \leftarrow -$	58588.60(4)	9
$\frac{5}{2} \leftarrow \frac{3}{2}$	$\frac{5}{2} \leftarrow \frac{5}{2}$	$+ \leftarrow -$	58617.30(4)	139
$\frac{5}{2} \leftarrow \frac{3}{2}$	$\frac{3}{2} \leftarrow \frac{3}{2}$	$+ \leftarrow -$	58611.15(4)	− 22
$\frac{5}{2} \leftarrow \frac{3}{2}$	$\frac{7}{2} \leftarrow \frac{5}{2}$	$- \leftarrow +$	58659.18(2)	− 78
$\frac{5}{2} \leftarrow \frac{3}{2}$	$\frac{5}{2} \leftarrow \frac{3}{2}$	$- \leftarrow +$	58674.52(2)	− 14
$\frac{5}{2} \leftarrow \frac{3}{2}$	$\frac{3}{2} \leftarrow \frac{1}{2}$	$- \leftarrow +$	58676.13(10)	− 43
$\frac{5}{2} \leftarrow \frac{3}{2}$	$\frac{5}{2} \leftarrow \frac{5}{2}$	$- \leftarrow +$	58591.98(5)	− 20
$\frac{5}{2} \leftarrow \frac{3}{2}$	$\frac{3}{2} \leftarrow \frac{3}{2}$	$- \leftarrow +$	58627.54(4)	−118
$\frac{7}{2} \leftarrow \frac{5}{2}$	$\frac{9}{2} \leftarrow \frac{7}{2}$	$- \leftarrow +$	82030.187(9)	− 10
$\frac{7}{2} \leftarrow \frac{5}{2}$	$\frac{7}{2} \leftarrow \frac{5}{2}$	$- \leftarrow +$	82031.721(12)	− 18
$\frac{7}{2} \leftarrow \frac{5}{2}$	$\frac{5}{2} \leftarrow \frac{3}{2}$	$- \leftarrow +$	82035.467(5)	− 25
$\frac{7}{2} \leftarrow \frac{5}{2}$	$\frac{7}{2} \leftarrow \frac{7}{2}$	$- \leftarrow +$	82070.444(16)	10
$\frac{7}{2} \leftarrow \frac{5}{2}$	$\frac{5}{2} \leftarrow \frac{5}{2}$	$- \leftarrow +$	82064.860(50)	138
$\frac{7}{2} \leftarrow \frac{5}{2}$	$\frac{9}{2} \leftarrow \frac{7}{2}$	$+ \leftarrow -$	82108.526(8)	12
$\frac{7}{2} \leftarrow \frac{5}{2}$	$\frac{7}{2} \leftarrow \frac{5}{2}$	$+ \leftarrow -$	82115.153(9)	6
$\frac{7}{2} \leftarrow \frac{5}{2}$	$\frac{5}{2} \leftarrow \frac{3}{2}$	$+ \leftarrow -$	82116.070(9)	− 12

Table G.3 continued:

$J' \leftarrow J''$	$F' \leftarrow F''$	Parity	$\nu_{\text{obs.}}$ [MHz]	$(o-c)^{(a)}$ [kHz]
$\frac{7}{2} \leftarrow \frac{5}{2}$	$\frac{7}{2} \leftarrow \frac{7}{2}$	$+ \leftarrow -$	82048.060(100)	171
$\frac{7}{2} \leftarrow \frac{5}{2}$	$\frac{5}{2} \leftarrow \frac{5}{2}$	$+ \leftarrow -$	82069.300(60)	94
$\frac{9}{2} \leftarrow \frac{7}{2}$	$\frac{11}{2} \leftarrow \frac{9}{2}$	$+ \leftarrow -$	105479.958(5)	15
$\frac{9}{2} \leftarrow \frac{7}{2}$	$\frac{9}{2} \leftarrow \frac{7}{2}$	$+ \leftarrow -$	105480.848(7)	8
$\frac{9}{2} \leftarrow \frac{7}{2}$	$\frac{7}{2} \leftarrow \frac{5}{2}$	$+ \leftarrow -$	105483.260(10)	− 18
$\frac{9}{2} \leftarrow \frac{7}{2}$	$\frac{9}{2} \leftarrow \frac{9}{2}$	$+ \leftarrow -$	105521.039(9)	− 39
$\frac{9}{2} \leftarrow \frac{7}{2}$	$\frac{7}{2} \leftarrow \frac{7}{2}$	$+ \leftarrow -$	105516.274(10)	13
$\frac{9}{2} \leftarrow \frac{7}{2}$	$\frac{11}{2} \leftarrow \frac{9}{2}$	$- \leftarrow +$	105556.945(13)	19
$\frac{9}{2} \leftarrow \frac{7}{2}$	$\frac{9}{2} \leftarrow \frac{7}{2}$	$- \leftarrow +$	105560.673(6)	− 7
$\frac{9}{2} \leftarrow \frac{7}{2}$	$\frac{7}{2} \leftarrow \frac{5}{2}$	$- \leftarrow +$	105561.333(19)	24
$\frac{9}{2} \leftarrow \frac{7}{2}$	$\frac{9}{2} \leftarrow \frac{9}{2}$	$- \leftarrow +$	105500.058(10)	3
$\frac{9}{2} \leftarrow \frac{7}{2}$	$\frac{7}{2} \leftarrow \frac{7}{2}$	$- \leftarrow +$	105515.374(11)	7
$\frac{11}{2} \leftarrow \frac{9}{2}$	$\frac{13}{2} \leftarrow \frac{11}{2}$	$- \leftarrow +$	128928.517(12)	− 27
$\frac{11}{2} \leftarrow \frac{9}{2}$	$\frac{11}{2} \leftarrow \frac{9}{2}$	$- \leftarrow +$	128929.213(12)	66
$\frac{11}{2} \leftarrow \frac{9}{2}$	$\frac{9}{2} \leftarrow \frac{7}{2}$	$- \leftarrow +$	128930.876(7)	0
$\frac{11}{2} \leftarrow \frac{9}{2}$	$\frac{11}{2} \leftarrow \frac{11}{2}$	$- \leftarrow +$	128970.294(34)	12
$\frac{11}{2} \leftarrow \frac{9}{2}$	$\frac{9}{2} \leftarrow \frac{9}{2}$	$- \leftarrow +$	128966.271(18)	− 26
$\frac{11}{2} \leftarrow \frac{9}{2}$	$\frac{13}{2} \leftarrow \frac{11}{2}$	$+ \leftarrow -$	129004.593(9)	13
$\frac{11}{2} \leftarrow \frac{9}{2}$	$\frac{11}{2} \leftarrow \frac{9}{2}$	$+ \leftarrow -$	129007.018(8)	− 9
$\frac{11}{2} \leftarrow \frac{9}{2}$	$\frac{9}{2} \leftarrow \frac{7}{2}$	$+ \leftarrow -$	129007.436(60)	− 58
$\frac{11}{2} \leftarrow \frac{9}{2}$	$\frac{11}{2} \leftarrow \frac{11}{2}$	$+ \leftarrow -$	128950.143(18)	− 13
$\frac{11}{2} \leftarrow \frac{9}{2}$	$\frac{9}{2} \leftarrow \frac{9}{2}$	$+ \leftarrow -$	128962.127(44)	− 54
$\frac{13}{2} \leftarrow \frac{11}{2}$	$\frac{15}{2} \leftarrow \frac{13}{2}$	$+ \leftarrow -$	152376.402(*)	209
$\frac{13}{2} \leftarrow \frac{11}{2}$	$\frac{13}{2} \leftarrow \frac{11}{2}$	$+ \leftarrow -$	152376.402(*)	−235
$\frac{13}{2} \leftarrow \frac{11}{2}$	$\frac{11}{2} \leftarrow \frac{9}{2}$	$+ \leftarrow -$	152377.976(10)	36
$\frac{13}{2} \leftarrow \frac{11}{2}$	$\frac{13}{2} \leftarrow \frac{13}{2}$	$+ \leftarrow -$	152418.383(16)	9
$\frac{13}{2} \leftarrow \frac{11}{2}$	$\frac{11}{2} \leftarrow \frac{11}{2}$	$+ \leftarrow -$	152415.074(14)	− 15
$\frac{13}{2} \leftarrow \frac{11}{2}$	$\frac{15}{2} \leftarrow \frac{13}{2}$	$- \leftarrow +$	152451.453(12)	31
$\frac{13}{2} \leftarrow \frac{11}{2}$	$\frac{13}{2} \leftarrow \frac{11}{2}$	$- \leftarrow +$	152453.367(*)	202
$\frac{13}{2} \leftarrow \frac{11}{2}$	$\frac{11}{2} \leftarrow \frac{9}{2}$	$- \leftarrow +$	152453.367(*)	−169

Table G.3 continued:

$J' \leftarrow J''$	$F' \leftarrow F''$	Parity	$\nu_{\text{obs.}}$ [MHz]	$(o-c)^{(a)}$ [kHz]
$\frac{13}{2} \leftarrow \frac{11}{2}$	$\frac{13}{2} \leftarrow \frac{13}{2}$	$- \leftarrow +$	152398.726(13)	− 15
$\frac{13}{2} \leftarrow \frac{11}{2}$	$\frac{11}{2} \leftarrow \frac{11}{2}$	$- \leftarrow +$	152408.649(16)	− 42
		$^2\Pi_{\frac{3}{2}}$		
$\frac{5}{2} \leftarrow \frac{3}{2}$	$\frac{7}{2} \leftarrow \frac{5}{2}$	$+ \leftarrow -$	58140.97(4)	175
$\frac{5}{2} \leftarrow \frac{3}{2}$	$\frac{5}{2} \leftarrow \frac{3}{2}$	$+ \leftarrow -$	58161.49(6)	75
$\frac{5}{2} \leftarrow \frac{3}{2}$	$\frac{3}{2} \leftarrow \frac{1}{2}$	$+ \leftarrow -$	58171.71(5)	36
$\frac{5}{2} \leftarrow \frac{3}{2}$	$\frac{5}{2} \leftarrow \frac{5}{2}$	$+ \leftarrow -$	58108.44(4)	277
$\frac{5}{2} \leftarrow \frac{3}{2}$	$\frac{3}{2} \leftarrow \frac{3}{2}$	$+ \leftarrow -$	58138.64(20)	313
$\frac{7}{2} \leftarrow \frac{5}{2}$	$\frac{9}{2} \leftarrow \frac{7}{2}$	$- \leftarrow +$	81404.300(5)	4
$\frac{7}{2} \leftarrow \frac{5}{2}$	$\frac{7}{2} \leftarrow \frac{5}{2}$	$- \leftarrow +$	81413.120(5)	2
$\frac{7}{2} \leftarrow \frac{5}{2}$	$\frac{5}{2} \leftarrow \frac{3}{2}$	$- \leftarrow +$	81418.385(2)	− 5
$\frac{7}{2} \leftarrow \frac{5}{2}$	$\frac{7}{2} \leftarrow \frac{7}{2}$	$- \leftarrow +$	81380.623(∗)	137
$\frac{7}{2} \leftarrow \frac{5}{2}$	$\frac{5}{2} \leftarrow \frac{5}{2}$	$- \leftarrow +$	81395.278(12)	− 24
$\frac{7}{2} \leftarrow \frac{5}{2}$	$\frac{9}{2} \leftarrow \frac{7}{2}$	$+ \leftarrow -$	81404.813(5)	16
$\frac{7}{2} \leftarrow \frac{5}{2}$	$\frac{7}{2} \leftarrow \frac{5}{2}$	$+ \leftarrow -$	81413.573(6)	16
$\frac{7}{2} \leftarrow \frac{5}{2}$	$\frac{5}{2} \leftarrow \frac{3}{2}$	$+ \leftarrow -$	81418.884(4)	14
$\frac{7}{2} \leftarrow \frac{5}{2}$	$\frac{7}{2} \leftarrow \frac{7}{2}$	$+ \leftarrow -$	81380.623(∗)	−171
$\frac{7}{2} \leftarrow \frac{5}{2}$	$\frac{5}{2} \leftarrow \frac{5}{2}$	$+ \leftarrow -$	81395.934(12)	− 6
$\frac{9}{2} \leftarrow \frac{7}{2}$	$\frac{11}{2} \leftarrow \frac{9}{2}$	$+ \leftarrow -$	104665.278(11)	8
$\frac{9}{2} \leftarrow \frac{7}{2}$	$\frac{9}{2} \leftarrow \frac{7}{2}$	$+ \leftarrow -$	104670.139(6)	− 8
$\frac{9}{2} \leftarrow \frac{7}{2}$	$\frac{7}{2} \leftarrow \frac{5}{2}$	$+ \leftarrow -$	104673.371(6)	− 5
$\frac{9}{2} \leftarrow \frac{7}{2}$	$\frac{9}{2} \leftarrow \frac{9}{2}$	$+ \leftarrow -$	104646.328(10)	− 9
$\frac{9}{2} \leftarrow \frac{7}{2}$	$\frac{7}{2} \leftarrow \frac{7}{2}$	$+ \leftarrow -$	104655.566(8)	6
$\frac{9}{2} \leftarrow \frac{7}{2}$	$\frac{11}{2} \leftarrow \frac{9}{2}$	$- \leftarrow +$	104666.098(11)	8
$\frac{9}{2} \leftarrow \frac{7}{2}$	$\frac{9}{2} \leftarrow \frac{7}{2}$	$- \leftarrow +$	104670.905(10)	0
$\frac{9}{2} \leftarrow \frac{7}{2}$	$\frac{7}{2} \leftarrow \frac{5}{2}$	$- \leftarrow +$	104674.173(6)	2
$\frac{9}{2} \leftarrow \frac{7}{2}$	$\frac{9}{2} \leftarrow \frac{9}{2}$	$- \leftarrow +$	104646.928(14)	26
$\frac{9}{2} \leftarrow \frac{7}{2}$	$\frac{7}{2} \leftarrow \frac{7}{2}$	$- \leftarrow +$	104656.552(9)	− 2

Table G.3 continued:

$J' \leftarrow J''$	$F' \leftarrow F''$	Parity	$\nu_{\text{obs.}}$ [MHz]	$(o-c)^{(a)}$ [kHz]
$\frac{11}{2} \leftarrow \frac{9}{2}$	$\frac{13}{2} \leftarrow \frac{11}{2}$	$- \leftarrow +$	127924.987(10)	21
$\frac{11}{2} \leftarrow \frac{9}{2}$	$\frac{11}{2} \leftarrow \frac{9}{2}$	$- \leftarrow +$	127928.041(14)	− 5
$\frac{11}{2} \leftarrow \frac{9}{2}$	$\frac{9}{2} \leftarrow \frac{7}{2}$	$- \leftarrow +$	127930.222(10)	8
$\frac{11}{2} \leftarrow \frac{9}{2}$	$\frac{11}{2} \leftarrow \frac{11}{2}$	$- \leftarrow +$	127909.047(13)	− 67
$\frac{11}{2} \leftarrow \frac{9}{2}$	$\frac{9}{2} \leftarrow \frac{9}{2}$	$- \leftarrow +$	127915.592(11)	− 35
$\frac{11}{2} \leftarrow \frac{9}{2}$	$\frac{13}{2} \leftarrow \frac{11}{2}$	$+ \leftarrow -$	127926.215(7)	30
$\frac{11}{2} \leftarrow \frac{9}{2}$	$\frac{11}{2} \leftarrow \frac{9}{2}$	$+ \leftarrow -$	127929.194(10)	− 6
$\frac{11}{2} \leftarrow \frac{9}{2}$	$\frac{9}{2} \leftarrow \frac{7}{2}$	$+ \leftarrow -$	127931.402(12)	0
$\frac{11}{2} \leftarrow \frac{9}{2}$	$\frac{11}{2} \leftarrow \frac{11}{2}$	$+ \leftarrow -$	127910.072(18)	60
$\frac{11}{2} \leftarrow \frac{9}{2}$	$\frac{9}{2} \leftarrow \frac{9}{2}$	$+ \leftarrow -$	127917.040(14)	− 11
$\frac{13}{2} \leftarrow \frac{11}{2}$	$\frac{15}{2} \leftarrow \frac{13}{2}$	$+ \leftarrow -$	151183.729(8)	− 14
$\frac{13}{2} \leftarrow \frac{11}{2}$	$\frac{13}{2} \leftarrow \frac{11}{2}$	$+ \leftarrow -$	151185.631(*)	−223
$\frac{13}{2} \leftarrow \frac{11}{2}$	$\frac{11}{2} \leftarrow \frac{9}{2}$	$+ \leftarrow -$	151187.436(5)	40
$\frac{13}{2} \leftarrow \frac{11}{2}$	$\frac{13}{2} \leftarrow \frac{13}{2}$	$+ \leftarrow -$	151170.002(17)	0
$\frac{13}{2} \leftarrow \frac{11}{2}$	$\frac{11}{2} \leftarrow \frac{11}{2}$	$+ \leftarrow -$	151174.921(30)	− 56
$\frac{13}{2} \leftarrow \frac{11}{2}$	$\frac{15}{2} \leftarrow \frac{13}{2}$	$- \leftarrow +$	151185.631(*)	191
$\frac{13}{2} \leftarrow \frac{11}{2}$	$\frac{13}{2} \leftarrow \frac{11}{2}$	$- \leftarrow +$	151187.436(5)	− 46
$\frac{13}{2} \leftarrow \frac{11}{2}$	$\frac{11}{2} \leftarrow \frac{9}{2}$	$- \leftarrow +$	151189.043(13)	− 13
$\frac{13}{2} \leftarrow \frac{11}{2}$	$\frac{13}{2} \leftarrow \frac{13}{2}$	$- \leftarrow +$	151171.264(21)	− 45
$\frac{13}{2} \leftarrow \frac{11}{2}$	$\frac{11}{2} \leftarrow \frac{11}{2}$	$- \leftarrow +$	151176.881(14)	− 26

[a] Residuals of the fit.

[b] The numbers in parentheses are the uncertainties in units of the last decimal place. The symbol '*' denotes blended lines given zero weight.

Table G.4: Combination differences giving the $(000)\,^2\Pi_{\frac{1}{2}} \leftarrow ^2\Pi_{\frac{3}{2}}$ interval in NCO ($\tilde{X}^2\Pi$) and included in the fit of the $1_0^1\,^2\Pi$ band. Calculated from the $\tilde{A} \leftarrow \tilde{X}$ transition.

$J^{(a)}$	$\tilde{\nu}$	$(o-c)^{(b,c)}$	$J^{(a)}$	$\tilde{\nu}$	$(o-c)^{(b,c)}$
	[cm^{-1}]	[10^{-2} cm^{-1}]		[cm^{-1}]	[10^{-2} cm^{-1}]
$\frac{3}{2}$	96.364	− 1	$\frac{55}{2}$	98.783	−10
$\frac{5}{2}$	96.385	5	$\frac{57}{2}$	98.961	− 7
$\frac{7}{2}$	96.406	4	$\frac{59}{2}$	99.141	− 8
$\frac{9}{2}$	96.435	4	$\frac{61}{2}$	99.322	−13
$\frac{11}{2}$	96.467	2	$\frac{63}{2}$	99.521	− 6
$\frac{13}{2}$	96.509	3	$\frac{65}{2}$	99.727	2
$\frac{15}{2}$	96.555	1	$\frac{67}{2}$	99.927	− 2
$\frac{17}{2}$	96.607	5	$\frac{69}{2}$	100.131$^{(d)}$	− 7
$\frac{19}{2}$	96.668	1	$\frac{71}{2}$	100.349	− 3
$\frac{21}{2}$	96.728	− 5	$\frac{73}{2}$	100.564	− 8
$\frac{23}{2}$	96.804	− 1	$\frac{75}{2}$	100.797	− 1
$\frac{25}{2}$	96.882	− 2	$\frac{77}{2}$	101.026	− 3
$\frac{27}{2}$	96.964	− 5	$\frac{79}{2}$	101.261	− 5
$\frac{29}{2}$	97.053	− 6	$\frac{81}{2}$	101.501	− 6
$\frac{31}{2}$	97.146	−10	$\frac{83}{2}$	101.764	9
$\frac{33}{2}$	97.253	− 7	$\frac{85}{2}$	102.024	17
$\frac{35}{2}$	97.361	− 8	$\frac{87}{2}$	102.271	6
$\frac{37}{2}$	97.473	−11	$\frac{89}{2}$	102.538	11
$\frac{39}{2}$	97.589	−17	$\frac{91}{2}$	102.797	2
$\frac{41}{2}$	97.726	− 7	$\frac{93}{2}$	103.097	29
$\frac{43}{2}$	97.868$^{(d)}$	1	$\frac{95}{2}$	103.377	30
$\frac{45}{2}$	97.994	−12	$\frac{97}{2}$	103.648	18
$\frac{47}{2}$	98.142	−10	$\frac{99}{2}$	103.934	16
$\frac{49}{2}$	98.282	−21	$\frac{101}{2}$	104.238	27
$\frac{51}{2}$	98.451	−10	$\frac{103}{2}$	104.531	22
$\frac{53}{2}$	98.611	−13	$\frac{105}{2}$	104.802$^{(d)}$	− 9

$^{(a)}$Calculated for $\Delta J = 0$.

$^{(b)}$Residuals of the fit.

$^{(c)}10^{-2}$ cm^{-1} uncertainty assigned to each combination difference.

$^{(d)}$Calculated from blended line(s) and given zero weight.

Table G.5: Diode laser observations of the $1_0^1\,^2\Pi$ band of NCO ($\tilde{X}^2\Pi$), included in the fit of the $1_0^1\,^2\Pi$ band.

Transition	$\tilde{\nu}_{\text{obs.}}$ [cm^{-1}]	$(o-c)^{(a,b)}$ [10^{-4} cm^{-1}]	$\tilde{\nu}_{\text{obs.}}$ [cm^{-1}]	$(o-c)^{(a,b)}$ [10^{-4} cm^{-1}]
	$^2\Pi_{\frac{1}{2}}$		$^2\Pi_{\frac{3}{2}}$	
R($\frac{45}{2}$)	—	—	1936.9351	−11
R($\frac{37}{2}$)	—	—	1934.4159	− 1
R($\frac{35}{2}$)	1935.2407	0	1933.7675	−18
R($\frac{33}{2}$)	1934.5899	52	1933.1145	−14
R($\frac{31}{2}$)	1933.9268	49	—	—
R($\frac{29}{2}$)	—	—	1931.7879	−13
R($\frac{27}{2}$)	1932.5757	− 1	—	—
R($\frac{25}{2}$)	1931.8956	31	—	—
R($\frac{23}{2}$)	—	—	1929.7476	−18
R($\frac{21}{2}$)	—	—	1929.0547	−14
R($\frac{19}{2}$)	1929.8003	−12	—	—
R($\frac{17}{2}$)	1929.0913	6	1927.6492	− 6
R($\frac{15}{2}$)	—	—	1926.9347	−20
R($\frac{13}{2}$)	1927.6499	10	1926.2161	− 9
R($\frac{11}{2}$)	1926.9152	−25	—	—
R($\frac{9}{2}$)	1926.1760	−37	1924.7567	−10
R($\frac{5}{2}$)	1924.6831	− 3	—	—
R($\frac{3}{2}$)	—	—	1922.5190	− 1

Table G.5 continued:

Transition	$\tilde{\nu}_{\text{obs.}}$ [cm^{-1}]	$(o-c)^{(a)}$ [$10^{-4}\,\text{cm}^{-1}$]	$\tilde{\nu}_{\text{obs.}}$ [cm^{-1}]	$(o-c)^{(a)}$ [$10^{-4}\,\text{cm}^{-1}$]
	$^2\Pi_{\frac{1}{2}}$		$^2\Pi_{\frac{3}{2}}$	
$P(\frac{9}{2})$	1918.4217	−43	—	—
$P(\frac{13}{2})$	—	—	1915.4458	−16
$P(\frac{15}{2})$	1915.9657	−20	1914.6308	20
$P(\frac{17}{2})$	1915.1341	− 6	1913.8033	− 2
$P(\frac{19}{2})$	1914.2913	−36	1912.9751	33
$P(\frac{21}{2})$	1913.4475	−10	—	—
$P(\frac{23}{2})$	1912.5947	− 6	—	—
$P(\frac{27}{2})$	—	—	1909.5765	−24
$P(\frac{29}{2})$	—	—	1908.7162	20
$P(\frac{31}{2})$	1909.1184	33	1907.8405	−26
$P(\frac{33}{2})$	1908.2329	46	1906.9634	−20
$P(\frac{35}{2})$	1907.3325	−22	—	—
$P(\frac{37}{2})$	1906.4338	− 6	—	—

[a] Residuals of the fit.

[b] $2 \times 10^{-3}\text{cm}^{-1}$ uncertainty assigned to each datum.

Table G.6: EPR observations[a] of $(020)\,^2\Delta_{\frac{5}{2}}$, $J = 5/2$ NCO ($\tilde{X}^2\Pi$), included in the fit of the $1_0^1 2_1^1\,^2\Delta$ band.

$M'_J \leftarrow M''_J$	M_I[b]	$B_{\text{obs.}}$ [T]	$\frac{\partial\nu}{\partial B}$[c] [MHzG^{-1}]	$(o-c)$[d,e] [kHz]
$\frac{5}{2} \leftarrow \frac{3}{2}$	1	1.10302	0.880	434
$\frac{5}{2} \leftarrow \frac{3}{2}$	0	1.10491	0.880	−139
$\frac{5}{2} \leftarrow \frac{3}{2}$	−1	1.10689	0.880	− 64
$\frac{3}{2} \leftarrow \frac{1}{2}$	1	1.13852	0.823	229
$\frac{3}{2} \leftarrow \frac{1}{2}$	0	1.14037	0.823	409
$\frac{3}{2} \leftarrow \frac{1}{2}$	−1	1.14236	0.823	− 11
$\frac{1}{2} \leftarrow -\frac{1}{2}$	1	1.17281	0.776	130
$\frac{1}{2} \leftarrow -\frac{1}{2}$	0	1.17475	0.776	− 49
$\frac{1}{2} \leftarrow -\frac{1}{2}$	−1	1.17666	0.776	−191
$-\frac{1}{2} \leftarrow -\frac{3}{2}$	1	1.20598	0.736	21
$-\frac{1}{2} \leftarrow -\frac{3}{2}$	0	1.20796	0.736	−125
$-\frac{1}{2} \leftarrow -\frac{3}{2}$	−1	1.20985	0.736	−445
$-\frac{3}{2} \leftarrow -\frac{5}{2}$	1	1.23809	0.701	43
$-\frac{3}{2} \leftarrow -\frac{5}{2}$	0	1.24011	0.701	− 85
$-\frac{3}{2} \leftarrow -\frac{5}{2}$	−1	1.24193	0.701	−202

[a] Observed at a frequency of 9270.00 MHz.

[b] $\Delta M_I = 0$.

[c] Tuning rate at resonance.

[d] Residuals of the fit.

[e] 300 kHz uncertainty assigned to each datum.

Table G.7: Microwave observations of $(010)\,^2\Delta$ of NCO ($\tilde{X}^2\Pi$), included in the fit of the $1_0^1 2_1^1\,^2\Delta$ band.

$J' \leftarrow J''$	$F' \leftarrow F''$	$\nu_{\text{obs.}}$ [MHz]	$(o-c)^{(a)}$ [kHz]
		$^2\Delta_{\frac{3}{2}}$	
$\frac{5}{2} \leftarrow \frac{3}{2}$	$\frac{7}{2} \leftarrow \frac{5}{2}$	58769.73(4)$^{(b)}$	35
$\frac{5}{2} \leftarrow \frac{3}{2}$	$\frac{5}{2} \leftarrow \frac{3}{2}$	58796.56(4)	− 6
$\frac{5}{2} \leftarrow \frac{3}{2}$	$\frac{3}{2} \leftarrow \frac{1}{2}$	58809.69(4)	− 10
$\frac{7}{2} \leftarrow \frac{5}{2}$	$\frac{9}{2} \leftarrow \frac{7}{2}$	82287.07(4)	125
$\frac{7}{2} \leftarrow \frac{5}{2}$	$\frac{7}{2} \leftarrow \frac{5}{2}$	82298.75(4)	186
$\frac{7}{2} \leftarrow \frac{5}{2}$	$\frac{5}{2} \leftarrow \frac{3}{2}$	82305.69(4)	143
$\frac{9}{2} \leftarrow \frac{7}{2}$	$\frac{11}{2} \leftarrow \frac{9}{2}$	105800.919(8)	− 1
$\frac{9}{2} \leftarrow \frac{7}{2}$	$\frac{9}{2} \leftarrow \frac{7}{2}$	105807.439(17)	− 7
$\frac{9}{2} \leftarrow \frac{7}{2}$	$\frac{7}{2} \leftarrow \frac{5}{2}$	105811.856(18)	− 2
$\frac{9}{2} \leftarrow \frac{7}{2}$	$\frac{9}{2} \leftarrow \frac{9}{2}$	105778.190(13)	0
$\frac{9}{2} \leftarrow \frac{7}{2}$	$\frac{7}{2} \leftarrow \frac{7}{2}$	105790.021(45)	30
$\frac{11}{2} \leftarrow \frac{9}{2}$	$\frac{13}{2} \leftarrow \frac{11}{2}$	129313.226(13)	17
$\frac{11}{2} \leftarrow \frac{9}{2}$	$\frac{11}{2} \leftarrow \frac{9}{2}$	129317.429(17)	13
$\frac{11}{2} \leftarrow \frac{9}{2}$	$\frac{9}{2} \leftarrow \frac{7}{2}$	129320.479(21)	− 3
$\frac{13}{2} \leftarrow \frac{11}{2}$	$\frac{15}{2} \leftarrow \frac{13}{2}$	152824.242(12)	− 13
$\frac{13}{2} \leftarrow \frac{11}{2}$	$\frac{13}{2} \leftarrow \frac{11}{2}$	152827.189(19)	− 21
$\frac{13}{2} \leftarrow \frac{11}{2}$	$\frac{11}{2} \leftarrow \frac{9}{2}$	152829.460(14)	− 20

Table G.7 continued:

$J' \leftarrow J''$	$F' \leftarrow F''$	$\nu_{\text{obs.}}$ [MHz]	$(o-c)^{(a)}$ [kHz]
		$^2\Delta_{\frac{5}{2}}$	
$\frac{7}{2} \leftarrow \frac{5}{2}$	$\frac{9}{2} \leftarrow \frac{7}{2}$	81613.04(4)	61
$\frac{7}{2} \leftarrow \frac{5}{2}$	$\frac{7}{2} \leftarrow \frac{5}{2}$	81627.30(4)	102
$\frac{7}{2} \leftarrow \frac{5}{2}$	$\frac{5}{2} \leftarrow \frac{3}{2}$	81636.35(4)	− 92
$\frac{9}{2} \leftarrow \frac{7}{2}$	$\frac{11}{2} \leftarrow \frac{9}{2}$	104935.676(7)	− 12
$\frac{9}{2} \leftarrow \frac{7}{2}$	$\frac{9}{2} \leftarrow \frac{7}{2}$	104943.579(4)	− 4
$\frac{9}{2} \leftarrow \frac{7}{2}$	$\frac{7}{2} \leftarrow \frac{5}{2}$	104949.187(8)	− 4
$\frac{9}{2} \leftarrow \frac{7}{2}$	$\frac{9}{2} \leftarrow \frac{9}{2}$	104905.591(13)	− 4
$\frac{9}{2} \leftarrow \frac{7}{2}$	$\frac{7}{2} \leftarrow \frac{7}{2}$	104919.354(24)	10
$\frac{11}{2} \leftarrow \frac{9}{2}$	$\frac{13}{2} \leftarrow \frac{11}{2}$	128256.625(9)	7
$\frac{11}{2} \leftarrow \frac{9}{2}$	$\frac{11}{2} \leftarrow \frac{9}{2}$	128261.637(21)	14
$\frac{11}{2} \leftarrow \frac{9}{2}$	$\frac{9}{2} \leftarrow \frac{7}{2}$	128265.417(16)	28
$\frac{13}{2} \leftarrow \frac{11}{2}$	$\frac{15}{2} \leftarrow \frac{13}{2}$	151576.463(20)	59
$\frac{13}{2} \leftarrow \frac{11}{2}$	$\frac{13}{2} \leftarrow \frac{11}{2}$	151579.858(40)	14
$\frac{13}{2} \leftarrow \frac{11}{2}$	$\frac{11}{2} \leftarrow \frac{9}{2}$	151582.556(23)	17

[a] Residuals of the fit.

[b] The numbers in parentheses are the uncertainties in of the last decimal place.

Table G.8: Combination differences giving the $(010)\,^2\Delta_{\frac{3}{2}} \leftarrow ^2\Delta_{\frac{5}{2}}$ interval in NCO ($\tilde{X}^2\Pi$) and included in the fit of the $1_0^1 2_1^1\,^2\Delta$ band. Calculated from the $\tilde{A} \leftarrow \tilde{X}$ transition.

$J^{(a)}$	Parity	$\tilde{\nu}$	$(o-c)^{(b,c)}$	Parity	$\tilde{\nu}$	$(o-c)^{(b,c)}$
		[cm^{-1}]	[10^{-2} cm^{-1}]		[cm^{-1}]	[10^{-2} cm^{-1}]
$\frac{7}{2}$		95.837$^{(d)}$	5			
$\frac{9}{2}$		95.826$^{(d)}$	1			
$\frac{11}{2}$		95.863$^{(d)}$	1			
$\frac{13}{2}$		95.898$^{(d)}$	1			
$\frac{15}{2}$		95.949$^{(d)}$	1			
$\frac{17}{2}$		95.988$^{(d)}$	0			
$\frac{19}{2}$		96.037$^{(d)}$	−2			
$\frac{21}{2}$		96.102$^{(d)}$	−2			
$\frac{23}{2}$	$-\leftarrow-$	96.227$^{(d)}$	3	$+\leftarrow+$	96.180$^{(d)}$	−1
$\frac{25}{2}$	$+\leftarrow+$	96.281	1	$-\leftarrow-$	96.256$^{(d)}$	−2
$\frac{27}{2}$	$-\leftarrow-$	96.361	0	$+\leftarrow+$	96.357	0
$\frac{29}{2}$	$+\leftarrow+$	96.422$^{(d)}$	−3	$-\leftarrow-$	96.477$^{(d)}$	3
$\frac{31}{2}$	$-\leftarrow-$	96.537$^{(d)}$	−1	$+\leftarrow+$	96.548	0
$\frac{33}{2}$	$+\leftarrow+$	96.666$^{(d)}$	1	$-\leftarrow-$	96.648	−1
$\frac{35}{2}$	$-\leftarrow-$	96.750$^{(d)}$	−2	$+\leftarrow+$	96.771	1
$\frac{37}{2}$	$+\leftarrow+$	96.885	0	$-\leftarrow-$	96.889	1
$\frac{39}{2}$	$-\leftarrow-$	97.012	1	$+\leftarrow+$	97.006	0
$\frac{41}{2}$	$+\leftarrow+$	97.142$^{(d)}$	1	$-\leftarrow-$	97.140	0
$\frac{43}{2}$	$-\leftarrow-$	97.263	−1	$+\leftarrow+$	97.282	1
$\frac{45}{2}$	$+\leftarrow+$	97.414	0	$-\leftarrow-$	97.380$^{(d)}$	−3
$\frac{47}{2}$	$-\leftarrow-$	97.553$^{(d)}$	−1	$+\leftarrow+$	97.555	−1

Table G.8 continued:

$J^{(a)}$	Parity	$\tilde{\nu}$ [cm^{-1}]	$(o-c)^{(b,c)}$ [10^{-2} cm^{-1}]	Parity	$\tilde{\nu}$ [cm^{-1}]	$(o-c)^{(b,c)}$ [10^{-2} cm^{-1}]
$\frac{49}{2}$	$+ \leftarrow +$	97.716	0	$- \leftarrow -$	97.713	0
$\frac{51}{2}$	$- \leftarrow -$	97.899	3	$+ \leftarrow +$	97.861	-1
$\frac{53}{2}$	$+ \leftarrow +$	98.056	2	$- \leftarrow -$	98.005[d]	-3
$\frac{55}{2}$	$- \leftarrow -$	98.199	-1	$+ \leftarrow +$	98.208	0
$\frac{57}{2}$	$+ \leftarrow +$	98.381	-1	$- \leftarrow -$	98.375	-1
$\frac{59}{2}$	$- \leftarrow -$	98.558	-1	$+ \leftarrow +$	98.551	-2
$\frac{61}{2}$	$+ \leftarrow +$	98.773	1	$- \leftarrow -$	98.739[d]	-2
$\frac{63}{2}$	$- \leftarrow -$	98.957	0	$+ \leftarrow +$	98.958	0

[a] Calculated for $\Delta J = 0$.

[b] Residuals of the fit.

[c] 10^{-2} cm^{-1} uncertainty assigned to each combination difference.

[d] Calculated from blended line(s) and given zero weight.

Table G.9: EPR observations[a] of $(020)\,^2\Phi_{\frac{7}{2}}$, $J = 7/2$ NCO ($\tilde{X}^2\Pi$), included in the fit of the $1_0^1 2_2^2\,^2\Phi$ band.

$M'_J \leftarrow M''_J$	M_I[b]	$B_{\text{obs.}}$ [T]	$\frac{\partial\nu}{\partial B}$[c] [MHzG^{-1}]	$(o-c)$[d,e] [MHz]
$\frac{7}{2} \leftarrow \frac{5}{2}$	1	1.4320	0.680	0.71
$\frac{7}{2} \leftarrow \frac{5}{2}$	0	1.4339	0.680	−0.07
$\frac{7}{2} \leftarrow \frac{5}{2}$	−1	1.4361	0.680	−1.45
$\frac{5}{2} \leftarrow \frac{3}{2}$	1	1.4614	0.651	1.35
$\frac{5}{2} \leftarrow \frac{3}{2}$	0	1.4633	0.651	0.87
$\frac{5}{2} \leftarrow \frac{3}{2}$	−1	1.4653	0.651	0.58
$\frac{3}{2} \leftarrow \frac{1}{2}$	1	1.4907	0.626	−1.37
$\frac{3}{2} \leftarrow \frac{1}{2}$	0	1.4925	0.626	0.97
$\frac{3}{2} \leftarrow \frac{1}{2}$	−1	1.4945	0.626	−1.48
$\frac{1}{2} \leftarrow -\frac{1}{2}$	1	1.5185	0.603	1.54
$\frac{1}{2} \leftarrow -\frac{1}{2}$	0	1.5206	0.603	0.34
$\frac{1}{2} \leftarrow -\frac{1}{2}$	−1	1.5227	0.603	−0.99
$-\frac{1}{2} \leftarrow -\frac{3}{2}$	1	1.5464	0.582	0.35
$-\frac{1}{2} \leftarrow -\frac{3}{2}$	0	1.5484	0.582	−0.01
$-\frac{1}{2} \leftarrow -\frac{3}{2}$	−1	1.5504	0.582	−0.92
$-\frac{3}{2} \leftarrow -\frac{5}{2}$	1	1.5736	0.563	0.16
$-\frac{3}{2} \leftarrow -\frac{5}{2}$	0	1.5756	0.563	0.01
$-\frac{3}{2} \leftarrow -\frac{5}{2}$	−1	1.5774	0.563	0.05
$-\frac{5}{2} \leftarrow -\frac{7}{2}$	1	1.6002	0.546	0.47
$-\frac{5}{2} \leftarrow -\frac{7}{2}$	0	1.6022	0.546	0.52
$-\frac{5}{2} \leftarrow -\frac{7}{2}$	−1	1.6040	0.546	0.37

[a] Observed at a frequency of 9270.00 MHz.

[b] $\Delta M_I = 0$.

[c] Tuning rate at resonance.

[d] Residuals of the fit.

[e] 300 kHz uncertainty assigned to each datum.

Table G.10: Microwave observations of (020) $^2\Phi$ of NCO ($\tilde{X}^2\Pi$), included in the fit of the $1_0^1 2_2^2\,{}^2\Phi$ band.

$J' \leftarrow J''$	$F' \leftarrow F''$	$\nu_{\text{obs.}}$ [MHz]	$(o-c)^{(a)}$ [kHz]
		$^2\Phi_{\frac{5}{2}}$	
$\frac{11}{2} \leftarrow \frac{9}{2}$	$\frac{13}{2} \leftarrow \frac{11}{2}$	129671.707(11)$^{(b)}$	23
$\frac{11}{2} \leftarrow \frac{9}{2}$	$\frac{11}{2} \leftarrow \frac{9}{2}$	129678.364(31)	72
$\frac{11}{2} \leftarrow \frac{9}{2}$	$\frac{9}{2} \leftarrow \frac{7}{2}$	129683.293(46)	42
$\frac{13}{2} \leftarrow \frac{11}{2}$	$\frac{15}{2} \leftarrow \frac{13}{2}$	153248.597(14)	−25
$\frac{13}{2} \leftarrow \frac{11}{2}$	$\frac{13}{2} \leftarrow \frac{11}{2}$	153253.235(23)	−15
$\frac{13}{2} \leftarrow \frac{11}{2}$	$\frac{11}{2} \leftarrow \frac{9}{2}$	153256.887(17)	2
$\frac{15}{2} \leftarrow \frac{13}{2}$	$\frac{17}{2} \leftarrow \frac{15}{2}$	176824.175(29)	−61
$\frac{15}{2} \leftarrow \frac{13}{2}$	$\frac{15}{2} \leftarrow \frac{13}{2}$	176827.666(36)	− 5
$\frac{15}{2} \leftarrow \frac{13}{2}$	$\frac{13}{2} \leftarrow \frac{11}{2}$	176830.451(57)	−12
		$^2\Phi_{\frac{7}{2}}$	
$\frac{11}{2} \leftarrow \frac{9}{2}$	$\frac{13}{2} \leftarrow \frac{11}{2}$	128591.990(15)	− 3
$\frac{11}{2} \leftarrow \frac{9}{2}$	$\frac{11}{2} \leftarrow \frac{9}{2}$	128598.790(13)	−15
$\frac{11}{2} \leftarrow \frac{9}{2}$	$\frac{9}{2} \leftarrow \frac{7}{2}$	128604.132(23)	−37
$\frac{13}{2} \leftarrow \frac{11}{2}$	$\frac{15}{2} \leftarrow \frac{13}{2}$	151973.325(15)	− 2
$\frac{13}{2} \leftarrow \frac{11}{2}$	$\frac{13}{2} \leftarrow \frac{11}{2}$	151978.037(19)	5
$\frac{13}{2} \leftarrow \frac{11}{2}$	$\frac{11}{2} \leftarrow \frac{9}{2}$	151981.850(17)	−14
$\frac{15}{2} \leftarrow \frac{13}{2}$	$\frac{17}{2} \leftarrow \frac{15}{2}$	175353.657(29)	66
$\frac{15}{2} \leftarrow \frac{13}{2}$	$\frac{15}{2} \leftarrow \frac{13}{2}$	175357.100(36)	76
$\frac{15}{2} \leftarrow \frac{13}{2}$	$\frac{13}{2} \leftarrow \frac{11}{2}$	175359.974(57)	84

$^{(a)}$Residuals of the fit.

$^{(b)}$The numbers in parentheses are the uncertainties in of the last decimal place.

Table G.11: Microwave observations of (010) $\mu, \kappa\,^2\Sigma$ in NCO ($\tilde{X}\,^2\Pi$), included in the fit of the $1_0^1 2_1^1\,^2\Sigma$ bands.

$N'_{F'_i} \leftarrow N''_{F''_i}$	$F' \leftarrow F''$	$\nu\,\mu^2\Sigma$ [MHz]	$(o-c)^{(a)}$ [kHz]	$\nu\,\kappa^2\Sigma$ [MHz]	$(o-c)$ [kHz]
$2_1 \leftarrow 1_1$	$\frac{7}{2} \leftarrow \frac{5}{2}$	48558.774$^{(b)}$	29	48551.193	− 61
$2_1 \leftarrow 1_1$	$\frac{5}{2} \leftarrow \frac{3}{2}$	48563.596	17	48547.340	128
$2_1 \leftarrow 1_1$	$\frac{3}{2} \leftarrow \frac{1}{2}$	48564.346	53	48544.258	141
$2_2 \leftarrow 1_2$	$\frac{5}{2} \leftarrow \frac{3}{2}$	45113.964	82	45078.763	−174
$2_2 \leftarrow 1_2$	$\frac{3}{2} \leftarrow \frac{1}{2}$	45121.682	− 32	45042.063	−127
$3_1 \leftarrow 2_1$	$\frac{9}{2} \leftarrow \frac{7}{2}$	71978.924	52	71955.863	− 64
$3_1 \leftarrow 2_1$	$\frac{7}{2} \leftarrow \frac{5}{2}$	71980.950	17	71954.172	− 33
$3_1 \leftarrow 2_1$	$\frac{5}{2} \leftarrow \frac{3}{2}$	71981.343	36	71952.470	− 13
$3_2 \leftarrow 2_2$	$\frac{7}{2} \leftarrow \frac{5}{2}$	68535.400	80	68481.454	− 61
$3_2 \leftarrow 2_2$	$\frac{5}{2} \leftarrow \frac{3}{2}$	68536.953	86	68474.158	− 4
$3_2 \leftarrow 2_2$	$\frac{3}{2} \leftarrow \frac{1}{2}$	68539.019	78	68472.443	− 17
$3_2 \leftarrow 2_2$	$\frac{5}{2} \leftarrow \frac{5}{2}$	68544.734$^{(c)}$	93	—	
$3_2 \leftarrow 2_2$	$\frac{3}{2} \leftarrow \frac{3}{2}$	68544.734$^{(c)}$	−110	—	
$4_1 \leftarrow 3_1$	$\frac{11}{2} \leftarrow \frac{9}{2}$	95398.780	53	95361.214	− 65
$4_1 \leftarrow 3_1$	$\frac{9}{2} \leftarrow \frac{7}{2}$	95399.997$^{(c)}$	133	95360.242	− 89
$4_1 \leftarrow 3_1$	$\frac{7}{2} \leftarrow \frac{5}{2}$	95399.997$^{(c)}$	− 96	95359.186	− 54
$4_2 \leftarrow 3_2$	$\frac{9}{2} \leftarrow \frac{7}{2}$	91954.386	54	91885.061	− 19
$4_2 \leftarrow 3_2$	$\frac{7}{2} \leftarrow \frac{5}{2}$	91955.116	132	91881.934	− 4
$4_2 \leftarrow 3_2$	$\frac{5}{2} \leftarrow \frac{3}{2}$	91956.205	79	91881.027	31
$4_2 \leftarrow 3_2$	$\frac{7}{2} \leftarrow \frac{7}{2}$	91964.126$^{(c)}$	−180	—	
$4_2 \leftarrow 3_2$	$\frac{5}{2} \leftarrow \frac{5}{2}$	91964.126$^{(c)}$	22	—	

Table G.11 continued...

$N'_{F'_i} \leftarrow N''_{F''_i}$	$F' \leftarrow F''$	$\nu\,\mu^2\Sigma$ [MHz]	$(o-c)^{(a)}$ [kHz]	$\nu\,\kappa^2\Sigma$ [MHz]	$(o-c)$ [kHz]
$5_1 \leftarrow 4_1$	$\frac{13}{2} \leftarrow \frac{11}{2}$	118818.301	6	118766.663	− 70
$5_1 \leftarrow 4_1$	$\frac{11}{2} \leftarrow \frac{9}{2}$	118819.111$^{(c)}$	98	118766.062	− 75
$5_1 \leftarrow 4_1$	$\frac{9}{2} \leftarrow \frac{7}{2}$	118819.111$^{(c)}$	− 54	118765.331	− 56
$5_2 \leftarrow 4_2$	$\frac{11}{2} \leftarrow \frac{9}{2}$	115372.196	44	115288.374	− 26
$5_2 \leftarrow 4_2$	$\frac{9}{2} \leftarrow \frac{7}{2}$	115372.573	67	115286.672	10
$5_2 \leftarrow 4_2$	$\frac{7}{2} \leftarrow \frac{5}{2}$	115373.267	42	115286.045	− 23
$6_1 \leftarrow 5_1$	$\frac{15}{2} \leftarrow \frac{13}{2}$	142237.441	− 57	142171.941	− 84
$6_1 \leftarrow 5_1$	$\frac{13}{2} \leftarrow \frac{11}{2}$	142238.025$^{(c)}$	34	142171.610	− 8
$6_1 \leftarrow 5_1$	$\frac{11}{2} \leftarrow \frac{9}{2}$	142238.025$^{(c)}$	− 72	142170.981	− 92
$6_2 \leftarrow 5_2$	$\frac{13}{2} \leftarrow \frac{11}{2}$	138789.047$^{(c)}$	72	138691.146	35
$6_2 \leftarrow 5_2$	$\frac{11}{2} \leftarrow \frac{9}{2}$	138789.047$^{(c)}$	−146	138689.858$^{(c)}$	−153
$6_2 \leftarrow 5_2$	$\frac{7}{2} \leftarrow \frac{7}{2}$	138789.799	115	138689.858	254$^{(c)}$
$7_1 \leftarrow 6_1$	$\frac{17}{2} \leftarrow \frac{15}{2}$	165656.467$^{(c)}$	231	165576.754	−229
$7_1 \leftarrow 6_1$	$\frac{15}{2} \leftarrow \frac{13}{2}$	165656.467$^{(c)}$	−126	165576.754	64
$7_1 \leftarrow 6_1$	$\frac{13}{2} \leftarrow \frac{11}{2}$	165656.467$^{(c)}$	−126	165576.754	476
$7_2 \leftarrow 6_2$	$\frac{15}{2} \leftarrow \frac{13}{2}$	162204.884$^{(c)}$	94	162093.149	133
$7_2 \leftarrow 6_2$	$\frac{13}{2} \leftarrow \frac{11}{2}$	162204.884$^{(c)}$	− 51	162092.102$^{(c)}$	−158
$7_2 \leftarrow 6_2$	$\frac{11}{2} \leftarrow \frac{9}{2}$	162204.884$^{(c)}$	−406	162092.102$^{(c)}$	136

$^{(a)}$Residuals of the fit.

$^{(b)}$Each datum assigned an uncertainty of 40 kHZ.

$^{(c)}$Partially resolved components are assigned the same transition frequency.

Table G.12: Optical combination differences calculated from the $01^10\,^2\Pi \leftarrow 01^00\,\mu^2\Sigma^{(+)}$ and $01^10\,^2\Pi \leftarrow 01^00\,\kappa^2\Sigma^{(-)}$ bands of NCO $\tilde{A} \leftarrow \tilde{X}$, included in the fit of the $1^1_0 2^1_1\,^2\Sigma$ bands. The interval calculated is $(010)\,\kappa^2\Sigma^{(-)}\,(N', F_i) - (010)\,\mu^2\Sigma^{(+)}\,(N'', F_i)$

$\kappa\, N'_{F_{i'}} \leftarrow \mu\, N''_{F_{i''}}$	$\tilde{\nu}$ [cm^{-1}]	$(o-c)^{(a)}$ [10^{-3}cm^{-1}]	$\tilde{\nu}$ [cm^{-1}]	$(o-c)^{(a)}$ [10^{-3}cm^{-1}]
	$\mu R_1(N) - \kappa Q_1(N+1)$		$\mu Q_1(N) - \kappa P_1(N+1)$	
$23_1 \leftarrow 22_1$	—		198.800[b]	−34
$24_1 \leftarrow 23_1$	199.607[c]	3	199.598	− 6
$25_1 \leftarrow 24_1$	—		200.375[c]	1
$26_1 \leftarrow 25_1$	201.181[c]	38	201.117[c]	−26
$27_1 \leftarrow 26_1$	—		201.901	−11
$28_1 \leftarrow 27_1$	202.647	−34	202.707	26
$29_1 \leftarrow 28_1$	203.458	9	203.470[c]	21
$30_1 \leftarrow 29_1$	204.287[c]	70	204.236[c]	19
$31_1 \leftarrow 30_1$	205.054[c]	70		
$32_1 \leftarrow 31_1$	205.829[c]	78		
$33_1 \leftarrow 32_1$	206.572[c]	55		
$34_1 \leftarrow 33_1$	207.324[c]	41		
$35_1 \leftarrow 34_1$	208.123[c]	75		
$36_1 \leftarrow 35_1$	208.778[c]	−35		
$37_1 \leftarrow 36_1$	209.597	19		
$38_1 \leftarrow 37_1$	210.360	18		
$39_1 \leftarrow 38_1$	211.158	52		
$40_1 \leftarrow 39_1$	211.919	50		
$41_1 \leftarrow 40_1$	212.686	54		
$42_1 \leftarrow 41_1$	213.396[c]	2		
$43_1 \leftarrow 42_1$	214.175[c]	18		

[a] Residuals of the fit.

[b] Each datum assigned an uncertainty of 10^{-2} cm^{-1}.

[c] Calculated from blended line(s) and given zero weight.

Table G.13: Optical combination differences calculated from the $01^10\,^2\Pi \leftarrow 01^00\,\mu^2\Sigma^{(+)}$ and $01^10\,^2\Pi \leftarrow 01^00\,\kappa^2\Sigma^{(-)}$ bands of NCO $\tilde{A} \leftarrow \tilde{X}$, included in the fit of the $1^1_02^1_1\,^2\Sigma$ bands. The interval calculated is $(010)\,\kappa^2\Sigma^{(-)}\,(N', F_i) - (010)\,\mu^2\Sigma^{(+)}\,(N'', F_i)$

$\kappa\, N'_{F_{i'}} \leftarrow \mu\, N''_{F_{i''}}$	$\tilde{\nu}$ [cm^{-1}]	$(o-c)^{(a,b)}$ [10^{-2}cm^{-1}]	$\kappa\, N'_{F_{i'}} \leftarrow \mu\, N''_{F_{i''}}$	$\tilde{\nu}$ [cm^{-1}]	$(o-c)^{(a,b)}$ [10^{-2}cm^{-1}]
$\mu Q_1(N) - \kappa R_1(N-1)$ and $\mu P_1(N) - \kappa Q_1(N-1)$					
$9_1 \leftarrow 10_1$	173.034[c]	− 7	$22_1 \leftarrow 23_1$	162.806	1
$10_1 \leftarrow 11_1$	172.227[d]	−29	$23_1 \leftarrow 24_1$	162.005	−10
$11_1 \leftarrow 12_1$	171.428[c]	−42	$24_1 \leftarrow 25_1$	161.257[c]	32
$12_1 \leftarrow 13_1$	—		$25_1 \leftarrow 26_1$	160.449[c]	15
$13_1 \leftarrow 14_1$	169.904	6	$26_1 \leftarrow 27_1$	159.656[c]	13
$14_1 \leftarrow 15_1$	169.124	12	$26_1 \leftarrow 27_1$	159.551[c]	−92
$15_1 \leftarrow 16_1$	168.291	−33	$27_1 \leftarrow 28_1$	158.871[c]	19
$16_1 \leftarrow 17_1$	167.521	−16	$28_1 \leftarrow 29_1$	158.046	−15
$17_1 \leftarrow 18_1$	166.725	−24	$29_1 \leftarrow 30_1$	157.278	9
$18_1 \leftarrow 19_1$	165.955	− 6	$30_1 \leftarrow 31_1$	156.530[c]	53
$19_1 \leftarrow 20_1$	165.137	−35	$30_1 \leftarrow 31_1$	156.477	0
$20_1 \leftarrow 21_1$	164.401[c]	17	$31_1 \leftarrow 32_1$	155.686	1
$21_1 \leftarrow 22_1$	163.571	−23	$31_1 \leftarrow 32_1$	155.754[c]	69

[a] Residuals of the fit.

[b] Where the same combination difference has been calculated from un-blended lines in both bands, the average was taken; otherwise both combination differences were included separately.

[c] Calculated from blended line(s) and given zero weight.

[d] Each datum assigned an uncertainty of $10^{-2}\,\mathrm{cm}^{-1}$.

Table G.14: Optical combination differences calculated from the $01^10\,^2\Pi \leftarrow 01^00\,\mu^2\Sigma^{(+)}$ and $01^10\,^2\Pi \leftarrow 01^00\,\kappa^2\Sigma^{(-)}$ bands of NCO $\tilde{A} \leftarrow \tilde{X}$, included in the fit of the $1^1_02^1_1\,^2\Sigma$ bands. The interval calculated is $(010)\,\kappa^2\Sigma^{(-)}\,(N', F_i) - (010)\,\mu^2\Sigma^{(+)}\,(N'', F_i)$

$\kappa\,N'_{F_{i'}} \leftarrow \mu\,N''_{F_{i''}}$	$\tilde{\nu}$ [cm^{-1}]	$(o-c)^{(a)}$ [10^{-2}cm^{-1}]	$\kappa\,N'_{F_{i'}} \leftarrow \mu\,N''_{F_{i''}}$	$\tilde{\nu}$ [cm^{-1}]	$(o-c)^{(a)}$ [10^{-2}cm^{-1}]
		$\mu\mathrm{R}_2(\mathrm{N}) - \kappa\mathrm{Q}_2(\mathrm{N}+1)$			
$18_2 \leftarrow 17_2$	194.868$^{(b)}$	31	$30_2 \leftarrow 29_2$	204.066$^{(c)}$	5
$19_2 \leftarrow 18_2$	195.550$^{(b)}$	−58	$31_2 \leftarrow 30_2$	—	
$20_2 \leftarrow 19_2$	196.423$^{(b)}$	44	$32_2 \leftarrow 31_2$	205.538$^{(b)}$	− 53
$21_2 \leftarrow 20_2$	197.182$^{(b)}$	32	$33_2 \leftarrow 32_2$	206.317$^{(b)}$	− 39
$22_2 \leftarrow 21_2$	197.974$^{(b)}$	55	$34_2 \leftarrow 33_2$	207.213$^{(b)}$	93
$23_2 \leftarrow 22_2$	198.669$^{(b)}$	−20	$35_2 \leftarrow 34_2$	207.895$^{(b)}$	12
$24_2 \leftarrow 23_2$	199.402$^{(b)}$	−56	$36_2 \leftarrow 35_2$	208.729	82
$25_2 \leftarrow 24_2$	200.185$^{(b)}$	−41	$37_2 \leftarrow 36_2$	—	
$26_2 \leftarrow 25_2$	200.967$^{(b)}$	−27	$38_2 \leftarrow 37_2$	210.161$^{(b)}$	− 11
$27_2 \leftarrow 26_2$	201.752$^{(b)}$	− 9	$39_2 \leftarrow 38_2$	211.044$^{(b)}$	111
$28_2 \leftarrow 27_2$	202.502$^{(b)}$	−26	$40_2 \leftarrow 39_2$	211.784$^{(b)}$	89
$29_2 \leftarrow 28_2$	203.254$^{(b)}$	−41			

$^{(a)}$Residuals of the fit.

$^{(b)}$Calculated from blended line(s) and given zero weight.

$^{(c)}$Each datum assigned an uncertainty of $10^{-2}\,\mathrm{cm}^{-1}$.

Table G.15: Optical combination differences calculated from the $01^10\,^2\Pi \leftarrow 01^00\,\mu^2\Sigma^{(+)}$ and $01^10\,^2\Pi \leftarrow 01^00\,\kappa^2\Sigma^{(-)}$ bands of NCO $\tilde{A} \leftarrow \tilde{X}$, included in the fit of the $1^1_0 2^1_1\,^2\Sigma$ bands. The interval calculated is $(010)\,\kappa^2\Sigma^{(-)}\,(N', F_i) - (010)\,\mu^2\Sigma^{(+)}\,(N'', F_i)$.

$\kappa\, N'_{F_{i'}} \leftarrow \mu\, N''_{F_{i''}}$	$\tilde{\nu}$ [cm^{-1}]	$(o-c)^{(a)}$ [10^{-2}cm^{-1}]	$\kappa\, N'_{F_{i'}} \leftarrow \mu\, N''_{F_{i''}}$	$\tilde{\nu}$ [cm^{-1}]	$(o-c)^{(a)}$ [10^{-2}cm^{-1}]
		$\mu Q_2(N) - \kappa R_2(N-1)$			
$6_2 \leftarrow 7_2$	175.495$^{(b)}$	− 7	$18_2 \leftarrow 19_2$	166.050	− 8
$7_2 \leftarrow 8_2$	—		$19_2 \leftarrow 20_2$	165.263$^{(b)}$	− 6
$8_2 \leftarrow 9_2$	173.909$^{(c)}$	−23	$20_2 \leftarrow 21_2$	164.494$^{(c)}$	15
$9_2 \leftarrow 10_2$	173.133	−13	$21_2 \leftarrow 22_2$	—	
$10_2 \leftarrow 11_2$	172.345$^{(c)}$	−15	$22_2 \leftarrow 23_2$	162.965$^{(c)}$	66
$11_2 \leftarrow 12_2$	171.557	−17	$23_2 \leftarrow 24_2$	162.139$^{(c)}$	31
$12_2 \leftarrow 13_2$	170.800	13	$24_2 \leftarrow 25_2$	161.297$^{(c)}$	−20
$13_2 \leftarrow 14_2$	169.997	− 3	$25_2 \leftarrow 26_2$	160.468$^{(c)}$	−58
$14_2 \leftarrow 15_2$	169.258$^{(c)}$	46	$26_2 \leftarrow 27_2$	159.762$^{(c)}$	28
$15_2 \leftarrow 16_2$	168.419	− 5	$27_2 \leftarrow 28_2$	158.929$^{(c)}$	−14
$16_2 \leftarrow 17_2$	167.613	−23	$28_2 \leftarrow 29_2$	158.216$^{(c)}$	65
$17_2 \leftarrow 18_2$	166.853$^{(c)}$	6	$29_2 \leftarrow 30_2$	157.353	− 5

$^{(a)}$Residuals of the fit.

$^{(b)}$Each datum assigned an uncertainty of 10^{-2} cm^{-1}.

$^{(c)}$Calculated from blended line(s) and given zero weight.